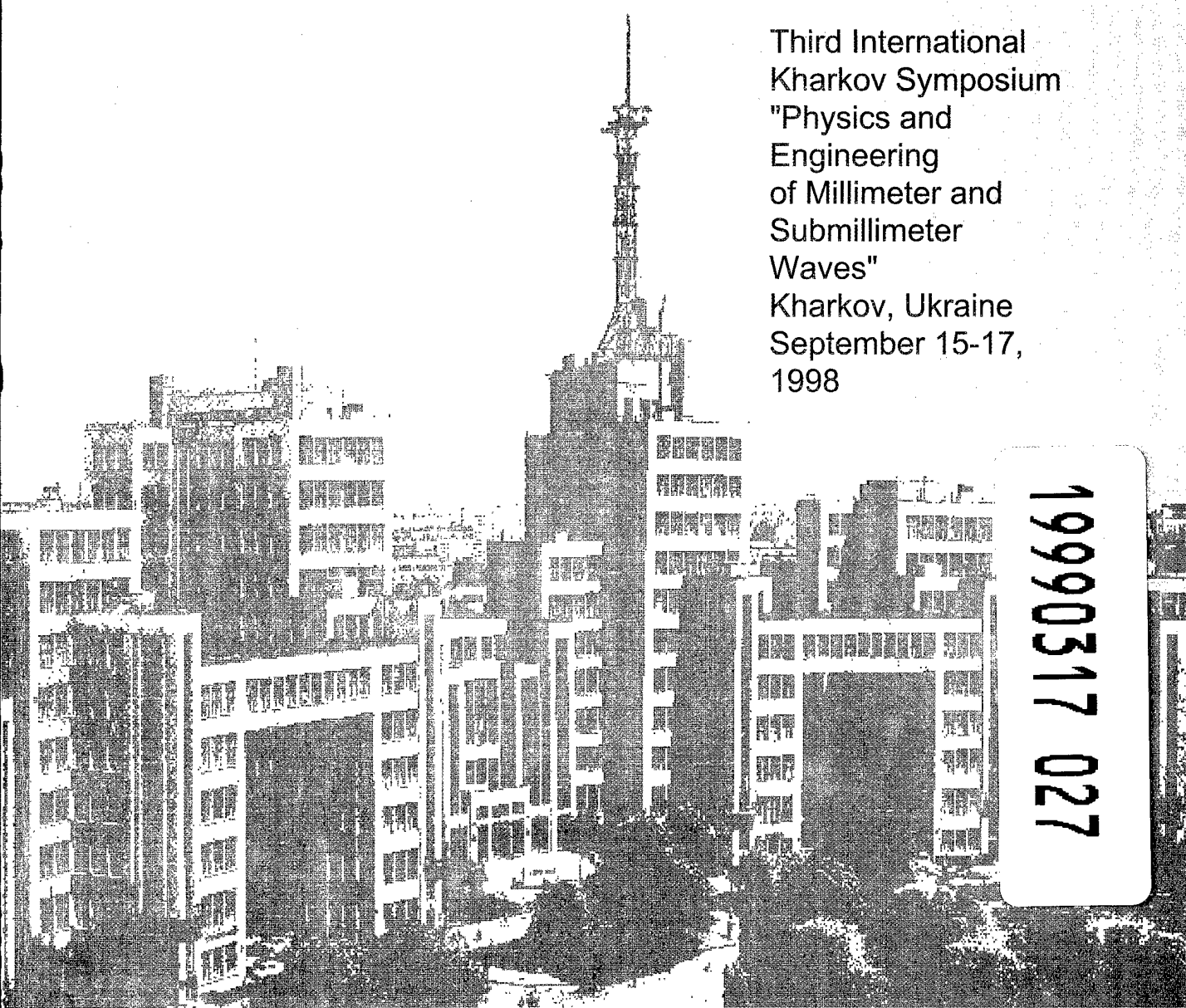


MSMW'98

SYMPOSIUM PROCEEDINGS

Third International
Kharkov Symposium
"Physics and
Engineering
of Millimeter and
Submillimeter
Waves"
Kharkov, Ukraine
September 15-17,
1998

19990317 027



DISTRIBUTION STATEMENT AS

Approved for Public Release
Distribution Unlimited



QUALITY INSPECTED

AQ F99-06-1176

**THIRD INTERNATIONAL KHARKOV SYMPOSIUM
"PHYSICS AND ENGINEERING
OF MILLIMETER AND SUBMILLIMETER WAVES"**



MSMW'98
Symposium Proceedings

Volume 1

**Kharkov, Ukraine
September 15-17, 1998**

DISTRIBUTION STATEMENT A
Approved for Public Release
Distribution Unlimited

**THIRD INTERNATIONAL KHARKOV SYMPOSIUM
"PHYSICS AND ENGINEERING
OF MILLIMETER AND SUBMILLIMETER WAVES"**

Organized by

**Usikov Institute for Radiophysics and Electronics,
National Academy of Sciences of Ukraine**

**Institute of Radio Astronomy,
National Academy of Sciences of Ukraine**

**Kharkov State University,
Ministry of Education of Ukraine**

IEEE AP/ED/MTT/AES Societies Joint Chapters of Ukraine

Ukrainian URSI Committee

Sponsored/Technically Sponsored by

URSI - International Union of Radio Science

IEEE ED/MTT Societies

US Army European Research Office

UNTC - Science and Technology Center in Ukraine

Proceedings of Third International Kharkov Symposium "Physics and Engineering of Millimeter and Submillimeter Waves" (September 15-17, 1998)

IEEE Catalog Number: 98EX119
ISBN: 0-7803-4389-1

Microfiche Edition

Copyright and Reprint Permission: Abstracting is permitted with credit to the source. Libraries are permitted to photocopy beyond the limit of U.S. copyright law for private use of patrons those articles in this volume that carry a code at the bottom of the first page, provided the per-copy fee indicated in the code is paid through Copyright Clearance Center, 222 Rosewood Drive, Danvers, MA 01923. For other copying, reprint or republication permission, write to IEEE Copyrights Manager, IEEE Service Center, 445 Hoes Lane, P.O. Box 1331, Piscataway, NJ 08855-1331. All rights reserved. Copyright @ 1998 by the Institute of Electrical and Electronics Engineers, Inc.

Prepared directly from the authors' camera-ready copies.
Design by a computer group of Usikov Institute for Radiophysics and Electronics,
National Academy of Sciences of Ukraine.
c/o IRE NASU, 12 Ac. Proskura St., Kharkov, 310085, Ukraine
Phone/ Fax: +380 (572) 441105 E-mail: <symposium@ire.kharkov.ua>

Printed by Business Inform Co.
Office 319, 28, Marshal Bazhanov St., Kharkov, 310002, Ukraine
Phone/ Fax: +380 (572) 142755

MSMW'98 Organizing Committee

Chairman

Prof. V.M. Yakovenko (Ukraine)

Co-Chairmen

Prof. L.N. Litvinenko (Ukraine)

Prof. V.A. Svich (Ukraine)

Co-Organizers

Dr. A.A. Kostenko (Ukraine)

Prof. A.I. Nosich (Ukraine)

Members

Prof. V.P. Churilov (Ukraine)

Prof. B.I. Makarenko (Ukraine)

Dr. P.N. Melezhik (Ukraine)

Dr. V.F. Mescheryakov (Ukraine)

Dr. V.G. Pavlovsky (Ukraine)

Dr. I.E. Pochanina (Ukraine)

Mr. A.D. Ustimenko (Ukraine)

Prof. I.I. Zalubovsky (Ukraine)

MSMW'98 International Program Committee

Dr. V.M. Chmil (Ukraine)

Prof. S.F. Dyubko (Ukraine)

Dr. O.P. Fedorov (Ukraine)

Dr. L.I. Fedoseev (Russia)

OC Special Representative in Nizny Novgorod

Prof. Dr. H.C.C. Fernandes (Brazil)

Prof. L.G. Gassanov (Ukraine)

Dr. H.F. Harmuth (USA)

Dr. M. Henini (UK)

Prof. Dr.-Ing. R.H. Jansen (Germany)

Prof. A.A. Kirilenko (Ukraine)

Prof. Dr. P. Kordos (Germany)

Prof. V.F. Kravchenko (Russia)

Dr. M.J. Lancaster (UK)

Prof. V.V. Meriakri (Russia)

OC Special Representative in Moscow

Prof. Koji Mizuno (Japan)

Prof. N.G. Nakhodkin (Ukraine)

Prof. A.P. Naumov (Russia)

Prof. G. Nusinovich (USA)

Prof. Yu.K. Požela (Lithuania)

Prof. A. Räisänen (Finland)

Prof. V.B. Razskazovsky (Ukraine)

Prof. B.A. Rozanov (Russia)

Prof. Dr.-Ing. K.Schünemann (Germany)

Prof. V.P. Shestopalov (Ukraine)

Prof. Ya.S. Shifrin (Ukraine)

Prof. V.M. Shulga (Ukraine)

Dr. K.S. Sunduchkov (Ukraine)

Prof. M. Thumm (Germany)

Prof. O.A. Tretyakov (Ukraine)

Prof. D.M. Vavriv (Ukraine)

Prof. O.G. Vendik (Russia)

Prof. A.A. Verity (Ukraine)

Prof. Kiyotoshi Yasumoto (Japan)

Table of MSMW'98 Geography

<i>Country</i>	<i>Papers</i>
<i>Kharkov</i>	134
<i>Russia</i>	46
<i>Ukraine non-Kharkov</i>	22
<i>Germany</i>	7
<i>Ukraine + Russia</i>	7
<i>Brazil</i>	4
<i>Russia + Belarus</i>	3
<i>Ukraine + Turkey</i>	3
<i>Japan</i>	2
<i>Russia + Germany</i>	2
<i>UK</i>	2
<i>Ukraine + Mexico</i>	2
<i>Belarus</i>	1
<i>China</i>	1
<i>Finland</i>	1
<i>Germany + Switzerland</i>	1
<i>India</i>	1
<i>Italy</i>	1
<i>Switzerland</i>	1
<i>Ukraine + Finland</i>	1
<i>Ukraine + Germany</i>	1
<i>Ukraine + Italy</i>	1
<i>Ukraine + Russia + Mexiko</i>	1
<i>Ukraine + Sweden</i>	1
<i>USA</i>	1
Total	247

*Ladies and gentlemen,
Dear colleagues and friends,*

I am proud to be able to welcome the MSMW'98 participants in Kharkov.

First and foremost, I should say that we highly appreciate your interest in the 3-rd International Kharkov Symposium "Physics and Engineering of Millimeter and Submillimeter Waves". We are confident that your contributions will certainly be helpful in making this meeting a real success. Your presence here will add significantly to the prestige of the MSMW'98.

MSMW symposia have been held in Kharkov since 1978 as a regular Soviet Union meeting on MM and SubMM waves and used to provide an extremely wide exchange of information, ideas, approaches, technological concepts and applications in this particular field of radiophysics and electronics.

Following the break-up of the Soviet Union a decision was made to maintain that tradition by periodically convening MSMW symposia. As a matter of fact, in 1991 the research community put forward a suggestion that it should be called as the International Kharkov Symposium "Physics and Engineering of Millimeter and Submillimeter Waves". It is owing to this decision that Kharkov had received a fairly wide recognition as one of the leading centers of fundamental and applied research on radiophysics and electronics, particularly, in the development of MM and SubMM waves.

Over a long span time the basic research of the Ukrainian radiophysicists had been carried out for the benefit of the military-industrial complex which was hugely financed by the Soviet government. As a result, we developed a great scientific potential with the aid of highly experts, engineers and technicians who were able to deal with many sophisticated problems.

Unfortunately, nowadays the close ties that had been earlier maintained broke down, and researchers found themselves isolated. Therefore, it became extremely imperative to preserve those groups of researchers who are still capable of pursuing investigations.

We are very hopeful that the present MSMW'98 Symposium will contribute towards integrating the experts in radiophysics and electronics into the world-wide research community. It will offer an ample opportunity to find new ways of resolving numerous issues.

At the same time we would be pleased to see the new ideas, all kinds of innovations and problems implemented on a large scale. We believe that in this context the borders separating our nations should never stand in the way of achieving whatever results by joint effort.

Let me express my gratitude to all those prestigious international institutions: URSI (International Union of Radio Science), IEEE (Institute of Electrical and Electronics Engineers) ED/MTT Societies, US Army European Research Office, UNTC (Science and Technology Center in Ukraine), which committed themselves to provide their share of financial support. We are grateful to all authors who have submitted their papers to MSMW'98. It was a pleasure to work with the members of Organizing and Program Committees.

We will do our best to make you feel satisfied and impressed so that you could remember it for a long time and have a strong desire to come back to the future MSMW in the next millennium.

Thank you very much for your participation.

Yours sincerely,



*Prof. Vladimir M.Yakovenko
MSMW'98 Chairman*

Contents

Volume 1

INV. INVITED PAPERS

<p>INV.1. A Review of the Principles of Holographic Power Combining at Millimeter and Submillimeter-Wave Frequencies <i>H.-G.Unger, M.Shahabadi, and K.Schünemann</i>.....</p> <p>INV.2. InP Transferred Electron Devices for Power Generation at Frequencies above 130GHz <i>R.Judaschke and K.Schünemann</i>.....</p> <p>INV.3. Transition Radiation of Charged Particles and the Possibility of Submillimeter Waves Generation in the Semiconductor Structures <i>V.M.Yakovenko</i></p> <p>INV.4. Measurements of High Gain Antennas at Millimeter Wavelength Using Hologram CATR <i>A.Räisänen, T.Hirvonen, J.Ala-Lauriaho, A.Lehto</i>.....</p> <p>INV.5. The Synergy of Submillimetre and Infrared Spectroscopy in Predicting Global Warming Effects of CFC Replacement Molecules <i>G.Duxbury, K.Smith, M.McPhail, R.McPheat, J.Ballard, and D.Newnham</i></p> <p>INV.6 New Trends in GaAs-Based Devices For Generation of Millimeter and Submillimeter Waves <i>P.Kordos</i>.....</p> <p>INV.7. Microwave Components and Devices Based on High Temperature Superconductors <i>O.G.Vendik</i></p> <p>INV.8. Radar Estimations of Soil Parameters by Multichannel Methods <i>G.P.Kulemin</i></p> <p>INV.9. State of the Art of Gyrotron Developments and Investigations <i>A.Goldenberg</i>.....</p> <p>INV.10. Detection System for the Measurements of Collective Thomson Scattering Spectra in Fusion Plasma <i>L.V.Lubyako, E.V.Suvorov, A.B.Burov, A.M.Shtanuk, Yu.A.Dryagin, L.M.Kukin, and N.K.Skalyga</i></p> <p>INV.11. Hypersonic Delay Lines: Physical Base, Technology and Application in the Space Radar Engineering <i>V.N.Balabanov, E.M.Ganapolskii, A.V.Golik, V.B.Efimov, A.P.Korolyuk, A.C.Kurekin, A.G.Sergeev, V.V.Tarakanov, and V.N.Tcymbal</i></p> <p>INV.B1. MM-Wave Transmitters Using Magnetrons with Cold Secondary-Emission Cathode <i>V.D.Naumenko, K.Schünemann, V.Ye.Semenuta, D.M.Vavriv, and V.A.Volkov</i>.....</p> <p>INV.C1. Superconducting Passive Microwave Components for Mobile Communications <i>M.J.Lancaster, J.-S.Hong, D.Jedamzik, and R.B.Greed</i></p> <p>INV.E1. Value Estimations of the Third Stokes-Vector Component Both Precipitation Microwave Emission and Sun Scattered Radiation Observations <i>B.G.Kutuza, G.K.Zagorin, A.Hornbostel, and A.Schroth</i></p> <p>INV.F1. Remote Sensing of the Atmospheric Ozone at Millimeter Waves <i>E.P.Kropotkina, A.N.Lukin, S.B.Rozanov, and S.V.Solomonov</i>.....</p> <p>INV.F2. Millimeter Wave Noise Radar Technology <i>K.A.Lukin</i></p> <p>INV.G1. Millimeter and Submillimeter Wave Spectroscopy of Interstellar Medium <i>I.I.Zinchenko and V.M.Shulga</i></p> <p>INV.G2. Low-Noise Millimeter and Submillimeter Wave Receivers <i>B.A.Rozanov and S.B.Rozanov</i>.....</p> <p>INV.H1. Integrated Software Package for Synthesis, Analysis and Optimization of Frequency-Selective Devices of Millimeter and Centimeter Waves <i>A.A.Kirilenko, L.A.Rud', V.I.Tkachenko, L.P.Mos'pan, and D.Yu.Kulik</i>.....</p>	<p>22</p> <p>24</p> <p>30</p> <p>35</p> <p>40</p> <p>44</p> <p>50</p> <p>53</p> <p>60</p> <p>64</p> <p>70</p> <p>76</p> <p>82</p> <p>88</p> <p>91</p> <p>94</p> <p>98</p> <p>104</p> <p>110</p>
---	---

INV.I1. Precise Measurements in Millimeter and Submillimeter-Wave Range Based on Phase-Locked Primary Radiation Sources <i>A.F.Krupnov, M.Yu.Tretyakov, V.N.Markov, E.N.Karyakin, G.Yu.Golubyatnikov, V.V.Parshin, S.A.Volokhov, A.M.Schitov, V.V.Bychkov, and I.I.Leonov.....</i>	115
INV.I2. Material Properties in the Millimeter Range <i>V.V.Meriakri</i>	121
INV.J1. Multifunctional Millimeter Wave Radar Sensor for Vehicle Applications <i>M.Wollitzer, J.Büchler, J.-F.Luy, U.Siart, and J.Detlefsen</i>	124
INV.J2. High Temperature Processing of Materials Using Millimeter-Wave Radiation <i>Yu.V.Bykov, A.G.Eremeev, V.V.Holoptsev, K.I.Rybakov, and V.E.Semenov</i>	130
INV.K1. The Elaboration Measurement Accuracy Problems of the Frequency Characteristics of the Sources of High Stability Oscillations in the Millimeter and Submillimeter Range and of the Means of Their Traceability <i>A.S.Kleiman</i>	136
INV.L1. Mechanism of Interaction of EHF Radiation with Biological Systems <i>O.V.Betskii, N.N.Lebedeva, and Yu.G.Yaremenko.....</i>	139

Session A. NEW PRINCIPLES OF GENERATING AND RECEIVING MM AND SUBMM WAVES

A1. Harmonic Mode Operation of GaAs-IMPATT Devices above 200 GHz <i>M.Claassen and H.Böhm</i>	142
A2. Mixing of 28 THz CO ₂ -Laser Radiation by Nanometer Thin-film Ni-NiO-Ni Diodes with Difference Frequencies up to 176 GHz <i>C.Fumeaux, W.Herrmann, F.K.Kneubühl, H.Rothuizen, B.Lipphardt, and C.O.Weiss.....</i>	145
A3. Infrared Raman Solitons, Self-phase Modulation and Self Focusing in CO ₂ -Laser Pumped NH ₃ <i>M.O.Baumgartner and F.K. Kneubühl</i>	147
A4. Semiconductor Microwave Device in HSRI of China. <i>Li Songfa.....</i>	149
A5. Antenna - Coupled Schottky Diodes for Millimeter Wave Receivers <i>E.O.Iounevitch and V.E.Lioubtchenko.....</i>	152
A6. Dynamic and Noise Parameters of the Power Adders Using the Multistructural IMPATT Diodes <i>A.A.Nikitin and A.S.Shapovalov.....</i>	155
A7. Thesis's About Gunn Diode Work with Two Transit-Time Regions and Heterojunction Between them <i>I.Storozhenko</i>	157
A8. Power and Frequency Characteristics of Gunn GaAs-Diodes with Tunnel Injection of Cold Electrons <i>Yu.V.Arkusha, E.D.Prokhorov, and I.P.Storozhenko.....</i>	159
A9. Compensated GaAs Diodes Oscillator <i>O.V.Botsula and E.D.Prokhorov</i>	161
A10. Frequency Dependence of MM-Wave GaAs Gunn Diode Oscillators Efficiency Operated on 2-nd or 3- rd Harmonic <i>A.V.Dyadchenko, A.A.Mishnjov, and E.D.Prokhorov.....</i>	163
A11. Efficiency Possibilities of the RTD Generators <i>E.D.Prokhorov, V.V.Medvedev.....</i>	166
A12. Whispering Gallery Oscillations in an Anisotropy Ball <i>Yu.F.Filipov and Z.E.Eremenko</i>	168
A13. Exact Simulation Method for Analysis of Open Resonators with Step-Like Deformation of Mirrors <i>O.I.Belous, AI.Fisun, A.A.Kirilenko and V.I.Tkachenko.....</i>	170
A14. Millimeter Wave Signals Detection by Means of Monocrystal Hexagonal Ferrite Ellipsoid <i>M.Yu.Koledintseva, A.A.Kitaytsev</i>	173

A15.	Gunn Diode Cathode Contacts Part in the Increase of the Oscillation Efficiency <i>Yu.V.Arkusha</i>	176
A16.	MESFET VCO for Use in MM-Wave Communications <i>S.S.Slesarenko</i>	178
A17.	Basic Principles of Elaborated of Solid-State Millimeter Wave Sources with Dispersive Open Oscillating Systems <i>O.I.Belous, B.M.Bulgakov, and A.I.Fisun</i>	181
A18.	Efficiency of the Aperture of the Reconstructive Interferometer <i>V.N.Uvarov</i>	183

**Session B. ELECTRONICS OF MM AND SUBMM WAVES, INCLUDING QUANTUM
AND RELATIVISTIC ELECTRONICS**

B1.	Gyrotron as a Source of Probing Radiation for Collective Thomson Scattering Experiments <i>E.V.Suvorov, W.Kasperek, L.V.Lubyako, N.K.Skalyga, V.Erckmann, and T.H.Lqua</i>	188
B2.	Relativistic Gyrotron at the 5th Cyclotron Harmonic <i>V.L.Bratman, Yu.D.Grom, Yu.K.Kalynov, V.N.Manuilov, M.M.Oftserov, and S.V.Samsonov</i>	191
B3.	Simulation of the Excitation Mechanisms of Oscillation in Diffraction Electronics Devices on Coupled Open Resonators <i>G.S.Vorobjov and A.I.Ruban, and A.I.Tsvyk</i>	194
B4.	Simulation of the Excitation Processes of Diffraction-Cerenkov Radiation by the Electron Beam Space Charge Waves on Metal-Dielectric Periodic Structures <i>G.S.Vorobjov, K.A.Pushkaryov, A.I.Ruban and A.I.Tsvyk</i>	196
B5.	Installation for Investigation of Electron Beams of Vacuum Electronic Devices of Millimeter Wave Band <i>G.S.Vorobjov, D.A.Nagornyi, K.A.Pushkaryov, Ye.V.Belousov, and V.G.Korzh</i>	198
B6.	Investigation of Phase-Locked Diffraction Radiation Generator <i>M.Yu.Demchenko, G.P.Ermak, and I.D.Revin</i>	200
B7.	On Mechanism for Oscillation Excitation by Electron Beam in Cavity <i>V.A.Buts and I.K.Kovalchuk</i>	203
B8.	The Peniomagnetron with Barrel-Shaped Resonator <i>V.D.Yeremka and O.P.Kulagin</i>	206
B9.	Autosoliton Mode of the Oscillations in the Smooth Anode Magnetron <i>O.P.Kulagin</i>	209
B10.	Effect of Load on Characteristics of a Magnetron Cavity <i>A.E.Serebryannikov and A.V.Sova</i>	212
B11.	HCN-Laser with Combined Pumping of Active Medium <i>Yu.E.Kamenev</i>	215
B12.	Submillimetre Discharge HCN Laser with the Inside Film Electrodes <i>N.F.Dachov, Yu.E.Kamenev, V.K.Kiseliov, E.M.Kuleshov, and V.P.Radionov</i>	216
B13.	Quantum Chaos in the 3D Electrodynamic Systems of Millimeter Wave Range <i>E.M.Ganapolski</i>	218
B14.	Investigation of Critical Regimes in Periodical Structure of FEL, Formed by Coupled Grooved Waveguides <i>V.S.Miroshnichenko</i>	221
B15.	"Buch" Oscillations in Diffraction Radiation Oscillator <i>I.K.Kuz'michev and B.K.Skrynnik</i>	224

B16.	Experimental Detection and Analysis of the Morse Critical Point of Open Electrodynamical Structure Involved in Diffraction Radiation Oscillator <i>I.K.Kuz'michev</i>	227
B17.	Analysis of the Steady-State Mode of the Ormotron <i>G.A.Alexeev</i>	230
B18.	Analysis of Electron-Wave Interaction in Cathode Driven Crossed-Field Amplifiers by Coupled-Mode Method <i>G.I.Churyumov and T.I.Frolova</i>	233
B19.	Simulation of an Inverted Cold Secondary Emission Magnetron Gun invited design <i>D.B.Eremin, G.I.Churyumov, N.I.Ayzatskiy, A.N.Dovbnya, V.V.Zakutin</i>	236
B20.	The MM-Wave Cold Cathode Peniometer <i>V.D.Yeremka</i>	239
B21.	Slow-Wave Structure High-Power MM Band TWT <i>V.D.Yeremka, M.O.Khorunzhii, and V.N.Koshparenok</i>	242
B22.	Millimeter Band Magnetron Triodes with Lens Optics <i>V.D.Yeremka, G.Ya.Levin, S.N.Teryokhin, and O.P.Kulagin</i>	245
B23.	Diffraction Radiation Generator with Local Inhomogeneity of Magnetostatic Field in the Interaction Space <i>A.I.Tsvyak, A.V.Nesterenko, and V.N.Zheltov</i>	248
B24.	Low-Noise MM Traveling-Wave Maser with Instantaneous Bandwidth of 470 MHz <i>N.T.Cherpak, A.A.Lavrinovich, T.A.Smirnova</i>	251

Session C. WAVE PROCESSES IN FINITE-SIZE SEMICONDUCTORS, SOLID-STATE STRUCTURES AND HTSC MATERIALS

C1.	Connection of Residual Losses of a Microwave Energy in Superconductive State of $\text{YBa}_2\text{Cu}_3\text{O}_{7-\delta}$ Films on Saphire Substrates with Their Resistance in a Normal State <i>O.D.Poustylnik</i>	254
C2.	Phenomenological Approach to Radiofrequency Response of HTS Thin Samples to Microwave Irradiation <i>N.T.Cherpak, E.V.Izhyk, A.Ya.Kirichenko, and A.V.Velichko</i>	257
C3.	Interaction of Magnetostatic Surface Waves with Film Granular HTSC Structure <i>V.A.Krakovskiy</i>	260
C4.	Evolution of Oscillations of Semibounded Electron Plasma <i>V.L.Falko, S.I.Khankina, and V.M.Yakovenko</i>	263
C5.	Semiquantal Dynamics of the Electrons in a Periodic Potential Under the Microwave Excitation <i>L.V.Yurchenko and V.B.Yurchenko</i>	266
C6.	Influence of Microcorrugated Surface on Electron States in 2D Quantum Well <i>V.A.Pogrebnyak</i>	269
C7.	Resonant Field Emission in Multilayer Cathods with Quantum Well <i>N.M.Goncharuk, V.E.Chayka, V.G.Litovchenko, A.A.Evtukh, and Yu.M.Litvin</i>	272
C8.	Negative Dynamic Conductivity in Diode Structure with the Cone Cathode <i>V.E.Chayka, N.M.Goncharuk, and D.V.Mironov</i>	275
C9.	Losses in Diamonds at Millimeter Range <i>B.M.Garin, A.N.Kopnin, M.P.Parkhomenko, E.E.Chigryai, Y.V.Parshin, A.B.Mazur, V.G.Ralchenko, and V.I.Konov</i>	278
C10.	Polariton Excitations in Two-Dimensional Electron Magnetoplasma <i>V.V.Popov, T.V.Teperek, and G.M.Tcymbalov</i>	281
C11.	Perturbation of Quasioptical Dielectric Resonator by a Radial Slot with Anisotropic Substrate <i>N.T.Cherpak, E.V.Izhyk, A.Ya.Kirichenko, A.Ya.Dan'ko, A.T.Budnikov, and V.G.Pedyash</i>	284

C12.	On Collisionless Damping of Surface Plasmons <i>V.M.Yakovenko and I.V.Yakovenko</i>	286
C13.	Quantizing of Transition Radiation of the Surface Polaritons by the Charge, Intersecting Two-Layer Two-Dimensional Electron System, Placed Into Strong Magnetic Field <i>Yu.O.Averkov, N.N.Beletskii, and V.M.Yakovenko</i>	289
C14.	Non-Radiative Polaritons in a GaAs/AlGaAs Heterostructures Under Quantum Hall Effect Conditions <i>N.N.Beletskii and S.A.Borisenco</i>	292
C15.	Features of a Spectrum of Magneto-Plasma Waves in Periodic Semiconducting Lattice <i>A.A.Bulgakov, O.V.Shamkova</i>	295
C16.	Surface Polaritons in the Finite Superlattice Placed Into the Quantizing Magnetic Field <i>J.V.Bludov</i>	298
C17.	Non-Linear Magnetoplasma Excitations in Compensated Metals: Periodic and Solitary Waves <i>N.M.Makarov, G.B.Tkachev, and V.E.Vekslerchik</i>	301
C18.	Acoustic Wave Resonances in a Solid Layer with Periodically Irregular Boundary <i>A.S.Bugaev and V.V.Pogrebnyak</i>	304
C19.	Optical Surface Modes in a Random System of Small Metallic Particles <i>A.Ya.Blank, L.V.Garanina, L.G.Grechko</i>	307
C20.	Interaction of Submillimeter Electromagnetic Waves with Ferroelastic Solid-State Structures <i>Ya.O.Shablovsky</i>	310
C21.	Peculiarities of Electron-Wave Interactions in the Resonance System with a Semiconductor <i>V.A.Abdulkadyrov</i>	313
C22.	The Theory of an Electromagnetic Radiation by a Semiconducting Heterostructure with Periodic Screens <i>V.A.Abdulkadyrov</i>	316

Session D. PROBLEMS OF THE THEORY OF WAVE DIFFRACTION

D1.	A Regularization Method for a Class of Dual Series Equations in Diffraction Theory <i>A.V.Brovenko and A.Ye.Poyedinchuk</i>	320
D2.	Harmonic Filters on Ridger Waveguides <i>A.A.Kirilenko, L.A.Rud', and V.I.Tkachenko</i>	323
D3.	Waveguide Band Pass Filters with Increased Stop Band Attenuation <i>M.E.Ilchenko, A.A.Kirilenko, A.G.Yushchenko, L.A.Rud', and V.I.Tkachenko</i>	326
D4.	Investigation of Different Non-Uniform Grids in Waveletbased Planar Circuit Analysis <i>K.Bubke, G.Oberschmidt and A.F.Jacob</i>	329
D5.	Fundamental and Applied Synthesis Problems for Periodic Structures <i>L.G.Velychko</i>	332
D6.	An Efficient Educational Program for a Fin Line Coupler on Semiconductor <i>H.C.C.Fernandes</i>	334
D7.	Microstrip Line with Superconductivity in Multilayer Semiconductor <i>H.C.C.Fernandes, G.A.de B.Lima, and W.P.Pereira</i>	337
D8.	Project and Analysis of Unilateral Fin Line Power Dividers <i>H.C.C.Fernandes, R.L.M.Lima, and E.L.Freitas</i>	340
D9.	HTc Superconducting Planar Antennas Design Using the TTL Method in the Fourier Transform Domain <i>H.C.C.Fernandes</i>	343
D10.	Analysis of Wave Diffraction on the Systems of Screens by the Method of the Product of Parabolic Regions <i>I.V.Petrusenko</i>	346

D11.	Method of Analysis of the Thin-Film Dielectric Parameters <i>V.N.Derkach, A.E.Pojedinchuk, A.V.Brovenko, and A.A.Vertij</i>	349
D12.	Bandpass and Bandstop Multiaperture Irises for Millimeter and Centimeter Wave Range <i>A.A.Kirilenko and L.P.Mos'pan</i>	352
D13.	The Analytical and Numerical Solution Method of the Wave Diffraction Problem for a One-Dimensional Periodic Grating with Chiral Medium <i>S.B.Panin and A.Ye.Poyedinchuk</i>	354
D14.	Fractal Electrical and Magnetical Radiators <i>E.I.Veliev and V.M.Onufrienko</i>	357
D15.	The Morse Critical Points and Problems of Synthesis and Analysis Dielectric Layer <i>V.V.Yatsik</i>	360
D16.	Scalar Wave Diffraction by Axially Symmetrical Flat System of Infinitely Thin Perfectly Conducting Circular Rings <i>Y.A.Tuchkin, E.Karacuha, and F.Dikmen</i>	363
D17.	A Rigorous Approach to the Analysis of Transients in Complete-Parametric Periodic Structures <i>A.O.Perov</i>	366
D18.	Resonance Effects in Electromagnetic Wave Diffraction by a Thin Strip with Anisotropic Conductivity <i>A.D.Shatrov and P.A.Malyshkin</i>	370
D19.	Proper and Improper Waves of Strip with Anisotropic Conductivity <i>E.N.Korshunova, I.P. Korshunov, A.N.Sivov, and A.D.Shatrov</i>	373
D20.	The Diffraction of Nonsinusoidal Radio Waves on Natural Media <i>S.O.Masalov, O.O.Puzanov, and A.I.Timchenko</i>	376
D21.	Excitation of Electromagnetic Waves in Space with Spherical-Layerd Structure <i>Yu.M.Penkin</i>	379
D22.	Coherent Backscattering by a Medium of Randomly Oriented Multiple-Sphere Clusters <i>V.P.Tishkovets and P.V.Litvinov</i>	382
D23.	Modelling and Visualisation of the Electromagnetic Fields in Channel Waveguides <i>G.F.Zargano, K.V.Vdovenko, and G.P.Sinyavskij</i>	385
D24.	Analysis of Line Current Wave Diffraction from Metal-Backed Dielectric Strip by Extended PO Method <i>A.S.Andrenko and Makoto Ando</i>	387
D25.	The Effective Mathematical Model of Microstrip Frequency Selective Surfaces <i>A.O.Kasyanov, V.A.Obukhoveths</i>	390

Subsession ATOMIC FUNCTION

D26.	Atomic Functions and Wavelet Matrix Transform Approach for Efficient Solution of Electromagnetic Integral Equations in the Boundary Value Problems of Millimeter Wave Diffraction <i>V.F.Kravchenko and A.A.Zamyatin</i>	393
D27.	Optimization of the Profile of the Electrodynamic System of a Powerful Gyro-Traveling-Wave-Tube (Gyro-TWT) <i>V.F.Kravchenko, A.A. Kuraev, and S.V.Kolosov</i>	396
D28.	Applications of Atomic Functions to the Boundary Value Problems and Signal Processing Millimeter Band <i>V.F.Kravchenko, V.L.Rvachev, and V.A.Rvachev</i>	399
D29.	Relativistic Travelling-Wave-Tube-O (TWT-O) with an Irregular Moderating System <i>V.F.Kravchenko, A.A.Kuraev, and A.B.Zakalyukin</i>	402
D30.	Optimization of the Variation of a Phase Velocity Wave in an Orotron of Millimeter Band Based on Atomic Functions <i>V.F.Kravchenko, A.A.Kuraev, A.K.Sinitsyn, and A.I.Shakirin</i>	405

D31.	Computation of Electrodynamical Characteristics of Arbitrarily Shaped Domains Based on R-functions Method <i>V.F.Kravchenko, V.L.Rvachev, and V.V.Torchinov</i>	407
D32.	Calculation of a Millimeter Wave Electrooptical Modulator of Laser Bundles by a Method of R-functions <i>V.F.Kravchenko, N.I.Kravchenko, and N.D.Sizova</i>	410
D33.	An effective Solution of Electromagnetic Integral Equations in the boundary Value Problems of Millimeter Wave Diffraction Based on Atomic Functions <i>V.F.Kravchenko and A.A.Zamyatin</i>	413
D34.	Application of R-functions Method to the Calculation of Microstrip Element of Pentagonal Shape <i>V.F.Kravchenko, V.L.Rvachev, and V.V.Torchinov</i>	416
D35.	Analytical and Numerical Methods in the Boundary Value Problems of Superconducting Electrodynamics of Structures in the Millimeter Band <i>V.F.Kravchenko</i>	418
	Authors Index	421

Volume 2

Session E. MM AND SUBMM WAVE PROPAGATION

E1.	Research of the Propagation of Broadband Signals of Millimetre Range in the Near-Earth Layer of an Atmosphere <i>L.F.Chornaya, S.V.Titov, and G.K.Zagorin</i>	450
E2.	Monitoring Spatially - Temporary Distributions of Fields of Harmful Impurities in Atmosphere by Methods of Microwave Sounding it from a Surface of the Earth and from Space <i>S.D.Dubko, L.V.Kostenko, L.N.Litvinenko, B.I.Makarenko, and E.I.Solokha</i>	453
E3.	Attenuation Factor of X-and Ka-Band Field Near Sea Surface <i>V.B.Razskazovsky, Yu.A.Pedenko, and Yu.F.Logvinov</i>	455
E4.	Spectral and Correlation Characteristics of Fluctuations of a Point Radiation Source Bearing Under Strong Effect of a Sea Surface in W-Range <i>N.V.Gorbach, L.I.Sharapov, and N.V.Ryazantseva</i>	458
E5.	Prediction of Millimeter Wave Attenuation in Indian Continent <i>T.K.Bandopadhyaya and P.Saxena</i>	460
E6.	Theory of Waveguide Propagation in Randomly Corrugated Channels <i>N.M.Makarov and A.V.Moroz</i>	463
E7.	Localization of Waves in a Single-Mode Waveguide with Statistically Identical Rough Boundaries <i>N.M.Makarov and Yu.V.Tarasov</i>	466
E8.	Estimation of Electrical Path Delay Fluctuations in the Atmosphere by Microwave Radiometry <i>B.G.Kutuza</i>	469
E9.	Quasi-Synchronous Measurements of Radiowave Attenuation by Falling Snow at 138 and 247 GHz <i>N.I.Furashov and B.A.Sverdlov</i>	472
E10.	Computer Simulation of Radiowave Attenuation in Snowfalls at 138 and 247 GHz <i>A.M.Osharin</i>	474
E11.	Some Peculiarities of Vegetation Doppler Spectra and Estimation of Their Influence on the Selection Performance of the 2mm Wavelength Radar <i>N.V.Gorbach, V.G.Gutnic, and L.I.Sharapov</i>	476
E12.	On the Influence of an Ionised Above-Surface Layer on Wave Propagation <i>G.A.Alexeev</i>	478

Session F. COMMUNICATIONS AND RADARS; REMOTE SENSING

F1.	Application of Millimeter Radio Waves in Radio Engineering Systems (Review) <i>V.N.Antifeev, A.B.Borsov, R.P.Bystrov, E.V.Vashenko, and A.V.Sokolov</i>	482
F2.	Experimental Research on Detection and Recognition of Ground Objects on the Basis of Polarization Parameters <i>N.S.Akinshin, V.N.Antifeev, A.B.Borsov, R.P.Bystrov, V.A.Nikolaev, A.V.Sokolov, I.A.Panin, and D.A.Nosdrachev</i>	485
F3.	Radar-Tracking Converters in Alarm Systems <i>R.P.Bystrov, E.V.Vashenko, and A.V.Sokolov</i>	492
F4.	Alarm Complex for Detection and Recognition of Ground Objects <i>R.P.Bystrov, E.V.Vashenko, and A.V.Sokolov</i>	493
F5.	Digital Computer Simulation of Radar Scattering Fields for Complex Shape Objects <i>V.N.Antifeev, A.B.Borsov, R.P.Bystrov, D.A.Nosdrachev, G.L.Pavlov, and A.V.Sokolov</i>	494
F6.	The Analysis of Radar-Tracking Scenes VIA Mathematical Simulation Method <i>V.N.Antipeev, A.B.Borsov, R.P.Bystrov, D.A.Nosdrachev, A.V.Sokolov, V.B.Suchkov</i>	496
F7.	Methodology of Multichannel Radar Image Processing and Interpretation <i>G.P.Kulemin, A.A.Zelensky, V.V.Lukin, A.A.Kurekin, and K.P.Saarinen</i>	497
F8.	The Influence of Phase and Amplitude Fluctuations of Microwaves in Troposphere on Sar Operation <i>G.P.Kulemin, V.V.Lukin, and A.A.Zelensky</i>	500
F9.	Use of Homomorphic Transforms for Low Contrast Edge/Detail Detection and Filtering of MM-Band Images <i>V.I.Chemerovsky, A.N.Dolia, A.A.Kurekin, V.V.Lukin, and A.A.Zelensky</i>	503
F10.	Remote Sensing of the Minor Gas Constituents of the Lower and Middle Atmosphere <i>Sh.D.Kitaj, A.P.Naumov, N.N.Osharina, and A.V.Troitskij</i>	506
F11.	The Influence of Air-Water Interface Boundary Conditions on Thermal Radio Emission at 2, 5 and 8 mm <i>K.P.Gaikovich and R.V.Troitsky</i>	509
F12.	Detection of Small Scale Structures in Ozone Layer by Microwave Sounding <i>A.A.Krasilnikov, Y.Y.Kulikov, V.G.Ryskin, and L.I.Fedoseev</i>	512
F13.	Polarization of Atmospheric Millimeter-Wave Radiation from Scattering Particles Cloud, and Remote Sensing of Volcanic Eruption Column <i>A.A.Shvetsov</i>	515
F14.	Frequency-Temporal Distributions of Radar-Returns from Sea Surface in X- and Ka-Band <i>V.A.Kirichenko, G.P.Kulemin, and V.G.Sugak</i>	517
F15.	Polarization Selection of Non-Doppler Ground Objects in MM-Wave Range <i>A.N.Zubkov, N.S.Akinshin, and B.V.Sukhinin</i>	520
F16.	Clutter Rejection in Short-Range Radar with Uncoded and Wideband Pulsed Signals <i>G.P.Kulemin</i>	523
F17.	Rough Sea Surface Observation Scheme Optimization at Microwave Radiometric Sensing <i>V.A.Komyak, S.A.Shilo, and Ya.I.Stephanishin</i>	526
F18.	Millimeter Band Scanning Multi-Beam Radiometer <i>S.A.Shilo and V.A.Komyak</i>	529
F19.	Methods of Remote Sensing of Stratified Mediums and Their Applications <i>V.M.Velasco Hererra, V.K.Volosyuk, S.E.Falkovich, O.A.Gorbunenko, and A.V.Sokolnikov</i>	532
F20.	Optimized Complex Signal Processing in Multichannel Synthesized Aperture Radar <i>V.K.Volosyuk, V.F.Kravchenko, A.V.Sokolnikov, O.A.Gorbunenko, V.A.Onishchuk, and V.M.Velasco Hererra</i>	535

F21.	To the Accuracy of Small Slope Approximation of Kirchhoff Technique <i>D.V.Mikhailova and L.V.Stulova</i>	538
F22.	Millimeter Wave Null-Modem Radio Communication <i>N.M.Zaitsev and V.E.Lioubtchenko</i>	541
F23.	On Energy Potential of a Millimeter-Wave Radar <i>B.A.Rozanov and G.V.Cheslavsky</i>	543
F24.	Optimum Synthesis of Transmitting-Receiving Sections of an Underground Radar <i>A.A.Orlenko and P.V.Kholod</i>	546
F25.	The Problems of the Possible Non-Linear Radiolocation on the Objects of Low Perception <i>S.A.Gayvoronskaja and V.I.Sergeev</i>	549
F26.	Brightness Variations Resistant Algorithms of Object Location on Radiometric Images <i>V.I.Antyufeev, V.N.Bykov, B.I.Makarenko, and A.M.Grichaniuk</i>	552
F27.	Reconstruction of the Continuum Object from the Sampled Radio Image <i>A.S.Viltchinsky, B.I.Makarenko, E.D.Prilepsky, and M.G.Shokin</i>	555
F28.	Influence of the Oil Film on Spectral and Polarization Features of S-, KA- and V-Band Water Surface Back Scattering <i>V.I.Lutsenko, S.I.Homenko, A.A.Uzlenkov, and V.A.Kirichenko</i>	558
F29.	Two-Parametric Representation of Nonstationary Random Signals in Millimeter Wave Radar <i>K.A.Lukin and A.A.Mogila</i>	561
F30.	Mathematical Models and Spatial Characteristics of Coherent and Incoherent Imaging Systems <i>I.Pрудюс, С.Волошиновский, and Т.Холотяк</i>	562

Session G. MM AND SUBMM WAVE RADIO ASTRONOMY

G1.	Observations of Total Solar Eclipses at Short Millimeter Waves <i>B.A.Rozanov, N.A.Zharkova, and V.G.Nagnibeda</i>	566
G2.	The Interferometric Method of Image Formation and Associated Mathematical Problems <i>Yu.V.Kornienko</i>	569
G3.	Optimization of Non-redundant Apertures on Integer Grids <i>L.E.Kopilovich</i>	572
G4.	A Calculated Choice in the Problem on the Input Aperture of an Optical Multibeam Interferometer <i>L.V.Stulova</i>	575
G5.	Construction on Nonredundant Apertures for Interferometric Radiotelescope by Method on Random Search <i>Yu.V.Kornienko</i>	578
G6.	Immunity of the Interferometric Method for Image Formation to Phase Distortion of the Wave Front <i>Yu.V.Kornienko</i>	581

Session H. MM AND SUBMM DEVICES BASED ON THE PLANAR AND QUASI-OPTICAL TRANSMISSION LINES (PASSIVE AND ACTIVE COMPONENTS, ANTENNAS)

H1.	A New De-embedding Method for Microstriplines with Coaxial Adapters <i>J.Marquardt and J.Passoke</i>	586
H2.	Coupled-Mode Formulation for Double-Strip NRD Waveguides Based on Singular Perturbation Technique <i>K.Watanabe and K.Yasumoto</i>	589
H3.	A Microstrip Array Fed by a Non-Homogeneous Stripline Feeding Network <i>N.I.Herscovici, N.K.Das, and J.Klugman</i>	592
H4.	Properties of Oversized Corrugated Waveguides at Moderate Diameter-Wavelength Ratio <i>D.A.Lukovnikov, A.A.Bogdashov, and G.G.Denisov</i>	595

H5.	Integrated P-I-N-Structures Designed for MM and SubMM Wave Quasi-Optical Modulators <i>V.V.Grimalsky, Ya.I.Kishenko, I.P.Moroz, and S.V.Koshevaya</i>	598
H6.	Wide-Range System of Turning Mirrors for the Waveguide Laser Resonator <i>V.A.Svich, V.M.Tkachenko, A.N.Topkov, V.A.Maslov, and I.M.Militinskiy</i>	601
H7.	Short Pulse Generation in a Cavity with an Active Layer and a Dielectric Mirror <i>L.V.Yurchenko and V.B.Yurchenko</i>	604
H8.	Resonant Reflection of Electromagnetic Wave from Thin Strip Grating <i>I.K.Kuzmichev, S.N.Vorobiov</i>	607
H9.	On the Diffraction Coupling Organisation in Open Resonators <i>D.G.Afonin and A.K.Malyshkin</i>	610
H10.	Computer Analysis of Side Radiation of Narrow-Beam Antenna Array <i>N.N.Gorobets, Yu.N.Gorobets, and V.I.Kiyko</i>	611
H11.	Influence of Side Radiation on One-Reflector Antenna Parameters <i>N.N.Gorobets and S.S.Vyazmitinova</i>	615
H12.	Millimetre-Range Multi-Channel Two Polarization Horn Antenna <i>N.N.Gorobets, V.M.Dakhov, and I.V.Cherny</i>	618
H13.	The Principles of Electrodynamics of Planar Periodic Structures <i>V.V.Khoroshun</i>	620
H14.	Optimization of the Eigenmodes Spectrum of Parallel-Plate Waveguide with Knifelike Diaphragm <i>V.V.Khoroshun, I.E.Pedchenko, and N.A.Syvozalizov</i>	623
H15.	Super Narrow-Band Low-Dimentional Ultra-High Frequency Filter on the Basis of Waveguide-Dielectric Resonator <i>A.A.Zvyagintsev, A.V.Strizhachenko, V.V.Chizhov, and V.V.Popov</i>	624
H16.	Surface Wave HTS Resonators <i>G.A.Melkov, Y.V.Yegorov, A.N.Ivanyuta, and V.Y.Malyshev</i>	625
H17.	The Phased Array Antenna for the Radar of a Millimetric and Centrimetric Range <i>B.N.Bakhvalov, A.V.Gomozov, and L.V.Kostenko</i>	628
H18.	Ring Antenna Array of Millimeter Wavelength Band <i>V.N.Rudenko, E.I.Solokha, V.I.Gomozov, and L.V.Kostenko</i>	631
H19.	Electromagnetic Modelling of Microwave High Power Multiplexers <i>B.I.Makarenko, A.S.Soroka, and I.S.Tsakanyan</i>	633
H20.	Simulation of Multichannel Waveguide Power Dividers <i>A.S.Soroka, A.O.Silin, V.I.Tkachenko, and I.S.Tsakanyan</i>	634
H21.	On Application of Multicomponent Copper Alloys for Making Microstrip Line Conductors of EHF Microcircuits <i>V.A.Bessonov, S.A.Barantsev, and I.I.Uliyanova</i>	636
H22.	Waves in Irregular Rectangular Waveguide with Inhomogeneous Anisotropic Impedance of Wall <i>V.F.Borulko</i>	638
H23.	Two-Dimensional Bragg Resonator with Nonperiodic Radial Perturbation of Parameters <i>V.F.Borulko and V.E.Ivanilov</i>	641
H24.	Polarizable-Spectral Characteristics of Revolving Linear Polarizer <i>V.N.Polupanov, Y.M.Kuleshov, B.N.Knyaz'kov, and M.S.Yanovsky</i>	644
H25.	Consideration of Optimum Sectional Waveguide Tapers for Quasi-Optical Transmission Lines <i>V.K.Kiseliov</i>	647
H26.	Stochastical Resonator for the Accumulation of Millimeter Wave Range Electromagnetic Field Energy <i>E.M.Ganapolskii</i>	650
H27.	Open Hemispherical Imagine Dielectric Resonator with Whispering Gallery Modes <i>Z.E.Eremenko, Yu.F.Filipov, and S.N.Kharkovsky</i>	653

H28.	Three-Mirror Open Resonator with a Saturating Paramagnetic <i>I.Gudim and N. Popenko</i>	655
H29.	Diffraction Radiation Oscillator with the Long-Focus Small-Aperture Open Resonator <i>M.Demchenko, I.Ivanchenko, and V.Korneyenkov</i>	658
H30.	Millimeter Wave Linear Antenna Arrays Based on Ridge Dielectric and Groove Waveguides <i>A.P.Yevdokimov and V.V.Krizhanovsky</i>	661
H31.	Millimeter Wave Planar Cosecant Antenna Array for Airborne Radar for the Ukrainian Ministry of Extreme Situations <i>A.P.Yevdokimov and V.V.Krizhanovsky</i>	663
H32.	Automobile Radars for Collision Avoidance <i>A.P.Yevdokimov and V.V.Krizhanovsky</i>	666
H33.	Airborne Radiometer Broadband Quasi-Optical Scanning Antenna System <i>G.I.Khlopov, V.A.Komyak, A.A.Kostenko, and S.P.Martynuk</i>	667
H34.	Excitation of the Whispering-Gallery-Modes at the Shielded Hemispherical Dielectric Resonator <i>S.N.Kharkovsky, V.V.Kuzov, A.E.Kogut, and V.A.Solodovnik</i>	669
H35.	Open Radiating systems for Microwaves and Millimeter Waves <i>V.K.Korzenkov, V.I.Lutsenko, V.S.Miroshnichenko, and V.I.Uzlenkov</i>	671
H36.	The Main Type of Oscillations in Waveguide Branching of Three Orthogonal Below Cutoff Waveguides <i>Yu.G.Makeev</i>	674
H37.	Charactors of Waveguide-Dielectric Resonator <i>Yu.G.Makeev and A.P.Motornenko</i>	677

Session I. MM AND SUBMM WAVE SPECTROSCOPY

I1.	Wide-Range Millimeter-Wave Spectrometer for High-Resolution Investigation of Molecular Rotational Spectra <i>E.A.Alekseev, V.V.Ilyushin, and S.F.Dyubko</i>	682
I2.	Millimeter Wave Spectrometer and Its Application <i>A.N.Kopnin and V.V.Meriakri</i>	685
I3.	The Registration of Distortions by Microwave Components of Measurements of the Multifrequency Radiointerferometer of Millimeter Waves <i>M.V.Andreev</i>	687
I4.	Time Spectroscopy of a Film Bolometric Response to MM-Waves Power as a Method of the Thermodynamic Coefficients Diagnostics in a Film Structures <i>A.M.Grishin, Yu.V.Medvedev, and Yu.M.Nicolaenko</i>	690

Session J. MM AND SUBMM WAVELENGTH INSTRUMENT-MAKING FOR SCIENTIFIC RESEARCH (HOT-PLASMA DIAGNOSTICS, CONTROL OF TECHNOLOGICAL PROCESSES)

J1.	Heterodyne Spectrometer for Remote Sensing of the Atmospheric Ozone <i>V.A.Gusev, E.P.Kropotkina, S.V.Logvinenko, A.N.Lukin, P.L.Nikiforov, S.B.Rozanov, AM.Shtanjuk and S.V.Solomonov</i>	694
J2.	Optimisation of UHF Reflectometer Device for Study of Plasma Density Profile and Fluctuation in Magnetically Confined Plasmas <i>A.I.Skibenko, L.V.Bereznyj, O.S.Pavlichenko, V.L.Ocheretenko, I.B.Pinos and I.P.Fomin</i>	697
J3.	Graphit-Made UHF Resonator of Fabry-Perot Type for Investigation of the Plasma Divertor Flow in Fusion Devices and the Small-Scale Particles of a Substance <i>V.L.Jereshnyj, V.S.Voitsenya, V.L.Ocheretenko, A.I.Skibenko, and I.P.Fomin</i>	700

J4.	Extension of Functional Possibilities of MM-Range Modulation Radiometers <i>Yu.A.Skripnik and A.F.Yanenko</i>	703
J5.	Investigation of a New Quasi-Optical Waveguide Modeling Method for Backward and Forward Scattering Study in Millimeter and Submillimeter Wave Bands <i>V.K.Kiseliov, T.M.Kushta, and P.K.Nesterov</i>	706
J6.	About Digital Processing Signals of the Dynamic Spectrum Fourier <i>V.K.Laptyn</i>	709
J7.	Profound Spectral-Frequency Analysis of the Cardiograms <i>V.K.Laptyn</i>	712

Session K. ELECTROMAGNETIC METROLOGY

K1.	Electromagnetic Metrology of Millimeter and Submillimeter Wavelength Bands at Last Years in Ukraine <i>B.I.Makarenko</i>	716
K2.	Thin-wire Bolometers of Intensive Electromagnetic Radiation <i>V.M.Kuzmichov</i>	719
K3.	Measurement of the Generalized Laser Beam Cross Section Area <i>V.M.Kuzmichov, S.N.Pokhil'ko</i>	722
K4.	Intensive Laser Radiation Elliptical Polarization Measurement by Thin-wire Bolometers <i>V.M.Kuzmichov and E.V.Kuzmichova</i>	725
K5.	Nonlinearity of the Characteristic of Transformation Thin-wire Bolometer of Focused Laser Radiation <i>V.M.Kuzmichov and S.V.Pogorelov</i>	728
K6.	Microwave Diagnosis of Protective Coatings Quality <i>O.B.Ijashchuk and Z.T.Nazarchuk</i>	731
K7.	The Error's Influence on the Accuracy of Inverse Problems Solution for the Microwave Electromagnetic Diagnosis of Multilayer Materials <i>O.B.Ijashchuk</i>	734
K8.	Measurement of a Dielectric Permeability of Solutions by a Resonator Aperture Method <i>A.V.Koberidze</i>	737
K9.	Realization of Principle of Fourier Holographic Processing in Multifrequency Measurements in Range 126.6-145.4 GHz <i>O.O.Drobakhan, D.Yu.Saltykov, and A.Yu.Velikiy</i>	739
K10.	Vibratory String as a Perturbation Body in Order to Measurement Electromagnetic Field of Microwave Radiators <i>A.Ya.Kirichenko and O.A.Suvorova</i>	742

Session L. BIOMEDICAL APPLICATIONS OF MM AND SUBMM WAVES

L1.	Radiothermograph Millimeters of a Range for Medical Diagnostics <i>B.I.Makarenko, V.E.Kudryashov, E.V.Khomenko, and D.V.Martinenco</i>	746
L2.	Using of the EHF Method for Investigation of Radiation-Induced Changes in DNA Hydration Shell <i>O.V.Dubovitskaya, V.A.Kashpur, A.A.Krasnitskaya, and V.Ya.Maleev</i>	748
L3.	The Physical Evidence of the Weak Electromagnetic Field Action in the 30-300 GHz Region upon Biological System <i>L.I.Berezhinsky and G.I.Dovbeshko</i>	751
L4.	Dynamics of Indexes Water-Electrolytic Composition of the Blood for Patients with Alcoholic Psychosis under EHF-Therapy <i>M.Yu.Ignatov, A.V.Malihin, V.N.Derkach, and L.I.Zolotuhina</i>	754

L5.	Effects of Low Power Microwave Electromagnetic Fields on Brain Neurodynamics <i>T.N.Sulima and A.I.Fisun</i>	757
L6.	Research of Controlling Connection Systems of Cell Macromolecul Mechanisms by Method Dielectrometry in MM Range of Radiowaves <i>T.Yu.Shchegoleva and V.G.Kolesnikov</i>	760
L7.	About Possible Low-Intensive Combined Fields of Various Physical Nature Mechanisms of Interaction with Bioobjects <i>Yu.V.Chovnjuk</i>	763
L8.	EHF Radiation Impact on Drosophila Melanogaster Viability <i>V.G.Shachbazov, B.M.Bulgakov, S.P.Sirenko, L.M.Chepel', A.I.Fisun, O.I.Belous</i>	766
L9.	Using of EHF and IR Methods for Studying Hydration of Polycytidylc Acid <i>V.A.Kashpur, M.A.Semenov, and N.N.Sagaidakova</i>	768
L10.	Study of the Weak Electromagnetic Field Action upon the Biological Molecules and Tissues by Holographic Interferometer <i>L.I.Berezhinsky, G.I.Dovbeshko, and N.Ya.Gridina</i>	771
L11.	Method of EHF-Therapy at Treatment of Endogene Mental Diseases <i>A.N.Bacherikov and V.N.Derkach</i>	774
L12.	The Research of Molecular Mechanisms of Sperm Control Systems Functioning <i>M.V.Zubez, V.G.Kolesnikov, and T.Yu.Shchegoleva</i>	776
L13.	Application of Method of EHF-Dielectrometry in Analysis of Mechanisms, Stipulating Individual Lever of Coronary Risk <i>L.N.Gridasova, T.Yu.Shchegoleva, V.G.Kolesnikov, and U.J.Nicolenko</i>	779
L14.	EHF-Dielectrometry Method in Investigation Molecular Mechanisms of Stress Realization <i>O.Kovaljova, D.Sidorov, V.Smirnova, T.Ju.Shchegoleva, and E.A.Lepeeva</i>	782
L15.	Application of Dielectrometry in MM Range of Radiowaves for Research of Molecular Mechanisms of Pharmacological Preparations Action <i>N.E.Kiselova, T.Yu.Shchegoleva, and V.G.Kolesnikov</i>	785
L16.	Research of a Singularities of Drugs Toxycological Action on the Pregnant Women Blood by Method EHF-Dielectrometry <i>N.E.Kiselova, T.Yu.Shchegoleva, V.G.Kolesnikov, and N.S.Nikitina</i>	788
L17.	The Methodology of the Analysis of Molecular Mechanisms of Antrogenous Influence by Method of HF-Dielectrometr <i>T.Yu.Shchegoleva, V.G.Kolesnikov, L.A.Begma, A.A.Begma, and N.E.Kiselova</i>	791
	Authors Index	794

Volume 1

INV



INVITED PAPERS

A



**NEW PRINCIPLES OF GENERATING
AND RECEIVING MM AND SUBMM
WAVES**

B



**ELECTRONICS OF MM AND SUBMM
WAVES, INCLUDING QUANTUM AND
RELATIVISTIC ELECTRONICS**

C



**WAVE PROCESSES IN FINITE-SIZE
SEMICONDUCTORS, SOLID-STATE
STRUCTURES AND HTSC MATERIALS**

D



**PROBLEMS OF THE THEORY
OF WAVE DIFFRACTION**

INV  **INVITED PAPERS**

MSMW'98

A Review of the Principles of Holographic Power Combining at Millimeter and Submillimeter-Wave Frequencies

H.-G. Unger, M. Shahabadi, and K. Schünemann
Invited Paper

Abstract

In this contribution, we present a review of the principles of holographic power combining, a new concept for power combining at millimeter and submillimeter wavelengths. This approach which is based on the principles of holography utilizes a computer-generated hologram to transform the wavefront radiated by an array of sources into a plane wave, and establishes spatial power combining. The primary advantages of this method are its scalability up to arbitrarily high frequencies, high combining efficiency, and broad-band characteristics. Moreover, it will be shown that a holographic power combiner has a simple structure, and its design shows no dependence on the number of sources. With regard to the above mentioned advantages, this power-combining technique can replace many of the common methods of power combining and open the way to all-solid-state power sources for millimeter and submillimeter waves.

1 Introduction

In most applications of millimeter and submillimeter waves, e.g. in active imaging and radar systems, the required power level for transmitters cannot be supported by a single solid-state source. On the other hand, solid-state sources exhibit innumerable advantages compared with other millimeter-wave sources such as tubes or lasers. To gain these advantages and simultaneously meet the requirements on the power level, one should usually combine the power generated by a large set of solid-state sources.

The existing methods of power combining are assigned to two categories: *resonant* and *nonresonant* approaches [1]. In resonant methods, the sources coherently inject their energies into an eigenmode of an open resonator [2] while nonresonant methods are mainly based on spatial combining of the energy radiated by an array of mutually locked oscillators [3]. To avoid mode competition in resonant methods and grating lobes in nonresonant ones, the single sources should be arranged within a spacing dictated by the wavelength. In either method, the distance between neighboring devices should typically be less than a fraction of the wavelength. At millimeter-wave frequencies, this requires a geometrically small inter-element spacing and consequently circuit miniaturization. However, regarding the fact that solid-state sources usually possess a low power efficiency, the individual sources must be equipped with heat sinks, which are as large as several wavelengths. This explains the main disadvantage of the above mentioned methods, namely the necessity of miniaturization which is none but an obstacle for the installation of required heat sinks.

Recently we have developed a novel approach to power combining based on the principles of holography [4], [5]. In this method, which may be applied to power-combining of low-power solid-state sources of millimeter and submillimeter waves, a computer-generated hologram transforms the wave generated by an array of sources into a plane wave, and establishes spatial power combining. Since this scheme shows flexibility both in orientation and number of sources, it can overcome the shortcomings mentioned above.

In this contribution, we firstly review the operation principle of a holographic power combiner. This is followed by a discussion on the concrete configuration of such a power combiner. Finally, we summarize the outstanding features of the proposed method.

2 Principle of Operation

This section deals with a simple explanation of the operating principle of a holographic power combiner. To begin, consider the case in which the power generated by a group of arbitrarily oriented, identical sources is to be combined in free space. By power combining in free space we mean the generation of a single electromagnetic beam which carries the sum of power radiated by single sources. During this process the most important step is the formation of a *desired wavefront* for the sum beam. To explain this more precisely, we should add that although the wavefront radiated by a group of sources always contains the sum of total input power, in the case that this wavefront does not possess the "right" characteristics, the sum power is distributed among many beams propagating in different directions, and no free-space power combining can take place.

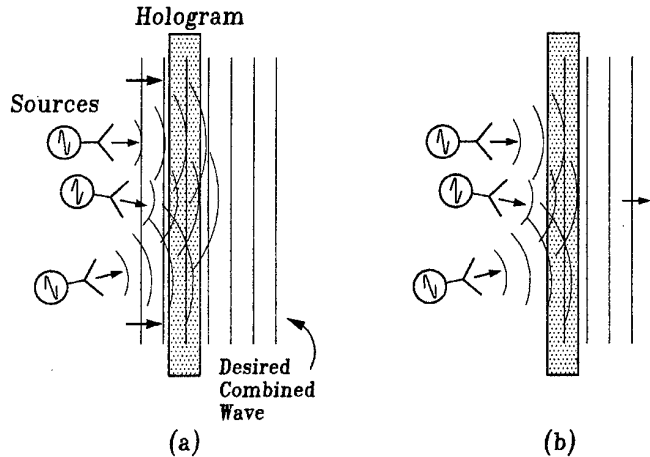


Fig. 1: (a) Interference of the desired output beam with the waves generated by the sources: The interference pattern is stored in a hologram. (b) Illumination of this hologram with the input waves reconstructs the desired output beam.

To avoid this case, we suggest a wavefront transformation by means of a quasi-optical component which primarily affects the phase of the radiated wavefront. The final output of this transformation must be an electromagnetic beam with the required wavefront. In what follows, we demonstrate how a hologram can perform the above transformation.

Looking at Fig. 1(a), suppose that the arbitrarily oriented sources the power of which is to be combined are oscillating synchronously. Thus the wave emerging from each source may be imagined as a wave originating from one of the scattering centers of an imaginary object illuminated by a monochromatic source. On the other hand, we can assume the desired output beam as a portion of the wave illuminating this fictitious object. According to the principles of holography [6], it is well known that the interference pattern of the above waves can be stored in a hologram (Fig. 1(a)), so that the desired output beam will be reconstructed if the hologram is imposed to the input waves (Fig. 1(b)). This observation describes the basic concept of holographic power combining.

It is worth mentioning that this method does not place any stringent constraint on the orientation of the sources. As a consequence, enough room can be devoted to heat sinks, and high-power sources are allowable. This explains the main advantage of holographic power combining, namely its scalability to very high frequencies at which the dimensions of the required heat sinks can be quite large.

In order to demonstrate other essential characteristics of this approach, a concrete configuration of a holographic power combiner will be discussed in the next section.

3 Periodic Arrangement of the Sources

In the special case that the sources are arranged in an equi-distant array, the configuration of the holographic power combiner takes the simple form of Fig. 2(a) where the hologram is realized using a dielectric periodic structure. This is due to the fact that the holographic image of a periodic arrangement of sources is periodic as well [4].

Since the wave issuing from the periodic structure shown in Fig. 2(a) consists of a set of discrete plane waves, the optimum design of this spatial power combiner is the one which maximizes the power in the perpendicular component (i.e. $m = 0$ in Fig. 2(a)). In [5], we have developed an equivalent network for modeling the energy transfer between the modes of input waveguides and each component m of the radiated wave, i.e. the space harmonics. In this model, which is depicted in Fig. 2(b), ideal TEM transmission lines are used to model the propagation of different space harmonics, whereas two multi-port networks \mathcal{N}_A and \mathcal{N}_H model the function of the horn array and the hologram, respectively. The analysis of this network yields the voltages and currents (V_m, I_m) on each transmission line and consequently the power contained in each space harmonic. Using the above analysis in an optimization algorithm, we can determine the physical parameters of the power combiner in a way that the largest possible portion of the power injected into the input waveguides is transferred to the zeroth space harmonic, so that the spatial power combining will be optimal. In the next section, the results obtained from such an optimization process will be presented.

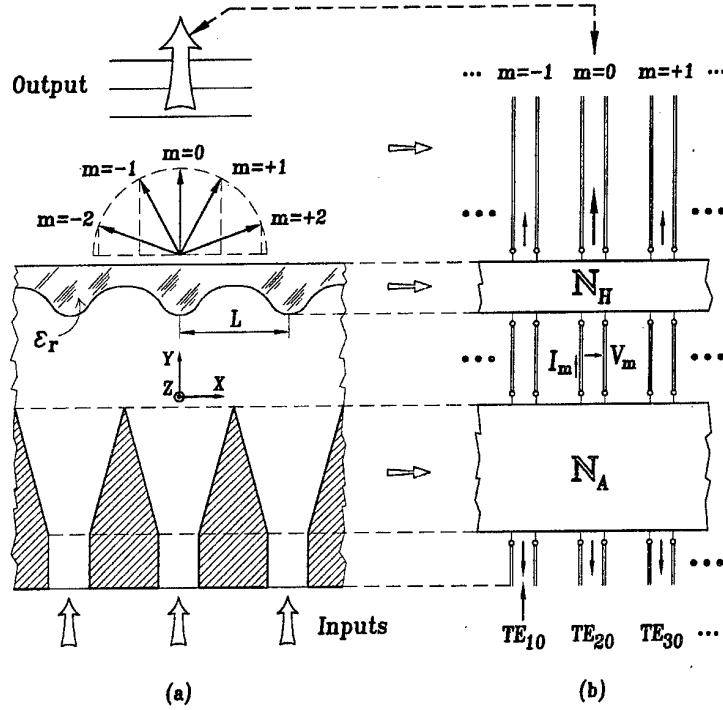


Fig. 2: (a) A holographic power combiner consisting of an array of horn antennas and a dielectric periodic structure. (b) An equivalent network for modeling the energy transfer between the waveguide modes and the transmitted space harmonics.

4 General Characteristics of a Holographic Power Combiner

The diagrams of Figs. 3(a) and (b) illustrate the values to be expected for the combining efficiency and bandwidth for an optimized holographic power combiner as a function of the normalized inter-element spacing, i.e. L/λ_o , (see Fig. 2(a)), where λ_o denotes the free-space wavelength. For each marked point in these diagrams, the optimum structure of the power combiner has been found by assuming a simple rectangular groove shape for the periodic structure. As can be seen, a combining efficiency of better than 97% and a bandwidth of larger than 11% can be maintained by the power combiner independent of the spacing L/λ_o . This leads to one of the notable features of our method, i.e. its scalability up to very high frequencies.

Fig. 3(c) demonstrates the impact of the optimum hologram on the radiation pattern of a single element of the array. $|F_2|$ is this pattern in the absence of the hologram, while $|F_1|$ clearly shows the effect of the hologram on this pattern. Note that the hologram reduces the radiation in the directions of the grating lobes ($\text{azimuth} = \sin^{-1}(m\lambda_o/L)$) to zero. As a result, the radiation pattern of the array seen in Fig. 3(d) does not suffer from grating lobes, no matter how many of the antennas are used for power combining. That is to say, the failure of the end oscillators does not cause any serious degradation in the operation of the power combiner, or equivalently, its design does not depend on the number of sources.

Another remarkable feature of the proposed method is the possibility of parallel coupling of sources. Since in parallel coupling each source affects all others with the same coupling coefficient, the oscillators lock on to each other very tightly and a stable mutual synchronization will be established. As shown in [7], to realize this type of coupling, one can add a semi-transparent reflector to the output side of the power combiner to reflect a portion of the sum beam. The reflected wave will be split by the hologram and injected into the input waveguides. If the number of oscillators gets very large, the value of coupling coefficients tends to be equal for all input ports.

5 Conclusions

This paper has reviewed the basic characteristics of holographic power combining at very high frequencies. It has been shown that regarding the scalability, high efficiency, broad-band character, and flexibility in both orientation and number of sources the proposed method can become the favorite candidate for millimeter and submillimeter-wave applications.

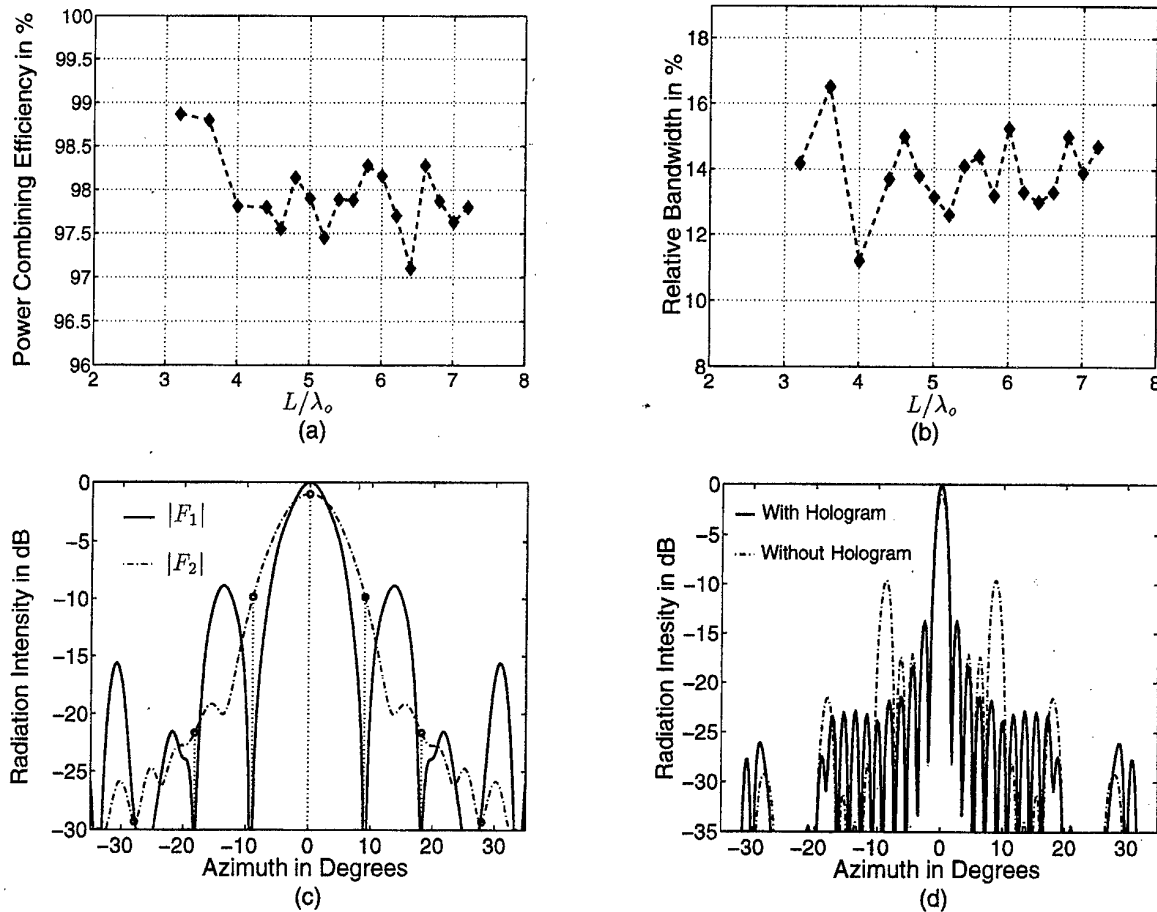


Fig. 3: Achieved combining efficiency (a) and bandwidth (b) for the power combiner shown in Fig. 2. The influence of the periodic structure on the element (c) and array (d) radiation pattern.

Acknowledgment

The authors wish to thank the Deutsche Forschungsgemeinschaft for financial support of this work.

References

- [1] K. Chang and C. Sun, "Millimeter-wave power-combining techniques," *IEEE Trans. Microwave Theory Tech.*, vol. MTT-31, pp. 91–107, Feb. 1983.
- [2] L. Wandinger and V. Nalbandian, "Millimeter-wave power combiner using quasi-optical techniques," *IEEE Trans. Microwave Theory Tech.*, vol. MTT-31, pp. 189–193, Feb. 1983.
- [3] K. D. Stephan, "Inter-injection-locked oscillators for power combining and phased arrays," *IEEE Trans. Microwave Theory Tech.*, vol. MTT-34, pp. 1017–1025, Oct. 1986.
- [4] M. Shahabadi and K. Schünemann, "Holographic power combining: A new principle for millimeter and submillimeter-wave power combining," in *Proc. 26th European Microwave Conf.*, Prague, Czech Republic, Sept. 9–12, 1996, pp. 115–119.
- [5] M. Shahabadi and K. Schünemann, "Millimeter-wave holographic power splitting/combining," *IEEE Trans. Microwave Theory Tech.*, vol. MTT-45, pp. 2316–2323, Dec. 1997.
- [6] H. M. Smith, *Principles of Holography*, 2nd ed. New York: Wiley, 1975.
- [7] M. Shahabadi, *Application of Holography to Millimeter-Wave Power Combining*, Ph.D. Dissertation (in German), Technische Universität Hamburg-Harburg, 1998.

InP TRANSFERRED ELECTRON DEVICES FOR POWER GENERATION AT FREQUENCIES ABOVE 130 GHz

R. JUDASCHKE AND K. SCHÜNEMANN

Arbeitsbereich Hochfrequenztechnik, Technische Universität Hamburg-Harburg,
Wallgraben 55, D-21071 Hamburg, Germany,
Phone +49 40 7718-2746, FAX +49 40 7718-2755, E-mail judaschke@tu-harburg.de

Abstract— InP Gunn devices of modulated impurity profile have been theoretically investigated for fundamental- and harmonic-mode operation at frequencies above 130 GHz. The results are based on an efficient and accurate hydrodynamic simulator which analyzes the device for impressed terminal voltages and in practical oscillator circuits. In comparison with state-of-the-art graded profile diodes, improved performance is demonstrated for both modes of operation. Especially for power generation above 200 GHz, the proposed modulated impurity concentration diodes are expected to be advantageous in comparison with Si IMPATT diodes.

Introduction:

At millimeter-wave frequencies, there is a growing interest in low-noise solid-state oscillators for applications as transmitters in high-resolution radars, local oscillators, and drivers for multipliers. Typical state-of-the-art RF output power levels of different types of oscillators are depicted in Fig. 1. InP Gunn devices operating in the fundamental- and second-harmonic mode have shown to be suitable for the generation of low-noise oscillations at frequencies up to 170 GHz [1], [2]. However, the performance of Gunn oscillators at higher frequencies is still limited (e. g. less than 1 mW beyond 250 GHz [3], [4]). Thus, for power generation at frequencies above 170 GHz either multipliers or Silicon IMPATT oscillators are used. The latter exhibit poor phase noise characteristics. In this contribution, the performance of InP Gunn devices in both fundamental- and harmonic-mode operation is theoretically investigated. Special emphasis is attached to the influence of different doping profiles as well as the harmonic-mode driving voltage-to-phase relationship on the overall device performance.

Active device model:

Due to the small characteristic device dimensions, nonstationary transport effects become significant in the millimeter-wave region. Hence, the drift-diffusion equations are often inappropriate and instead, hydrodynamic (HD) models or Monte Carlo (MC) methods are applied. However, the main drawback of the latter methods is their large computational effort. Thus, the hydrodynamic model is a compromise between accuracy and computational efficiency.

In the present work, a hydrodynamic device simulator which carefully includes effects of thermal energy as well as diffusive heat flow [5] has been applied. The steady-state transport coefficients have been calculated by a MC simulation. The solution of the resulting system of partial differential equations is accomplished by a fully implicit, decoupled, yet unconditionally stable finite-difference scheme. Results of the present model closely agree with those of several MC simulations as well as with measured results of Gunn oscillators in the millimeter-wave region. In order to investigate the device properties in dependence of the impurity variation, extensive simulations are necessary. These are performed under impressed voltages at the device terminal according to

$$V(t) = V_0 + V_1 \sin(2\pi f_1 t) + V_2 \sin(2\pi f_2 t + \varphi),$$

and under realistic load impedance conditions as well.

Gunn devices:

Typical doping profiles under investigation are shown in Fig. 2. Since the time required for the evolution of the electron charge instability is comparable to the average transit time, Gunn devices for fundamental-mode operation are limited in length to approximately 1 μ m which is the common active length of all devices in the present analysis. Furthermore, the doping shows a linear increase from cathode to anode in order to stimulate the electron charge instability to grow. As a modification of this graded doping profile which has been successfully designed, fabricated, and tested around 130 GHz in [1], a doping notch at the cathode and/or a doping mesa located in the center of the active region have been added. The former creates an above-threshold electrical field near the cathode which insures exclusive nucleation and launching of dipole layers from the cathode, whereas the latter results in a modulation of the strong fundamental current oscillation in order to produce a higher quantity of harmonic output power [6].

The diameter of the different devices is adjusted to result in equal DC-power dissipation for given AC-conditions, and the device temperature is assumed to be 400 K.

Results:

For each doping profile shown in Fig. 2, both fundamental- and harmonic-mode simulations have been performed. Fig. 3 shows RF output power, diode efficiency, and device impedance for fundamental-mode operation. Taking into account the inclusion of series losses (Fig. 6), the output power for the graded profile (solid line) is in close agreement with the measured results in [1]. Furthermore, Fig. 3 clearly depicts the increase in RF power and efficiency for the modified profiles. The charge instability evolution over one period of oscillation for the graded profile and mesa profile, respectively, is illustrated in Fig. 4. In comparison, premature instability appearance can be observed for the mesa profile which is advantageous for RF power generation. Finally, the steady-state voltage/current characteristic of a free-running oscillator with single-resonant load impedance has been calculated for a fixed DC voltage (Fig. 5). The fundamental output power of 240 mW is in slight agreement with the result for impressed conditions (Fig. 3).

For harmonic-mode operation, power extraction at 260 GHz can be expected only in a limited range of the phase angle φ , as shown in Fig. 7. Thus, a careful adjustment of the load impedance at both fundamental and harmonic frequency has to be fulfilled. As an additional result, higher harmonic power levels are corresponding to mesa profiles, the harmonic device resistance of which is larger in magnitude in comparison to that of the graded profile. This is an important result since series losses due to bulk resistance and skin effect are responsible for a dramatic degradation of the power generation capability at frequencies above 150 GHz (Fig. 6). The charge instability evolution in Fig. 8 indicates that the dipole is modulated as it drifts through the doping mesa what confirms the appearance of a higher quantity of harmonic output power. Finally, in Fig. 9, graded and mesa profile devices are compared as a function of the 2nd-harmonic voltage V_2 .

Conclusions:

InP Gunn devices of various doping profiles have been theoretically investigated for fundamental- and harmonic-mode operation at frequencies up to 260 GHz. The results are based on an efficient and accurate hydrodynamic simulator which analyzes the device under impressed terminal voltage conditions. In comparison with state-of-the-art graded profile diodes, improved performance is demonstrated for modulated impurity-concentration devices for both modes of operation.

Acknowledgement:

The authors are indebted to M. Curow for helpful discussions and to D. Liebig for supplying the steady-state transport coefficients.

References

- [1] Eisele, H., Haddad, G.I., "High-Performance InP Gunn Devices for Fundamental-Mode Operation in D-Band (110–170 GHz)," *IEEE Microwave and Guided Wave Letters*, vol. 5, Nov. 1995, pp. 385–387.
- [2] Crowley, J.D. et al. "140 GHz Indium Phosphide Gunn Diode," *Electronics Letters*, vol. 30, No. 6, Mar. 1994, pp. 499–500.
- [3] Eisele, H., Haddad, G.I., "D-band InP Gunn Devices with Second-Harmonic Power Extraction up to 290 GHz," *Electronics Letters*, vol. 30, No. 23, Nov. 1994, pp. 1950–1951.
- [4] Rydberg, A., "High Efficiency and Output Power from Second- and Third-Harmonic Millimeter-Wave InP-TED Oscillators at Frequencies above 170 GHz," *IEEE Electron Device Letters*, vol. EDL-11, Oct. 1990, pp. 439–441.
- [5] Curow, M., "Konsistente Simulation von Millimeterwellen-Oszillatoren mit Gunn-Elementen und IMPATT-Dioden," Ph. D. thesis, Technical University of Hamburg–Harburg, Hamburg, Germany, Mar. 1996.
- [6] Jones, S.H., Tait, G.B., Shur, M., "Modulated-Impurity-Concentration Transferred-Electron Devices Exhibiting Large Harmonic Frequency Content," *Microwave and Optical Technology Letters*, vol. 5, No. 8, Jul. 1992, pp. 354–359.

Figures

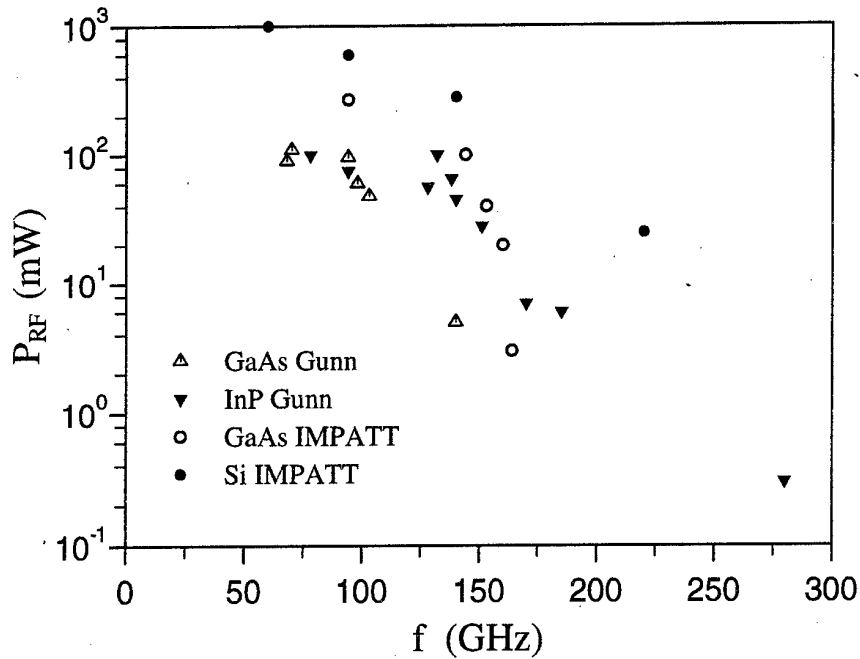


Fig. 1: CW output power of state-of-the-art millimeter-wave solid-state oscillators.

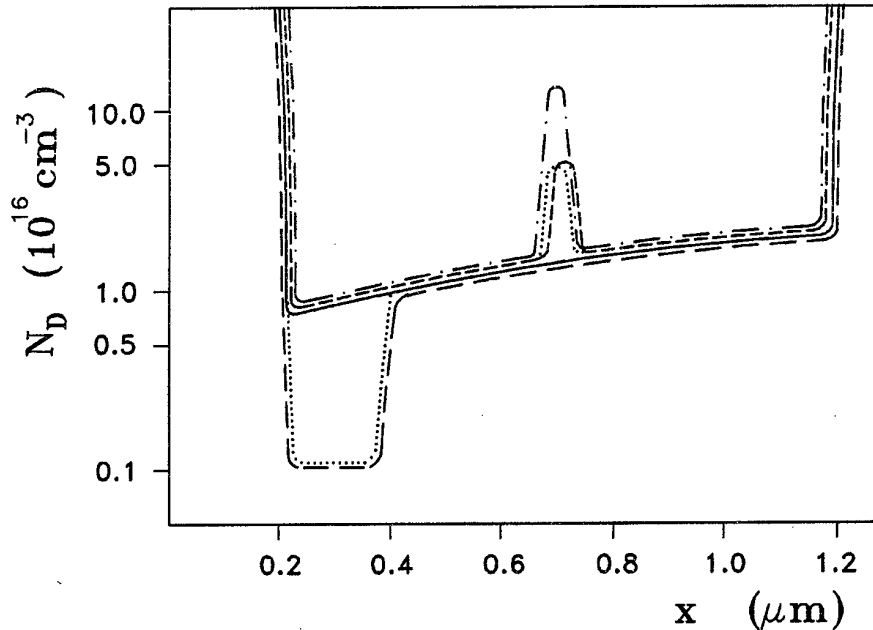


Fig. 2: Doping profiles under investigation: Graded profile (—) [3], cathode notch profile (---), mesa profiles (- - -), (- · - -), combination of cathode notch and mesa profile (· · · · ·).

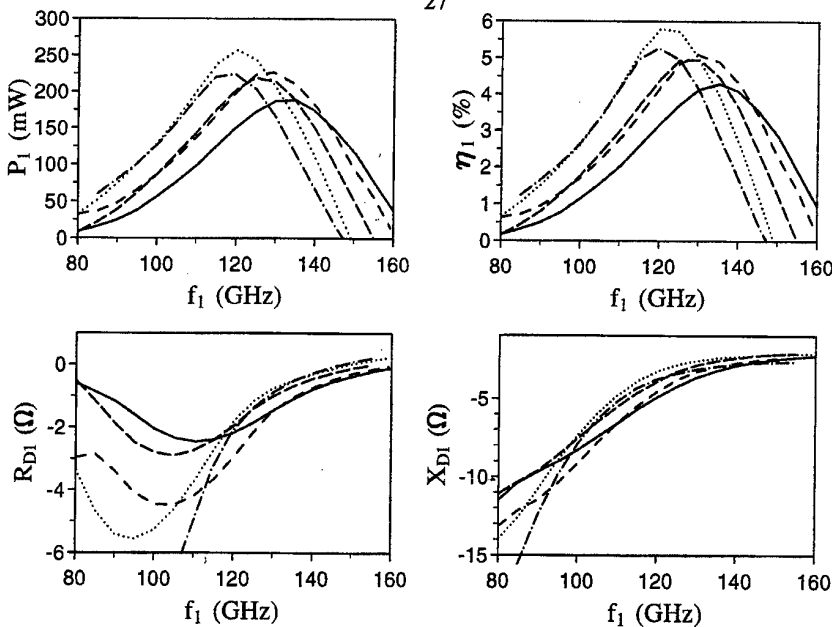


Fig. 3: Fundamental-mode operation, impressed terminal voltages $V_0 = 4.5$ V, $V_1 = 2.0$ V, doping profiles as defined in Fig. 2.

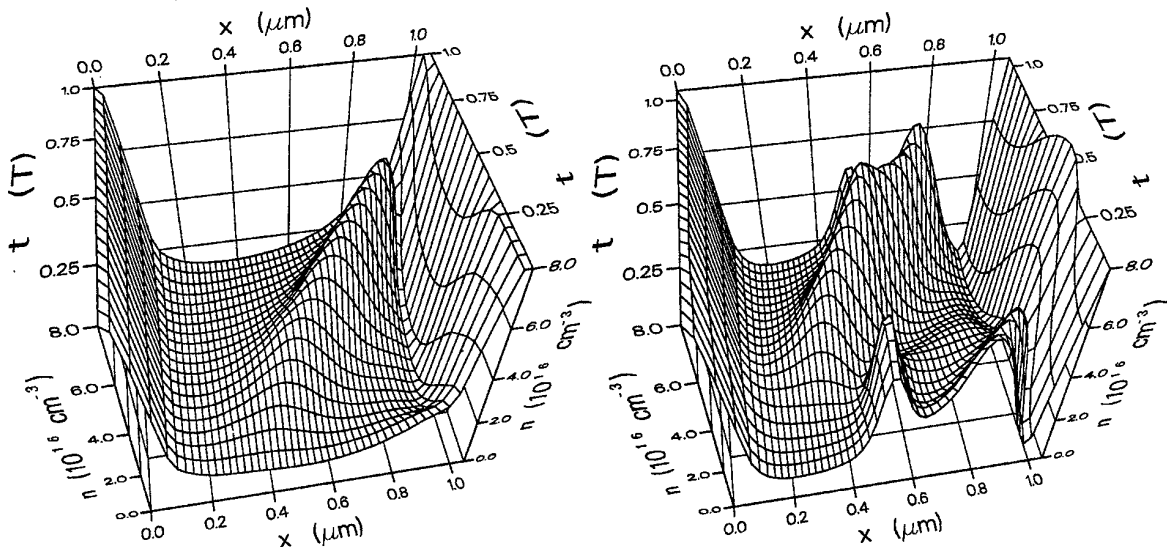


Fig. 4: Electron density evolution over one period for graded profile (—) [3] (left plot) and mesa profile (---) (right plot), fundamental-mode operation, impressed terminal voltages $V_0 = 4.5$ V, $V_1 = 2.0$ V.

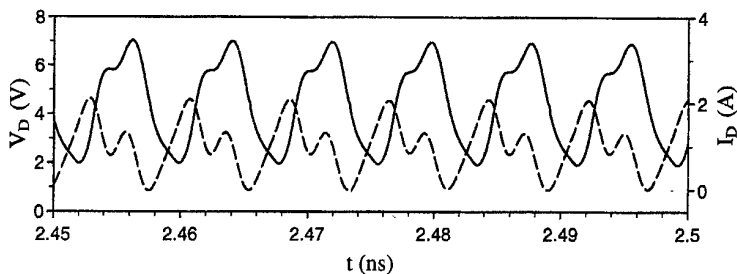


Fig. 5: Steady-state terminal voltage (—) and current (---) characteristics of a Gunn-oscillator with single-resonant load impedance, $f_1 = 128$ GHz, $P_1 = 240$ mW, $V_0 = 4.4$ V, $I_0 = 1.0$ A, mesa doping profile as defined by (----) in Fig. 2.

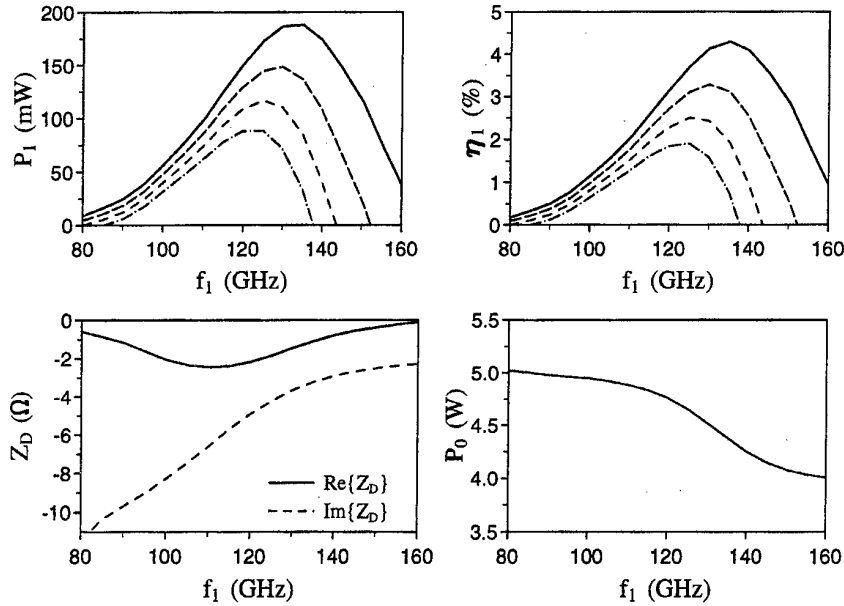


Fig. 6: Degradation of diode performance due to series losses: Fundamental-mode operation, impressed terminal voltages $V_0 = 4.5$ V, $V_1 = 2.0$ V, graded diode profile (—) [3] as defined in Fig. 2, $R_s = 0.0 \Omega$ (—), $R_s = 0.3 \Omega$ (— · —), $R_s = 0.6 \Omega$ (— · — · —), and $R_s = 0.9 \Omega$ (— · — · — · —).

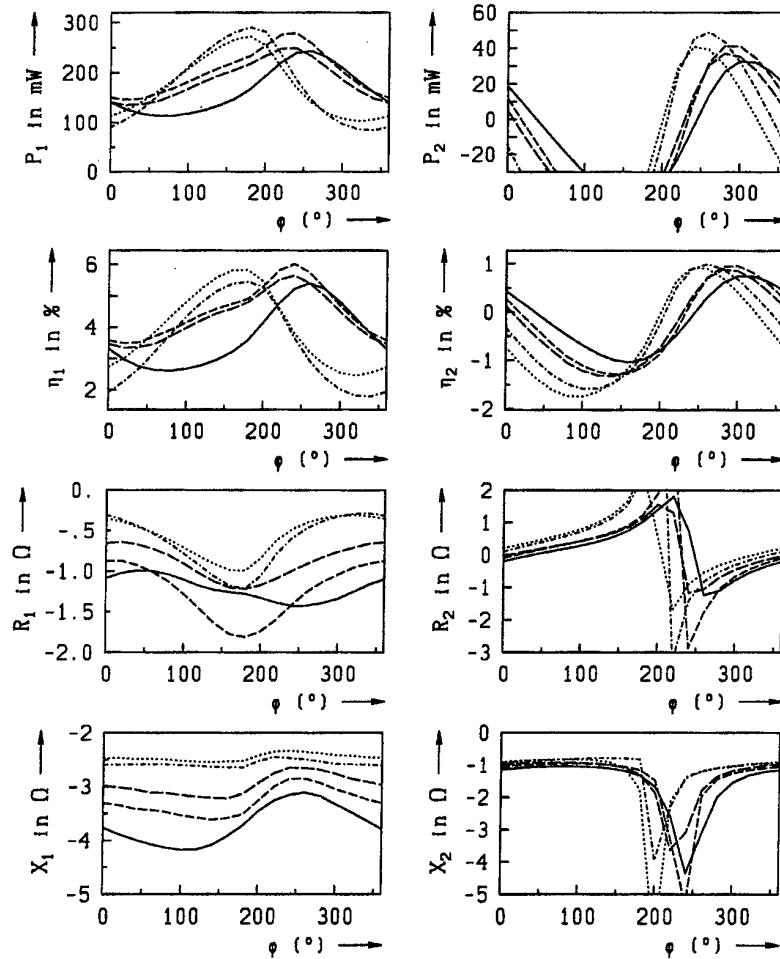


Fig. 7: Harmonic-mode operation $f = 130/260$ GHz, impressed terminal voltages $V_0 = 4.5$ V, $V_1 = 2.0$ V, $V_2 = 0.5$ V, doping profiles as defined in Fig. 2.

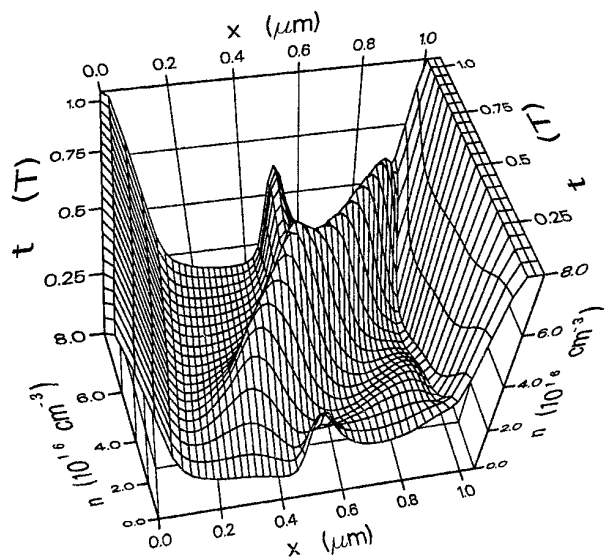


Fig. 8: Harmonic-mode, impressed terminal voltages $V_0 = 4.5$ V, $V_1 = 2.0$ V, $V_2 = 0.5$ V, $\varphi = 260^\circ$.

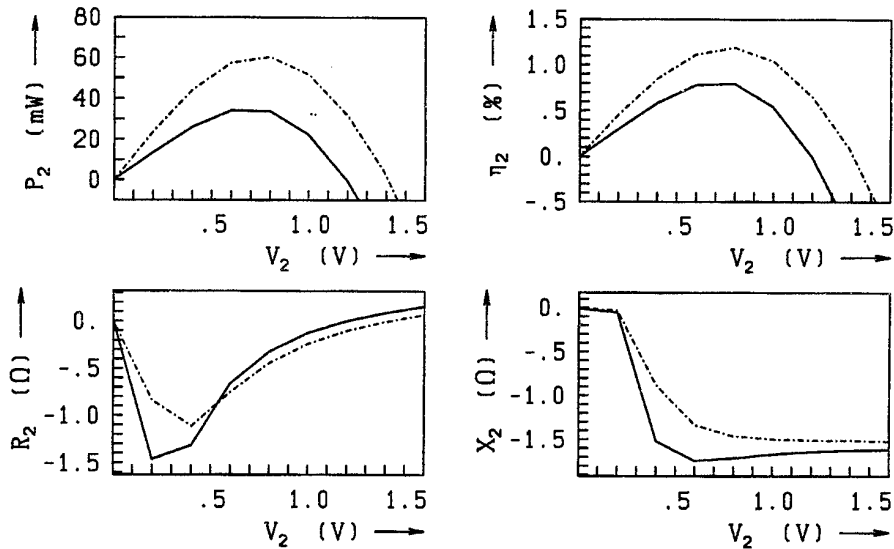


Fig. 9: Harmonic-mode operation $f = 130/260$ GHz, impressed terminal voltages $V_0 = 4.5$ V, $V_1 = 2.0$ V, graded profile (—) $\varphi = 290^\circ$, mesa profile (---), $\varphi = 260^\circ$.

**TRANSITION RADIATION OF CHARGED PARTICLES
AND THE POSSIBILITY OF SUBMILLIMETER WAVES
GENERATION IN THE SEMICONDUCTOR STRUCTURES**

V. M. Yakovenko

Institute for Radiophysics and Electronics of National Academy of Sciences of Ukraine,
12 Acad. Proscura St., Kharkov, 310085, Ukraine
Tel. (380)572-441129, Fax (380)572-441105, E-mail: yakovenko@ire.kharkov.ua

Abstract

The hamiltonian of an interaction of charged particles with surface plasmons on the basis of elementary effects of the transition radiation of a charge in inhomogeneous media has been found. A kinetic equation has been set up for surface plasmons, the conditions of arising of the instability (generation) at their interaction with an electron flow and a value of the increment in the submillimeter wave range have been determined.

1. Introduction

Mastering of the short-wave region of millimeter and submillimeter electromagnetic wave range is a very important problem of the modern solid state electronics. There are two different approaches to the solution of this problem and both of them have brought essential results. From the side of the low frequencies the investigations are carried out to improve parameters of Gunn diodes, avalanche-transit diodes and transistors. Besides, one can deal with a number of other physical phenomena which result from both the electron plasma heating by external fields and the Josephson effect. In the high frequency region there are attempts to use the laser principle for generation and amplification of the electromagnetic waves. It is based on the particle transitions between energy levels in the inverted system. However this idea was successfully realized in the semiconductor lasers.

I should like to point out the possibility of using charged particle transition radiation for generation of electromagnetic waves (oscillations) on the frequencies about 10^{14} Hz.

2. The physical model investigated

It is well known that the charged particle radiates an electromagnetic field when it crosses the boundary between the media of different electromagnetic properties.

The radiation mechanism lies in the following. The electromagnetic field connected with particle depends not only on the radiator properties but also on the properties of medium. Therefore, at the boundary between two media the reconstruction of the field takes place and the part of this field breaks away from the particle. Then a free field arises. This field can be an eigen oscillation of system. So, the kinetic energy of the particles can be transformed into energy of oscillations of the system. The opposite process exists also. It is clearly that instability (generation) of eigen oscillations can arise if the first process prevails over the second one. As such process of mutual transformation (exchange) of the energy of the waves and the particles takes place on the two-media interface it is more advisable to investigate the interaction particles with surface oscillations (surface plasmons).

Let a semiconductor occupy the space region $y > 0$ and vacuum (dielectric with ϵ_1) is at $y < 0$. It follows from Maxwell equations and boundary conditions that there are the surface electromagnetic oscillations with spectrum

$$q^2 = \frac{\omega^2}{c^2} \frac{\epsilon_1 \epsilon_2}{\epsilon_1 + \epsilon_2}; \quad \epsilon_2 \equiv \epsilon_2(\omega) = \epsilon_0 - \frac{\omega_0^2}{\omega^2}; \quad \epsilon_2(\omega) < 0, \quad \epsilon_1 > 0, \quad (1)$$

where ω is the frequency of plasmon, q is the wave vector along the surface, $\omega_0 = (4\pi e^2 n_0 / m)^{1/2}$ is the plasma frequency; n_0 is the electron concentration, m is the effective mass of electron, ϵ_0 is the dielectric constant of a crystal lattice of the semiconductor (semimetal). If $c \rightarrow \infty$, the dispersion law is $\omega = \omega_0 / \sqrt{\epsilon_0 + \epsilon_1}$.

Suppose further that an external flow of charged particles (free electrons) passes through the dielectric-semiconductor interface.

Most simply and clearly one can describe their interaction with surface plasmons in the representation of the second quantization.

Hamiltonian of the system have got the following appearance:

$$\hat{\mathcal{H}} = \hat{\mathcal{H}}^{(F)} + \hat{\mathcal{H}}^{(e)} + \hat{\mathcal{H}}^{(int)}, \quad (2)$$

where $\hat{\mathcal{H}}^{(F)} = \frac{1}{2} \sum_q \hbar \omega_q [\hat{a}_q^\dagger(t) \hat{a}_q(t) + \hat{a}_q(t) \hat{a}_q^\dagger(t)]$ is the hamiltonian of electromagnetic field (surface plasmons), $\hat{\mathcal{H}}^{(e)} = \sum_k \mathcal{E}_k \hat{b}_k^\dagger(t) \hat{b}_k(t)$ is the hamiltonian of a electron system; $\mathcal{E}_k = \hbar^2 k^2 / 2m$ is the dispersion law of electrons; \mathbf{k} is the wavevector of the electron; $\hat{a}_q^\dagger(t) = \hat{a}_q^\dagger \exp(i\omega_q t)$, $\hat{a}_q(t) = \hat{a}_q \exp(-i\omega_q t)$, $\hat{b}_k^\dagger(t) = \hat{b}_k^\dagger \exp(i\mathcal{E}_k t / \hbar)$, $\hat{b}_k(t) = \hat{b}_k \exp(-i\mathcal{E}_k t / \hbar)$, \hat{a}_q^\dagger , \hat{a}_q , \hat{b}_k^\dagger , \hat{b}_k are the creation and annihilation operators for the plasmons and the electrons in the states \mathbf{q} and \mathbf{k} ;

$$\hat{\mathcal{H}}^{(int)} = \sum_{k'qk'} W_{k'qk'} \hat{b}_k^\dagger(t) [\hat{a}_q(t) + \hat{a}_{-q}^\dagger(t)] \hat{b}_{k'}(t) \quad (3)$$

is the hamiltonian of the electron-plasmon interaction.

To find the expression for the matrix element $W_{k'qk'}$ it is necessary to use the expression

$$\hat{\mathcal{H}}^{(int)} = -\frac{1}{c} \sum_{\alpha=1}^2 \int \hat{\mathbf{j}}(\mathbf{r}, t) \hat{\mathbf{A}}_\alpha(\mathbf{r}, t) d\mathbf{r}, \quad (4)$$

where

$$\hat{\mathbf{j}}(\mathbf{r}, t) = \frac{e\hbar}{2m_0 V} \sum_{\mathbf{k}, \mathbf{k}'} (\mathbf{k} + \mathbf{k}') \hat{b}_k^\dagger(t) \hat{b}_{k'}(t) \exp i(\mathbf{k}' - \mathbf{k}) \mathbf{r}$$

is the operator of an electron current density,

$$\hat{\mathbf{A}}_\alpha(\mathbf{r}, t) = \sum_{\mathbf{q}} \left(\frac{4\pi\hbar c^2}{V\omega_q} \right)^{1/2} \mathbf{e}_\alpha [\hat{a}_q(t) + \hat{a}_{-q}^\dagger(t)] e^{i\mathbf{q}_\alpha \cdot \mathbf{r}}$$

is the operator of the vector-potential of the surface wave electromagnetic field; \mathbf{e}_α is the unit of the polarization vectors: $e_x = e_{1x} = e_{2x} = (q_x / |q|) \sqrt{L|q| / (\epsilon_1 + \epsilon_0)}$, $e_{1y} = -e_{2y} = ie_x$, $e_z = (q_z / q_x) e_x$, $\mathbf{q}_{1,2} = (q_x, \mp iq, q_z)$, $V = LS$ is the volume of the interaction space, S is the cross-section of the sample.

The peculiarity of this matrix element consists in that the conservation laws of momentum are fulfilled only along the interface plane (the axis Ox , Oz).

3. Results and discussion

Carrying out the standard procedure [1,2] we obtain the following kinetic equation which describes the change of the surface plasmon number N_q as the result of their radiation and absorption with the electrons n_k

$$\frac{\partial N_q}{\partial t} = \frac{2\pi}{\hbar} \sum_{\mathbf{k}_1 \mathbf{k}_2} |W_{\mathbf{k}_1 \mathbf{q} \mathbf{k}_2}|^2 [(N_q + 1)n_{\mathbf{k}_1}(1 - n_{\mathbf{k}_2}) - N_q n_{\mathbf{k}_2}(1 - n_{\mathbf{k}_1})] \delta(\mathcal{E}_{\mathbf{k}_1} - \mathcal{E}_{\mathbf{k}_2} - \hbar\omega_{\mathbf{q}}), \quad (5)$$

where [2]

$$W_{\mathbf{k}_1 \mathbf{q} \mathbf{k}_2} = \frac{q_x(k_1^2 - k_2^2)}{m_0 L |q_x| [q^2 + (k_{1y} - k_{2y})^2]} \left(\frac{2\pi e^2 q \hbar^3}{S \omega_q (\epsilon_0 + \epsilon_1)} \right)^{1/2}. \quad (6)$$

From here for $N_q \gg 1$ we shall obtain the expression for the decrement or increment of the surface plasmons $\gamma = (1/2)N_q^{-1}(\partial N_q / \partial t)$;

Suppose that injected electron energy is distributed near some value $\mathcal{E}_{k0} = p_0^2 / 2m_0 = \hbar^2 k_o^2 / 2m_0$. Then one can present the electron number $n_k \ll 1$ as

$$n_k = \frac{n_{0b} (2\pi\hbar)^3}{(2\pi m_0 T)^{3/2}} e^{-\frac{\hbar^2 (k_y - k_0)^2}{2m_0 T}} e^{-\frac{\hbar^2 (k_x^2 + k_z^2)}{2m_0 T}}, \quad (7)$$

where $n_{0b} = \sum n_k / V = \int n_k d\mathbf{k} / (2\pi)^3$ is the density, T is the temperature of the electrons beam.

If conditions $\frac{\hbar^2 k_0^2}{2m_0} \gg T, \hbar\omega \gg T$ are fulfilled then one can consider $T = 0$ and $n_k = (2\pi)^3 n_{0b} \delta(k_x) \delta(k_y - k_x) \delta(k_z)$.

After the integration of equation (5) over the wave vectors \mathbf{k}_1 and \mathbf{k}_2 one can obtain the following expressions for the growth rate of the instability of the surface plasmons

$$\gamma = \frac{2n_{0b} VLm_0}{\hbar^3} \left[\frac{|W_-|^2 + |W'_-|^2}{k_-} - \frac{|W_+|^2 + |W'_+|^2}{k_+} \right], \quad (8)$$

where $k_{\pm} = \sqrt{k_0^2 - q^2 \pm 2m_0\omega_q/\hbar} > 0$, $W_{\pm} = W_{k_1 q k_2}(k_{x1} = k_{z1} = 0; k_{y1} = k_0; k_{2x} = q_x; k_{y2} = \pm k_0; k_{2x} = q_z)$, $W'_{\pm} = W_{\pm}(-k_{\pm})$. At here it is necessary that $\gamma > \nu$, where ν is the frequency of electron collisions.

The value $|W_{\pm}|^2$ describes the probability of the transition from the state " k_0 " to the state " k_{\pm} " (the scattering "forward" of the particles with absorption (+) or radiation (-) of quantum); W'_{\pm} describes the scattering "backward", respectively. If $k_0^2 \gg q^2 + 2m_0\omega_q/\hbar$ we have:

$$(k_{\pm} - k_0)^2 \sim \frac{\omega_q^2}{v_0^2}; \quad \frac{W_+^2}{W_-^2} = 1; \quad |W_{\pm}|^2 \gg |W'_{\pm}|^2 \quad \text{and}$$

$$\gamma \approx \frac{4\omega_b^2 \omega_q^2 q v_0}{(\omega_q^2 + q^2 v_0^2)^2}; \quad \omega_b^2 = \frac{4\pi e^2 n_{0b}}{m_0(\epsilon_0 + \epsilon_1)}. \quad (9)$$

One can see that the increment has maximum $\gamma_{max} = \frac{3}{4} \frac{\omega_b^2}{q v_0}$ at the condition $\omega_q^2 = 3q^2 v_0^2$.

Thus, when the directed electron beam interacts with the surface plasmons the induced radiation processes dominate over the absorption ones and the oscillations become instable at the condition $\frac{p_0^2}{2m} \gg \hbar\omega_q \gg T$. This is due to the fact that the probability for the electron to pass to the state with a smaller energy exceeds the probability to pass to the state with a grater energy. In the former case the probability is proportional to k_-^{-1} , in the latter case it is proportional to k_+^{-1} . This mechanism of the instability of the oscillations takes place at the different inhomogeneous solid state structures: semiconductor superlattice [3], two-dimensional gas [4], and others [5].

The instability increment can also be obtained by using the formula for the energy losses of the particle passing through the interface of two media to the excitation of the surface plasmons (the effect of the transition radiation [6]). Let us start from the following equations

$$\text{rot} \vec{\mathbf{E}}(\vec{\mathbf{r}}, t) = 0; \quad \text{div} \vec{\mathbf{D}}(\vec{\mathbf{r}}, t) = 4\pi e \delta(x) \delta(y - v_0 t) \delta(z) \quad (10)$$

$$\vec{\mathbf{D}}(\vec{\mathbf{r}}, t) = \int_{-\infty}^t \hat{\epsilon}(t - t') \vec{\mathbf{E}}(\vec{\mathbf{r}}, t') dt',$$

where

$$\hat{\epsilon} = \begin{cases} \epsilon_1 \delta(t - t') & y < 0 \\ \epsilon_2 \delta(t - t') & y > 0 \end{cases}$$

e is the charge, v_0 is the particle velocity moving along the positive direction of axis y and crossing the boundary $y = 0$ at the time moment $t = 0$. Using the Fourier expansion

$$\mathbf{E}(\vec{\mathbf{r}}, t) = \sum_{q_x, q_z} \int_{-\infty}^{\infty} \mathbf{E}(\omega, \vec{\mathbf{q}}, y) \exp[i(\vec{q}\vec{r} - \omega t)] d\omega$$

we obtain the expression for the field components in each medium as

$$E_{1x}(\omega, \vec{\mathbf{q}}, y) = A_1 \exp(qy) - \frac{B}{\epsilon_1} \exp(i\frac{\omega}{v_0}y), \quad y < 0,$$

$$E_{2x}(\omega, \vec{\mathbf{q}}, y) = A_2 \exp(-qy) - \frac{B}{\epsilon_2} \exp(i\frac{\omega}{v_0}y), \quad y > 0,$$

$$E_{1,2y}(\omega, \vec{q}, y) = -\frac{i}{q_x} \frac{\partial E_{1,2x}(\omega, \vec{q}, y)}{\partial y}; \quad E_{1,2z}(\omega, \vec{q}, y) = \frac{q_z}{q_x} E_{1,2x}(\omega, \vec{q}, y), \quad (11)$$

where $B = i \frac{2e q_x v_0}{S(\omega^2 + q^2 v_0^2)}$, $q = \sqrt{q_x^2 + q_z^2}$, $\varepsilon_2(\omega) = \int_0^\infty \hat{\varepsilon}_2(\tau) \exp(i\omega\tau) d\tau$, $S = L_x L_z$, $q_{x,z} = 2\pi n_{x,z}/L_{x,z}$; $n_{x,z}$ are the integer numbers.

From the boundary conditions we find

$$A_1 = \frac{B}{\varepsilon_1} \frac{\varepsilon_2 - \varepsilon_1}{\varepsilon_1 + \varepsilon_2}, \quad A_2 = -\frac{\varepsilon_1}{\varepsilon_2} A_1. \quad (12)$$

The energy losses of the particle on the excitation of the surface oscillations representing the solution of the homogeneous equation are written as follows

$$\Delta\mathcal{E} = ev_0 \left\{ \int_{-\infty}^0 E_{1y}(\vec{r}, t) dt + \int_{-\infty}^0 E_{2y}(\vec{r}, t) dt \right\} \quad (13)$$

Here the field value is taken at the point of finding the particle $x = 0$, $y = v_0 t$, $z = 0$. As a result of integration (13) we obtain ($\omega_q^2 \gg q^2 v_0^2$)

$$\Delta\mathcal{E} = \sum_{q_x, q_z} \Delta\mathcal{E}_q, \quad \Delta\mathcal{E}_q = -\frac{8\pi e^2 v_0^2 q}{S(\varepsilon_0 + \varepsilon_1) \omega_q^2}. \quad (14)$$

Taking into account that the time of the particle transit τ through the whole system is equal to $\tau = L/v_0$, we find the average value of the energy losses of the particle in a unit time

$$\frac{d\mathcal{E}_q}{dt} = \frac{\Delta\mathcal{E}_q}{\tau}. \quad (15)$$

This value (with an opposite sign) can be considered as the spontaneous radiation of the surface plasmons N_q in unit time

$$\hbar\omega_q \frac{\partial N_q}{\partial t} = -\frac{d\mathcal{E}_q}{dt}. \quad (16)$$

On the other hand, it is possible to make the kinetic equation of the following form for plasmon number (6). Hence at $N_q \rightarrow 0$, $n_k^0 = \delta_{kk_0}$, $\vec{k}_0 = (0, k_0, 0)$ we obtain:

$$\frac{\partial N_q}{\partial t} = \frac{2Lm_0}{\hbar^3} \int_0^\infty |W_{k_0 q k}|^2 \delta(k_0^2 - k_y^2 - \frac{2m_0 \omega}{\hbar}) dk_y = \frac{Lm_0 |W_{k_0 q k_-}|^2}{\hbar^3 k_-}, \quad (17)$$

$$\text{where } k_- = \sqrt{k_0^2 - \frac{2m\omega}{\hbar}}.$$

The integration is carried out with the positive values k'_y for the comparison with (17) it is necessary to take into account only the process of electron scattering "forward" as the particle moves along. If we take the case $k_0^2 \gg 2m\omega/\hbar$ and use equality (17) then $|W_{k_0 q k}|$ takes on the form

$$|W_{k_0 q k}| = \left(\frac{8\pi e^2 v_0^4 \hbar q}{LV \omega_q^3 (\varepsilon_0 + \varepsilon_1)} \right)^{1/2}. \quad (18)$$

It is shown that this expression coincides with formula (7) at $|k_{1y} - k_{2y}| = \omega/v_0$ and $|k_1^2 - k_2^2| = 2m\omega/\hbar$.

4. Conclusion

Thus, when the directed electron beam crosses the boundary of plasma-like media the surface plasmons became unstable at the condition $\frac{p_0^2}{2m} > \hbar\omega_q > T$. One can show that if the conditions $\frac{p_0^2}{2m} \gg T \gg \hbar\omega_q$ are met place the absorption processes dominate over the induced processes and the surface plasmons

fade away. In this case the spontaneous radiation of the surface plasmons is interested. The power of an emission is equal to

$$\hbar\omega_q \frac{\partial N_q}{\partial t} \simeq 2m_0 q v_0^3 \frac{\omega_b^2}{\omega_q^2}. \quad (19)$$

So, $n_{0b} = 10^{11} \text{ cm}^{-3}$, $q = 10^3 \text{ cm}^{-1}$, $v_0 = 3 \cdot 10^9 \text{ cm/s}$, $\epsilon_0 = 16$, $\omega_q \sim 10^{12} \text{ s}^{-1}$, $\hbar\omega_q \frac{\partial N_q}{\partial t} \simeq 9 \cdot 10^{-8} \text{ watt}$.

These processes are very important for diagnostics of a surface of solids.

References

- [1] J.M.Ziman, *Elements of Advanced Quantum Theory*. 1971, Mir, M., 288 p.
- [2] N.N. Beletsky, V.M. Svetlichny, D.D. Khalamejda, V.M. Yakovenko, *Electromagnetic phenomena UHF in inhomogeneous semiconductor structures*, 1991, Naukova Dumka, K., 216 p.
- [3] M.V.Burtyka, O.V.Glukhov, V.M.Yakovenko, *Interaction of hot electrons with two-dimensional gas in semiconductor superlattices* Solid-State Electronics, 1991, **34**, N 6, pp. 559-564.
- [4] M.V.Burtyka, V.M.Yakovenko, I.V.Yakovenko, *Interaction of charged particle beams with plasmons in a two-dimensional electron gas*, Low Temp. Phys., 1995, **26**, N.6, pp. 489-492.
- [5] I.V.Yakovenko, *Interaction of charged particles with surface waves at periodically rough ideally conducting boundary* Radiophysics and Electronics, The collected volume of the IRE NAS Ukraine, 1998, Kharkov, **3**, N 1, pp. 7-10.
- [6] V.L.Ginzburg, V.N. Tsytovich, *Transition Radiation and Transition Scattering*, M., Nauka, 1984, 360 p.

**MEASUREMENTS OF HIGH GAIN ANTENNAS AT MILLIMETER
WAVELENGTHS USING A HOLOGRAM CATR**
(invited paper)

Antti V. Räisänen, Taavi Hirvonen, Juha Ala-Laurinaho, Arto Lehto
Radio Laboratory, Institute of Radio Communications, Helsinki University of Technology
P.O. Box 3000, FIN-02015 HUT, Finland
Tel.: +358 9 451 2241, Fax: +358 9 451 2152, E-mail: ara@radio.hut.fi

Abstract

A compact antenna test range (CATR) has a great potential for testing electrically large antennas. However, the application of conventional reflector type CATRs becomes increasingly difficult, though not impossible, above 100 GHz due to the tight surface accuracy requirements for the reflectors. A CATR based on a planar hologram has been studied to overcome the problems incurred by the use of reflectors with insufficient surface accuracy. This paper summarises the recent results obtained for a hologram CATR at Helsinki University of Technology.

1. Introduction

Antenna testing of future remote sensing and radio astronomical satellites has given rise to a need for accurate measurements of electrically large reflector antennas at millimeter and submillimeter wavelengths. Previous studies have shown that a compact antenna test range (CATR) has the greatest potential for these kinds of tests [1,2]. In a CATR, a spherical (or a cylindrical) wave front is transformed into a plane wave with a collimating device which may be a reflector, a lens, or a hologram. The antenna under test (AUT) is placed in the plane wave region (quiet-zone) which is a part of the radiating near-field of the collimating element. A compact range simulates the conditions of the traditional far-field ranges in a distance which is only a small fraction of the corresponding far-field distance. Thus, a CATR makes it possible to measure electrically large antennas in an indoor environment, away from the changing weather.

A CATR is commonly realised with the use of one or more reflectors for which the surface accuracy needs to be better than about 0.01 wavelengths. As a result, tight surface-accuracy specifications at frequencies above 100 GHz are required. The use of a dielectric lens has been studied as a possible alternative to overcome the problems incurred by the use of reflectors with insufficient surface accuracy [3,4]. Recently, a new concept employing a planar hologram structure as a collimating element to form the desired plane wave in a CATR has been developed. The hologram CATR is a relatively low-cost easy-to-fabricate structure. The surface accuracy requirements for a transmission-type amplitude hologram are less stringent than those for a reflector [5].

This paper shows the principle of the hologram CATR, reviews the development work of the 2.4 m × 2.0 m hologram which will be used for the Odin satellite antenna tests at 119 GHz in 1998, and summarises the most important results of a feasibility study of a submillimeter wave hologram CATR.

2. Hologram CATR

Generating a conventional hologram means creating an interference pattern of two wave fronts on a surface. After the hologram has been created, one of the interfering fields can be recreated by illuminating the hologram with the other interfering field. A hologram can be simply formed at optical wavelengths by illuminating a photosensitive film with two light beams, a light reflected from an object and a reference light beam.

In many practical applications, in the optical and radiowave region, holograms are synthesised by computational methods (computer-generated hologram, CGH). The hologram pattern is determined by numerically calculating the structure required to change the known input field into the desired output field. In general, a hologram structure changes both the amplitude and phase of the field transmitted through or reflected from the structure. In practice, holograms are usually realised so that they modulate only the amplitude or the phase of the field (amplitude or phase hologram). Furthermore, due to fabrication limitations,

the structure has to be quantized in some way. The method for accomplishing this is usually called the coding scheme of the CGH. The two most widely used schemes are the binary amplitude and the binary phase quantizations. For example, the binary amplitude hologram either lets the incoming light pass through undisturbed or blocks it completely [6,7].

Figure 1 illustrates a facility layout employing a hologram CATR and shows an example of a computer-generated, binary amplitude hologram. The feed horn transmits a spherical wave onto one side of a computer-generated amplitude hologram structure that modulates the field such that a planar wave is emanated on the other side of the structure. The plane wave is designed to leave the hologram at a certain angle so that the other diffraction modes generated by the hologram do not disturb the plane wave. The antenna under test (AUT) is illuminated with this plane wave. The extent of the volume enclosing the plane wave is called the quiet-zone. The required field-quality of the quiet-zone is driven by the required measurement accuracy of the AUT. Typical requirements are a peak-to-peak amplitude ripple less than 1 dB and phase ripple less than 10° in the quiet-zone.

The theoretical analysis and the optimisation procedure of the hologram CATR are based on the coding scheme of the hologram and the combination of the finite difference time domain (FDTD) method and physical optics (PO) calculation. The complex aperture field needed in the PO analysis is determined with a two-dimensional FDTD calculation. The analysis method has been validated by comparison of theoretical and experimental results, and it is thoroughly described in [8,9].

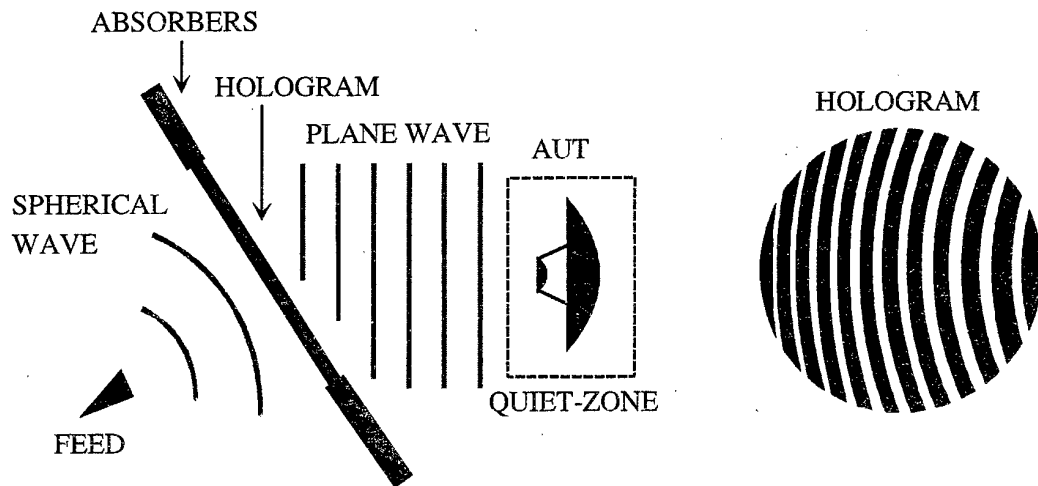


Figure 1. A hologram CATR and an example of a hologram pattern.

3. Hologram for Odin tests

The Radio Laboratory is participating in an international Odin satellite project. Odin satellite will carry a millimeter- and submillimeter-wave radio telescope for monitoring aeronomical and astronomical spectral lines. The radio telescope uses an offset reflector antenna with a 1.1 m diameter main reflector. The antenna will be tested with a hologram CATR at 119 GHz.

The purpose of the Odin tests is to verify the radiation pattern of the Odin antenna by measuring the main beam. For this purpose, a 2.4 m × 2.0 m elliptic hologram was designed. The corrugated horn as a feed was placed 6.0 m away from the hologram. The structure of the hologram optimises the quiet-zone field at vertical polarisation 6 m behind the hologram. The plane wave is designed to leave the hologram at an angle of 33.0°. The thickness of the dielectric film is 75 µm, and the thickness of the copper layer is 35 µm. The relative permittivity of the film is 3.3.

The hologram was manufactured with a silk screen printing process, which was capable of producing up to $1.2 \text{ m} \times 1.0 \text{ m}$ sized patterns. Thus, the hologram was made of seven pieces as shown in Figure 2 because it is highly desirable to avoid any kind of joints in the center of the structure. The curved lines in Figure 2 illustrate the slots of the hologram. The pieces were spliced together by using a 50 mm wide and 30 μm thick polyester tape on both sides of the film.

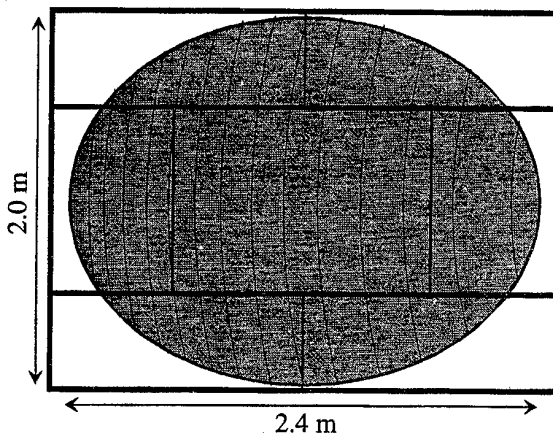


Figure 2. Layout of the hologram.

Figure 3a shows the theoretical and experimental quiet-zone amplitudes in the horizontal direction at the center of the quiet-zone. The curves have been vertically shifted in order to separate them from each other. The solid line is the optimized theoretical amplitude distribution. The line with the bullets is the theoretical amplitude distribution when the two vertical joints have been included in the analysis. The line with the stars is the measured amplitude distribution. Figure 3b shows the theoretical phase distributions in the quiet-zone in the horizontal direction. Figure 3c shows the measured quiet-zone amplitude in the vertical direction. Theoretical, optimised peak-to-peak amplitude and phase ripples are less than 1 dB and 10° . Measured peak-to-peak amplitude ripple is about 3 dB in the worst part of the quiet-zone and less than 1.5 dB in the most parts of the quiet-zone.

The extra amplitude ripple between the optimised and realised quiet-zone fields is clearly caused by the joints of the hologram. The position of the pieces relative to each other is not correct and they are 'out of phase'. The incorrect position of the pieces relative to each other causes amplitude and phase errors in the quiet-zone. Another source of error is the tape which is used to splice the pieces together. The tape changes the thickness of the dielectric layer. However, the effect of the changed thickness of the film on the quiet-zone field is less critical than the effect of the positioning errors (especially on the phase) [10].

The quality of the quiet-zone field is sufficient for measuring the main beam of the Odin telescope. The Odin telescope is scheduled to be tested in July 1998. However, for future purposes the manufacturing techniques of large holograms have to be improved or new methods must be found. The good accuracy of the theoretical analysis facilitates a careful study of the hologram CATR.

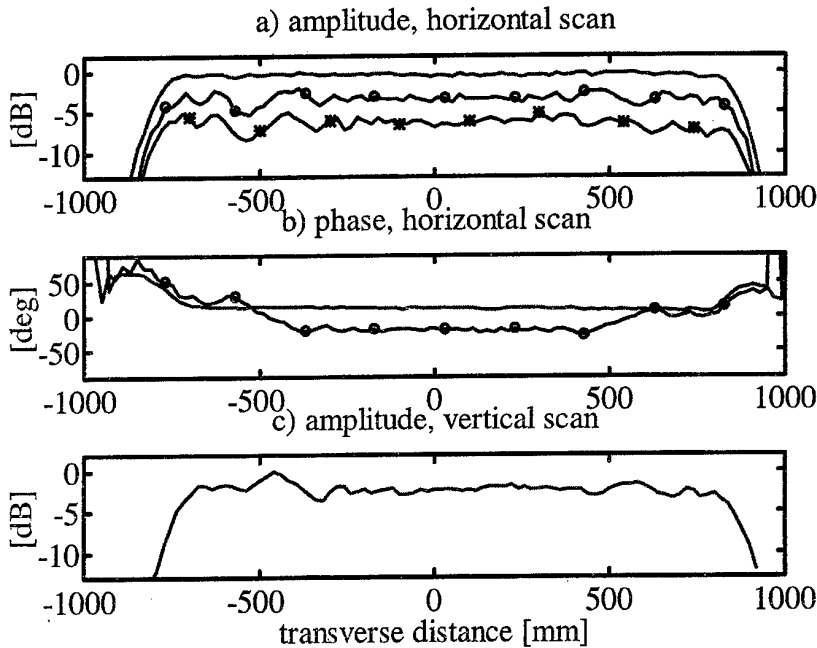


Figure 3. a) Quiet-zone amplitudes in the horizontal direction: optimised theoretical (—), theoretical with the joints (o), and measured (*), b) quiet-zone phases in the horizontal direction: optimised theoretical (—) and theoretical with the joints (o), c) measured quiet-zone amplitude in the vertical direction ($f = 119$ GHz, vertical polarisation).

4. Feasibility study of a submillimeter wave hologram CATR

The European Space Agency (ESA) is currently examining the use of space-based radiometric instruments to probe the atmosphere in the 200–1000 GHz region. Recently, the Radio Laboratory participated in a study where possible antenna measurement facilities for measuring 1.0, 2.0, and 4.0 m diameter antennas at frequencies 200, 500, 1000, and 1500 GHz were examined in detail [2,11]. A reflector type and a hologram type of compact ranges were found to be the most potential candidates for these tests.

The main emphasis was to estimate the uncertainties of the absolute gain and beam efficiency measurements. The feasibility study of the hologram CATR is based on a combined analysis of physical optics (PO) and finite difference time domain (FDTD) method. The feasibility study was carried out at 500 GHz and it is more thoroughly reported in [11,12].

The main advantages of the hologram were found to be the relatively inexpensive manufacturing costs and less stringent surface accuracy requirements than those of a reflector. The main disadvantages are the fairly strong polarisation and frequency dependences. The polarisation dependence of the hologram is due to the polarisation dependences of the transmission coefficients of narrow slots. The bandwidth of a hologram CATR is case specific (typically 5–20 %) depending on the feed antenna, focal length, and the size of the hologram relative to the wavelength. Generally, the hologram structure is optimized for a single frequency and a certain linear polarisation to produce a plane wave.

It was found that with the existing lithographic manufacturing techniques it should be possible to construct a hologram CATR which has the RMS phase error in the quiet-zone of less than about 6° even at 1500 GHz. This means a gain error of 0.05 dB (caused by the CATR). However, this estimation is optimistic because it does not include the effect of joints when the hologram is fabricated by joining several pieces together. Altogether, the overall uncertainties in the measurements of large millimeter and submillimeter wave reflector antennas are dominated by the uncertainties related to the measurement instrumentation: low available power

levels, high noise temperatures, low dynamic ranges, and the lack of calibrated attenuators. Thus it is difficult to give accurate estimations for the overall uncertainties. However, it is estimated that the overall uncertainty of the absolute gain is about 0.3 dB, when the gain of a highly directive antenna is measured with a gain comparison method at 200 GHz. The uncertainty of the beam efficiency is of the order of 0.1%, when the beam efficiency of the same antenna is determined from the truncated radiation pattern in a compact range [2,11].

5. Conclusions

A hologram type of compact antenna test range (CATR) utilises a computer-generated amplitude hologram to form the desired plane wave from the feed antenna spherical wave. The advantages of a hologram CATR over a reflector CATR are its less expensive fabrication costs and less stringent surface accuracy requirement. The disadvantages are a fairly strong dependence on frequency and polarisation. Especially, the fabrication of a large hologram needs to be further developed. The tolerance requirements of a submillimeter wave hologram are not too stringent for the fabrication techniques that are used for making printed circuits. The problem is that the present day fabrication techniques are not capable of fabricating large structures (situation in Finland). The next steps in this research are testing of the Odin satellite antenna (diameter 1.1 m) at 119 GHz with a hologram CATR and a design, construction and testing of a submillimeter wave CATR based on a 0.5 m hologram at 310 GHz. Furthermore, ways of reducing the polarisation dependence and the alternative manufacturing techniques are the subjects for the future studies.

References

1. J. Aurinsalo, S. Karhu, A. Koivumäki, A. Pitkäaho, A. Lehto, A. Räisänen, T. Tolmunen, J. Tuovinen, "Test methods and ranges for testing the millimeter wave sounder of the Meteosat second generation satellites", Final Report, *ESTEC Contract No. 7966/88/NL/PB(SC)*, 1990.
2. P.R. Foster, D. Martin, C. Parini, A. Räisänen, J. Ala-Laurinaho, T. Hirvonen, A. Lehto, T. Sehm, J. Tuovinen, F. Jensen, K. Pontoppidan, "Mmwave antenna testing techniques—Phase 2," MAAS Report 304, *ESTEC Contract No. 11641/95/NL/PB(SC)*, 1996.
3. A.D. Olver, A.A. Saleeb, "Lens-type compact antenna test range," *Electronics Letters*, Vol. 15, No. 14, pp. 409–410, 1979.
4. T. Hirvonen, J. Tuovinen, A. Räisänen, "Lens-type compact antenna test range at mm-waves," *Proceedings of the 21st European Microwave Conference*, Stuttgart, pp. 1079–1083, 1991.
5. J. Tuovinen, A. Vasara, A. Räisänen, "A new type of compact antenna test range," *Proceedings of the 22nd European Microwave Conference*, Espoo, pp. 503–508, 1992.
6. A. Vasara, J. Turunen, A. Friberg, "Realization of general nondiffracting beams with computer-generated holograms," *Journal of Optical Society of America A*, Vol. 6, pp. 1748–1754, 1989.
7. W.-H. Lee, "Computer-generated holograms: techniques and applications," In *Progress in Optics XVI*, E. Wolf (ed.), North-Holland, pp. 121–231, 1978.
8. T. Hirvonen, J. Ala-Laurinaho, J. Tuovinen, A.V. Räisänen, "A compact antenna test range based on a hologram," *IEEE Transactions on Antennas and Propagation*, Vol. 45, No. 8, pp. 1270–1276, 1997.
9. J. Ala-Laurinaho, T. Hirvonen, J. Tuovinen, A.V. Räisänen, "Numerical modeling of a non-uniform grating with FDTD," *Microwave and Optical Technology Letters*, Vol. 15, No. 3, pp. 134–139, 1997.
10. T. Hirvonen, J. Ala-Laurinaho, P. Piironen, J. Tuovinen, A.V. Räisänen, "A 119 GHz CATR based on 2.4 m hologram," *Proceedings of the 19th Meeting and Symposium of the Antenna Measurement Techniques Association (AMTA)*, Boston, MA, pp. 164–169, 1997.
11. T. Hirvonen, J. Ala-Laurinaho, A. Lehto, J. Tuovinen, A.V. Räisänen, "Feasibility of a hologram CATR for measuring large mm- and submm-wave antennas," *Proceedings of the 20th ESTEC Antenna Workshop on Millimetre Wave Antenna Technology and Antenna Measurement*, Noordwijk, pp. 355–362, 1997.
12. T. Hirvonen, J. Ala-Laurinaho, A.V. Räisänen, "Performance analysis of a submillimeter wave hologram CATR," *Proceedings of the 27th European Microwave Conference*, Jerusalem, pp. 681–686, 1997.

**THE SYNERGY OF SUBMILLIMETRE AND INFRARED SPECTROSCOPY IN
PREDICTING
GLOBAL WARMING EFFECTS OF CFC REPLACEMENT MOLECULES.**

Geoffrey Duxbury, Kevin Smith, Mark McPhail and Robert McPheat,
 Department of Physics and Applied Physics, John Anderson Building, 107 Rottenrow, Glasgow G4 0NG
 John Ballard and David Newnham,
 NERC Molecular Spectroscopy Facility, Rutherford Appleton Laboratory, Chilton,
 Didcot, Oxfordshire, OX11 0QX, UK.

The evaluation of the global warming effects of the CFC replacement gases is of very considerable interest following the Kyoto summit, since the main replacements, the HFC's are predicted to have both high global warming potential and atmospheric lifetimes of hundreds of years. In order to assess global warming potential it is essential to have available accurate temperature dependent absorption cross sections of the CFC replacement gases, particularly the HFC's. This requires not only the development of accurate and reproducible ways of experimental measurement of absorption cross sections, but also better methods of modelling their temperature dependence. Much of this has been developed by the authors as part of the SWAGG consortium

The CFC replacement gases, the HFC's, CF_3H , CH_2F_2 , C_2F_6 and CF_3CH_3 are used as examples of the measurement and interpretation of cross sections, of the evaluation of the effects of the low frequency torsional modes whose spectra occur in the submillimetre region, and of the temperature dependence of the absorption cross sections. This encompasses techniques for freezing out torsional hot bands, strategies for line by line calculations of the spectra of heavy molecules of this type, and the input of the resulting cross section information into radiation transport codes in K. Shine's group in the Department of Meteorology at Reading University.

The spectra were recorded using two Fourier transform spectrometers, a Bruker IFS 120HR spectrometer at R.A.L. and a Bomem DA3.002 at Strathclyde University. All measurements were made using coolable stainless steel absorption cells mounted in the sample compartments of the spectrometers. Most of the spectra were recorded in the range from 295 to 203 K. The collisionally cooled spectra were recorded at RAL. Great care was taken to ensure the purity of the gas samples used, and to minimise the effects of adsorption on the walls of the cells. Indium wire seals for the windows were used in all of the cells to eliminate the effects of sealants..

For cross section measurements the spectra were recorded at resolution of 0.03 to 0.1 cm^{-1} in the spectral region from 600 to 2000 cm^{-1} . An interferogram recorded with a maximum optical path difference of 1 metre was Fourier transformed to produce spectra of fluoroform with resolutions from 0.1 cm^{-1} to 0.01 cm^{-1} . These spectra were converted to absorption spectra and integrated. The resulting integrated intensities show a small change with resolution. The change was small but systematic and was corrected for. The effects of detector-amplifier nonlinearity and of drift were eliminated, and sample emission corrections were also made.

Internal rotation occurs in two of the four molecules, C_2F_6 and CF_3CH_3 , leading to a large number of torsional states being populated even at 200K. The other two molecules, CF_3H and CH_2F_2 have low lying vibrational states which have been studied using microwave spectroscopy. C_2F_6 does not possess a dipole moment, and its pure rotation spectrum could only be measured using Raman spectroscopy.

The room temperature absorption spectrum of fluoroform was recorded at resolutions of up to 0.0017 cm^{-1} . To avoid saturation of absorption the cell pressure was limited to below 0.5 Torr for measurements of the polyad centred around 1150 cm^{-1} , and to less than 1 Torr for the other bands. One band of fluoroform, ν_3 , is quite weak, and has only been recorded previously at a resolution of 0.03 cm^{-1} by Graner, Antilla and Kauppinen². With the enhanced resolution of 0.0017 cm^{-1} provided by the RAL Bruker, an almost completely resolved spectrum of the R and P branch regions was obtained and analysed. using of two computer programs developed by Pickett³ at the Jet Propulsion Laboratory. These programs are CALFIT for the least squares spectral fitting and CALCAT for calculation of the absorption spectrum using the constants derived from the fit.. Examples of the observed and calculated spectrum of this band are shown in Figure 1.

The polyad involving the ν_2 , $\nu_3 + \nu_6$ and ν_5 bands centred around 1150 cm^{-1} has a very complex structure, and was analysed in detail by Graner and Guelachvili⁴. A partial fit to the new high resolution spectrum has been carried out by Smith and Duxbury, making use of the simplification afforded by the newly recorded collisionally cooled spectrum⁵. The ν_4 band has had its intensity measured by several groups. One group, Sofue et al.⁶, has used a diode laser to measure the intensity of two well resolved vibration-rotation lines. They have compared their results with those obtained by the measurement of the integrated intensity of the band, and have pointed out

that hot bands make a large contributions to the integrated intensity across a band. The hot band contribution has been calculated for the ν_4 band at room temperature assuming that the transition dipole moment is the same for the hot bands, including the populations and degeneracies of the excited levels. New measurements of the submillimetre spectrum have also been made⁷.

The infrared band strengths and absorption cross sections of HFC-32, difluoromethane (CH_2F_2) were measured by Smith et al.⁸. We have completed a rotational analysis¹⁰ of the ν_3 and the ν_9 bands in the region from 1000 to 1300 cm^{-1} , combining high resolution (0.0019 cm^{-1}) room temperature spectrum with collisionally cooled spectra, and also the microwave data of Hirota⁹. These will be used to construct a line by line model of this section of the HFC-32 absorption spectrum.

The temperature dependence of the absorption cross sections of 1,1,1-tri-fluoro-ethane, CF_3CH_3 , has been measured by Smith et al.¹¹, showing extensive torsional hot band structure in the ν_3 band, which is absent in the collisionally cooled spectra⁵. In collaboration with Nivellini and his colleagues at the University of Bologna, we have analysed the part of the infrared spectrum in the region from 1370 to 1470 cm^{-1} . The two infrared active bands, of A_1 symmetry, have been assigned as ν_2 (CH_3 symmetric deformation) and the combination band $\nu_4 + \nu_5$. 1,1,1-tri-fluoro ethane is a prolate symmetric top of C_{3v} symmetry. Owing to its small and nearly equal A and B rotational constants¹² parallel and perpendicular bands appear in the spectrum with similar structures. A Raman spectrum obtained at LENS in Florence, to aid the reassignment of the CH_3CF_3 vibrational spectrum, shows that the two infrared active bands are of A_1 symmetry, while two further Raman active bands are of E symmetry. A detailed study of the 10 μm bands has been made by Fraser et al.¹² To complete a line-by-line study of this spectrum it will be necessary to record further microwave and submillimetre spectra.

The perfluoroethane spectra are examples of very compact spectra with a rotational structure whose spacing is close to the resolution limit of most commercial Fourier transform spectrometers. Two of these bands ν_5 , at 1117 cm^{-1} and ν_{10} , at 1251 cm^{-1} , have been studied by Hansford and Davies¹³ and by Nakanaga et al.¹⁴ at very low temperatures using diode laser spectroscopy of supersonic jet expansions. The spectra were analysed using a prolate symmetric rotor Hamiltonian in the rigid rotor limit, and the band centres of the fundamentals and some hot bands to be identified. We have recorded high resolution room temperature spectra, and slightly lower resolution spectra at 253 and 203 K using the RAL FTS.. The band centred at 713.7 cm^{-1} has been recorded with partial rotational resolution for the first time. The Q branch region of this latter band shows extensive hot-band structure, most of which is due to transitions from thermally populated levels involving multiple quanta of the torsional vibration, ν_4 . In Figure 1 the spectrum of the Q branch recorded at 203 K is compared with a simulated spectrum based on our assignment of the rotational structure of the P and R branches. We assumed that the transition moments of the hot bands are identical to that of the fundamental, and that the intensities are proportional to the product of the statistical weight and the population of the thermally excited torsional levels. The reasonable agreement shows that this assumption is a valid one.

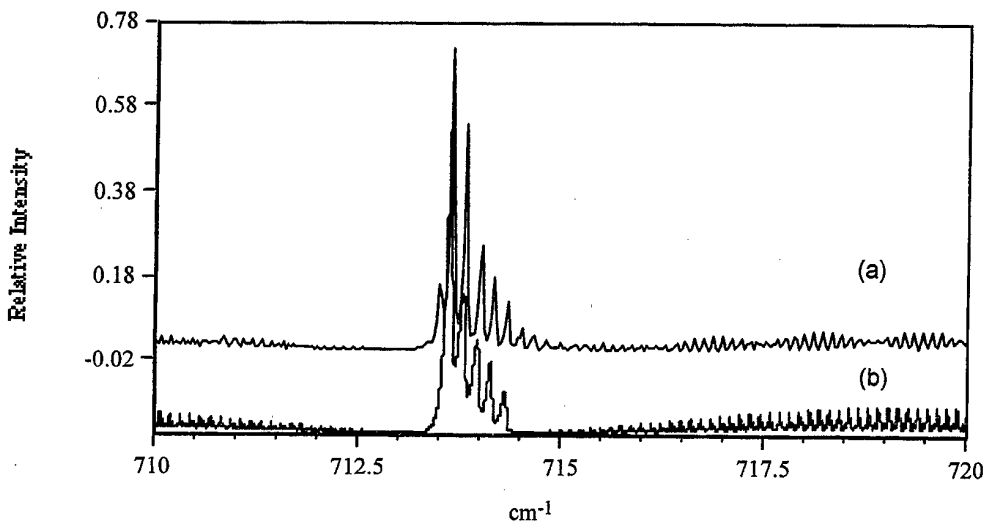
A rotational analysis was carried out using the ground state constants derived by Hansford and Davies¹². The effects of the K quantum number cannot be seen and the spectrum resembles that of a perpendicular band of a linear molecule. The odd 'beating' effect seen in the experimental spectrum is due to a Moiré fringe type of pattern arising from the slightly different line spacings in the transitions from the ground and lowest lying states. In the 253 and 293 K spectra this beating is largely damped and a more regular structure is seen in the spectra.

Many radiative transfer models, such as the NCAR Community Climate Model, use broad band absorption cross sections in the form of a mean absorption intensity over a wavenumber interval of 100 cm^{-1} . In considering the impact of heavy HFC's very large errors which may exceed 25% may be made when such large averaging intervals are used. In the recent models of Highwood, Freckleton and Shine¹⁵ of Reading University, it has been shown that 10 cm^{-1} wide bins can be used satisfactorily, but the integrated area under these "binned spectra" is derived from the much higher resolution spectra of the type described in this paper. Many of these molecules have very long atmospheric lifetimes and very large global warming potentials (GWP). The GWP is usually measured relative to CFC-11 which, over 20 years, is 6300 times more powerful than CO_2 . The values for the molecules discussed in this paper are given in Table 1.

Table 1 Lifetimes and global warming potential of perfluoroethane and selected HFC's

Molecule	Lifetime/years	GWP			GWP relative to CO ₂
		20 years	100 years	500 years	500 yearsr
C ₂ F ₆	10,000	1.20	2.25	9.15	16,472
HFC23 (CF ₃ H)	264	0.31	2.40	5.59	10,060
HFC32 (CH ₂ F ₂)	5.6	1.46	0.12	0.10	188
HFC-143a (CF ₃ CH ₃)	55.3	0.83	0.88	0.90	1628

Figure 1



Observed (a) and calculated (b) spectra of the ν_6 band of C_2F_6 at a temperature of 203 K. The sequence band structure is due to thermally populated levels of the torsional vibration ν_4 and its overtones. The missing hot bands in the calculation are associated both with more highly excited torsional levels, and also with the other thermally populated states built on ν_3 and ν_{12} .

References

1. "Spectroscopy and Warming Potential of Atmospheric Greenhouse Gases" (SWAGG); CEE ENV4 CT95 0069.
2. G. Graner, R. Anttila, and J. Kauppinen, "High resolution infrared spectrum of the ν_3 and ν_6 bands of HCF_3 and their hot bands", Mol. Phys. **38**, p. 103, (1979).
3. H. M. Pickett, "The Fitting and Predictions of Vibration-rotation Spectra with Spin Interactions" J. Mol. Spectrosc. **148**, 371-377 (1991).
4. G. Graner, and G. Guelachvili, "Fluoroform: The Polyad at 8-9 μm ", J. Mol. Spectrosc. **107**, 215-228 (1984).
5. K.M. Smith, G. Duxbury, D. Newnham and J. Ballard "High Resolution Mid-Infrared Molecular Absorption Spectroscopy Of Collisionally Cooled Hydrofluorocarbon Vapour", J. Chem. Soc.. Faraday Trans. **93**, 2735-2740 (1997)
6. S. Sofue, K. Kawaguchi, E. Hirota and T. Fujiyama, "Absolute Intensity Measurement of the ν_4 Band of Fluoroform by the Use of a Tunable Diode-laser Source" Bull. Chem. Soc. Jpn. **54**, 3546-3550 (1981).
7. R. Bosquet, D. Boucher, W.D. Chen, D. Papousek, G. Wlodarczak and J. Demaison, "the submillimetre-Wave Rotational Spectrum of Fluoroform: Analysis of the K=3 Line Doubling" J. Mol. Spectrosc **163**, 291 (1994)
8. K.M. Smith, D.A. Newnham, M. Page, J. Ballard and G. Duxbury, "Infrared Band Strengths and Absorption Cross-Sections of HFC-32 Vapour", J. Quant. Spectrosc. Radiat. Transfer, **56**, 73-82 (1996)

9. E. Hirota, J. Mol. Spectrosc **69**, 409 (1978)
10. K.M. Smith, G. Duxbury, D.A. Newnham and J. Ballard, "A high resolution Analysis of the and Absorption bands of Difluoromethane", (to be published)
- 11 K.M. Smith, D. Newnham, M. Page, J. Ballard and G. Duxbury "Infrared Band Strengths and Absorption Cross-Sections of HFC-134 and HFC-143a Vapour", J. Quant. Spectrosc. Radiat. Transfer **59**, 437-451 (1997)
- 12 G.T. Fraser, A.S. Pine, J.L. Domenech, and B.H. Pate, "Molecular-beam spectrum of the 970 cm⁻¹ Fermi triad of CF₃CH₃" J. Chem. Phys. **99**, 2396 (1993)
- 13 G. M. Hansford and P. B. Davies, "Resolution Infrared Laser Spectroscopy of Jet-Cooled C₂F₆ near 10 μm", J. Molec. Spectrosc. **180**, 345-354 (1996).
14. T. Nakanaga, F. Ito, J. Miyawaki, K. Sugawara, H. Takeo and A Suga, , " High Resolution Infrared Diode Laser Spectroscopy of C₂F₆ in a Supersonic Jet", J. Mol. Spectrosc. **178**, 40-44 (1996).
- 15 E.J. Highwood, R.S. Freckleton and K.P. Shine, "Radiative Forcing due to SWAGG Molecules", SWAGG Final report (1998)

NEW TRENDS IN GaAs-BASED DEVICES FOR GENERATION OF MILLIMETER AND SUBMILLIMETER WAVES

Peter Kordoš

Institute of Thin Film and Ion Technology, Research Centre Jülich

D-52425 Jülich, Germany

Tel.: +49-2461-612732, Fax: +49-2461-612333, E-mail: p.kordos@fz-juelich.de

Two examples of GaAs-based devices which can generate radiation with frequencies above 100 GHz are described. First one is the InGaAs/InP pseudomorphic HEMT which consists of Al-free 2-DEG material structure. Optimization steps towards an improvement of its performance are described. From the analysis resulting device, an $0.1 \mu\text{m}$ T-gate pHEMT with f_T/f_{\max} of 160/300 GHz, is demonstrated. Obtained cutoff frequencies are comparable to the record values reported on InGaAs/InAlAs HEMTs, however Al-free devices show higher breakdown voltages, no kink effects and better reliability. Another novel device is an MSM detector on nonstoichiometric GaAs which is suitable as a radiation source up to THz frequency range using optical heterodyne mixing. Intrinsic and extrinsic bandwidths of a detector as well as conditions for output power increase are analyzed. A 3-dB bandwidth of 550 GHz, higher than previously reported, is achieved on optimized device with interdigitated finger contacts. Further possibilities in performance improvement of both types of GaAs-based devices are finally discussed.

1. Introduction

Millimeter- and submillimeter- wave systems are currently of increasing interest because of their application in different areas, like wireless communications, material analysis, spectroscopy, medicine, sensoric systems, security technique, etc. Devices, sources as well as detectors, with cutoff frequencies above 100 GHz are needed in order to improve the system performance. In general, it can be reached by two different ways. One is by improving the properties of state-of-the-art devices, another by using novel types of materials or device principles.

An example in improvement of state-of-the-art devices is an InGaAs/InAlAs based pseudomorphic high-electron-mobility-transistor (HEMT) which support highest cutoff frequencies reported up to now on three-terminal device - f_T and f_{\max} are well in excess of 100 GHz [1,2]. Unfortunately various problems, which are mostly contributed to the Al-containing material structure, hinder its wide application [3]. Recently, we have reported on an efficient enhancement of the Schottky barrier height on n-InGaAs by p⁺-InGaAs or -InP instead of InAlAs [4], as well as on the optimization possibilities of strained Al-free InGaAs/InP heterostructures for HEMT applications towards high channel conductivity [5]. Simultaneously it was shown by others that Al-free InGaAs-based material structure can be used for HEMT preparation and f_T 's near to 100 GHz were achieved [6]. These results indicate that Al-free InGaAs-based 2-DEG material structure might be a good candidate for the preparation of high-efficient and reliable HEMTs with cut-off frequencies above 100 GHz.

Another way how to improve the properties of radiation sources is by using novel types of materials or device principles. This can be demonstrated by optical mixing in a broadband GaAs detector which acts as a tunable source of sub-mm wave radiation. Device consists of nonstoichiometric GaAs grown by molecular-beam epitaxy (MBE) at low temperatures (usually designated as LT GaAs) and its basic advantages like high resistivity, high breakdown field and short carrier lifetime are utilized for ultra-fast and broadband optical detection [7]. Recently, a tunable source of THz radiation on LT GaAs was proposed [8] and shortly after the radiation up to 3.8 THz was detected using MSM detector with a bandwidth of 405 GHz [9]. However, the radiation power in THz region is rather small and detailed studies of LT GaAs behavior regarding the performance optimization of a photomixer are therefore needed. As we reported recently, the properties of LT GaAs can be well optimized by choosing proper growth conditions [10].

Both above mentioned examples of novel GaAs-based devices for generation of millimeter and submillimeter waves are the subject of our studies and recent results related to their preparation and properties are presented in this paper. At first, results on pseudomorphic HEMTs based on Al-free InGaAs/InP structures are described. In the frame of our study developed $0.1\text{ }\mu\text{m}$ T-gate pHEMTs exhibit cut-off frequencies $f_T/f_{m,a}$ of 160/300 GHz. These are comparable values to the record ones reported on conventional InGaAs/InAlAs HEMTs. Further, our investigations on LT GaAs related to the optical mixer performance are presented. The preparation conditions of an LT GaAs MSM detector are described and conditions for the device bandwidth optimization are discussed. Achieved results are demonstrated on the device which exhibit 550 GHz bandwidth, higher than so far reported. Finally, possibilities in performance improvement of both types of GaAs-based devices are discussed in conclusion.

2. InGaAs/InP pseudomorphic HEMTs

2.1. Al-free material structure

Pseudomorphic InGaAs/InAlAs HEMTs have shown the best performance of all three-terminal devices in terms of high speed/high frequency and low noise performance [1,2]. The material structure is grown on InP substrate with an In-rich InGaAs 2-DEG channel. All other layers (buffer, carrier supplier, spacer and barrier enhancement) are InAlAs layers. However, the presence of the Al-containing InAlAs layers has following disadvantages: i) not high enough etching selectivity to stop the gate recess exactly at the InGaAs/InAlAs interface, ii) high density of deep traps at the InGaAs/InAlAs interface (DX centers), and iii) high oxidation of Al-containing materials. These properties are responsible for worse device parameters (high leakage currents, lower breakdown voltage and kinks in I-V characteristics) and mainly for poorer long-term device stability [3]. Similar problems are also observed on InGaAs/AlGaAs HEMTs grown on GaAs substrate and recently structures with GaInP instead of AlGaAs are proposed to achieve better device performance [11].

There are two main reasons of using InAlAs, high enough conduction band discontinuity at the InGaAs/InAlAs interface ($\Delta E_c = 0.55\text{ eV}$ instead of 0.36 eV for InGaAs/InP) as well as effective enhancement of the Schottky barrier height by InAlAs interlayer ($\Phi_B = 0.68\text{ eV}$ instead of 0.2 eV directly on InGaAs). However, we have shown before that the barrier height can be enhanced up to 0.66 eV also by using p^+ -InP layer of optimal thickness [4]. Further, we have optimized the properties of Al-free InGaAs/InP 2-DEG structures towards high channel conductivity. The influence of the InGaAs channel composition on the carrier mobility and carrier sheet density, as well as on the resulting channel conductivity is shown in Fig. 1 (open marks for $d_{ch} = 10\text{ nm}$). For optimal channel composition $x_{InAs} = 0.75$ we achieved further improvement of n_s , μ_n and G_{ch} by reducing the channel thickness to 7 nm (full marks in Fig. 1). Resulting channel conductivity is $G_{ch} = 5.5\text{ mS}$. For conventional InGaAs/InAlAs HEMTs an optimal value of 5.9 mS for $x_{InAs} = 0.77$ was found before [12]. This indicates that concerning both, the barrier height enhancement and the channel conductivity, nearly identical properties can be obtained for Al-free and Al-containing material structures of InGaAs-based HEMTs.

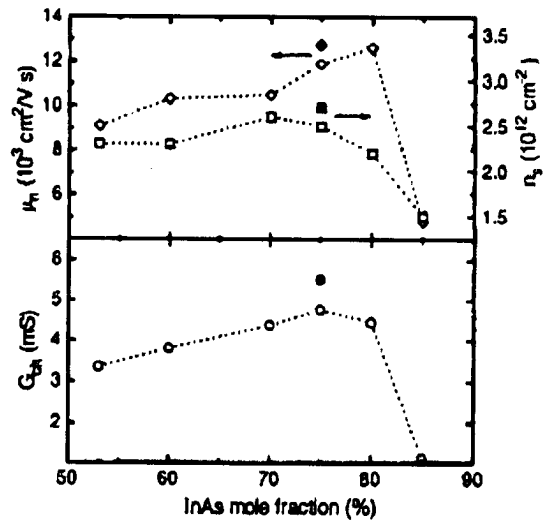


Fig. 1. Electron mobility μ_n , sheet carrier density n_s , and channel conductivity G_{ch} in InGaAs/InP 2-DEG structures as a function of the InGaAs channel composition x_{InAs} .

2.2. Preparation and properties of HEMTs

The layer structures of InGaAs/InP pHEMTs were grown by low-pressure MOCVD and consist, starting from semi-insulating InP substrate, as follows: 300 nm intentionally undoped i -InP buffer, InGaAs channel of

different thickness (7–15 nm) and indium mole fraction (mostly $x_{\text{InAs}} = 0.75$), 6 nm InP spacer, 5 nm InP carrier supplying layer ($n = 8 \times 10^{18} \text{ cm}^{-3}$), 15 nm i-InP separation layer, 15 nm p-InP barrier layer, and 20 nm InGaAs cap layer. Device fabrication consists of standard lithography, metal evaporation and lift-off processes. Devices with different gate length from 1.2 μm down up to 0.1 μm were prepared. The electron-beam lithography was used to define the gate length below 0.75 μm and T-gates were used for L_G below 0.3 μm . A three-layer resist is used for the formation of T-gates.

DC measurements show that the drain-to-source breakdown voltage is higher than 5 V and no kinks are observed. Extrinsic transconductances of 520 and 870 mS/mm are evaluated on devices with L_G of 0.7 and 0.25 μm , respectively. The channel width is 100 μm . High frequency S-parameter evaluation up to 26.5 GHz was performed using on-wafer measurements and cutoff frequencies of current gain (h_{21}) and unilateral power gain (GU) were extracted with -20dB/decade.

Figure 2 shows the current gain cutoff frequency f_T as a function of the gate length L_G evaluated on our Al-free InGaAs/InP pseudomorphic HEMTs with different nominal gate length ranging from 1.2 μm down to 0.1 μm (0.1 μm nominal is 0.12 μm real value). The $f_T \times L_G$ -product is about 25 GHz $\cdot\mu\text{m}$, which is comparable to conventional InAlAs/InGaAs HEMTs. The f_T increases from 21 GHz for devices with L_G of 1.2 μm to values above 100 GHz for pHEMTs with T-gate of the length $\leq 0.2 \mu\text{m}$. Similar increase of f_{\max} with decreasing the gate length is observed, from 35 GHz for $L_G = 1.2 \mu\text{m}$ to values above 200 GHz for $L_G \leq 0.2 \mu\text{m}$.

From the optimization process of our study resulting device with highest cut-off frequencies is the pHEMT with 0.1 μm T-gate. Figure 3 shows the current gain and unilateral power gain measurements on such optimized pHEMT. Extracted cutoff frequencies f_T and f_{\max} are 160 GHz and 300 GHz, respectively. The gates were placed asymmetrically between source and drain with $l_{GS} \approx 0.7 \mu\text{m}$. Short-channel effects appear at the 0.1 μm devices because of low-gate aspect ratio. They results in a reduction of DC transconductance of around 20 % in comparison with the ‘long gate’ devices. The total gate capacitance $C_G = C_{GS} + C_{GD}$ at optimum f_T conditions is 0.5 pF/mm.

From our study it follows that Al-free InGaAs/InP HEMT can be a good candidate for high performance amplifier applications above 100 GHz. On the other hand, further improvement should be still possible, as follows from our recent partial studies related to the thermionic field emission in p-barrier enhanced devices and resulting reduction in the gate leakage currents [13], as well as from the application of a nitrogen carrier gas instead of H₂ at the LP-MOCVD, which improves the growth process in terms of homogeneity, safety and costs [14]. Moreover, improvements reported recently on InGaAs/InAlAs HEMTs, like the use of a composite or a double-side-doped channel, can be simply applied to the Al-free material structures too.

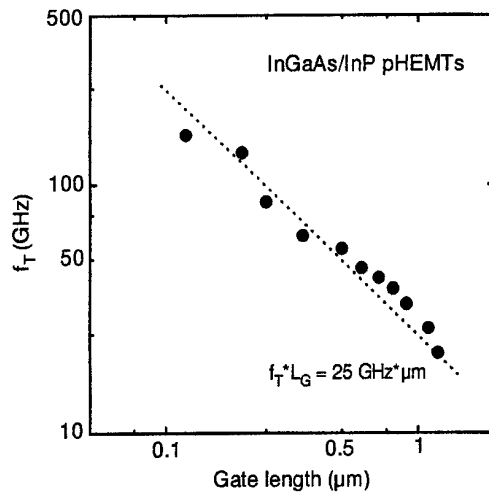


Fig. 2 Current-gain cutoff frequencies as a function of gate length of InGaAs/InP pHEMTs.

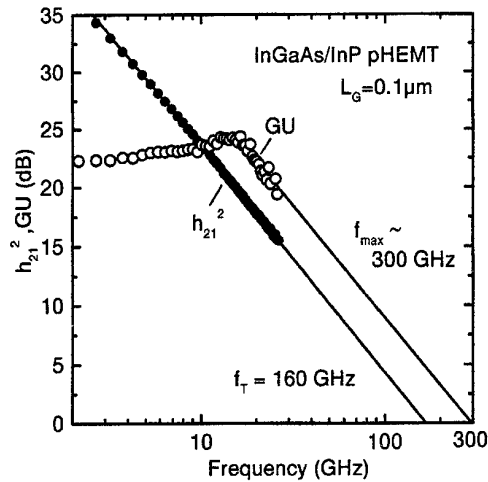


Fig. 3. Current gain h_{21}^2 and unilateral power gain GU of InGaAs/InP pHEMT with gate length $L_G = 0.1 \mu\text{m}$.

3. LT GaAs detectors for THz photomixing

3.1. General remarks

LT GaAs is nonstoichiometric (≈ 1 at. % excess As) and high resistive ($\leq 10^7 \Omega \text{ cm}$) and originally was proposed to reduce short-channel effects in MESFETs. Owing to an extremely high density of defects ($\geq 10^{18} \text{ cm}^{-3}$) in LT GaAs, it is a favourable material for high-speed optoelectronic applications [7]. However, the properties that are observed upon annealing depend critically on growth conditions of LT GaAs. The conduction of LT GaAs can be described by mixed band and hopping regime [15,16].

Recently, source of THz radiation using an LT GaAs was proposed [8]. The photomixer consists of two tunable single-mode lasers ($\lambda_1 \approx \lambda_2$) and LT GaAs photodetector (PD) with coupled planar antenna and a difference-frequency radiation is generated by optical heterodyne conversion. Coherent radiation from microwave frequencies up to 3.8 THz using LT GaAs PD with a bandwidth of 405 GHz has been measured [9]. However, the output power was rather small and the optimization of the photomixer performance is therefore needed [10].

3.2. Preparation and properties of LT GaAs MSM detectors

The LT GaAs layers were grown on (100)-oriented semi-insulating GaAs substrates at the temperature in the range between 200 and 400 °C (thermocouple reading only) [7,15]. An As/Ga beam-equivalent pressure ratio of 20 and a growth rate of 1 $\mu\text{m}/\text{h}$ were used at the growth. No post growth annealing was performed in MBE chamber. Wafers with GaAs layer were cleaved and a part was annealed for 10 min at 600–650 °C by rapid thermal processing under local arsenic overpressure. The fabrication of PDs consisted of optical lithography, metal evaporation (Ni/AuGe/Ni contacts) and lift-off processes. Interdigitated finger electrodes (MSM structures) with various finger-spacing s and -width w in the range 1–3 μm ($s+w = 3, 3.5$ and 4 μm) were used. The devices had an area of $20 \times 20 \mu\text{m}^2$ and $50 \times 50 \mu\text{m}^2$. Additional information about the LT GaAs layer growth, sample preparation and device processing can be found in our previous studies [7, 10, 15–17]. Scanning-electron micrograph of a LT GaAs PD with interdigitated finger contacts is shown in Fig. 4.

The photocarrier lifetime in LT GaAs using time-resolved reflectivity measurements was studied before [17]. On the best samples an extremely fast reflectivity decay and the carrier lifetime ≤ 0.24 ps were obtained. From this it follows that for intrinsically limited devices, i.e. if the RC time constant is smaller than the carrier lifetime, the bandwidth of about 640 GHz might be expected on LT GaAs PDs.

Transient behaviour of LT GaAs MSM PDs was studied by measurements of the photoresponse on the femtosecond pump pulse from a sapphire laser ($\lambda = 820$ nm). Fig. 5 illustrates the time-resolved photoresponse measured on two devices with the LT GaAs prepared at different conditions. Both devices have an active area of $20 \times 20 \mu\text{m}^2$ and interdigitated electrodes with finger-width and -spacing of $w = 1$

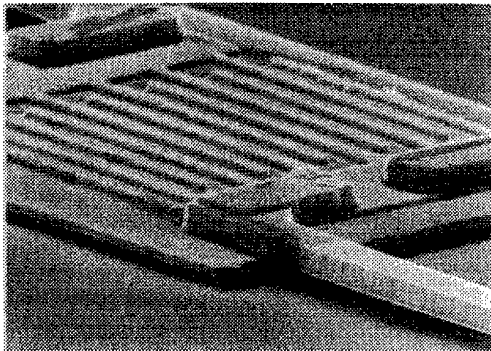


Fig. 4. SEM picture of GaAs photodetector with interdigitated finger contacts.

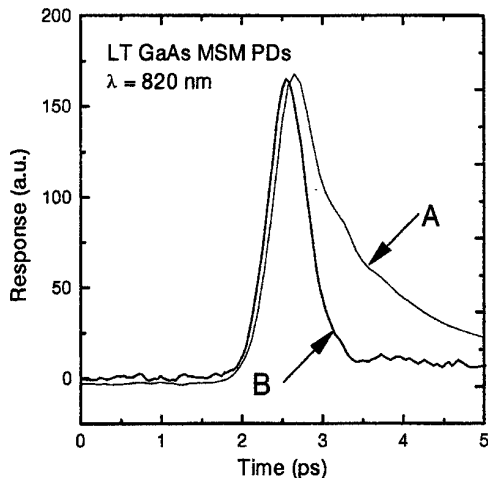


Fig. 5. Time resolved response of two different LT GaAs MSM PDs.

μm and $s = 2 \mu\text{m}$, respectively. In contradiction to device A, for a ‘good’ device (response B) the measured signal was nearly symmetric, i.e. without any tail. The rise and fall times (10-90) are 0.4 and 0.6 ps, respectively and the FWHM is 0.6 ps.

The frequency response of two LT GaAs MSM PDs obtained by Fourier transforming the detected pulse is shown in Fig. 6. The bandwidth of device A is only 130 GHz. However $f_{3\text{dB}} = 550$ GHz is obtained for device B, which is higher bandwidth than reported yet. On the other hand, measured bandwidth is smaller than expected 640 GHz for intrinsically limited PDs, as follows from our carrier lifetime measurements.

In order to estimate the RC time constant, we evaluated the capacitance of the MSM PDs by microwave measurements up to 26 GHz and using the MMICAD software. Obtained results for devices with different electrode geometry are compared with calculations according conformal mapping of a coplanar alternating electrode pattern in Fig. 7. The unit area capacitance of $0.014 \text{ fF}/\mu\text{m}^2$ was measured obtained for devices with electrode geometry of $w = 1 \mu\text{m}$ and $s = 2 \mu\text{m}$. This value is in good agreement with calculated $0.016 \text{ fF}/\mu\text{m}^2$.

The calculated bandwidth, considering both time constants and assuming 75Ω transmission line impedance, is about 500 GHz, i.e. nearly the same as the measured 550 GHz. However, the RC time constant is still larger than the carrier lifetime. This indicates that the bandwidth of studied LT GaAs PDs is RC limited. Further improvement of the bandwidth will be possible by decreasing the device capacitance, e.g. by using smaller device area and/or by optimizing the finger electrode geometry (in general, the capacitance decreases with increasing the $s+w$ and/or s/w , as shown in Fig. 7). On the other hand, PDs with the same area and a bandwidth of 405 GHz were successfully used by others for photomixers with generated power detected up to 3.8 THz [7]. From this it follows already now the potential of presented device.

4. Conclusions

Two examples of GaAs-based devices which can generate radiation power with frequencies above 100 GHz were described. First one is the $0.1 \mu\text{m}$ T-gate pHEMT prepared on Al-free InGaAs/InP material structure, which exhibit cut-off frequencies f_T/f_{\max} of 160/300 GHz. The HEMTs based on Al-free structures exhibit better performance, mainly concerning the long-term stability, than conventionally used InGaAs/InAlAs devices. Further improvement of HEMT parameters will be still possible, mainly by reducing the gate length below $0.1 \mu\text{m}$ and/or by introducing a composite or double-side-doped channel into the 2-DEG material structure. Second device is the GaAs photodetector prepared on low-temperature grown MBE layers. This PD shows extremely high 3-dB bandwidth of 550 GHz, higher than reported yet. The LT GaAs MSM PD can be used as a photomixer to produce radiation power in the THz frequency range. As it follows from our analysis, the bandwidth of PDs is RC -limited. The device capacitance can be reduced by reducing the active

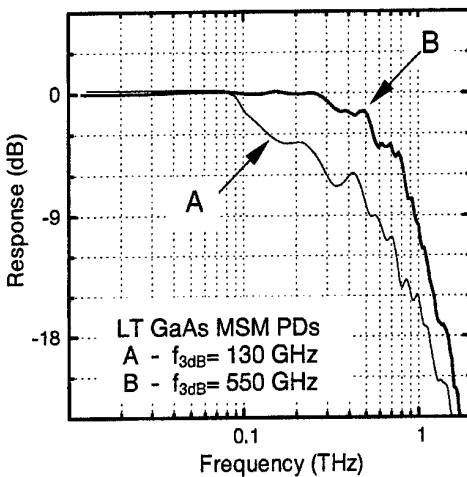


Fig. 6. Frequency response of two different LT GaAs MSM PDs.

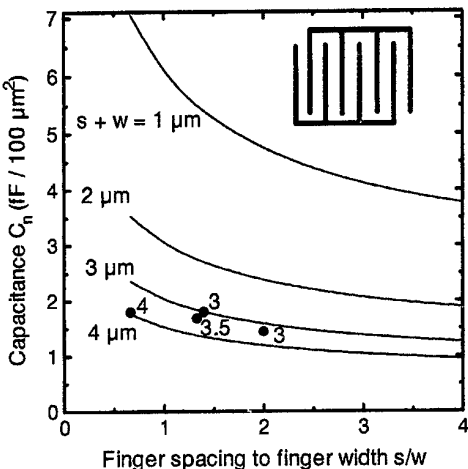


Fig. 7. Microwave capacitance of LT GaAs MSM PDs (lines - calculated, dots - measured for $s+w = 3, 3.5$ and $4 \mu\text{m}$).

area of PD and/or by optimizing the finger electrode geometry. However, in order to enhance the output power of the photomixer further optimization of material structure (carrier lifetime and mobility product) as well as of whole photomixer circuit (thermal properties, radiation antenna, etc.) should be made.

Acknowledgement

The author would like to acknowledge A. Fox, A. Förster, H. Hardtdegen, M. Horstmann, M. Marso, F. Rüders and K. Schimpf from the Institute of Thin Film and Ion Technology, Research Centre Jülich, Germany, for their contribution to this work.

References:

- [1] L. D. Nguyen, A. S. Brown, M. A. Thompson, and L. M. Jelloian, "50-nm self-aligned-gate pseudomorphic AlInAs/GaInAs high electron mobility transistors," *IEEE Trans. Electron Devices*, vol. 39, pp. 2007-2014, 1992.
- [2] M. Wojtowicz, R. Lai, D. C. Streit, G. I. Ng, T. R. Block, K. L. Tan, P. H. Liu, A. K. Freudenthal, and R. M. Dia, "0.10 μm graded InGaAs channel InP HEMT with 305 GHz f_T and 340 GHz f_{\max} ," *IEEE Electron Device Lett.*, vol. 15, pp. 477-479, 1994.
- [3] K. Inoue, "Recent advances in InP-based HEMT/HBT device technology," *Proc. 4th Intern. Conf. Indium Phosphide and Related Materials IPRM'92*, IEEE, Piscataway, pp. 10-13, 1992.
- [4] P. Kordos, M. Marso, R. Meyer, and H. Lüth, "Schottky barrier height enhancement on n-InGaAs," *J. Appl. Phys.* vol. 72, pp. 2347-2555, 1992.
- [5] R. Meyer, H. Hardtdegen, A. Leuter, M. Marso, P. Kordos, and H. Lüth, "Optimization of strained GaInAs/InP heterostructures for HEMT applications towards high conductivity," *Proc. 5th Intern. Conf. Indium Phosphide and Related Materials IPRM'93*, IEEE, Piscataway, pp. 485-488, 1993.
- [6] A. Mesquida Küsters, R. Wüller, H. J. Geelen, A. Kohl, and K. Heime, "Sub-half-micrometer pseudomorphic InP/InGaAs/InP HEMT's with very high f_T values," *IEEE Electron Device Lett.*, vol. 16, pp. 396-399, 1995.
- [7] P. Kordos, J. Betko, A. Förster, S. Kuklovsky, Ch. Dieker, F. Rüders, "Electrical and structural characterization of MBE GaAs grown between 200 and 600 °C," in *Compounds Semiconductors 1994*, Inst. Physics Conf. Series Nr. 141, IOP Bristol, pp. 295-300, 1995.
- [8] E. R. Brown, F. W. Smith, and K. A. McIntosh, "Coherent millimeter-wave generation by heterodyne conversion in low-temperature-grown GaAs photoconductors," *J. Appl. Phys.* vol. 73, pp. 1480-1484, 1993.
- [9] E. R. Brown, K. A. McIntosh, K. B. Nichols, and C. L. Dennis, "Photomixing up to 3.8 THz in low-temperature grown GaAs," *Appl. Phys. Lett.* vol. 66, pp. 285-287, 1995.
- [10] P. Kordos "Low-temperature grown molecular-beam epitaxial GaAs for terahertz photomixing," in *Heterostructure Epitaxy and Devices HEAD'97*, eds. P. Kordos and J. Novák, NATO Science Series, Kluwer Acad. Publ., vol. 48, pp. 169-178, 1998.
- [11] M. Chertouk, S. Bürkner, K. Bachem, W. Pletschen, S. Kraus, J. Braunstein, and G. Tränkle, "Advantages of Al-free AlInP/InGaAs PHEMTs for power applications," *Electron. Lett.*, vol. 34, pp. 590-592, 1998.
- [12] K. B. Chough, T. Y. Chang, M. D. Feuer, and B. Lalevic, "Comparison of device performance of highly strained GaInAs/AlInAs MODFETs," *Electron. Lett.*, vol. 28, pp. 329-330, 1992.
- [13] K. Schimpf, M. Horstmann, H. Hardtdegen, M. Marso, and P. Kordos, "Thermionic field emission in p-barrier enhanced InP/InGaAs HEMTs," *Electron. Lett.*, vol. 32, pp. 2132-2133, 1996,
- [14] K. Schimpf, M. Hollfelder, M. Horstmann, M. Marso, H. Hardtdegen, and P. Kordos, "0.2 μm T-gate InP/InGaAs/InP pHEMT with an InGaP diffusion barrier layer grown by LP-MOCVD using an N₂-carrier," *Proc. 26th European Solid-St. Device Research Conf. ESSDERC'96*, eds. G. Baccarani and M. Rudan, Editions Frontières, pp. 877-880, 1996.
- [15] P. Kordos, J. Betko, M. Morvic, J. Novák, and A. Förster, "Conductance properties of as-grown and annealed MBE GaAs layers grown at temperatures between 200 and 420 °C," *Proc. 9th Conf. Semicond. and Insulating Mater. SIMC-9*, IEEE, XXXX, pp. 37-XX, 1996.
- [16] P. Kordos, A. Förster, J. Darmo, J. Betko, and G. Nimtz, "Space-charge controlled conduction in low-temperature-grown molecular-beam epitaxial GaAs," *Appl. Phys. Lett.*, vol. 71, pp. 1118-1120, 1997.
- [17] P. Kordos, A. Förster, M. Marso, and F. Rüders, "550 GHz bandwidth photodetector on low-temperature grown molecular-beam epitaxial GaAs," *Electron. Lett.*, vol. 34, pp. 119-120, 1998.

MICROWAVE COMPONENTS AND DEVICES BASED ON HIGH TEMPERATURE SUPERCONDUCTORS

O.G. Vendik

Electrotechnical University, 5 Prof. Popov str., St. Petersburg, 197376, RUSSIA
Phone: +7 812 234 99 83, FAX: +7 812 234 48 09 E-mail: mcl@eltech.ru

High temperature superconductors (HTS), just after discovery, were investigated and oriented for practical applications at microwaves [1,2]. The following area of HTS study at microwaves can be specified:

1. Low loss transmission lines and high quality resonators and filters,
2. Signal limiters, switches and digital phase shifters based on transition from superconducting to normal state of the HTS material (S-N transition),
3. Bolometers and resistive type mixers for frequency up to a few THz,
4. Applications of Josephson effect to generation and detection of THz frequency signals and to frequency measurement and spectroscopy.

All these applications are realized at the operational temperature of 60-80 K. $\text{YBa}_2\text{Cu}_3\text{O}_7$ epitaxial films on single crystal substrate [3] are commonly used. The temperature of superconductive phase transition of the films is about 90 K. The films can be fabricated on the industrial level [4].

Low loss transmission lines and high quality resonators and filters

The most important characteristic of HTS films is the surface resistance R_{sur} (Fig. 1). For the best films $R_{\text{sur}} = 0.3 \text{ m}\Omega$ at $T = 78 \text{ K}$, $f = 10 \text{ GHz}$. R_{sur} of HTS is proportional to f^2 and at $f > 100 \text{ GHz}$ becomes to be comparable with R_{sur} of copper or gold. Important field of application of HTS films is narrow-band filters with extremely low insertion loss in pass band and sharp skirts, providing high power handling capability. The main goal of the investigations was development of design procedure of planar structure filters that allows to use the integrated technology of the filters without any trimming (Fig. 2) [5]. The trimming-less technology is based on a specified computer design procedure which is used as added tool to commercial software.

As an impressive example of HTS film applications, the planar disk resonator should be mentioned [6] with $Q = 10^5$ at $T = 78 \text{ K}$, $f = 4 \text{ GHz}$. The low-loss microwave delay lines form the specific area of the HTS film applications [7].

Microwave components based on S-N- transition

The essential feature of the superconducting films is not only the small microwave surface resistance but also the S-N- transition which can be induced by either *ac* or *dc* current and exhibits itself as a large change of the film surface resistance (See Fig. 3) [8].

The destruction of the S-state by the *ac* or *dc* current is a kinetic process in the electron subsystem of the film. Characteristic time of such a process is $10^{-11} - 10^{-12} \text{ s}$ for HTS. The returning from the N-state to the S-state is a thermal process with characteristic time about $10^{-7} - 10^{-8} \text{ s}$ [8]. The variety of the devices based on the S-N-transition can be found in literature [9, 10]. The phenomena of the S-N transition forms a wide field of investigations of relaxation processes and nonequilibrium noises in the HTS films in superconducting and resistive states. The efficiency of a switch can be characterized by the switching quality factor K , which in the case of the S-N transition is :

$$K = \frac{R_N}{R_S}, \quad (1)$$

For YBCO films at $f \leq 20 \text{ GHz}$ and $T = 77 \text{ K}$ the quality factor $K \geq 10^4$ [11]. However, the small value of $R_N = 1-3 \Omega$ complicates a design of the switch connected with a 50Ω transmission line. To obtain a higher value of the N-state resistance, a long narrow strip should be used as a switching element. Hence the S-N element should be considered as a resistor and inductance in series. Fig. 4 shows the equivalent diagram of reflection type phase shifter using the S-N element. Two port passive network provides the matching of the L-R load, where L is sum of geometric and kinetic inductance of the element, $R = R_M$ and is determined as follows

$$R_M = \sqrt{R_S R_N}. \quad (2)$$

For S- and N-states the reflection type phase shifter provides the phase of the reflection coefficient 180° and 0° with minimum return losses, for both states being equal to

$$a_{dB} = 13.76 \frac{1}{\sqrt{K}} \quad (3)$$

Bolometers and resistive type mixers

In recent years, a significant advance has been made in a development of high frequency low noise heterodyne receivers based on bolometric effects [12]. The idea is to thermally separate the electron and phonon subsystems in the superconducting film. It is possible, if the electron-electron scattering time is less than the electron-phonon scattering time. Such a device is called hot electron bolometric (HEB) mixer. HEB mixer based on low temperature superconducting films (NbN) demonstrated low noise operation up to several hundreds of GHz signal with IF about 10 GHz. The operational principle of a HEB mixer is illustrated by Fig. 5. The experience gained with low temperature superconductors is being successfully generalized to the HTS applications [13].

Applications of Josephson effect

Technology of Josephson junctions (JJ) based on HTS has been developed [14]. The circuits, in which the JJ and small size antenna are integrated, are used for detection of THz frequency signals. Applications of JJ to microwave spectroscopy makes possible to cover a wide frequency range with a high spectral resolution (so called Hilbert spectroscopy) [15]. As an example of JJ microwave applications, the quasi-optical integrated receiver with YBCO JJ can be considered [16]. A log-periodic antenna is integrated with JJ on a bicrystal MgO substrate (Fig. 6). The influence of 350-850 GHz radiation on YBCO JJ was experimentally demonstrated (Fig. 7).

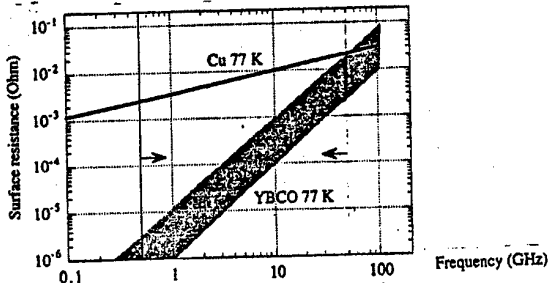


Fig. 1. Dependence of the surface resistance of YBCO and copper samples on frequency

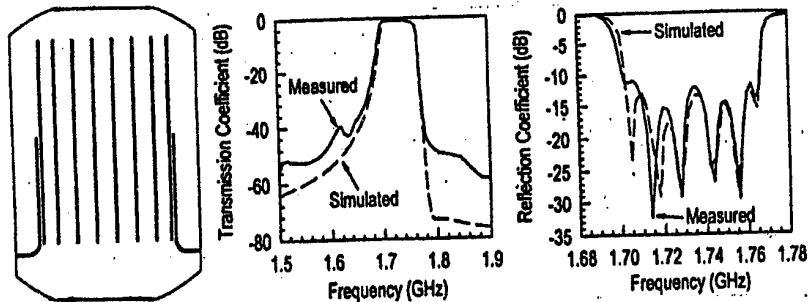


Fig. 2 Multi-pole YBCO strip line filter: layout and characteristics

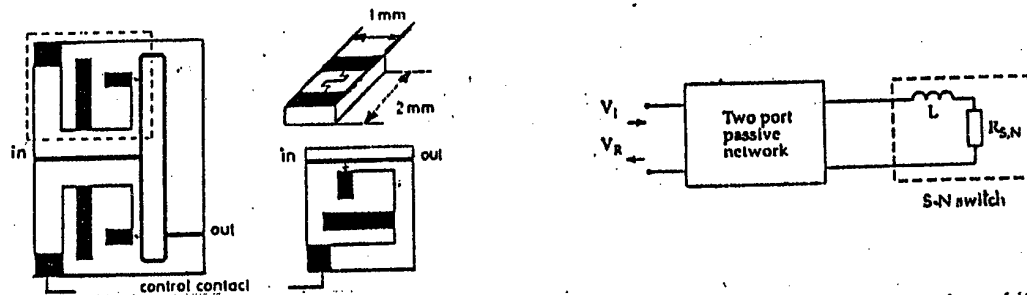


Fig. 3. Schematic of the 0-180° phase shifter.

Fig. 4 Equivalent diagram of reflection type phase shifter

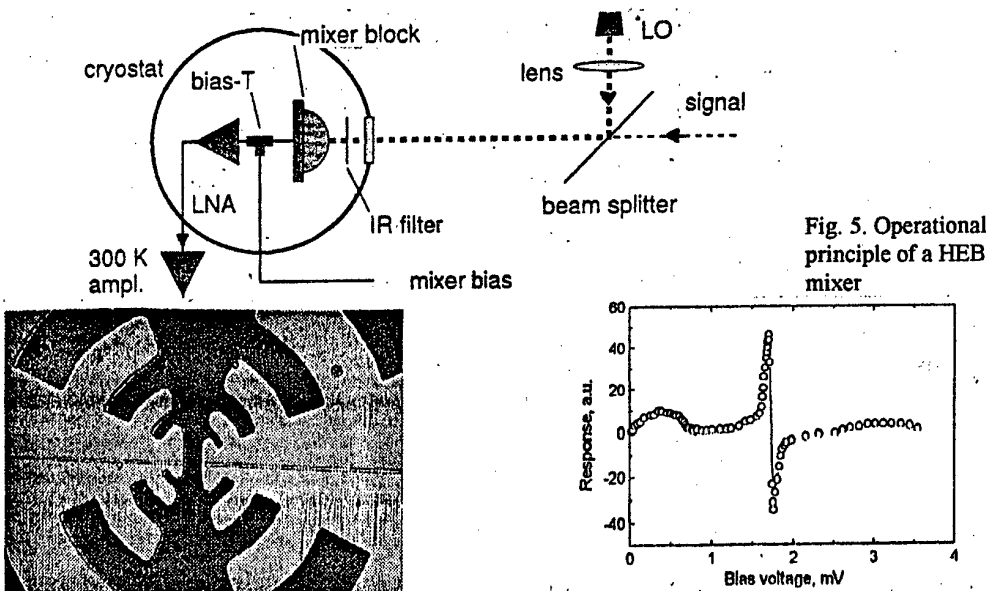


Fig. 6. Log-periodic antenna integrated with JJ.

Fig. 7. Current response of HTS JJ measured at 830 GHz.

References:

1. M. Bielski, O.G. Vendik, M.M. Gaidukov et al., "Surface resistance of Y-Ba-Cu-O ceramics in the region between RF and microwave frequencies", *JEPT Lett.*, Vol. 46, Suppl. pp. S145 - S147 (1987).
2. K.K. Likharev, V.K. Semenov, A.B. Zorin, "New potentialities of superconductor electronics" (In Russian), *ВИНИТИ АН СССР, сер. "Сверхпроводимость"*, том. 1 (1988).
3. E.K. Hollmann, O.G. Vendik, A.G. Zaitsev, B.T. Melekh, "Substrates for high-Tc superconductor microwave integrated circuits", *Supercond. Sci. Technol.* Vol. 7, pp. 609-622 (1994).
4. Special Issue on the Microwave and Millimeter Wave Applications of High temperature Superconductivity, *IEEE Trans. on MTT*, Vol. 44, No. 7, pp. 1193-1392 (1996).
5. I. Vendik, M. Gubina, A. Deleniv et al. "Linear and Nonlinear Characteristics of Microstrip and Coplanar Waveguide Microwave HTS Devices on Sapphire Substrate", *ISEC '97, Berlin*, Vol. 3, pp. 263-265 (1997).
6. H. Chaloupka, M. Jeck, B. Gurzinski, S. Kolesov, "Superconducting planar disk resonators and filters with high power handling capability", *Electronics Letters*, Vol. 32, No. 18, pp. 1735-1736 (1996).
7. W.G. Lyons, D.R. Arsenault, A.L. Keast et al., "Wide band compressive receiver based on advanced superconductor and semiconductor circuits", *IEEE Trans. on AS*, Vol. 7, No. 2, pp. 2462-2467 (1997).
8. M.M. Gaidukov, S.G. Kolesov, L. Kowalewicz et al., "Microwave power limiter based on high-Tc superconducting film", *Electronics Letters*, Vol. 26, No. 16, pp. 1229-1230 (1990).
9. D.I. Kaparkov, V.V. Kuznetsov, M. Löfgren, I.B. Vendik, "Nonreflective high-Tc superconductive modulator", *Electronics Letters*, Vol. 29, No. 11, pp. 1006-1007 (1993).
10. M.M. Gaidukov, A.B. Kozyrev, V.N. Osadchy, "Microwave phase shifter based on high-Tc superconducting films", *Electronics Letters*, Vol. 31, No. 12, pp. 983-985 (1995).
11. I.B. Vendik, "The limitation of the parameters of a one-bit phase shifter based on S-N transition in high-Tc superconductors", *Microwave and Optical technology Letters*, Vol. 7, No. 14, pp. 644-646 (1994).
12. G.N. Gol'tsman, E.M. Gershenson, "Phonon-cooled hot-electron bolometric mixers: overview of recent results", *ISEC '97 (Berlin)*, Vol. 1, pp. 89-91 (1997).
13. M. Danerud, D. Winkler, M. Zorin et al., "Nonequilibrium and bolometric photoresponse in patterned $\text{YBa}_2\text{Cu}_3\text{O}_{7-x}$ thin films", *J. Appl. Phys.*, Vol. 76, No. 3, pp. 1902-1909 (1994).
14. K.A. Delin, A.W. Kleinsasser, "Stationary properties of high Tc proximity effect Josephson junctions", *Supercond. Sci. Technol.* Vol. 9, pp. 227-239 (1996).
15. M. Tarasov, A. Shul'man, G. Prokopenko et al., "Quasioptical Hilbert transform spectrometer" *IEEE Trans. on AS*, Vol. 5, No. 2, pp. 2686-2689 (1995).
16. M. Tarasov, A. Shul'man, O. Polyansky et al., "Quasioptical integrated $\text{YBa}_2\text{Cu}_3\text{O}_7$ receiver for direct detection and Hilbert spectroscopy in 350-850 GHz band", *ISEC '97 (Berlin)*, Vol. 1, pp. 83-85 (1997).

RADAR ESTIMATIONS OF SOIL PARAMETERS BY MULTICHANNEL METHODS

G.P.KULEMIN

Institute of Radiophysics and Electronics of Ukrainian National Academy of Science, 12 Proskura St, 310085
Kharkov, Ukraine, tel. (0572) 448-508, E-mail gena@ireas.kharkov.ua

A possibility of separate estimation of soil moisture and surface roughness is considered, the results of numerical simulations are presented. It is shown that the use of multifrequency and dual-polarization radar methods permits to estimate the dielectric constant of soil, r.m.s values of roughness and spatial correlation radius. It is demonstrated also that a fractal approximation of surface spatial spectra enables to obtain the most accurate estimations of soil surface parameters. Experimental results for 3.0 and 0.8 cm are presented as well showing the possibility of dual-polarization data processing for land erosion degree determination.

The rational use of agricultural fields requires an urgent elaboration of remote sensing techniques for soil characteristic determination because the traditional methods of in situ measurements do not provide the obtaining of data detailed enough for practice and, besides, they are too labor consuming. During last decades, besides the optical and infrared methods, the radar methods of soil characteristic study have got an intensive development, in particular, the near-surface soil moisture estimation, the determination of humus content and soil erosion degree. The high resolution and the weather independence of radars determine their practical application to remote sensing of large terrains with the use of airborne and spaceborne carriers of radars (synthetic aperture radars-SAR or side-look radars-SLAR). For radar methods of remote sensing the electromagnetic field scattered by the objects serves as a source of information about the physical and chemical properties of sensed surfaces. Because of this reason the processes of microwave scattering from bare soil have been the subject of theoretical and experimental investigations for many years. This research activity was directed on the search of correlation between the parameters of scattered electromagnetic field and the statistical and agrophysical characteristics of soil.

The capability of active microwave techniques to be sensitive to near-surface soil moisture has a considerable research interest. The basis for microwave remote sensing of soil moisture is the dependence of the soil's dielectric properties on its moisture content due to a large contrast between the dielectric constant of water and that one of dry soil. Boundary conditions of interest to soil characteristics include the small-scaled random surface roughness generated by agricultural tillage practice, the soil erosion processes, the azimuthally dependent ridge/furrow patterns, the slope of a terrain element affecting the local angle of incidence, etc.

As is well known, the scattered signal intensity is determined by the statistical characteristics of surface and the medium dielectric constant. However, the range of the soil specific radar cross-section (RCS) variations due to moisture influence does not exceed 8 - 10 dB, at the same time the roughness variations can lead to 15 - 25 dB of RCS variations. Consequently, the effects of surface roughness create the obstacles to correct estimation of soil moisture.

The use of dual-polarization ratio of specific RCS for obtaining of unbiased estimation of real part of complex dielectric constant was first time proposed in [1], this ratio was also used in [2]. The application of radar multifrequency technique to determination of surface roughness was proposed in [3], this approach was used for small incidence angles and joint processing was not applied. In papers [4-5] the application of multichannel techniques to separate determination of near-surface soil moisture and surface roughness was proposed and the joint processing of data was used. Taking into account that roughness parameters mainly depend on mechanical and aggregate soil structure, the successful retrieval of this information provides the potential possibility to determine the soil lots with different degree of erosion and to analyse the dynamics of their evolution. This paper presents the results of theoretical and experimental investigations into multichannel remote sensing techniques application to estimation of soil parameters at the microwave band.

In modeling of the wave scattering from natural terrains one generally expects a combination of surface and volume scattering, especially when a dry soil medium is inhomogeneous. The soil medium can be treated as a volume consisting of variable fractions of soil solids, aqueous fluids, and air. Soil solid material is a mixture of sand, silt, and clay and it is characterized by a distribution of particle sizes (texture) and mineralogy of

their consistent particles (particularly, a clay fraction). The particle diameter of clay is less than 2μ , the particle diameter of silt is between 2μ and 50μ , and the particle diameter of sand is between 50μ and 200μ . The water in soil is classified as free and bounded water.

Modeling of scattering from bare natural and agricultural soils starts from a characterization of the surface roughness and dielectric behavior of materials. The latter one depends on several parameters including the bulk density, the particle size distribution, the mineralogical composition, the content of organic matter, the content of bound and free water, the soil salinity, and the temperature. All the models can be divided into two groups: the field-approach models and the intensity-approach ones [6]. The disadvantage of the existing field-approach models is that they cannot in practice include the multiple incoherent scattering beyond the second order. On the other hand, the intensity-approach models can include more multiple scattering terms and the interaction between surface and volume scattering but it assumes a far field interaction between scatterers. We restrict ourselves to rough surface scattering models only and neglect the volume scattering although in practice these two effects are sometimes difficult to separate. For the bare soil the surface scattering is dominant only if the terrain can be considered homogeneous.

Two rough surface scattering models are widely applied because of their simplicity: the Kirhhoff and the first-order small perturbation models [7]. In most backscattering applications the Kirhhoff model is used over the incidence angular region $0 < \theta < 20^\circ$. Besides, this model is restricted to high frequencies and indicates that for perfectly conducting surfaces the backscattering fields do not depend on polarization.

A small perturbation model is used over the remaining part of an angular range, $20^\circ < \theta < 60^\circ$. Larger influence angles are not considered because the scattering mechanisms for grazing incidence are likely to be different from a purely surface scattering phenomenon. Using a perturbational approach derived for surfaces with small gradients ($k\sigma_h < 0.3$ where $k=2\pi/\lambda$ is the wavenumber and σ_h is the r.m.s. of the roughness height), the backscattering field is shown to be strongly dependent upon the polarization of the incident and scattered waves.

There are other scattering models which are, perhaps, potentially more powerful than the previous ones but they have not yet been extensively applied to the interpolation of experimental measurements. Without going into any details, we mention three methods which seem potentially the most promising ones: the full-wave method of Bahar [8] bridging the wide gap existing between the perturbational solutions for rough surfaces with small slopes and the quasi-optics solutions, the diagram method [9], the stochastic Fourier method [10]. These methods are not fully developed yet but the results obtained appear to be very encouraging.

In all the models of rough surface scattering the specific RCS of surface characterizing the intensity of scattered field is a product of two functions

$$\sigma_{pp}^o(f, \theta_i) = D_{pp}[\epsilon_s(f, \theta_i)] \cdot S(f, \theta_i). \quad (1)$$

The first function $D(\cdot)$, or so-called dielectric function, characterizes the dielectric properties of the scattering medium and depends upon the polarization $pp = HH, VV$, the angle of incidence θ_i and the dielectric constant ϵ_s . For these models the dielectric functions are equal or proportional to the Fresnel reflectivity, i.e. they present equally the RCS dependence as a function of medium dielectric constant. Their main limitation is a non-adequate estimation of the scattering coefficients for cross-polarized components of the scattered signals. The second function $S(\cdot)$ takes into account the surface roughness influence on specific RCS, f denotes the radar frequency.

For analysis of the multichannel method capabilities we have used the simple surface scattering models, particularly, the small perturbation model. This is conditioned by some reasons. First of all, for agricultural soils with different types of tillage the condition $k\sigma_h > 1$ usually is fulfilled at microwave band. Then the small perturbation model can be used only for approximated estimation of the specific RCS. However, the model derivations of specific RCS dependences as the functions of incidence angles, the r.m.s. surface roughness heights, and the soil moisture coincide rather accurately with the experimental results up to $k\sigma_h > 2.5 - 3.0$ and more [9]. The most essential differences between the model and experimental results are observed for the cross-polarized components of the scattered signals. Besides, for the considered multichannel methods we have used the ratios of the specific RCS at different frequencies and polarizations when the absolute errors of RCS estimations from the perturbational model have not influenced greatly on the ratio values.

The moisture content determination is based on the correlation between the dielectric function and the soil dielectric constant and also on the dielectric function dependences on the frequency and the soil moisture. The results of simulation [5] have shown that the dielectric functions had a weak dependence upon frequency at microwave band while the soil dielectric constant differed essentially for different frequencies. Its analysis shows

that the maximal difference of dielectric functions do not exceed 1 dB if the ratio of two frequencies satisfies the condition

$$1 < f_2 / f_1 < 2 - 3, \quad (2)$$

i.e. for the microwave band the dielectric functions are practically frequency independent. The most obvious dependence of D on f takes the place for moisture $0.05-0.2 \text{ g cm}^{-3}$. The lower bound of this interval deals with a free water molecules appearance in soil, when the moisture content exceeds $0.2-0.25 \text{ g cm}^{-3}$ the saturation of dielectric functions occurs. This phenomenon leads to some important conclusions:

- the potential moisture content sensitivity is equal for all frequencies at microwave band;
- the weak frequency dependence of the dielectric functions provides the opportunity of soil moisture estimation for the upper soil layer and measurement of some other statistical characteristics on basis of the joint analysis of multichannel remote sensing data

As it is shown in [5], in the framework of small perturbation approach it is theoretically possible to separate and to estimate accurately the roughness and the moisture parameters on the basis of multichannel measurements without *a priori* knowledge of surface statistical characteristics. In the most simple case of two-frequency remote sensing it is possible to select the frequencies f_1, f_2 and the angles of incidence θ_1, θ_2 in such a way that the ratio of corresponding functions of roughness does not depend on surface statistical characteristics. The condition of such independence is described by the equation

$$k_1 \sin \theta_1 = k_2 \sin \theta_2 \quad (3)$$

Then the ratio of the RCS for two polarizations is equal to

$$\frac{\sigma_{pp,1}^o}{\sigma_{qq,2}^o} = \frac{\sigma_{pp,1}^o(f_1, \theta_1)}{\sigma_{qq,2}^o(f_2, \theta_2)} = \frac{D_{pp}(\varepsilon_1, \theta_1)}{D_{qq}(\varepsilon_2, \theta_2)} \cdot \frac{(k_1 \cos \theta_1)^4}{(k_2 \cos \theta_2)^4} \quad (4)$$

Here $pp, qq = HH$ or VV , $\varepsilon_1 = \varepsilon(f_1)$ and $\varepsilon_2 = \varepsilon(f_2)$. The ratio (8) is the function of dielectric constants, wavelengths, and angles of incidence and it does not depend on surface statistical characteristics. The remote moisture determination can be performed from (8) taking into account that the dielectric constants are the functions of the volume moisture content of the soil upper layer. Here we can consider five polarization ratios

$$R_1 = \frac{\sigma_{HH,1}^o}{\sigma_{HH,2}^o}; R_2 = \frac{\sigma_{HH,1}^o}{\sigma_{VV,2}^o}; R_3 = \frac{\sigma_{VV,1}^o}{\sigma_{HH,2}^o}; R_4 = \frac{\sigma_{VV,1}^o}{\sigma_{VV,2}^o}; R_5 = \frac{\sigma_{HH}^o}{\sigma_{VV}^o} \quad (5)$$

The polarization ratio R_5 is the particular case when $f_1 = f_2 = f$, $pp = HH$, $qq = VV$. It was for the first time proposed in [1], in this paper it was shown that this ratio served for obtaining of unbiased estimation of real part of complex dielectric constant. Moisture dependence R_5 for the operation frequency of $f = 10 \text{ GHz}$ and for the different angles of incidence is presented in [5]. The nonlinear behavior of this dependence is well seen. The variation range of R_5 value increases with the angle of incidence increase and for $\theta = 50 - 60^\circ$ it is approximately equal to 6 dB. The maximal moisture sensitivity is observed for volume moisture content less than 0.25 g cm^{-3} and it is approximately equal to $0.24 \text{ dB} / 0.01 \text{ g cm}^{-3}$. For more wet soil the saturation is observed, the sensitivity decreases more than 3 times.

Multichannel technique of statistical characteristics estimation for some surfaces in the framework of small perturbation method is based on the use of the following relationship [4]

$$SR_i = \frac{\sigma_{pp}^o(\theta_i, f_1)}{\sigma_{pp}^o(\theta_i, f_2)} = \frac{D_{pp}[\theta_i, \varepsilon_s(f_1)] \cdot S(\theta_i, f_1)}{D_{pp}[\theta_i, \varepsilon_s(f_2)] \cdot S(\theta_i, f_2)} \quad (6)$$

The weak frequency dependence of a dielectric function in microwave band permits to assume that

$$D_{pp}[\theta_i, \varepsilon_s(f_1)] \approx D_{pp}[\theta_i, \varepsilon_s(f_2)] \quad (7)$$

This assumption is permissible taking into account the fact that the instrumental accuracy of specific RCS estimation is 1.5 dB and especially if the operation frequencies f_1 and f_2 are comparable, i.e. when $(f_2 - f_1) \ll (f_1 + f_2)/2$ and $f_2/f_1 < 1.5$. In such conditions the expression (10) is the function of surface parameters only and it does not depend on $\varepsilon_s(f)$.

The further estimation of the statistical characteristics is determined by the model of a surface roughness spatial spectrum. Most often the surfaces with a Gaussian surface height distribution and any surface autocorrelation function are used. For surfaces with this height distribution and a Gaussian autocorrelation function analytical expressions available for cross checking. In addition, many surface scattering theories have been reported in the literature using the Gaussian height assumption, although the roughness spectrum of natural surfaces generally have more high frequency components than the Gaussian roughness spectrum.

The rapidly increasing number of applications of fractal models and fractal geometry in physics deserve the close attention of researches from various areas, particularly, in remote sensing of land. It was first demonstrated by M. Berry [10] that for Gaussian statistics the surfaces with a simple power spectrum of the type

$$W_1(\Lambda) = C_1 \Lambda^{-\alpha}, \quad 1 < \alpha < 3 \quad (8)$$

are fractal rough surfaces. We remark that the spectrum W is defined for any real Λ , therefore, the corresponding surface has no characteristic scales and the r.m.s. height is not defined ($\sigma_h \rightarrow \infty$). For the values of the spectral exponent α given by (8) the Fourier transform of W is a divergent integral, thus, the correlation function does not exist.

The second type surfaces have the same expression for the roughness spectra but with an outer (or large scale) cutoff Λ_o

$$W_2(\Lambda) = \begin{cases} C \Lambda^{-\alpha} & \text{for } \Lambda \geq \Lambda_o \\ 0 & \text{for } \Lambda < \Lambda_o \end{cases} \quad (9)$$

In view of the experimental data type II surfaces appear to be particular importance in the practice of remote sensing (here most often case is $\alpha = 2$). We should like to note that for large Λ the spectra form (7) and (8) are identical but type II spectra have finite r.m.s. height σ_h and infinite r.m.s. slope.

The estimation of the fractal spectrum exponent is equal to

$$\hat{\alpha} = \ln(SK_i)/\ln(\Lambda_{2,i}/\Lambda_{1,i}). \quad (10)$$

The constant C is linked with σ_h by the expression

$$\sigma_h = (\sqrt{C} \cdot \Lambda_o^{1-\alpha/2}) / [\alpha \cdot \sin(\pi/\alpha)] \quad (11)$$

The value of Λ_o is not greater than 2 when $\alpha = 1-3$; for $\alpha = 2$ the value of $C = \sigma_h^2$.

Therefore, it is obvious that in multichannel approach we can obtain only one characteristic of surface from the radar measurements: the fractal spectrum exponent.

The efficiency of considered multichannel approaches was investigated on basis of the experimental results obtained in [3] for a bare field. The experimental angular dependences of the specific RCS for this field are obtained at the frequency of 4.7 GHz for two polarization of radiation. The soil solid is characterized by the high clay content (about 40 %). The measurements have been carried out for dry soil (gravimetric moisture was 4.3 %) and for wet soil with gravimetric moisture about 30.2 %. The high clay content results in the temporal invariable r.m.s. of surface roughness heights of about 2.5 cm.

The estimations of exponent α were formed from data of σ^0 . The I_{eff} and α data for dry and wet soils are presented in Table 1.

The α values for dry soil are identical practically for both polarizations of radiation and they differ essentially for wet soil. With the use of C estimations we derived the values of surface roughness spectral density; their values are presented in Table 1, too. The application of Gaussian and exponential models for the autocorrelation function permits to estimate the correlation radius of field roughness. The surface roughness for this field does not satisfy the small perturbation model. In these conditions the derived values of I do not correspond to real values of I for agricultural fields. At the same time the fractal approximation of surface spectra seems to be more suitable because the spectral exponent is in a good agreement with the value range ($\alpha = 1 - 3$). Thus, the application of multichannel methods permits to obtain the soil dielectric constant and, consequently,

the soil moisture and the soil statistical characteristics with the use of the fractal model for the surface spectra even for rough surfaces when the limitations of small perturbation model are infringed.

The experimental study of the multichannel method applications to soil characteristics estimation was carried out at the end of September 1992 [11]. The agricultural field was located on a hill and its different lots had average slopes between 2 and 8°. The system tillage performed three weeks earlier across the slope included chisel, disking and harrowing. The soil type was chernozem with four stages of soil erosion. Visual inspection indicated that the periodic row structure was almost destroyed by many rainfalls.

The surface roughness was measured with a profile meter with density of 1 measurement per 10 mm which permitted to ensure the errors not greater than 5 mm. The common length of every surface profile was equal to 6 - 7.5 m. The profile processing included the obtaining of autocorrelation functions and spatial spectra along and across the directions of the mechanical tillage.

The method of soil tillage can result in the essentially different degree of roughness for the same agricultural region. It is worth noting that for fields with the periodical structure the r.m.s. surface height depends greatly on the profile orientation in respect to the ploughing furrows. However, for fresh-ploughed fields the periodicity is often essentially distorted by clodness. The small and rather large clods appearing for breast ploughing are oriented randomly. Their dimensions depend on the moisture and the soil type. In general, the surface normalized autocorrelation function can be approximated by the following expression

$$\rho(\xi) = \exp(-\gamma \cdot \xi) \cdot \cos(2\pi\xi / \beta) \quad (12)$$

where ξ is the spatial coordinate. The statistical dependence between parameters γ and β was not detected. The more general approximation can be used for dual-scale roughness (the typical cases are the ploughed and harrowed fields), it takes into account the peculiarities of the field tillage. For this case

$$\rho(\xi) = (1 - A) \cdot \exp(-\gamma\xi) \cdot \cos(2\pi\xi / L_p) + A \cdot \exp(-\eta\xi) \cdot \cos(2\pi\xi / L_h) \quad (13)$$

where the coefficient A is determined by the ratio of harrowing and ploughing depths, L_p denotes the distance between the furrows of ploughing, L_h defines the distance between the furrows of harrowing.

The observations show that the change dynamics of field roughness (if the fields are not subjected to additional tillage) is fully determined by the atmosphere humidity conditions, the aggregate and mechanical soil contents. On the initial stage the roughness smoothing caused by rainfalls can result in the increase of periodicity because the process of furrow destroying is more prolonged in comparison to the process of clod destroying.

It is worth noting that the percent content of clay in the soil is a basic factor determining the degree of field roughness after the furrow and the clod destroying under the influence of natural conditions. The mechanical and aggregate soil contents are subjected to slow permanent change and, as the result, to erosion. The field slope about of 5 - 10° is the reason for heavy- and middle-eroded areas forming. The mechanical and hydrophysical properties of such soils differ from those ones of non-eroded soils. Therefore, it is possible to expect that in the borders of the same terrain the different degree of erosion can be settled as the result of the same field tillage. For such fields the successful separation of the roughness and moisture effects and their accurate estimation offers the potential possibility to retrieve the information about the erosion process and its evolution. The process of furrow destroying manifests itself in removal of the periodical structure of the autocorrelation function. The autocorrelation functions of surface roughness along the direction of tillage almost do not differ from the autocorrelation functions of isotropic surfaces. In the spatial spectra the second maximum appeared rather often, it is connected with the tillage type. However, in our measurements it is not observed because of the soil washing off.

For roughness characteristics determination the fractal approximation of spatial spectra was used. The average values of σ_h and fractal exponent α are presented in Table 2. The averaged exponent in the experimental spectra was equal to $\alpha=1.61\pm0.89$. For profiles with a strongly marked periodic row structure without the non-averaged exponent α of a fractal spectra does not change considerably; its values were equal to $\alpha=1.64\pm1.02$.

The data analysis showed that the value of σ_h along the direction of tillage practically did not depend on soil erosion degree but we observed the decrease of σ_h with the increase of erosion degree across the direction of tillage. At the same time the decrease of α was observed along the direction of tillage when the erosion degree increased. This shows the increasing of the spatial correlation radius for non-eroded soils in comparison to eroded ones.

The results of the angular specific RCS dependence study have shown the following:

- the specific RCS for wavelength of 8 mm is greater by 3 - 6 dB than for wavelength of 3 cm for all selected surface areas and for both polarizations of radiation and reception of copolarized components;
- the specific RCS values for vertical polarization exceed those ones for horizontal polarization by 0.2-8 dB depending upon the surface erosion degree;
- the speed of the angular RCS variations depends on the erosion degree.

Dual-channel polarization processing (with the use of ratio R_s) has permitted to emphasize its sensitivity to variations of soil agrophysical parameters. It is seen from Table 3 data where the polarization ratios $\sigma_{HH}^0 / \sigma_{VV}^0$ are presented averaged for all region of incidence angles. The maximal value of this ratio at the wavelength of 3 cm equals to - 6.6 dB for heavy eroded lot and it equals to 7.7 dB for non- eroded lot. The good correlation between the ratio R_s and the agrophysical parameters of soil are observed.

For the incidence angles $\theta = 35 - 45^\circ$ the maximum sensitivity of R_s to agrophysical parameter variations is observed at the wavelength of 3 cm but at the wavelength of 0.8 cm the maximum sensitivity is observed for the incidence angles greater than 60° .

The angular dependences of the specific RCS ratios for the cross-polarized components reception seem to have no correlation with soil erosion degree . The depolarization increases with the wavelength decrease from - (10 - 13) dB for wavelength of 3 cm to -(5-8) dB for wavelength 8 mm, the correlation of these values with erosion degree is not observed

Thus, it is shown theoretically that the multichannel methods permit to separate and to estimate the roughness parameters and the dielectric constant of soil near-surface layer. The obtained ratios for multichannel approaches can be used when the small perturbation model conditions are not satisfied fully. The fractal spectra are the best approximations of the surface roughness spectra.

The existence of the correlation between the radar and agrophysical characteristics of soil was proved experimentally. In particular, the use of dual-polarization processing permits to increase the sensitivity of radar remote sensing techniques to the soil erosion change.

Table 1

The values of $|\epsilon|$, α and $W(k_1)$ for dry and wet soil.

Polarization	HH	HH	VV	VV
Gravimetric volume, %	4.3	30.2	4.3	30.2
$ \epsilon $	3	35	3	35
α	0.8-1.1	0.8-1.1	1.0-1.3	2.3-2.5
$W(k_1)$, dB	-(76.7-78.5)	-(76.7-78.5)	-(79.8-80.5)	-(87.4-88.1)

Table 2

Roughness characteristics of investigated lots

Erosion degree		Non - eroded	Weakly eroded	Middle eroded	Heavy eroded
Along furrows	σ_h , cm	1.7	1.54	1.46	1.28
	α	1.8	1.6	1.35	1.3
Across furrows	σ_h , cm	2.1	2.45	1.9	1.8
	α	1.9	1.75	1.85	1.7

Table 3
The ratio R_5 values of investigated lots at wavelengths 0.8 and 3 cm

Erosion degree	Non - eroded	Weakly eroded	Middle eroded	Heavy eroded
$\frac{\sigma_{HH}^{\rho}}{\sigma_{VV}^{\rho}}$, dB $\frac{0.8cm}{3cm}$	11.4 7.7	6.0 0.2	3.4 - 3.1	- 4.5 - 6.6

References

1. Yakovlev V.P. On radiometer and radar abilities for surface remote sensing, "Proc. of State Scientific Center of Natural Resources Study", Gidrometeoizdat, Leningrad, 1986, No 26, pp. 27-31 (in Russian).
2. Shi I., Soares I.V., Hess L. et. al. SAR-derived soil moisture measurements for bare fields," Proceedings of IGARSS" 91,1991, pp. 393 - 396.
3. Mo T., Wang J.R., Schmugge T.J. Estimation of surface roughness parameters from dual frequency measurements of radar backscattering coefficients, IEEE Trans. Geosci. and Remote Sensing, 1988, GE-26, pp. 574-579.
4. Kulemin G.P., Zerdev N.G., Application of multichannel radar methods of remote sensing for soil parameter estimations, " Electromagnetic Waves and Electronic Systems", 1997, v.2, No 5, pp. 82-92 (in Russian).
5. Kulemin G.P., Zerdev N.G., Soil moisture determination by multichannel radar techniques, "Soviet Journal of Remote Sensing", 1993, v. 1, No 11, pp. 139-152.
6. Ishimaru A. Wave propagation and scattering in random media , N.Y., London, Academic Press, 1978.
7. Bahar E. Full wave solutions for the scattered radiation fields from rough surfaces with arbitrary slopes and frequency, IEEE Trans. ANt. and Prop., 1980, AP-28, pp. 11-21.
8. Zipfel C.C., DeSanto J.A. Scattering of a scalar wave from a random rough surface: a diagrammatic approach, J. Math. Phys., 1972, 13, pp. 1903-1911.
9. Brown G.S. A stochastic Fourier transform approach to scattering from perfectly conducting randomly rough surfaces, IEEE Trans. Ant. and Prop., 1982, AP-30, pp. 1135-1144.
10. Feder J. Fractals , N.Y., John Waley , 1988.
11. Zerdev N.G., Kulemin G.P. Soil erosion effects in microwave backscattering from bare fields, "24 Europ. Microwave Conf. Proceedings" (Sept., 5-8, 1994, Cannes, France), 1994, v. 1, pp. 431-436.

STATE OF THE ART OF GYROTRON DEVELOPMENTS AND INVESTIGATIONS

A. Goldenberg

*Institute of Applied Physics of Russian Academy of Sciences; GYCOM Ltd.;
46 Ulyanov street, 603600, Nizhny Novgorod, Russia, FAX (8312) 362061*

Introduction

Gyrotrons are the most powerful radiation sources of the shortest microwaves at long pulses up to continuous wave (CW) regime. At frequencies from several gigahertz to almost 200 GHz they attain 1 MW output power level considerably exceeding other microwave devices. All high-energy and some high power applications of the microwaves are associated with gyrotrons.

Problems of increase in gyrotrons power, efficiency, and frequency were priority ones in their study and development during many years. Now in gyrotrons a technically reasonable power limit is reached with efficiency of electron beam - RF field interaction, near 40%, close to its maximum calculated value. Concerning the increase in frequency of gyrotrons, its possibilities are not exhausted though the advance is relatively slow due to rather weak stimulations.

Now the intense works on gyrotrons are being carried out for some important applications, first of all for heating of plasmas at nuclear fusion installations and high temperature processing of some materials [1]. These efforts has resulted in considerable progress in transfer from long pulses to real CW regime at the highest output power as well as in considerable increase in efficiency of gyrotrons. The modern tendencies in investigations and developments of gyrotrons are described below.

1. Enhancement of radiation energy

Since the 1 MW output power level was achieved at over-1 s pulses, their transfer to CW regime became the key problem of gyrotrons. On this way, the main difficulties are associated with possible overheating of some parts, primarily a resonance cavity and an output window.

Heating of a cavity wall by RF Ohmic losses is characterized by the density of the losses

$$P_{\text{ohm}} = \frac{5kdL}{\lambda^2 R_{\text{cav}}^2 \left[1 - \left(m\lambda / 2\pi R_{\text{cav}} \right)^2 \right]} P_{\text{out}}, \quad (1)$$

where $k \approx 1.5$ is an empirical coefficient, λ is a wavelength, d is the depth of the skin layer, R_{cav} and L are a diameter and effective length of a cavity, respectively, and P_{out} is output power.

Basing on experience, in cavities P_{ohm} is restricted by the maximum value 2 kW/cm^2 . At high-frequency near-1 MW gyrotrons the restriction of P_{ohm} leads to operation at high cavity modes TE_{mp} , with m up to 30 and p exceeding 10. A lot of theoretical and experimental works have shown that at such modes, the gyrotrons' cavities possess sufficient selectivity to oscillate at a fixed mode with rather high efficiency, $\eta \geq 30\%$. At higher modes with denser resonance spectrum, there is a tendency to lower efficiency because of narrowing of a stable mode oscillation zone. This restriction for output is stronger at higher frequencies since P_{ohm} is proportional to $f^{1/2}$.

To avoid the mode competition in gyrotrons it is possible to use a more selective coaxial cavity, in which higher mode can be used. In experimental gyrotrons with coaxial cavities outputs of 1.5-2 MW are achieved at modes with $m \approx 35$ and $p \approx 15$ conserving P_{ohm} admissible for CW performance.

Up to the current year, RF losses in an output window were the main factor limiting pulse duration and prohibiting transfer to CW regime in powerful gyrotrons. In tubes with output from 500 kW to 1 MW boron nitride (BN) disks were used which were heated to the limiting temperature near 800°C (and even higher) during 1 s or several second pulses depending on radiation frequency. Now there is firm opinion that the window problem will be solved soon using CVD diamond disks. Now there are diamond disks with $tg\delta$ near or below 10^{-5} (10-30 times below that of BN). Owing to the low losses and extremely high thermoconductivity the CVD diamond window is capable to transmit 1 MW CW power at frequencies up to 200 GHz, possibly higher. Gyrotrons with the diamond windows have been manufactured already and will be tested during the year.

2. Enhancement of efficiency

Applications of gyrotrons as sources of microwave energy stimulated new interest for increase of their efficiency. Since in them the radiation energy is got from gyration movement of electrons, the total efficiency η is presented usually as a product

$$\eta = \eta_g \cdot \eta_{\perp} \cdot \eta_{ed}, \quad (2)$$

where η_g is a ratio of power associated with the gyration power to the total initial electron beam power P_{beam} , η_{\perp} is a ratio of RF radiation power to P_{beam} , and η_{ed} is a transmission coefficient, taking into account all kinds of radiation losses including Ohmic losses and scattering at conversion and transmission of the radiation.

In (2) usually η_g does not exceed 0.8 and has a tendency to slow decrease at higher electron beam currents and higher operation frequencies. In cavities with optimized longitudinal distribution of RF field and static magnetic field, η_{\perp} can be close to 0.7-0.8, though in the most powerful gyrotrons such optimization leads to stronger mode competition; in them η_{\perp} is usually below 0.6. Total electrodynamical losses defining η_{ed} are near 0.25 in some gyrotrons. The optimization of gyrotron's mode converters based on recent advance in quasi-optics [2] can reduce them to near 0.1 resulting in $\eta_{ed} \approx 0.9$. Therefore in the powerful gyrotrons the efficiency η is usually between 0.3 and 0.4.

Still there is another way to increase the efficiency using energy recovery, that is taking-away part of energy of worked-out electrons in a collector with depressed potential U_{col} below the electron beam potential in a cavity, U_0 , (CPD scheme). Calculations and experiments have shown considerable increase of overall efficiency η_{rec} near 1.5 times, in one-stage CPD-gyrotron according to

$$\eta_{rec} = \eta \frac{U_0}{U_{col}}. \quad (3)$$

Increase of number of collector stages to 2 or 3 is not expedient because this can give rather small additional gain. Using the one-stage CPD, the overall efficiency of experimental gyrotrons η_{rec} was from 50% to 65% (at η between 30% and 40%) [3]. Calculations show that having higher quality electron beam and optimized distributions of the RF and static magnetic fields in a cavity, the efficiency η_{rec} near 80% can be reached [4].

3. Widening of frequency range

An operating frequency of a gyrotron is close to the gyrofrequency or one of its harmonic,

$$\omega = n\omega_B, \quad \omega_B = \frac{eB}{m_0} \sqrt{1 - v^2/c^2}, \quad (4)$$

where e and m_0 are electrons charge and mass of rest, v is its total velocity, c is the light velocity, and B is static magnetic field in a cavity.

The frequency range from several gigahertz to near 300 GHz can be regarded as natural one of gyrotrons. In it at the fundamental gyroresonance, they can attain near or over 1 MW output having rather high efficiency. At higher frequencies, their output and efficiency are restricted by a number of factors, primarily by fast increase in RF Ohmic losses and problems in generating static magnetic fields well over 10T. Then two ways are possible, either use of pulse magnetic fields or operation at 2nd, 3rd or higher harmonics of ω_B .

The pulse magnetic fields have allowed to attain over 600 GHz frequency with 40 kW output at 10 μ s pulses [5].

The operation at higher harmonics allows to reach and overcome 1 THz frequency. There is a lot of experimental efforts to excite rather high harmonics, $n \geq 5$, for this (rf. review [6]).

Such gyrotrons are to be used in various diagnostics of plasmas, gases and solids [1].

4. Gyrotrons for nuclear fusion

All nuclear fusion installations need additional heating of plasmas by sources of many megawatt power in several second pulse or CW regime. Such plasmas are confined by magnetic fields of several tesla corresponding to the electron cyclotron (EC) frequencies near or over 100 GHz as can be seen from (4). These frequencies fall into the natural frequency range of gyrotrons. Now it is widely recognized that heating of the plasmas by the EC resonance radiation has significant advantages over other means such as neutral beam injection and lower frequency RF heating at the ion cyclotron resonance (several tens megahertz) or the low hybrid resonance

(several gigahertz). The modern scenarios of heating and maintenance of nuclear fusion plasmas necessarily include of the EC radiation injection. Particularly this is accepted for the ITER program in which a share of the EC radiation among other heating means is rather high owing to recent progress of gyrotrons in their output power, efficiency and reliability.

Main parameters of gyrotrons now used in many experimental nuclear fusion installations are given in Table 1. All these gyrotrons have built-in mode converters of a cavity mode into a wave beam and all operate in cryomagnets generating the magnetic fields.

Table 1. Some experimental and industrial gyrotrons for heating of nuclear fusion plasmas.

Frequency, GHz	Output power, MW	Efficiency, %	Pulse duration, s	Cavity mode/ output mode	Institute or company
8	1.0	45	1	TE _{5,1} /TE _{5,1}	Thomson
28	0.34	37	CW	TE _{0,2} /TE _{0,2}	CPI (VARIAN)
28	0.5	40	0.1	TE _{4,2} /Gb ^a	GYCOM
53	0.5	40	0.2	TE _{8,3} /GB	GYCOM
83	0.5 0.65	35 50(CPD ^c)	2 1-2	TE _{10,4} /GB	GYCOM
100	2.1	30	3×10^{-5}	TE _{25,13} /TE _{25,13} (coax ^b)	IAP
110	0.9 0.35	35 35	2 10	TE _{19,5} /GB	GYCOM
110	0.35	48(CPD)	5	TE _{10,4} /GB	Toshiba
110	0.9	27	1-2	TE _{22,6} /GB	CPI
140	0.5	48(CPD)	10^{-3}	TE _{10,4} /GB	FZK (Karlsruhe)
140	0.55 0.85	38 51(CPD)	3 1	TE _{22,6} /GB	GYCOM

^a Gaussian beam

^b Coaxial cavity

^c Collector with depressed potential

Let us point out specially the results obtained with the highest frequency one-megawatt gyrotron intended for ITER program (see Table 2).

Table 2. Test results of 170 GHz/near-1 MW gyrotron with BN window

Pulse duration, s	1	2	5	10
Output power, kW	1030	500	350	270

Now the gyrotrons for nuclear fusion are close to satisfy the requirements for CW industrial energy sources.

5. Gyrotrons for technology

Prospects of gyrotrons can be tied up as well with thermal processing of materials, e.g. with sintering of some ceramics at high temperature close to 2000°C in ovens with relatively cold walls. Many pure crystalline materials absorb RF radiation rather intensely at frequencies not below the tens gigahertz order which can be provided for the ovens just by gyrotrons. The material processing using gyrotrons is being studied now at near 20 setups over the world.

The remarkable feature of heating of dielectrics in strong magnetic fields is its volumetric character providing high speed of the process – tens minutes instead of many hours using conventional ovens. This speed is important for sintering fine construction ceramics in which an average size of crystal grains must be rather small to provide plastic properties together with high firmness. There are a lot of experiments demonstrating denser and smaller-grain samples produced under the 30 GHz powerful radiation than in conventional ovens.

Gyrotrons for technology applications are demanded now to yield near 10 kW output power in CW regime at near 30 Hz frequency mostly. These ones operate in normal conducting copper solenoids or permanent

magnets. Though some higher frequency technological gyrotrons with cryomagnets are used as well. The main parameters of the technology gyrotrons are given in Table 3.

Table 3. Technological gyrotrons

Frequency, GHz	Output power, kW	Efficiency, %	Magnet system	Company
30	10-25	33-40	NS*	GYCOM
28	10	30	NS	CPI
28	10	30-39	PM** 600 kg	Mitsubishi
30	10	22	PM 68 kg	GYCOM
37.5	20-30	35	SCM***	GYCOM
83	20-30	30	SCM	GYCOM

*normal conducting solenoid **permanent magnet ***superconducting magnet

Depending on the demands, the output power and efficiency on industrial technological gyrotrons can be considerably enhanced to those of the gyrotrons for nuclear fusion installations.

Conclusion

Gyrotrons are now well studied and thoroughly developed powerful microwave sources. They dominate by their power at millimeter wavelengths and adjusting ranges, being the only available sources of considerable microwave energy. Many year practice of their use and development have resulted in rather feasible and reliable powerful sources and the total relevant set of equipment. Still possibilities of further progress of the gyrotrons for wider frequency range and more powerful and effective radiation have not been exhausted.

References

1. Applications of High-Power Microwaves, edited by A.V.Gaponov-Grekhov and V.L.Granatstein (Artech House, Boston, London, 1994)
2. G.G.Denisov, A.N.Kuftin, V.I.Malygin et.al. Int. Journ. of Electronics, 72(5-6), 1079(1992). A.A.Bogdashov, A.V.Chirkov, G.G.Denisov et.al. Int. Journ. of IR&M Waves, 16(4), 735 (1995)
3. A.L.Goldenberg and A.G.Litvak, Physics of Plasmas, 2(6), 256 (1965)
4. A.L.Goldenberg, V.N.Manuilov, M.A.Moiseev and N.A.Zavolsky. . Int. Journ. of IR&M Waves, 18(1), 435 (1997)
5. V.A.Flyagin, A.G.Luchinin, G.S.Nusinovich. Int. Journ. of IR&M Waves, 4(4), 629 (1983)
6. M.Thumm. State-of-the- art of High Power Gyrodevices and free electron masers update 1997, (Wissenschaftliche Berichte FZKA 6060, Karlsruhe, 1998)

DETECTION SYSTEM FOR THE MEASUREMENTS OF COLLECTIVE THOMSON SCATTERING SPECTRA IN FUSION PLASMA

L.V.Lubyako, E.V.Suvorov, A.B.Burov, A.M.Shtanuk, Yu.A.Dryagin, L.M.Kukin, N.K.Skalyga.
Institute of Applied Physics PAS, 46 Ulyanova st., N.Novgorod, Russia

Introduction

As is well known (see, e.g. [1,2] electron density fluctuations in the plasma with the frequencies ω and wavenumbers k , related by

$$\omega \approx k v_i \quad (1)$$

with v_i being characteristic ion velocity provide the information on the ion distribution function.

This information can be obtained from the spectral characteristics of electron density fluctuations due to the fact that every ion in the plasma is shielded by electron coating with the characteristic scale of the order of the electron Debye length. Collective Thomson Scattering (CTS) technique provides a rather general way for measuring electron density fluctuations. This diagnostics is based on the relation between angular/frequency spectra of scattered radiation and spatial/temporal spectra of electron density fluctuations in the plasma. Collective scattering process satisfies well known resonant conditions:

$$\omega_s = \omega_i + \omega_p , \quad k_s = k_i + k_p , \quad (2)$$

where ω_i , k_i , ω_p , k_p and ω_s , k_s are frequencies and wave vectors of the incident radiation, of the plasma turbulence and of scattered radiation correspondingly. The spectrum of scattered radiation is defined by relations (2) if so called Saulpeter parameter significantly exceeds unity:

$$1/k_p^2 r_d^2 \gg 1 , \quad (3)$$

where r_d is the electron Debye length.

Eqs. (2), (3) define possible scattering geometries with the fixed frequency of the probing radiation and Eq.(1) defines the frequency band subjected to spectrum analysis. Problems of measuring the ion distribution function (and the ion temperature, in particular) were the subject of lengthy discussions [1-9]. The main difficulty here is a very small scattering cross-section of equilibrium electron density fluctuations, which under the typical fusion conditions does not exceed 10^{-23} 1/Hz. This results in the natural requirement of powerful enough source of probing radiation and sensitive enough detection system. Historically first CTS experiments were performed in the optical and IR ranges where powerful enough sources were available; but for a long time gyrotrons were under discussion as a rather attractive source of probing radiation in CTS experiments. Contemporary powerful gyrotrons of mm wavelength region developed for electron cyclotron heating and current drive deliver a power approaching 1 MW in a few seconds pulse duration and are challenging cw operation. Their advantage as compared to infrared range generators (and, of course, optical) is possibility to use 90 degree scattering geometry, providing the opportunity of local measurements with good spatial resolution. The long pulse operation gives additional opportunity to increase essentially the sensitivity of CTS system based on gyrotron due to possibility of signal accumulation during long enough time. This advantage is not so critical in the case of ion temperature measurements where the signal level is relatively high, but becomes decisive in the challenging problem of alpha-particle diagnostics in the burning fusion plasmas.

In the present communication the detection system designed for the proof-of-principle CTS experiments using 140 GHz gyrotron as a source of probing radiation has been discussed. The system is aimed to the ion temperature measurements in a moderate size fusion installations W7-AS stellarator (Garching, Germany) and FTU tokamak (Frascati, Italy) as a first step in CTS experiments using gyrotrons with the prospects of its further upgrading for the alpha-particle diagnostics. It is capable of ion temperature measurements in a wide range of plasma parameters (H plasma, D plasma, density range from few times 10^{13} cm^{-3} to $2 \cdot 10^{14} \text{ cm}^{-3}$, ion temperatures from few hundred eV to few keV) in various scattering geometries with the scattering angles from 60° to 180° .

In general CTS system includes (see Fig.1) the powerful source of probing radiation (the gyrotron in our case); the high-power transmission line for transportation of probing radiation from the source to the plasma;

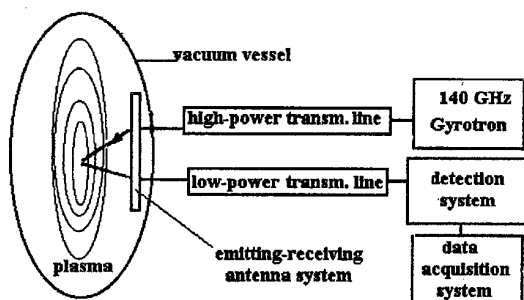


Figure 1. Schematic diagram of CTS experiment.

fluctuations the scattered radiation is of noise character with the spectrum symmetric with respect to the frequency of probing radiation (see, e.g., [1,2]). The shape of the spectrum depends on the scattering geometry, plasma ion composition and on electron and ion temperatures. The total bandwidth of CTS spectrum expected for H-plasma in the back-scattering geometry is about 1 GHz which defines the required band of spectral analysis. The expected value of scattered signal (see [9]) is within few tens eV. This allows to use the receiver with moderate sensitivity and to provide the wide dynamical range of measured signals. In order to specify the useful signal at the background noises the procedure of integration of scattered signal over considerable time interval should be provided.

Finally, the detection system should be reliably protected. During the time interval of CTS measurements the system needs the protection from the stray radiation at the main probing frequency. Outside this interval the system should be protected from other possible rather strong interferences which may overload or even destroy the system.

Composition of the detection system

The detection system (see Fig.2) is designed as multi-channel superheterodyne radiometer. It includes

protection system, heterodyne frequency converter based on the balanced Shottkey mixer with phase-locked BWO as a local oscillator, IF spectrum analyzer, analog-digital converter, data acquisition and data processing systems.

Heterodyne converter provides shifting of the scattered radiation spectrum from the high frequency range (around 140 GHz) to IF range (50-1200 MHz) where the spectrum analysis is performed. The specific feature of frequency conversion is the equality of heterodyne frequency operating regime) and double-band (without the suppression of the «mirror» band) regime of mixer operation. Taking into account the symmetry of the scattered radiation spectrum with respect to the frequency of probing radiation this operation regime allows to increase the value of registered signal by the factor of 2. To provide this the detuning between the probing radiation frequency and the heterodyne frequency should be less than the resolution of spectrum analyzer.

Protection system solves two main problems. The first is to diminish the stray radiation level at the mixer to values lower than the heterodyne power. The suppression of the stray radiation is achieved by introducing a notch-filter at the receiver input. It is a mechanically tuneable notch-filter based on the rectangular monomode waveguide with up to 20 coupled to it cylindrical cavities operating at H_{013} mode [10]. Such a filter (see Fig.3) provides maximum suppression in the line centre up to 100 dB and higher than 40 dB suppression within the band ± 30 MHz from the centre; additional attenuation introduced by the notch-filter outside ± 60 MHz is not higher than 3 dB and outside ± 90 MHz is not higher than 2 dB. This additional attenuation slightly decreases the sensitivity of the detection system, especially in the low frequency channels.

emitting-receiving antenna system, which defines the scattering geometry and allows, in principle, to vary the position of scattering volume within the plasma column; low-power transmission line for transportation of scattered radiation to the detection system; the detection system itself which is a spectral superheterodyne receiver; data acquisition and data processing systems.

Requirements to the detection system

Detection system parameters are specified by the characteristics of expected scattered signal. In the case of thermal density

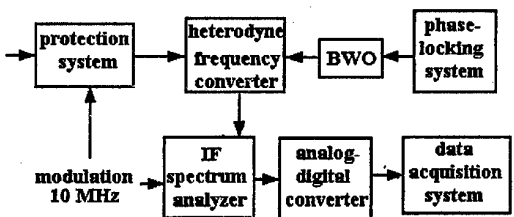


Figure 2. Bloc-diagram of detection system.

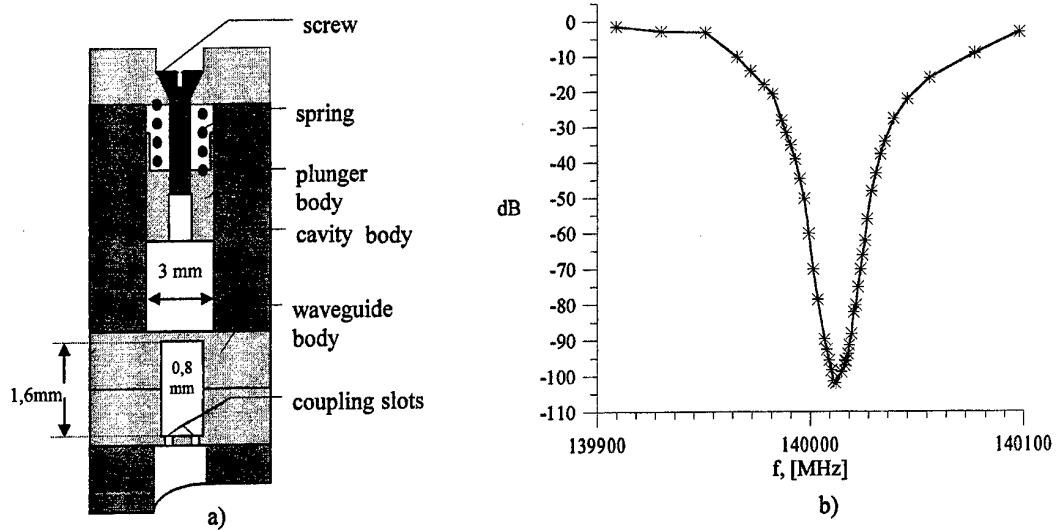


Figure 3. Cross-section cut (a) and transmission characteristic (b) of the notch-filter.

The second protection problem is related to the frequency drift of probing gyrotron radiation during RF pulse. To protect the detection system from the stray radiation when the gyrotron frequency is outside the suppression band of the notch-filter electronically controlled p-i-n diode is used. It provides more than 40 dB additional attenuation at the receiver input outside the gate and operates as a modulator within the gate. Gate is formed by a synchronizer which allows to vary gate parameters and to produce a rather sophisticated gate structures (like the sequence of two gates of different duration with controlled separation between them).

Protection system and heterodyne converter are placed together with the phase-locking system in a separate well screened box. Phase-locking system is based on the synthesizer of 4-8 GHz range with the only feed-back loop. Heterodyne frequency can be stabilized within the relative frequency shift not more than 10^{-8} in the whole frequency range of BWO operation (about 20 %). The band of phase locking is about 600 MHz, the band of the «trapping» is about 250 MHz and the minimum step of frequency change is 210 kHz. The resulting receiver noise temperature referred to the receiver input is about 0.6 eV.

Frequency spectral analysis is performed in the IF band; two filter banks provide spectrum measurements in two frequency ranges. The main 32 channel filter bank covers the range from 50 to 1200 MHz with the relative bandwidth of every channel and separation between adjacent channels about 10 %. For measurements of possible fine structures in the scattered signal «zoom» 20 channel system is operating in a limited frequency band about 100 MHz wide with enhanced frequency resolution; this band of analysis may be placed into the arbitrary position within total band covered by the main spectrum analyzer. Spectrum analysis can be performed with a rather high time resolution about 1 ms (which is inner integration time of the detection system).

Wide dynamical range of the detection system allows to register noise signals with the values varying from hundredths of eV to hundreds keV, or monochromatic signals with the power equivalent to that of the corresponding noise signal in full band of the spectral channel. Due to this fact the detection system was used not only for the main purpose (ion temperature determination from CTS on equilibrium electron density fluctuations) but also for the measurements of strong nonequilibrium plasma turbulence and for the measurements of gyrotron frequency evolution during RF pulse.

Measurement procedure

The output voltage at the every channel of spectrum analyzer may be presented as:

$$u_i = K_i (T_{ai} - T_0) + u_i^0, \quad (4)$$

where K_i is a throughout transmission coefficient of i -th channel from the antenna input, T_{ai} is antenna temperature averaged over the channel band and u_i^0 is some dc shift of the «device zero».

In general to measure the signal value at the receiving antenna input two calibration measurements are necessary to determine quantities K_i and u_i in every of spectrum analyzer channels for every selected part of the full dynamic range of the detection system. The ideal way of throughout calibration should be two separate measurements obtained by placing before the receiving antenna of standard noise sources with known and different enough temperatures. With the orientation of the receiving antenna in the equatorial plane of a stellarator a very nice calibration source is the plasma itself which emits black-body radiation at the second cyclotron harmonic of X-mode with the effective radiation temperature coinciding with the electron temperature in the resonance layer. Empty vacuum chamber may be taken as a second standard source with the effective temperature considered to be equal to the room temperature. The exact value of the last is of minor importance provided that it is essentially lower than the electron temperature. In this case the effective temperature of the measured signal is defined as:

$$T_{al} = \frac{u_i - u_i^{(c)}}{u_i^{(ECE)} - u_i^{(k)}} T_{ECE}, \quad (5)$$

where T_{ECE} is the effective temperature of calibration ECE radiation, u_i , $u_i^{(c)}$ and $u_i^{(ECE)}$ are output voltages in i -th spectral channel obtained from CTS measurements, from the vacuum chamber and from optically thick ECR layer correspondingly. With other orientation of the receiving antenna or when ECE come from optically thin layer radiation from the plasma may be used only for the relative calibration. This procedure allows to equalize transmission coefficients in different spectral channels under assumption that the spectrum of radiation is flat within the band of spectral analysis. Such an assumption seems to be rather reliable taking into account a rather narrow relative band (less than 1 %) of calibration radiation where the existence of some features with a fine structure is highly improbable. Absolute values of registered signals are obtained in this case with a rather poor accuracy which is determined either from indirect estimates of the effective ECE radiation temperature or from absolute calibration with a separate standard noise source and estimate of additional attenuation introduced by the part of transmission line from receiving antenna to the receiver input. An example of measured spectrum of ECE at the 4-th cyclotron harmonic with an absolute calibration performed using X-mode ECE at the second harmonic is given in Fig.4. In spite of rather high attenuation in the transmission line (about 25 dB) and very low signal level the spectrum is measured with good accuracy and its absolute value coincides with the value obtained from the independent ECE diagnostics. This demonstrates a rather good sensitivity of the detection system and the reliability of the proposed calibration procedure. Nevertheless the best way to measure CTS spectra is to perform a relative calibration in the same plasma shot in which scattered radiation is registered. To provide this a complicated (double) gate is used; it opens the receiver for the first time during the gyrotron pulse to register CTS spectrum and for the second time the receiver is opened after the end of gyrotron pulse to

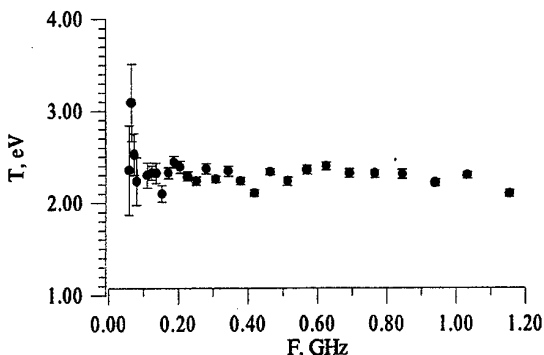


Figure 4. Measured ECE spectrum at the 4-th harmonic.

perform relative calibration (or absolute, if possible) by the radiation escaping from plasma supported by NBI heating.

Measured CTS spectra

The detection system described above was successfully used in a number of experimental series at W7-AS stellarator in two geometries: close to the back-scattering geometry and approximately 90 degree scattering. As an illustration we present here some CTS spectra obtained under different conditions [11, 12, 13, 14].

First CTS spectra from equilibrium fluctuation were obtained in the back-scattering geometry practically without spatial resolution under conditions of rather high level of stray radiation. Notch-filter provided reliable protection of the receiver but together with stray radiation eigen noise of the gyrotron was brought to the receiver input. Under these conditions CTS spectrum was obtained from alternative measurements when gyrotron pulse was fired to the empty chamber and to the plasma. CTS spectrum was obtained as the difference of signals registered from the plasma and from the empty chamber. CTS spectra thus obtained for two plasma densities [13]

are shown in Fig.5. It was not possible to get CTS spectra below 200 MHz because of very high level of gyrotron noise in low-frequency channels.

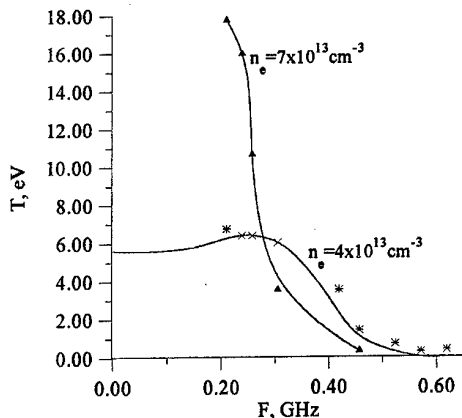


Figure 5. CTS spectra from thermal density fluctuations obtained in backscattering geometry [13].

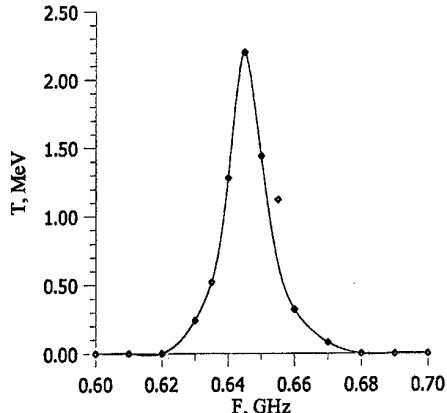


Figure 6. CTS spectrum from lower-hybrid turbulence [13].

Another example of CTS spectrum obtained in the back-scattering geometry is presented in Fig.6. This spectrum is the result of scattering by nonequilibrium lower-hybrid turbulence excited by injection into the plasma of a rather weak diagnostic neutral hydrogen beam [13]. The signal level is by 5-6 orders of magnitude higher than that obtained from scattering by equilibrium density fluctuations and the gyrotron noise is negligibly small compared to it. Enhanced spectrum resolution was obtained using «zoom» spectrum analyzer which allowed to measure a rather narrow bandwidth (about 2-3 %) of discovered feature.

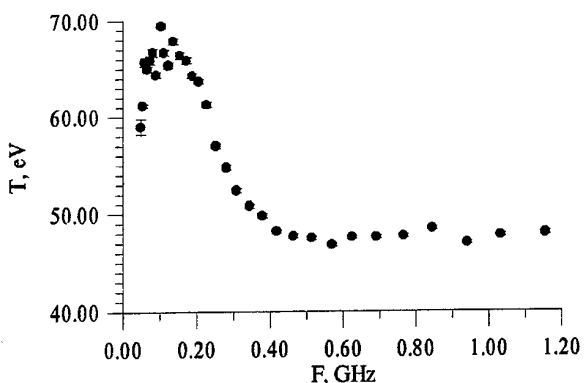


Figure 7. CTS spectrum at ECE background for 90 degree scattering geometry [14].

Example of local CTS spectrum obtained in the 90 degree scattering geometry with the spatial resolution about 4 cm is shown in Fig.7. It can be easily seen that CTS spectrum is distinctly separated from flat ECE background with the level about 3 times higher than that of CTS signal [14]. This kind of spectrum allows the determination of the local ion temperature provided that electron temperature, plasma density and ion composition are known.

Conclusion

In the course of the proof-of-principle CTS experiment it was demonstrated that the gyrotron can be successfully used as a source of probing radiation. General principles of the detection system design for the registration of

CTS spectra were tested and proved to be appropriate and reliable. The system may be upgraded up to routine diagnostics for the ion temperature profile measurements in the large-scale installations. More important is that the same principles may be used for the alpha-particle diagnostics under the condition of D-T fusion reaction. At present the gyrotron is the only really existing source which can provide long pulse probing radiation for scattering diagnostics with the enhanced sensitivity due to very large «radiometric gain» which can be reached by integrating the scattering signal over long enough time.

Authors greatly appreciate financial support from German Bundesministerium für Forschung und Technologie and Russian Foundation of Basic Research (project N° 96-02-19455-a).

References

1. J. Sheffield "Plasma Scattering of Electromagnetic Radiation", Academic Press, New York - San Francisco - London, 1975

2. Levin M. L., Rytov S. M., "Theory of Equilibrium Fluctuations in Electrodynamics" (rus.), Nauka, Moscow, 1967.
3. Hoekzema J.A., Costley A.E., et.al., "Collective mm-wave scattering fast ion and alpha-particle distribution in JET". Proc. of 15th Symp. on Fusion Technology, Utrecht, 1988, p.314.
4. Orsito F., BurattiP., Analysis of collective Thomson scattering for alpha-particle diagnostics on tokamaks. ENEA report 1988.
5. Benhn R., Dicken D., et. al., "Ion temperature measurements of tokamak plasma by collective Thomson scattering", J. Appl. Phys., 1991,v. 69,N 4,
6. Woskoboinikov P., Cohn D.R., et. al., "Gyrotron Thomson scattering diagnostics of ion in D-T burning tokamaks". Digest of 12 Int. Conf. on IR and MM waves, December 14-18, 1987, Orlando, Florida. IEEE catalog number 87CH2490-1, pp. 368-371.
7. Lubyako L.V., Luchinin A.G., Nusinovich G.S. et. al., Fizika plazmy (rus.), 1992, v.18, N 2, pp. 211-212.
8. Brodsky Yu. , Lubyako L. V., Nechuev S. I. et. al. Abstracts of workshop "Instruments, Technology and Propagation of mm and submm Waves" (rus.), Kharkov, Ukraine, 1992, pp.109.
9. Suvorov E.V. "Microwave scattering diagnostics". High power microwave generation and applications. Proceedings of the International school of plasma physics "Piero Caldirola", Villa Monastero - Varenna, Italy, 9-17 Sept., 1991, pp. 79-98.
10. Dryagin Yu., Skalyga N., Geist T. "A notch-filter for 140 GHz microwave radiation", Int. J. of Infrared and MM waves, 1996, v.17, N7, pp.1199-1204.
11. Suvorov E.V., Burov A.B., Dryagin Yu.A., et. al. "Collective scattering of powerful gyrotron radiation at W7-AS", Proc. of the Int. Workshop "Strong microwaves in plasma". N. Novgorod, 1993, v. 1, pp. 172-184.
12. Suvorov E.V., Dryagin Yu.A., Filchenkov S.E., et. al. First results on ion temperature measurements at W7-SA by collective scattering of 140 GHz gyrotron radiation", 9-th Joint Workshop on ECE and ECRH. Jan., 1995, Borrego Springs, California, World Scientific Publishing, Co. Pte LTD, Singapore, 1995, pp. 501-508.
13. Suvorov E.V., Erckmann V., Holzhauer E., et. al. "Ion temperature and beam-driven plasma waves from collective scattering of gyrotron radiation in W7-AS", Plasma Phys. Controlled Fusion, 1995, v.37, pp.1207-1213.
14. Suvorov E.V., Holzhauer E., W.Kasperek, et. al. "Collective Thomson scattering at W7-AS", Plasma Phys. Controlled Fusion, 1997, v.39, pp.B337-B351.

HYPERSONIC DELAY LINES: PHYSICAL BASE, TECHNOLOGY AND APPLICATION IN THE SPACE RADAR ENGINEERING

V.N.Balabanov, E.M.Ganapolskii, A.V.Golik, *V.B.Efimov, A.P.Korolyuk,

*A.S.Kurekin, A.G.Sergeev, V.V.Tarakanov, *V.N.Tcymbal

Institute for Radiophysics and Electronics of NAS of Ukraine

310085, Ukraine, Kharkov, 12 Ak.Proskura St.

Tel.(0572)448553, E-mail: ire@ire.kharkov.ua

*Center for Radiophysical sensing of the Earth NAS and NSA of Ukraine

310085, Ukraine, Kharkov, 12 Ak.Proskura St.

Tel.(0572)448397, E-mail: vnt@crse.kharkov.ua

The problem of the hypersonic delay lines (HDL) creating dates back to the late 50-s in connection with the development of radar engineering based on the use of the coherent impulse microwave signals. The HDL operation principle consists in the conversion of electromagnetic signal into hypersonic wave propagating in the acoustic line and the reverse conversion of the wave into a time-delayed electromagnetic signal. Due to the linearity of piezoelectric effect which is responsible for this conversion the time-delayed electromagnetic signal retain the time coherence with respect to the initial one. This characteristics is most important peculiarity of HDL. Owing to the low velocity of the hypersonic wave propagation inside the crystalline acoustic line using the HDL one can obtain the relatively long-time delay of the microwave signal with the conservation of the stored information. So it was found that the HDL are the most suitable devices to be widely employed in various coherent-impulse radar systems. In particular, determine coherent signal processing time directly in the waveguide transmission line. The HDL are also used in impulse radar both coherent and noncoherent for the automatic control and potential calibration of receiving and transmitting apparatus placed on the space modules

It should be noted that the HDL designing and their application in radar engineering in former Soviet Union is in most cases the result of long term investigations and works carried out in the IRE of NAS of Ukraine. The effective methods of hypersonic wave generation, transmission and reception it were suggested and realized for the first time. The technology of hypersonic transducer was developed and many problems dealing with the hypersonic wave propagation in crystalline acoustic lines were studied at this Institute as well. All that has provided the physical basis to use the hypersonic waves in the microwave storage devices intended for radar engineering. Due to this the HDL of centimeter and millimeter wave range were originally developed in the IRE of NAS of Ukraine. The main parameters of these HDL (delay time, pass band, insert losses) are not worse but in many cases they exceed similar devices developed abroad. HDL have found their applications in the side-looking radars (SLR) with a really and synthetic aperture and intended for remote sensing of the Earth. These facilities were engineered in the IRE of NAS of Ukraine.

The main scientific and engineering problems relating to the HDL development in the assigned microwave range deal firstly, with finding materials for an acoustic line characterized by the low energy losses of hypersonic waves propagating and, secondly, with developing effective hypersonic transducers which proved the low-loss conversion of electromagnetic signal into a hypersonic wave in the given frequency band. High quality crystals with the low concentration of crystalline defects and high Debay temperature are generally used as a material for the HDL. The main source of the hypersonic wave losses in a crystal is the scattering on heat phonons. Due to this the absorption of hypersonic waves at the relatively high temperatures of order of the Debay temperature is proportional to the square of the angular frequency ω^2 and weakly depends on temperature T^α ($\alpha < 1$). The hypersonic wave absorption mechanism [1] (Achiezer absorption) operates as follows. The state of phonon gas in a dielectric crystal changes under the influence of a hypersonic wave and it leads to an irreversible increase of entropy. The source of the required energy for these processes is the hypersonic wave energy. The Achiezer mechanism leads to the sufficient absorption. For instance, in quartz the hypersonic absorption at the frequency of 10GHz at room temperature which is comparable with the Debay temperature for this crystal reaches the value of 70 dB/ μ s. The large value of hypersonic wave absorption also occurs in other crystals having the relatively low Debay temperatures. The low hypersonic wave absorption was found to take place only in a few selected crystals. Those are diamond [2] and sapphire crystals [3]for the longitudinal hypersonic wave propagating along the 3-fold symmetry axis direction and the crystal aluminum yttrium garnet and magnesium aluminum spinel [4] for shear hypersonic waves propagating along the 2-fold symmetry axis direction. Thus, the absorption of longitudinal hypersonic wave in sapphire is 18 dB/ μ s at the frequency 9 GHz and a room tem-

perature. An exceedingly low absorption of a shear hypersonic wave was discovered in the crystal of magnesium aluminum spinel. Its value is $6.5 \text{ dB}/\mu\text{s}$ at the above-mentioned frequency and a room temperature. These materials were used to develop a number of HDL devices operating at different frequencies of the centimeter wave range.

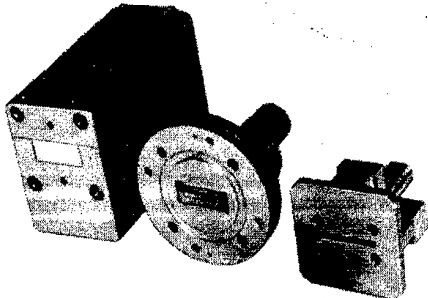


Figure 1. HDL of the 3 cm wave range. Parameters: The delay time is 8 μs , inserting signal loss is 85 dB, frequency bandwidth is 11%. [9]

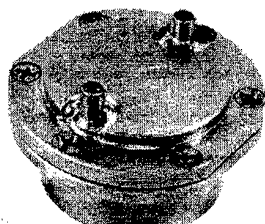


Figure 2. HDL of the 10 cm wave range. Parameters: The delay time is 6 μs , inserting signal loss is 35 dB, frequency bandwidth is 25%. [10]

The second important problem is to work out an effective method for transforming an electromagnetic field to a hypersonic wave in the acoustic line and reverse conversion of this wave into an electromagnetic field. The effective method for the hypersound excitation by using the slow-delayed surface electromagnetic wave propagating near the piezoelectric crystal surface was proposed and realized in the IRE of NAS of Ukraine [5]. For the first in the world the longitudinal and shear hypersonic waves in the quartz crystal at low temperatures at the record high frequencies up to 75 GHz were realized in this Institute. [5,6]. This made it possible to study of the longitudinal and shear hypersonic wave absorption in various crystalline materials over a wide temperature interval including the liquid helium temperature and to establish the main mechanisms of hypersonic wave dissipation [7]. Another method which was proposed and realized in IRE of NAS of Ukraine turned out to be very effective for the hypersonic wave translation from one body to another. This fact is very significant in the HDL development. This method is based on the use of thin textured piezoelectric zinc oxide films whose thickness is equal to the quarter of the hypersonic wave. These films are vacuum evaporated on the end face of the cylindrical acoustic line. For the effective conversion of electric field into hypersonic wave it is necessary that this field be concentrated in the piezoelectric film. For this purpose the "point" transformation hypersound method was proposed and realized [8]. It allows to concentrate the microwave electric field in the film area having a dimension of several hundreds of hypersonic wave length. Due to the very small area where the electric field is concentrated the "point" hypersonic transformer has the capacitive impedance comparable to the waveguide line characteristic impedance and could be matched with it in a very broad frequency range. The coefficient of the electric field transformation into a hypersonic wave achieves 0.1 in the frequency range of 20% in centimeter wave range. The number of HDL at the various frequencies of centimeter and millimeter wave range was developed in IRE of NAS of Ukraine. These devices are intended for the radar systems. The created HDL of the three- and ten-centimeter wave range are shown on the Fig.1,2.

The space radar engineering development requires that HDL should be developed with super long delay time of more than 1 ms which corresponds the time interval of electromagnetic signal propagation at a distance of 10^3 km. This problem was solved at first in the world. As a result a new class of the microwave memory devices - cryogenic hypersonic delay lines (CHDL) having the super long time delay were developed [11]. The effect which was discovered and realized in IRE of NAS of Ukraine and referred to as a reversal scattering of the longitudinal hypersonic wave in dielectric crystals at low temperatures has provided the basis of CHDL development [12]. As is known the hypersonic wave dissipation in dielectric crystals decreases with the dielectric crystal cooling and at low temperatures has the frequency-temperature dependence in the form ωT^4 [1] where ω is the angular frequency and T is the crystal temperature. But with the temperature decreasing below that of order of 0.01Θ where Θ is the Debye temperature the absorption decrease falls sharply and the curve of the absorption temperature dependence come out to the plateau. The temperature-independent hypersonic dissipation on the plateau area is usually called the residual hypersonic absorption (RHA). The RHA is the limit

absorption from the point of view of it decreasing by cooling a crystal acoustic line which is normally used by the HDL development. RHA is determined by the crystal defects (structure inhomogeneity, crystal axis deviation, etc.) and practically limits the HDL time delay to 100 μ s by with allowance for the acoustic line deep cooling. In consequence of this it was believed that the creation of HDL having the delay time over the 1 ms was impossible. The use of the effect of reversal scattering of longitudinal hypersonic wave in dielectric crystals at low temperatures allowed to solve this problem and to increase microwave signal delay time (which is required for the space radar systems) by one or two orders. The concept of the stability hypersonic wave propagation in crystal acoustic line makes it possible to get a better understanding of this effect.

The hypersonic wave propagation in the acoustic lines of an typical geometry takes place between the two plano-parallel end faces. It appears to be unstable in relation of the crystal inhomogeneities and the deviation of end faces from the rigid parallel alignment. Owing to this the inhomogeneities which always occur in crystalline acoustic lines add to the hypersonic wave front deflection from the normal to the end faces. As a result, the efficiency of the hypersonic wave transformation into microwave electromagnetic field decreases that results in the delayed microwave signal losses. The studies of the reversal scattering effect shown that in crystal one could create conditions for the stability propagation of hypersonic wave and to decrease the RHA significantly. This is achieved by using the new form of reflecting surfaces using instead of the usually plano-parallel geometry. In a new geometry one surface is plane and second is spherical with the curvature radius greater than the double distance between of the reflecting surfaces. In this case the plane and spherical surfaces were oriented so that the crystallographically axis of 3-fold symmetry passes through the center of the spherical surface.

With this geometry of reflecting surfaces the hypersonic wave propagation takes place in the area limited by caustic surfaces and due to this it is stable in respect to the crystal inhomogeneities and to the deflection of the reflection surfaces form. As a result of the plano-spherical geometry of reflecting surfaces using there was a significant decreasing of an attenuation for the longitudinal hypersonic waves in the crystals of quartz, lithium niobate and sapphire at a frequency of 3 GHz. The lower hypersonic absorption was achieved in the high quality lithium niobate crystal and amounts to 0.0055 dB/ μ s [12]. Using this crystal as a acoustic line of HDL the 12-ms delay was achieved at the liquid helium temperature as a result of total losses on the signal propagation of 60 dB. The echo-signals corresponding to the acoustical way of order of 100 m which is equivalent to the run distance of 10^4 km for an electromagnetic signal. Besides, it was found that the super long delay time can be realize in the niobate lithium acoustic line not alone at the liquid helium temperature but at higher temperatures up to the liquid hydrogen temperature 20.4 K. This permits to use the self-contained micro-cooling device of XM-20B type with the operation temperature 20-30 K for the HDL acoustic line cooling. The XM-20B device operates with the reverse closed thermodynamical Sterling cycle by using an invariable quantity of helium gas. The low power consumption, small clearances and weight and self-contained supply make this microcooling device very

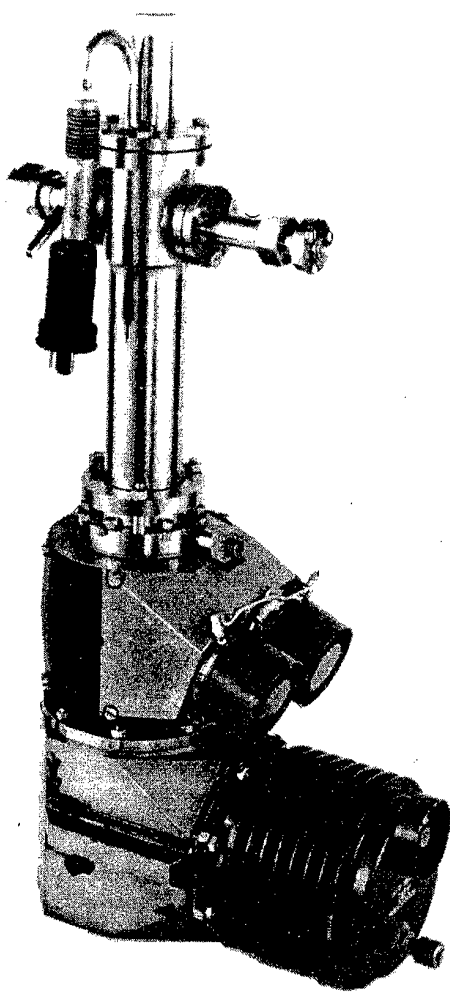


Figure 3.

suitable for the development for the super long-time delay of microwave signals based on the CHDL. The creation of such CHDL developed on the bases of the microcooling device is shown on the Fig. 3. Its main parameters are following: the operating frequency is 3 GHz, delay time (total) is 2.2 ms, the time interval between the echo-impulses is 12 μ s, frequency bandwidth is 0.1%, tuning range is 10%. [13] The CHDL was used for the development of the impulse-coherent side looking radar system with synthetic aperture. Using the cooling sapphire acoustic line and hypersonic transformers on the thin piezoelectric film based it is possible to create at first the HDL in eight-millimeter wave range at the frequency 36.7 GHz with the delay time of 4 μ s. [14].

It was also found that the line with the super long delay time can be realized by using the polyhedron acoustic line made of quartz crystal. In this acoustic line the time delay up to 3 ms was produced at the frequency 100 MHz and room temperature. The way rays in acoustic quartz line is shown on Fig. 4.

Now consider the HDL is applied to the remote sensing radar system that were designed and developed in the IRE of the NAS of Ukraine to measure the parameters of microwave signals scattered from the Earth's surface. These systems exhibit a resolving power ranging from units of meter to kilometers and are capable of addressing a great variety of research and practical issues. The dependence of back-scattering coefficient (σ^0) and the radar image contrasts upon a type of the surface being studied and its electrophysical properties is the basic factor in interpreting remotely-sensed data.

Therefore, the development of a radar system calls for a high accuracy in the measurement of scattered radio-signal characteristics. This accuracy is heavily dependent upon the calibration of a potential.

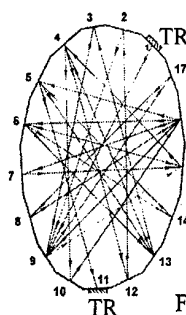


Figure 4.

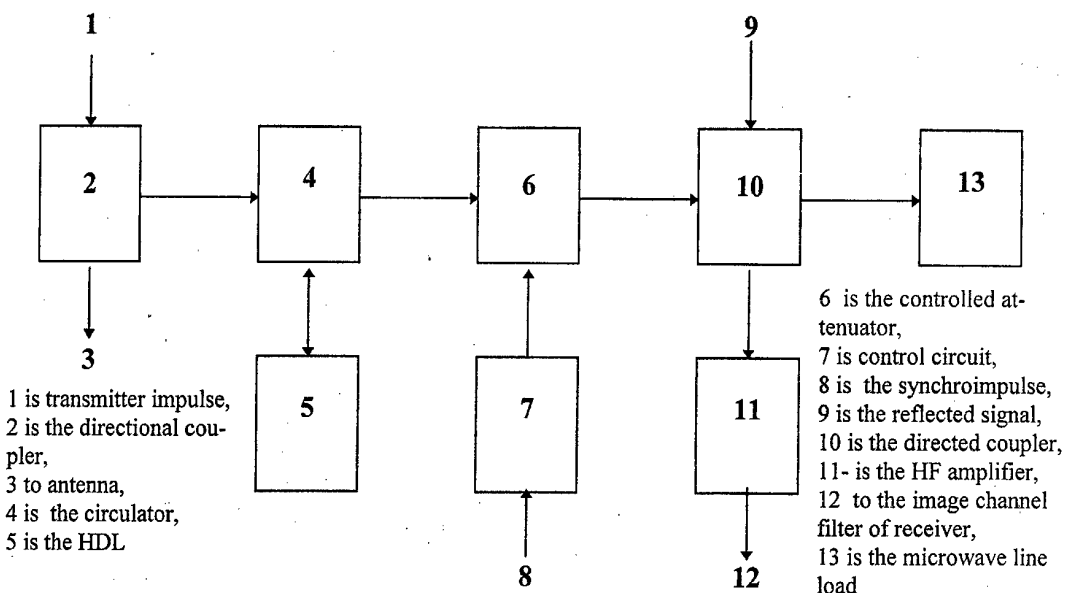


Figure 5. Block diagram of the SLR calibrator.

The most effective method for internal calibration is the use of time-delayed sensing pulses simulating the target-scattered signals generated by the HDL. The HDL-based calibrators were found their applications on airborne SLRs of the «Analogy» [15] and «MARS» [16] types and on the spaceborne SLRs of the «Cosmos-1500», «Okean» and «SICH-1» satellite series.

To calibrate the receive-transmit channel a transmitter pulse which was attenuated for a certain magnitude was utilized and delayed for a period required to restore the receiving system potential. In this case part of the transmitted power was applied to the HDL to generate the calibration signal, and a delayed pulse was fed to the receiver input. The block diagram of the calibrator is presented in Fig.5.

The calibration signals are passed through the entire measuring channel and are being recorded in synchrony with the returned signals [17]. This signal is automatically generated by changing the controlled attenuator, and its magnitude spans the whole range of the SLR input signals. This type of calibration ensures that the receive-transmit channel characteristics are automatically controlled in the course of experiments and does not necessitate any absolute measurements of transmitted and received signals. A high degree of measurement accuracy has been achieved through the thermostabilisation of the HDL device and calibration channel components. The error estimation in defining the σ^0 from the images acquired by the SLRs installed on the «Cosmos-1500» satellite, using the HDL-based internal calibrator, indicated that σ^0 measurement mean-square error caused by the equipment instability parameters does not exceed 1.5-2 dB. Similar results have been obtained for the airborne system as well. The spaceborne SLRs installed on the «SICH-1» satellite enable the processes that occur in the ocean-air system to be efficiently monitored on the sea surface [18]. In this case it is possible to record and evaluate the parameters of active atmospheric processes such as atmospheric fronts and storm zones. The SLRs can equally be utilized to record extra-tropical and tropical cyclones (hurricanes, typhoons) which are exceedingly hazardous and deadly natural phenomena that are most likely to cause considerable material damage and trigger off innumerable losses of human lives.

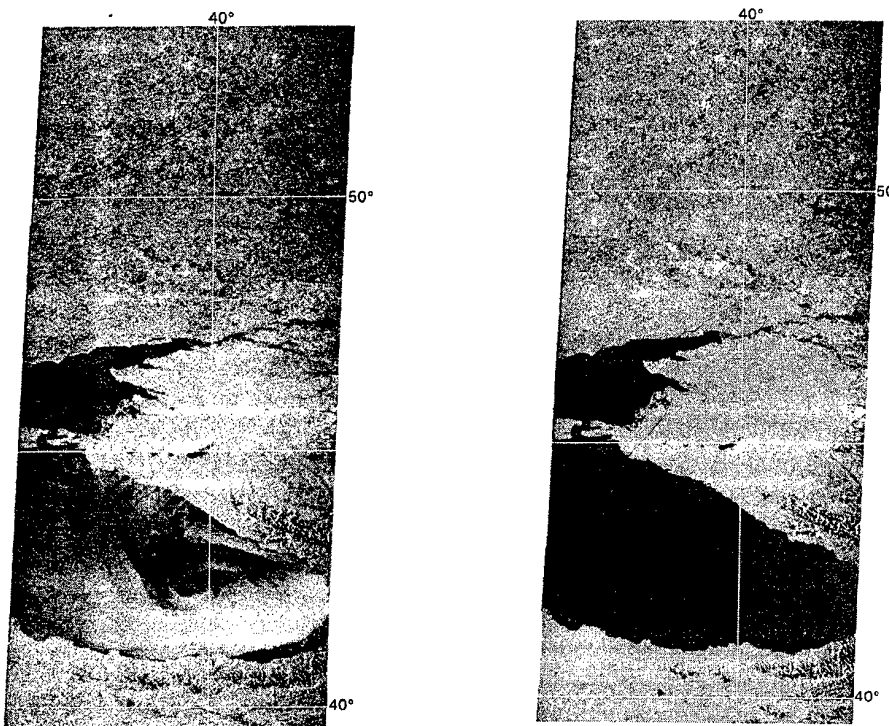


Figure 6. The Radar image of the Black Sea East part obtained by SLR installed on the «SICH-1» satellite (October 27, 1996)..

Many years of experience in analyzing and using the spaceborne SLR data strongly suggest that these processes can be traced not only over the sea surface in the initial stages of their development but also serve as the precursors of the nascent tropical and extratropical cyclones. Of significant importance is the application of the SLRs to monitor extratropical cyclones known to seriously affect the weather conditions across the vast expanses of any country [19]. The storms and squalls resulting from these cyclones tend to pose great threat. For instance, just one stormy event that broke out in the wakes of the intensive extratropical cyclone on November 15, 1992 was highly ruinous for Ukraine and the resultant damage was put at more than 100 mln. hryvnas.

An example of the radar image of the intensive cyclone over the Black Sea waters, which was detected by the «SICH-1» SLR in the night-time is illustrated in the Fig.6. The image clearly displays a peculiar structure of the near-sea surface cyclone-induced wind. The maximum wind speed was recorded in the eastern region of the Black Sea close to the Turkish coast.

Thus, the SLRs abroad the spaceborn carriers make it possible to provide reliable data on the processes of ocean-atmosphere interaction. Specifically, the excellent SLR performance results from using the HDLs whose high technical parameters are conducive to the precise measurements of the microwave scattering characteristics on the Earth's surfaces under study.

References

- [1] J.W.Tucker, V.W.Rampton Microwave ultrasonics in Solid state physics. North-Holland Publishing Company. Amsterdam. 454p. 1992
- [2] V.N.Balabanov, A.A.Bulgakov, A.N.Chernetz Absorption of hypersound in diamond. Letters in JETP, v.11, p.486-488, 1970.
- [3] E.M.Ganapolskii, A.N.Chernetz. Absorption of hypersound in quartz and ruby crystals. JETP, v.51, p.388-391, 1966.
- [4] M.P.Lewis, E. Paterson. Microwave Phonon Attenuation in Magnesium Aluminate Spinel J. Appl.Phys. v. 39, p.3420-3425, 1968
- [5] E.M.Ganapolskii, A.N.Chernetz Excitation of hypersound by means of the slow electromagnetic waves Doklady AS of SSSR, v. 149, p. 72-77, 1963
- [6] E.M.Ganapolskii, R.V.Kicelev, A.N.Chernetz Excitation of hypersound in millimeter wave range. Doklady AS of SSSR, v.191, p.1015-1018, 1970
- [7] E.M.Ganapolskii, A.N.Chernetz Absorption of hypersound in quartz and ruby crystals. JETP, v. 51, p. 388-397, 1966.
- [8] E.M.Ganapolskii. Hypersonic transducer. A.s. # 314560 (SSSR). B.I., # 28, 1971.
- [9] V.N.Balabanov, A.A.Grintchenko, A.O.Silin Small size broadband hypersonic delay lines of centimeter wave range. Preprint № 193, 21p. IRE AS USSR 1982
- [10] A.P.Korolyuk, A.S.Sergeev, V.V.Tarakanov, N.A.Kusnetzova Hypersonic delay line of centimeter wave range with the many-element ZnO-transducer. Pribory i technika experimenta, # 6, p.204, 1988
- [11] E.M.Ganapolskii, A.P.Korolyuk, V.A.Nezhivenko, V.E.Popov Hypersonic lines of super long time delay for the X-band signals. Preprint # 77, 40p. IRE AS USSR, 1977
- [12] E.M.Ganapolskii, A.P.Korolyuk, V.V.Tarakanov The reversal of residual dissipation of longitudinal hypersound in dielectric crystals. JETP, v.182, p. 82-95, 1982
- [13] E.M.Ganapolskii, A.P.Korolyuk, V.V.Tarakanov. Hypersonic delay lines on single crystal acoustic lines with caustics. Preprint # 166, 36 p. IRE AS USSR, 1981
- [14] E.M.Ganapolskii Cryogenic hypersonic delay line for the microwave signals of 8-mm wave range. Pribory i technika experimenta. # 3 p. 58-62, 1991
- [15] A.S.Gavrilenko, V.V.Krihanovskii, U.A.Kuleschov et all.. Complex radiofizicheskoy apparaturi dlya distanzionnogo zondirovaniya prirodnoy sredy. Preprint # 321, 39 p. IRE AS USSR 1986.
- [16] A.I.Kalmikov, B.N.Tsymbal, A.N. Blinkov et all. Mnogozelevoy radiolocatzionniy samoletniy complex issledovaniya Zemli. Preprint # 90-21, 34 p. IRE AS USSR, 1990.
- [17] A.I.Kalmikov, V.B.Efimov, S.S.Kaverin et all. Radiolocazionnaya sistema ISZ «Kosmos-1500». V kn.: Issledovaniya Zemli iz Kosmosa. # 5, p.84-93, 1984.
- [18] A.I.Kalmikov, A.P.Pithugin, V.N.Tsymbal, V.P.Shestopalov Radiophysicheskie nabludeniya iz Kosmosa krupnomashtabnich obrasovany na poverchnosti okeana. Doklady AS SSSR, v.279, p.860-862, 1984.
- [19] V.I.Dranovsky, A.I.Kalmykov, V. B. Efimov et al. Possibilities of Ecological Environment Monitoring the using SICH-1. Proc. of IV Ukraine-Russia-China Symposium of Space Science and Technology, p. 1-7, Kyiv, 1996.

MM-WAVE TRANSMITTERS USING MAGNETRONS WITH COLD SECONDARY-EMISSION CATHODE

V. D. Naumenko¹, K. Schuenemann²,
V. Ye. Semenuta¹, D. M. Vavriv¹, and V. A. Volkov¹

1) Radio Astronomy Institute of Ukrainian Academy of Sciences

4 Chervonopraporna Street, 310002 Kharkov, Ukraine

Tel.: +380-572-448718; Fax: +380-572-476506; E-mail: vavriv@rian.kharkov.ua

2) Technical University Hamburg-Harburg, Arbeitsbereich Hochfrequenztechnik
D-21071 Hamburg, Germany

Tel.: +49-40-77 18 30 19; Fax: +49-40-77 18 27 55; E-mail: schuenemann@tu-harburg.d400.de

ABSTRACT. We present here the recent results on the development of efficient millimeter wave transmitters, which employ spatial-harmonic magnetrons with cold secondary-emission cathode and solid-state modulators. Design and characteristics of 94 GHz transmitters with the output power level of several kilowatts and suitable for radar applications are described.

1. INTRODUCTION

Nowadays, a number of potential applications has appeared in using radar systems operating at frequencies of 94 GHz and higher for civil applications, such as vehicle guidance systems, meteorological and navigation radars, environmental monitoring systems, etc. [1-3]. The development of such radar systems is strongly limited by the lack of cost-efficient, compact transmitters with a kilowatt output power level and higher. It is clear now that only vacuum devices can satisfy the needs for such sources for these frequencies.

For lower frequencies, the problem has been solved to a large extent by utilizing classical magnetrons, which have demonstrated a number of clear advantages compared to other types of vacuum tubes. However, such magnetrons cannot fit many of the requirements for the frequencies of 94 GHz and higher from the point of view of reliability and output power. It was found that spatial harmonic magnetrons with cold secondary-emission cathode [4, 5] are superior to the classical magnetrons from this point of view. Although magnetrons with cold secondary-emission cathode are known from the 50ies, but only recently they became suitable for the development of compact and highly efficient transmitters for radar applications [6, 7]. A substantial advance in the performance of the transmitters has been achieved due to several factors. At first, the magnetron design has been optimised and the technology of the magnetron manufacturing has been essentially improved what have resulted in improving reproducibility of the output characteristics and upgrading reliability and stability of the magnetrons. At second, recent advances in semiconductor devices and, in particular, the advent of high voltage MOSFETs, have opened a way for the development of solid-state modulators. All these have culminated in the development of efficient, reliable, and cost-effective transmitters with the output peak power of several kilowatts at the frequencies around 94 GHz and higher. In the present paper, the research activities, which have led to the development of the transmitters, are described. Characteristics of these transmitters are discussed along with the description of the transmitter main units – the solid-state modulator and the spatial harmonic magnetron with cold secondary-emission cathode.

II. SPATIAL HARMONIC MAGNETRONS WITH COLD SECONDARY-EMISSION CATHODE

It is well known that the dimensions of the oscillatory circuit of the classical magnetrons scale proportionally to the operating wavelength λ , and the dc magnetic field is proportional to λ^{-1} . For example, at frequencies around 94 GHz the anode block of classic magnetrons should have diameter about 1 mm, and the operating magnetic field of 20 kGs. Another problem is related with a thermal cathode, which is placed usually inside the magnetron interaction space. The life time of the cathode is rather short because it is difficult to provide its effective cooling. This is due to both a large amount of heat produced by the cathode itself in a

small volume and a severe bombarding of the cathode by electrons rotating in the interaction space. Due to these factors the classical magnetrons with highest frequency equal to 94 GHz are commercially available.

The radical solution to these problems came from the spatial-harmonic magnetrons with cold secondary-emission cathode. The distinctive features of these magnetrons are as following: (i) they utilise a backward-wave harmonic of the $\pi/2$ resonator mode for the magnetron operation, distinct from the conventional π -mode, and (ii) a cold secondary emission cathode is introduced instead of the conventional thermionic cathode. It was found that these solutions result in a number of advances, like: the dimensions of the oscillatory system can be increased, the frequency separation between neighbouring modes is improved, the needed values of the dc magnetic field is smaller, a higher stability of magnetron operation is achieved, and the life time of the magnetrons is essentially extended.

Type of magnetrons	classical		proposed	
Wavelength, mm	3.3	6.3	3.1	6.8
Anode diameter, mm	1.27	2.44	3.3	4.5
Magnetic field, kGs	25	13	6.25	6
Anode voltage, kV	8-13	10-16	18	20
Pulse power, kW	20	44	20	60
Efficiency, %	15	19	12	17
Life time, hours	100	200	800	2000

Table 2. The operation conditions and characteristics of classical and proposed magnetrons.

Wave-length, mm	Peak output power, kW	Average output power, W	Pulse duration, μ s	Peak anode voltage, kV	Weight, kg	Life time, hours
8.1	150	40	0.1	23	2.5	1000
8.1	75	80	0.2	19	2.0	2000
8.1	75	20	0.2	19	2.2	2000
8.1	20	80	3	13	1.7	2000
8.1	20	20	1	13	2.0	2000
6.8	120	30	0.1	26	2.7	1000
6.8	40	50	0.2	19	2.2	2000
6.8	40	20	0.2	19	2.5	2000
4.1	35	20	0.1	18	2.0	1000
4.1	20	30	0.2	16.5	2.0	1500
4.1	20	15	0.2	16.5	2.2	1500
3.1	20	20	0.1	18	2.0	800
3.1	13	20	0.2	16.5	1.8	800
3.1	13	10	0.2	16.5	2.0	800
3.1	5	5	0.3	15	1.5	1000
3.1	5	20	1	12	2.0	1000
3.1	1	1	0.3	6.5	0.3	1000
3.1	2	2	0.2	7.5	0.3	1000
3.1	4	4	0.2	9.5	0.6	1000
2.2	10	10	0.07	15	1.7	500
2.2	3	3	0.1	13	1.5	500

Table 3. Specifications of mm-wave spatial-harmonic magnetrons with cold secondary-emission cathode.

As for the cold secondary-emission cathode, it was found that a platinum foil placed on copper core serves as an effective cathode providing a high level of the secondary emission under electron bombarding. The secondary emission is initiated by an auxiliary thermal cathode placed outside the interaction space. For comparison the typical operation conditions and characteristics of classical magnetrons and spatial-harmonic magnetrons with cold secondary-emission cathode are summarised in Table 1.

It should be noted that the proposed magnetrons operate with the magnetic field values, which are smaller by factor around 4 for 3 mm-wave magnetrons, what gives possibility to decrease the weight of the magnetic system by factor 4. This resulted in an essential decrease of the magnetron dimensions and the weight as well. The anode diameter is larger by factor 2 compared to this value for classical magnetrons. The dramatic improvement in life time of the magnetrons is also evident from this table.

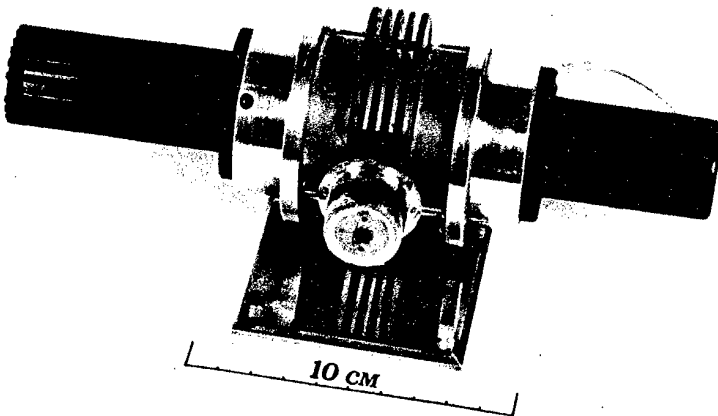


Fig. 1. Photograph of 10 kW, 140 GHz magnetron.

The above mentioned approaches have resulted in the appearance of magnetrons capable for efficient operation throughout the whole millimeter wave band. Characteristics of the magnetrons developed and produced at the Institute of Radio Astronomy of the National Academy of Sciences of Ukraine are summarised in Table 2. A photograph of 10 kW, 94 GHz magnetron is shown in Fig. 1 as an example. Magnetrons are water or air cooled depending on the level of the averaged power. Usually, if the averaged power is below 5 W, then air cooling is sufficient. The authors call the reader's attention to low voltage 3 mm-wave magnetrons, which operate with the anode voltage of 9 kV and lower. The weight of these magnetrons is only several hundred grams. Such magnetrons have been developed recently, and they accumulated the latest advances of the theoretical and experimental studies in this field [6 - 8].

III. SOLID-STATE MODULATORS

To drive the magnetrons, two kinds of lightweight solid-state modulator have been developed. The first type is a switch modulator, which uses a series stack of high voltage MOSFETs as power key and a direct coupling to magnetron. This modulator is used to drive magnetrons having the anode voltage of 10 kV and below.

The modulator scheme is shown in Fig. 2. The scheme comprises such sub-assemblies as high voltage converter, filament power supply, MOSFET switching stack, and a driver for MOSFETs. Some features of the design should be mentioned. The required high voltage is procured by using a single ended backward converter, which is synchronised at the pulse repetition frequency (PRF). This allows achieving small physical dimensions of the modulator along with a high efficiency (about 80%). The slow high voltage built-in within power turning on has been used to provide a safe start-up process of the magnetron oscillation. The filament power supply is based on a converter operating at doubled PRF, which is produced by using a phase lock loop circuit. In order to provide a high degree of stability of the heating current, linear pre-regulator is used owing to a small power consumed by the auxiliary cathode. The high voltage switch consists of ten MOSFETs connected in series. A transformer coupling is used to drive these transistors.

The second modulator is used to drive magnetron with anode voltage over 10 kV. It is a line modulator built by using thyristors and transformer coupling.

The scheme of the modulator is shown in Fig. 3. It contains high voltage converter, switching thyristor stack, filament power supply and a driver for the thyristors. Due to a greater power consumed by the filament of this magnetron the converter operates at a multiplied transmitter clock frequency that allows reducing physical dimensions of the filament transformer.

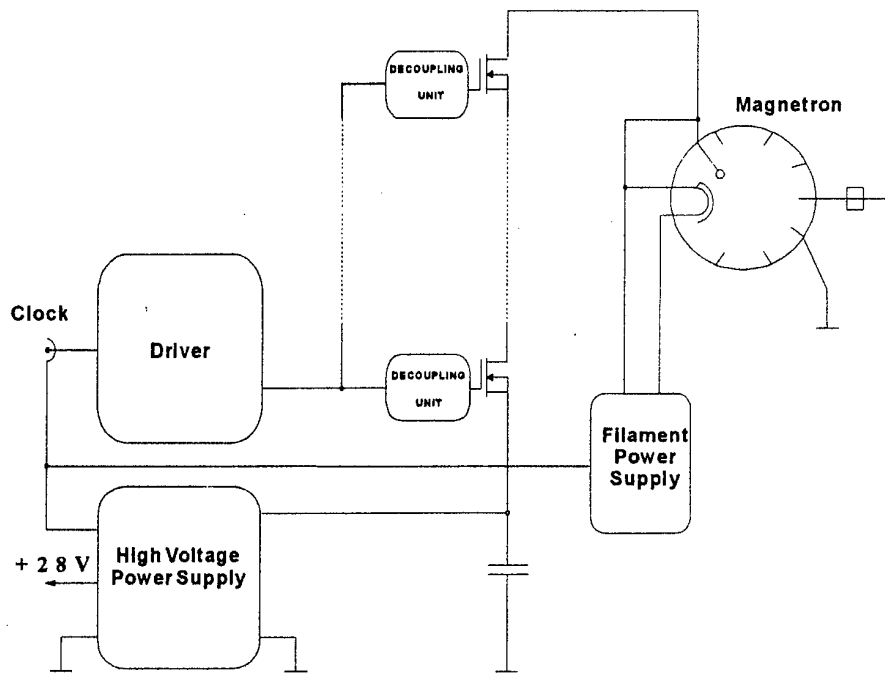


Fig. 2 Scheme of transistor modulator.

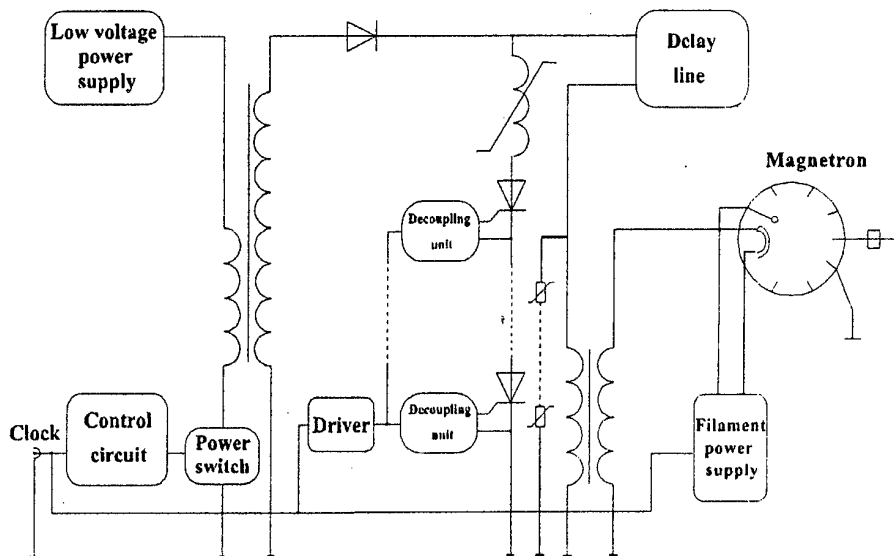


Fig. 3. Scheme of thyristor modulator.

The delay line is charged from a high voltage supply via a charging choke what implies the necessity of using a smoothing capacitor at the output of this supply. The application of such choke and the capacitor is undesirable, especially for airborne systems, since both are high voltage components and they have large dimensions and weight. An advanced solution has been introduced in the modulator design. Namely, the pulse synchronous charge of a delay line by using intermediate inductive storage has been implemented. This resulted in a decrease of dimensions and weight of the modulator and gives a possibility to increase the duty cycle compared to the conventional approaches to the modulator design. In the described scheme these components are absent at all, moreover the delay line charge becomes possible directly from a low voltage DC source. Since it is necessary to provide a comparatively large average power level, the delay line is charged by four pulses, i.e., the high voltage converter operates at equivalent frequency of 20 kHz.

The following solutions have been included in the described modulator. To improve efficiency and make easier the operation mode of the thyristors a saturated reactor was used. This is especially important for the operation with small values of the pulse duration at a large duty cycle. Varistors are introduced to shunt the magnetron and to provide a better matching of the magnetron with the delay line during pulse leading edge.

To summarize, all above mentioned approaches allow us to achieve the following advantages: (i) A charge choke and a smoothing capacitor are rejected, thereby, the modulator dimensions and weight are significantly reduced. (ii) The thyristors are recovered under a non-current mode, which enables us to increase significantly the duty cycle values. (iii) In the absence of the synchronisation there is no high-voltage applied to the circuit elements and the magnetron. Remote control of the modulator is also realised.

IV. PERFORMANCE OF THE TRANSMITTERS

The low-voltage magnetrons have been used to develop and produced 94 GHz transmitter suitable for radar applications. The modulator is built as a direct drive unit with a series of standard 10 MOSFET stacks as power key. Parameters of 1 and 4 kW transmitters are given in Table 3.

Peak output power, kW	1	4
Average power (max), W	1	2
Pulse duration, ns	50-200	50-200
Pulse repetition frequency (max), kHz	10	5
Volume, cm³	2000	3000
Weight, kg	2.5	4
DC supply voltage, V	28	28
Watt consumption (max)	80	120

Table 3. Parameters of the 94 GHz transmitters.

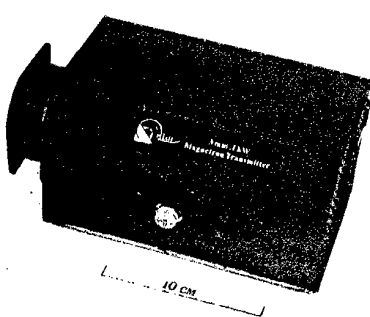


Fig. 3. Photograph of the 94 GHz, 1 kW transmitter.

The transmitters are built as single units with a forced-air cooling system incorporated in them. The cooling for both switch elements and magnetron is relied by using a single, low-power fan. A photograph of the 94 GHz, 1 kW transmitter is given in Fig. 3.

CONCLUSION

The development and realisation of effective mm-wave transmitters have become feasible due to the availability of several recent achievements. First of all, a new generation of compact mm-wave spatial-harmonic magnetrons with cold secondary-emission cathode has been successfully developed, including low voltage magnetrons. Advances in semiconductor technologies and novel circuit solutions have enabled the creation of compact and reliable solid state magnetron modulators. The realised transmitters by its combined characteristics (weight, dimensions, reliability, power, efficiency and spectral characteristics) have no analogues and can find a wide application in practical systems. In this paper, 3 mm transmitters have been mainly described, however transmitters for other frequency bands with attractive characteristics are now available as well.

ACKNOWLEDGEMENTS

The authors thank N. Khyzshnjak, A. Suvorov, A. Syrov, and B. Trush, for their contributions to the work presented here. This work was supported in part by EC under contract BIC15CT960816 and by DFG in the frame of the project "Millimeter Wave Magnetrons".

REFERENCES

1. J. B. Mead, A. L. Pazmany, S. M. Sekelsky, and R. E. McIntosh, "Millimeter-wave radars for remotely sensing clouds and precipitation", Proc. IEEE, vol. 82, no. 12, pp. 1891-1906 (1994).
2. F. Sadjadi, M. Helgeson, J. Radke, and G. Stein, "Enhanced vision for adverse weather aircraft landing", Int. J. of Infrared and Millimeter Waves, vol. 17, no. 1, pp. 1-49 (1996).
3. H. Meinel, "Commercial applications of millimeter-waves. History, present status and future trends", IEEE Trans. MTT, vol. 43, no. 7, pp. 1-16 (1995).
4. I. D. Truten, I. G. Krupatkin, O. N. Baranov, N. M. Galushko, and V. E. Ignatov, "Pulse magnetrons of millimeter wavelength under condition of space harmonics", Ukr. Phys. J., vol. 20, no. 7, pp. 1170-1176 (1975) (in Russian).
5. I. M. Vigdorchik, V. D. Naumenko, and V. P. Timofeev, "The secondary-emission cold cathode pulse magnetrons of the millimeter waveband", Rep. Ukr. Acad. Sci., Ser. A, no. 7, pp. 633-636 (1975) (in Russian).
6. V. Naumenko, A. Suvorov, and A. Sirov, "Tunable magnetron of a two-millimeter-wavelength band", Microwave and Opt. Techn. Let., vol. 12, no. 3, pp. 129-131 (1996).
7. V. Naumenko and D. Vavriv, "Millimeter wave magnetrons with secondary-emission cathode: Theory and experiments", Proc. of the 21st Int. Conf. on Infrared and Millimeter Waves, Berlin, Germany, 1996.
8. D. M. Vavriv and A. E. Serebryannikov: "On the analysis of magnetron oscillatory systems", Radiotekhnika i Elektronika, vol. 40, no. 1, pp. 71-78 (1995) (in Russian).

SUPERCONDUCTING PASSIVE MICROWAVE COMPONENTS FOR MOBILE COMMUNICATIONS.

M. J. Lancaster¹, J.-S. Hong¹, D. Jedamzik², R. B. Greed³¹The University of Birmingham

School of Electronic and Electrical Engineering, Edgbaston, Birmingham, UK

Tel. +44 121 414 4317, Fax. +44 121 414 4291, E-mail M.J.Lancaster@bham.ac.uk

²GEC-Marconi Materials Technology, Borehamwood, UK³GEC-Marconi Research Centre, Chelmsford, UK***Abstract***

A superconducting receive filter and duplexer are described with application in a mobile communications receiver. The design of an 8-pole quasi-elliptic filter is outlined, and the filter performance given. In addition, the design of an associated superconducting duplexer is discussed together with appropriate measurements. The components are for a DCS1800 base station.

Introduction

High temperature superconducting (HTS) passive microwave devices have been of interest for over 10 years [1]. However, it is only recently that a promising mass market for these high performance, miniature devices has begun to emerge. This market is in mobile communications base station applications. There have been a number of companies in the US set up to exploit HTS technology, and they are now producing mobile communications base station receivers. Operators around the world are currently evaluating these products. A European project partly sponsored by the European Commission entitled "SUperconducting systems for COMunicationS" or SUCOMS is developing a superconducting air interface for DCS1800 base stations. It is the receive passive components that this article describes.

The reasoning and advantages behind using superconducting materials in the mobile communications environment will not be described here. This has been detailed in a number of other publications [2, 3, 4, 5, 6]. All the advantages come from the reduced surface resistance of the superconducting material, giving filters and other components with low insertion loss together with an ability to have filters with very steep skirts. There have been only a small number of filter designs previously reported for mobile communications applications [7, 8, 9, 10].

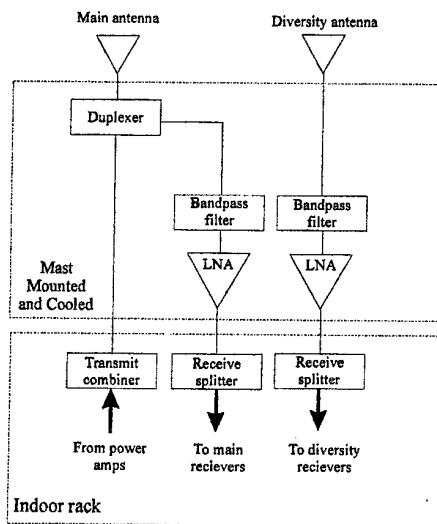


Figure 1 The SUCOMS receiver front end showing how it interfaces with a conventional DCS1800 base station.

The SUCOMS project initially involves the production of a receive front-end, consisting of six receive channels. Three channels consist of a duplexer, bandpass filter and amplifier and three channels consist of just the filter and amplifier for the diversity antenna. Two channels are shown in Figure 1. The design and performance of the filter and duplexer are briefly described in this paper. A description of the rest of the system including the amplifiers, microwave packaging and cryogenics can be found elsewhere [11]. The whole receive front-end will be tested by three separate operators as an antenna mounted system during 1998.

Filter Design

The DCS1800 receive band frequencies are 1710-1785MHz, the bandpass filter is designed to work in a 15MHz sub-band from 1770MHz to 1785MHz. A simplified specification for the filter is

Centre frequency 1777.5MHz
 Bandwidth 15MHz
 Insertion loss <0.3dB
 Return loss <-20dB
 30dB rejection bandwidth 17.5MHz;
 Transmit band (1805-1880MHz) rejection >66dB

A quasi-elliptic function filter was chosen to achieve this specification. Careful consideration of other filter types was given [12,13,14]. However, the quasi-elliptic filter gives passband nulls which provide a very sharp roll-off close to the band edge, although this is at the expense of stopband attenuation. The specification above can be met by using a significantly lower number of poles than other types of filter.

The structure of the microstrip filter is shown in Figure 2, it consists of 8 meander loop resonators above a ground plane. The particular structure was chosen in order to minimise the size of the filter whilst still retaining the required performance. The quasi-elliptic filter design requires unloaded Q values of 50,000 for the resonators. Measurements on a single packaged resonator at 60K, show the meander line resonator achieves this. This unloaded Q value has been obtained by careful consideration of the losses associated with the dielectric, the HTS material and importantly the housing for the filter.

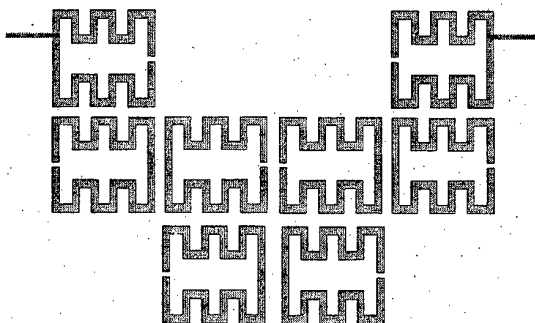


Figure 2: A microstrip 8-pole quasi-elliptic function filter using meander open-loop resonators.

The coupling structure of the quasi-elliptic function filter is shown in Figure 3. The cross coupling M_{36} shown as a dotted line is required in order to give the quasi-elliptic response. This cross coupling has to be electric coupling rather than the magnetic coupling of the other resonator couplings. This is achieved by placing the open circuit of the resonators close to one another, rather than the high current regions as in the other resonator couplings.

The filter synthesis starts with a low pass prototype, consisting of shunt capacitance and J inverters. The low pass prototype is converted to bandpass with parallel resonant sections of the same value. The J inverters provide values of the coupling coefficients between the meander loop resonators. The required distances between the resonators are then found by using a full wave electromagnetic simulator [15, 16, 14].

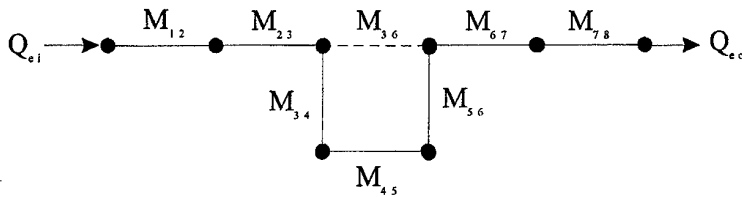


Figure 3 A general coupling structure of the filter of Figure 2

Filter fabrication and Measurements

The filter is fabricated out of 350nm thick $\text{YBa}_2\text{Cu}_3\text{O}_7$ thin film superconductor on both sides of a 0.3mm thick MgO substrate. The substrate measures 22.5mm by 39mm. In order to match thermal expansion of the MgO, it is mounted in a titanium box, the outer dimensions being 50x38x13mm. For the final system six of these filters plus their amplifiers fits in a box measuring 113x85x19mm

A sensitivity analysis has shown that the thickness of the substrate is the most important parameter regarding the performance of the filter [14]. The sensitivity of the centre frequency to the change in substrate thickness has been calculated to be $0.7\text{MHz}/\mu\text{m}$. The tolerances on the substrates are only $\pm 5\%$, therefore the filter must be tuned. This is done by a series of 16 sapphire tuning screws placed above the resonator. 8 of the screws are over the coupling gaps, and 8 over the open circuit ends of each of the resonators.

Measurements of S21 and S11 for a filter tuned in liquid nitrogen are shown in Figure 4. The filter shows a good response approaching the required specifications, cooling to 60K with appropriate tuning will improve the response further. Out of band rejection is above 70dB and no spurious responses are observed up to a frequency of 3GHz. The shape of the passband response does not change up to input powers of 5dBm; the specification requires a power handling capability of 0dbm. Further measurements at lower temperature and of power handling performance are underway.

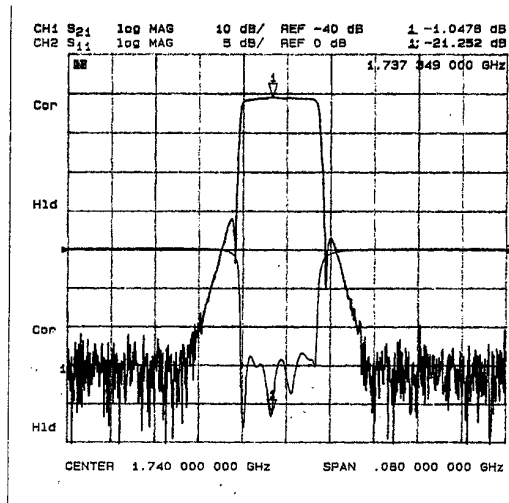


Figure 4 Frequency response of the superconducting DCS1800 filter in liquid nitrogen at 77K.

Duplexer Design

A duplexer is required in order to use a single antenna for both transmit and receive operations. Traditionally, duplexers have been large and cumbersome and can in some cases contribute to a reduction in system performance. The superconducting duplexer described here is very small and has an excellent performance. It is integrated into the cryogenic encapsulation together with the other components described above.

The layout of the microstrip duplexer is shown in Figure 5(a). It consists of two 3dB couplers and two bandstop filters. An individual coupler is shown in Figure 5(b). The coupler used is a tandem coupler rather than the conventional hybrid coupler, this is in order to reduce the size of the element and also to increase the

bandwidth. The disadvantage of using this coupler is that bond wires are required to bridge the two-coupled lines. The coupler has the action of power splitting the input signal into two, with a 90° phase shift between the outputs.

An individual bandstop filter is shown in Figure 6(a) and is designed from the prototype circuit shown in Figure 6(b). It consists of three resonators placed a quarter of a wavelength apart coupled to a transmission line. The bandstop filters are at the receive frequency band. As the resonators do not resonate at the transmit frequency, the 12W maximum transmit power only travels along the transmission lines, hence the power requirements for the HTS is minimised.

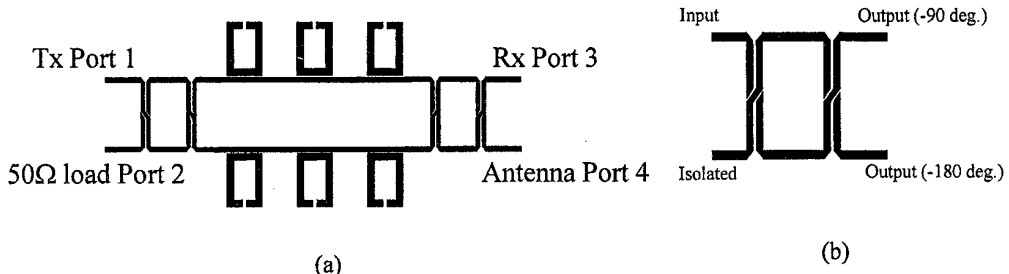


Figure 5 (a) Duplexer, including two tandem couplers and two bandstop filters (b) Tandem coupler used in the duplexer

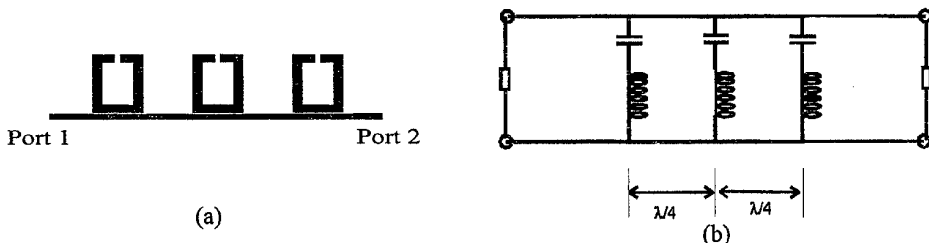


Figure 6 Bandstop filter. (a) Layout (b) Prototype circuit

Duplexer fabrication and measurements.

The duplexers are fabricated out of $\text{YBa}_2\text{Cu}_3\text{O}_7$ HTS on 0.5mm thick LaAlO_3 substrates. The tandem couplers measure 15.5mm by 22.5mm each and the pair of bandstop filters measure 38mm by 13mm each. The four elements are packaged together with bond wires connecting the components. Tuning screws are used to tune the bandstop filters.

The tandem couplers and the hybrids were tested separately. The tandem couplers were tested by replacing the bandstop filters in Figure 5(a) by two superconducting transmission lines. This produces a component that should produce transmission from port 1 to port 4 and port 2 to port 3, over the coupler bandwidth. Measurements indicate that all the isolations S_{21} , S_{34} , S_{24} and S_{13} are $>30\text{dB}$ and all the return losses S_{11} , S_{22} , S_{33} , S_{44} are better than -20dB . The values of S_{14} and S_{23} could not be differentiated from the connectors and bond wires. Individual measurements were also made on a single bandstop filter shown in Figure 6(a). When tested and tuned as an individual component, it shows S_{21} to be almost -30dB at the receive frequency and S_{11} to be -20dB in the transmit frequency band.

The performance of the full HTS duplexer is shown in Figure 7. The transmit and receive bands are shown as shaded areas. The transmitted signal to the antenna, S_{41} , shows very low attenuation in the transmit band and an almost 30dB rejection in the receive band. The path from antenna to receiver shows low loss in the receive band, and almost 20dB rejection in the transmit band. The isolation between the transmit port to the receive port, S_{31} , is mostly greater than 30dB, but increases to almost 50dB in the receive band. Measurements of the return loss of all four ports are better than -20dB over all the bands. All the above measurements we done in liquid nitrogen.

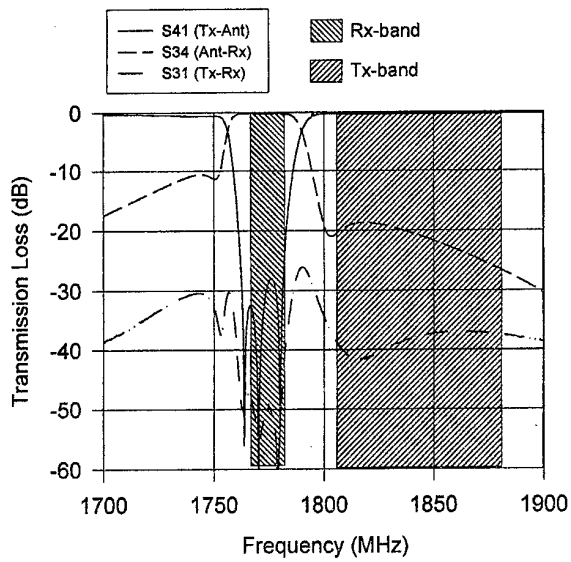


Figure 7 Performance of the superconducting duplexer

Conclusions

Measurements on a HTS bandstop filter and duplexer for mobile communications have been given. These initial measurements show that an excellent performance can be achieved. Further measurements are in progress on the power handling capability and at lower temperatures. These components are currently being integrated into a cryogenic system that will go on field trials with telecommunications operators.

Acknowledgements

The SUCOMS project participants are: Universität Wuppertal, Germany, GEC-Marconi Materials Technology, UK, GEC-Marconi Research Centre, UK, Thomson CSF Communications, France, Thomson CSF – LCR, France, Leybold, Germany and the University of Birmingham, UK. The authors would like to acknowledge the participants in the project from these establishments. The project was partially funded by the European Commission through the ACTS initiative (project AC115). Dr Lancaster was supported from funding from the Nuffield foundation.

¹ Lancaster M. J. "Passive microwave device applications of superconductors" Cambridge University Press, Cambridge UK 1997

² Reeder D. "A cryogenic option for expanding coverage" Mobile Communications International June 1996 p57 (SCT)

³ STI Inc. "A receiver front end for wireless base stations" Microwave Journal April 1996 p 116

⁴ Dawson F. "Technical innovations expand coverage" Wireless Week August 12th 1996

⁵ Yourc'h Y., Auger G., Chaloupka H. J., Jedamzik D. "Architecture of Future base stations using high temperature superconductors" Acts Mobile Summit, Aalborg Denmark September 1997

⁶ M. J. Lancaster, J.-S. Hong H. J. Chaloupka, D. Jedamzik, R. B. Greed, G Auger, Y Yourc'h, J. C. Mage "Superconducting Filters for Mobile Communication Base Stations" Acts Mobile Summit, Aalborg Denmark September 1996

⁷ Zhang D., Liang G.-C., Shih C. F., Lu Z. H., and Johansson M. E. "A 19-pole cellular bandpass filter using 75mm diameter high-temperature superconducting thin films" IEEE Microwave and guided wave letters V5(11) pp 405-407

⁸ Liang G.-C., Zhang D., Shih C. F., Withers R. S., and Johansson M. E "High-power HTS microstrip filters for wireless communications" IEEE MTT-S International Microwave Symposium Digest pp 183-186 1994

-
- ⁹ Liang G.-C., Zhang D., Shih C. F., Withers R. S., and Johansson M. E. "Compact forward-coupled superconducting microstrip filters for cellular communications" IEEE MTT-S International Microwave Symposium Digest pp 2656-2659 1995
- ¹⁰ Liang G.-C., Zhang D., Shih C. F., Withers R. S., and Johansson M. E., Oates D. E., Anderson A. C., Polakos P., Mankiewich P., Obaldia E., Miller R. E., "High-power HTS microstrip filters for wireless communication" IEEE Transactions on Microwave Theory and Techniques pp 3020-3029 1995
- ¹¹ Greed R. B., Häfner H. U., Mistry R. "Cold communications in Europe" Acts Mobile Summit, Aalborg Denmark September 1997
- ¹² Hong J.-S., Lancaster M. J., Jedamzik D., and Greed R. B., "8-pole superconducting quasi-elliptic function filter for mobile communications application" IEEE MTT-S International Microwave Symposium, Baltimore, USA June 1998
- ¹³ J.-S.Hong, M.J.Lancaster, R.B.Greed, D.Jedamzik "Superconducting Microstrip Filter for DCS1800 Base Station", Submitted to ICMMT'98
- ¹⁴ Hong J.-S., Lancaster M. J., Jedamzik D., and Greed R. B., "On the development of superconducting microstrip filters for mobile communications applications" Submitted to IEEE Trans on Microwave Theory and Techniques.
- ¹⁵ Hong J-S., Lancaster M. J. "Couplings of Microstrip square open-loop resonators for cross-coupled planar microwave filters" IEEE Trans. on Microwave Theory and Techniques V44(11) 1996 pp 2099-2109
- ¹⁶ Hong J.-S. and Lancaster M.J., "Theory and experiment of novel microstrip slow-wave open-loop resonator filters", IEEE Trans., MTT-45, Dec. 1997.

**VALUE ESTIMATIONS OF THE THIRD STOKES-VECTOR COMPONENT
BOTH PRECIPITATION MICROWAVE EMISSION AND SUN SCATTERED
RADIATION OBSERVATIONS**

B.G.Kutuza, G.K.Zagorin

Russian Academy of Sciences, Institute of Radio Engineering & Electronics
11, Mokhovaya st., Moscow, 103907, Russia
Tel: (7095) 203-4793, Fax: (7095) 203-8414, e-mail: kutuza@mail.cplire.ru

A.Hornbostel, A.Schroth

DLR, Deutsches Zentrum fuer Luft- und Raumfahrt, Institut fuer Hochfrequenztechnik
D-82230 Oberpfaffenhofen, P.O. Box 1116, Germany
Tel: (0049) 8153-28-2318/2325, Fax: (0049) 8153-28-1135
e-mail: achim.hornbostel@dlr.de; arno.schroth@dlr.de

Heat emission of the many natural objects is partially polarized. This fact was found by Arago at 1824 [1]. The microwave emission of the both water surfaces and nonspherical raindrops is a good examples of this natural phenomenon. In general case this polarization is elliptic. However so far the microwave emission polarization parameters dependence on the natural sources state characteristics are studied insufficiently. Four parameters (the angle inclination ψ , the ellipticity angle $\varepsilon = \arctan(b/a)$, where a is the larger axis and b is the smaller axis of polarization ellipse, the phase difference between electric field orthogonal components and the full electric field amplitude) determine both the location and shape of the microwave emission polarized component polarization ellipse completely.

The quantitative description of the partially polarized quasi-monochromatic waves is based on the coherence matrix conception. The linear combinations of this matrix elements, so-called the Stokes parameters are used successful in radio-astronomy, as well as lidar and radar polarimetry. The relations between the both polarization and Stokes parameters are expressed by the formula [2]

$$I = I_u + I_p, \dots Q = I \cdot p \cdot \cos 2\psi \cdot \cos 2\varepsilon, \dots (-\pi/2 \leq \psi \leq \pi/2), (-\pi/4 \leq \varepsilon \leq \pi/4),$$

$$U = I \cdot p \cdot \sin 2\psi \cdot \cos 2\varepsilon, \dots V = I \cdot p \cdot \sin 2\varepsilon,$$

where I is the total radiation intensity; I_u, I_p are non-polarized and polarized components

intensity, respectively; $p = \frac{\sqrt{Q^2 + U^2 + V^2}}{I} = \frac{I_p}{I}, \dots (0 \leq p \leq 1)$ is the polarization degree,

and $\psi = \frac{1}{2} \arctan(\frac{U}{Q}), \varepsilon = \frac{1}{2} \arcsin \frac{V}{\sqrt{Q^2 + U^2 + V^2}}$, the sign of Q is equal to sign of ψ .

The angle ψ is determinated by the principal value of $\arctan \psi_0$ with expression

$$\psi = \psi_0 + \pi(1 - \text{sign}Q)\text{sign}U/4.$$

Within the Stokes parameters (Q, U, V) subspace the quasi-monochromatic wave polarization state is presented by the point with the polar coordinates $(p, \pi/2 - 2\varepsilon, 2\psi)$. The unity sphere ($p=1$) within the Stokes subspace is called the Poincare sphere. In [3] was proposed to use the three first Stokes parameters for the presentation with pseudo-color the polarization state of the observed scenario radiation like color TV.

All the Stokes parameters have dimension of intensity. The third Stokes parameter U similar to the second parameter Q define the linear polarized orthogonal components intensity difference but the third parameter relate to the intensity difference in coordinate system rotated around the propagation direction on angle $\pm \pi/4$ compare to reference system. Fourth Stokes parameter indicate the circular polarized orthogonal components intensity difference.

It is clear from the rotation (at angle ϕ around propagation direction) transformation Stokes parameters expressions [2] I_p, I, V are invariant. The parameter U at $\phi=0$ is expressed with value at $\phi=\pi/4$ by means relation

$$U(\phi=0) = 2(U(\phi=\pm\pi/4) - I)$$

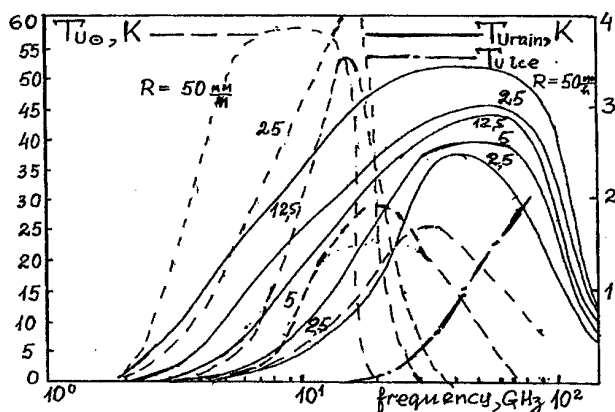
For the passive microwave remote sensing using it is suitable the concept of the brightness temperature vector $\vec{T} = \{T_I, T_O, T_U, T_V\}$ which proportionate to the Stokes parameters due to linearity of the Rayleigh-Jeans expression for the microwave range.

There are both surface distributed and volume sources of the microwave emission at $T_U \neq 0$ within the system: "rainy atmosphere over underlying surface". Up-welling and down-welling microwave emission are formed within top- and down-lying layer of the system, respectively. These layer optical depth value is order ~ 1 . If the rain layer optical thickness more than 1 there is intermediate screening layer where both the up-welling emission from the underlying surface and down-welling emission from the top layer attenuate. The principal cause of emission at $T_U \neq 0$ is the azimuth asymmetry of the environment emission. The microwave emission with $T_U \neq 0$ from surface is conditioned by the asymmetric distribution of the small-scale roughness slopes. Its distribution function described by Gram-Charlie series in case sea surface, as shown by Cox and Munk. The atmosphere emission back-scattered by these roughness carries in additional contribution to the up-welling emission third Stokes parameter. The microwave emission volume sources with $T_U \neq 0$ are partially oriented non-spherical particles (raindrops, hail, melting snowflakes and so on). The volume source intensity in this case is proportionate $\sim \Delta A \sin \beta$ where ΔA is the difference attenuation at horizontal and vertical polarization and β is the particle symmetry axis declination from the local vertical angle. Additional mechanism of generation radiation with $T_U \neq 0$ is the volume scattering (including multiple scattering) microwave emission by the non-spherical partially oriented particles (ice crystals, raindrops, hail and so on). The two scattering mechanisms the coherent forward scattering and non-coherent (diffuse) scattering take place. The coherent forward scattering by non-spherical particles is described with attenuation matrix in radiation transfer equation. Due to this effect the initial non-polarized Sun microwave emission after the passing through raindrops layer is polarized. The incoherent (diffuse) microwave emission scattering by the raindrops and ice cloud crystals transformed the polarization state too.

The precipitation microwave emission third Stokes parameter (T_U) contributions from rain, hail and ice crystals value estimations have been carried out in order to investigate the possibilities for its measurement. The calculations are based on the approximate solutions of the boundary problems for the set of radiative transfer equations which describes the propagation of polarised microwave emission through homogeneous plane parallel layers of oriented, non-spherical rain, hail and ice particles. The general problem formulation is considered in [4].

The thickness of the rain layer was supposed to be 4 km, and 3 km both for the hail and ice crystal layers. The rain drop size distribution was described by the Marshall-Palmer law. The hail and ice crystals were considered as monodisperse with major particle dimensions of 6.5 mm and 2 mm, respectively. The raindrops were modelled by spheroids which are close to the Pruppacher-Pitter shape. The shape of hail was assumed to be the same as for raindrops with equal dimensions. Plate form ice crystals were modelled as described by Auer and Veal.

The calculations have been carried out for frequencies of 6, 13, 20, 35 and 90 GHz at rain rates of 2.5, 5, 12.5, 25, 50 and 100 mm/h. The ice water content was set to 0.13 g/m³ for hail and to 0.15 g/m³ for ice crystal clouds. The thermodynamical temperatures of the layers were +20° C within rain volume, 0°C within hail cloud and -15° C within ice crystal cloud. The particle orientation effective declination angle was assumed equal to 5 degree. Results are presented on Fig. 1 for an observation angle of 50 degree (from zenith for down-welling radiation and from nadir for up-welling radiation). Fig. not contains the results of calculations for hail. Only the curve which describes the ice crystal scattering rain emission is relate to up-welling emission. The scale of the rain down-welling emission $T_{U_{rain}}$ and the ice crystal scattered up-welling emission curves is indicate at right-hand side of fig., and the scale of the raindrop scattered the Sun emission curves is indicate at the left-hand side of fig.



It is shown that T_u depends both on the shape and orientation of the particles. For the third Stokes parameter of microwave emission from precipitation the sin-component of the first azimuthal harmonic is predominant among the azimuthal Fourier harmonics. For comparison, in the case of microwave emission from sea surface the predominant harmonic is the second one. The T_u maximum values are located near 2-3 K at rain rates $R=5-25$ mm/h for the rain microwave emission and 25-60 K for the Sun microwave emission scattered by rain. The contribution into third Stokes vector component of the upwelling microwave emission increase due to scattering by the ice crystal clouds from $T_u=1$ K at 35 GHz to $T_u=2.5$ K at 90 GHz. For the dry hail these values are 2-3 times larger. The Sun emission scattered by hail decreases with frequency from $T_u=30$ K at $f=20$ GHz to $T_u=20$ K at $f=30$ GHz.

It is clear from the Fig. the T_u maximums in case rain scattered Sun emission increase and move to lower frequency range if rain rate increase. Opposite rain layer microwave emission T_u maximums demonstrate tendency to move into more high-frequency area a little. The T_u value of the rain layer microwave emission scattered by ice crystal monotonously grows with increasing of both rain and surface microwave emission intensity and grows of radiation frequency.

The results of our calculations show real possibilities of measurements of microwave emission third Stokes parameter due to precipitation. The obtained values exceed essentially the sensitivity threshold of modern microwave radiometers.

Third Stokes parameter measurements of microwave emission from precipitation enable an additional independent channel to obtain information about the shape, orientation and phase state of precipitation particles.

References

- 1.O.Sandus A Review of the Emission Polarization Appl.Opt.1965,v.4,pp.1634-1642.
- 2.S.Chandrasekhar Radiative Transfer.Oxford,1950.
- 3.J.E.Solomon Polarization imaging.Appl.Opt.1981,v.20,9,pp.1537-1544.
- 4.Kutuzza,B.G. et.al. Physical Modeling of Passive Polarimetric Observations of the Atmosphere with Respect to the Third Stokes Parameter. Radio Sci. 1998,v.33,№3, pp.677-695.

REMOTE SENSING OF THE ATMOSPHERIC OZONE AT MILLIMETER WAVES

E.P.Kropotkina, A.N.Lukin, S.B.Rozanov, S.V.Solomonov
 P.N.Lebedev Physical Institute of the Russian Academy of Sciences
 53 Leninsky prospect, Moscow V-333, 117924 RUSSIA
 Tel.: (007)(095) 132-64-62, Fax: (007)(095) 135-24-08, E-mail: solomon@sci.lpi.msk.su

1. Ground-based remote sensing of the atmospheric ozone at millimeter (MM) waves is necessary for continuous day-and-night monitoring of the ozone layer. A valuable feature of the method and its advantage over observations at shorter wavelengths is low dependence on weather conditions because of low influence of aerosols and clouds on propagation of MM waves in the atmosphere. Low-noise heterodyne MM-wave radio spectrometer [1, 2] was built at the P.N.Lebedev Physical Institute (LPI) for ground-based measurements of the atmospheric ozone spectral line of 142.175 GHz central frequency. High sensitivity and frequency resolution of the spectrometer allow to get accurate pressure-broadened ozone spectra which are used for solution the inverse problem - retrieval the vertical ozone distribution (VOD) in the atmosphere.

Regular ground-based ozone measurements are being carried out at the LPI since 1987 to study various processes and changes in the Earth's ozonosphere. The VOD for altitudes about from 15-20 to 75 km is retrieved from the spectra measured. The upper boundary of the altitude range is essentially higher than one for balloons and ozone sondes (about 35 km), ground-based optical spectrometers and lidars (up to 40-50 km). The LPI MM-wave spectrometer was incorporated to ground-based network for ozone measurements during international campaigns DYANA (1989-90), CRISTA/MAHRSI (1994), and CRISTA/MAHRSI-2 (1997).

2. The ozone spectrometer (ozonometer) is mounted before radio transparent window in a laboratory room at the LPI in Moscow. The instrument measures thermal emission spectra of the atmospheric ozone molecules in 283 MHz band centered with the 142.175 GHz [1, 2]. Its 80-channel filter-bank spectrum analyzer is adapted to shape of the spectra measured due to stepped increase of frequency resolution towards the line center. Additionally a broadband channel is used for measurements of brightness temperature of the atmospheric background radiation (oxygen and water vapour thermal emission). The broadband data are necessary to determine tropospheric attenuation and to calculate the "above-troposphere" ozone spectra which are used for following retrieval of the VOD. Typically zenith angle of the observations is of 60°.

The retrieval procedure is based on the iteration algorithm [3] where the Tikhonov's method in form of generalized mismatch is used at every step. Accuracy of the VOD retrieval by the procedure is no worse than 5-7 % for altitudes of 20-50 km and no worse than 15-20 % for other parts of the altitude range covered.

3. Regular ground-based ozone observations at the LPI allowed to obtain detailed altitude-temporal picture of the ozone distribution over Moscow and its variations. Some examples of the VOD (relative ozone content in ppm units (10^{-6}) versus altitude) for various states of the atmosphere in 1996-98 are given in Fig. 1. A graph of annual behaviour of the relative ozone content at 35 km altitude (i.e. close to its normal maximum for the Moscow latitude 55°N [4]) for the period is presented in Fig. 2. Qualitatively the annual VOD variations observed are constituent with the Keating's model [4]. Additionally short-term changes in the VOD were detected. In summer seasons deviations of the measured vertical ozone profiles from the model ones were essentially smaller than in winter seasons, and the summer profiles were close to model [4] in average.

A new effect of strong and long-term ozone depletion in stratosphere over the Moscow region in 25-45 km layer in winter seasons was discovered for the first time by the MM-wave observations (Fig. 1). Comparison with results of our ozone measurements in 1987-90 [5] shows that so noticeable and long-term ozone content decrease in stratosphere over the Moscow region was not observed in late 80s.

When comparison of the VOD measured at the beginning of 1996 (Fig. 1, a, curves 1-5), and in cold seasons of 1996-97 (Fig. 1, b, curves 1,2,4,5,7) and 1997-98 (Fig. 1, c, curves 1,2,3,5,7) it is important to note coincidence of altitude regions (25-45 km) where the most prominent ozone decrease occurred for all the periods.. Shape of the VOD measured in cold seasons of 1996-98 is essentially different from VOD of both the model [4] for proper winter/spring months and vertical ozone profiles of summer seasons. The recurrence of the altitude region (25-45 km) where the most strong relative ozone depletion was observed in stratosphere of middle latitudes together with repeating the unusual VOD shape for the periods of the cold seasons indicate

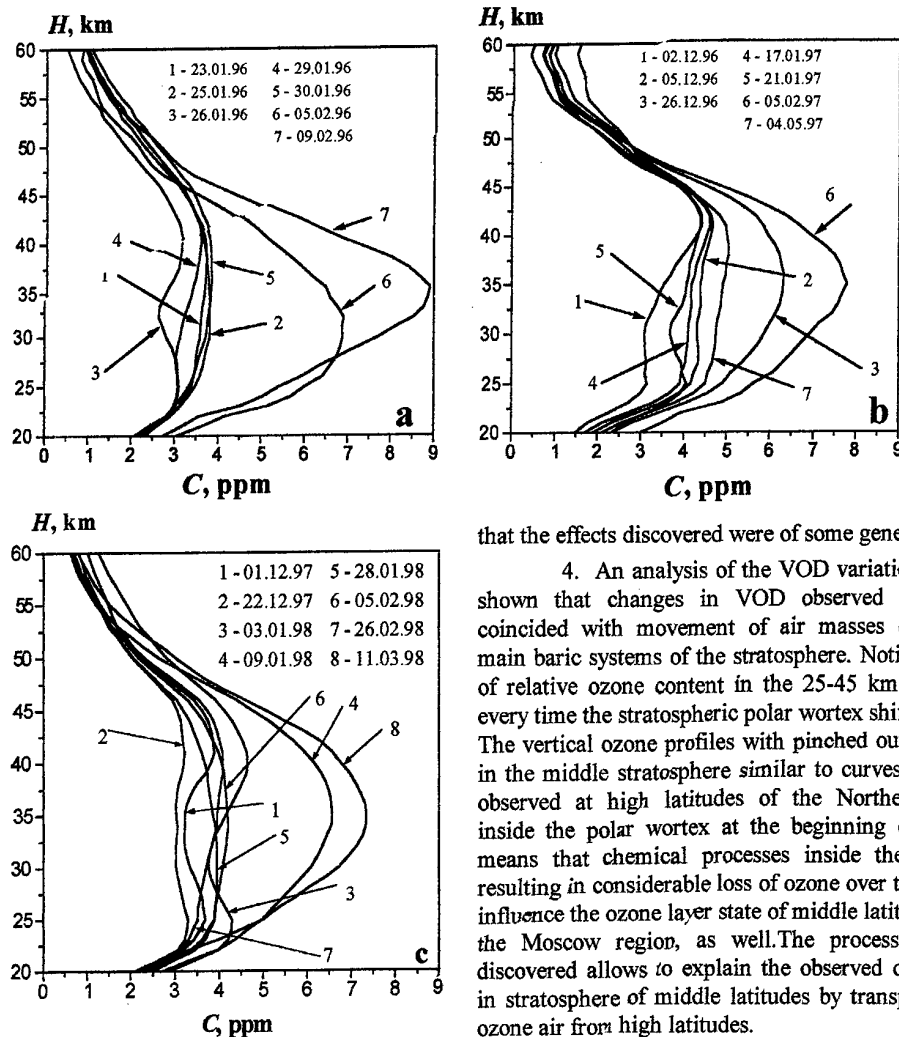


Fig. 1

The remote sensing of the atmospheric ozone at MM waves open unique possibilities for monitoring the ozone layer and continuous control of its changes under unlimited industrial pollutions to the atmosphere.

The research was supported by Grant No. 96-02-19093 from the Russian Foundation for Basical Research.

that the effects discovered were of some general nature.

4. An analysis of the VOD variations (Fig. 1) has shown that changes in VOD observed at MM waves coincided with movement of air masses connected with main baric systems of the stratosphere. Noticeable decrease of relative ozone content in the 25-45 km layer occurred every time the stratospheric polar vortex shifted to Moscow. The vertical ozone profiles with pinched out ozone content in the middle stratosphere similar to curves of Fig. 1 were observed at high latitudes of the Northern hemisphere inside the polar vortex at the beginning of 1996 [6]. It means that chemical processes inside the polar vortex resulting in considerable loss of ozone over the polar region influence the ozone layer state of middle latitudes, including the Moscow region, as well. The processes and effects discovered allows to explain the observed ozone depletion in stratosphere of middle latitudes by transport of poor in ozone air from high latitudes.

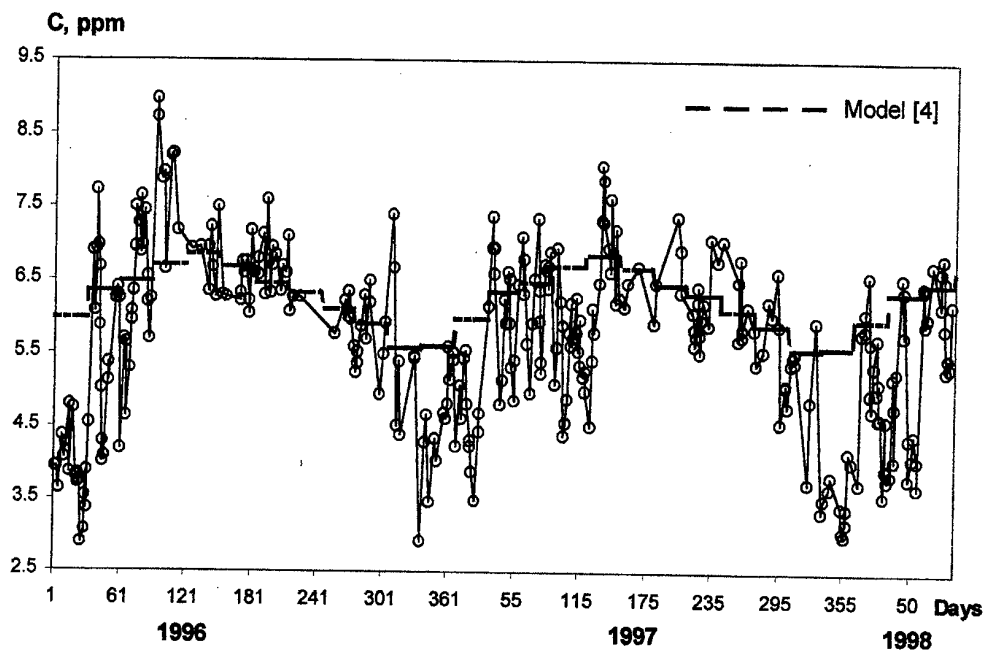


Fig. 2

References

1. S.V.Solomonov, S.B.Rozanov, E.P.Kropotkina, A.N.Lukin, "Techniques of ground-based remote sensing of the ozone layer by millimeter-wave heterodyne spectroscopy", Proc. SPIE, Vol.3406, 1998.
2. V.A.Gusev, E.P.Kropotkina, S.V.Logvinenko, A.N.Lukin, P.L.Nikiforov, S.B.Rozanov, A.M.Shtanjuk, S.V.Solomonov, "Heterodyne spectrometer for remote sensing of the atmospheric ozone", this issue.
3. K.P.Gaikovich, E.P.Kropotkina, S.V.Solomonov, "New possibilities of ground-based ozone radiometry", Abstr.XXV Gen. Assembly URSI, Aug.28-Sept.5, 1996, Lille, p.291.
4. G.M.Keating, L.S.Chiou, N.C.Hsu, "Improved ozone reference models for the COSPAR international reference atmosphere" Adv. Space Res., Vol.18, No.9/10, pp.11-58, 1996.
5. S.V.Solomonov, E.P.Kropotkina, A.N.Lukin, N.I.Ponomarenko, S.B.Rozanov, J.Elder, "Some features of the vertical ozone distribution from millimeter wave measurements at Pushchino and Onsala observatories" J. Atmos. Terr. Phys., Vol.56, No.1, pp.9-15, 1994
6. G.Hansen, T.Svonoe, M.Chipperfield, A.Dahlback, U.-P.Hoppe, "Evidence of substantial ozone depletion in winter 1995/96 over Northern Norway", Geophys. Res. Lett., Vol.24, No.7, pp.799-802, 1997.

MILLIMETER WAVE NOISE RADAR TECHNOLOGY

Konstantin A. Lukin

Institute of Radiophysics and Electronics National Academy of Sciences of Ukraine
 12 Academika Proskura St., Kharkov 310085, Ukraine
 Phone/Fax: +38 0572 448349/441105; E-mail: lukin@ire.kharkov.ua
 and
 Space Applications Institute, Joint Research Center of EC, 21020 Ispra (Va), Italy

1. Introduction

Millimeter Wave (MMW) electromagnetic signals are the most appropriate ones to be used when solving various practical problems of our daily life on the basis of radar sensors, such as environment monitoring, remote sensing, target detection, vehicle collision warning systems, automatic landing and docking systems and many others. Development of a light, compact, low energy consumption and low cost MMW sensor, having capability of a coherent radar with half of meter range resolution and 10 cm/s velocity resolution is a challenging problem for today's radar technology. Such kind of radar sensor will provide a new ability for radar system design and find a number of applications. Optimal reception of coherent (pulsed or CW) radar signals and pulse compression technique are the principles formed the basis of the modern radar design. Avoidance of ambiguities in range and velocity measurements, as well as minimization of ambiguity function side lobes are the primary goals for a radar designer that, being properly achieved, supply him with big benefits in the radar performances. From those viewpoints, the **noise continuous waveform (NCW)** is known to be a most appropriate one for the radar design. In spite of that, the NCW was not used mainly because of the lack of the hardware needed for its realization. However, today's advances in chaotic dynamics and fast digital electronics make it possible to revise the idea of **Noise Radar Technology (NRT)** and implement the development of noise radars with performances allowing their realistic applications.

In the paper, we present main results of theoretical and experimental development of the NRT for MM Waveband which has been studying in the Laboratory of Nonlinear Dynamics of Electronic Systems (LNDES) of the Institute of Radiophysics and Electronics, National Academy of Sciences of Ukraine since 1990 [1]-[10]. The key points of the NRT developed are the use of chaotic waveform generator as a source of noise signals and digital-analog correlator with electronically controllable delay line as the main part of correlation receiver of the noise radar. Besides, so called double spectral processing of NCW has been also using for the development of the noise radars and range measurement devices.

2. Noise Radar Technology

The NRT is the radar technology which uses the NCW as a probe signal and correlation processing (or double spectral one) of the radar returns for their optimal reception (matched filtration). Its development includes the following main sub-tasks: 1.Theoretical consideration of the NCW generation and simulation of NCW optimal processing. 2.Numerical simulation of the noise radar working regimes. 3.Development of the NCW generators with required parameters. 4.Design and development of the correlation receiver for the NCW optimal reception. 5.Development of the noise radar for specific application.

2.1. Theoretical Consideration and Development of the Noise Radar

The radar signals, such as coherent pulses, linear frequency modulated (both pulsed and CW) and bi-phase coded waveforms, etc., have received wide acceptance mainly because they don't need controllable delay lines for the optimal processing of radar returns, on the one hand, while developments of single

frequency and pulsed signal generators have made a considerable progress, on the other hand. Those signals, allow to perform with a good approximation the optimal reception and pulse compression of the radar returns, simultaneously. However, they normally have the power spectrum of rectangular shape which gives raise side lobes in both range and Doppler frequency measurements. At the same time, it is well known that the NCW with a wide enough Gaussian power spectrum and fast decay of correlation allows to regulate independently the signal compression, its optimal reception and minimization (or even elimination) of the ambiguity function side lobes. Besides, the use of the NCW provides such an advantages as single-validity of the radar ambiguity function, no peak power in the transmitted signals and simplicity of its forming scheme, etc. However, many experiments which have been carried out before 90's years showed very restricted abilities of the noise radar under development in comparison with conventional radars. This was because of availability at that time only narrow band NCW generators and correlation receivers. Meanwhile, quick developments in the science on dynamical chaos gives the methods for generation of wideband NCW, while the integrated circuit electronics provides fast digital components for design the appropriate digital correlator allowing to perform the optimal processing of the NCW. This gives the chance to go around the mentioned above difficulties of the NRT development and take its advantages for the design of various remote sensing systems.

Theoretical evaluation of the performances of the noise radar main units has been carried out before its development. The following sub-tasks have been solved analytically and numerically: a. Noise Radar Power consideration; b. Affect of the NCW power spectrum shape and width on the Ambiguity function, its side lobes, etc.; c. Affect of the sampling rate, number of quantization levels, integration time, etc. on the SNR and other parameters. Numerical simulation of the noise radar working regime and evaluation of its performances showed its feasibility, high performances and provide theoretical basis for the NRT development.

The noise radars of several types have been developed in the LNDES on the basis of the approaches described above. Generally, the noise radar developed consists of the following main units:

1. Transmitting and Receiving Antennas.
2. The NCW Generator-Transmitter.
3. Workingband-to-Baseband Frequency Converter.
4. Correlation Receiver.
5. Processor/Display of Receiver Output Signals.

The Units 1, 3 and 5 are similar to those of conventional radars. The main effort have been spent to develop the Unit 2, containing the NCW generator, as well as the Unit 4, the main part of which is the Digital-Analog Real-Time Correlator.

2.2. Generators of Noise Continuous Waveforms

The advantages of NCW generators developed in comparison with, say, thermal noise signal sources consist in the much higher spectral density of the generated signals, as well as availability of their parameters control and simplicity of the generator construction, etc. For the correlation processing, it does not matter how the NCW has been obtained, if it has no any auto-correlation during measurement time. This statement has been completely confirmed by the experiments carried out with the use of millimeter wave NCW generators developed on the principles of the dynamical chaotization of nonlinear system motion [1],[5]-[10]. The MMW solid-state NCW generators of two kinds were designed on the basis of IMPATT- and Gunn-diodes. Chaotic regimes are provided via special design of the coupled resonators, as well as by the use of the special working regime of the diode itself. These generators allow to generate NCW with output power up to 100 mW and controlled frequency bandwidth from 30 MHz up to 300 MHz. The NCW having much higher power could be obtained from the NCW generator developed on the basis of the weak-resonant backward wave oscillator (WRBWO) [5]-[7]. The WRBWO noise generators produce the tunable NCW with bandwidth from 50 MHz up to 1000 MHz with central frequency about 36 GHz and 60 GHz and output power up to 15 W and 3 W respectively. The IMPATT noise generator of special design generates NCW having bandwidth up to 2 GHz and integrated power about 40 mW.

2.3. Digital-Analog Correlator

For the correlation processing of the received quasi-stationary NCW radar returns the digital-analog real-time correlator was designed and constructed on the basis of fast digital components with clock frequency up to 500 MHz. To avoid the use of analog-to-digital converters the principle of two-level quantization of the reference signal has been used. The correlator designed and constructed [1]-[4], allows to process the NCW with bandwidth about of 250 MHz. The clock frequency used allows to provide the accuracy of time delay measurements about of 2 ns. Additional channel for measurements of Doppler shift of the carrier frequency caused by a target movement (or vibration) is available and allows to measure this shift in the range of 100 Hz to 200 KHz . This corresponds to the velocity range of 0.4 m/s to 750 m/s for the carrier frequency 40 GHz. Integration time could be varied from 5 μ s to 1500 μ s. To perform measurements for bi-static radar version, as well as to evaluate the NCW auto-correlation function the two additional channels for the NCW correlation processing have been also constructed. The controllable digital delay lines (CDDL) of two kinds were designed, namely: the CDDL on the basis of shift registers has been developed for short distances, while CDDL on the basis fast RAM memory has been used for long distances. Note that it is possible on the basis of the GaAs-technology to design digital delay lines in a single chip with required delay times and the clock frequency up to 4 GHz..

2.4. Test Experiments

In the case of the correlation processing of the NCW radar returns the target's distance is defined via the time delay measured as the coordinate of the cross-correlation function maximum. To perform the corresponding experiments the noise radar was constructed using the NCW generators and digital-analog real time correlator developed. The cross-correlation of the reference and received signals as a function of the CDDL delay time is observed on the oscilloscope screen. Observation time (oscilloscope swiping) could be varied from 0.32ms to 32 ms. The Doppler signal from the moving reflector was observed on a second oscilloscope screen and spectrum analyzer, simultaneously. Digital output for input into a computer is also provided in the correlator. Experiments carried out showed that the noise radar designed provides the distance resolution value of 100 cm with accuracy about 50 cm. The Doppler signal was observed from the moving target, having velocity within the range from 0.5 m/s to 50 m/s. The cross-correlation function of the signal, reflected by a moving car, people and dog was observed in the form of Gaussian-like curve moving across the oscilloscope screen in real time scale. Immunity against interference was tested by the feeding into the receiver antenna an external NCW having the same power spectrum bandwidth. Normal working regime of the noise radar took place when the voltage in the HF mixer-diode caused by the interference exceeded the useful signal voltage by 30 dB for the integration time about 0.5 ms.

3. Applications

The NCW with a wide and smooth enough power spectrum, having fast decay of correlation allows to perform simultaneously the signal compression with a high rate, its optimal reception, providing high SNR values, and minimization the ambiguity function side lobes. Besides, the NCW ambiguity function has no additional maximums, while for the periodical waveforms this is always the case. From that, particularly, follows that there is no contradiction for the NRT when providing the optimal conditions for simultaneous measurements of target distances and velocities; no theoretical limitations on the non-ambiguous working range; no needs in the high peak power in the transmitted signals for a given working range. Besides, that means the ability of the noise radar to perform coherent (preserving a phase) measurements even for negative (in dBs) SNR values provided a long enough integration time. Also, the correlation processing of the NCW in the time domain performed by the correlator developed provides always their optimal reception, maximizing the SNR values. To the most important of the expected advantages of the noise radar implementation we can relate the following:

- a. Simplicity and low cost of the forming scheme for the NCW, in this sense the NCW generator is equivalent to a single frequency CW oscillator.
- b. Correlation receiver and low power of the radiated NCW give possibility to use a low voltage and low energy consumption components;
- c. High electromagnetic compatibility characteristics of noise radars and their resistance against external electromagnetic interference, allowing simultaneous work of many similar devices at the same area.

- d. The use of the suggested NCW generators, digital-analog real time correlator, as well as MMW solid state electronic components allows to employ the IC technology for the development of a fully solid-state radar having high performances for a short and super-short range radars.

The advantages of the NRT and the results in the noise radar developments described above, in combination with those of the MMW technology (small sizes, light weights of antennas and other RF components, etc.) makes MMW Noise Radar Technology to be very promising technology for the development of the compact, low energy consumption and low cost radar systems for many different areas of civil applications. For example, they could be used for the development of the efficient MMW sensors for the following remote sensing systems:

- Car collision warning and intelligent traffic control systems, where high resolution, accuracy and fast processing, as well as small sizes and light weights are required.
- Navigation and surveillance systems with a high range resolution, as well as high reliability and environmentally save characteristic.
- Ground Based Interferometric Synthetic Aperture Radar.
- Noise radar-reflectometer for measurements of the cut-off layer position in fusion plasma reactors.
- Forward Looking Radar for the aircraft automated landing systems.

References

- 1.K.A.Lukin, "Noise Radar Technology For Civil Applications", Proceedings of the 1st EMSL User Workshop. 23-24 April 1996,JRC-Ispra,ITALY, Ed. By G.Nesti, Org. by Space Application Institute, Advanced Techniques Unit, ECSC-EC-EAEC Brussels, Luxembourg, 1997, pp.105-112.
- 2.K.A.Lukin, "Noise Radar with Correlation Receiver as the Basis of Car Collision Avoidance System", 25-th European Microwave Conference, Bologna; Conference Proceedings, UK, Nexus, 1995, pp.506-507, 1995.
- 3.K.A.Lukin, "K_a-band Noise Radar", Proceedings of the Int. Symposium "Physics and Engineering of Millimeter and Submillimeter Waves", June 7-10 1994, Kharkov, Ukraine; Vol.2, pp.322-324, 1994.
- 4.K.A.Lukin, Yu.A.Alexandrov, V.V.Kulik, et. al., "Wideband Millimeter Wave Noise Radar", Int. Conference on Modern Radars, 1994, Kiev, Ukraine, pp.30-31.
- 5.V.A.Rakityansky and K.A.Lukin, "Excitation of the Chaotic Oscillations in Millimeter BWO", Int. Journal of Infrared and Millimeter Waves, Vol.16, No.6, pp.1037-1050, June 1995.
- 6.K.A.Lukin and V.A.Rakityansky, "Excitation of Intensive Chaotic Oscillations of Millimeter Waveband", Proceedings of ISSSE, 1-4 Sept.1992, Paris, pp.454-457, Sept. 1992.
- 7.K.A.Lukin and V.A.Rakityansky, "Sources of Millimeter Noise Oscillations", Proceedings of the Int. Symposium "Physics and Engineering of Millimeter and Submillimeter Waves", June 7-10 1994, Kharkov, Ukraine; Vol.2, pp.322-324, 1994.
- 8.K.A.Lukin, V.V.Kulik and V.A.Rakityansky, "Autodyne Effect in BWO Operating in Chaotic Regime", Proceedings of the SPIE 2250, Ed. by M.Afsar, pp.207-208, 1994.
- 9.B.P.Efimov, K.A.Lukin and V.A.Rakityansky, "Transformation of Chaotic Oscillation Spectrum by Reflection", Journal of Technical Physics, Vol.58, No.12, pp.2398-2401, 1988 (In Russian).
- 10.B.P.Efimov, K.A.Lukin and V.A.Rakityansky, "Chaotic Interaction of Modes in the Electron-Wave Auto-Oscillator with Two Feedback Channels", Letters to Journal of Technical Physics; Vol.15, No.18, pp.9-12, 1989 (in Russian).

MILLIMETER AND SUBMILLIMETER WAVE SPECTROSCOPY OF INTERSTELLAR MEDIUM

I.I. Zinchenko

Institute of Applied Physics, Russian Academy of Sciences
46 Ulyanov str., Nizhny Novgorod, Russia

Tel.: +7-8312-367253, Fax: +7-8312-362061, E-mail: zin@appl.sci-nnov.ru

V.M. Shul'ga

Institute of Radio Astronomy, Ukrainian Academy of Sciences
4 Chervonopraporna str., Kharkiv, Ukraine

Tel.: +380-572-448591, Fax: +380-572-476506, E-mail: shulga@rian.kharkov.ua

1. Introduction

Millimeter and submillimeter wave astronomy is one of the most rapidly developing areas of astrophysical research. In recent years we see an enormous progress in the equipment: the noise level of receiving systems is approaching the fundamental quantum limit; the available frequency range is extending to higher and higher frequencies; the efficiency of mapping observations is greatly increased by introducing multibeam technique. Further important developments are foreseen in coming years: new large ground-based facilities will be constructed and there are ambitious space projects in this field.

What is the scientific motivation for these technical efforts? One of the most important is understanding the process of star formation which is a basic problem of modern astrophysics. The stars are born in so-called "molecular clouds" where most of hydrogen is present in molecular form. These clouds contain a number of various molecules which emit line radiation mostly at millimeter and submillimeter waves. In addition, some fine structure transitions of important interstellar atoms and ions fall in this range too. Observations of these lines provide an information on density, temperature, mass and other physical parameters of interstellar medium. The peak of cold dust emission lies at submillimeter waves. As a result millimeter and submillimeter wave observations turn out to be the most efficient tool for studying the regions of star formation.

Of course, there are other areas of astrophysics from cosmology to solar system studies where spectral millimeter and submillimeter wave observations provide very important and sometimes crucial information. They might be helpful in other fields too, e.g. for molecular spectroscopy. Some unstable molecules have been discovered first in space and some spectroscopic parameters can be most easily derived from such observations.

The radio astronomical groups from the Institute of Applied Physics RAS and Institute of Radio Astronomy NASU collaborate for several years in this area. Here we review the main results of these studies and describe the general situation in this field with the emphasis on the topics which seem to us the most important (though the selection might be subjective).

2. Facilities

Spectral line millimeter and submillimeter wave observations impose severe requirements for the facilities. First, the system noise temperature should be as low as possible. Normally, the aim is to reduce the noise below the background level. Most of millimeter and submillimeter wave observatories are located high in mountains to reduce the atmospheric opacity. At normal conditions the atmospheric emission constitutes several tens K. For astronomical instruments in space this level is determined only by cosmic background radiation which is close to 3 K microwave background at these wavelengths. However, this 3 K blackbody emission at millimeter and submillimeter waves is below the quantum limit on the noise temperature ($\sim h\nu/k$). Thus, we need receivers with the noise temperature close to this quantum limit. At present the basic type of receivers which fulfills this requirement is a heterodyne receiver with the superconductor-insulator-superconductor (SIS) mixer. At frequencies below ~ 700 GHz they are approaching the quantum limit on the noise temperature (Fig. 1). At $\lambda \sim 3$ mm masers provide equally good or even better noise level. However, at frequencies > 700 GHz the performance of niobium SIS mixers deteriorates fast since the photon energy exceeds the superconducting gap. The most promising way to improve the receiver performance at these higher frequencies is the usage of hot electron bolometer (HEB) mixers (Fig. 1). In principle their parameters do not depend on frequency since a thermal effect is used.

The required spectral resolution depends on the physical conditions in the sources and observing frequency. In order to investigate narrow features in cold clouds at ~ 3 mm wavelength the resolution of ~ 10 kHz might be needed. At the same time the total extent of the emission including the line wings and/or extragalactic sources can reach ~ 1 GHz. This shows the requirements to spectrum analyzers which are to be used for these

measurements. The easiest way to approach them is to use acousto-optical spectrometers (AOS) which provide several thousands channels within wide bandwidths. However, it is problematic to achieve resolutions better than ~ 100 kHz. Higher resolutions are frequently realized now by digital devices (autocorrelators). Traditional filter banks are still in use too.

Next, the substructure in molecular clouds exists at all scales down to at least ~ 0.1 pc which corresponds to few tens of arc seconds at the distance of ~ 1 kpc. Moreover, there are much smaller clumps, e.g. maser spots in the vicinity of young stellar objects. To investigate this substructure we need large antennas and even interferometers.

In most cases it is necessary to map the sources in order to understand their structure and to derive the physical parameters. The mapping efficiency can be greatly improved if we have a possibility to observe several positions simultaneously. This is the reason for introducing multibeam technique. Focal-plane receiver arrays have been developed in several laboratories. At present they comprise up to 16 elements with a common local oscillator.

There are several very efficient millimeter and submillimeter wave observatories in the world (e.g. IRAM 30m, CSO 10m, JCMT 15m, SEST 15m, NRAO 12m, FCRAO 15m, BIMA, IRAM Plateau de Bure interferometer, etc.). There are ambitious new projects including instruments in space (e.g. Large Millimeter Array, Large Millimeter Telescope, SWAS, Odin, Millimetron, etc.).

The best antenna within FSU appropriate for these researches is RT-22 CrAO. We used it regularly with our own receiving systems based on 3 mm maser and SIS mixer. The noise performance of these receivers is close to the best world results. The maser receiver [2] noise temperature was ~ 60 K (SSB) and the tuning range was 85-93 GHz. However, it consumes a large amount of liquid He which makes its exploitation rather costly. In the SIS receiver [3] the mixer developed at the Institute of Radio Engineering and Electronics (Moscow) with niobium junctions is used. The receiver noise temperature is ~ 80 K (DSB) and the tuning range as determined by the local oscillator (BWO) is about 80-115 GHz. The photo of the receiver and its block diagram are presented in Fig. 2.

As a backend we used for many years a filter bank of 120 channels with 100 kHz resolution developed at IAP. Recently an acousto-optical spectrometer (AOS) developed at the S.-Petersburg technical university was successfully attached to this system. It has a total bandwidth of about 70 MHz and ~ 150 kHz spectral resolution. An example of the spectra obtained with AOS in combination with the SIS receiver is presented in Fig. 3.

3. Studies of dense molecular gas in regions of star formation

Regions of star formation are divided traditionally into 2 categories: low and high mass star forming regions. It is not well known which factors determine the mass of a new star but it might be that the underlying physical mechanisms are significantly different for low and high mass star formation. Myers and co-workers (e.g. [4]) investigated a number of dense cores in nearby dark nebulae where low mass stars are born. As a result the basic parameters of these cores have been determined, some correlations between them revealed, etc. Studies of dense cores in regions of high mass star formation have been limited to a few of the most prominent objects like Orion Molecular Cloud. This approach does not enable to investigate the general properties of these cores.

For systematic studies of dense cores we need first a representative sample of these objects, i.e. we have to search for dense cores in regions of high mass star formation. There are several commonly used indicators of such areas: powerful IR sources, H II regions, water masers. We used all of them in our studies. In the beginning we surveyed about 100 Sharpless H II regions in the HCN and HCO⁺ lines with the RT-22 CrAO [5,6]. These lines are excited at enhanced densities and, therefore, trace dense cores within molecular clouds. We detected an emission in these lines in about a half of our targets.

The next survey was performed in the CS line towards H₂O masers both in the southern and northern hemispheres [7,8]. The observations have been performed with the 20-m Onsala radio telescope and 15-m SEST in Chile. The CS emission indicative of dense gas was detected towards practically all (90%) of the target masers. Most of the detected sources have been mapped in the CS line. In addition, the CS emission peaks have been observed in CO and optically thin C³⁴S lines. As a result the basic physical parameters of the cores (size, mass, mean density, velocity dispersion, kinetic temperature) have been derived. The statistical distributions of these parameters have been constructed. In particular, it was found that the *mean* density of the cores is rather low, 10^3 - 10^5 cm⁻³, which is 1-2 orders of magnitude lower than the density in regions of line formation derived from multi-transitional data. Most probably this is explained by strong small-scale density inhomogeneities in the cores. An analysis of these data shows that the mean density decreases with increasing galactocentric distance [8,9]. Therefore, the local properties of star forming regions are determined to a great extent by large scale processes in the Galaxy.

These surveys provide important statistical information on the dense core properties. However, understanding details of the star formation process is impossible without thorough investigations of individual objects. It means that we have to map selected cores in various molecular lines with adequate angular and spectral resolu-

tion. Different species are sensitive to different parameters. For example, CO lines give information at first about the kinetic temperature. Even better estimates of this temperature in the cloud interior can be obtained from ammonia. Abundances of some molecules (e.g. SiO) are very enhanced in shocks and in post-shock gas. Otherwise, N_2H^+ and some other species trace probably a quiescent gas. This explains why maps in many different molecular transitions are needed to understand the source structure.

Moreover, investigations of the physical conditions in the vicinity of young stellar objects require an angular resolution of a few arcsec. It can be achieved with interferometers which operate now at frequencies up to ~ 300 GHz. Another way to obtain a high angular resolution is to use higher frequencies and special deconvolution technique, e.g. Maximum Entropy Method (MEM) [10].

For our studies we selected a few both high mass and low mass star forming cores. A good example of the latter category is TMC-1. It has been investigated in many lines already. However, our HCN data obtained with the very low noise maser reveal new features, especially in so-called hyperfine intensity anomalies [11]. We observed very unusual ratios of the hfs components (Fig. 4).

One of the most interesting phenomena in regions of star formation is high velocity bipolar outflows detected mostly in CO lines in a large number of objects. Its significance for the process of star formation is in the fact that most probably it removes an extra angular moment from the system. We attempted to investigate bipolar objects in the lines of high density tracers like HCN and CS (Fig. 5).

4. Conclusions and perspectives

Millimeter and submillimeter wave astronomy is a powerful tool for investigations of star formation and other astrophysical phenomena. This is a rapidly developing field of research which imposes severe requirements to the facilities. The main directions of the technical developments include multibeam receivers, high frequency (up to ~ 1 THz) systems, interferometry. A large amount of important information on the physical and chemical processes in the vicinity of newly born stars and protostars is expected from these new techniques.

This work was supported by INTAS (grants 93-2168 and 93-2168-ext) and Russian Foundation for Basic Research (grants 96-02-16472 and 97-02-31011).

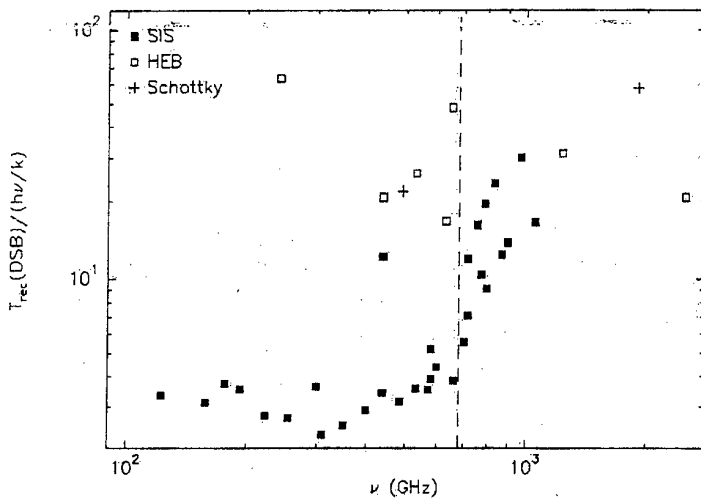


Fig. 1. Ratio of DSB receiver noise temperature to frequency for different types of receivers obtained by various groups as summarized in [1]. The vertical dashed line marks the frequency corresponding to the energy gap in Nb.

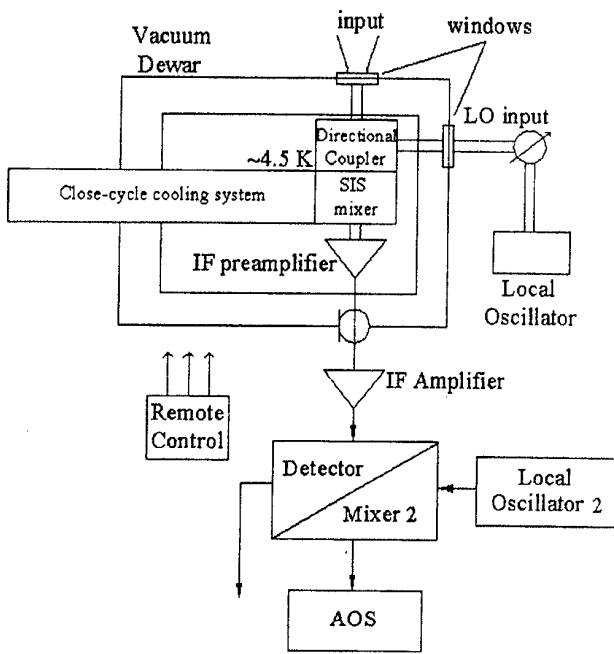
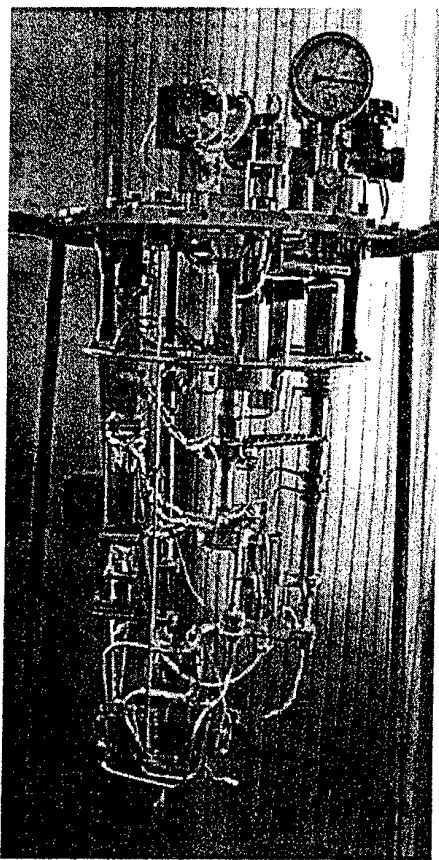


Fig. 2. The general view and the block-diagram of the 3 mm SIS receiver used for observations at RT-22 CrAO. The receiver is placed into a vacuum dewar.

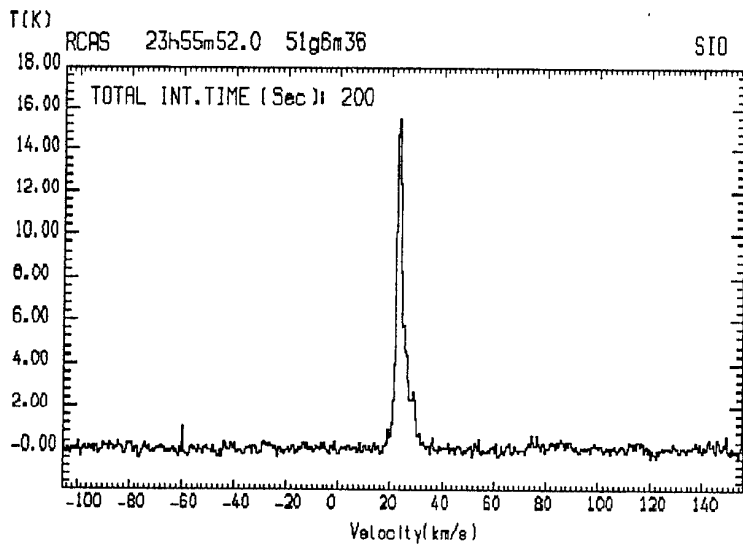


Fig. 3. An example of the spectra obtained at RT-22 with the SIS receiver and acousto-optical spectrum analyzer.

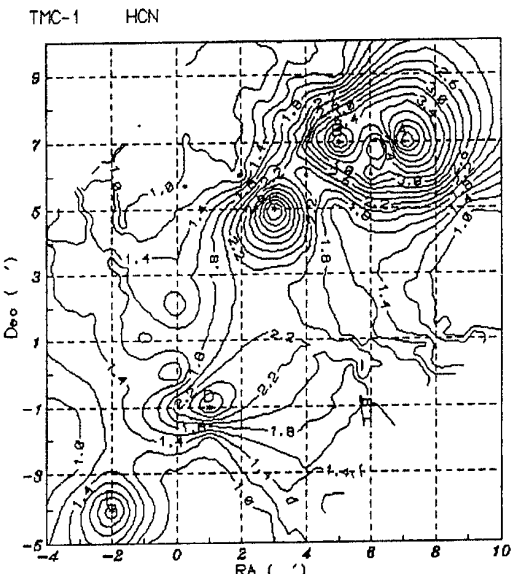


Fig. 4 A spatial distribution of the HCN molecular radiation toward TMC-1 dark molecular cloud.

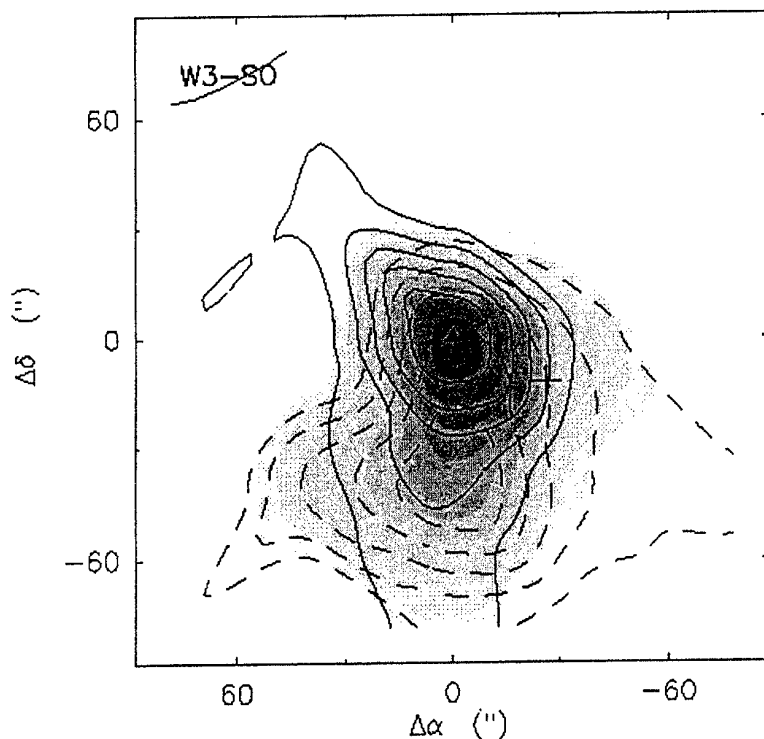


Fig. 5. An example of the source map with an apparently bipolar structure. The grey-scale image represents the total intensity map. The solid contours correspond to the blue part of the emission and the dashed contours correspond to the red part. The data are obtained in the SO line at 3 mm with Onsala 20-m antenna.

References

1. J. Zmuidzinas, «Recent progress in submillimeter heterodyne receiver development», Proc. 30th ESLAB Symp. «Submillimetre and Far-Infrared Space Instrumentation», The Netherlands, ESA SP-388, 1996, p.151
2. V.M. Shulga, I.I. Zinchenko, N.S. Nesterov, et al. "Molecular line observations in the 85-90 GHz band using maser receiver at the Crimean Astrophysical Observatory 22-m radio telescope", Pis'ma v Astron. Zh., 17, 1084-1089, 1991
3. I.I. Zinchenko, A.M. Baryshev, V.F. Vdovin, et al., "Spectroscopic radioastronomical observations with the RT-22 radio telescope of the Crimean Astrophysical Observatory equipped with a 3 mm SIS receiver", Pis'ma v Astron. Zh., 23, 145-148, 1997
4. P.C. Myers, "Molecular cloud cores", In: Protostars and Planets II, eds. D.C. Black, M.S. Matthews, Univ. Arizona Press, 1985
5. A.B. Burov, V.F. Vdovin, I.I. Zinchenko, et al., "A J=1-0 HCN line survey of molecular clouds associated with Sharpless H II regions: observational results", Pis'ma v Astron. Zh., 14, 492-502, 1988
6. I.I. Zinchenko, A.V. Lapinov, L.E. Pirogov, "Survey in the J=1-0 HCN line of molecular clouds associated with H II regions in Sharpless catalog. Analysis of spectral observations", Astron. Zh., 66, 1142-1153, 1989
7. I. Zinchenko, K. Mattila, M. Toriseva, "Studies of dense molecular cores in regions of massive star formation. II. CS J=2-1 survey of southern H₂O masers in the longitude range l = 260°-310°", Astron. Astrophys. Suppl., 111, 95-114, 1995
8. I. Zinchenko, L. Pirogov, M. Toriseva, «Studies of dense molecular cores in regions of massive star formation. VII. Core properties on the galactic scale», Astron. Astrophys. Suppl., in press
9. I. Zinchenko, «Studies of dense molecular cores in regions of massive star formation. V. Statistics of the core parameters», Astron. Astrophys., 303, 554-560, 1995
10. A.V. Lapinov, P. Schilke, M. Juvela, I. Zinchenko, «Studies of dense molecular cores in regions of massive star formation. VI. Multitransitional CS and CO observations of G 261.64-2.09, G 268.42-0.85, G270.26+0.83 and G 301.12-0.20», Astron. Astrophys., in press
11. V.M. Shulga, V.V. Myshenko, E.A. Nazarov, et al., "Molecular cloud TMC-1 in HCN (J=1-0) molecular line", Radiofizika i Radioastronomia, 1, 54-60, 1966

LOW-NOISE MILLIMETER AND SUBMILLIMETER WAVE RECEIVERS

B.A.Rozanov¹, S.B.Rozanov²

¹ N.E.Bauman Moscow State Technical University

5, 2nd Baumanskaya street, Moscow, 105007 RUSSIA

Tel.: (007)(095) 263-65-98, Fax.: (007)(095) 267-75-96, E-mail: rozanov@rl-1.bmstu.ru

² P.N.Lebedev Physical Institute of the Russian Academy of Sciences

53, Leninsky prospect, Moscow V-333, 117924 RUSSIA

Tel.: (007)(095) 132-64-62, Fax: (007)(095) 135-24-08, E-mail: solomon@sci.lpi.msk.su

Advances in design and performance of millimeter (MM) and subMM wave receivers result in appearance of new applications of the devices in various branches of science and technique. MM and subMM receivers are used now in communications, radar's, radio astronomy, remote sensing, medicine, ecology, plasma physics, military technique, navigation, etc. [1-5]. In most MM-wave applications, when frequency increasing, problems connected with radiometric measurements of noise emissions become the main ones in comparison with detection of coherent signals, and extremely high sensitivity of receivers is necessary typically for the MM-wave radiometry.

General trends of evolution of MM and subMM wave receivers are increasing their operation frequencies, improving sensitivity within the operation bands developed, and design of devices suitable for serial manufacturing taking into account various operation conditions. Especially high sensitivity of the receivers is required in radio astronomy. Impressive progress of MM and subMM wave receivers (their noise decreased by 1-2 orders for the last two decades) was caused in large part by tasks of radio astronomy.

At present heterodyne receivers with an input mixer are widely used at short MM and subMM waves, and HEMT amplifier following with a mixer became the typical receiver at long MM waves. State of art of heterodyne receivers employing main usable types of input mixers together with data on various MM-wave amplifiers are presented in Fig. 1. The figure includes data on receivers based on (1) superconductor-insulator-superconductor (SIS) junction mixers [6-14], (2) Schottky barrier diode (SBD) mixers employing (i) honey comb diode structures at room temperature [15-20] and under cooling [15-17, 20-23] and (ii) planar Schottky diodes at ambient [24-28] and cryogenic temperatures [24, 25, 29-31] as well, (3) Josephson mixers with external local oscillator (LO) pump [32, 33], and (4) semiconducting [34-36] and superconducting [37-42] bolometric mixers. Single sideband (SSB) noise temperatures of the heterodyne receivers T_{RSSB} are given in Fig. 1 versus frequency. Data on amplifier noise temperatures T_{amp} are presented in Fig. 1 for (5) masers [43-45], (6) high electron mobility transistor (HEMT) amplifiers operating at room temperature [46-52] and under cooling [46, 53-55], and (7) parametric amplifiers, both room temperature [56-59] and cryogenic ones [57, 58] as well.

When studying data of Fig. 1 it is necessary to take into account some important features. Firstly, in many cases in Fig. 1 twice values of double sideband (DSB) noise temperature were used for the heterodyne receivers instead of true SSB values. This could result in underestimating of the true SSB values up to 1.5-2 times because contribution of image termination noise was not included in the cases. Secondly, for almost all amplifiers the noise temperature given represent only their own noise without contributions of input units and following stages of the receivers. Additionally, noise temperature of heterodyne receivers built before middle 80s could be much more better today provided modern ultra-low-noise intermediate frequency (IF) amplifiers were used with the same mixers (especially it concerns Josephson mixer receivers).

Main results, advances and trends of development the MM and subMM wave receivers for the last decade commenting data of Fig. 1 may be summarized as follows:

1) Progress in MM-wave mixers and amplifiers resulted in pushing detector receivers out of many practical applications in the range. For today detector receivers are rarely used at frequencies lower 100 GHz. At higher frequencies they are helpful mainly for those applications when very broadband signals should be detected with low noise level and for various measurements where extremely high sensitivity is not so important. For applications where high relative frequency resolution $f/\delta f$ is necessary heterodyne receivers provide better sensitivity. Boundary dividing regions of "low" and "high" relative frequency resolution and determining choice of detector or heterodyne receivers goes now approximately from $f/\delta f$ values of $10^1\text{-}10^2$ at 100 GHz to $10^4\text{-}10^5$ at 3 THz [3];

2) HEMT amplifiers (especially those based on InP) having gate length about 0.1 μm reached frequencies up to 140 GHz without cooling and to 100 GHz under cooling. The amplifiers are planned for frequencies up to 220 GHz [48]. At long MM waves receivers based on the HEMT amplifiers have now lower noise temperature than traditional Schottky diode heterodyne receivers. Monolithic MMIC technology allows to make extremely compact HEMT modules for various applications;

3) Technically complex long-MM-wave masers operating with considerable running costs, are being replaced by more practical and less expensive receivers using cooled HEMT amplifiers or SIS mixers having noise temperature approximately as the masers. Additionally, HEMT and SIS receivers typically have broader instantaneous input bandwidth in comparison with the masers;

4) Receivers employing quasiparticle SIS tunnel junction mixers based on Nb technology with barrier of AlO_x (both single junctions and various arrays) reached frequencies close to 1 THz. They have demonstrated excellent performance at frequencies of 50-700 GHz. Really, at 100-300 GHz their DSB noise temperature of 17-23 K is only 2-4 times of fundamental quantum limit hf/kT ; and the factor grows smoothly to approximately 10 when frequency increases to 700 GHz. At many MM and subMM wave radio telescopes, especially ones placed in mountains at altitudes of 2-4 km, the SIS receivers are used now instead of previous cooled SBD receivers. It occurred that Josephson mixers actively studied in 70s-80s couldn't compete with the SIS receivers because of increased intrinsic noise level of Josephson junctions. It is believed that using of SIS junctions based on NbN technology with increased value of energy gap in comparison with Nb will allow to increase operation frequencies of SIS mixers up to 1.2-1.3 THz;

5) Traditional receivers with GaAs-based honey comb Schottky diode mixers moves to 3-5 THz operation frequencies due to progress in diode manufacturing and design of quasi-optical mixers. At MM waves performance of SBD receivers employing honey comb diodes practically weren't improved since middle 80s. In early 90s planar diode mixers covered all MM range where they have now performances close to ones of the best honey comb diode mixers. Both waveguide and quasi-optical planar SBD mixers are being designed for frequencies up to approximately 1 THz. Despite of impressive advances in development of superconducting receivers, the Schottky diode receivers remain the most widely used devices in practical short-MM-wave applications because only they provide good sensitivity at frequencies above 100 GHz without cooling the receivers;

6) Superconducting bolometric hot electron mixers are intensively studied in 90s. It is expected now that the mixers will be the most sensitive receiving elements at frequencies above 1 THz. Using the NbN thin (1-100 nm) and short (0.1-10 μm) films allowed to increase intermediate frequencies of the mixers up to 1-10 GHz [40]. Traditional limitation of the IF value by 1-10 MHz for InSb-based MM and subMM wave bolometric mixers was overcame by using semiconducting GaAs-based heterostructures with two-dimensional electron gas. It was demonstrated that the IF may be increased up to 1-2 GHz for the MM-wave mixers [60];

7) Persistent and continuous efforts are directed to development of integrated and matrix (array) MM and subMM wave receivers which can radically decrease observation time when mapping objects or space surveying. Every element of matrix receivers may include antenna, mixer or amplifier, and auxiliary matching circuits and filters (see for example [61-64]). Integration of IF amplifiers for heterodyne array receivers is possible as well. Planar integrated circuits may be used together with both horn-waveguide and quasi-optical planar or lens antennas.

Gunn diode oscillators using varactor frequency multipliers are developed up to 800 GHz [65]. They became the main type of LOs for heterodyne receivers employing SIS junction mixers and SBD mixers at frequencies up to 600 GHz. MM and subMM oscillators and frequency multipliers using diode arrays and quasi-optical elements are actively studied as well. At frequencies close to 1 THz and higher optically pumped subMM lasers are used usually as LOs [66]. Else one prospective type of oscillator for frequencies higher than 100 GHz is flux-flow oscillator (FFO) based on long Josephson junction. The FFOs were successfully used in SIS receivers at frequencies up to 500 GHz [61]. They may be integrated to monolithic SIS receivers.

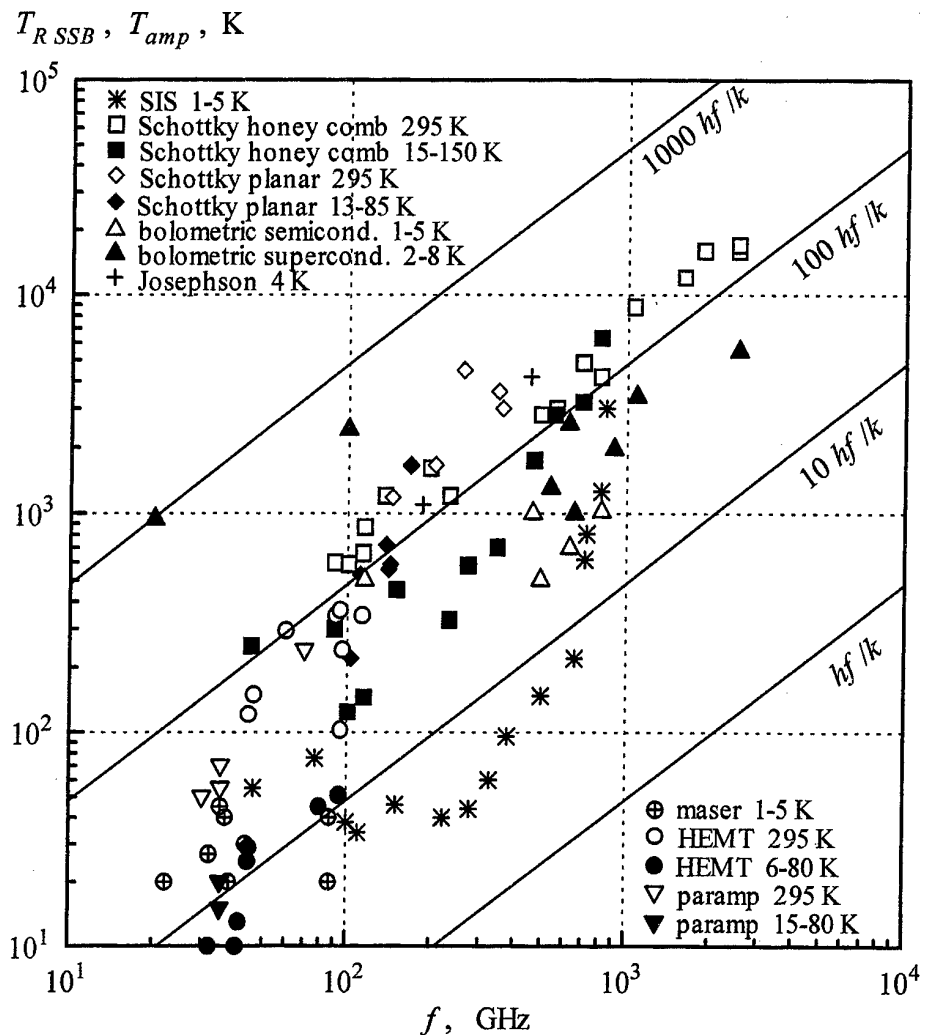


Figure 1. State of art of MM and sub MM wave receivers

References

1. B.A.Rozanov, S.B.Rozanov, "Millimeter-wave receivers", Rus. Radio i svyaz, Moscow, 1989 (in Russian).
2. I.I.Sobel'man, S.V.Solomonov, R.L.Sorochenko, "Millimeter wavelengths: new possibilities for ozonosphere monitoring", Herald Rus. Acad. Sci., Vol.63, No.8, pp.597-604, 1993.
3. P.J.Encrenaz, G.Beaudin, G.Pilbratt, "Submillimetre wave technologies for the future Earth and space applications", Proc. 24th Europ. Microwave Conf., Cannes, Sept. 5-8, 1994, Vol.1, pp.1-7.
4. B.A.Rozanov, S.B.Rozanov, "Millimeter and submillimeter wave receivers for radio astronomy and remote sensing", Proc. XXI URSI/IEEE/IRC Convent on Radio Sci., Otaniemi, Oct. 2-3, 1996, pp.219-220.
5. A.V.Ipatov, B.A.Rozanov, "Radiometers - from decimeter to millimeter waves", Proc. XXVII Rus. Radio Astron. Conf., S.-Petersburg, Nov. 10-14, 1997, Vol.1, pp.14-19 (in Russian).
6. D.W.Face, D.E.Prober, W.R.McGrath, P.L.Richards, "High quality tantalum superconducting tunnel junctions for microwave mixing in the quantum limit", Appl. Phys. Lett., Vol.48, No.16, pp.1098-1100, 1986.
7. S.-K.Pan, M.J.Feldman, A.R.Kerr, "Low-noise 115-GHz receiver using superconducting tunnel junctions", Appl. Phys. Lett., Vol.43, No.8, pp.786-788, 1983.

8. G.Pance, M.J.Wengler, "Broadband quasi-optical SIS mixers with large area junctions", IEEE Trans. Microwave Theory Techn., Vol.42, No.4, pp.750-752, 1994.
9. J.M.Payne, J.W.Lamb, J.G.Cochran, N.Bailey, "A new generation of SIS receivers for millimeter-wave radio astronomy", Proc. IEEE, Vol.82, No.5, pp.811-823, 1994.
10. H.Ogawa, "A 100-115 GHz SIS receiver for radio astronomy", Dig. 16th Int. Conf. on IR and MM Waves, Lausanne, Aug. 26-30, 1991, SPIE Vol.1576, pp.133-134.
11. A.R.Kerr, S.-K.Pan, A.W.Lichtenberger, F.L.Lloyd, N.Horner, "A new SIS mixer for 2-mm band", Proc. 4th Int. Symp. on Space THz Technol., Los Angeles, 1993, pp.1-10.
12. A.Karpov, J.Blondell, K.H.Gundlach, D.Billion-Pierron, "Low noise SIS mixer for 230 GHz receivers of Plateau de Bure interferometer" Int. J. IR and MM Waves, Vol.18, No.2, pp.301-317, 1997.
13. J.W.Kooi, M.Chan, B.Bumble, H.G.LeDuc, P.Schaffer, T.G.Phillips, "230 and 492 GHz low noise SIS waveguide receivers employing tuned Nb/A_xO_y/Nb tunnel junctions", Int. J. IR and MM Waves, Vol.16, No.12, pp.2049-2068, 1995.
14. A.Karpov, J.Blondell, M.Voss, K.H.Gundlach, B.Lazareff, "Four photons sensitivity heterodyne detection of submillimeter radiation with superconducting tunnel diodes" Proc. IR and MM Waves Conf., 1994.
15. A.M.Korolev, S.A.Peskovatsky, V.I.Pod'yachy, "Low-noise cooled 3-mm band receiver", Abstr. XXI Sov. Conf. "Radio Astron. Techn.", Yerevan, Oct. 19-21, 1989, pp.125-126 (in Russian).
16. C.R.Predmore, A.V.Raisanen, N.R.Erickson, P.F.Golgsmith, J.L.R.Marrero, "A broad-band, ultra-low-noise Schottky diode mixer receiver from 80 to 115 GHz" IEEE Trans. Microwave Theory Techn., Vol.32, No.5, pp.498-507, 1984.
17. J.W.Archer, M.T.Faber, "A very low noise receiver for 80-120 GHz", Int. J. IR and MM Waves, Vol.5, No.8, pp.1069-1081, 1984.
18. H.-I.Cong, A.R.Kerr, R.J.Mattauch, "The low-noise 115-GHz receiver on the Columbia-Giss 4-ft radio telescope", IEEE Trans. Microwave Theory Techn., Vol.27, No.3, pp.245-248, 1979.
19. I.I.Eru, "Low-noise quasioptical 2.0-mm and 1.5-mm Schottky mixer receivers", Int. J. IR and MM Waves, Vol.15, No.7, pp.1315-1323, 1994.
20. N.R.Erickson, "A very low-noise single sideband receiver for 200-260 GHz", IEEE Trans. Microwave Theory Techn., Vol.33, No.11, pp.1179-1188, 1985.
21. N.J.Keen, K.-D.Mischerikow, G.A.Ediss, "Three facility low-noise receivers for millimeter and submillimeter radioastronomy", Proc. 16th Europ. Microwave Conf., Dublin, 1996.
22. J.W.Archer, "Low-noise heterodyne receivers for near-millimeter-wave radio astronomy" Proc. IEEE, Vol.73, No.1, pp.109-130, 1985.
23. J.Hernichet et al., "Submillimeter receiver development at the University of Cologne", Proc. 2nd Int. Symp. Space THz Technol., Jet Propulsion Lab., California, Feb. 1991, pp.641-647.
24. S.B.Rozanov, A.N.Lukin, S.V.Solomonov, "Low-noise cooled planar Schottky diode receiver for ground-based ozone measurements at 142 GHz" Int. J. Infrared and Millimeter Waves, Vol.19, No.2, 1998.
25. V.G.Bozhkov, V.F.Vdovin, V.N.Voronov, V.A.Genneberg, Yu.A.Dryagin, I.V.Kuznetsov, L.M.Koukin, K.I.Kourkan, L.I.Fedoseev, "Investigation of monolithic balanced short millimeter wave mixer", Rus. Radiotekhn. i Elektron., Vol.37, No.4, pp.736-743, 1992 (in Russian).
26. V.G.Bozhkov, V.A.Genneberg, V.N.Romanovskaya, L.I.Fedoseev, A.D.Friger, A.A.Shvetsov, "Investigation of monolithic balanced 1.5-mm band mixer", Rus. Radiotekhn. i Elektron., Vol.41, No.7, pp.876-881, 1996 (in Russian).
27. S.S.Gearhart and G.M.Rebeiz, "A monolithic 250 GHz Schottky-diode receiver", IEEE Trans. Microwave Theory Techn., Vol.42, No.12, pp.2504-2511, 1994.
28. T.Newman, W.L.Bishop, K.T.Ng, S.Weinreb, "A novel planar diode mixer for submillimeter-wave applications", IEEE Trans. Microwave Theory Techn., Vol.39, No.12, pp.1964-1971, 1991.
29. Y.Dryagin, I.Lapkin, V.Vdovin, I.Zinchenko, K.Kuittinen, E.Oinaskallio, J.Peltonen, "Low-noise beam-lead diode mixer for the 3 mm radio astronomical receiver at the Metsähovi Radio Research Station", Experim. Astron., Vol.5. - P.279-287, 1994.
30. O.P.Koistinen, H.T.Valmu, A.Räisänen, V.F.Vdovin, Yu.A.Dryagin, I.V.Lapkin, "A 110 GHz ozone radiometer with a cryogenic planar Schottky mixer", IEEE Trans. Microwave Theory Techn., Vol.41, No.12, pp.2232-2236, 1993.
31. M.Boheim, L.-P.Schmidt, J.Ritter, V.Brancovic, R.Beyer, F.Arndt, U.Klein, K.Künzi, G.Schwaab, T.W.Crowe, "A new 140 GHz planar diode finline mixer for radiometer applications", Proc. 24th Europ. Microwave Conf., Cannes, Sept. 5-8, 1994, Vol.1, pp.664-669.
32. T.Poorter, "Josephson heterodyne detection at high thermal background levels", J. Appl. Phys., Vol.53, No.1, pp.51-58, 1982.

33. T.G.Blaney, "Josephson mixers at submillimeter wavelengths: Present experimental status and future developments", in "Future Trends in Superconductive Electronics", B.S.Deaver, Jr. et al., Eds. New York, AIP Conf. Proc., 1978, Vol.44, pp.230-238.
34. T.G.Phillips, K.B.Jefferts, "A low temperature bolometer heterodyne receiver for millimeter wave astronomy", Rev. Sci. Instrum., Vol.44, No.8, pp.1009-1014, 1973.
35. R.Padman, G.J.White, R.Barker, D.Bly, N.Johnson, H.Gibson, M.Griffin, J.A.Murphy, R.Prestage, J.Rogers, A.Scivetti, "A dual-polarization InSb receiver for 461/492 GHz", Int. J. IR and MM Waves, Vol.13, No.10, pp.1487-1513, 1992.
36. E.R.Braun, J.Keene, T.G.Phillips, "A heterodyne receiver for the submillimeter wavelength region based on cyclotron resonance in InSb at low temperature", Int. J. IR and MM Waves", Vol.6, pp.1121-1138, 1985.
37. H.Ekström, B.S.Karasik, E.L.Kollberg, K.S.Yngvesson, "Conversion gain and noise of niobium superconducting hot-electron-mixers", IEEE Trans. Microwave Theory Techn., Vol.43, No.4, pp.938-947, 1995.
38. G.N.Gol'tsman, "Terahertz technology in Russia", Proc. 24th Europ. Microwave Conf., Cannes, Sept. 5-8, 1994. Vol.1, pp.113-121.
39. A.Scalare, W.R.McGrath, B.Bumble, H.G.LeDuc, P.J.Burke, A.A.Verheijen, R.J.Schoelkopf, D.E.Prober, "Large bandwidth and low noise in a diffusion-cooled hot-electron bolometer mixer", Appl. Phys. Lett., Vol.68, No.11, pp.1558-1560, 1996.
40. H.Ekström, E.Kollberg, P.Yagoubov, G.Gol'tsman, E.Gershenson, S.Yngvesson, "Gain and noise bandwidth of NbN hot-electron bolometric mixer", Appl. Phys. Lett., Vol.70, No.24, P.3296-3298, 1997.
41. P.A.Yagoubov, "Quasioptical terahertz mixers based on electron heating in thin NbN films", Ph.D.Th., Mosc. State Pedagog. Univ., 1997 (in Russian).
42. B.S.Karasik, M.C.Gaidis, W.R.McGrath, B.Bumble, H.G.LeDuc, "Low noise in a diffusion-cooled hot-electron mixer at 2.5 THz", Appl. Phys. Lett., Vol.71, No.11, pp.1567-1569, 1997.
43. N.T.Cherpak, "Quantum millimeter-wave amplifiers", Rus. Izv. Vuzov. Radiophyz., Vol.27, No.7, pp.815-851, 1984 (in Russian).
44. L.G.Abakoumov, L.E.Abramyan, A.Sh.Aroutunyan, E.D.Baranov, K.G.Erzinkanyan, A.V.Ipatov, R.M.Martirosyan, N.G.Pogosyan, "Broadband quantum amplifier using closed cycle refrigerator", Abstr. XXI Sov. Conf. "Radio Astron. Techn.", Yerevan, Oct. 19-21, 1989, pp.169-170 (in Russian).
45. L.B.Knyazkov, A.M.Korolev, V.V.Myshenko, S.A.Peskovatsky, V.I.Pod'yachy, V.M.Shoulga, "Quantum amplifier of 3-mm band radiometer", Abstr. XXI Sov. Conf. "Radio Astron. Techn.", Yerevan, Oct. 19-21, 1989, pp.130-131 (in Russian).
46. T.Gaier, M.Seiffert, P.Meinholt, P.Lubin, M.Sholley, R.Lai, H.Wang, B.Allen, B.Osgood, T.Block, P.H.Liu, C.Jackson, C.R.Lawrence, "Noise performance of a cryogenically cooled 94 GHz InP MMIC amplifier and radiometer", IEEE Trans. Microwave Theory Techn., Vol.45, 1997.
47. G.I.Ng, R.Lai, Y.Hwang, H.Wang, D.C.W.Lo, T.Block, K.L.Tan, D.C.Streitt, R.M.Dia, P.H.Liu, P.D.Chow, J.Berenz, "A fully passivated ultra low noise W-band monolithic InGaAs/InAlAs/InP HEMT amplifier", Dig. IEEE Microwave and MM-wave Monolithic Circuits Symp., Orlando, Florida, May 1995, pp.63-66.
48. J.Berenz, InP MMICs: Coming of age", Microwave J., No.8 pp. 113-114, 1993.
49. Y.Itoh, K.Nakahara, T.Sakura, N.Yoshida, T.Katoh, T.Takagi, Y.Ito, "W-band monolithic low noise amplifiers for advanced Microwave Scanning radiometer", IEEE Microwave and Guided Wave Lett., Vol.5, No.2, pp. 59-61, 1995.
50. K.W.Chang, H.Wang et al., "A W-band image-rejection downconverter", IEEE Trans. Microwave Theory Techn., Vol.40, No.12, pp.2332-2338, 1992.
51. H.Wang, R.Lai, D.C.W.Lo, D.C.Streit, P.H.Liu, R.M.Dia, M.W.Pospieszalski, J.Berenz, "A 140-GHz monolithic low noise amplifier", IEEE Microwave and Guided Wave Lett. Vol.5, No.5, pp. 150-152, 1995.
52. H.Wang, T.N.Ton, R.Lai, D.C.W.Lo, S.Chen, D.Streit, G.S.Dow, K.L.Tan, J.Berenz, "Low noise and high gain 94 GHz monolithic InP-based HEMT amplifiers", Dig. IEEE Int. Electron Device Techn. Meeting, Washington D.C., Dec. 1993, pp.239-242.
53. M.W.Pospieszalski et al., "Millimeter-wave cryogenically-coolable amplifiers using AlInAs/GaInAs/InP HEMT's", Dig. IEEE MTT-S Int. Microwave Symp., Atalanta, GA, June 1993, Vol.2, pp.515-518.
54. H.Wang, D.C.-W.Lo, R.Lai, C.-C.Yang, J.Berenz, "Cryogenically cooled performance of a monolithic 44-GHz InP-based HEMT low-noise amplifier", IEEE Microwave and Guided Wave Lett., Vol.5, No.9, pp. 281-283, 1995.
55. S.Weinreb, Workshop on Low Noise MM Wave Amplifiers, Santa Barbara, California, Feb. 1995.
56. V.B.Khaikin, A.V.Yaremenko, "Dual-channel phase-stable amplifier based on low-noise parametric amplifier", Abstr. XXI Sov. Conf. "Radio Astron. Techn.", Yerevan, Oct. 19-21, 1989, p.117 (in Russian).

57. R.E.Borovsky, V.V.Kogorod, I.A.Strukov, "Cooled millimeter-wave parametric amplifier", Abstr. XVII Sov. Conf. "Radio Astron. Techn.", Yerevan, Oct. 10-12, 1985, pp.122-123 (in Russian).
58. R.E.Borovsky, V.V.Kogorod, I.A.Strukov, "Low-noise cooled 8-mm parametric module with high-stable gain", Abstr. XXI Sov. Conf. "Radio Astron. Techn.", Yerevan, Oct. 19-21, 1989, p.160 (in Russian).
59. F.A.Grigoryan, A.S.Berlin, "Parametric 70 GHz amplifier for radio astronomy", Rus. Radiotekhn. i Elektron., Vol.18, No.2 pp.426-428, 1973 (in Russian).
60. J.-X.Yang, F.Agahi, D.Dai, C.F.Musante, W.Grammer, K.M.Lau, K.S.Yngvesson, "Wide-bandwidth electron bolometric mixers: A 2DEG prototype and potential for low-noise THz receivers", IEEE Trans. Microwave Theory Techn., Vol.41, No.4, pp.581-589, 1993.
61. V.P.Koshelets, S.V.Shitov, L.V.Filippenko, A.M.Baryshev, A.V.Shchukin, G.V.Prokopenko, P.G.Litskevitch, Th. de Graaw, W.Luinge, H. van de Stadt, H.Golstein, H.Schaeffer, T.M.Klapwijk, J.R.Gao, P.Leikonen, J.Mygind, "Integrated submillimetre heterodyne receiver", Proc. 30th ESLAB Symp. "SubMM and Far-IR Space Instrumentation", ESTEC, Noordwijk, Sept. 24-26, 1996.
62. N.R.Erickson, P.F.Goldsmit, G.Novak, R.M.Grosslein, P.J.Viscuso, R.B.Erickson, C.R.Predmore, "A 15 element focal plane array for 100 GHz", IEEE Trans. Microwave Theory Techn., Vol.40, No.1, pp.1-11, 1992.
63. Yu.M.Zabytov, Yu.V.Lebsky, L.I.Fedoseev, E.N.Fel'dman, A.G.Gel'fer, "Multi-beam heterodyne millimeter-wave receiver", Rus. Radiotekhn. i Elektron., Vol.38, No.12, pp.2240-2248, 1993 (in Russian).
64. P.A.Smitson, R.J.Dengler, H.G.LeDuc, S.R.Cypher, P.H.Siegel, "A planar quasi-optical SIS receiver", IEEE Trans. Microwave Theory Techn., Vol.41, No.4, pp.609-615, 1993.
65. A.Rydberg, B.N.Lyons, S.U.Lindholm, "On the development of a high efficiency 750 GHz frequency tripler for THz heterodyne systems", IEEE Trans. Microwave Theory Techn., Vol.40, No.5, pp.827-830, 1992.
66. G.Clin, "Optically pumped submillimeter laser heterodyne receivers: Astrophysical observations and recent technical development", Proc. IEEE, Vol.80, No.11, pp.1788-1799, 1992.

INTEGRATED SOFTWARE PACKAGE FOR SYNTHESIS, ANALYSIS AND OPTIMIZATION OF FREQUENCY-SELECTIVE DEVICES OF MILLIMETER AND CENTIMETER WAVES

A.A. Kirilenko, L.A. Rud, V.I. Tkachenko, L.P. Mos'pan, and D.Yu. Kulik

Institute of Radiophysiks and Electronics of National Academy of Sciences of Ukraine
12 Ac. Proscura St., Kharkov, 310085, Ukraine

Tel. 38(0572)448518, Fax 38(0572)441105, e-mail:<kirilenko@ire.kharkov.ua>

The state of the art of theory and practice of signal frequency selection in the millimeter and centimeter wave ranges can be described from one hand as going to more sophisticated schemes of filter building and from another hand, especially in millimeter waves, by extensive usage of practically non-tuning configurations. The first direction as well as the second one is based on the powerful software and on modern production processes, that provide minimal tolerances. Below is a summary of the results that have been obtained in IRE NASU regarding to one of this two sides if filter problems: the short description of the set of software packages for the synthesis and analysis of low-pass (LPF), wide-band and narrow-band band-pass (BPF), and band-stop (BSF) rejection waveguide filters.

These packages have been performed as unitary system, that consists of six main subsystems:

- 1). SES-library (the first version of such a system of electromagnetic modeling has been described in [1]) for exact modeling of complicated components in rectangular, circular, ridged and partially filled waveguides, based on S-matrix technique and wide set of algorithms for the calculation of key-building elements. Among them there are such twoports as steps in rectangular, circular and ridged waveguides, junctions of above mentioned waveguides; such threeports as bifurcations and tees in rectangular waveguide; such multiport as multifurcations, and plane junction of three and more different waveguides and crosses in rectangular waveguides.
- 2). The programs for the synthesis of filter and multiplexer prototypes, basing on circuit theory and the algorithms by Cohn, Rhodes, Levy, Wanselow, Williams, and other.
- 3). The set of program modules for the searching of the geometry of objects that are physical equivalents of prototype elements. Among them there are the procedures for searching of K-invertors physical equivalents on one free parameter, the procedure for searching the dimensions of a resonator with the given qualities and central frequencies on two free parameters; the program for determination of diaphragm aperture sizes, that provides the given coupling between two cavities or between two orthogonal modes within the same cavity, and so on.
- 4). The set of tuning or optimizing procedures, beginning with different iterative procedures for tuning of filter central frequencies and passbands and ending with gradient procedures of sophisticated "pulling" one frequency response to another one or with conventional procedures of frequency response optimization.
- 5). The program modules for on-line response processing with the aim of determination of generalized characteristic data about frequency response and the data that are some derivatives of response, for example, standing wave ratio, the variation of the group delay within given frequency band, and so on.
- 6) "Internal" and "external" Windows interface software that is intended for the debugging and tuning different actual problem-oriented packages as well as for the users of CAD packages with fixed topology of the device. With the aim of problem-oriented language and "internal" interface the various versions of frequency-selective device building may be verified and investigated. The best configuration is accepted as the physical base for the final version of CAD software and equipped with user's interface.

Such a tool for software creation and investigation of different new filter and diplexer configurations made it possible to find some new solutions or new configurations even in this, relatively well-developed field of microwave technique. Do not claim for the completeness of state of the art describing, we will give an account of the peculiarities of the design, physical backgrounds or frequency responses for filters and diplexers, that were considered in IRE NASU.

Band pass filters on all-metal inserts

The main configurations of millimeter waves BPFs are basing on planar (or fin-line) technologies. The most known studied BPF is the filter with all-metal E-plane inserts (Fig. 1a). Peculiarities of design of such BPF are described in [1]. Owing to the possibility to use the calculation of the waveguide bifurcation S-matrix only and slow dispersion of its elements, it makes possible to use exact interpolation for the coefficients of mul-

timode matrix. The process of design, tuning and optimization such a filter takes 20-30 sec. on Pentium 200. At possible bandwidth up to 20% such a configuration has essential drawback caused by proximity of higher parasitic pass bands. If passband of such a BPF lies in low part of waveguide operation band then the parasitic pass band may appear in the upper part of operating band. The worse performances are characteristic for the filters, based on unilateral fin-lines, however they may be more exactly fabricable (Fig. 1b).

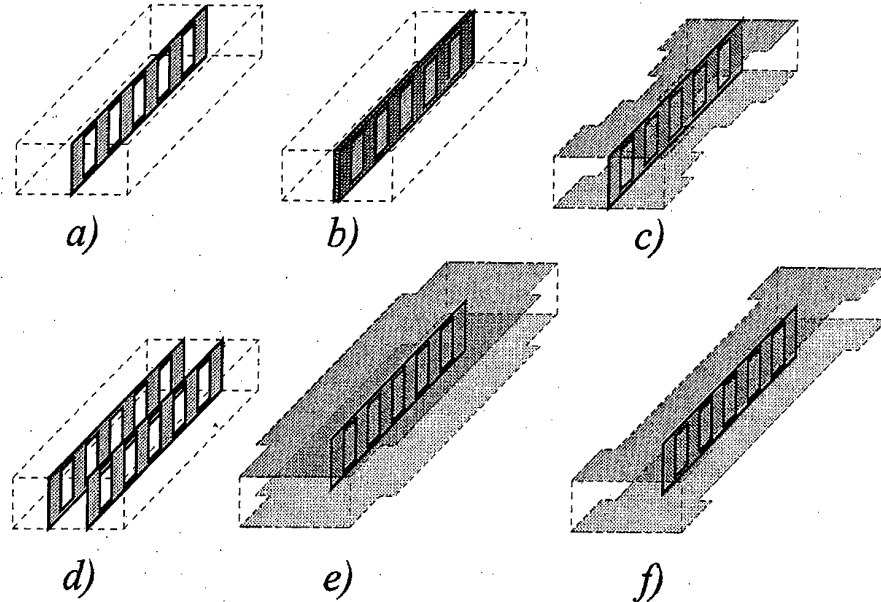


Figure 1. Configurations all-metal band-pass filters

Some improvement of situation may be achieved by stepped construction of filter housing [9], when different sections of the filter have distinguishing wide walls (see Fig. 1c) and, correspondingly, the different frequencies of second resonances due to differing dispersions (see, more detailed report in this Proceedings). There is also the possibility to design some complicated constructions based on double metal inserts (Fig. 1d, increasing a suppression in upper part of stop band) [2], on decreased cross-section of housing (Fig. 1e, increasing a suppression in low part of stop band) [3], and on widened cross-sections (Fig. 1f, some reduction of insertion loss within pass band) [3].

Band-pass filters on ridged waveguides

The BPFs on ridged waveguides made it possible radically to solve the problem of extra-band suppression. The matter is the resonators of such filters are based on very short sections of ridged waveguides and the second resonant frequency of the filter resonators may dispose very far. As the result, we obtain the frequency response with increased stop band attenuation and range of suppression that extends up to second-third frequency harmonic. The physical reason of the possibility radically to short the resonators is the value of phase of reflection coefficient for the junctions between resonator waveguide and bounding loads. Usually corresponding phase corrections, that provide $\lambda_g/2$ electrical length of the section, led to some geometrical shortening of actual section. However for the case of ridged waveguide sections, bounded by evanescent mode sections, end phase corrections led to the lengths some more than $\lambda_g/2$, and consequently to the possibility to reduce the section length by entire $\lambda_g/2$ and obtain very short sections. Such resonators are known as bar resonators, our contribution into the design of such kind filters consists in new design technology based on initial K-invertors approach, determination of new Q-factors of filter resonators, that are reducing due to $\lambda_g/2$ -shortening, and finally, on redesign the filter geometry basing on the new set of K-invertors, that provide required Q-factors of each section.

Another essential issue of described LPFs on ridged waveguides is the in/output transformers of a new type. They can be used in BPFs too and are the sections of ridged waveguide with the external dimensions equal to the ones for rectangular waveguide and with the ridge thickness equals to the one for other ridges of the filter. Thus the transformer ridges may be performed on the same septum, as the filter as itself, without additional steps of external waveguide walls and, consequently on the base of simplest housing.

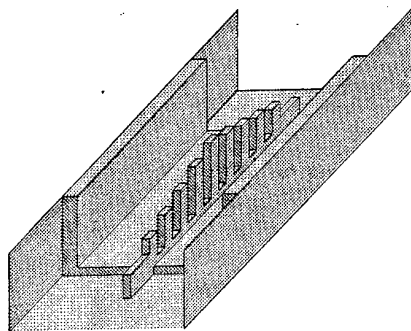


Figure 4. Low-pass filter on ridged waveguide.

limeter wave range because of very small slot widths that are required to provide the needed qualities of full transmission resonances [6]. It impedes their usage even in centimeter wave range. Except of the software for the synthesis of conventional BPFs on rectangular resonant windows the new one for multiaperture windows and for the windows with special configurations are developing. The matter is that there are the physical possibility (see the more detailed report in this Proceedings [7]) to increase essentially Q -factor of full-transmission resonances at the same width of slot by means of a II-shaped slots with possible non-centered placement (Fig. 5b, c). This increasing may be so essential (one-two orders) that such a filter may be used even in long-wave part of millimeter waves.

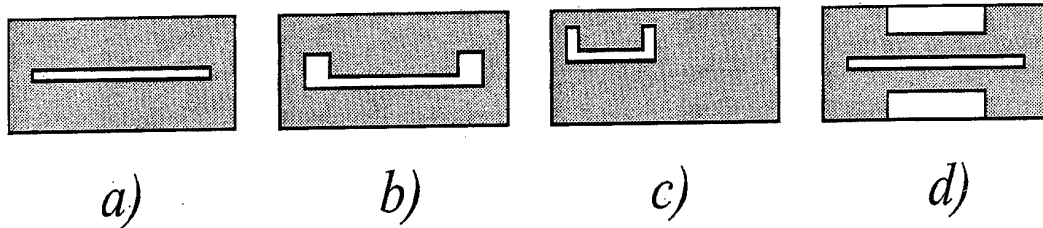


Figure 5. II-shaped and multiaperture diaphragms.

Another interesting phenomenon has been found at the investigation of multiaperture diaphragms (Fig. 5d). It turned out that electromagnetic interaction of several apertures or, in other words, overlapping of two or more full-transmission resonances leads to the appearance of the full rejection resonances in between. It is very important that the geometries that provide wide frequency bands with good matching below and upper rejection point may be successfully found numerically. Another valuable feature is relatively wide slots of corresponding diaphragms. Together they open the way to create a new type of filters of centimeter and, may be, millimeter waves.

Non-tuning dual-mode band-pass filters

The filters with elliptic or pseudo-elliptic characteristics provide the solution of the most complicated problems of frequency selections. The existence of the couplings between non-adjacent sections makes it possible to improve the skirt selectivity, placing the poles of insertion loss near edge frequencies of pass band. On the other hand, the usage of dual (or three)-mode resonators permit to reduce the weight and the dimensions of filters and multiplexers. The main problem of dual-mode filters was the complexity of their exact design and the problems associated with their tuning. At the present time some new configurations were proposed that can be precisely calculated and therefore are not needed any essential tuning after exact fabrication. One of them is four-pole dual-mode filter that was firstly described in [8]. Its special feature consists in replacement conventional tuning screws by large-aperture tilted rectangular diaphragm that can be precisely calculated by mode-matching technique.

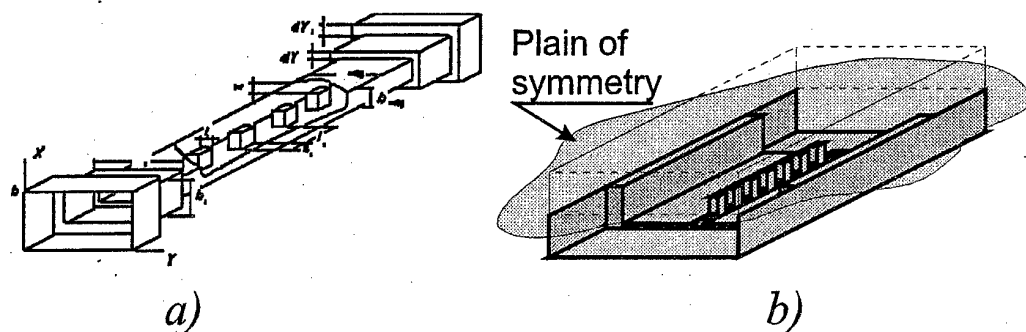


Figure 2. Band-pass filters on ridged waveguides.

There are two geometries of BPFs on the ridged waveguides: with additional in/output transformers (Fig. 2a) and without them (Fig. 2b). The matter is the transformer free configuration has indeed the upper boundaries of possible values of in/output K -invertors, defined by the step junction between main and given ridged waveguide. The wider pass band of the filter the bigger the value of in/output BPF K -invertors and consequently we obtain that simplest configuration Fig. 2b can not be used if pass band is more 10-12%.

Low-pass filters on tapered corrugated waveguides

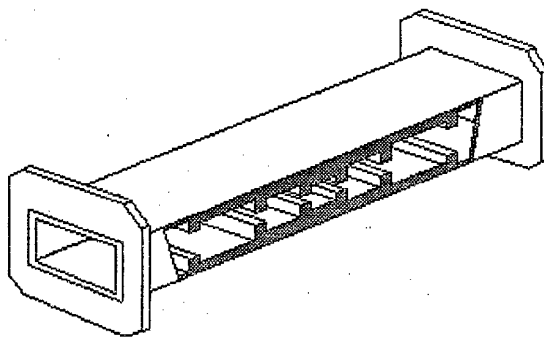


Figure 3. Tapered-corrugated low-pass filter

Low-pass filters (LPFs) on tapered corrugated configurations may be used up to short millimeter waves, taking into account the possibilities of electric discharge or electroforming machining. These filters are based on the series of successive E -plane symmetrical steps in rectangular waveguide with thin capacitive irises in between (Fig. 3). Using the lumped-distributed Levy's circuit theory prototypes and exact 2D electromagnetic models for actual configuration it is possible to obtain very fast algorithm for the design of these LPFs [4]. Even without using the more time-consuming optimization

procedures, i.e. immediately after the reconstruction of K -inverter geometries and some adjustment of section lengths taking into account multimode iris-to-iris interaction, it is possible to obtain a low insertion loss within passband and good suppression up to fourth frequency harmonic of the main signal. For example, for 11-sections filter the return losses are non worse than 20 dB practically within entire waveguide operating band and calculated insertion loss within stop band, which begins closely to the end of operating band, lie in the range 60 to 100 dB. The exception is possible parasitic resonance between second and third harmonics bands, however it may be shift on frequency placement or essentially suppressed by changing set of heights of successive steps or some parameters of prototype. In the worse case the band of bad suppression can be placed between the bands of harmonics of useful signal.

Low-pass filters on ridged waveguides

The main features of LPFs on ridged waveguides (Fig. 4) derive from the fact of very high second resonant frequency of shortened sections (see above) that provide very efficient rejection of the signals including the fourth harmonic with more than 80 dB level of insertion loss (more detailed information see in special report in this Proceedings [5]). Corresponding software is based on the same algorithms as in tapered-corrugated case, however it is supplied by power optimization procedure. It turned out possible owing to special program SES-library tools that provide the possibility to save S-matrixes of a set of discontinuities in the hundreds of frequency points.

We succeeded in the development software for the design not only four-pole filters, based on such a configuration, but for much more complicated six-pole and 8-pole filters as well (Fig. 6). Creation of generalized software has required to solve a lot of separate problems and to elaborate the set of special algorithms and procedures: 1) procedure of synthesis of circuit theory prototypes according to the filter specification, taking into account possible nonstandard cases of specifications, for example non-symmetrical ones; 2) procedure of preliminary estimation of possible fields of diaphragm geometrical parameters and creation of the data base for

the following multidimensional approximating models (the latter makes possible to design such a filter even on Pentium 200); 3) procedure of intermediate fine-adjustment of prototype on the base of frequency response, obtained with electromagnetic model, aiming to take into account possible response distortion due to diaphragm-to-diaphragm interaction. At the final stage of the filter fine-adjustment, the multidimensional optimization procedure is used directly to whole geometry of the filter. The software was repeatedly used for the design of filter the different frequency ranges from decimeter waves to millimeter waves.

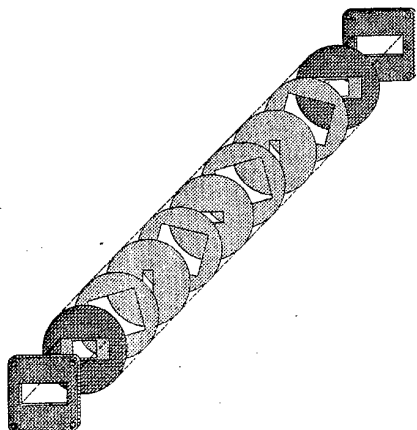


Figure 6. 8-poles dual-mode band-pass filter

References

1. A.A. Kirilenko, V.I. Tkachenko, "System for electromagnetic modeling of microwave – millimeter-wave devices", Izv. vuzov. Radioelektronika, Vol. 39, No. 9, pp.17-28, 1996 (in Russian).
1. A.A.Kirilenko, L.A.Rud', V.I.Tkachenko, "Iterative scheme of optimization of waveguide band-pass filters of millimeter-wave range", Radiotekhnika i Elektronika, Vol. 24, No. 4, pp. 54-62, 1997 (in Russian).
2. A.A.Kirilenko, S.L.Senkevich, B.G. Tysik, "Comparative analysis of filters on the single and double longitudinal strip diaphragm", Elektronnaja tehnika, Ser. Elektronika SVCH, Vyp. 8 (412), 1988 (in Russian).
3. A.A.Kirilenko, S.L.Senkevich, B.G. Tysik, "Synthesis of microwave filters in stepped widening and narrowing of waveguide", Elektronnaja tehnika, Ser. Elektronika SVCH, Vyp. 2 (436), 1991 (in Russian).
4. A.A.Kirilenko, L.A.Rud', S.L.Senkevich, V.I.Tkachenko, "Synthesis and analysis of small-size low-pass filters (LPF) on corrugated rectangular waveguides", Radiofizika i Elektronika, Sb. nauchn. trudov IRE NASU, Vol. 1, No. 1, pp. 5-16, 1996
5. A.A Kirilenko, L.A. Rud', V.I. Tkachenko, "Harmonic filters on ridged waveguides", See this Proceedings.
6. A.A.Kirilenko, L.A.Rud', S.L.Senkevich, V.I.Tkachenko, "Electromagnetic synthesis and analysis of wide band waveguide filters on resonant diaphragms", Izv. VUZov, Radioelektronika, Vol. 40, No. 11, (in Russian).
7. A.A. Kirilenko, L.P. Mospan, "Bandpass and bandstop multiaperture irises for millimeter and centimeter wave range", See this Proceedings.
8. L.Accatino, G. Bertin, M. Mongiardo, "A four-pole dual mode filter in circular cavity without screws", IEEE Trans on MTT, Vol. 44, No. 12, pp. 2680-2687, 1996.
9. M.E. Ilchenko, A.A. Kirilenko, A.G. Yuschenko, L.A. Rud', V.I. Tkachenko, "Waveguide bandpass filters with increased stop band attenuation", See this Proceedings.

PRECISE MEASUREMENTS IN MILLIMETER AND SUBMILLIMETER-WAVE RANGE BASED ON PHASE-LOCKED PRIMARY RADIATION SOURCES

A.F. Krupnov, M.Yu. Tretyakov, V.N. Markov, E.N. Karyakin, G.Yu. Golubyatnikov, V.V. Parshin, S.A. Volokhov, A.M. Schitov, V.V. Bychkov and I.I. Leonov

Institute of Applied Physics of Russian Academy of Sciences
Uljanova St. 46, Nizhny Novgorod 603600, Russia
Tel. +7 (831) 238 4366, Fax. +7 (831) 236 3792, E-mail: trt@appl.sci-nnov.ru

Exclusive kind of microwave radiation generators continuously covering whole millimeter and submillimeter wave range are backward wave oscillator (BWO) tubes. Series of such tubes was developed by Golant with coauthors [1] in sixties and now are commercially available from "Istok" (Fryazino, Moscow region). The report is devoted to a new developments of phase lock loop (PLL) kind of frequency stabilization systems for these sources in the range up to beyond Terahertz as well as application of these systems for scientific and technical measurements.

The operation of the first PLL stabilization system of millimeter and submillimeter-wave BWOs of kind of [1] in the range up to 350 GHz was demonstrated by our group in 1970 [2]. Then the operation range of the system was extended by steps up to 500 GHz in 1976 [3], up to 600 GHz in 1979 [4], up to 820 GHz in 1984 [5]. Next considerable step towards high frequency range we made after joint development with Institute of Electronic Measurements "Kvarz" (Nizhny Novgorod) of series of commercial millimeter-wave frequency synthesizers covering all together the range 35-178 GHz [6]. The synthesizers are based on BWOs of kind of [1] stabilized by PLL system against stable radio signal. The synthesizers were used as source of reference radiation for stabilization of submillimeter-wave tubes as well as primary radiation sources. In 1994 working in collaboration with Cologne's University (Germany) we introduced the BWO PLL system operating up to 970 GHz [7]. Later the range of the setup was extended up to the range of highest frequency tube - 1267 GHz [8-10]. Block-diagram of the system is presented in Fig.1.

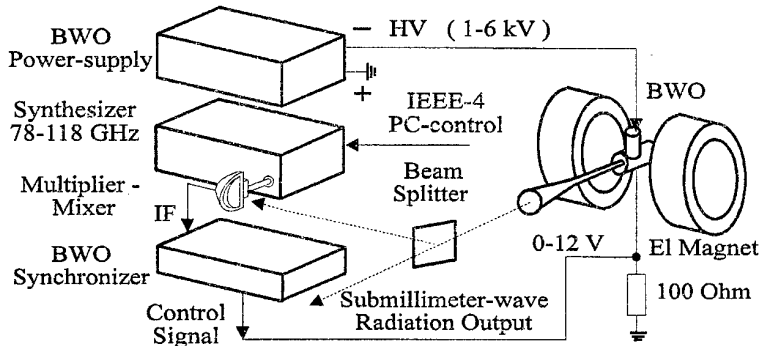


Fig. 1. Block-diagram of submillimeter wave frequency synthesizer.

The system performs stabilization of submillimeter-wave source radiation frequency against harmonic of radiation of millimeter-wave synthesizer, so function of controlling of the source is passed to the synthesizer. The synthesizer is one of the crucial part of the system since the basic properties of output submillimeter-wave radiation such as spectrum purity and bandwidth, frequency stability and accuracy, scanning abilities and step-width etc. are determined by corresponding properties of the synthesizer but multiplied by number of harmonic used for the PLL stabilization. The synthesizer and consequently output submillimeter-wave radiation is computer controlled through standard GPIB interface. Another crucial element of the system is specially

developed in our laboratory broad-band quasi-optical multiplier-mixer. The multiplier-mixer consists of a planar Schottky diode, mounted at the end of ridged 3-millimeter waveguide. The diode is placed in the focal point of a semiparabolic mirror illuminated by submillimeter-wave radiation. Once the mixer is properly adjusted, no further tuning is required. Construction of the mixer is shown in Fig. 2.

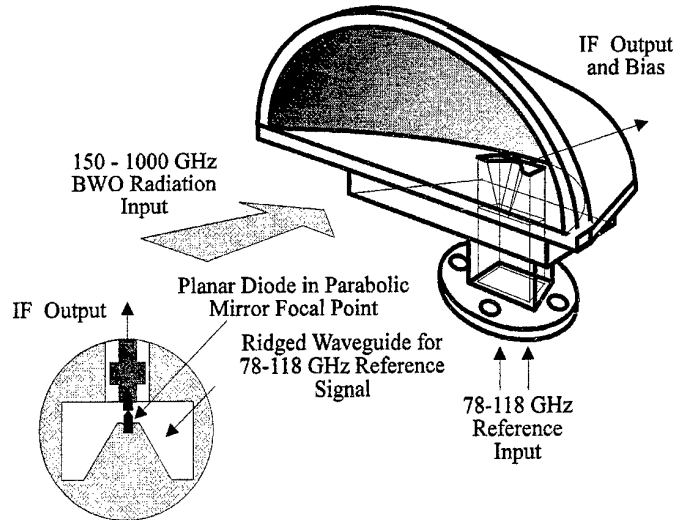


Fig. 2. Broad-band multiplier-mixer for submillimeter-wave range.

Synchronizer includes low noise intermediate frequency amplifier, phase sensitive detector, output amplifier and serving electronics. For the first time this system was installed and used for the high resolution spectroscopy at Cologne's University (Germany) and later spread all over the world from Canada, to Japan. A sub-Doppler spectral resolution, a few kilohertz accuracy of frequency measurements, availability of non-stop single frequency scan length up to 200 GHz with a minimum step of 500 Hz, were demonstrated [7-10]. At present time the spectrometer has highest performance in the world.

Similar but a bit different approach to output radiation control we used developing the laboratory prototype of commercial frequency synthesizer in the range 178 - 370 GHz (covered by two BWOs of corresponding range). The device is designed by analogy with, and as continuation of aforementioned series of "Kvarz" synthesizers [6]. Block-diagram of the device is presented in Fig. 3.

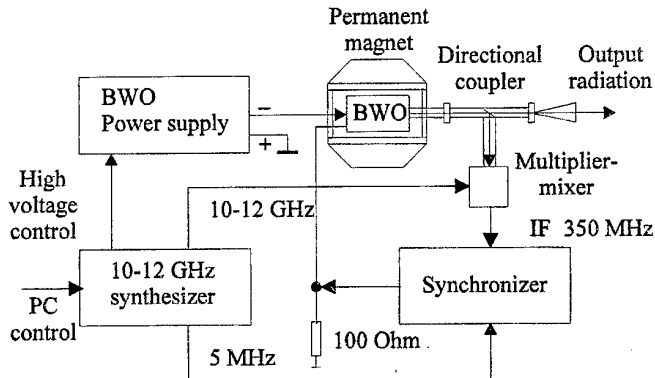


Fig. 3. Block-diagram of 178-370 GHz frequency synthesizer.

Three previous examples demonstrate as frequency stabilization of radiation source leads to development of high precision frequency measurements. Two following examples shows that use of precise frequency methods allows to perform precise "amplitude" measurements.

While working on BWO radiation frequency multiplication [13] and having precisely controlled by use of PLL system source of radiation in the range of 1-3 mm we developed universal method of measurement of conversion losses for every separate harmonic with numbers from 2 to 5 produced and radiated by multiplier. The method is based on measurement of absorption of radiation in spectral lines with known intensity and acoustic detection of this absorption. Block-diagram of the experiment is shown in Fig. 5.

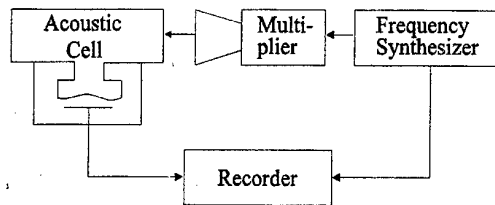


Fig. 5. Block-diagram of radiation frequency multiplication experiments.

The radiation of the source passed through the multiplier and containing both fundamental radiation and harmonics is directed into acoustic gas cell (radio-acoustic detector [4]) commonly used in our spectroscopic experiments. The cell is filled by gas with well known spectrum. Observed spectral lines are recorded and analyzed by PC. Following properties of the acoustic detector in addition to its high sensitivity make it crucial element of the method: i) sensitivity of radio-acoustic detector is independent from frequency range, polarization and space mode of the radiation; ii) there is no signal from the acoustic detector if there is no absorption in the spectral line of gas inside the cell; iii) output signal has linear dependence from the radiation power which was absorbed inside the gas cell. Thus a minor power of a few nanowatt at any particular harmonic may be detected in spite of the fact that at the same time hundreds of milliwatt of fundamental power and other harmonics are passing through the cell but do not produce any signal. So spectral lines of the gas are that frequency-selective element which allows us to distinguish one harmonic from another and those from fundamental. The main criterion of identification of observed line is coincidence of its frequency with calculated line frequency taken from the spectrum data base. The use of PLL stabilization of the fundamental radiation source supports the method with so high accuracy of line frequency measurement that the line identification is undoubtedly. The observed spectral line width is an additional criterion for the line identification. Due to the principle of lines observation the frequency step of radiation scanning through a range is determined by frequency step of fundamental radiation, but for radiation on harmonics the value of the step should be multiplied by corresponding harmonic number. So if higher is the harmonic number then narrower is the linewidth of observed line. The amplitude of observed line is in direct proportion to the line intensity (except the case of too strong absorption which can be estimated beforehand) and to the power of radiation. So comparison of amplitude of observed lines with known intensities allows us to perform quantitative comparison of power in different harmonics. In particular such important characteristic of multiplier as conversion losses can be determined. Dynamic range of such measurements is limited by the acoustic cell sensitivity and in our experiment it was about 55 dB. Accuracy of the method is limited by variation of power of radiation inside the acoustic cell due to parasitic interference when frequency of radiation is changed from one line to another. In our experiments the accuracy of measurements was about 20%. Use of this method for the first time gave possibility in real time to make tuning and adjusting of submillimeter-wave multipliers at every harmonic.

Computer controlled and stabilized by PLL system microwave source of radiation in combination with spectral line shape processing software and Fabry-Perot cavity with quality factor more than 600000 helped us to develop method of ultralow absorption measurements in dielectrics [14]. Open Fabry-Perot resonators are uniquely suitable for studying dielectric properties of low-loss materials. The absorption measurements in this case come to measurements of quality factor of the empty and loaded resonator. There is a sufficient variety of measurement and calculation techniques to obtain a dielectric properties of gas, liquid and solid samples but in

Conventional BWO tube from Istok of kind of OB-24 or OB-30 is placed in a compact permanent magnet system. The output radiation of the tube is stabilized by PLL system against harmonic of 10-12 GHz signal. This signal is generated by base block of "Kvarz" synthesizer which is in fact precise frequency synthesizer of this range. The base block produces also a signal for the BWO power supply to address the radiation of the tube to required frequency range where it will be automatically caught and locked by PLL system. Further precise control of the tube output radiation is performed by controlling of the 10-12 GHz signal of the base block by PC through GPIB interface. The multiplier-mixer is of balance type based on couple of planar Schottky diodes glued on a fin-line inside a 3-millimeter wave-guide. The synchronizer is of the same kind as we use for stabilization of submillimeter-wave BWOs. Workability of the synthesizer in such configuration was demonstrated up to 500 GHz. Main parameters of the synthesizer output radiation are following: relative frequency stability - 10^{-8} with inner quartz reference oscillator and 10^{-11} with use of external 5 MHz signal from rubidium standard; radiation bandwidth - 1 kHz; minimal frequency step 100 Hz.; output power 5-50 mW (depending from BWO output). The synthesizer was successfully used for high resolution spectroscopy [11].

In close collaboration with spectroscopy group of Lille's University (France) the aforementioned PLL technique developed for frequency stabilization of BWOs was successfully used for stabilization of continuous wave far infrared laser. The preliminary work done in this direction is described in ref. [12]. The FIR laser working in the range 0.6 - 2.5 THz and serving as radiation source in sideband spectrometer was for the first time stabilized against harmonic of 78-118 GHz synthesizer. Block-diagram of the setup is presented in Fig.4.

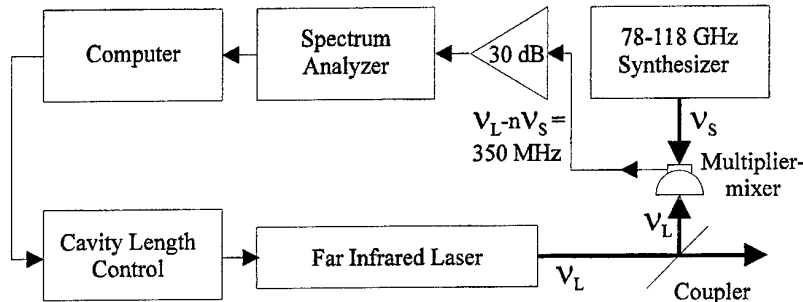


Fig. 4. Block-diagram of FIR laser stabilization.

Minor part of laser radiation is split and mixed with radiation of 78-118 synthesizer by quasi-optical multiplier-mixer of the same kind as described above. The beat-note signal at frequency 350 MHz after low noise preamplifier is analyzed by commercial HP spectrum analyzer. For the laser stabilization achievement we used two facts. First, that internal frequency-meter of the analyzer allows to measure frequency of beat-note signal in a "marker tracking" mode with accuracy 1 kHz, and second that the full information about the beat-note signal may be in real time transferred to computer through GPIB interface. The computer in a real time processes the information and through fast GPIB card and special interface controls micro-step motor. The motor changes the laser cavity length and consequently frequency of radiation of the laser by such way that frequency of beat-note signal remains constant. As it's seen, such stabilization is not of PLL kind but just ordinary so called frequency stabilization, when the system reacts in proportion to frequency difference between stable reference signal and signal which has to be stabilized, so the frequency of the last one is constant only in average. Nevertheless in such frequency lock loop we achieved the frequency stability of the laser radiation better than 50 kHz. Such good result became possible due to the fact that emission of the laser itself has narrow bandwidth and is quite stable in a short time but its frequency is slowly drifting due to temperature effects which can be easily eliminated by our stabilization system. Advantage of our system in comparison with other systems with frequency stabilization loop is - it doesn't need frequency modulation of the laser radiation. The stabilization increased accuracy of frequency measurements of the spectrometer in about order of magnitude.

any case all the information about absorption is contained in a broadening of resonance width of loaded resonator in comparison with the empty one. For achieving the highest sensitivity of absorption measurements, the highest quality factor of the resonator together with precise method of the resonance curve width measurements should be developed. In course of the work we concentrated on increase signal-to-noise ratio, optimization of radiation source and resonator geometry, coupling, detection and signal processing. Special work had been performed to reach the highest possible quality factor of the cavity. We minimized coupling, diffraction and atmospheric losses and maximized the reflection coefficient of mirrors. Quality from 560000 up to 670000 depending from working frequencies and different resonator geometries (which is practical limit of the quality factor of the Fabry-Perot resonator with non-cooled mirrors) has been achieved. To increase signal-to-noise ratio we used 100% amplitude modulation of radiation, selective amplifier at the modulation frequency and synchronous detection of the signal from detector as well as data accumulation and long time averaging. The software used in this measurements was developed earlier for precise studies of molecular collisional broadening. Block-diagram of the experiment is given in Fig.6.

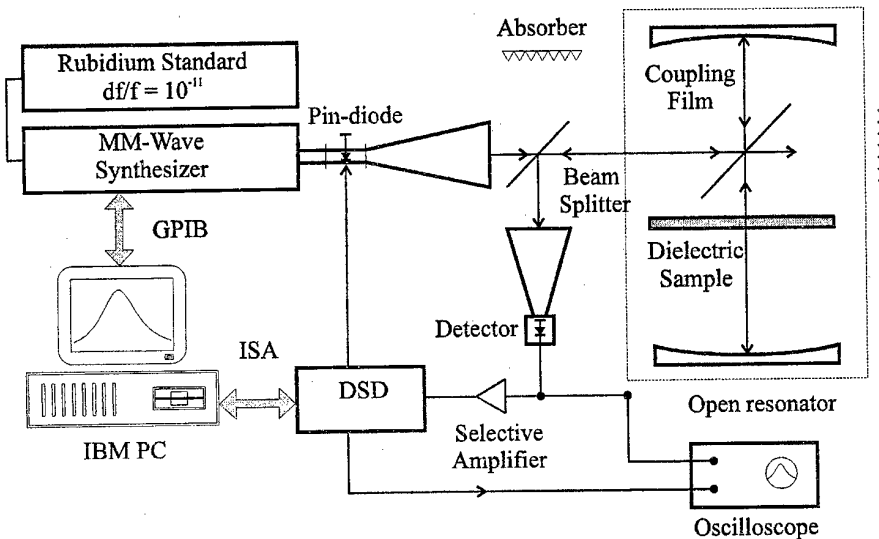


Fig. 6. Block-diagram of ultralow absorption measurements in dielectrics.

"Kvarz" microwave synthesizer [6] of 78-118 GHz range is used as source of radiation. The resonator is connected with synthesizer and detector by quasioptical 3 dB splitter. Amplitude modulation of the synthesizer radiation is made by pin-diode. The teflon film placed under 45 degrees angle to the resonator axis serves for coupling the resonator. A plane parallel sample of a dielectric is placed in the center of the resonator perpendicular to its axis. Computer controls the synthesizer scanning step-by-step over frequency range of resonance band of the resonator and for each step captures the amplitude of the signal from detector. Digital synchronous detector (DSD) mounted in plug-in PC board was used for data acquisition. Resonance curve obtained by such way was fitted to the Lorentzian profile by least-squares method.

After optimization of experimental conditions the absolute accuracy of measurement of the cavity respond width was increased up to 500 Hz at 110 GHz frequency of radiation. Total measurement time was 130 sec. (15 resonance curve records). The limit sensitivity recalculated from such accuracy corresponds to the loss tangent less than 10^{-8} minimal detectable absorption for case of completely filled by dielectric cavity. Counting in absolute units it means that absorption of 0.1 dB/km can be detected by use of Fabry-Perot resonator of 300 millimeter length. For the interpretation of obtained accuracy in terms of absorption measurement in solid or liquid dielectric sample situated in the resonator a real case must be considered. We used the method when a plane-parallel dielectric placed in the resonator perpendicular to its axis has "resonant" optical thickness: i.e. constituting exactly integer number of half wavelengths at one of the resonator eigenfrequencies. In this case rather simple expressions for calculation of loss tangent from experimental data may be used [15]. The

condition of "resonant" thickness can be easily obtained by tuning the synthesizer frequency. Then assuming 10% of standard deviation of measurement error (what corresponds to about 7 kHz resonance curve difference of loaded and empty resonator) we get following loss tangent values: $6.9 \cdot 10^{-7}$ for sapphire plate and $5.5 \cdot 10^{-7}$ for silicon plate both of about 3 mm thickness and $6 \cdot 10^{-6}$ for diamond plate of thickness 0.57 mm. (This estimation is made for materials and their thicknesses practically used for windows of powerful gyrotrons.) Such accuracy is more than sufficient for loss tangent measurements at the present state of low-loss materials development.

The achieved level of sensitivity exceeds the one obtained earlier by more than two orders. The method can be used not only for gyrotron output windows analysis (the problem of developing of ultralow absorbing windows was mentioned as the main difficulty at the creation of 1 MW CW gyrotrons) but for diagnostics of high purity semiconductors, for measurements of thin films properties, for investigation of absorption temperature dependencies etc.

The same method may be used for precise measurements of radiation reflection coefficient from highly reflective surfaces.

Although the experiment was made in 3 millimeter-wave range, similar techniques exist up to frequencies exceeding 1 THz, so described measurements are affordable at the whole millimeter and submillimeter wave bands.

The work described at this report was supported in part by Russian Fund for Basic Research (RFBR) Grant No 97-02-16593 and joint RFBR-DFG Grant No 98-03-04072 and State Program "Fundamental Metrology".

References:

1. M.B. Golant, R.L. Vilenkin, E.A. Zulina, Z.F. Kaplun, A.A. Negirev, V.A. Parilov, E.B. Rebrova, V.S. Saveliev, Pribori i Tekhnika Eksperimenta, No. 4, pp. 136-139, (1965); M.B. Golant, Z.T. Alekseenko, Z.S. Korotkova, L.A. Lunkina, A.A. Negirev, O.P. Petrova, T.B. Rebrova, V.S. Saveliev, Pribori i Tekhnika Eksperimenta No.3, pp. 231-232, (1969).
2. A.F. Krupnov, L.I. Gershtein, Pribori i Tekhnika Eksperimenta, No. 6, pp. 143-144, (1970).
3. A.F. Krupnov, A.V. Burenin, in Molecular Spectroscopy: Modern Research, K.N. Rao, Ed, Academic Press, N.Y, pp. 93-126, (1976).
4. A.F. Krupnov, in Modern Aspects of Microwave Spectroscopy, G.W. Chantry, Ed, Academic Press, L, pp. 217- 256, (1979).
5. L.I.Gershtein, V.L.Vaks, A.V.Maslovsky, Pribori i Tekhnika Eksperimenta, No.6, pp. 201-202, (1984).
6. A.F. Krupnov, O.P. Pavlovsky, Int J. of IR and MM Waves, Vol. 15, pp. 1611 - 1624, (1994).
7. G. Winnewisser, A.F. Krupnov, M.Yu. Tretyakov, M. Liedtke, F. Lewen, A.H. Saleck, R. Shieder, A.P. Shkaev, S.A. Volokhov, J. Mol. Spectrosc, Vol. 165, pp. 294 - 300, (1994).
8. S.P. Belov, K.M.T. Yamada, G. Winnewisser, L. Potenu, R. Bocquet, J. Demaison, M.Yu. Tretyakov, O. Polyansky, J. Mol. Spectr., Vol.173, No. 2, pp. 380-390, (1995).
9. S.P. Belov, F. Lewen, Th. Klaus, and G. Winnewisser, J. Mol. Spectr., Vol. 174, pp. 606-612, (1995); G. Winnewisser, S.P. Belov, Th. Klaus, and R. Schieder, J. Mol. Spectr., Vol.184, pp. 468-472, (1997).
10. A.F. Krupnov, M.Yu. Tretyakov, M. Bogeay, S. Bailleux, A. Walters, B. Delcroix, S. Civis, Journ. Molec. Spectrosc, Vol. 176, pp. 442-443, (1996).
11. G.T. Fraser, F.J. Lovas, R.D. Suenram, E.N. Karyakin, A. Grushow, W.A. Burns, K.R. Leopold, J. Molec. Spectr., Vol. 181, pp. 229-245, (1997); E.N. Karyakin, G.T. Fraser, F.J. Lovas, R.D. Suenram, M. Fujitake, J. Chem. Phys., Vol.102, pp. 1114-1121, (1995).
12. R. Bocquet, M.Yu. Tretyakov, A.F. Krupnov, L. Poteau, O. Boulogne, Int. J. of IR and MM Waves, Vol. 17, pp. 1031-1039, (1996); R. Bocquet, M.Yu. Tretyakov, A.F. Krupnov, S.A. Volokhov, L. Poteau, Int. J. of IR and MM Waves, Vol. 17, pp. 1181-1192, (1996).
13. A.F. Krupnov, M.Yu. Tretyakov, Yu.A. Dryagin, S.A. Volokhov, J. Mol. Spectrosc, Vol. 170, pp. 279-284, (1995); A.F. Krupnov, M.Yu. Tretyakov, S.A. Volokhov, JETP Letters, Vol.61, No.1, pp. 79-81, (1995).
14. A.F. Krupnov, V.N. Markov, G.Yu. Golubyatnikov, I.I. Leonov, V.V. Parshin, Yu.N. Konoplev, IEEE Transactions on Microwave Theory and Techniques, accepted for publication.
15. Yu.A. Dryagin, V.V.Parshin, Int.J.Infrared and Millimeter Waves, Vol.13, pp.1023-1032, (1992).

MATERIAL PROPERTIES IN THE MILLIMETER RANGE.

V.V.Meriakri

Institute of Radio Engineering and Electronics, Russian Academy of Sciences

Address: 1 Vvedensky sq. Fryazino, Moscow region, 141120, Russia

Tel: (095)5269266, Fax: (095)7029572, E-mail: ask@ms.ire.rssi.ru

Here we present some results of our investigations of the different material properties (complex refractive index, permittivity, transmission and reflection coefficients) of dielectrics, semiconductors, ferrites, composite materials, and materials for practical use at wavelengths from 3 to 0.6 mm [1-4].

We have used beam waveguide technique [1] and backward wave oscillators as the sources. The interval of the real part n of the complex index is from 1.05 to 20, and the interval of loss tangent $\tan \delta = 2nk/(n^2 - k^2)$ is from 10^{-5} to 1. Here n and k are real and imaginary parts of the complex refractive index. For n , k and $\tan \delta$ determination we have used beam waveguide versions of complex transmission $t = |t|e^{i\varphi_t}$ and reflection $r = |r|e^{i\varphi_r}$ measurement methods including interferometers. The measurement errors are about (1-2)% for $|t|^2$ and $|r|^2$, and 3°-5° for $\arg t$ and $\arg r$.

Tables 1-5 present the measured values of n and $\tan \delta$ ore $\varepsilon' = n^2 - k^2$ and $\varepsilon'' = 2nk$ of the main materials under test.

Table 1. Low loss liquids properties

No	liquid	$n \pm 0.3\%$	$\tan \delta \times 10^3 \pm 10\%$	λ, mm
1	octane	1.396	0.74	0.63
2	nonane	1.405	0.93	0.63
3	decane	1.407	0.83	0.63
4	cyklohexane	1.424	0.5	0.63
5	crude oil	1.47-1.51	0.8 ± 1.5	2.0

Here we present the liquids with the minimum loss in the near millimeter region.

Table 2. Lossy liquids properties.

No	liquid	$\varepsilon' \pm 5\%$	$\varepsilon'' \pm 10\%$	λ, mm
1	H ₂ O	6.3	8.8	2.0
	H ₂ O	5.1	5.1	1.03
	H ₂ O	4.7	4.0	0.74
	H ₂ O	4.5	3.5	0.58
2	DMCO	3.39	1.6	0.9
3	(CH ₃) ₂ CO	3.04	3.23	0.99
4	CH ₃ COC ₂ H ₅	2.69	2.19	1.02
5	CH ₃ NO ₂	3.19	5.16	1.02
6	C ₆ H ₁₀ O	2.62	1.06	1.02

We investigated also water-alcohol solutions, NaCl -water and KCl - water solutions, and water crude oil emulsions.

For water content determination we use some methods and blockdiagrams: modus and phase of transmission coefficient measurements using different types of waveguides and coupling with material under test.

For example, moisture meter in spirit is based on dielectric waveguide prepared from Si and has sensitivity 0.5-0.7 db/1% H₂O for moisture <10% at frequencies 26-30 Ghz.

The Table 3 presents low loss solid dielectrics properties.

Table 3. Low loss dielectrics properties.

No	Material	$n \pm 0.5\%$	$\tan \delta \times 10^3 \pm 10\%$	λ, mm
1	Teflon (unsintered)	1.35-1.44	0.23-0.26	0.63
2	Teflon (sintered)	1.43	0.7	1.3
3	Polyethylene	1.53	0.6	0.63
4	Polypropylene	1.51	0.6	0.63
5	TPX	1.44	0.41	1.3
6	Polystyrene	1.59	2.4	0.9
7	Rexolite-1422	1.59	2.4	1.0
8	Duroid-5880	1.48	0.9	3.0
9	Teflon -4MB	1.42	1.2	0.63

Here unsintered Teflon had density from 1.3 to 2.2 g/cm³.

The Table 4 presents the measured values of n and $\tan \delta$ of low loss materials with $n > 1.7$.

Table 4. Low loss solid.

No	Material	$n \pm 0.5\%$	$\tan \delta \times 10^3 \pm 10\%$	λ, mm
1	SiO ₂ (crystal)	$n_e = 2.45$	0.55	2.18
	SiO ₂ (crystal)	$n_o = 2.10$	0.56	2.18
2	SiO ₂ (fused)	1.95	1.4	0.85
3	SiO ₂ (ceramic)	1.92	0.67	1.0
4	Al ₂ O ₃ (ceramic)	3.10	0.26	2.18
5	BeO	2.63	1.2	1.0
6	MgF ₂	1.16	0.6	1.2
7	AlN	2.88	0.7	1.4
8	GGG	3.51	1.3	1.15
9	NB	1.72	1.5	0.87
10	MgAl ₂ O ₄	2.90	1.0	1.0
11	GaAs ($\rho > 10^8 \text{ Om} \cdot \text{cm}$)	3.60	0.2	2.24
12	Si ($\rho = 25 \cdot 10^4 \text{ Om} \cdot \text{cm}$)	3.42	0.08	1.46
13	YIG, Ni-Zn, Li- ferrites	3.54-3.95	0.8-1.5	2.0

Table 5. Building materials characteristics, $\lambda=2 \text{ mm}$

No	Material	$n \pm 1\%$	$\tan \delta \times 10^2 \pm 20\%$
1	Brick ($\rho = 1.5 \text{ g/cm}^3$)	1.8	3.5-4.2
2	Concrete ($\rho = 1.7 \text{ g/cm}^3$)	2.4	5.0-5.5
3	Asphalt ($\rho = 1.3 \text{ g/cm}^3$)	1.5	8.0
4	Sand ($\rho = 1.8 \text{ g/cm}^3$)	1.6	2.5
5	Pine-tree wood (moisture <7%)	1.4	3.4 / 2.0
6	Glass	1.45	5.0
7	Veneer (d=7.6 mm)	1.5	2.6 / 1.4
8	Marble	1.5	1.0
9	Organic glass	1.6	1.5
10	Cardboard	1.8	6.0

There are many lossy solids materials with ϵ' up to 300, and absorption up to 100 db/mm (BaTiO_3 , TGS, RDP, $\text{La}_{0.5}\text{Li}_{0.5}\text{TiO}_3$, ferroepoxy). Some of these materials are anisotropic, other are composites.

Building materials properties (Table 5) are of interest for communications and other applications as well as for nondestructive test.

In Table 5, less value of $\tan \delta$ for pine-tree wood corresponds to electrical field perpendicular to wood fiber. For some application it is interesting to know clothes and other common use materials characteristics at millimeter wavelengths.

Transparency of clothes decreases, as frequency increases, from 99.84% at $\lambda = 1.6$ mm to 76.37% at $\lambda = 0.4$ mm.

References.

1. V.V.Meriakri et al, Submillimeter beam spectroscopy and its applications. Problems of Modern Radio Engineering and Electronics., edd. by V.A.Kotelnikov, pp.179-197, Nauka, Moscow, 1982.
2. V.V.Meriakri, I.P.Nikitin, E.E.Chigrai, Dielectric Materials properties in near millimeter range, Radiotekhnika, No. 6, pp. 88-95, 1995 (in Russian)
3. V.V.Meriakri and E.E.Chigrai, Properties of material for practical use at the mm and submm wavelengths, 17 Int. Conf. on IR and MM waves, Digest, pp.68-69, Colchester, UK, 1993
4. V.V.Meriakri, Low Loss Ceramic Properties in the Near Millimeter Wave Range, Electroceramics V Intern. Conf. Pp.107-109, Aveiro, Portugal, 1996.

MULTIFUNCTIONAL MILLIMETER WAVE RADAR SENSOR FOR VEHICLE APPLICATIONS

M. Wollitzer, J. Büchler, J.-F. Luy^{*}
U. Siart, J. Detlefsen[†]

*Daimler-Benz Research Ulm, Wilhelm-Runge-Str. 11, 98081 Ulm, Germany
e-mail address of corresponding author: m.wollitzer@dbag.ulm.DaimlerBenz.com

[†]Technische Universität München

INTRODUCTION

Important aspects in future automotive concepts are comfort, reduced energy consumption and particularly improved safety. To optimize these points a precise sensing of the vehicle parameters and the environmental conditions is necessary. For example the velocity of a vehicle, the tilt angle, the height above ground and especially for active distance control and for autonomous driving the road condition have to be known. Well suited to carry out these tasks are radar sensors in the millimeter wave range. However, separate sensors for each purpose are uneconomic. Thus the merging of such sensor types to one multifunctional sensor system is needed. Therefore a millimeter wave radar system which is mounted at the bottom of a car was conceived to measure the mentioned values and to get information about the road condition. The sensor consists of two modules with a combined bistatic/monostatic arrangement. Module 1 acts as a transceiver whereas module 2 is a receiving frontend. A schematic view of the arrangement of both modules is shown in Fig.1.

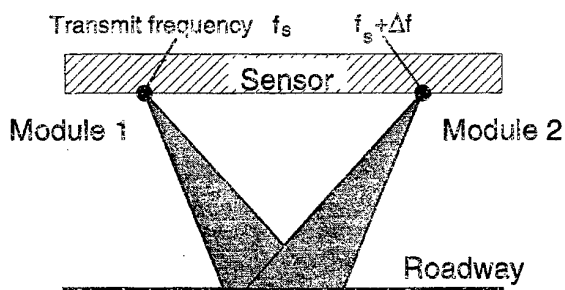


Figure1: Schematic view of the arrangement of the bistatic (module 1) and monostatic (module 2) frontends of the multifunctional radar system.

The transmitting part (module 1) radiates a frequency modulated signal alternately in two orthogonal polarizations at the frequency f_s . The receiving parts work with an LO frequency $f_s - \Delta f$ and detect both polarizations of the scattered signal simultaneously. From the resulting Doppler spectra and a distance measurement, the velocity, the tilt angle and the height with respect to ground and the direction of the movement of a vehicle can be derived as is described in [1]. From the polarimetric information a classification of the road condition is possible. The polarization of the backscattered signals is projected on the Poincare-sphere. Qualitative changes of the polarization state for transitions from smooth to rough asphalt and dry to wet surface are depicted in Fig. 2.

In a first approach the sensor was built in conventional waveguide technique. In this evaluation system, the transmit signal in the ISM-band at 61 GHz is generated by a varactor quadrupler. The transmit polarisation is changed by a pin-switch. The transmit signal is radiated by a corrugated feed horn which is fed by an orthomode-transducer. Isolation between transmitted and reflected signals is realized by circulators. The received signals are downconverted in subharmonically pumped mixers. Photographs of the transmit and receive frontends are shown in Fig. 3a, b. The corresponding block circuit diagrams of the modules are also depicted.

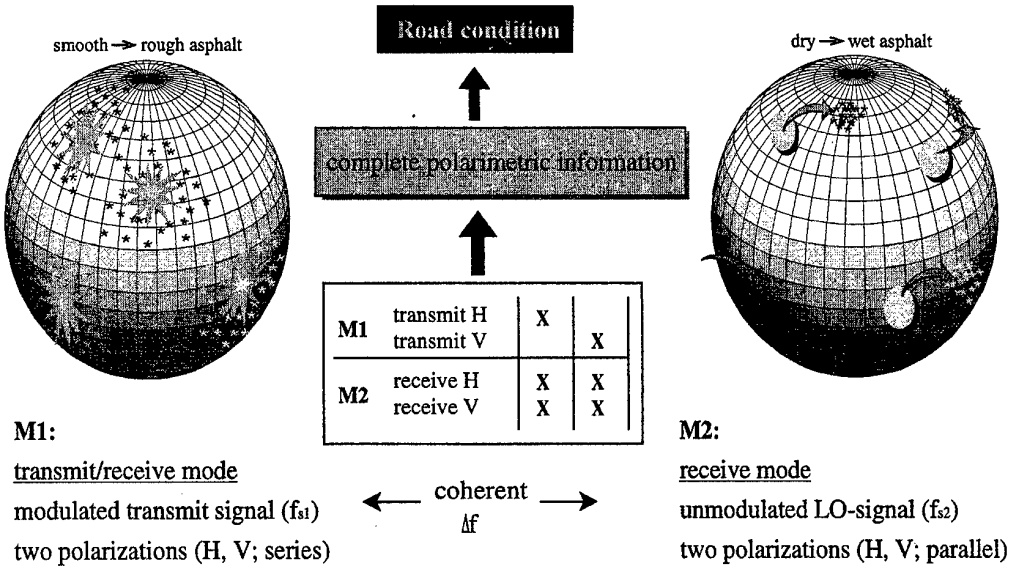


Figure 2: Change of the polarization state of the backscattered waves for the transition from smooth to rough asphalt and from dry to wet roadway.

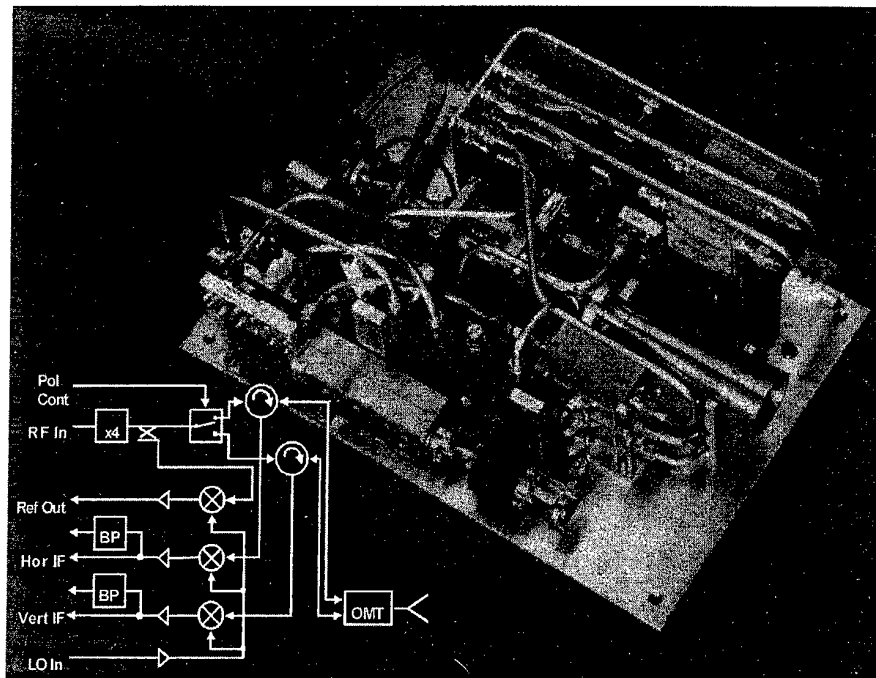


Figure3a: Photograph and block circuit diagram of the bistatic frontend (module 1).

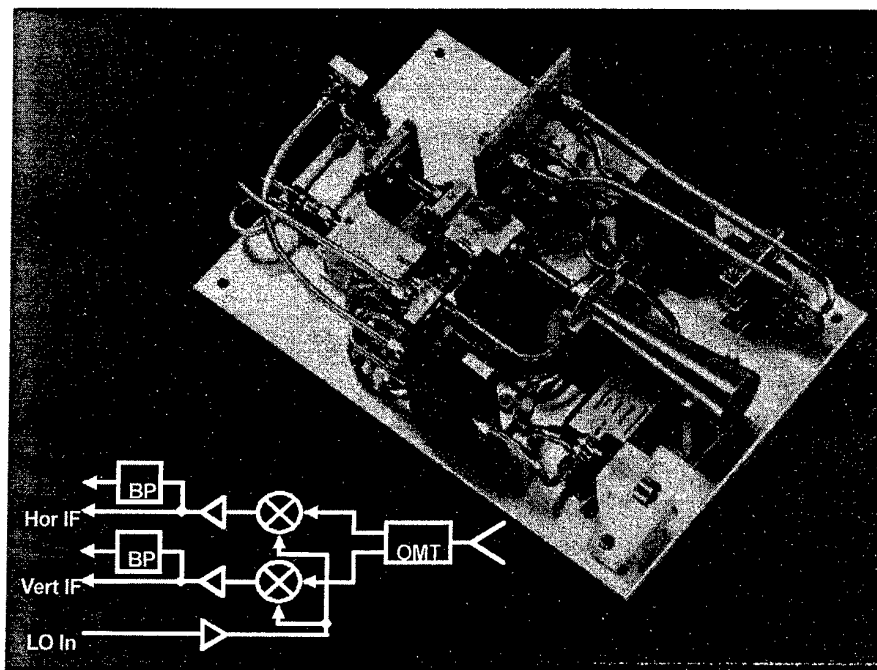


Figure3b: Photograph and block circuit diagram of the monostatic frontend (module 2).

To meet the low cost requirement for mass production SIMMWIC (Silicon Millimeter-wave Integrated Circuits) technology is a promising way [2]. The monolithic integration of active devices combined with antenna structures on high resistivity silicon leads to complete single chip transmitter or receiver circuits. Therefore the second step was to realize the millimeter wave circuits of both modules with monolithic SIMMWICs. To achieve a flat arrangement which can easily be mounted at the bottom of a car a leaky wave antenna [3] was developed and coupled to the SIMMWIC chips. The antenna consists of a dielectric plate with a thickness of $n\lambda_{dielectric}/4$ and a relative permittivity of 20, which is located at half a free-space wavelength of the radiated signal above a conducting plane. With this configuration, an antenna gain of 20 dB is achieved. A schematic cross-sectional view of the integrated frontend is depicted in Fig. 4.

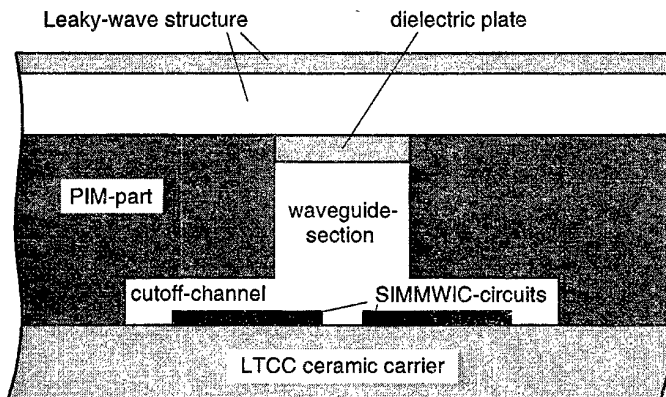


Figure 4: Cross-sectional view of the integrated frontend

The planar silicon millimeterwave oscillators are located in cutoff channels. The generated signal is guided by a waveguide section. The chips are protected from environmental influences by a $\lambda/2$ dielectric plate through which the rf-signal is coupled to the leaky-wave antenna structure. Phase coherence of the system is realized by subharmonic injection locking [4] of the millimeterwave circuits to a source at a third (20.4 GHz) of the operating frequency of the radar system which could, for example be realized by a phase locked SiGe-HBT oscillator. In the receiver frontends, the received signals are downconverted to an intermediate frequency by application of the self-mixing properties of the SIMMWIC-oscillators [5]. A

block diagram of the millimeterwave frontend is shown in Fig. 5. A view of a milled structure for evaluation purposes and a photograph of the realized injection moulded frontend structure are depicted in Fig. 6.

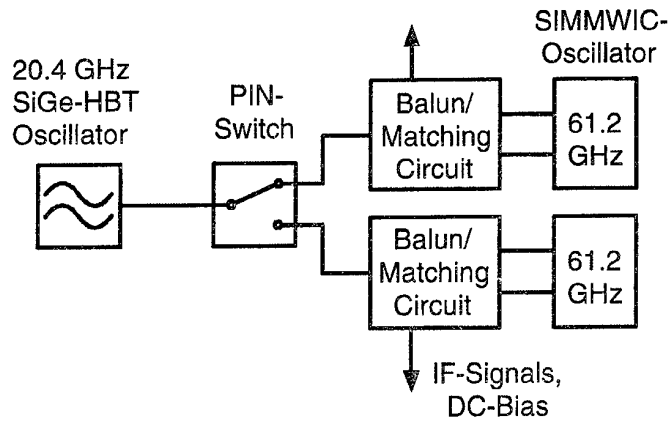


Figure 5: Block diagram of the integrated radar frontend

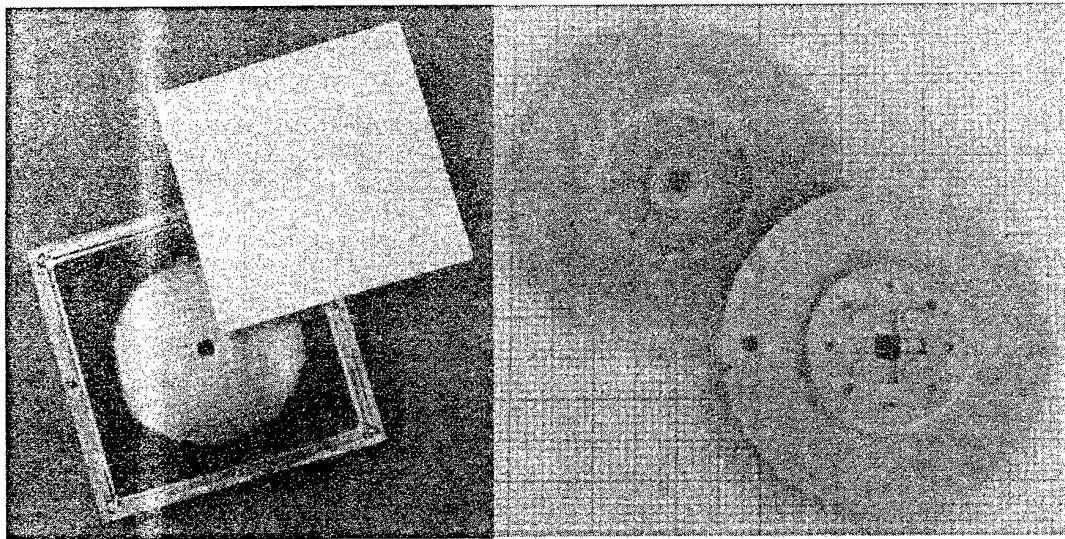


Figure 6: Left: Milled structure for the evaluation of the frontend concept
 Right: Powder injection moulded frontend housing.

REFERENCES

- [1] M. Wollitzer, J. Buechler, J.-F. Luy, U. Siart, E. Schmidhammer, M. Esslinger, „Multifunctional Radar Sensor for Automotive Applications“, *IEEE Trans. Microwave Theory Techn.*, vol. 46, pp. 701-708, May 1998.
- [2] J.-F. Luy, K. M. Strohm, H.-E. Sasse, A. Schueppen, J. Buechler, M. Wollitzer, A. Gruhle, F. Schaeffler, U. Guettich, A. Claassen, „Si/SiGe-MMICs“.
- [3] H. Ostner, E. Schmidhammer, J. Detlefsen, D. R. Jackson, „Radiation from Dielectric Leaky-Wave Antennas with Circular and Rectangular Apertures“, *Electromagnetics*, vol. 17, no. 5, pp. 505-535, Sept./Oct. 1997.
- [4] M. Wollitzer, J. Buechler, E. Biebl, „Subharmonic Injection Locking (of) Slot Oscillators“, *Electron. Lett.*, vol. 29, no. 22, pp. 1958-1959, 1993.
- [5] M. Claassen, U. Guettich, „Conversion Matrix of Self-Oscillating Mixers“, *IEEE Trans. Microwave Theory Techn.*, vol. 29, pp. 25-30, April 1991.

HIGH TEMPERATURE PROCESSING OF MATERIALS USING MILLIMETER-WAVE RADIATION

Y.V. Bykov, A.G. Eremeev, V.V. Holopsev, K.I. Rybakov, V.E. Semenov

Institute of Applied Physics, Russian Academy of Sciences,

46 Ulyanov St., Nizhny Novgorod 603600 Russia

Tel. +7 831 238 4300, Fax +7 831 236 2061, E-mail byk@appl.sci-nnov.ru

INTRODUCTION

As a rule, an advent of new high-power sources of coherent electromagnetic radiation is followed by development of novel technological applications. The invention of a gyrotron made it possible to master the millimeter wave range (frequencies from 10 to 300 GHz). Until recently, the main application area of high-power gyrotrons was plasma heating in nuclear fusion reactors. A radically new interest in the use of the millimeter-wave (mm-wave) radiation arose in the late 80's. New expectations were associated with the potential offered by the mm-wave power for industrial applications. Owing to an intermediate position of the mm-wave radiation on the frequency scale, this radiation can be used either as a wave beam similar to the laser beam, or for feeding applicators in which the microwave energy is spread over a large volume. In the former case, intense wave beams can be utilized for surface treatment of materials. In the latter case, volumetric heating of materials provides a basis for various applications. Along with the benefits for applications provided by the controllable, inertialess nature of the mm-wave heating, there is much evidence in favor of specific nonthermal influence of the high-frequency electromagnetic fields on the materials, which may further increase the industrial potential of the mm-wave processing methods. This paper outlines the research in the field of mm-wave processing of materials undertaken at the Institute of Applied Physics (IAP) over the last decade.

EXPERIMENTAL FACILITIES

Since the invention of a gyrotron, IAP has been keeping leadership both in the fundamental studies of gyrotron operation and in the development and production of gyrotrons. In addition to gyrotrons operating in pulse mode with the output power up to a megawatt at frequencies 50 – 170 GHz, a specialized 20 kW CW, 30 GHz gyrotron for the processing of materials was developed [1]. As a result, today IAP has a unique set of facilities for the feasibility studies in the potential application areas of the mm-wave power.

The 20 kW CW, 30 GHz gyrotron is a key component of the Gyrotron Heating System (see Fig. 1). The System includes the following major components:

- gyrotron with variable output power, complete with a warm magnet system,
- three-mirror quasioptical transmission & focusing line,
- microwave furnace 50 cm in diameter and 60 cm in height,
- furnace vacuum system for operation in the pressure range $(1 - 2 \cdot 10^5)$ Pa,
- temperature measurement and computer-based process control system.

The same structure of equipment is used in the systems operating with gyrotrons having the output power about 20 kW CW at frequencies 37 and 84 GHz. These gyrotrons (available commercially from the GYCOM company, Nizhny Novgorod, Russia), have built-in converters for shaping the output radiation as a Gaussian wave-beam.

The set of equipment currently available at IAP allows implementation of a broad-scale study of both volumetric and surface processing of materials. The diversity of the radiation parameters, viz. frequency, power range, modes of operation, is of paramount importance whenever the research pursues either of the two goals: to clarify the specific effect inherent to the mm-wave processing, and to determine optimal conditions for yielding high-quality final products.

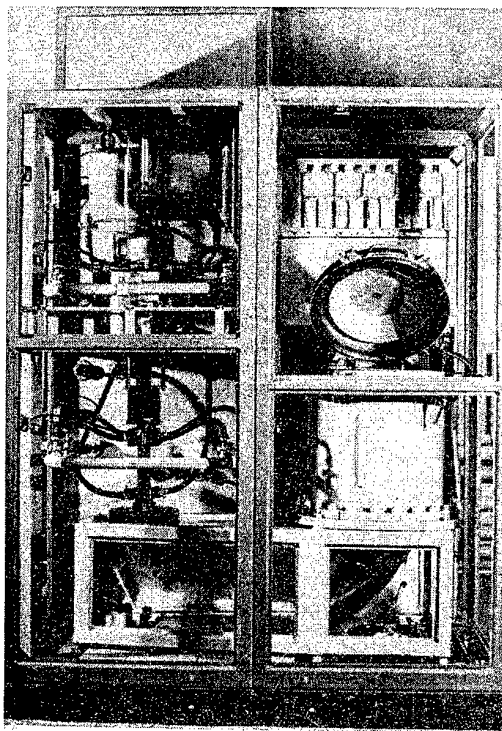


Fig.1. 20 kW CW 30 GHz Gyrotron System.

EXPERIMENTAL RESEARCH

The volumetric nature of the microwave heating is a distinctive feature that underlies virtually all industrially implemented processes. From a physical standpoint, volumetric absorption of microwave radiation eliminates the need in energy transfer by thermal conduction which is relatively slow in dielectric materials. Technically, the absence of massive furnaces and heaters leads to significant reductions in process duration and energy consumption. These and other factors contributed to broad utilization of microwave energy for such industrial applications as food processing, wood drying, rubber vulcanization etc. [2] All processes industrially implemented to date utilize decimeter-wavelength or radio-frequency (rf) radiation which is efficiently absorbed in the mentioned materials due to high content of water and/or organic substances in them. The temperatures needed for these processes are relatively low ($\leq 100 - 200$ °C).

In recent years, application of microwave energy to high-temperature processing of materials, such as sintering and joining of ceramics, deposition of various functional coatings, etc., has been extensively investigated. The interest drawn to these applications is not even due to potential energy savings (although these can be especially substantial for high-temperature processes) but mostly due to the prospects of creating materials with novel properties. For example, densification of ceramic materials during sintering is always accompanied by recrystallization grain growth, which leads to the coarsening of microstructure and deterioration of mechanical properties [3]. A reduction in the sintering time due to volumetric heating results in obtaining ceramic materials with fine and uniform microstructure and enhanced mechanical properties.

The advantages of the use of mm-wave power for high-temperature processes based on volumetric heating of materials are well recognized now (see, for example, [4, 5]). Mastering the new frequency range means a significant extension of the range of materials which can be processed effectively with electromagnetic radiation. For example, among the structural ceramic materials most promising are those based on silicon nitride and pure oxides. It is well known how low the dielectric losses of these materials are at frequencies ≤ 2.45 GHz. Their processing by microwaves in that frequency range is only possible with the so-called hybrid systems which utilize at the initial stage of heating additional heat sources or additional objects with high microwave loss. However, since microwave absorptivity of the ceramic materials increases rapidly with frequency, they can be directly processed by the mm-wave radiation.

Another advantage of the mm-wave processing is higher uniformity of the electromagnetic energy distribution within the applicator. Because of productivity requirements, for most industrial purposes it is necessary to utilize overmoded cavities as applicators. The degree of uniformity of electromagnetic field in such cavities depends upon the ratio L / λ , where L is cavity dimension, and λ is wavelength. In the mm-wave range it is possible to use untuned multimode applicators with $L / \lambda \geq 100$. High uniformity of the electromagnetic energy distribution is achieved as a result of the superposition of hundreds modes excited simultaneously. Perhaps the most convincing demonstration of the feasibility of mm-wave processing for producing large-size and complex-shape ceramic parts was the sintering of silicon nitride buckets $\varnothing 200$ mm $\times 200$ mm performed in Japan [6].

The volumetric nature of mm-wave/microwave heating, combined with surface heat losses, gives rise to a specific dome-like temperature distribution within the material undergoing processing. Under these conditions, processes involving the gas phase, such as reaction sintering and infiltration of porous structures, occur in the form of propagation of the reaction/transformation front from the (hotter) core of the material towards its surface. Due to slower densification at the periphery, the gas phase retains access to the core, which results in a drastic reduction of the total process time. In particular, a more than an order of magnitude rate enhancement has been observed in reaction synthesis of silicon nitride, sintering of HTSC ceramics, and membrane infiltration [4].

In our studies of mm-wave sintering of ceramics we were mostly interested in the physical aspects of the processes and in those factors which could be responsible for their specific features. The existence of such features follows directly from a comparison between the regimes of the mm-wave and conventional sintering of various ceramic materials. As seen from Table 1, mm-wave sintering typically requires significantly shorter hold times (about an order of magnitude less than the conventional sintering times) and a lower temperature. Apparently, the duration of the high-temperature stage of sintering is reduced by about an order of magnitude for virtually all ceramic materials, independent of their chemical composition, atomic bond type, and crystalline structure of the initial powder material. Higher heating rates and shorter hold times reduce the duration of the entire thermal treatment phase of the production cycle from 20 \div 40 hours (typical in conventional sintering) down to 5 \div 10 hours; energy consumption is reduced by more than an order of magnitude.

Table 1. Comparison between the regimes of microwave and conventional sintering [7-10]

Material	Heating rate, °C/min	T_{\max} , °C mm-wave / conventional	Hold time, min mm-wave / conventional
Al_2O_3	50 \div 200	1500 / 1550	10 / 120 \div 150
BaTiO_3 , $\text{Pb}(\text{Zr Ti})\text{O}_3$	50 \div 100	1250 / 1350	5 \div 10 / 120
Si_3N_4 (+ Al_2O_3 & Y_2O_3)	50	1700 / 1800	10 \div 15 / 120

As a typical example of the difference between the microstructures of the mm-wave and conventionally sintered materials, shown in Fig. 2 are scanning electron microscopy images of technical grade Al_2O_3 ceramics. As a consequence of a finer and more uniform microstructure obtained via the mm-wave sintering, structural Al_2O_3 - and Si_3N_4 -based ceramics possess noticeably higher strength and fracture toughness, whereas piezoceramics and electroceramics exhibit enhanced functional properties [10].

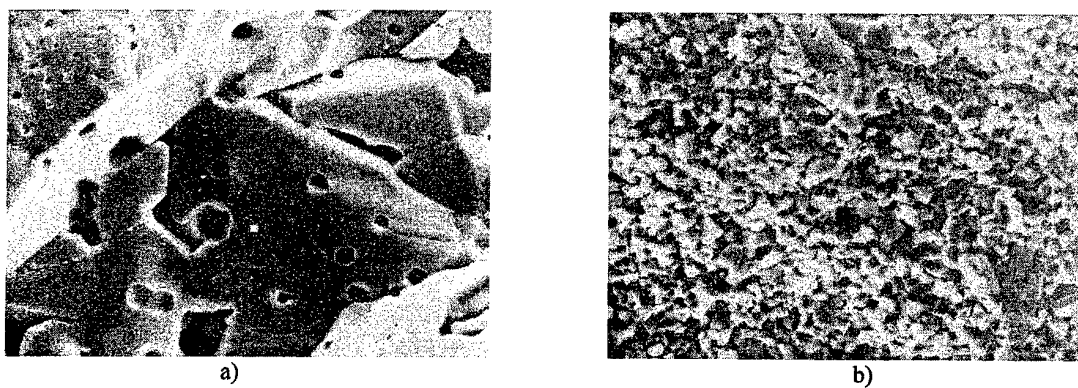


Fig. 2. Microstructure of Al_2O_3 -based ceramics ($\times 4000$): a) sintered conventionally, b) sintered with mm-waves

High thermal treatment rates and short sintering times make the mm-wave heating a promising method for obtaining nanostructured ceramics. The ductility and deformation rates of polycrystalline materials increase with decreasing crystallite size, d , as $d^{-2} \dots d^{-4}$. A transition from a 1 μm grain size (as in today's fine ceramics) to grain sizes on the order of tens of nanometers would render the ceramic material ductile at moderate temperatures. This would facilitate net-shape forming of ceramic parts and eliminate the need in expensive and ecologically hazardous finish machining. The results of experiments with TiO_2 ceramics [11] have demonstrated that by mm-wave heating at rates $100 \div 300 \text{ }^{\circ}\text{C}/\text{min}$ it is possible to obtain a sufficiently dense ceramic material while retaining the average grain size in the nanometer range. The mechanical properties of the nanostructured TiO_2 are noticeably different from those of common ceramics; in particular, its microhardness exceeds the microhardness of a single crystalline rutile by more than 30 %.

Processing of materials with intense mm-wave beams has been studied at IAP since the 80's [12]. In principle, processing of materials based on local heating with mm-wave beams can be considered as one more method for surface treatment of materials by intense energy flows, which is alternative or additional to such widely used in practice techniques as electron and ion beams, plasma processing, and laser irradiation. The systems using intense mm-wave beams appear to be very similar to the systems based on infrared lasers. In fact, when exploiting an up-to-date gyrotron, a power density as high as 10^6 W/cm^2 can be achieved by focusing the radiation in a spot of about λ^2 in size. Wave beams can easily be transported virtually without attenuation over a distance of tens of meters and scanned across the surface using a simple guiding system. The processing itself can be performed in any atmosphere and at any pressure. Yet, mm-wave systems possess a number of advantages from the viewpoint of their potential application. Among them are: higher efficiency of the source of radiation ($\geq 40\%$; 60% for gyrotrons with a depressed collector); higher output power from a single source (when necessary, power on the order of 100 kW can be produced); much simpler quasi-optical systems for wave beam transmission. Such systems are capable of transporting the radiation virtually without any loss and hence without their own heating, which is very important for applications. The most serious limitation of the use of the mm-wave beam system is a lower threshold for the microwave gas breakdown, which decreases even more in the case of high-temperature surface processing of materials.

An example illustrating wavebeam processing of materials is an experimental study of the joining of high-temperature superconductive layers to metal tapes [13]. Tapes of various metal alloys were covered with a slurry of YBaCuO mixed with an organic binder. By varying the processing conditions, viz., the wavebeam intensity, tape motion velocity, temperature value and temperature profile along the tape, different types of joining conditions were achieved. Among them were the joining via solid-state reactions, via partial melting of the YBaCuO layer, and via melting and subsequent crystallization in a temperature gradient. In the latter case, layers with a well-textured structure which had good adhesion to the metal tape and the critical temperature of transition to the superconductive state above 90 K were obtained. However, as it is common for the YBaCuO ceramics, the critical current density was low (about 100 A/cm^2).

It is easy to roughly estimate the output that can be achieved in such energy-demanding process as melting of a refractive coating layer on a substrate. Taking typical values for the coating layer parameters and assuming that 50 % of the incident power is absorbed in the layer, from energy balance considerations it follows that the melted area is linked to the wavebeam intensity as $S (\text{cm}^2/\text{s}) \sim P (\text{kW})$, i.e., when using a gyrotron with power of several tens of kilowatts, the output of the process is quite acceptable for industrial applications.

On the whole, it can be argued that the use of the mm-wave beam technique for surface processing of materials possesses a considerable potential, and only a few of possible applications have been investigated to date.

THEORETICAL STUDIES

The search for the physical mechanism(s) underlying the field-specific (non-thermal) effects in the microwave processing of materials involved theoretical studies. These started from the observation that in the solids with ionic crystalline structure, electrically charged vacancies can act as the recipients of the microwave field action. The vacancy flux, \mathbf{J} , thus consists of the diffusion and drift parts:

$$\mathbf{J} = -D \nabla N + D N q \mathbf{E} / kT, \quad (1)$$

where D is diffusivity, N is concentration, and q is effective electric charge of vacancies, \mathbf{E} is the vector of electric field. Even in comparatively weak electric fields, the amplitude of the drift part of the vacancy flux exceeds the characteristic value of the diffusion part [14]. However, since vacancy drift in HF fields is oscillatory, a non-zero averaged effect can only exist due to a nonlinear "rectification" of currents. The

nonlinearity in ionic crystals can originate from the field-induced space charge perturbations. This effect can be described quantitatively within a model consisting of the continuity equations (written for each sort of vacancies),

$$\partial N_{\pm} / \partial t + (\nabla \cdot \mathbf{J}_{\pm}) = 0, \quad (2)$$

and the Maxwell equations,

$$(\nabla \cdot \mathbf{E}) = 4\pi \rho / \epsilon, \quad (3)$$

$$(\nabla \times \mathbf{E}) = 0, \quad (4)$$

where $\rho = (|q_+|N_+ - |q_-|N_-)$ is density of space charge, and ϵ is the lattice dielectric constant of the material under consideration. The quasistatic approximation used here corresponds to an ionic crystalline body (i.e., a powder particle in ceramics) whose dimensions are small compared with the electromagnetic wavelength.

In a uniform single crystal the electromagnetic field, varying sinusoidally in time, does not perturb the concentration of vacancies and induces only homogeneous oscillatory fluxes of vacancies. At the same time, in the vicinity of a grain boundary (or interface) oscillatory fluctuations of the concentration of vacancies arise due to their oscillatory drift. These fluctuations are in phase with the HF electric field. Therefore, net (averaged over the field period) drift flux is non-zero. The direction of the net flux is same for both positive and negative vacancies, which means that a transport of neutral mass occurs. Since the mobility of positive and negative vacancies is generally different, there should also be a charge transport.

The final result for the net drift flux can be presented as a product of the effective mobility and the average volumetric ponderomotive force:

$$\mathbf{J} = \frac{D_+ D_-}{D_+ + D_-} <\rho \mathbf{E}>. \quad (5)$$

A general measure of the ponderomotive action is the magnitude of the radiation pressure of the electromagnetic field, $E^2/8\pi$. However, in contrast to mechanical stresses, the ponderomotive force in the ionic crystalline solid is applied directly to mobile vacancies. It can be shown [14] that its efficiency with respect to the mass transport drive is enhanced by a large factor, $N_0/N \cong 10^5$, compared to the value of the radiation pressure (here N_0 is the concentration of atoms in the solid). An additional enhancement of the ponderomotive mass transport drive is caused by the action of the tangential component of the HF electric field [15]. This component induces net fluxes of vacancies only within the near-surface layer where the HF space charge is localized. The mobility of vacancies in that layer is much higher than in the bulk. This results in an additional mass transport enhancement factor, $(D_V/D_S + a/R)^{-1}$, which may reach several orders of magnitude (here D_S is the diffusivity in the near-surface amorphized layer, D_V is the diffusivity in the bulk crystal, a is thickness of the amorphized layer, and R is a characteristic size of crystal). As a result, the ponderomotive action of an electric field of about 1 kV/cm, which is a typical value in the microwave sintering, can influence mass transport in ionic crystalline solids significantly.

The efficiency of the ponderomotive effect on mass transport depends upon the correlation between the values of field frequency and ionic conductivity of the solid. Estimates show that depending on the material type and temperature, the optimum frequency range for the effect can vary from rf to microwaves and mm-waves.

Recent numerical studies [16] have revealed a considerable intensification of the electric field in the neck regions between individual grains in ceramics undergoing sintering. Depending upon the dielectric properties of the material and the relative neck size, the energy density of the microwave electric field has been demonstrated to be 1..3 orders of magnitude higher in this region than the energy density averaged over the volume of the grain. Since the mass transport in the course of sintering occurs predominantly within the neck region, this result suggests that the role of ponderomotive forces in microwave sintering is even more significant than it was anticipated. Another study [17] has shown that the microwave ponderomotive action facilitates removal of stable faceted pores from ceramic thus enhancing the sintering process rate.

An interesting application of the solid-state ponderomotive effect was suggested in [18]. It was shown that a microwave field with the E-vector directed tangentially to a surface of a solid (or an interface of a doped layer inside a solid) can develop a deformation-type instability. This results in the formation of a corrugated profile on that surface (interface) with the spatial period on the order of 1 μm . The period can be controlled by adjusting the microwave power.

CONCLUSION

Development of material processing methods is a promising application area for the mm-wave technology. Order-of-magnitude reductions in process duration and energy consumption determine high industrial potential of mm-based methods. Specific features in the interaction of the electromagnetic field with materials during processing open prospects for engineering novel materials with enhanced properties.

ACKNOWLEDGMENT

This research is supported in part by the Commission of the European Communities under the Cooperation with Third Countries and International Organizations programme, International Association for the promotion of cooperation with scientists from the New Independent States of the former Soviet Union (INTAS); and the Russian Basic Research Foundation (grant # 97-02-17252).

REFERENCES

1. Y. Bykov, A. Eremeev, V. Flyagin *et al.*, "The gyrotron system for ceramics sintering", in *Microwaves: Theory and Applications in Material Processing III*, eds. D.E. Clark, D.C. Folz, S.J. Oda, R. Silbergliit (*Ceramic Transactions*, Vol. 59), Amer. Ceram. Soc., Westerville, OH, 1995, pp. 133 – 140.
2. R.F. Shiffman, "Commercializing microwave systems: paths to success or failure", *Ibid*, pp. 7 – 16.
3. R.M. German, *Sintering Theory and Practice*, Wiley, New York, 1996.
4. D.E. Clark, W.H. Sutton, D.A. Lewis, "Microwave processing of materials", in *Microwaves: Theory and Applications in Material Processing IV*, eds. D.E. Clark, W.H. Sutton, and D.A. Lewis (*Ceramic Transactions*, Vol. 80), Amer. Ceram. Soc., Westerville, OH, 1997, pp. 61 – 96.
5. Yu.V. Bykov and V.E. Semenov, "Processing of material using microwave radiation", in *Applications of High Power Microwaves*, eds. A.V. Gaponov-Grekhov and V.L. Granatstein, Artech House, Boston, MA, 1994, pp. 319 – 351.
6. T.Saji, "Microwave sintering of large products", in *Microwave Processing of Materials V*, eds. M.F. Iskander, J.O. Kiggans, and J.-C. Bolomey (Materials Research Society Symposium Proceedings, Vol. 430), Materials Research Society, Pittsburgh, PA, 1996, pp. 15 – 20.
7. Y.V. Bykov, A.E. Eremeev, V.V. Holoptsev, "Experimental study of the non-thermal effect in microwave sintering of piezoceramics", in *Microwave Processing of Materials IV*, eds. M.F. Iskander, R.J. Lauf, and W.H. Sutton (Materials Research Society Symposium Proceedings, Vol. 347, Pittsburgh, PA, 1994), pp. 585 – 590.
8. Y.V. Bykov, A.E. Eremeev, V.V. Holoptsev, "Influence of specific absorbed microwave power on activation energy of densification in ceramic materials", *loc. cit.* [6], pp. 385 – 390.
9. Y.V. Bykov, A.E. Eremeev, V.V. Holoptsev, "Comparative study of Si_3N_4 -based ceramics sintering at frequencies 30 and 83 GHz", *loc. cit.* [6], pp. 613 – 618.
10. Y.V. Bykov, A.G. Eremeev, V.V. Holoptsev, C. Odemer, A.I. Rachkovskii, and H.J. Ritzhaupt-Kleissl, "Sintering of piezoceramics using millimeter-wave radiation", *loc. cit.* [4], pp. 321 – 328.
11. Yu. Bykov, A. Eremeev, S. Egorov *et al.*, "Sintering of nanostructural titanium oxide using millimeter-wave radiation", *Nanostructured Materials*, 1998, to be published.
12. Yu.V. Bykov and A.G. Eremeev, "The possibilities of the technological use of a powerful electromagnetic radiation of the millimeter wavelength range", in *Vysokochastotnyj razryad v volnovyh polyah (High-Frequency Discharge in Wave Fields)*, ed. A.G. Litvak, IAP, Gorkii, 1988, pp. 265 – 289 (in Russian).
13. Yu.V. Bykov, T. Borodacheva, and A. Sorokin, "Microwave heating for joining HTSC thick layers with metals", in *Abstracts of the Materials Research Society 1992 Spring Meeting*, MRS, San Francisco, CA, 1992.
14. K.I. Rybakov and V.E. Semenov, "Possibility of plastic deformation of an ionic crystal due to the non-thermal influence of a high-frequency electric field", *Phys. Rev. B* 49 [1], pp. 64 – 68 (1994).
15. K.I. Rybakov and V.E. Semenov, "Mass transport in ionic crystals induced by the ponderomotive action of a high-frequency electric field", *Phys. Rev. B* 52 [5], pp. 3030 – 3033 (1995).
16. J.P. Calame, K.I. Rybakov, Y. Carmel, D. Gershon, "Electric field intensification in spherical neck ceramic microstructures during microwave sintering", *loc. cit.* [4], pp. 135 – 142.
17. K.I. Rybakov and V.E. Semenov, "Non-thermal effects in microwave sintering of ceramics", in *Proc. CIMTEC '98 – World Ceramics Congress*, to be published; *see also*, J.H. Booske, R.F. Cooper, S.A. Freeman, K.I. Rybakov, V.E. Semenov, "Microwave ponderomotive forces in solid-state ionic plasmas", *Phys. Plasmas*, 5 [5], pp. 1664 – 1670 (1998).
18. K.I. Rybakov and V.E. Semenov, "Possibility of microwave-controlled surface modification", *loc. cit.* [6], pp. 435 – 440.

THE ELABORATION MEASUREMENT ACCURACY PROBLEMS OF THE FREQUENCY CHARACTERISTICS OF THE SOURCES OF HIGH STABILITY OSCILLATIONS IN THE MILLIMETER AND SUBMILLIMETER RANGE AND OF THE MEANS OF THEIR TRACEABILITY

A.S. Kleiman

State Scientific-Research Industrial Association "Metrology"

42, Mironositskaya st., Kharkov, 310002, Ukraine

Tel. (572) 403 020, Fax (572) 436 193, E-mail bondarew@metrog.kharkov.ua

The intensive mastering of submillimetric range stimulates the development both measurement equipment of this range and metrological assurance equipment for high-precision measurements of frequencies and frequency characteristics.

The method of direct multiplication of frequency from standard sources has a number of essential limitations which makes impossible its use for standard frequencies transfer into submillimetric range and higher as when multiplication ratios are 10^4 the phase noise increases intolerably. The complicated problem of high-stable generators development for realization of such sources in the metrological systems take a particular place in the problems of submillimetric range systems realization. The creation of sources for metrological systems and also for the united time, frequency and length standard is realized by the use of various-type generators which are stabilized by means of phase lock. We suggested the method of phase lock multiringed optimal systems computation, which permits to maximize the stabilized generator output signal S/N ratio. The generalized formula of output phase fluctuation power spectral density determination at various numbers of phase lock rings is:

$$S_{\varphi g} = S_{\varphi g}^0 \left| K_1^{(I)} \right|^2 + N^2 \left\{ S_{\varphi g} \prod_{i=1}^x \left| K_1^{(i)} \right|^2 + \sum_{i=1}^x \left| K_1^{(i)} \right|^2 S_{org}^0 \frac{\prod_{g=i+1}^x \left| K_2^{(g)} \right|^2}{\prod_{i=1}^x \prod_i^2} + \frac{\sum_{i=1}^x S_{ymi} \prod_{g=i}^x \left| K_2^{(g)} \right|^2}{\prod_{i=1}^x N_i^2} \right\}$$

The results of calculation are presented in table1.

The principles of high-stable sources of oscillations construction for metrological purposes are discussed. The result of the investigation of some metrological high-stable on frequency sources of oscillations are adduced. The inherent relative instability of output frequency of one of the realized metrological sources on the frequency of 70 GHz is $(1-2) 10^{-14}$ for measurement time of 100 s.

The problems of creation of metrological assurance equipment which permits to measure the main metrological characteristics of oscillation sources in the wide range of carriers (1 MHz to 300 GHz) are discussed.

It is known that source frequency characteristics including LF are characterized most completely by the spectral density of phase fluctuations power (SDPFP) - $S_\varphi(F)$ which may be represented for the most known generators as:

$$S_\varphi(F) = \frac{K_0}{1 + \left(\frac{F}{\Delta F^2} \right)^2} + \frac{K_1}{F^{0.5}} + \frac{K_2}{F} + \frac{K_3}{F^{1.5}} + \dots + \frac{K_n}{F^{n/2}},$$

where $K_0 - K_n$ are the noise constants defined by the generator scheme and noise characteristics of its elements; F is amplifier bandpass. The exponent ($n=0,5$ to 8) characterizes source phase noise spectrum and is typical for the laser phase noise spectrum at large n ($n=5$ to 8).

Frequency instability is defined by the characteristic series and may be estimated both by measurement results in the time domain and by measurement results in the frequency one. The method with use of the phase

discriminator (FD), i.e. the method of determining the parameter, which characterizes instability in the time domain ("Allan dispersion") by means of filtration which is realized in the frequency domain, has the large resolution and a number of advantages: high dynamics which is typical for FD, the absence of data statistical treatment (statistical averaging is realized by r.m.s. voltmeter), less measurement time than one at the measurements in the time domain. In common case the expression for the "Allan dispersion" with account of "dead time" may be presented as following:

$$\sigma_y^2(\tau) = \frac{8\pi^2 S_0 \tau}{(\pi\tau)^{3-n}} \int_{\pi F_i \tau}^{\pi F_i} \frac{\sin^2 x \cdot \sin^2 Mx}{x^n} dx.$$

The results of integral value calculation for various values of exponent N and "dead time" M show the essential contribution to the "dead time" instability determination error, permit to take into account this error and indicate the possibility of the noise character determination by "dead time" change. The device Y7-42, which permits measurement of frequency relative instability $(1-3) \cdot 10^{-14}$ for measurement time 1 s, has been developed in SSIA "Metrology" and is turned out serially for the purpose of excluding the essential error which is related with "dead time" and measurement error decrease and realizes the upon mentioned theoretical consideration. The measurement of frequency longtime instability for $\tau=10^3$ with resolution 10^{-15} is possible.

It is intended for automated measurement of the main characteristics of signals of oscillation stable and high-stable sources (frequency instability, phase and frequency fluctuations power spectral density, parasite and determined deviation of phase and frequency, microdeviation of phase and frequency and so on). It is used at scientific & research, experiment & design works conduced under the conditions of production and verification practice. The equipment complex corresponds to the world technical level. The operating principle is based on the use of the methods of phase detection, parallel analysis and fast Fourier transform. A basic set includes: input amplifiers, phase detectors, low-noise amplifiers, band-pass filters, interface system, mean square value voltmeters, a phase shifter, a phase lock system and a number of auxiliary units, software set and IBM compatible PC. The basic set measures signal characteristics (phase fluctuations power spectral density (PFPSD), frequency microdeviation and instability) for carriers of 1 to 20 MHz in the analysis frequency band of 0.001 Hz to 60 kHz. PFPSD measurement is carried out both with the use of fast Fourier transform and with the use of a built in two-channel spectrum analyzer with a variable analysis band. The use of SHF1 synthesizer permits to enlarge the carriers range to 100 GHz and, if necessary, to 300 GHz. Meter software system provides measurement mode selection and tuning a number of parameters, automatic measurement of noises in the given analysis band, representation of results in a table and diagram form on the display, diagrams and tables copies on the paper. The system is simple for study and control.

CONCLUSION

Methods of increased stability of frequency of generators in a wide range of frequencies are developed. Generators in microwave range (above 70 GHz) with stability $(1-2) \cdot 10^{-14}$ for a time of measurements 100 s are created. A complex of equipment for measurement characteristics of such generators is created.

Table 1. - Comparison of characteristics Super High Frequency Sources.

GHz	Wimber a phase lock system	Retiones multiply			"Allan dispersion" for $\tau=1$ s		dB/Hz
5,9	1	1130	-	-	-	$1,2 \cdot 10^{-12}$	51,0
7,5	1	1521	-	-	-	$0,9 \cdot 10^{-12}$	48,3
43,51	2	6	1460	-	-	$2,0 \cdot 10^{-12}$	46,0
48,7	2	7	1202	-	-	$1,9 \cdot 10^{-12}$	45,2
74,2	3	9	69	24	-	$0,8 \cdot 10^{-12}$	48,4
94	3	10	79	2	-	$0,1 \cdot 10^{-12}$	43,5

Table 2. - Oscillation sources frequency characteristics meter.

SPECIFICATIONS	
Frequency range in Hz	106 to 4.1010
Frequency instability is determined for any interval of measurement time which is in the range of s.	10-5 to 103
Mean square relative random frequency deviation measurement resolution at the frequency of 5.0 MHz for measurement time of 1 s.	3.10-14
Phase fluctuations power spectral density measurement resolution at the analysis frequency of 1 kHz in dB/Hz	-176
Display screen (and the table) show phase fluctuations power spectral density diagram which is taken without information loss at the analysis frequency band in Hz	2.5 to 600,000
Phase fluctuations power spectral density shown on the display screen (table) is measured in the transmission band of at the level of - 3 dB in Hz	5 ± 2 150 ± 40 1500 ± 200

Table 3. - Spectrum analyzer comparative characteristics.

Characteristics	SPECTRUM ANALYZER TYPE	
	Hewlett Packard HP3048A	SSIA "Metrology"
Frequency range	5 MHz to 40 GHz	1 MHz to 40 GHz
Analysis frequency range	10-2Hz to 40 MHz	10-3Hz to 600 k Hz
Resolution of power spectral density on the analysis frequency:		
100 Hz	-150	-160
1 kHz	-160	-176
10 kHz, dB/Hz	-170	-176
Frequency instability is determined for any measurement time interval which is within, s		10-5 to 103
Resolution of frequency mean square relative chance variation measurement on the frequency of 5 MHz for measurement time of 1 s	-	3.10-14

MECHNISM OF INTERECTION OF EHF RADIATION WITH BIOLOGICAL SYSTEMS

O.V.Betskii, N.N.Lebedeva, Yu.G.Yaremenko. (IRE RAS)

Address: ul Mohovaya 11, Moscow, 103907, Russia

tel: 2034489, fax: 2038414, E-mail: ygy169@ire216.msk.su

Per last years in medicine large attention to therapeutic possibilities of electromagnetic waves of EHF (extremaly high frequencies, 30-300 ГГц, length of a wave of 1-10 mm) range is given. For optimization of methods of EHF-therapy and magnification of its effectiveness understanding mechanisms of action of mm waves on living organisms, including, human are being necessary.

It is possible are to state with confidence, that perception and radiation of electromagnetic oscillations are not only possible, but also essential properties of an alive substance. In the complicated process of perception of electromagnetic radiation it is possible conditionally to select some stages conventionally. The first of them is biophysical. It is primary mechanisms of interaction electrical component of field with dipol molecules and also with separate fragments of biomacromolecules, having except a dipol moment, some degrees of mechanical freedom.

Today it is possible to speak seriously about the several approaches to the explanation of biophysical mechanisms of action of mm waves on a living cell. Complete and agreed is the hypothesis offered and developed in works by N.D.Devyatkov and M.B.Golant (1981), consisting that homeostasis of an organism is connected to generation by cells of electromagnetic fields in mm range, which are used for a synchronization of functions of separate cells and coordination of work of multicell-like formations. Parameters of radiation of ill and healthy organisms are different, as any pathology is a pathology of cells. The exterior medical EHF-radiation from a device for EHF therapy imitates the radiation of a healthy organism, fulfilling a synchronizing role and imposing an organism lost for want of disease "healthy" rhythm. The exterior radiation affects the informative and controlling system of an organism.

The primary events take place in cell membrane and consist in coherent energization of sites of a membrane (G.Frolich) as acustoelectric waves. Q-factor of a cell membranes, as a resonator defines frequency - dependently biological effects of mm radiation. Under an operation of these waves the synthesis of various substances in a cell varies, there are new structural elements fulfilling a role of antennas for connection between cells. These elements remain until a cell (cells) restores the normal functions.

Other approach to the explanation of primary mechanisms of an operation of mm waves is advanced in the works O.Betskii and Yu.Khurgin and co-authors (1985). It is based on a representation about a primary absorption of mm-wave radiation by free molecules of water with a large dipol moment (1.84D). It will be recalled, that a flat stratum of water by a thickness 1 mm loosens an electromagnetic energy at the length of a wave $\lambda=2$ mm in 10^4 times and at $\lambda=8$ MM in 10^2 times. According to this hypothesis the basic events also occur at a membrane level of cell, but the principal elements are albuminous molecules of membrane, which under the action of a mm-wave radiation change their conformation, reset in a functional active condition, control the processes of metabolism and thus normalize vital functions of cells.

Immediately mm-wave radiation in a skin is perceived by molecules of a free, untied, quasigas fraction of water, which increase the kinetic (rotary) energy. Such thermalisation of mm-wave energy by molecules of water strengthens interchanging by energy between these molecules and molecules of water which is included in a hydrative shell of albumins. For albuminous molecules there is a critical (trigger) point of hydration, for which the connected amount of molecules of water on the surface of albumins does not exceed 1/3 full hydrative shell. As this takes place under an action of mm-wave radiation is formed functionally active conformation of albuminous molecules. Such molecules under functional-active condition control natural and chemical processes included in the common scheme of metabolism and normalize the vital functions of cells through albuminous receptors.

Skin consists of water approximately on 65 % and mm waves practically completely damp in it outside stratum , which thickness is ~0.5 mm. And, it is consequently just here in zone of a direct operation of mm waves the primary physiological targets, specialized cells realizing the whole varieties of biological effects of mm waves. Therefore skin is key plant for understanding the second biochemical stage perception of a mm-wave radiation by a human organism. Now it is possible to allocate at least four primary physiological targets. They are 1) receptors of a central nervous system (mechanoreceptors, nociceptors, free nervous terminations); 2) cells of a diffuse endocrine system (must cells, Mercel-cells); 3) immune cells (T-lymphocytes, Langergance-cell) and, at last, 4) microcapillary channels.

Studies of immunological response and reactions for mm-wave radiation were begun in an extremity 80-s'. by V.Govallo and his colleagues (CITO, 1991). They found out that under the action of mm-wave radiation on human lymphocytes and fibroblastes in vitro the factor increasing growth and functional activity of these cells - fitokin is produced in citoplasm. They demonstrated that the concentration of lactatdehydrogenese in irradiated cells increases as much as 3-5 times. Clinical investigations done by several groups of medical workers (V.Zaporoghan et al. 1991; Pivovarova et al. 1991; L.Guedymin et al. 1995; S.Zaitseva and S.Donetskaia, 1995) confirmed an important role of the human immune system in forming a responce for mm-wave radiation in treatment of a number of various diseases.

There exist some biochemical effects observed in the process of irradiation of some biological objects. I.Petroff (1992) reports in his works with wegetable cells that some increase of ATF (a universal source of energy of any cells) synthesis was observed. In agreat number of works devoted to mm-wave irradiation of blule-green aqlgal (spirulina) A.Tambiev and N.Kirikova (1990) proved convincingly, that after mm-wave radiation biologically active substances having medicinal properties are additionally produced. Experimental data and clinical studies obtained at present make it possible to state, that the mm-wave radiation at this (biochemical) reception stage first of all initiated increase of medicinal substances synthesis in organisms.

The following level is the physiological reception, when through receptors of the CNS (central nervous system), located in the skin, apudoreceptors, skin depot of T-lymphocytes, capillary channels hemovascular and lymphatic systems basic regulatory systems get included, i.e. CNS, neuroendocrine (apud-system), immune and vascular systems. The physiological mechanisms of mm-wave ineraction with the organism of humans and animals were studied in works of I.Rodshtat, N.Lebedeva and N.Temur'yan. It was shown, that the nonspecific reaction of activation developed on the various functional systems of an organism under the influence of mm-wave radiation.

The leading role among the regulatory- adaptation systems of human organism belongs to CNS. Experimental researches of N.Lebedeva with the employees (1990-98) show, that CNS reactions for a pheripheral action of low-intensity mm waves can arise both at subsensory, and sensory levels. At this pronounced character of these reactions depends on the wavelength of electromagnetic stimulus. The greatest response is observed at the impact of all therapeutic wavelengths. The resulting pattern of the cortex bioelectric activity testifies that both an advantageous participation of the nonspecific (extralemnisk) sensor system in the mm-wave radiation reception and the development of a nonspecific activation reaction, that is increase of the tonicity of the cortical area, can be observed. This opens perspectives for use of the mm-wave application in the treatment of depressipus as well as a whole number of psychosomatic diseases.

The original physiological concept is developed I.Rodshtat (1991). A key moment of his hypothesis is molecules of the skin protein-collagen fibers and its brightly expressed piezoelectric properties. They manifest themselves at the absorption of mm-wave radiation by the hydrate envelope of collagen, which results in exitation of the sensitive nervous termination in skin receptors - Ruffini corpuscles. Further on the excitation of preganglionary sympathetic neurons of the side horns of the spinal cord, exitation of the myth-neurons, which reliase adrenalin and noradrenalin into synaptic rinnal and vascular ducts.



NEW PRINCIPLES OF GENERATING AND RECEIVING MM AND SUBMM WAVES

HARMONIC MODE OPERATION OF GaAs-IMPATT DEVICES ABOVE 200 GHz

M. Claassen and H. Böhm

*Lehrstuhl für Allgemeine Elektrotechnik und Angewandte Elektronik, Technische Universität München
Arcisstraße 21, D-80333 München, Germany, E-mail: aet@ei.tum.de*

1. Introduction: IMPATT diodes deliver highest output power at microwave and mm-wave frequencies. Cw-power generation of GaAs devices in the fundamental mode is, however, limited to frequencies well below 200 GHz. This is due to the oscillation condition which requires a negative dynamic device resistance that exceeds the loss resistances of device contacts and resonator. The negative diode resistance decreases with frequency and cannot be further enhanced by higher dc-current density because of thermal considerations.

The operation principle of IMPATT devices bases on periodic carrier generation by impact ionisation and transit-time delay of drifting carriers. The carrier multiplication by impact ionisation causes a strong nonlinearity that acts as a nonlinear inductance in the avalanche region. This effect can be used for internal frequency multiplication in the oscillating device thus generating output power at harmonic frequencies. There exists only few work about this specific property of the IMPATT diode [1], whereas for Gunn devices harmonic mode operation is a well practised method to achieve output power at elevated frequencies [2].

In this paper, the harmonic operation of self-pumped mm-wave IMPATT diodes is described and the power conversion is explained. Numerical calculation of both, active device and resonator, is compared with the experimental result of 1mW output power at 210 GHz.

2. Diode Simulation: In order to study the harmonic mode operation of IMPATT devices, a time domain large-signal drift-diffusion model [3] was applied which had been adjusted to Monte Carlo simulations in the high-field high-frequency regime. For the device structure, a double-drift Read-type diode (Fig. 1) with variable drift-region lengths is chosen which is similar to devices that have been applied experimentally with success for fundamental mode operation above 100 GHz [4]. To the active region of this device, fundamental as well as second harmonic voltage excitation at 105 GHz and 210 GHz, respectively, is applied with a dc-current density of 50 kA/cm². The corresponding ac-currents are determined by Fourier analysis.

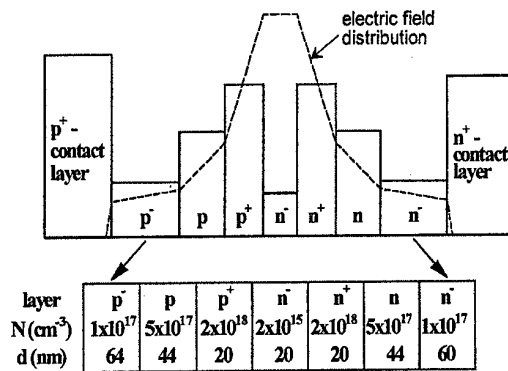


Fig. 1: *GaAs double-drift Read-type IMPATT diode structure with doping and electric field distribution*

Optimum operating conditions are found as follows: At the fundamental frequency, the oscillation condition must be fulfilled which determines fundamental frequency and amplitude. The capability of harmonic power generation improves with increasing fundamental amplitude. Therefore, a purely reactive resonator impedance is advantageous at the fundamental frequency leading to high oscillation amplitude. In the simulations, this is attained by choosing in each case a fundamental amplitude where the negative device resistance just compensates the losses. At the harmonic frequency, it is found that the active region of the device can in the interesting operation range be represented by an ideal current source I_{20} (driven by the fundamental voltage) and a constant internal admittance Y_{12} (Fig. 2). To this, the loss resistance R_{loss} has to be added in series.

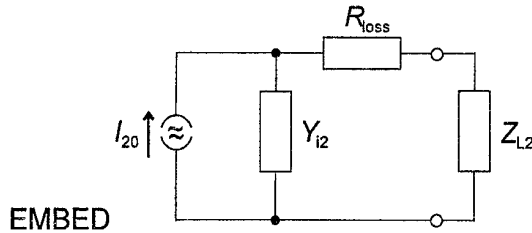


Fig. 2: The equivalent circuit of the self-pumped IMPATT device at the harmonic frequency.

Maximum output power at the harmonic frequency is achieved when the load impedance Z_{L2} is matched to the sum of $1/Y_{12}$ and R_{loss} . The attainable harmonic output power $P_{L2,max}$ is thus easily found from the equivalent circuit elements:

$$P_{L2,max} = \frac{|I_{20}|^2}{8 |Y_{12}|^2 \cdot \operatorname{Re} \left\{ \frac{1}{Y_{12}} + R_{loss} \right\}}$$

To calculate I_{20} and Y_{12} , only two simulations are required: one without harmonic voltage to attain I_{20} and one with arbitrary harmonic to derive Y_{12} from the change of harmonic current. This is sufficient to describe the device capabilities in harmonic mode operation and can be used for optimisation of the device structure, primarily of the appropriate drift region lengths. The lengths of the drift zones must be reduced with respect to the optimum lengths at the fundamental frequency, but they should be larger than for fundamental mode operation at the double frequency. Lengths of about 100 nm were found to be advantageous for both drift regions (n plus n'-zone and p plus p'-zone adjacent to the contacts in Fig. 1) for a selected harmonic frequency of 210 GHz (from which an optimum frequency in the fundamental mode of about 140 GHz would arise).

The further results for optimum harmonic operation at 210 GHz are as follows: Using a device area of $4 \cdot 10^{-6} \text{ cm}^2$, a purely inductive resonator impedance of $j 10 \Omega$ is needed at the fundamental frequency. This leads to a fundamental voltage amplitude of nearly 10 V, whereas the dc-voltage is about 11 V. The internal current source amplitude amounts to $|I_{20}| = 120 \text{ mA}$ and the internal admittance to $Y_{12} = (0.026 + j 0.227) 1/\Omega$. With a typical contact loss resistance of $R_{loss} = 1 \Omega$, this results in an attainable harmonic output power of $P_{L2,max} = 23 \text{ mW}$. The corresponding resonator impedance at the harmonic frequency is $Z_{L2} = (1.5 + j 4.35) \Omega$.

3. Resonator Simulation: For harmonic mode operation, the resonator should exhibit an inductive load at the fundamental frequency, whereas at the harmonic frequency an appropriate impedance for power matching is desirable. The resonator used for the experiments has a disc structure in a full height D-band waveguide (Fig. 3). In order to minimise mounting parasitics, a self-carrying structure is applied. This mounting technique - three monolithically integrated diodes below a common cap - can be achieved with high precision and reproducibility using monolithic processing which has been applied successfully for fundamental mode power generation in the mm-wave range [5].

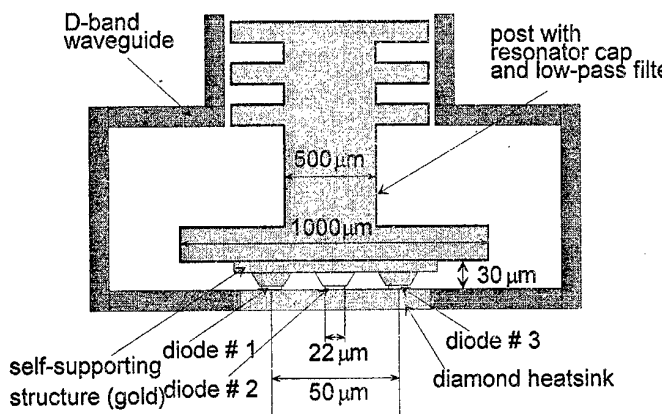


Fig. 3: Waveguide mount with self-carrying structure of three monolithically integrated diodes

The resonator impedance as seen from each single diode was numerically calculated by the help of the High Frequency Structure Simulator (HFSS) from Hewlett Packard. At the fundamental frequency, the desired inductive load of $j 10 \Omega$ is quite well achieved independently from sliding short position. The impedance at the harmonic frequency can be shifted in some range by the sliding short, but the minimum attainable value amounts to about $(10 + j 55) \Omega$. This is fairly far from the above calculated optimum impedance for power matching, but some output power can always be extracted from a device as characterised by the equivalent circuit in Fig. 2. This property of harmonic mode oscillators differs distinctly from the fundamental mode, where impedance matching to the oscillation condition is necessary to get any oscillation. In Fig. 4, the output power P_{L2} of each diode is shown versus the load impedance Z_{L2} . With the calculated impedance of the experimental resonator, only 0.5 mW output power can be expected per diode.

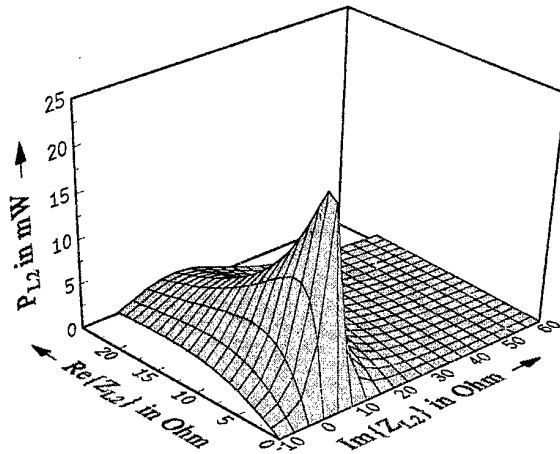


Fig. 4: Output power P_{L2} at harmonic frequency versus load impedance Z_{L2}

4. Experimental Results: For the first experimental investigations, a D-band disc resonator as described above with three monolithically integrated double-drift Read-type IMPATT diodes is used. The diode structure is similar to a typical 140 GHz double-Read IMPATT diode [4]. The diodes (device area $4 \cdot 10^{-6} \text{ cm}^2$) are driven with a dc-current density of 50 kA/cm^2 . The achieved total output power is 1 mW at the harmonic frequency of 210 GHz [6]. This fits quite well to the calculations.

5. Conclusion: In this work, theoretical and experimental investigations concerning power generation by second harmonic operation of self-pumped IMPATT diodes are described. The active device is characterised by a time-domain drift-diffusion model driven at fundamental and superimposed second harmonic frequency. The applied disc-type resonator structure is investigated by a commercial simulation program. Using a low parasitic encapsulation method and power combining of three active devices, 1 mW cw-output power at 210 GHz were obtained, a value which was not achievable in fundamental mode operation so far.

Acknowledgement: Financial support of Deutsche Forschungsgemeinschaft (SFB 348) is kindly acknowledged.

References

- [1] Rolland, P. A., Vaterkowsky, J. L., Constant, E., Salmer, G., "New modes of operation for avalanche diodes: Frequency multiplication and upconversion", IEEE MTT-24, 1976, pp. 768-775
- [2] Barth, H., "A wideband backshort-tunable second harmonic W-band Gunn-oscillator", IEEE-MTT-S Int. Microwave Symp. Dig. 1981, pp. 334-337
- [3] Gaul, L., Claassen, M., "Pulsed high-power operation of p^+pnn^+ -avalanche diodes near avalanche resonance", IEEE Trans. Electron Dev., 41, 1994, pp. 1310-1318
- [4] Tschernitz, M., Freyer, J., "140 GHz Double-Read Impatt diodes", Electron. Lett., 31, 1995, pp. 582-583
- [5] Bauer, T., Freyer, J., "New mounting technique for two-terminal millimeter-wave devices", Electron. Lett., 30, 1994, pp. 868-869
- [6] Böhm, H., Freyer, J., Claassen, M., Harth, W., Bauer, T., "Second harmonic power generation from GaAs-IMPATT diodes at 210 GHz", Int. J. Infrared and Millimeter Waves, 19, 1998, pp. 587-593

Mixing of 28 THz CO₂-Laser Radiation by Nanometer Thin-film Ni-NiO-Ni Diodes with Difference Frequencies up to 176 GHz

C. Fumeaux¹, W. Herrmann¹, F.K. Kneubühl¹, H. Rothuizen², B. Lipphardt³, C.O. Weiss³

¹ Institute of Quantum Electronics, Swiss Federal Institute of Technology (ETH), CH-8093 Zürich, Switzerland

(Tel.: +41-1-633 23 40, Fax: +41-1-633 10 77, e-mail: infrared@iqe.phys.ethz.ch)

² IBM Research Laboratory, Säumerstrasse 4, CH-8803 Rüschlikon, Switzerland

³ Physikalisch-Technische Bundesanstalt (PTB), D-38116 Braunschweig, Germany

Abstract

Difference frequencies up to 176 GHz between CO₂-laser transitions at 28 THz (10.7 μm) are generated by thin-film nanometer-scale Ni-NiO-Ni diodes (MOM, MIM) with integrated bow-tie antennas and rhodium waveguides.

high-frequency transmission and permit the illumination of the antenna from the back side of the substrate.

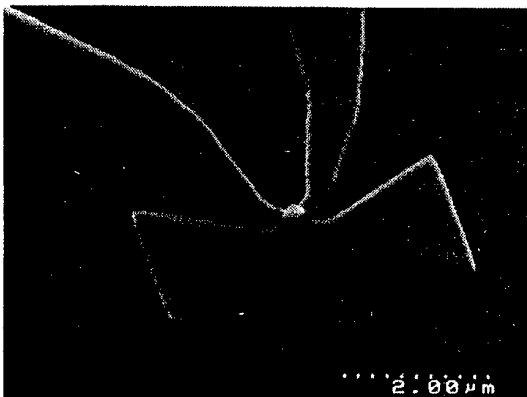


Fig. 1: Electron micrograph of our thin-film Ni-NiO-Ni diode with integrated bow-tie antenna

The mixing of infrared radiation with point-contact Metal-Oxide-Metal (MOM) diodes was first demonstrated by Hocker et al. in 1968 [1]. Since then, the range of operation of these devices has been extended to the visible [2]. These diodes have been intensively used in absolute frequency measurements and high-resolution spectroscopy. In 1973, Javan and co-workers [3] reported the first fabrication of thin-film diodes and demonstrated their mixing capability at approximately 1 THz. In this paper we report on the first successful mixing of two 28 THz (10.7 μm) CO₂-laser transitions in the 10P branch with difference frequencies up to 176.2 GHz performed by thin-film Ni-NiO-Ni diodes with integrated bow-tie antennas (Fig. 1) and new integrated rhodium waveguides. The fast response of our Ni-NiO-Ni diodes is due to their extremely thin NiO layer required for nonlinear electron tunneling and to their sufficiently small contact area of 110 nm × 110 nm that implies a short RC time constant. The fabrication and development of our thin-film Ni-NiO-Ni diodes with integrated dipole, bow-tie and spiral antennas and their application to the detection of 10 μm CO₂-laser radiation is described elsewhere [4-6]. First mixing experiments with our thin-film diodes are reported in [7]. They resulted in difference frequencies up to 85 MHz.

For the measurements described here, the diode is based on a high-resistivity (> 3 kΩ·cm) silicon substrate with weak losses in the microwave region [8] and low attenuation of the antenna currents at infrared frequencies. The previous connections to the diode with bond-wires [7] have now been replaced by coplanar rhodium waveguides and indium solder flip-chip connections, which guarantee excellent

The radiation of two CO₂-lasers with wavelengths near 10.7 μm was focused on the diode. The total infrared power on the diode was approximately 400 mW. The two lasers constitute part of the permanent frequency-measurement chain of the PTB (Braunschweig, Germany) [9]. Part of the mixing performed is shown in Table 1. In the second-order mixing experiment, the difference-frequency signal of two adjacent laser lines at 58.7 GHz was externally mixed with microwaves and measured with a spectrum analyzer. The higher-order mixing processes required irradiation of the diode with the microwaves produced by a Gunn oscillator working at the frequencies 58.8 GHz ± 50 MHz. The measured mixing signals listed in Table 1 show significant signal-to-noise (S/N) ratios, especially in the third-order mixing with 47 dB for a bandwidth of 100 kHz (Fig. 2). The highest difference frequency of 176.19 GHz was generated by mixing the 10P(30) and 10P(36) emissions with the third harmonic of the Gunn oscillator in a fifth-order mixing process.

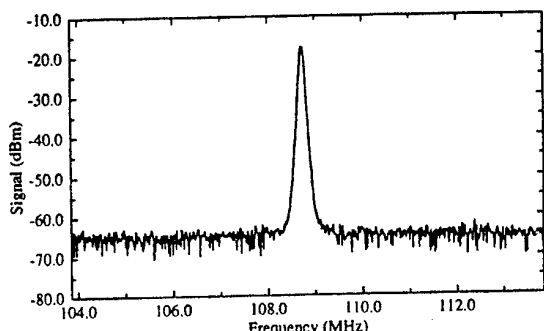


Fig. 2: Third-order mixing signal with a laser difference frequency of 58.7 GHz and a 100 kHz detection bandwidth

The mixing signals as a function of the polarization of the incident 10.7 μm CO₂-laser radiation are represented in Fig. 3 in the case of third-order mixing. The perfect polarization dependence demonstrates that our bow-tie antennas show almost complete polarization as predicted by the antenna theory of microwave techniques [10]. This can be explained by the fact that in our range of difference frequencies, the polarization-independent thermal effects are too slow to influence the mixing signal.

Our experiments represent the first mixing of 10 μm CO₂-laser radiation with thin-film MOM diodes with difference frequencies in the 50 to 200 GHz range.

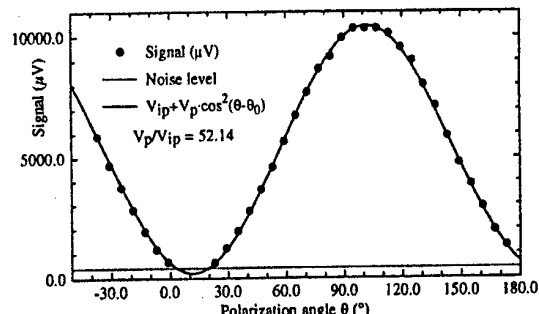


Fig. 3: Polarization dependence of the third-order mixing signal with a difference frequency of 58.7 GHz between the two CO₂-lasers

Mixing process	Mixing order	Lasers difference frequency $\Delta\nu$	S/N ratio	Bandwidth	Pol. contrast
10P32-10P34 (external mixing)	2	58.7 GHz	22 dB	100 kHz	34.4 dB
10P32-10P34 + MW 58.8 GHz	3	58.7 GHz	47 dB	100 kHz	34.4 dB
10P30-10P34 + 2 × MW 58.8 GHz	4	116.7 GHz	19 dB	100 kHz	> 25 dB
10P36-10P30 + 3 × MW 58.8 GHz	5	176.2 GHz	14 dB	300 kHz	-

Table 1: Mixing with our thin-film Ni-NiO-Ni diodes.

References:

- [1] L.O. Hocker, D.R. Sokoloff, V. Daneu, A. Szoke, A. Javan: *Appl. Phys. Lett.* **12**, 401-402 (1968)
- [2] H.-U. Daniel, M. Steiner, H. Walther: *Appl. Phys.* **25**, 7-12 (1981)
- [3] J.G. Small, G.M. Elchinger, A. Javan, A. Sanchez, F.J. Bachner, D.L. Smythe: *Appl. Phys. Lett.* **24**, 275-279 (1974)
- [4] I. Wilke, W. Herrmann, F.K. Kneubühl: *Appl. Phys. B* **58**, 87-95 (1994)
- [5] I. Wilke, Y. Oppliger, W. Herrmann, F.K. Kneubühl: *Appl. Phys. A* **58**, 329-341 (1994)
- [6] C. Fumeaux, G.D. Boreman, W. Herrmann, H. Rothuizen, F.K. Kneubühl: *Appl. Opt.* **36**, 6485-6490 (1997)

[7] C. Fumeaux, W. Herrmann, H. Rothuizen, P. De Natale, F.K. Kneubühl: *Appl. Phys. B* **63**, 135-140 (1996)

[8] A. Rosen, M. Caulton, P. Stabile, A.M. Gombar, W.M. Janton, C.P. Wu, J.F. Corboy, C.W. Magee: *RCA Rev.* **42**, 633-660 (1981)

[9] H. Schnatz, B. Lipphardt, J. Helmcke, F. Riehle, G. Zinner: *Phys. Rev. Lett.* **76**, 18-21 (1996)

[10] J.D. Kraus: "Antennas", second edition, McGraw-Hill, New York (1988)

Acknowledgements:

This study is supported by GR/EMD, Bern; Swiss Federal Institute of Technology (ETH), Zürich; and IBM Research Laboratory, Rüschlikon.

Infrared Raman Solitons, Self-phase Modulation and Self Focusing in CO₂-Laser Pumped NH₃

M. O. Baumgartner and F. K. Kneubühl

Institute of Quantum Electronics, Swiss Federal Institute of Technology (ETH), CH-8093 Zürich, Switzerland
(Tel: +41-1-633 23 40 Fax: +41-1-633 10 77, e-mail: infrared@iqe.phys.ethz.ch)

Stimulated Raman scattering is a nonlinear process, that has been studied extensively by many groups. Nevertheless, the presence of soliton-like pulses in the depletion region of the pump pulse is not yet completely understood. The origin of such spontaneous solitons is the rapid phase variation of the Stokes field induced by the quantum fluctuations of the electromagnetic field in vacuum.

With the aid of a pulsed CO₂-laser system [1] including a fast plasma shutter we have observed the first spontaneous Raman solitons in the forward stimulated Raman scattering (SRS) by the far-infrared-active laser gas NH₃. The measured SRS processes are rotational transitions at 58 μm and 72.6 μm optically pumped with pulses of preselected duration and wavelengths of 10.37 μm and 10.35 μm respectively. Our experimental arrangement shown in Fig. 1 enables us to measure the depleted pump pulse with the SRS solitons and simultaneously the scattered far-infrared radiation (FIR) with the corresponding dip. Such a measurement is shown in Fig. 2.

In addition we have measured the statistics of the relative delays and relative amplitudes of these spontaneous Raman solitons at 10.37 μm wavelength. We performed these statistics of 1000 shots with a shot to shot variation of the pulse intensity within the limit of 10%. They are shown in Fig. 3.

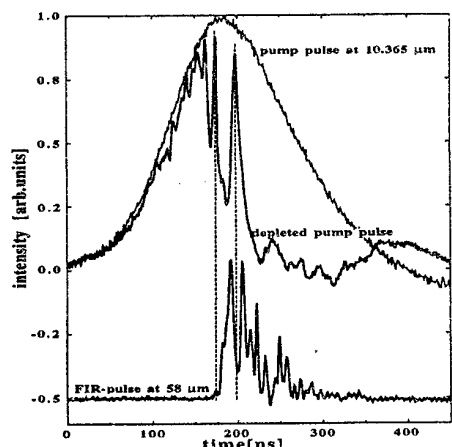


Fig.2: Multiple SRS solitons in the depleted pump pulse with the corresponding dips in the FIR

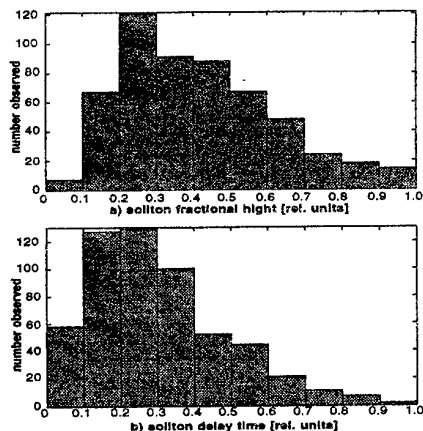


Fig. 3: Distribution of spontaneous SRS soliton fractional heights a) and soliton delay times b) measured relative to the duration of the temporal depletion region

For 260 of these 1000 shots we observed unambiguous multiple solitons within one pump pulse. In total we measured 550 solitons in our 1000 pump pulses. Subsequently, we compared these results with earlier measurements performed by MacPherson et al. [2] in para-hydrogen pumped by a frequency doubled Nd:YAG laser and with the calculations by Englund and Bowden [3].

As reported by Girdauskas et al. [4] the mutual diffractive focusing of laser and Stokes beams has a strong influence on the gain of the observed SRS as well as on the process of Raman soliton generation. Therefore, we have measured the

magnitude of self focusing shown in Fig. 4 for two different intensities of the CO₂ 10(R4) laser transition. In this figure the relative intensity is the intensity transmitted through an aperture at the end of the FIR cell versus the total intensity of the laser beam. In order to determine the nonlinear refractive index n₂ for NH₃, we have measured for the first time the corresponding self-phase modulation with the set-up shown in Fig. 5. Fig. 6 shows the result for the 10.37 μm (10R4) CO₂ emission. The total self-phase modulation is a linear function of the NH₃ gas pressure due to the maximal relative refractive index change of Δn_{max}/n₀ = 5*10⁻⁷. Making use of these data we evaluated the cubic refractive index n₂ as a function of the NH₃ pressure. Thus we determined the nonlinear refractive index n₂ for the CO₂-laser emissions 10(R4), 10(R6) and 10(R8). No phase change could be observed at 9(P20). This is in agreement with the fact that NH₃ has no vibrational resonance at that wavelength.

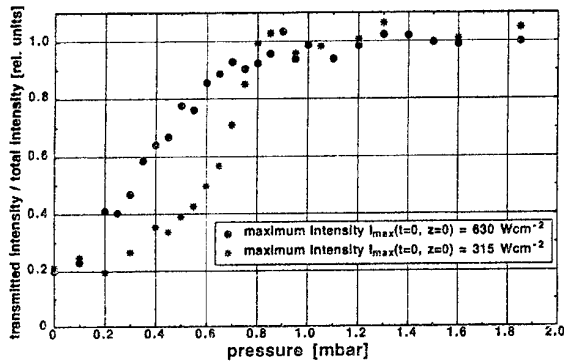


Fig. 4: Self focusing of a TEM₀₀ CO₂-laser pulse with a transversal radius of the intensity r_e = 8.4 mm and a duration of t_e = 88 ns.

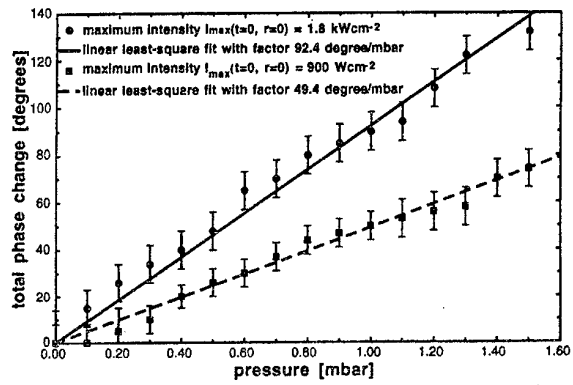


Fig. 6: Self-phase modulation of 10(R4) CO₂-laser pulses as function of the NH₃ pressure in the 7.5 m FIR cell.

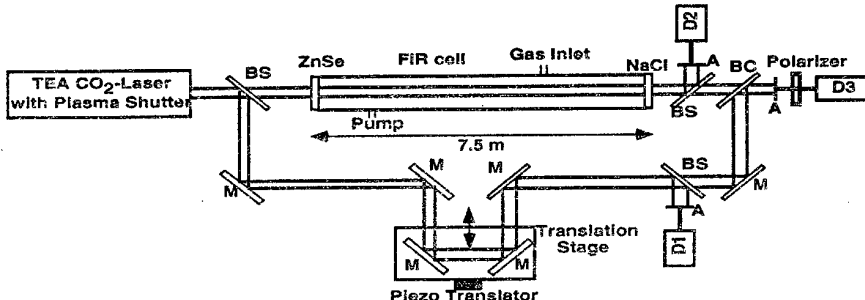


Fig. 5: The set-up for the measurement of the total self-phase modulation in NH₃ includes BS: beam splitter, BC: beam combiner, M: mirror, A: aperture, D1-D3: fast HgCdTe-photocurrent detectors for 10 μm radiation. Aperture A insures that only the onaxis modulation is measured.

References:

- [1] A. W. Kälin, R. Kesselring, Cao Hongru and F. K. Kneubühl, *Infrared Phys.* **33**, 73-112 (1992)
- [2] D. C. MacPherson, R. C. Swanson and J. L. Carlsten, *Phys. Rev. A* **40**, 6745-6747 (1989)
- [3] J.C. Englund and M. C. Bowden, *SPIE Conference Proceedings No. 874*, "Nonlinear Optical Beam Manipulation, Beams Combining in Atmospheric Propagation", 218 (1988)
- [4] A. Dement'ev, V. Girdauskas and A. Rodin, *SPIE Conference Proceedings No. 2800*, ICONO95, "Nonlinear Optical Interactions and Wave Dynamics", 341-350 (1995)

Acknowledgements:

This study is supported by the Swiss National Science Foundation and ETH Zürich.

SEMICONDUCTOR MICROWAVE DEVICE IN HSRI OF CHINA

Li Songfa, Hebei Semiconductor Research Institute
 P.O.Box 179, Shijiazhuang, Hebei, 050002, China
 Tel: +86 311 7041921 Fax: +86 311 7045695
 E-mail: hsri@public.sj.he.cn

Abstracts: The paper introduces some progress on semiconductor microwave devices in Hebei Semiconductor Research Institute (HSRI) of China. The scope of this paper will include silicon power transistor, A_3B_5 materials and devices, InP crystal, GaAs and InP based heterostructure epi-wafers, power microwave transistor and MMIC as well as Various 8mm monolithic IC.

1. Introduction

HSRI was founded in 1956, Beijing. In 1963 HSRI was moved to Shijiazhuang, the capital city of Hebei province. The main developing direction of the Institute is to develop various semiconductor devices. In the recent years, we have got some progress in the area of Si VDMOS high power transistor and power GaAs MESFET. We also got some results on the GaAs and InP based heterostructure epi-wafers and devices. The main result is stated as following.

2. Silicon power VDMOS RF transistor

Si VDMOS power transistor has good future. It has been widely used in the electronics systems, because of its special features on the electrical performance and excellent reliability. We developed Si power VDMOS RF transistor with Mo-Al gate electrode using normal diffusion and ion-implantation process. In order to improve the parameters of the transistor, special oxidation and some additional annealing steps also adapted. We developed VDMOS transistor with one chip from which could get 80W output with 11dB gain under 400MHz and class B configuration. The transistor with two or four chips also gets good results. The main typical parameters of these VDMOS transistors are listed in table 1.

Table 1. typical parameters of VDMOS transistors

Transistor number*	Test Conditions		P_{out} W	I_D A	η_D %	G_P dB
	V_{DD} V	P_{in} W				
1-34	50	6	82	2.7	60.7	11.4
1-35	50	6	80	2.65	60.4	11.2
2-26	50	12	146	5.2	56.2	10.9
2-28	50	15	156	5.2	61.1	10.2
4-14	50	35	302	11.1	54.4	9.4
4-15	46	25	250	10.0	54.3	10.0

* The first number means the number of chips.

All of the multichip devices without internal-matching give some flexible selection on the frequency-band. But losing some power capability. Some necessary improvement will be done in near future.

3. Microwave power GaAs MESFET

Power GaAs MESFET could be mainly used in the C, X and Ku band, it also could be used in the L and S band even more lower frequency band with excellent performance under reasonable electric circuit design. For manufacturing of the power GaAs MESFET we start from MBE multilayer epi-wafer with n^+ contact layer, the chip manufactured with $0.5\mu m$ TiPtAu recessed gate, AuGeNiAu multilayer Ohmic contact metallization, silicon nitride passivation, plated via holes and $50\mu m$ -thick chip with additional heat sink to provide excellent thermal performance and very low source-grounding inductance. HSRI has developed a series of power GaAs MESFET products for different frequency band. Some of them are listed in table 2.

table 2. Performance of GaAs MESFET products

Type	RF Test Condition			P-1dB	G-1dB	Idss (mA)	G_m (ms)	$V_{G(on)}$ (V)
	V_{DS}	Idss	f	(dBm)	(dB)			
CS0467	8	0.4-0.6 Idss	12GHz	21	7	170	60	-3
CS0536	8	0.4-0.6 Idss	4GHz	27	13	300	150	-2.5
			8GHz	26	10			
CS0513	8	0.4-0.6 Idss	4GHz	32	10	800	350	-2.5
			8GHz	31	8			
DX0012	8	0.4-0.6 Idss	4GHz	34	9	1000	600	-2.5
			8GHz	33	7			

All the devices listed in table 2 were assembled with single chip. HSRI also uses chip and some larger gate-width chip internal matched power transistor. HSRI has developed 4GHz 25W, 6GHz 20W, 11-12GHz 15-16W, 12-14GHz 8-10W internal matching power GaAs MESFET in the laboratory, but now we are going to produce these high power GaAs MESFET, if some customers request these internal matching devices.

4. A_3B_5 heterostructure epi-materials and devices

A_3B_5 heterostructure epi-materials has been researched for more than 10 years with MBE and MOCVD system in HSRI. We use SI GaAs and InP substrate to growth different structure mainly for HEMT(PHEMT) combined with $0.1-0.25\mu m$ T-gate technology. HSRI has developed HEMT low noise monolithic amplifier at $f_c=36GHz$ with $F_n \leq 4dB$ and $G_a \geq 20dB$ as well as PHEMT medium power devices at 35GHz with $P_o=80mW$ and $G_a=5.1dB$. But these devices are only the samples in laboratory. HSRI wish to speed up the development of these new devices and make it to be more practical and useful in the nearest period.

5. InP crystal

HSRI has more than 20 years experience on pulling InP crystal. These InP crystal could be used for microwave and millimeter wave devices as well as optical-electronics devices. Their typical parameters are

listed in table 3. The feature of the pulling process is high purity Indium and Phosphide directly composed in the high-pressure chamber then directly pulling out single crystal ingot to avoid additional contamination. High quality of the crystal has been confirmed by several labs both in domestic and abroad.

Table 3. Some performance of InP crystal ingot.

Conductive type	N			ρ	Semi-insulator
Dopant	None	S	Sn	Zn	Fe
carrier concentration (cm^{-3})	$2-10 \times 10^{15}$	$3-10 \times 10^{18}$	$5-30 \times 10^{17}$	$4-6 \times 10^{18}$	Resistivity 1. $\geq 10^6$ 2. $\geq 10^7$ ($\Omega \cdot \text{cm}$)
mobility $\text{cm}^2/\text{V.S}$	3500-4500	800-1500	1200-2500	50-100	
E.P.D. cm^{-2}	10^4-10^5	1. $<5 \times 10^3$ 2. <500	$<5 \times 10^4$	$<5 \times 10^3$	5×10^4
Diameter	$\Phi 35\text{mm}$ $\Phi 50\text{mm}$ ($\Phi 75\text{mm}$)				
Orientation	$<111>$, $<100>$				

6. Conclusion

Some good result on semiconductor material and microwave device has been gotten in HSRI, our institute is going to look for the new cooperation partners.

Thanks for your attention.

ANTENNA - COUPLED SCHOTTKY DIODES FOR MILLIMETER WAVE RECEIVERS

E.O. Iounevitch, V.E. Lioubtchenko
 Bildg.1, Vvedenskii sq., Fryazino, Moscow Region, 141120, Russia
 Tel.: 8(095)526-92-17, E-mail: dvl176@ire216.msk.su

One of the most actual tasks in creation of communication and imaging systems in millimeter wavelength range is the creation of miniature receiving modules, including antenna and nonlinear element. These modules can be dipole planar antenna loaded directly by the detector diode (rectenna). For increasing an effective area the receiving rectennas can be coupled in arrays. A dipole log-periodic rectenna at thick dielectric lens was investigated in [1] and a slot antenna, coupled with a cavity 0.21λ in depth was investigated in [2]. In both cases the antenna has smooth unidirectional radiation pattern (RP), however its width is rather large ($50 - 60^\circ$). In [3] it was shown that metallization of back side of dielectric plane increases rectenna sensitivity, however the effect of such metallization on RP and dependence of it on dielectric thickness were not studied.

In this work a microstrip log-periodic rectenna was formed by photolithography at dielectric substrate and microwave diode 3A147B was mounted directly in the arms of it (fig. 1).

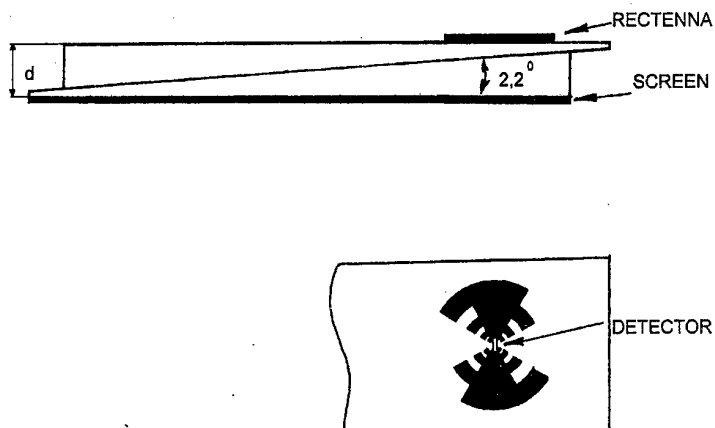


Fig. 1. Model of tuned rectenna.

A metal screen layer was deposited on the back side of the substrate. Substrates were made as wedges with angle of 2.2° and shifting them relatively to each other one could change the distance from rectenna to the screen smoothly, with cavity being tuned under rectenna. Rectenna response dependency on dielectric thickness expressed in wavelengths in dielectric is shown in figure 2.

From this figure one can see that rectenna sensitivity is minimal at the dielectric thickness of 0.5λ and λ and reaches its maximum at those of $\lambda/4$ and $3\lambda/4$ that in general corresponds to the picture of standing waves. Investigation of the radiation pattern of rectennas with different thickness and in frequency range shows that at the absence of the screen RP is rather wide ($\sim 60^\circ$) and very nonuniform (fig. 3), the position of maxima and minima depending on frequency. This results in strong frequency dependency of the response when the antenna is stable.

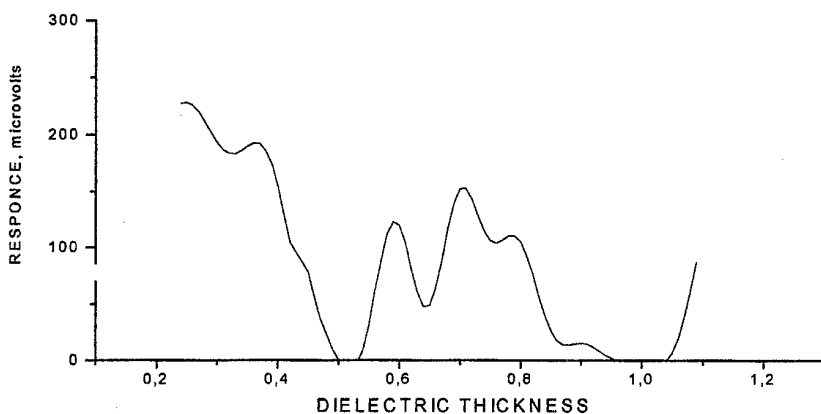


Fig.2. Rectenna response on dielectric thickness (d/λ).

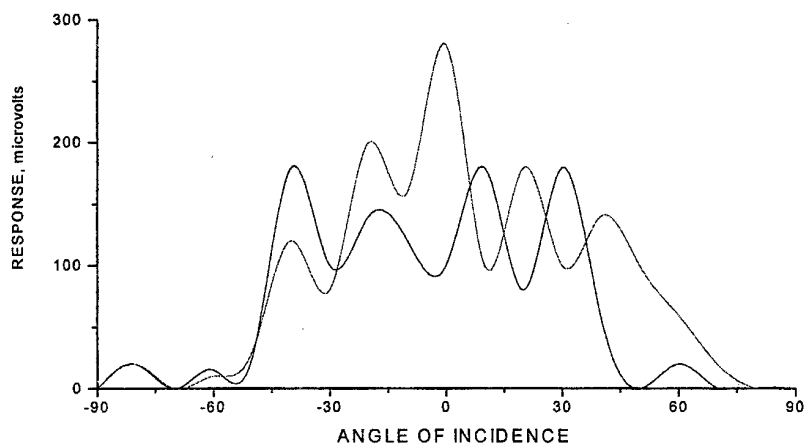


Fig. 3. RP of rectenna without screen at 42 and 45 GHz.

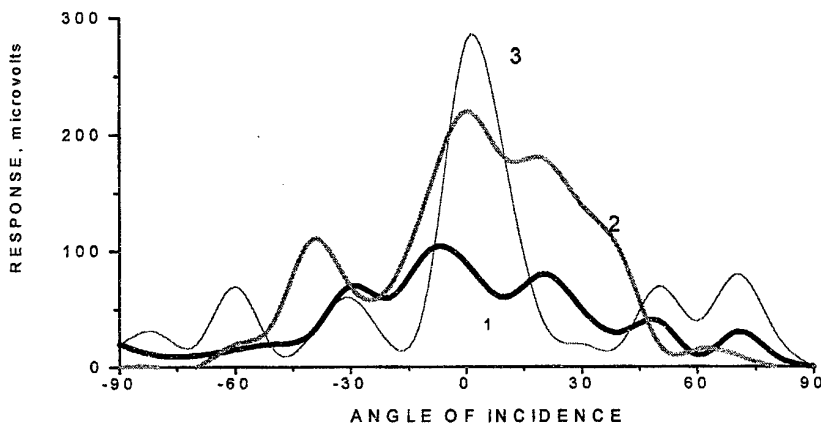


Fig. 4. RP of rectenna: 1 - without screen; 2 - the screen is at the distance of $0,31\lambda$; 3 - the screen is at the distance of $0,59\lambda$.

Using of the reflecting plane allows to get an antenna with much more narrow and smooth radiation pattern. RP of rectennas at 60 GHz in E-plane without a screen and with the screen at two different dielectric thickness are shown in figure 4.

According to measurements of general parameters the log-periodic rectenna without the screen has the width of the main peak 60° at the level of 0,7 and sensitivity in maximum is equal to $600 \text{ mV}/(\text{mW/cm}^2)$; rectenna with the screen at the distance of $0,31\lambda$ has correspondingly 40° and $1500 \text{ mV}/(\text{mW/cm}^2)$, and rectenna with the screen at the distance of $0,59\lambda - 12^\circ$ and $2000 \text{ mV}/(\text{mW/cm}^2)$. It is necessary to note that all rectennas with the reflective screen are narrow-banded ($\sim 2 \text{ GHz}$) and there can be some narrow bands of receiving in the frequency range under investigation ($30 - 60 \text{ GHz}$). Despite a general complexity of the picture the measurements allowed to discover some general features. So while using rectennas with dielectric thickness $0,25 - 0,4\lambda$ RP in E-plane has large width ($30 - 40^\circ$) and a large level of side peaks is sometimes more than the main peak. RP in H-plane has as a rule two main peaks.

At the dielectric thickness about $0,6\lambda$ RP becomes narrower up to 10° , the level of side peaks decreases too up to -15dB . In this case the radiation pattern in H-plane is formed with a centralized and very narrow peak.

The results obtained qualitatively can be explained as follows. With a quite large thickness of a dielectric and the presence of a reflective screen conditions for propagation of a surface wave in a dielectric are formed, with a power part being transformed into the antenna increasing its sensitivity. Contradiction in sensitivity received in this work and shown in [3] and [4] where sensitivity was obtained of the order of $300 \text{ mV}/(\text{mW/cm}^2)$ is probably explained by this phenomenon. The conditions of wave existence in a dielectric are of resonant character and depend both on the angle of incidence of a space wave and the distance between the antenna and the screen, it determining strong dependency of the RP form on a substrate thickness.

For increasing of the output signal and consequently the distance of communication rectennas can be coupled in arrays. This coupling was made either in series or in parallel. The parallel coupling provides individual bias and optimization of diode operation regime, operation reliability being maximum. In this case failure of certain diode does not affect the operation of the others. However the creation of individual bias network for every diode is necessary and output impedance decreases that makes difficult matching with amplifier at a low or intermediate frequencies. At coupling in series in this case one bias source is necessary but reliability decreases and impedance increases. Furthermore because of diode parameter dissipation a common current of bias is not optimal. Experiments show that an output signal grows proportionally to diode amount only for to 3 - 4 diodes. Compromise can be achieved at mixed switching as parallel chains of 3 - 4 diodes coupled in series. Using of low barrier diodes appears to be very prospective, as their maximum response takes place at zero bias. In [5] detective characteristics of diodes with different barriers were investigated and it was found that optimal barrier height is the value of $0,25 - 0,35 \text{ eV}$.

Multielement arrays of antenna-coupled diodes may be applied for portable telecommunication systems instead of microstrip antenna arrays like used in [6]. In contrast to them rectenna arrays allow to summarize the signals from detectors at low and intermediate frequencies, that simplifies the technology and design of the receiving devices.

References

1. C.Richard Compton, C.Ross McPhedran at al., "Bow-Tie Antennas on a Dielectric Half-Space: Theory and Experiment", IEEE Trans. On Antennas and Propagation, Vol.AP-35, No. 6, pp. 622-631, 1987.
2. H.Peter Siegel, "A Planar Log-Periodic Mixtenna for Millimeter and Submillimeter Wavelengths", IEEE MTT-S Digest, pp. 649-651, 1986.
3. Л.В. Волков, В.Е.Любченко, С.А.Тихомиров, "Двумерные матрицы антенно-связанных диодов с барьером Шоттки для формирования изображений в миллиметровом диапазоне волн", Радиотехника и Электроника, Т.40, № 2, с. 322-324, 1995.
4. K.M.Strohm, J.Buecher, J.F.Luy, "90 GHz SIMMWIC Rectennas", Proc. XXII European Microwave Conf. Helsinki, pp. 608-613, 1992.
5. Т.А.Брянцева, В.Е.Любченко, Е.О.Юневич, "Диоды Шоттки с пониженным барьером на основе тонкопленочных контактов Au+Ge/GaAs", Радиотехника и Электроника, Т.40, № 8, с.1306-1310, 1995.
6. T.Ninomiya, T.Saito, Y.Ohashi, H.Yatsuka, "60-GHz Transceiver for High-Speed Wireless LAN System", IEEE MTT-S Digest, p.1171, 1996.

DYNAMIC AND NOISE PARAMETERS OF THE POWER ADDERS USING THE MULTISTRUCTURAL IMPATT DIODES

A.A. Nikitin, A.S. Shapovalov

Address: 83, Astrakhanskay St., Saratov State University, Physics Dept., Saratov, 410026, Russia
Tel.: 51-46-88, Fax: +7(845-2)24-04-46, E-mail: Post master @ scnit. saratov.su

The development of a modern microwave semiconductor electronics in a direction of increase power level of the generated oscillations results in necessity of use in the circuits of power addition at a level of a common resonator multistructural Impatt diodes (MSID). Specific features of the impedance performances of MSID of a short-wave part of a centimetric range are presence of a resonance of a parallel type near to the top border of a working range of frequencies, the high meanings of resonant resistance (thousands Ohm) and Q-factor (tens units) oscillatory system MSID, formed by the reactive elements of the case of the diode. The brightly expressed resonant properties and essential reactance so distinguish MSID from one-structural analogues, that direct use of results earlier carried out researches on problems of the matching, frequency retuning, power summation, decrease of noise and designing of adders as a whole appears impossible. These circumstances cause significant difficulties with creation of the tunable generators of the indicated frequency range having an increased level of power and a low level of noise. The overcoming of these difficulties causes the necessity of introduction into known designs of power adders (in particular, in the Kurokawa waveguide-coaxial circuit) the principal changes influencing to a certain extent on various output parameters. It is necessary to take into consideration that the realization of the given complex of generator output parameters needs the quite certain changes in a design. For clearing up of a parametrical potential of various modifications two-diodes waveguide-coaxial adder on MSID and possibility of a choice of the circuit with an optimum combination of output parameters appropriate to a functionality of generator, the several variants of its constructions were carried out and comparative experimental investigated.

A Kurokawa circuit was used as the initial design of the power adder. Coaxial modules of the initial design containing MSID of the type 3A748 at one end and matched load at the opposite end were placed in the planes of the narrow walls of the rectangular waveguide resonator. Diode fastening unit allowed to adjust its displacement along an axis of a coaxial and by that to change the length of the reentrant coaxial resonator. The steady generation of such design was observed only with use in the coaxial resonator of a complex matching chain — impedance transformer containing three sections of a coaxial line. The similar generator was characterized by criticality for tuning and its complicity; difficulty of the selection of geometry matching circuits with three degrees of freedom and coupling element with waveguide; low efficiency ratio owing to losses in matched load, impedance transformer and coupling elements; insignificant mechanical (by short-circuiting piston of the waveguide) and electrical (by feeding current of the diodes) retuning on frequency; high noise level. While diod power of the order 2,5 W, the level of generated power reached only hundreds of milliwatts, frequency retuning was restricted to several megahertz the level of amplitude noise at 10 kHz from the carrier was equal to (-125) dB/Hz, the level of phase (frequency) noise for a named tuning off a carrier was equal to (-50 ± 55) dB/Hz.

The second design of the power adder differed from the previous one by the construction of coaxial modules. The central conductor of coaxial was cut off. It means that it was a pin radiator with adjustable depth of immersion in the summing resonator. The matched load at the end of coaxial was replaced by a short-circuiting coaxial piston, which was an additional element of the matching and tuning of the generator. The design provided an opportunity of independent change of lengths both of the coaxial reentrant resonator and of the short-circuited coaxial line. The indicated constructive changes in a design provided the possibility of easier tuning and stability in operation of the generator, occurrence of electrical retuning of frequency, high power and noise parameters. The power output level reached 4,6 W, factor of summation — 0,92. The electrical frequency retuning band was within the limits of 10–30 MHz. The mechanical frequency retuning range has remained insignificant. The level of amplitude noise at the mentioned tuning off a carrier has decreased to (-147 ± 150) dB/Hz, level of phase noise — to (-87 ± 90) dB/Hz.

The basic difference of the third variant of the adder from the second one was that the pin radiator was changed by an extended central conductor, which passes through all coaxial module from the diode up to short, but has an adjustable capacitance gap in the field of the summing resonator. With some reduction of quality of the power and noise characteristics in such design there is a mechanical retuning of frequency in a band of width 260 MHz, and the electronic retuning band extends up

to 45 MHz. The power of generated oscillations was 4,15 W, factor of summation — 0,83. The level of amplitude noise was equal (-150) dB/Hz, level phase noise — (- 65) dB/Hz.

With the purpose of expansion of a band of mechanical retuning of frequency the fourth modification of the adder was developed. This modification differed from previous designs both composition and arrangement of coaxial modules. Coaxial modules were displaced from planes of narrow walls of the summing resonator to its centre at a distance of $a/4$ (and a — size of a wide wall of the resonator). The central conductors of coaxials were continuous. For increasing the quality factor of the reentrant coaxial matching resonator the diaphragm was been put at the plane of intersection of each coaxial module with a wide wall waveguide from the side of the diode. Possessing much higher quality factor than at the summing resonator, the reentrant coaxial matching resonator ordains the parameters of the generated oscillations, including their fluctuation level. Therefore the increase of its quality factor partially compensates the reduction of output power and the increase of noise level of generated signal, which, as a rule, accompany with the effect of extension of the frequency retuning range. The bandwidth of the mechanical frequency retuning of the similar adder (on a level 3 dB) reached 1,2 GHz, and electrical — 100 MHz, i.e. accordingly 6 % and 0,5 % of carrying frequency. Power output reached 4,75 W, and summing factor -0,95. Fluctuations level of signal remained approximately such as in the third version of the unit. The amplitude noise level was $-(145 \pm 150)$ dB/Hz, and a phase noise level was (-65) dB/Hz.

The comparison of the parameters of the investigated modifications of the waveguide coaxial generator showed, that from the point of view of power and noise parameters. the second variant of a design was the best. The fourth design is most attractive from a position of a range of mechanical and electrical retuning of frequency. Besides, the fourth unit version is preferable because of the best complex of all output parameters.

The experimental researches also have shown, that the last three modifications of the two-dioid oscillators are able to effective work both autonomously and as a part of a multiunit summing device, when they are connected in a sequent chain. It leads to a significant increase of output power while keeping high enough summing ratio and other output parameters.

The constructive principles of power summing, frequence retuning and noise decrease in power adders with MSID, designed for short wave part of a centimetric band, seems to be promising for millimetric band (some experimental samples of such diodes worked at the frequency range up to 30 GHz). Taking it into consideration we may say, that the results of the present study will find a use for solving such problems of generatorsa on the base of MSID also in millimetric band.

THESIS'S ABOUT GUNN DIODE WORK WITH TWO TRANSIT-TIME REGIONS AND HETEROJUNCTION BETWEEN THEM

I.Storozhenko

Radiophysical department of Kharkov State University
4, Svoboda sq., Kharkov, 310077, Ukraine
Tel. (0572) 43-08-83

One the methods of increasing the output power and enlarging the work range frequency of Gunn diodes is search of optimal diodes construction. There were shown research works of GaAs diodes use with different semiconductor compounds in $In_xGa_{1-x}As$, $InP_{1-x}As_x$, $Al_xGa_{1-x}As$ cathodes in references [1-2]. If length and concentration of admixtures are close to means in cathode and active regions, this diode should be browsed as diode with two active regions. Output diodes characteristics will be determined of the active region. were could appeared unstable current. There were taken $m-n:In_{0.45}Ga_{0.55}As-n:GaAs-n+:GaAs$ structure of diode for this research. The purpose of research is to check assumption about spreading work range frequency opportunities. to discover physical processes, which are going in it and to obtain output characteristics.

Two-temperature model was used for characteristic calculations, that was enlarged for heterojunction [1-2] and metal cathode contact [3]. There were used semiconductor parameters [2], temperature of crystal lattice $T_0=300K$, diodes length, doping profile, generation frequency (f), voltage (U_0 , U_1) as initial data. Concentration of admixtures was equal to 10^{16} cm^{-3} in $n:In_{0.45}Ga_{0.55}As$ (1) and $n:GaAs$ (2) active regions. The length of first active region is 1.5 and 2.5 μm , and of the second active region 2.5 μm . The heigh of potential band is 0.06 eV on the metall-semiconductor contact.

The research works had shown, that dipole domains and accumulation layers can appear only in first or second active regions of diode in dependence of displacement U_0 and amplitude U_1 .

Accumulation layers spread by the high voltage in the first region. Regime is predominated over output power and efficiency of generation in dependence of work frequency. The diode work is determined with dipole domains regime on the low-frequency layers and with accumulation layers on the high-frequency layers. The frequency diode work range is ~ 55 GHz (from ~ 27 to ~ 82 GHz) by the equal length active regions 2.5 μm . Two transit-time region diodes have been provided for future spreade-frequencey range use different of transit regions length (the $n:In_{0.45}Ga_{0.55}As$ -region less than $n:GaAs$ -region). The first (low-frequency) corresponds to dipole domains regime, the second one (high-frequency) determined by accumulation layers regime. Dipole domains determine diodes work on less than ~ 70 GHz frequency at the second region. Increase of diode frequency work take place by loosing of efficiency and output power generation.

Taken researches were shown that specific characters of diodes have heavy current unsteady interconnection in different transit-time regions, what strongly changed its output data.

There were obtained following results.

1. Two works regimes could be in dependence of voltage in $m-n:In_{0.45}Ga_{0.55}As-n:GaAs-n+:GaAs$ diode. There are one regime with dipole domains in $n:GaAs$ and second one with accumulation layers in $n:In_{0.45}Ga_{0.55}As$.
2. Output diode characteristics have been determined by regime with dipole domains on the low-frequency range. Output diode characteristics have been determined by regime with accumulation layers in the high-frequency range.
3. Diode with equal transit-time region lengths of $l_1=l_2=2.5 \mu\text{m}$ has frequency range ~ 55 GHz (from ~ 27 to ~ 82 GHz) at the maximal generation frequency $\sim 5.6\%$. Diode with $n:In_{0.45}Ga_{0.55}As$ region length 1.5 μm and $n:GaAs$ region 2.5 μm has frequency range ~ 103 GHz (from ~ 22 to ~ 125 Ghz).

References

1. Ю.В.Аркуша, Э.Д.Прохоров, И.П.Стороженко "Гетеропереход $InP_{1-x}As_x/GaAs$ в диоде с междолинным переносом электронов", Радиотехника и электроника, т. 41, № 2, с. 248. 1996.

2. Ю.В.Аркуша, Э.Д.Прохоров, И.П.Стороженко "Гетеропереход In_xGa_{1-x}As/GaAs в арсенид-галлиевом диоде Ганна". Применение радиоволн мм и субмм диапазонов. Сб. науч. тр. Харьков. ИРЭ НАН Украины. с. 78. 1994.
3. Ю.В.Аркуша, А.А.Дрогаченко, Э.Д.Прохоров "Антизапорный металлический катодный контакт к коротким диодам Ганна" Радиотехника и электроника, т. 33, № 6, с. 1295. 1988.

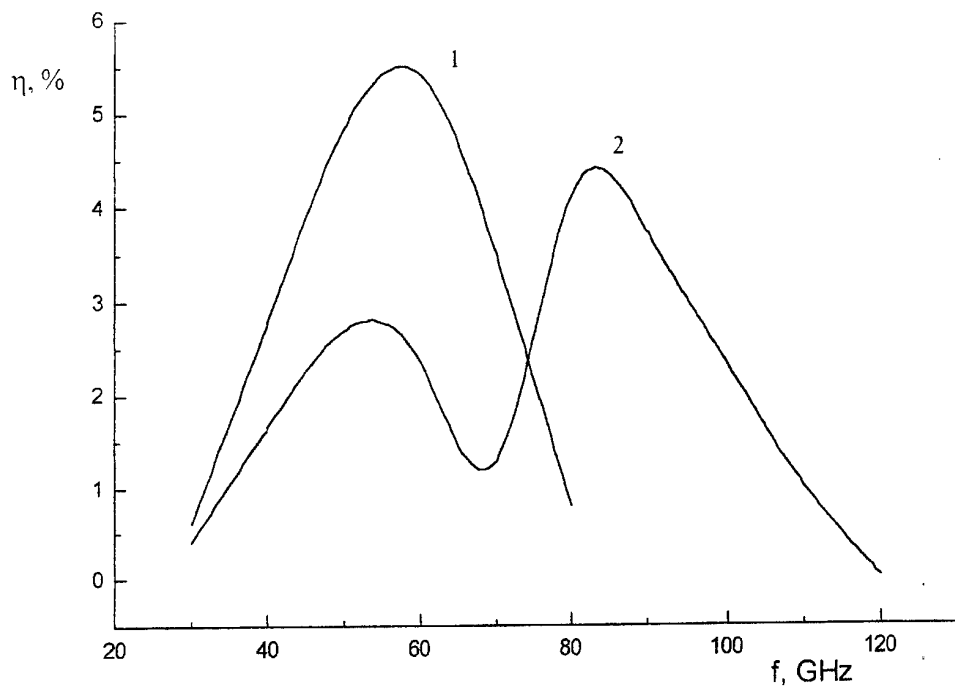


Figure. Dependence of diode efficiency generation from frequency (1 - $l_f=l_H=2.5 \mu\text{m}$, 2 - $l_f=1.5 \mu\text{m}$. $l_H=2.5 \mu\text{m}$)

POWER AND FREQUENCY CHARACTERISTICS OF GUNN GAAS-DIODES WITH TUNNEL INJECTION OF COLD ELECTRONS.

Yu.V.Arkusha, E.D.Prokhorov, I.P.Storozhenko
 Radiophysical department of Kharkov State University
 4, Svoboda sq., Kharkov, 310077, Ukraine
 Tel. (0572) 47-19-88, (0572) 43-08-83

To use Gunn diodes in mm-wave range it is necessary to decide two problem: inertia of the electron intervalley transfer and presence "dead zone" -initial electron heating region near the cathode. To decrease of the "dead zone" length it is usually used the local increasing of the cathode electric field [1-3]. Other method to remove the "dead zone" and electron transfer inertia influences is the active zone conductivity control. One from such methods of the conductivity control is electron injection of the active zone, for example, through the tunnel p^{++} - n^{++} -junction [4]. There p^{++} - n^{++} - n^- :GaAs-structure it was considered. The research purpose is to study the physical processes that take place in the diode with tunnel cathode and to obtain its output characteristics. For research it was used the two-temperature model [1]. In this model p^{++} - n^{++} -junction presence was taken into account by follow way [5]:

1. Electron tunnelling to the conductivity band central valley having energy.
2. Any processes in the degenerating p^{++} and n^{++} regions is not taken in to account.
3. Presence of p^{++} - n^{++} -junction is written by certain boundary conditions determination [5].
4. Voltage are given both to the diode and to p^{++} - n^{++} -junction independently.
5. All processes are considered for second period of microwave oscillations.

The diodes having active region lengths 1.0, 0.8, 0.5, 0.4 μm and 2.5, 3.1, 5.0, 6.2 10^{16} cm^{-3} impurity densities are considered. The contact potential difference on p^{++} - n^{++} -junction was equal 1.44 V, GaAs diode parameters were taken from [3,4].

The tunnel injection influence to the diode work has been studied in detail for diode having 0.8 μm length. It was found the accumulation layers are propagated in the diode what is an interesting fact at the such active region length.

It was shown that there is optimum voltage on p^{++} - n^{++} -junction when oscillation efficiency is maximally. It is conditioned by such facts that when voltage increases the amplitude characteristics are charged for the worse but the phase characteristics the wrong way are improved.

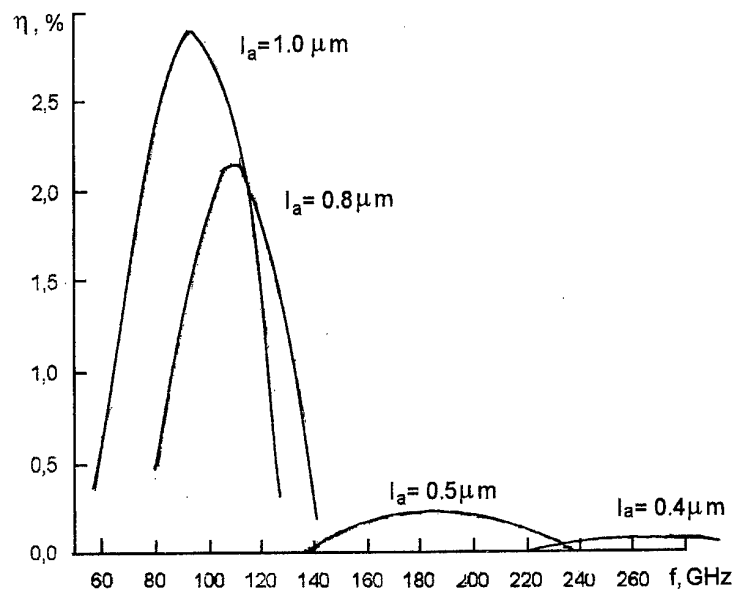
To find the frequency possibilities it was researched the output characteristics of the diode having different lengths. The electron injection leads to the "dead zone" length shorting. If the diodes having different lengths if the cathode electric field is low the electron energy in the central valley and the side valley electron population are enough to form the accumulation layers. Out of this the "dead zone" length is shortened without the electric field local increase. So far as the accumulation layers propagation velocity higher them dipole domains velocity the tunnel cathode diodes have the frequency limit higher and frequency range wider.

Thus preliminary researched of the Gunn diodes having tunnel injective to the active zone give the foundation to think about their effective using in the mm- and submm-ranges.

References

1. Ю.В.Аркуша, А.А.Дрогаченко, Э.Д.Прохоров "Влияние формы напряжения на энергетические характеристики коротких диодов Ганна с длиной менее 1 мкм" Радиотехника и электроника, т. 33, № 5, с. 1050-1054, 1987.
2. Ю.В.Аркуша, А.А.Дрогаченко, Э.Д.Прохоров "Влияние запорного металлического контакта на коротких диодов Ганна" Радиотехника и электроника, т. 33, № 6, с. 1295-1299, 1988.
3. Ю.В.Аркуша, Э.Д.Прохоров, И.П.Стороженко "Гетеропереход $\text{InP}_{1-x}\text{As}_x/\text{GaAs}$ в диоде с междолинным переносом электронов", Радиотехника и электроника, т. 41, № 2, с. 248, 1996.
4. Э.Д.Прохоров, Н.И.Белецкий "Полупроводниковые материалы для приборов с междолинным переносом электронов". Харьков: Вища школа, изд-во при Харьковском госуниверситете. 144 с., 1982.

5. Ю.В.Аркуша, Э.Д.Прохоров, И.П.Стороженко "Высокочастотные физические процессы в диоде Ганна с туннельным катодом" Труды 6-й Международной Крымской конференции "СВЧ-техника и телекоммуникационные технологии" Севастополь, 1996, с. 322-324.



COMPENSENTED GaAs DIODES OSCILLATOR

O. V. Botsula, E. D. Prokhorov
 Kharkov State University, Radiophysical department
 4 sq. Svobody, Kharkov, 310077, Ukraine
 Tel. 430-883

The purpose of this work is to examined influence of impurities on operate of high frequency oscillators based on Gunn diodes (in particular, GaAs diodes doped with chromium (GaAs:Cr)). Unfortunately, it was small paired attention to this problem the more so that in the real semiconductor together with main impurities (donor for n-type semiconductor) are always present other impurities. The present of impurities in semiconductor led to strong dependence of electron concentration in conductivity zone. If electron-capture coefficient of the deep level increases with increasing electric field the electron concentration decreases. Since concentration can't be smaller than one being determined by Kromer criterion: $nL > 10^{11} \text{ cm}^{-2}$ (n – carrier concentration, L – active region length) for high frequency instabilities to arise, it led to halt of oscillators. This case have been investigated very well.

The electron-capture coefficient of deep level associated with chromium in GaAs weakly depended on electric field and traps electron in slight fields and when field is absent. Thus, in the thermodynamic equilibrium state, values of electron concentration in conductivity zone is small and product nL may be smaller than 10^{11} cm^{-2} . Due to energy position of chromium associated levels in the forbidden zone GaAs, an impact ionization of electrons from traps resulting in a superlinear current increase may occur even in rather weak fields (several kilovolts). In result of the Kromer criteria is true and instabilities take place [1]. The possibility of appearance of high frequency instabilities in GaAs diodes compensated by chromium have been considered in work [2]. It have been showed that instabilities in the diodes determined by impact impurities ionization.

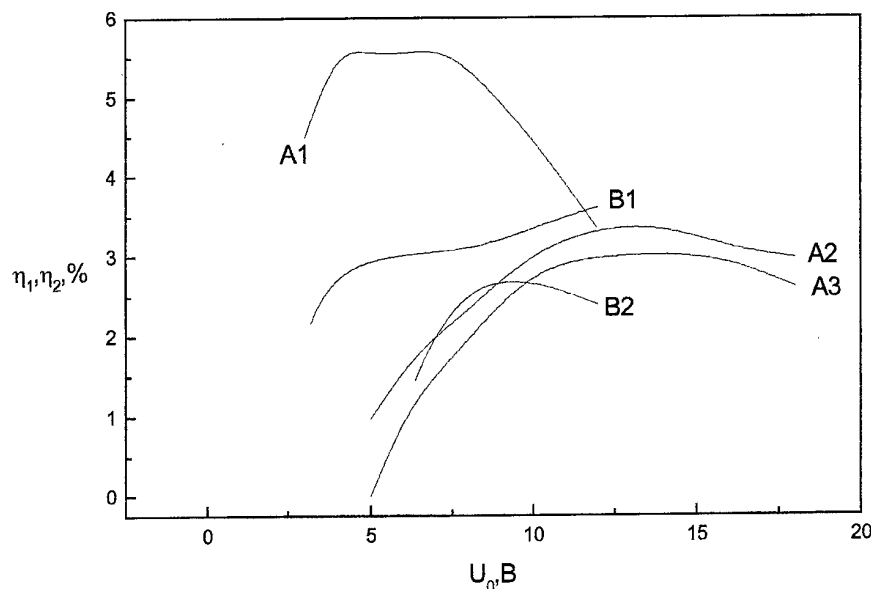


Fig. 1. The maximum efficiency versus dc voltage component for operate in fundamental harmonic A1-A3 and second harmonic - B1,B2. The curves A1and B1 for $\beta=0$, A2 for $\beta= 0.6$, A3 and B3 for $\beta= 0.9$.

A one - dimensional computer simulation of compensated GaAs Gunn diodes operating in resonance circuit has been made. We considered the operate of Gunn oscillators on the basic two diodes with different donor doping profiles of an $n^+ - n - n^+$ and $n^+ - n^- - n - n^+$ types. The active region length and donor concentration are taken as $\sim 9 \mu$ and an order of 10^{15} cm^{-3} , respectively. The both of diodes have being doped uniformly by chromium. A mathematics model for investigation has been described in [2]. The voltage waveform consist of only a fundamental and second harmonic components:

$$U(t) = U_0 + U_1 \sin(2\pi \cdot f \cdot t) - U_2 \cos(4\pi \cdot f \cdot t) \quad (1)$$

where U_0, U_1, U_2 are amplitudes of dc, fundamental and second harmonic voltage components, f - frequency of the fundamental component of applied voltage waveform. The influence of the degree of compensation ($\beta = N_0/N_D$, N_0, N_D are compensating impurities and donor in active region concentration) on efficiency of oscillation on fundamental and second harmonic have being investigated. The efficiency have being calculated by method described in [3]. The results of a calculation have being compared with ones obtained for same diodes without deep impurities. The maximum oscillation efficiency versus dc voltage plotted in Fig. 1 for $n^+ - n^- - n - n^+$ diode operating on fundamental A1-A3 and second B1- B2 harmonica. As may be expected oscillation efficiency decreased when β increase. First, ratio maximum to minimum current in compensated diodes is small and observed only dynamic state. Second, the active diodes region are determined by impart ionization region. Since, length of the last may be reduce , a times of a formation and extinguished will be grow and domain width will be grow too.

A I-V diodes characteristics is modified when impact ionization take place. Therefore, may be possible a operate in higher current harmonic component. For this purpose the diodes of $n^+ - n^- - n - n^+$ type has been selected. As seen from figure 1 operation on second harmonic efficiency drops if value of impurity concentration increase but it is approximately the same one in fundamental frequency operation. Thus , may be hope using other semiconductor parameters , for example higher donor concentration, if value of β have being constant , to reach high efficiency.

Reference

1. O.V. Botsula, E. D. Prokhorov, " Conductivity modulation of GaAs:Cr diodes ", p. 51-56, Functional Material, 4, No.1, 1997
2. О. В. Бонула , Э.Д. Прохоров, " Неустойчивости тока в GaAs в условиях захвата электронов на ловушки", Доповіді Національної академії наук України, №1, с. 107-111, 1998
3. Ю.В. Аркуша , А.А. Дрогаченко , Э.Д. Прохоров , " Влияние формы напряжения на энергетические характеристики коротких диодов Ганна с длиной менее 1 мкм", Радиотехника и электроника, т. 33, №5, с.1050-1054, 1987.

FREQUENCY DEPENDENCE of MM-WAVE GaAs GUNN DIODE OSCILLATORS EFFICIENCY OPERATED on 2-nd or 3-rd HARMONIC

Dyadchenko A.V., Mishnjov A.A., Prokhorov E.D.
Kharkiv State University, 4, Svoboda sq., Kharkiv, 310077, Ukraine
phone (0572) 47-19-88

One from different ways of moving to the short *mm*-wave range is an working out the oscillator on harmonic frequency [1]. As has been shown in the series works [2...4] when Gunn-diode operates in some resonator giving several contours it is possible to obtain considerable increasing of the efficiency and frequency range widening.

The results of numerical calculation of the efficiency dependence on frequency of GaAs Gunn-diode placing to the double-contour resonator are shown in this note. The first resonator contour was tuned on 1-st harmonic frequency f_1 (main frequency), second - on 2-nd $f_2 = 2f_1$ (or on 3-rd $f_3 = 3f_1$) harmonics. The main frequency microwave power was picked out on the load ρ_1 matching with first contour but 2-nd (or 3-rd) harmonics power - on the load ρ_2 , matching with second contour. It was used two-temperature model of Gunn-diode, in which kinetic Boltzman equation with displacing Maxwell function of the electron distribution was averaged taking into account it space change caused by electron diffusion (accounting «non-localization»).

It was researched the operation of Gunn diode with n^+ -n anode contact and m-n metalic cathode contact (in these cases «dead zone» near cathode is absent) and active n-region length $L_n = 2,5 \mu\text{m}$ and $L_n = 1,0 \mu\text{m}$. The transit regime of generation ensured by choice of electron concentration in active n-region Gunn-diode: $n_o = 1 \cdot 10^{16} \text{ cm}^{-3}$ ($L_n = 2,5 \mu\text{m}$) and $n_o = 2,5 \cdot 10^{16} \text{ cm}^{-3}$ ($L_n = 1,0 \mu\text{m}$). At the same time transit frequency was: $f_t = 45 \text{ GHz}$ ($L_n = 2,5 \mu\text{m}$) and $f_t = 110 \text{ GHz}$ ($L_n = 1,0 \mu\text{m}$). The anode n^+ -region concentration was $n_o^+ = (8...10) \cdot 10^{16} \text{ cm}^{-3}$.

It is obtained when Gunn-diode operates in the double-contour resonator on 1-st and 2-nd (or 1-st and 3-rd) harmonics it is observed maximum efficiency on any from these frequency while efficiency on other harmonic is lower and so the wrong way. This may be explained by redistribution of the microwave power between connected resonator contours and is defined by that contours parameters in particular by correlation between their wave resistance ρ_1 and ρ_2 . Thus for each harmonic frequency it is possible to find optimum efficiency η . Therefore it were calculated and analyzed frequency dependencies of Gunn-diode optimum efficiency on 1-st (f_1) and 2-nd (f_2) (or on 1-st (f_1) and 3-rd (f_3)) harmonics that are shown on Fig.1...Fig4.

Lower f_d and higher f_u boundaries of $\eta(f)$ dependencies define the Gunn-diode frequency range $\Delta f = (f_u - f_d)$ on corresponding harmonic. So far as these curves usually are crossed it is may be say about the common frequency range of Gunn-diode operation: when it operates on 1-st and 2-nd harmonics it is $\Delta f_{1,2} = (f_{u2} - f_{d1})$, when operates on 1-st and 3-rd harmonics - $\Delta f_{1,3} = (f_{u3} - f_{d1})$.

Follows results had been obtained:

1. Gunn-diode with $L_n = 2,5 \mu\text{m}$.

When Gunn-diode with such parameters operates in one-contour resonator ($f_t = 45 \text{ GHz}$) it gives efficiency $\eta_{1\max} \approx 8\%$.

a) an operation on 1-st and 2-nd harmonics:

$\eta_{1\max} = 11,5\%$ ($f_1 = 45 \text{ GHz}$; $\rho_1 = 4,7 \text{ Ohm}$; $\rho_2 = 25,3 \text{ Ohm}$); $\eta_{2\max} = 5,1\%$ ($f_2 = 66 \text{ GHz}$; $\rho_1 = 32,2 \text{ Ohm}$; $\rho_2 = 5,4 \text{ Ohm}$); on level η_1 , $\eta_2 = 1\%$: $\Delta f_1 = 44 \text{ GHz}$; $\Delta f_2 = 42 \text{ GHz}$; $\Delta f_{1,2} = 68 \text{ GHz}$.

b) an operation on 1-st and 3-rd harmonics:

$\eta_{1\max} = 11,6\%$ ($f_1 = 31 \text{ GHz}$; $\rho_1 = 9,3 \text{ Ohm}$; $\rho_2 = 21,4 \text{ Ohm}$); $\eta_{3\max} = 0,85\%$ ($f_3 = 123 \text{ GHz}$; $\rho_1 = 19,4 \text{ Ohm}$; $\rho_2 = 8,6 \text{ Ohm}$); on level η_1 , $\eta_3 = 0,4\%$: $\Delta f_1 = 36 \text{ GHz}$; $\Delta f_3 = 50 \text{ GHz}$; $\Delta f_{1,3} = 126 \text{ GHz}$.

2. Gunn-diode with $L_n = 1,0 \mu\text{m}$.

a) an operation on 1-st and 2-nd harmonics:

$\eta_{1\max} = 3,1\%$ ($f_1 = 125 \text{ GHz}$); $\eta_{2\max} = 1,85\%$ ($f_2 = 225 \text{ GHz}$); on level η_1 , $\eta_2 = 0,5\%$: $\Delta f_1 = 100 \text{ GHz}$; $\Delta f_2 = 265 \text{ GHz}$; $\Delta f_{1,2} = 335 \text{ GHz}$.

b) an operation on 1-st and 3-rd harmonics:

$\eta_{1\max} = 2,8\%$ ($f_1 = 125 \text{ GHz}$); $\eta_{3\max} = 0,6\%$ ($f_3 = 335 \text{ GHz}$); on level η_1 , $\eta_3 = 0,2\%$: $\Delta f_1 = 95 \text{ GHz}$; $\Delta f_3 = 310 \text{ GHz}$; $\Delta f_{1,3} = 435 \text{ GHz}$.

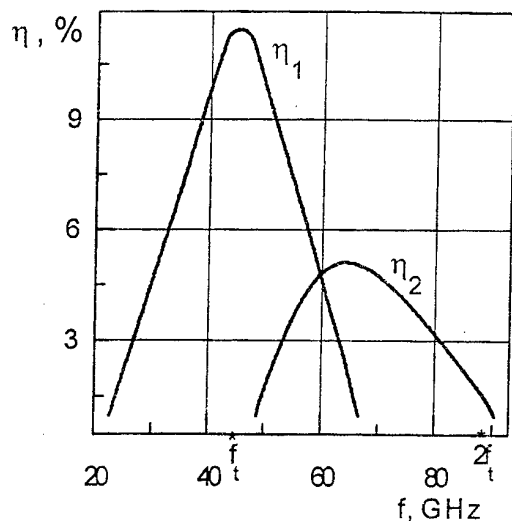


Fig.1. Gunn-diode $\{L_n = 2.5 \mu m\}$ operated on 1-st & 2-nd harmonics.

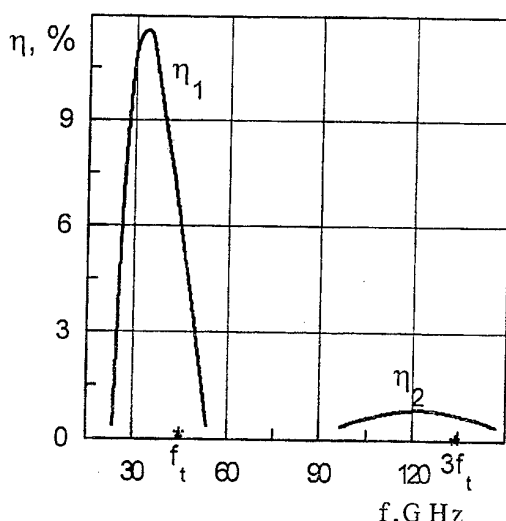


Fig.2. Gunn-diode $\{L_n = 2.5 \mu m\}$ operated on 1-st & 3-nd harmonics.

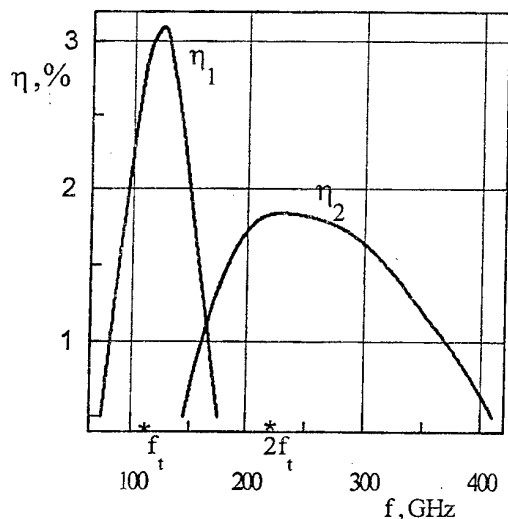


Fig.3. Gunn-diode $\{L_n = 1.0 \mu m\}$ operated on 1-st & 2-nd harmonics.

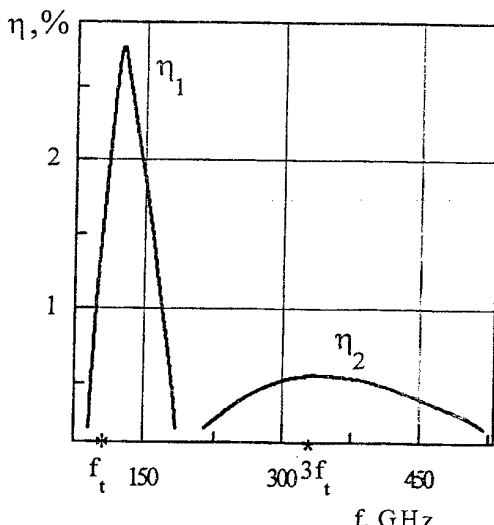


Fig.4. Gunn-diode $\{L_n = 1.0 \mu m\}$ operated on 1-st & 3-rd harmonics

The inductance of resonator contours in the optimum regimes were changed from 10 pH to 130 pH and capacitance - from 0,07 pF to 0,5 pF.

On base obtaining results it is possible to give follow conclusions:

1. On each harmonic frequency it is possible to have efficiency higher than in one-contour resonator.
2. Maximum efficiency on 2-nd (or 3-rd) harmonic take place on the frequencies lesser (or higher) than transit frequency. This may be explained by change for the worse of the phase correlation between Gunn-diode current and voltage.

3. Maximum efficiency is reached on that harmonic frequency whose resonant contour has lower wave resistance.
4. Decrease of Gunn-diode active region length leads to increase frequency and essential expanding of the frequency range.
5. It is possible to obtain sufficiently wide frequency range passing from main frequency oscillation to 2-nd (or 3-rd) harmonic oscillation.

These theoretically obtaining dependencies is confirmed by experiments and they may be usefull when GaAs *mm*- and sub-*mm* waves generator is elaborated and it parameters are optimised.

References

1. А.С.Косов, В.Г.Еленский, «Генераторы гармоник миллиметрового диапазона» (обзор), Зарубежная радиоэлектроника, N2, С.54-85, 1987.
2. Э.Д.Прохоров, Н.И.Белецкий, А.В.Дядченко, «О возможности увеличения высокочастотного предела работы диодов Ганна», Радиотехника и электроника, т.17, N5, С.1103-1108, 1972.
3. Ю.В.Аркуша, А.А.Дрогаченко, Э.Д.Прохоров, «Влияние формы напряжения на энергетические характеристики коротких диодов Ганна», Радиотехника и электроника, т.32, N9, С.1947-1954, 1987.
4. Ю.В.Аркуша, Э.Д.Прохоров, С.И.Санин, «Влияние типа катодного контакта, профиля легирования и температуры на эффективность генерации диодов Ганна», Радиотехника и электроника, т.39, N8-9, С.1435-1438, 1994.

Efficiency possibilities of the RTD generators.

E. D. Prohorov, V.V. Medvedev

Address: 4, Svoboda sq., Kharkov, 310077, Ukraine

Tel. 43-08-83

One from perspective active element for the mm- and submm-wave generation is the resonantly-tunnel diode (RTD) - some structure with double barrier quantum wells. It is interesting to estimate efficiency of RTD both on main frequency and on harmonics frequency. Since the oscillation power on main frequency is limited by influence of the diode capacitance and resistance of losses it is actually to research the oscillation of the RTD on the harmonics. By means of analyses of current-voltage characteristics of different RTD $\text{Al}_{0.2}\text{Ga}_{0.8}\text{As}/\text{GaAs}/\text{Al}_{0.2}\text{Ga}_{0.8}\text{As}$ that has I_{\max} at 0.3 V and the extensive region with small current and $\text{GaAs}_{0.4}\text{P}_{0.6}/\text{GaAs}/\text{GaAs}_{0.4}\text{P}_{0.6}$ that has two current maximum with small current region between them (it is two levels in the quantum well) was chosen. It was investigated the oscillation efficiency both on main frequency and on harmonics. Dependences of the generation efficiency of RTD $\text{Al}_{0.2}\text{Ga}_{0.8}\text{As}/\text{GaAs}/\text{Al}_{0.2}\text{Ga}_{0.8}\text{As}$ generator for different constant diodes voltages, different amplitudes of the variable signals, different diodes parameters: width of well and barriers were presented on fig. 1-4. Were demonstrated the existing of variable signal amplitude optimum (maximum of efficiency) for every voltages. Were presented the maximum efficiency dependences from voltage for optimum agreement between generator and burden. The first harmonic efficiency higher in 2-2.5 times than efficiency of Gunn-diode generator, that caused by quantity of RTD minimum current (the maximum current in some orders higher than minimum current).

Same dependences were obtained for generation on harmonics (2, 3-th), the diode were under influence of first and n_{th} harmonics of signal (RTD worked in double contour resonator). Efficiency in 2-3 times less than on main frequency.

RTD generator on $\text{GaAs}_{0.4}\text{P}_{0.6}/\text{GaAs}/\text{GaAs}_{0.4}\text{P}_{0.6}$ were analysed. It was shown the possibilities of maximum efficiencies on 4-th harmonic for certain voltages and amplitudes of the variable signals.

The influence of the capacity and the resistance of losses on the RTD frequency properties were shown. It was estimated on what frequencies begin to evidence the influence of the external parameters on the RTD negative differential conductivity.

Figure 1. Dependences of efficiency from voltage for different barriers width b1,b2

Figure 2. Dependences of efficiency from voltage for different well width a

Figure 3. Dependences of efficiency from voltage

Figure 4. Dependences of efficiency from voltage for different N

References

1. Тагер А.С. Размерные квантовые эффекты в субмикронных полупроводниковых структурах и перспектива их применения в электронике СВЧ. Электронная техника. сер. Электроника СВЧ, вып. 9(403), 21-34, 1987.
2. Аркуша Ю.В., Прохоров Э.Д., Санин С.И., Оптимальные параметры диодов с ДБКС. Техника мм и субмм диапазонов радиоволн., сб. науч. тр. ИРЭ НАН Украины, 43-49, 1993.

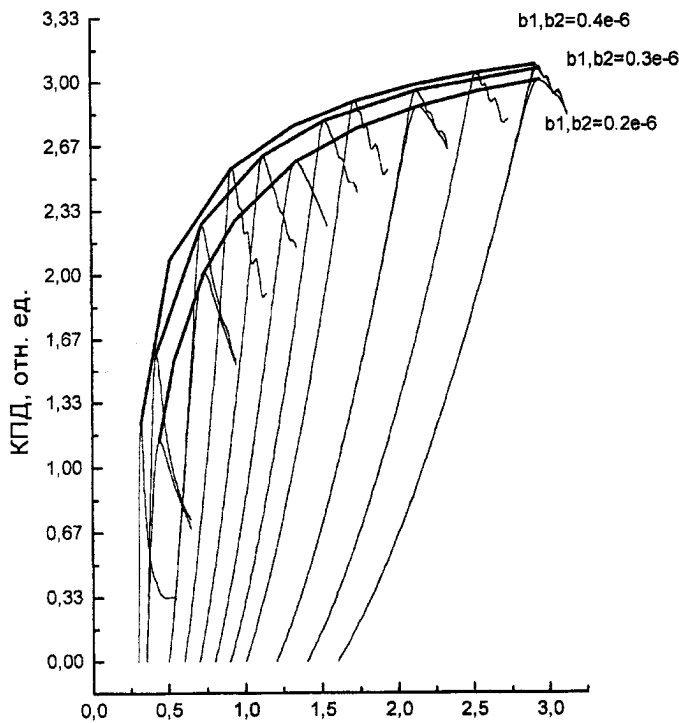


Fig.1. V, B
 $N=0.1e18, a=0.6e-6$

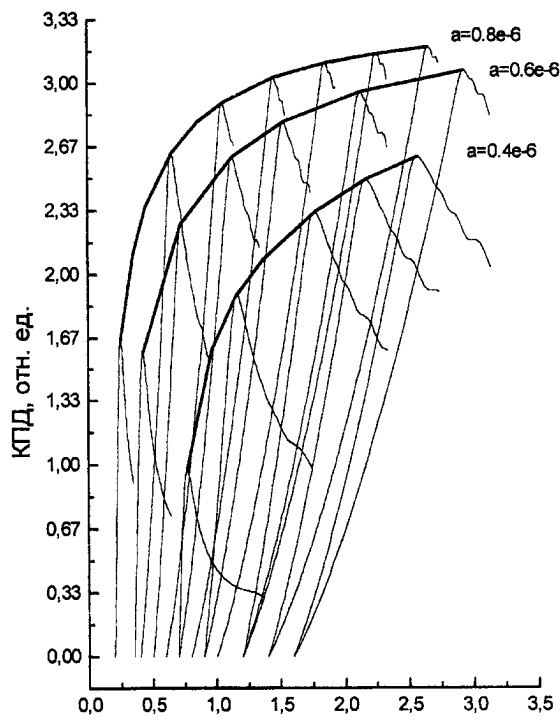


Fig.2. V, B
 $N=0.1e18, b1,b2=0.3e-6$

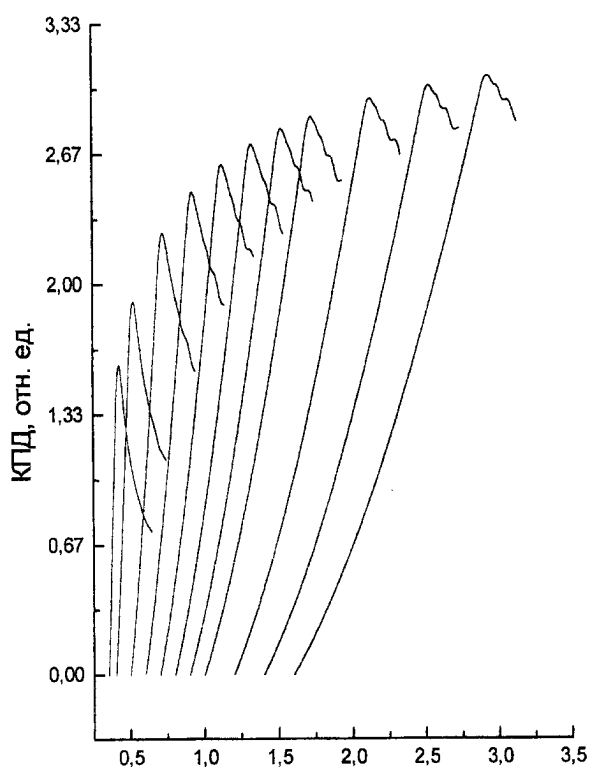


Fig.3. V, B
 $N= 0.1e18$; ширина: барьера- 0.3×10^{-6} см,
ямы- 0.6×10^{-6} см.

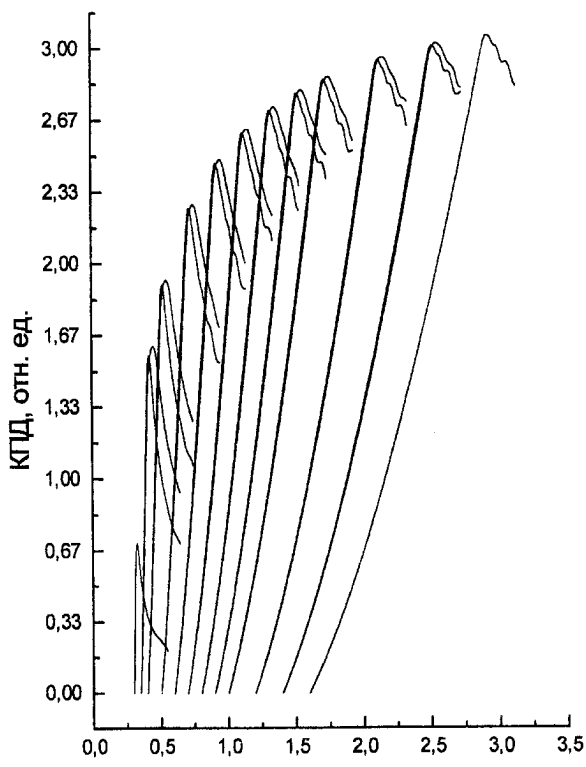


Fig.4. V, B
 $N= 0.5e17; a= 0.6e-6; b1,b2= 0.3e-6$
 $N= 0.5e18$

**WHISPERING GALLERY OSCILLATIONS
IN AN ANISOTROPY BALL**

Yu.F.Filipov ,Z.E.Eremenko

Institute for Radiophysics and Electronics National Academy of Science of Ukraine
12 Str. Proskura , Kharkov, 310085 , Ukraine
Tel.: 380 572 448 593; Fax: 380 572 441 105; E-mail : eremenko@ire.kharkov.ua

Resonant oscillations of homogeneous isotropic dielectric ball was investigated analytically and numerically [1]. It was shown that at big polar index n whispering gallery modes (WGM's) are excited in it. The special peculiarity of these modes is electromagnetic field concentration along the ball interface. It is known that WGM's have high Q-factor. At the first time they were observed in stimulated radiation of a spherical pattern, later in nuclear cavitation experiments, Raman light scattering in aerosols, and in ruby ball and so on {2-4}. High Q-factor, discovering the areas of the field localization of the resonant modes allowed to suggest set of devices with new unique properties, to calculate quite small losses in crystals and liquids [2-5].

In the present paper we consider a ball with radius r_0 , which is made of a single-crystal.

For azimuth - homogeneous modes $\left(\frac{\partial \vec{E}}{\partial \varphi} = \frac{\partial \vec{H}}{\partial \varphi} = 0\right)$ the anisotropy influences only on TM modes

$(H_r = 0)$. We introduce a potential V by following correlation $E_r = \left(\frac{\partial^2}{\partial r^2} - \frac{\epsilon_{\theta\theta}}{c^2} \frac{\partial^2}{\partial \theta^2} \right) V$

The investigation of Maxwell equations leads to the solution of the equation

$$\left\{ \epsilon_n \frac{\partial^2}{\partial r^2} + \frac{1}{r^2 \sin \theta} \frac{\partial}{\partial \theta} \sin \theta \left[\frac{\partial}{\partial \theta} \epsilon_{\theta\theta} - \epsilon_{r\theta} \left(1 + r \frac{\partial}{\partial r} \right) \right] - \frac{\epsilon_{r\theta}}{r} \frac{\partial^2}{\partial \theta^2} - \frac{\epsilon_{xx} \epsilon_{zz}}{c^2} \frac{\partial^2}{\partial \theta^2} \right\} V = 0 \quad (1)$$

Here $\epsilon_n = \epsilon_+ + \epsilon_- \cos 2\theta$, $\epsilon_{\theta\theta} = \epsilon_+ - \epsilon_- \cos 2\theta$, $\epsilon_{r\theta} = \epsilon_- \sin 2\theta$, $2\epsilon_{\pm} = \epsilon_{zz} \pm \epsilon_{xx}$.

ϵ_{zz} and ϵ_{xx} are the dielectric permittivities of crystal along the parallel and perpendicular directions to the anisotropy axes.

The solution Eq.1 we are looking for in the form

$$V = \sum_n \exp(-i\omega t) P_n(\cos \theta) \begin{cases} A_n j_n(qr) & r \leq r_0 \\ B_n h_n(kr) & r \geq r_0 \end{cases} \quad (2)$$

where A_n and B_n are constants, $k = \omega / c$, q is radial component of wave vector at $r < r_0$, $P_n(y)$ is

Legander polynom, $j_n(y) = \sqrt{\frac{\pi y}{2}} J_{\frac{n+1}{2}}(y)$; $h_n^{(1)}(y) = \sqrt{\frac{\pi y}{2}} H_{\frac{n+1}{2}}^{(1)}(y)$; $J_v(y)$ and $H_v^{(1)}(y)$ are

cylindrical functions of Bessel and Hankel of first kind.

Substituting Eq.2 into Eq.1, using recurrent relations for $j_n(y)$ and $P_n(y)$ we obtain for $r \leq r_0$ a system of algebraic equations for amplitude A_n

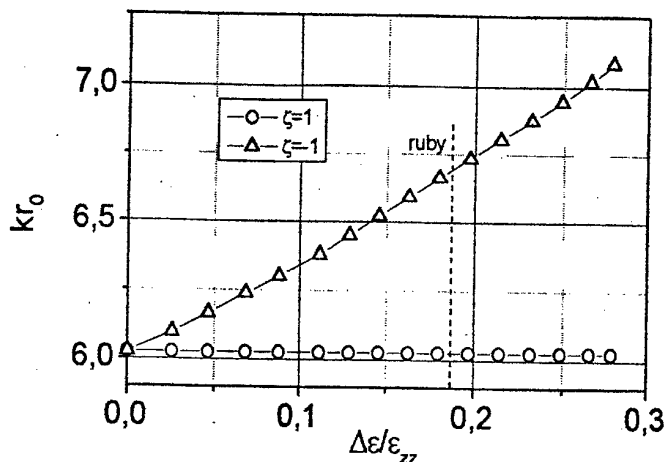
$$\left[\varepsilon_{xx} \varepsilon_{zz} k^2 - \left(\varepsilon_+ - \frac{\varepsilon_-}{(2n+3)(2n-1)} \right) q^2 \right] A_n + \\ 2\varepsilon_- q^2 \left[\frac{n(n-1)}{(2n-1)(2n+3)} A_{n-2} + \frac{(n+1)(n+2)}{(2n-3)(2n+5)} A_{n+2} \right] = 0 \quad (3)$$

For the big values of polar index n the system (3) has the approximate solution.

$$A_{n+2} = A_{n-2} = \xi A_n, \quad \xi = \pm 1, \quad q^2 = \varepsilon_{xx} \varepsilon_{zz} (\varepsilon_+ - \varepsilon_- \xi)^{-1} k^2 \quad (4)$$

Satisfying the boundary conditions at $r = r_0$, we obtain a dispersion equation, which determines resonant frequencies of whispering gallery modes ($x_0 = kr_0$, $x = qr_0$)

$$\frac{(x^2 - 2\varepsilon_- \xi x_0^2) j_{n-1}(x) - nx j_n(x)}{(\varepsilon_+ - \varepsilon_- \xi) x j_n(x)} = x_0 \frac{h_{n-1}^{(1)}(x_0)}{h_n^{(1)}(x_0)} - n \quad (5)$$



The dependence of value kr_0 for TM modes on $(\varepsilon_{zz} - \varepsilon_{xx}) / \varepsilon_{zz}$ at $\varepsilon_{zz} = 11.53 \cdot (1 + i10^{-4})$, $n = 15$, is shown in Fig. At the fixed polar index n and the variation number along of radial coordinate in the isotropic ball ($\varepsilon_{xx} = \varepsilon_{zz}$) there exists the only one resonant mode. The influence of anisotropy ($\varepsilon_{xx} \neq \varepsilon_{zz}$) leads to appearance two TM modes with different frequencies.

References

1. M. Gastine, L. Courtois, J. Dorman, » Em resonances of free dielectric spheres», IEEE Trans. , 1967, MTT-15, p.694
2. V.B.Braginsky, V.G.Ilchenko, M.L.Gorodetsky,»Quality factor and non-linear properties an optical whispering gallery modes», Phys. Lett. Ser.A, 1989, V.137, p.393
3. E.M.Ganapolsky, A.V.Golik,A.P.Koroluk, «Quasi-optical method of measurement of small dielectric losses in condensed media» Soviet J. Low Temp. Phys. (USA), 1993,v.19,No.11, p.1255
4. S.Sottini, E.Giogetti,C.Marcelino,» Whispering propagation optical frequency for spherical geodesic processor», Pure and Appl. Optics, 1992, V.1, N0.6,p.359
5. S.N.Kharkovsky, A.E.Kogut, V.V.Kutuzov, « Optical resonators with modes types of whispering gallery », Lett. in Tech. Phys. (USA), 1996, 22, N0.20, p.3

EXACT SIMULATION METHOD FOR ANALYSIS OF OPEN RESONATORS WITH STEP-LIKE DEFORMATION OF MIRRORS.

O.I.Belous, A.I.Fisun, A.A.Kirilenko and V.I.Tkachenko.

Institute for Radiophysics and Electronics

12, Proskura Str., Kharkov, 310085, Ukraine

Tel. 44-87-41, Fax. 44-11-05, E-mail obel@ire.ire.kharkov.ua

Introduction: Several effective methods of analysis of quasi-optical open resonators (ORs) with smooth mirrors exist. The analysis of the OR with the diffraction grating is a more challenging task, because the grating is an additional dispersive element in the OR and has an inhomogeneous surface [1,2]. There are many such ORs of a complicate configuration, where the inhomogeneous mirrors can be conceived as a step-like regular surface. Several ORs of this type are presented schematically in Fig. 1. 2-D models are shown here. The period l of the structures being studied is commensurable with the wave length λ or it is far beyond that of λ . As will be noted, that the condition $1 \ll \lambda$ can be used for the approximation of curved surfaces specifically for spherical mirror [3]. An efficient rigorous solution of the excitation problem of the complicate OR is presented in this report. As an example, the spectrum and the mode field topology of the corner-echelette OR [4] are calculated and several results are shown.

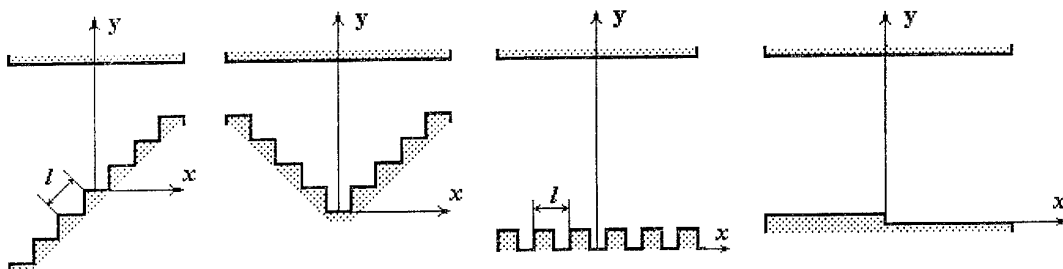


Figure 1.

Principle: The waveguide conception of keeping back electromagnetic field in the OR in the vicinity of critical frequency proposed by L.Vaenshtein [5], and the generalized scattering matrix method [6] represent the basis of this solution. From this standpoint, the complex electrodynamical problem of the OR excitation is reduced to the equivalent waveguide problem and to the subsequent decomposition of the component object into elementary key blocks with known scattering matrices (S -matrix). The open-ended plane waveguide, the elementary one-sides and bilateral steps in the plane guide, E -and H -plane tees and others guide components are defined as the key blocks in the current problem. Basically, the S -matrices of listed blocks are well known [6].

In the termin of quasi-optics a waveguide model has the same special features:

- the higher-order matrices are applied in the quasi-optical problems as opposed to the waveguide problems;
- the necessity of the minimum OR field distortion involves to use the small excited aperture; for this purpose the narrow-height dominant mode waveguide (for H-polarization) and standard-size waveguide with the inductive diaphragm (for E-polarization) are applied to the OR excitation.

Theoretical analysis: We have considered this method as an example of the solution to the corner-echelette OR excitation problem. The corner-echelette OR is employed in the quasi-optical solid-state mm-wave devices [4], and has numerical positive points. Among all choose the scheme of the corner-echelette OR decomposition where is shown in Fig. 2. It comprises of three successive stages. The echelette model is produced in the first stage as the set of the step-type transitions to the open-ended waveguide. For this purpose, the computational algorithm of the generalized S -matrix of the guide know is formed by the two quadripoles M and N . These quadripoles are connected by the i -th regular waveguide piece and are located between the $i-1$ th and $i+1$ th regular waveguide pieces (see Fig. 2a). In the matrix element form we obtain

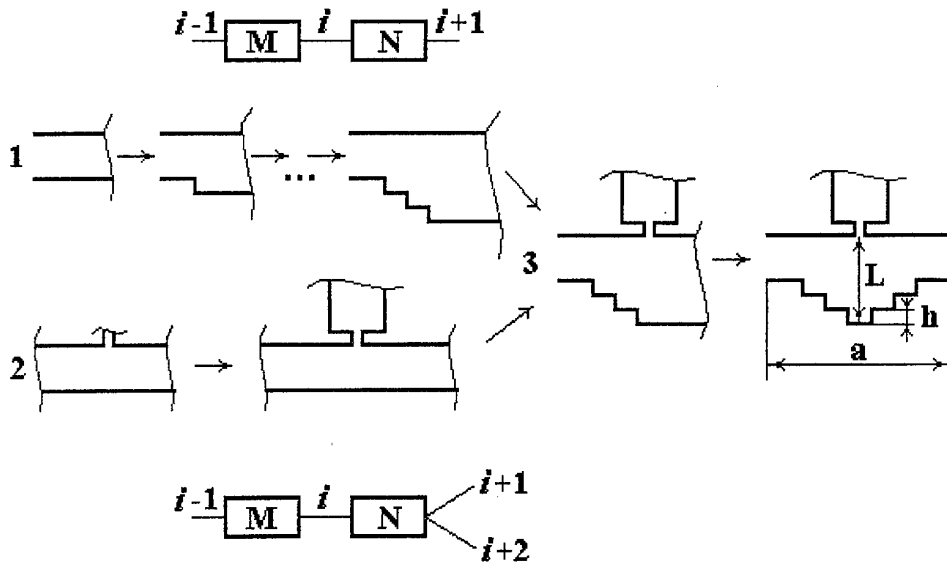


Figure 2.

$$S^{i-1,i-1}(MN) = S^{i-1,i-1}(M) + S^{i-1,i}(M)E_iS^{i,i}(N)E_iX_i \quad (1)$$

$$S^{i+1,i-1}(MN) = S^{i+1,i}(N)E_iX_i \quad (2)$$

$$S^{i+1,i+1}(MN) = S^{i+1,i+1}(N) + S^{i+1,i}(N)E_iS^{i,i}(M)E_iY_i \quad (3)$$

$$S^{i-1,i+1}(MN) = S^{i-1,i}(M)E_iY_i \quad (4)$$

where the matrices X_i and Y_i is the solution for the simultaneous linear equations

$$X_i - S^{i,i}(M)E_iS^{i,i}(N)E_iX_i = S^{i,i-1}(M) \quad (5)$$

and

$$Y_i - S^{i,i}(N)E_iS^{i,i}(M)E_iY_i = S^{i,i+1}(N) \quad (6)$$

The diagonal matrix E_i describes the phase progression or the exponential amplitude taper of the i -th waveguide wave between the reference planes of the unified objects M and N . This process is illustrated in Fig.2a.

The algorithm of the unification of the quadripole M and the three-port N is used in the second and third stages. The H -plane tee or E -plane tee with the inductive diaphragm in the lateral shoulder appear as the three-port network. Assume that the three-port N loads on i , $i+1$ and $i+2$ th waveguide and the quadripole M loads on i and $i-1$ th waveguides (see Fig. 2b,c). This fact indicates that the eqn. 1-6 is valid for the cells $S^{i-1,i-1}(MN)$, $S^{i+1,i-1}(MN)$, $S^{i+1,i+1}(MN)$ and $S^{i-1,i+1}(MN)$ of the generalized scattering matrix $S(MN)$. Other cells $S(MN)$ are obtained

$$S^{i+2,i}(MN) = S^{i+2,i}(N)E_iX_i \quad (7)$$

$$S^{i+2,i+1}(MN) = S^{i+2,i+1}(N) + S^{i+2,i}(N)E_iS^{i,i}(M)E_iX_i \quad (8)$$

$$S^{i,i+2}(MN) = S^{i-1,i}(M)E_iZ_i \quad (9)$$

$$S^{i+1,i+2}(MN) = S^{i+1,i+2}(N) + S^{i+1,i}(N)E_iS^{i,i}(M)E_iZ_i \quad (10)$$

$$S^{i+2,i+2}(MN) = S^{i+2,i+2}(N) + S^{i+2,i}(N)E_iS^{i,i}(M)E_iZ_i \quad (11)$$

where the matrix Z_i has been obtained from the solution of

$$Z_i - S^{i,i}(N)E_iS^{i,i}(M)E_iZ_i = S^{i,i+2}(N) \quad (12)$$

Numerical results: The realization of this method is performed by the System Electromagnetic Simulation (SES-04) [7]. The corresponding calculated procedure 1-11 is implemented using the SES-04 compilator automatically as a transformation from the problem-oriented input language. The accuracy of the key blocks computational algorithm and the accuracy of the exponent convergent relations 1-11 are chose no worse them

1% in the S-matrix elements of the OR, in so far as this analysis of the 2-dimensional OR model is intended to determine of the quality characteristics of a real physical phenomenon. Furthermore, this system provides different servicing means for a computing result processing, notably the production of amplitude-frequency characteristics (AFC), a field topology, an outer radiation diagrams, etc. As an example, the result of the investigation of the corner-echelette OR model, having the length $L=5h$, the mirror aperture $2a=7h$, where h is a step height, is presented. The OR is loaded on the outer space from the lateral aperture $l'=2h$. The dimensionless frequency $k=L/\lambda$ is used as a independent parameter. The spectrum of the corner-echelette OR as the AFC singular points is shown in Fig. 3, from below. The typical field topology of waveguide mode and quasi-optical H -polarized fundamental mode is depicted in Fig. 3a,b. The so called quasi-fundamental modes are of great interest. These modes have high Q, because the energy of these modes is concentrated into the immediate vicinity of a resonator axis. It can be easily observed in the Fig. 3c. The excitation of the E -polarized oscillation and the concentration of the field for the next modes in the corner-echelette OR was predicted by this particular method and experimentally verified in the orotron [7].

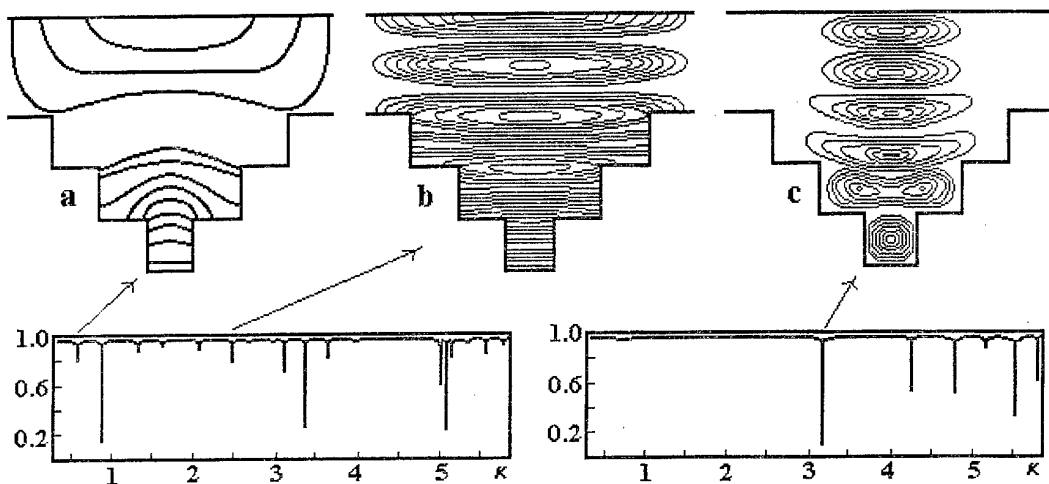


Figure 3.

Conclusion: The method involving the use of the waveguide concept and decomposition of the complex-shapes model into the key blocks is very useful medium for the analysis of the OR with a step-like deformation of its constituent surfaces in the quasi-optic. It permits to obtain accurate results for a small-size aperture OR ($a \sim 10\lambda$) where the application of the regroups diffraction theory is incorrect. This method is best suited to the problem of the OR excitation by the outer source, which maximally correlates with the elaboration of mm wave devices, e.g. the quasi-optic solid-state generators and the orotrons.

References.

1. V.P.Shestopalov, "Spectral Theory and Open Structure Excitation", Naukova Dumka, Kiev, pp. 288, 1987.
2. V.P.Shestopalov, A.A.Kirilenko, A.S.Masalov, Yu.K.Sirenko, "Resonance in Wave Scattering. Vol.1. The Diffraction Gratings", Naukova Dumka, Kiev, p. 232, 1986.
3. A.A.Kirilenko, M.V.Orlov, V.I.Tkachenko, "Stepped Model of Smooth Irregularities Corrected for Location of Equivalent Reflection Surface", Electronic Letters, No. 29(25), pp. 2180–2181, 1993.
4. A.V.Archipov, O.I.Belous, B.M.Bulgakov, A.I.Fisun, "Quasi-Optical Gunn and IMPATT Generators with Sphere-Corner-Echelette Resonator", Instrument and Experimental Techniques, No. 3, pp. 106–109, 1991.
5. L.A.Vainshtain, "Open Resonators and Open Waveguides", Moscow, p. 475, 1966.
6. R.Mittra, S.W.Lee, "Analytical Techniques in the Theory of Guided Waves", N.Y., 1971.
7. A.A.Kirilenko, V.I.Tkachenko, "System of Electromagnetic Simulation of SHF-and EHF-devices", Radioelectronics and Communication System, No. 39(9), pp. 17–28, 1996.

MILLIMETER WAVE SIGNALS DETECTION BY MEANS OF MONOCRYSTAL HEXAGONAL FERRITE ELLIPSOID

Marina Yu. Koledintseva, Alexander A. Kitaytsev

Moscow Power Engineering Institute (Technical University)
Krasnokazarmennaya, 14, MPEI, 111250, Moscow, Russia,
Tel. (095)362-7958, Fax: (095)362-8938, e-mail: koled@orc.ru

Frequency-selective ‘panorama’ devices on base of gyromagnetic converters (GC) for detection, visualization and measurement of power parameters of middle and high-intense microwave signals in wide frequency band (several octaves) have found application [1].

The principle of the GC operation is based on stable nonlinear resonance effects (SNLREs) at ferromagnetic resonance (FMR), taking place in ferrite resonators (FR) at power levels less than that of spin-wave instability. At interaction of microwave irradiation and FR with unmodulated resonance frequency (“resonance detection”) or modulated resonance frequency (“cross-multiplication”) nonlinear relations between transversal and longitudinal components of the FR magnetization vector are evident [1]. Thus, the longitudinal component and envelope of microwave signal, reradiated by the FR, contain information of spectrum power density of microwave radiation at the resonance frequency.

SNLREs have been already studied in crystallographically ‘isotropic’ ferrogarnet FR [2], employed in the frequency range of 300 MHz to 30 GHz. Application of prospective hexagonal monocrystal ferrites with large field of crystallographic magnetic anisotropy leads to the possibility of the GC design for mm waveband (from 30 to 200 GHz) without massive external magnets. This paper deals with the analysis of a more general case with taking into account both crystallographic H_A and form H_F anisotropy of HFE as well as its arbitrary orientation of the main crystallographic axis θ with respect to the constant field of external magnetization H_0 .

Let us consider the HFE to be a single-domain, magnetically uniaxial saturated small (compared to wavelength) ellipsoid. For an arbitrarily oriented HFE with arbitrary modulation frequencies the solution of the problem is intractable. So we make some simplifications, which correspond to real situation in GC design: (1) $H_A > H_0$; and modulation frequency is essentially less than relaxation one ($\Omega \ll \omega_r$). (2) We consider small angles of magnetization vector precession and small deviations of the HFR resonance frequency, $\omega_m \ll \omega_{res}$.

The HFE resonance frequency can be controlled (‘modulated’) in two ways. One way is the same as used in GC with ferrogarnets, that is, ‘field’ control by alternating current in the microcoil surrounding the FR. The second way is specific for the HFE, it is ‘angular’ control via deviation of the angle θ of H_A orientation.

The resonance frequency of the uniaxially anisotropic HFE with arbitrary oriented crystallographic axis and ellipsoid axis in respect to the external magnetic field H_0 is determined by method of effective demagnetization factors (sum of demagnetization tensors of form and crystallography),

$$\vec{N} = \vec{N}_F + \vec{N}_C$$

and the solution of a static problem for the equilibrium magnetization moment M_0 [3].

For both “field” and “angular” resonance frequency control with modulation frequency Ω we can represent the resonance frequency at small amplitudes of deviation as following:

$$\omega_{res} = \omega_{r0} + \omega_m \cos \Omega t, \quad (1)$$

ω_m is proportional to the magnitude of bias magnetic field variation h_z at “field” control and to the deviation of the HFE crystallographic anisotropy field orientation $\Delta\theta$ at “angular” control.

The mm-wave magnetization vector components have slowly varying amplitude and phase [4],

$$m_\alpha = G_\alpha \cos(\omega t + \varphi_\alpha), \text{ at } \alpha = x, y \quad (2)$$

where $G_\alpha = \sqrt{\left| \chi_{\alpha x} \right|^2 h_{xm}^2 + \left| \chi_{\alpha y} \right|^2 h_{ym}^2 + 2 h_{xm} h_{ym} \Delta_x}$ (3)

and h_x, h_y are components of mm-wave field (for instance, mode H_{10} in rectangular waveguide), each component of the HFE susceptibility tensor $\chi_{\alpha\beta}$ written in Cartesian coordinates in 9-component form with Landau-Lifshits dissipation term [3, 5], contains real and imaginary parts, $\Delta_\chi = \chi_{\alpha\alpha} \chi_{\alpha\alpha}'' - \chi_{\alpha\alpha}'' \chi_{\alpha\alpha}'$.

The amplitude G_α can be expanded into Fourier series,

$$G_\alpha = g_0^\alpha / 2 + \sum_{n=1}^{\infty} (g_n^\alpha \cos n\Omega t + f_n^\alpha \sin n\Omega t) \quad (4)$$

Harmonics of the envelopes of mm-wave signals, coupled by the HFE into the waveguide (transfer and reflection coefficients), also carry information on the input power at the certain frequency. They are determined via the HFE representation as an elementary magnetic dipole radiating into the waveguide, using the technique of eigenwaves and the solution of 'self-matched field' problem [3]. Then the modulation coefficient of the transferred wave approximately is [4],

$$Q \approx 0.5 \left(\frac{\omega \mu_0 V_f}{N} \right)^2 (G_x h_{xm}^2 + G_y h_{ym}^2), \quad (5)$$

where V_f is ferrite resonator volume, N is the main wave norm, $h_{xm,ym}$ are amplitudes of the mm-wave magnetic field components.

Spectra of $G_{x,y}$ determine the spectra of modulation coefficient Q . The form of the modulation coefficient harmonic amplitudes versus the relative detuning $\alpha = (\omega - \omega_0)/\delta$ coincides with the form of correspondent harmonics of the susceptibility tensor components and with the forms of analogous dependencies for the 'isotropic' case [2]. The harmonic amplitudes almost linearly increase with the normalized amplitude of modulation $q = \omega_m/\Omega$ growth at low modulation frequency Ω . Amplitudes of the harmonics in the envelope of the transferred signal are proportional to the intensity of the input signal. They also depend on the HFE physical parameters: anisotropy field, relaxation frequency, orientation, value of the external field of magnetization, waveguide path parameters, point of the HFE placement in the waveguide, etc. Maximum amplitude of any harmonic is achieved at certain combination of H_0 and angle of orientation θ for the ferrite with given H_A . Computations for the spherical HF resonator (which has the only resonance response due to the only main magnetostatic type of precession) show that at the 'field' control maximum modulation depth on the 1-st harmonic of modulation frequency corresponds to the 'zero' orientation, $\theta=0$. And at the 'angular' control with the fixed angular deviation the optimum angle of orientation this angle lies in the interval 30-70 degrees [6].

Now let us assume the HFE to be excited by the modulated mm-wave signal having the following components of the magnetic field

$$\begin{cases} h_x = h_{xm} (1+Q) \cos(\omega t + \Phi) \\ h_y = h_{ym} (1+Q) \sin(\omega t + \Phi) \end{cases}, \quad (6)$$

where $Q(t), \Phi(t)$ -modulated amplitude and phase, correspondingly.

Since the variation of the M_z follows from the geometry of the problem (see [5]):

$$\Delta M_z = \frac{m_x^2 + m_y^2}{2M_0} \cos \theta_M, \quad (7)$$

then taking into account the relation between mm-wave components m_α and h_α via susceptibility tensor voltage, we get E induced in spiral microcoil with the constructive coefficient Z :

$$E = \frac{Z}{2M_s} \cos \theta_M Q' (1+Q) (h_{xm}^2 g_x^2 + h_{ym}^2 g_y^2), \quad (8)$$

where

$$g_x^2 = \frac{(\omega \omega_M \alpha)^2 + (\omega_M \omega_1)^2 + (\omega \omega_M \cos \theta_M)^2}{(\omega \omega_1 - \omega^2 (1 + \alpha^2))^2 + (\omega \alpha (\omega_1 + \omega_2))^2}, \quad (9)$$

$$g_y^2 = \frac{(\omega \omega_M \alpha)^2 + (\omega_M \omega_2 \cos^2 \theta_M)^2 + (\omega \omega_M \cos \theta_M)^2}{(\omega \omega_1 - \omega^2 (1 + \alpha^2))^2 + (\omega \alpha (\omega_1 + \omega_2))^2}. \quad (10)$$

This output voltage has resonance character and reaches maximum at the FMR by choosing corresponding external field of magnetization and angle of orientation. The voltage increases with the reduction of the parameter

α , i.e. with the decrease of the HFE FMR width line. If the signal is non-modulated, the voltage is equal to 0. If the signal has amplitude modulation

$$Q(t) = m \cos \Omega t, \quad (11)$$

then the voltage E contains the 1-st and the 2-nd harmonics of the modulation frequency, because

$$Q' (1+Q) = -\Omega m \sin \Omega t + (m^2 \Omega / 2) \sin 2\Omega t, \quad (12)$$

and with the increase of the modulation frequency the voltage rises linearly (in the limits of 'quasistatic' approximation at relatively low modulation frequencies). With the growth of the modulation depth m the amplitudes of the voltage harmonics also increase: the first one - linearly, the second one as a square.

There is no dependence upon the phase of mm-wave signal, because of the square-law relation between the longitudinal and transversal components of the magnetization vector. Harmonics of the voltage contain information on the mm-wave power at the certain frequency. These results coincide with the solution of the same problem for 'isotropic' ferrite at low frequency and depth of modulation [2].

The processes of modulation and demodulation considered above lay the principles of design of an automodulation measuring system on HFE with feedback on the intermediate frequency and narrow-band amplifier in the feedback loop. This system operation and analysis (choosing the elements of the feedback loop, amplitude and phase relations in the circuit, threshold power level of signal detection, analysis of the generations zones width versus input microwave power) and experimental results on getting zones of generation are described in our paper [7].

The device has a number of advantages in comparison with the conventional GC and cascade junction of the GC with the crystal detector in mm-waveband: high sensitivity (10^{-7} W), high selectivity, due to the automodulation comparable to that realized in the GC on base of YIG resonators with narrow line width, about 5 MHz), larger linear dynamic range (about 50 dB), independence of the output voltage amplitude on the input power, leading to better measurement reliability. Tolerance control and power measurements become more reliable. The described system application reduces strictness of demands to the preselectors at the input of mm-wave measuring devices and thus eliminates difficulties connected with the technology of their production.

References

1. Balakov V. F. et al. "Application of gyromagnetic effects in the ferrite monocrystals for electromagnetic signals parameters measurement". *Proc. 5th ICMF'80*. Moscow. V.3, p.86-99.
2. Kitaytsev A. A., Savchenko N. I. Characteristics of monocrystal ferrite ellipsoid at alternative magnetization. *Proc. 2 Int. Conf. on microwave ferrites ICMF'74*, Zuhl, GDR, p.205-213.
3. Gurevich A.G. "Magnetic resonance in ferrites and antiferromagnetics". Moscow, "Nauka", 1973.
4. Pollak B.P. "Analysis of the hexagonal ferrite susceptibility tensor features". *Trans. of Moscow Power Engineering Institute No 320*. Moscow. pp.45-53, 1977.
5. Kitaytsev A.A., Koledintseva M.Yu. "Quasistatic approach to the analysis of magnetization vector behavior of monocrystal hexagonal ferrite with controlled resonance frequency". *Proc. 13th Int. Conf. on Microwave Ferrites ICMF'96*. Sept.23-27, 1996, Busteni, Romania, p. 33-40.
6. Koledintseva M.Yu. "The modulation of microwave field by means of acoustically controlled hexagonal ferrite resonator", *Proc. of the 1995 URSI Int. Symp. on Electromagnetic Theory*. Russia, St.-Petersburg, May 23-26, 1995, pp.735-737.
7. Kitaytsev A.A., Koledintseva M.Yu. "Millimeter wave hexagonal ferrite power converter with automodulation for frequency-selective power tolerance control and measurement". *Proc. 13th Int. Wroclaw Symp. and Exhibition on Electromagnetic Compatibility EMC'96*, June 25-28, 1996. Poland. P.372-374.

GUNN DIODE CATHODE CONTACTS PART IN THE INCREASE OF THE OSCILLATION EFFICIENCY.

Yu.V. Arkusha

*Kharkiv State University, 4, Svoboda sq., Kharkiv, 310077, Ukraine
phone (0572) 47-19-88*

By sole method basing on two-temperature model [1] n+-n, n+-n⁻-n - cathode contacts, bloking and antibloking metallic cathode contacts, bloking and antibloking heterojunctions on the cathode contact in the GaAs diodes working as on the fundamental frequency so on second and third harmonics it were investigated.

Let us examine some fundamental results for each contact when diode length is equal to 2,5 μm or less.

1. *n+-n cathode contact in the diode having unhomogeneous doping of the active region [2].*

If electron density near the cathode n_k is equal to the anode electron density n_a then diode is homogeneous doped and there are accumulation layers are propagated in it. In this case maximum efficiency is equal to ~3,4% and it was obtained on the transit mode f=45 Ghz. When k = n_a / n_k < 1 then initial heating region (IHR) near cathode is increased and efficiency is decreased quickly. When k > 1 the dipole domains are propagated in the diode and oscillation frequency are increased. Max efficiency ~ 8,2% at 300K was obtained for k = 1,5.

2. *The metallic cathode contact [3,4,5].*

In dependence from the output works correlation on the cathode it is formed either blocking metallic cathode contact (φ_m > φ_{n/n}) or antiblocking (φ_m < φ_{n/n}).

a). *Blocking metallic cathode contact (m-n).*

For the diode having l_a = 2,5 μm the optimum potential barrier height is 0,03 eV and efficiency at the optimum voltage is equal to ~ 8% on the 33 Ghz frequency. When the potential barrier height foll the cathode electric field is decreased and consequently the initial heating region length is increased and the diode efficiency is decreased. When the potential barrier increase the cathode field is increased but at the sametime increases the cathode region carrier charge deplection. An application of the blocking m-n contact in the diodes having ~1 μm and less length does not percpitive.

High electric field near cathode it is possible to obtain by help the blocking m-n⁺-n contact having high potential barrier height on m-n⁺ boundery. Whith this high contact field on m-n⁺ boundery is decreased owing to n⁺ region presence and from it magnitude depends the complex m-n⁺-n contact properties. The maximum efficiency is equal to ~ 5% (l_a = 2,5 μm)< but frequency range expanded from 10 to 65 Ghz.

b). *Antiblocking mmetallic cathode contact [m-n].*

This contact is analogi to n⁺-n cathode contact and also has one defect - low field near the cathode what undesirable in case of the short sample. Therefore m-n cathode contact is unfit for the diode having submicrometer length.

For the increase cathode field it is created narrow low doping region (n⁻ - region). In dependence from n⁻ - region length impurity concentration in it and from the output difference there are the dipole domaines or occumulation layers can propagate in the diode. With active region length 2-3 μm m-n⁻-n diodes have efficiency higher then m-n diodes. The frequency range of the m-n diode is wider then it has m-n⁻-n structure.

3. *Heterojunction on cathode contact [6,7].*

It is possible to create high cathode field by help isotype inversely biased heterojunction.

a). *Blocking isotype heterojunction on the cathode contact.*

It is studied GaAs diodes with In_xGa_{1-x}As and InP_{1-x}As_x heterocathodes. It was shown for different diodes lengthes and different semiconductor compounds in the cathode that it is optimum conductivity zone gap (ΔE_C) when the diode efficiency is maximum. GaAs diode with l_a -2,5 μm and with In_xGa_{1-x}As cathode has ~12% max efficiency (for optimum x) and with InP_{1-x}As_x cathode - ~ 9%. Frequency limit of such diodes is : for diode with In_xGa_{1-x}As cathode it equal to ~ 190 Ghz, with InP_{1-x}As_x cathode - ~ 180 Ghz.

b). *Antiblocking isotype heterojunction on the cathode contact.*

GaAs diodes with Al_xGa_{1-x}As heterocathode and with different active region length were studied. In the diode with such contact the accumulation layers are propagated. IHR near the cathode a few shortenes owing this it is possible to use the diodes having active region length less then 1μm. The frequency limit of GaAs diodes with Al_xGa_{1-x}As cathode is equal to ~ 160 Ghz.

It is big interest call the influence of the cathode contact type and active region doping profile to second and third harmonic oscillation. It is studied the diodes with m-n cathode contact, with $n^+ - n^- - n$ cathode and with unhomogeneous active region doping profile when $l_a = 2,5 \mu\text{m}$ and less.

It was shown using complex form of the voltage on the diode leads to shortening IHR near the cathode and to efficiency increase on fundamental frequency by $\sim 30\text{-}80\%$. The best diodes on second harmonic are diodes having m-n contact but on third harmonic - diodes with $n^+ - n^- - n$ contacts. Diode having $l_a = 1 \mu\text{m}$ and m-n contact has frequency range from 70 to 550 GHz on both fundamental and second and third harmonics but a frequency range of the diode with $n^+ - n^- - n$ contact is 90 - 580 GHz.

A problem of mm- and submm-wave range mastering by Gunn diodes it is possible to decide applicating the diodes based on perspective A_3B_5 semiconductor compounds. It is such compounds as $In_xGa_{1-x}As$, $InP_{1-x}As_x$, $In_{1-x}Ga_xP_{1-y}As_y$. Conducting researches were shown that when x and y in the complex A_3B_5 compounds are optimum then diode efficiency preparing on base such compounds are higher then GaAs diodes efficiency. $In_xGa_{1-x}As$ diodes with dipole domain mode can work on fundamental frequency to ~ 250 GHz, $InP_{1-x}As_x$ diodes - to ~ 180 GHz frequency. The efficiency of $In_xGa_{1-x}As$ and $In_{1-x}Ga_xP_{1-y}As_y$ diodes with accumulation layers mode by two factor higher then efficiency GaAs diode having $l_a = 2,5 \mu\text{m}$.

References

1. Аркуша Ю.В., Дрогаченко А.А., Прохоров Э.Д. "Влияние формы напряжения на энергетические характеристики коротких диодов Ганна", Радиотехника и электроника, т.32, № 9, С. 1947-1954, 1987.
2. Аркуша Ю.В., Попов А.М., Прохоров Э.Д. "Оптимальные профили легирования мм диодов Ганна при 300 и 500 К", Радиотехника и электроника, т.35, № 7, С. 1552-1553, 1990.
3. Аркуша Ю.В., Дрогаченко А.А., Прохоров Э.Д. "Влияние контакта металл-полупроводник с низкой высотой потенциального барьера на работу диода Ганна", В кн.: Электроника мм и субмм диапазонов. ИРЭ АН УССР, Н. Думка, С. 184-189, 1988.
4. Аркуша Ю.В., Дрогаченко А.А., Прохоров Э.Д. "Влияние запорного металлического катодного контакта на работу коротких диодов Ганна", Радиотехника и электроника, т.33, № 6, С. 1295-1301, 1988.
5. Аркуша Ю.В., Дрогаченко А.А., Прохоров Э.Д. "Антизапорный металлический катодный контакт к коротким диодам Ганна", Радиотехника и электроника, т.33, № 6, С. 1336-1337, 1988.
6. Аркуша Ю.В., Прохоров Э.Д., Стороженко И.П. "Гетерокатод в диодах Ганна миллиметрового диапазона", Труды 5-ой Крымской конференции и выставки "СВЧ-техника и спутниковые телекоммуникационные технологии", том 1, Севастополь, С. 127-130, 1995.
7. Аркуша Ю.В., Прохоров Э.Д., Стороженко И.П. "Гетеропереход $In_xGa_{1-x}As / GaAs$ в арсенид-галлиевом диоде Ганна", В кн.: Применение радиоволн миллиметрового и субмиллиметрового диапазонов. Сб. научн. тр.- Харьков. Ин-т радиофизики и электроники НАН Украины, С. 78-85, 1994.

MESFET VCO FOR USE IN MM-WAVE COMMUNICATIONS

S.S.Slesarenko

National Technique University of Ukraine "Kiev Polytechnic Institute"

Address: 2230, 37 Peremogi av., Kiev-056, Ukraine

E-mail: sles@slescom.kiev.ua

Introduction

Rapid increase in the number of people using personal communication systems has pushed the capacity of all channels to their limit and the problem will become even more severe with the implementation of high-speed data/video transmission services. Therefore, there is an urgent need to develop systems that use millimeter waves range. Such systems have several attractive features beyond those offered by microwave or UHF-wave systems [1]:

- 1) they have a wide frequency bandwidth, therefore, a large transmission capacity can be obtained. This solves the frequency bandwidth shortage problem faced by existing systems when high-speed mobile communication are considered.
- 2) they have large penetration losses through walls and diffraction losses. This result in compact and well-defined cell boundaries. Micro cellular or Wireless Local Area Network systems, in particular, benefit from this characteristic.
- 3) the small wavelengths allow miniaturise of the size of components - such as antennas and active devices. Miniaturized components are very important for portable sets as well as Base Station facilities, which need to be readily installed.

Therefore, many applications in the millimeter-wave frequency range (above 50 GHz), such as low-power radar and sensor systems, car navigation, noncontact identification, mobile communication, indoor Local Area Network, etc., require highly stable mm-wave sources with reasonable output power. Although the Gunn and IMPATT diodes are the conventional power sources for mm-wave radio-systems, their DC to RF conversion efficiencies, cost and power supply is not optimal. Perfectly justify using a low cost MESFET for the active device in miniature VCO [2].

Modeling

In the generalized problem of VCO design using a two-port active device that the embedding networks for oscillating systems are those that result in net power flow out of the active device.

The total power delivered to the device is given by:

$$P = \frac{1}{2} Re(V_1 I_1 + V_2 I_2) \quad (1)$$

where P is negative for net power flow out of the device.

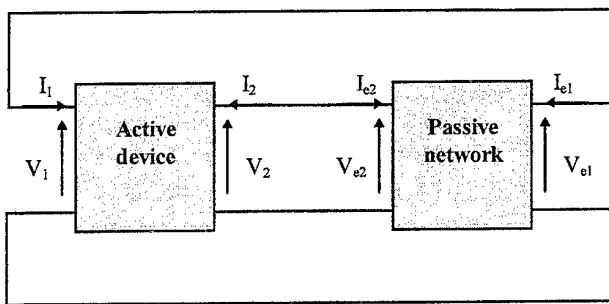


Figure 1. Equivalent circuit for generalized two-port oscillator design

The complex ratio of the port 2 voltage (V_2) and the port 1 voltage (V_1) is defined as:

$$A = \frac{V_2}{V_1} = A_r + j A_i \quad (2)$$

The active device is described by Y-parameter matrix:

$$\begin{bmatrix} I_1 \\ I_2 \end{bmatrix} = \begin{bmatrix} y_{11} & y_{12} \\ y_{21} & y_{22} \end{bmatrix} \begin{bmatrix} V_1 \\ V_2 \end{bmatrix} \quad (3)$$

The total power delivered to the active device can be expressed in terms of V_1 , A_r , A_i and the Y-parameters:

$$P = (g_{11} + g_{22})(A_r^2 + A_i^2) + (g_{12} + g_{21})A_r - (b_{12} - b_{21})A_i \cdot |V_1|^2 \quad (4)$$

where g_{ij} and b_{ij} are the real and imaginary parts of y_{ij} , respectively.

When V_1 is assumed to be a constant, the values of the real and imaginary parts of A that result in the negative minimum of P correspond to the maximum power output from the device. The value of A that corresponds to this optimum point can be found from the partial derivatives of (4) with respect to A_r and A_i . This value is:

$$A_{opt} = -\frac{y_{21} + y_{12}}{2g_{22}} \quad (5)$$

An oscillator at steady state will have the following relationships between the voltages and currents of the active device and the voltages and currents of the embedding network:

$$\begin{aligned} V_1 &= V_{el} & V_2 &= V_{e2} \\ I_1 &= -I_{el} & I_2 &= -I_{e2} \end{aligned} \quad (6)$$

A good starting point for designing the embedding network for an oscillator is to use the Y-parameters of the active device at the gain compression point corresponding to the maximum oscillator power. This value of gain is given by:

$$G_{ME} = \frac{G_0 - 1}{\ln G_0} \quad (7)$$

where G_0 - small signal uncompressed value, G_{ME} - large signal compressed value of the maximum efficient gain

The Y-parameters at this point can be estimated by reducing the transconductance in the equivalent circuit of the active device or by simply reducing the magnitude of the S-parameter S_{21} until the desired value of gain is obtained.

It is not clear that the magnitude of the port 1 voltage (V_1) will remain constant for all values A. A better way to maximize the output power is to determine the value of A, which gives the maximum two-port added power for the oscillating system. The two-port added power is defined as:

$$P_{add} = P_{out} - P_{in} \quad (8)$$

The added power in a two-port oscillator design can be maximized by the next method [3]:

The power delivered to port 2 ($P_2 = -P_{out}$) is taken to be any arbitrary negative constant, (power is going out), and the power delivered to port 1 ($P_1 = P_{in}$), which is positive (power is going in), is minimized. Since the phase in the oscillating system is arbitrary, we can select the phase angle of V_2 to be zero ($V_2 = V_{2r}$). This establishes a relationship between the real part of I_2 (denoted by I_{2r}) $V_{2r} I_{2r}$ and the negative power delivered to port 2 (P_2).

$$P_2 = \frac{1}{2} \operatorname{Re}(V_2 I_2) = \frac{1}{2} V_{2r} I_{2r} \quad (9)$$

$$I_{2r} = \frac{2 P_2}{V_{2r}} \quad (10)$$

The imaginary part of I_2 (denoted by I_{2i}) and V_{2r} are taken as independent variables. The real part of I_2 is a function of P_2 and V_{2r} . The imaginary part of V_2 has been set to zero. The current and voltage at port 1 (V_1, I_1) are functions of the port 2 variables as determined from the Y-parameter matrix. The power delivered to port 1 is given by:

$$P_1 = \frac{1}{2} \operatorname{Re}(V_1 I_1) \quad (11)$$

$$V_1 = \frac{I_2 - y_{22} V_2}{y_{21}} \quad (12)$$

$$I_1 = y_{11} \left(\frac{I_2 - y_{22} V_2}{y_{21}} \right) + y_{12} V_2 \quad (13)$$

The input power can be minimized by taking the partial derivatives of P_1 in terms of V_{2r} and I_{2i} , and setting them equal to zero. The corresponding values of the independent port 2 variables for maximum added power are:

$$I_{2i} = -\frac{V_2 (g_{12} b_{21} + g_{21} b_{12} - 2 g_{11} b_{22})}{2 g_{11}} \quad (14)$$

$$V_{2r} = 2 \cdot \sqrt{\frac{P_2^2 g_{11}^2}{N}} \quad (15)$$

$$N = 4 g_{11} g_{22} (g_{11} g_{22} + b_{12} b_{21} - g_{12} g_{21}) - (g_{12} b_{21} + g_{21} b_{12})^2 \quad (16)$$

The port 1 variables (V_1, I_1) can be calculated from these optimum port 2 variables through the Y-parameters. The value of A_{opt} is given by V_2 / V_1 :

$$A_{opt} = \frac{-2 g_{11} y_{21}}{\sqrt{N + 2 g_{11} g_{22} + j \cdot (g_{12} b_{21} + g_{21} b_{12})}} \quad (17)$$

The ratio of the arbitrary constant $P_2 = -P_{out}$ and the minimum input power at port 1 (P_1) is equal to the maximum power gain of the active device. This optimization of A is equivalent to simultaneously matching the input and output ports for maximum added power in the feedback loop.

Results

The final circuit was constructed on waveguide-microstrip performance. Voltage controlled oscillator based on 0.25 μ m GaAs MESFET. When biased at $V_{ds} = 3$ V and $I_{ds} = 25.5$ mA, this VCO oscillated at 62 GHz with an output power of 5 dBm. The DC to RF conversion efficiency is estimated to be 4.2 %. Out of oscillator is fabricate like standard waveguide 3.6x1.8 mm.

References

1. L.G.Gassanov, N.N.Kobak, S.S.Slesarenko, "A New Concept for Wireless Local Area Network", In: Proc. 5th Int. Symp. on Recent Advances in Microwave Technology, Kiev, pp.46-48, September 1995.
2. U.Guttich, "Active Elements Used in Microstrip Dielectric Resonator Oscillators", Microwave Journal, No.4, pp.92-95, April 1996.
3. Brian K. Kormanyos, Gabriel M. Rebeiz, "Oscillator Design for Maximum Added Power", IEEE Microwave and Guided Wave Letters, Vol.4, No.6, pp.205-207, June 1994.

BASIC PRINCIPLES OF ELABORATED OF SOLID-STATE MILLIMETER WAVE SOURCES WITH DISPERSIVE OPEN OSCILLATING SYSTEMS.

O.I.Belous, B.M.Bulgakov and A.I.Fisun.
 Institute for Radiophysics and Electronics
 12, Proskura Str., Kharkov, 310085, Ukraine
 Tel. 44-87-41, Fax. 44-11-05, E-mail obel@ire.ire.kharkov.ua

One way decreasing the frequency stabilization is to use the oscillating contour of generator with high-unloaded Q -factor. This way is manifested in the development of quasi-optical solid-state oscillators [1]. However, the problem of the matching of the active nonlinear element (Gunn-or IMPATT-diode) and the distributed-parameter system such as an open resonator (OR) up to now has not optimum solution. The matching circuits consists of several components. A typical flowchart of matching circuit and OR shows in Fig. 1, where 1 is active element with eigen oscillating contour, 2 is matching circuit, 3 is quasi-optical oscillating system and 4 is load. The system depicted here has a several losses at the matching and radiating components.



Figure 1.

The matching function combination with h high unloaded Q -factor of the oscillating system is effected by OR with impedance transformation on the one of mirrors [2,3]. In this situation the quasi-optical flowchart will be presented as indicated in Fig. 2. Here, OR plays a broad spectrum of roles. Under this flowchart, we list basic principles of elaborated of solid-state millimeter wave sources.

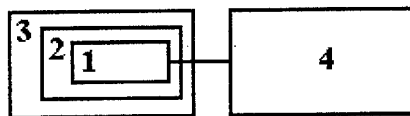


Figure 2.

1. A dispersive mirror allows one to rarefy the spectrum of eigen mode of OR and increase the Q -factor of operating mode while retaining the fundamental advantages of OR with smooth reflectors, which have the same reflecting factor in the wide frequency band. This improves the spectral characteristics and the dynamic stability of oscillators. There fore, a dispersive mirror OR is more advantageous for application in oscillation systems with matching components.
2. The frequency of quasi-optical oscillator determined by OR. The influence of the tuner on the frequency oscillation can be expressed by

$$\Delta\omega = \frac{1}{\sum_{j=1}^2 \left(\frac{\partial B_j}{\partial \omega} \right)} \text{ in condition } \omega \approx \omega_r,$$

where $\Delta\omega$ is the variation of the operating frequency of the oscillator due to the shift of the mirror or variation of the matching parameter, B_1 is the susceptance of OR and B_2 is the susceptance of the matching circuit at the diode terminans. Let us take into account that (in resonance condition $\omega \approx \omega_r$)

$$\frac{\partial B}{\partial \omega} = \frac{2G}{\omega_r} Q,$$

where G is the active conductance of resonance circuit. The Q -factor of the OR is greater by several orders of magnitude than the matching circuit Q . Hence, the OR controls the generator frequency.

3. A multicircuit impedance matching can best be allow in quasi-optical solid-state oscillators. The circular-disk resonator is used as a first matching circuit for IMPATT-diodes. It consists of a metal to ceramic diode case and radial cap with a bias pin. A Gunn-diode is matched without a circular-disk resonator. A rectangular waveguide section serves as an intermediate matching element.

The key feature of the corner-echelette OR is in the matching properties of the corner-echelette mirror, by virtue of impedance transformed property one [3].

The high Q of several modes and the field transformation near the impedance transformed mirror are a new quality of the open resonator with additional restriction of resonance space of OR. They allow one to improve both the spectral and power characteristics of the quasi-optical oscillator

References.

1. J.Bac, Y.Aburacava, H.Kondo, T.Tanaka and Mizuno, "Millimeter and Submillimeter Wave Quasi-Optical Oscillator with Gunn-Diode", IEEE Trans. MTT-41, No.10, pp.1851-1855, 1993.
2. A.T.Fialkovsky, "Open resonator shaped by plane mirror with impedance stepped on borders" Technical Physics Journal, vol. 26, No. 6, pp. 1100-1108. 1966.
3. A.I.Fisun, "Constructive Synthesis of Dispersive Oscillation Systems of Quasi-Optical Solid-State Millimeter-Wave Sources", EW&ES, Vol.2, No.5, pp.37-43, 1997.

EFFICIENCY of the APERTURE of the RECONSTRUCTIVE INTERFEROMETER

Vladimir N. Uvarov

Institute of Radiophysics and Electronics of National Academy of Science of Ukraine
 Acad. Proskura str, 310085 Kharkov, UKRAINE
 FAX 38 (0572) 441-105, Phone 38 (0572) 440-011,
 E-mail: ire@ire.kharkov.ua.

1. 90 -th XX century in optical astronomy is note by the system appearance, allowing get the image with millisecond angular resolution. At present the projects such system with the efficient aperture scale subkilometer and size subaperture before ten metre already are realized [1]. The projects with the size of aperture up to 100 km are discussed [2].

Particularity these system - use rarefy aperture. Using the rarefying apertures is stipulate by the desire to reach a high angular resolution with the minimum area very costly optical surface.

2. As the aperture is the filter of space frequencies its rarefying leads to defects in the frequency area and to worsening of the quality of the received image. The optimization of the rarefied aperture for the improvement of the quality of the image may be achieved on the basis of one from the existing criterions developed as in the theory of the synthesis of the antennas as the adaptive optics: minimization of mean or maximum value of the lateral lobes of the directional diagram, the criterions of the sharpness of the image or the integral interferometrical criterions. All these criterions are rather effective for the one pointlike source. For the more complicated objects the application of these criterions does not guaranteeig the maximum similarity of the received image to the investigated object. Therefore optimization of the aperture should be based on the criterions which are taking into account the space frequencies properties of the objects.

The existing assessments of the efficiency of the vision systems (imaging systems, system of vision with before and post detection processing, system of aperture synthesis) are based on the Reley criterions defining minimum size of an independent pixel [3]. However this criterion is applicable only at a qualitative level to modern astronomical systems as corresponds to a case of the circle and filled aperture at rather large (order 10) signal-to-noise ratio. The modern reconstructive interferometrical systems has the rarefied apertures. The conditions of registration are characterized by a low level of a signal and strong photon noise accordingly.

In this work the generalization of the resolution criteria on the basis of the decision theory and the space frequencies properties of the investigated objects carried out. On particular examples the efficiency of these assessments is shown.

3. The imaging system effectiveness can be defined as a posteriory probability of the correct recognition of the objects on the registered image. On the basis the decision theory the binary problem [4] about observation of the objects H1 and H2 the probability the correct choise can be recorded as

$$P(R|H1) = \int [1 + 2/\pi^{1/2} \int_{-\infty}^z \exp\{-x^2\} dx]/2, \quad (1)$$

$$z = 1/2 \int [F(H2 - H1) * T(f)]^2 df / D(R|H1)]^{1/2}, \quad (2)$$

$$\text{where } T(f) = \int |A(r-f) * A(r)| dr / \|A(r)\| dr \quad (3)$$

There F (*) - Fourier-transformation, T (*) - the optical transfer function of the aperture, A (*) - the aperture function, D (R | H1)] - the dispersion of the obtained image relative to the priori image H1.

From here follows, that two objects can be distinguished one from other if the spectrum of the difference image is nonzero within the passband of the optical system. The influence of the optical properties of the aperture on the probability of the correct choice can be appreciated on the basis of this equation. Besides it is possible to use a spectrum of the difference image as a value space - frequent standard for optimization of the aperture.

4. For the measure of influence of the aperture on the efficiency of the system it must to execute the Reley test experiment, at which the object H1 is $\delta(x, y)$, that is one pointlike object emitting I_s of photons per the subaperture; H2 is $\delta(x - x/2, y) + \delta(x + x/2, y)$, that is two pointlike objects each of them emitting $I_s/2$ photons per the subaperture.

For this case

$$F(H1 - H2) = 2 * I_s * \sin^2(\pi/2 f_x \Delta x). \quad (4)$$

Substitute (4) in (2) receive

$$z = ((I_s^2 / D)^{1/2} \sin^4(\pi/2 f_x \Delta x) T(f_x f_y)^2 df_x df_y)^{1/2} \quad (5)$$

Let's brings the relative spatial frequencies ($v = fx / f_{\max}$, $u = fy / f_{\max}$, $\rho = (u^2 + v^2)$, $\psi = \arctg(v/u)$) and the factor of a posterior resolution as the relation of the given system resolution to the diffraction limited resolution with the aperture size $R = \delta x * f_{\max}$. Taking into account (1), (2) and the photons registration process of submits to the Poisson statistics ($I^*S = D$) the results for verisimilitude of the image is

$$P = (1 + \text{Erf}\{\sqrt{I_S * M * U(R)}\})/2, \quad (6)$$

Here $\text{Erf}\{\cdot\}$ - the integral of probability (Gaussian integral), M - the number of the subapertures in the whole aperture, U - effectiveness factor of the aperture structure.

$$U = \int_0^1 T^2(\rho, \psi) \rho d\rho \int_0^{2\pi} \sin^4(\pi/2 R \rho \cos(\psi)) d\psi. \quad (7)$$

5. It is possible to install from expressions (6) and (7) follow.

- The system effectiveness P depends on the light flow intensity on one subaperture I_S , the number of the subapertures M and the efficiency factor of the aperture structure U by an identical way.
- The efficiency factor of the aperture structure U is a function of the aperture configuration, spectrum of the difference test image and the factor of the posterior resolution R .
- The spectrum of the difference test image can be considered as the measure of the value of the received information and to use for optimization of the aperture.

6. Obtained results may be illustrated by a few examples.

⇒ Ideal system with the circle aperture and large signal-to-noise ration. There are for the parameter of efficiency of the structure and the verisimilitude of the received image assuming the optical transfer function of the aperture as a circle cone $T(\rho) = 1 - \rho$, ($1 > \rho > 0$,) for the circle aperture ($M = \pi N^2$) is

$$U_{ID} = \int (1-\rho)^2 \rho d\rho \int \sin^4(\pi/2 R \rho \cos(\psi)) d\psi. \quad (8)$$

$$P_{ID} = 0.5 * [1 + \text{ERF}\{\sqrt{\pi I_S * U_{ID}}\}]. \quad (9)$$

In this case the aperture efficiency U does not depend on the size of the aperture N . The growth of the verisimilitude of the obtained image P is depended on increasing of the test spectrum value on the high spatial frequencies and the general energy of the image.

⇒ For assessment of the effectiveness of the system in conditions of the phase instability with recovery of the specke interferometry method we take the results of [5]

$$\langle |T(\rho)|^2 \rangle = 0.4 * T(\rho) / N^2, \quad (10)$$

There N - the linear size of the apertures in the numbers of the Fride parameter (which corresponds to diameter of the coherence field area). It is obtained for case of the circle aperture ($M = \pi N^2$)

$$U_{SP} = 0.4 J(R) / N^2, \quad (11)$$

$$P_{SP} = 0.5 * [1 + \text{ERF}\{\sqrt{0.4 \pi I_S * J(R)}\}]. \quad (12)$$

$$J(R) = \int (1-\rho) \rho d\rho \int \sin^4(\pi/2 R \rho \cos(\psi)) d\psi, \quad (13)$$

It is resulted from these expressions that the efficiency factor U_{SP} varies in inverse proportion to the size of the aperture N . The verisimilitude P_{SP} does not depend on the sizes.

⇒ The nonredundant aperture. A geometric properties of the such aperture structure is enough well approximated by the properties of the fractal cluster [6]. It can be written the relationship for the circle shape of the aperture

$$M = \pi N^D = \pi N_0^D r^D, \quad N = N_0 * r, \quad 0 < r < 1, \quad (14)$$

Here M - number of elements ('weight' of a cluster), N - linear cluster size, D - fractal dimensions.

Let's enter the concept an cluster aperture function as a probability density of the arrangement of the subapertures

$$A(r) = dM/dN / (2 \pi N) = D * (N_0 r)^{D-2} / 2; \quad (15)$$

The expression obtaining from (3) and (14) for an optical transfer function is

$$T(\rho) = (D-1)^2 * \Theta(\rho); \quad (16)$$

$$\Theta(\rho) = \int_0^1 dx \int_0^{1-x} dy \int_0^1 [(x-y)^2 + y^2]^{(D-2)/2} dy \quad (17)$$

$$U_{NRD} = (D-1)^4 * \Phi(D); \quad (18)$$

$$P_{NRD} = 0.5 * [1 + \text{ERF}\{(D-1)^2 * \sqrt{N_0^D * I_S * \Phi(D)}\}]; \quad (19)$$

$$\text{where } \Phi(D) = \int_0^1 \Theta(\rho)^2 \rho d\rho \int \sin^4(\pi/2 R \rho \cos(\psi)) d\psi \quad (20)$$

The expressions (18) and (19) allow to determine the effectiveness of the system depending on a level of the signal, the size and the structure of the aperture. They are brought on drawings, from which is seen that

- efficiency of aperture decreases with the growing of it fractal dimentions;
- plausibility grows with increasing the size of the aperture;

- for smaller values the fractal dimentions the plausibility is more. This result becomes understandable if to taking into account that quantity of light energy per one passing window of the space frequency (and accordingly on one the Fourier component of the image) decreases with the size of the aperture as $1 / (N-1)$. Thence follows that the more rarefied apertures with the alike number of the subapertures are more efficient.
7. As the efficiency of the filled phase outraged or rarefied aperture decreases with increasing the size it is more perspective strategy to partition of the aperture with large number of the subapertures into a set of partial systems with small number of the subapertures and independent registration for the further synthesis of the resulting image, as it was offered in [7].

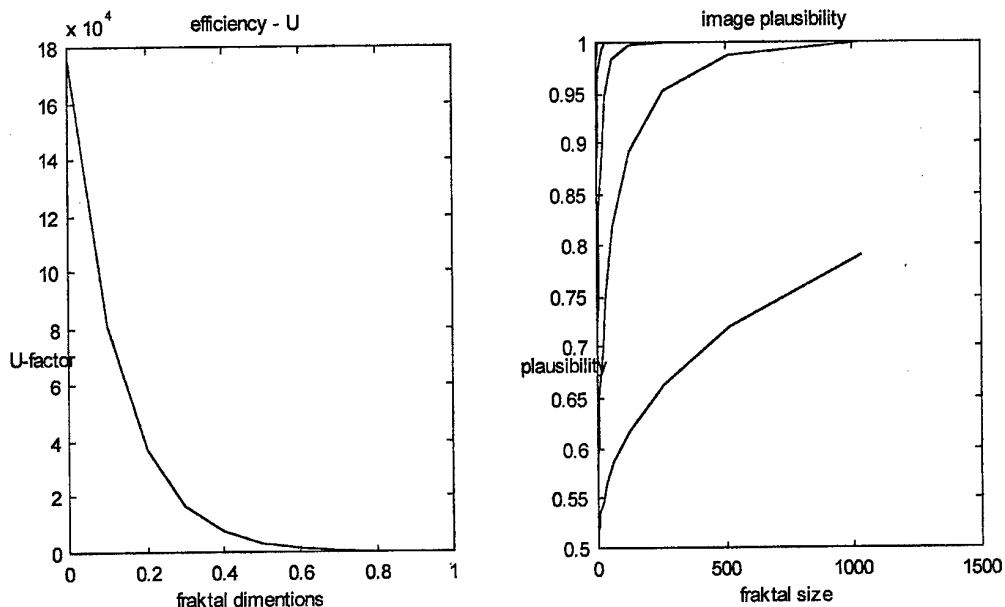


Figure 1 Efficency factor and plausibility of rarefied apertures

8. References

- 1) Luhe O. An Introduction to Interferometry with ESO Very Large Telescope./Recent publication on VLTI. European southern observarory. Technical preprint N 73. Science with the VLTI, ESO Workshop, F.Paresce (Ed.), June 1996.
- 2) Labeyrie A. Resolved imaging of extra-solar planets with future 10-100 km optical interferometric arrays. *Astronomy and Astroph. Supp. Ser.* 1996,118, p.517-524.
- 3) Born M., Wolf E.. The principles of optics. Pergamon Press. 1968
- 4) Harris J.L. Resolving power and decision theory.- *J.Opt. Soc. Am.*, 1964, 54, 5, p.606-611.
- 5) Korf D. Analysis of method for obtaining near-difraction-limited information in presence of atmospheric turbulence. - *J. Opt. Soc. Am.*, 1973.63.8.p.971-980.
- 6) E.Feder. Fractals. 1991 260 pages.
- 7) Uvarov V.N. About a capability of obtaining of the difraction limited images through inhomogeneous media. // Reports Sci.Ac USSR. A.- 1979, № 10, page 839 - 841.



**ELECTRONICS OF MM AND SUBMM
WAVES, INCLUDING QUANTUM AND
RELATIVISTIC ELECTRONICS**

**GYROTRON AS A SOURCE OF PROBING RADIATION FOR COLLECTIVE THOMSON
SCATTERING EXPERIMENTS**

E.V. Suvorov, W. Kasperek*, L.V. Lubyako, N.K. Skalyga, V. Erckmann**, TH. Laqua**,

Institute of Applied Physics, Russian Academy of Sciences

46 Ulyanov Str., Nizhny Novgorod 603600, Russia

**Institut für Plasmaforschung, Universität Stuttgart*

D-70569 Stuttgart, Germany

***Max-Planck-Institut für Plasmaphysik, EURATOM Association*

D-85748 Garching, Germany

Collective Thomson scattering (CTS) of electromagnetic radiation from thermal electron density fluctuations in principle allows to measure the velocity distribution of plasma ions and their composition. The main concept of CTS diagnostic is based on the measurements of CTS spectra in some fixed scattering geometry. Because of extremely low level of scattered radiation a powerful source of probing radiation and a sensitive spectrum analyzing system are required for CTS. Powerful gyrotrons of mm wavelength region developed for electron cyclotron heating and current drive seem to have also good prospects to be used in collective scattering experiments. Their advantage as compared to infrared range generators is possibility to use 90 degree scattering geometry, providing the opportunity of local measurements with good spatial resolution. These sources at present deliver a power approaching 1 MW in a few seconds pulse duration and are challenging cw operation. The long pulse duration gives additional opportunity to increase essentially the sensitivity of CTS system based on gyrotron due to averaging procedure. These are the main reasons why CTS experiments with gyrotron as source of probing radiation were widely planned and even performed at a number of installations.

There are, however, some essential differences in gyrotron radiation features required for CTS in contrast to plasma heating. Additional rather strong requirements to the source of probing radiation for CTS experiments are: high mode purity, low frequency drift during RF pulse and very high shot-to-shot stability of operating regime.

Before starting CTS experiments at W7-AS (Garching, Germany) a number of 140 GHz gyrotrons designed for ECRH and ECCD experiments were examined from point of view their applicability also in CTS experiments. In the course of upgrading ECRH system newly arriving gyrotrons were also tested. As a result characteristics of the seven 140 GHz gyrotrons routinely operating during different periods in W7-AS ECRH system were examined. The most of data were obtained using the detection system designed for registration of CTS spectra with the total band of the spectrum analysis from 50 to 1200 MHz (more information about it is presented in the report "Detection system for the measurements of collective Thomson scattering spectra in fusion plasma"). With receiving CTS antennas being installed at W7-AS the stray gyrotron radiation scattered from the empty vacuum chamber was mainly used in this analysis.

First we present results concerning the mode purity of the gyrotron output radiation. Five of seven tubes investigated demonstrated no signs of spurious modes in the bandwidth of ± 1.2 GHz from the line center. One of the tubes ("CI" namely) in every shot demonstrated two satellites 130 MHz apart from the line center. The spectrum of "CI" RF pulse measured with the spectrum analyzer of low sensitivity is shown in Fig.1. It was impossible to use this tube in CTS experiment. More sophisticated behavior was demonstrated by "EIP" tube. In the course of CTS measurements it was discovered that in

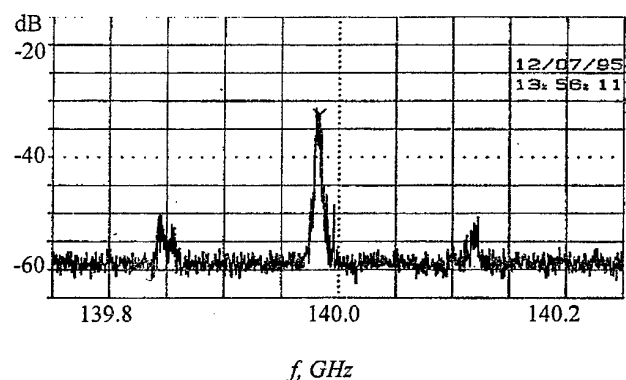


Figure 1. Spectrum of gyrotron "CI" output radiation.

identical operation regimes in some shot no spurious modes were seen with a rather sensitive CTS detection system, while in other shots the system was overloaded in channels corresponding to the frequency about 130 MHz and its 3-4 harmonics. It was not clarified either these harmonics were presented in the spectrum of gyrotron radiation or they were generated by the overloaded detection system itself.

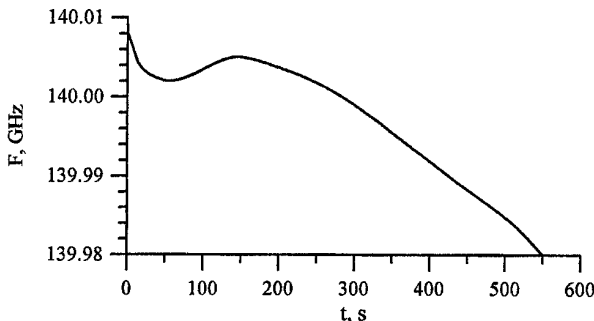


Figure 2. Gyrotron "AII" frequency evolution during RF pulse.

pulse. "AII" tube demonstrated the frequency drop with approximately constant rate about 100 MHz/sec during 1 sec RF pulse. Similar behavior is typical also of "AIII" tube but with lower frequency drift, - about 40 MHz in a 1 sec RF pulse.

For tubes "CI", "CII", "EI", "EII" (long pulse tubes up to 3 sec pulse duration) with the intense water cooling of the cavity and programmed establishing of quasi-steady-state regime of microwave power generation two significantly different stages of RF pulse can be distinguished. In the initial stage frequency is decreasing with a rather high rate after which the quasi-steady-state phase of RF pulse is established. The latter stage is characterized by random slow variations in the central line frequency with not more than 10 MHz deviation and reliable shot-to-shot stability of operating regime within the same limit. Transient stages are significantly different for tubes «C» and «E»: for "CI" and "CII" the duration of transient stage is a few hundred ms, and the drop in the central line frequency during it is about 600 MHz. The corresponding values for "EI" tube are 70 ms and 100 MHz, and for "EII" - even less than for "EI". Very fast frequency variation in the transient stage makes it impossible to use "CI" and "CII" tubes for CTS measurements in a short pulse (which are preferable for moderate-size installation like W7-AS). Gyrotrons "EI" and "EII" demonstrate tolerable repetition stability also in the transient stage, which allows to use them in a short pulse for CTS measurements.

As a summary plots of frequency evolution during RF pulse for tubes of «C» and «E» types are presented in Fig.3 together with the same characteristics of «AII» tube shown for comparison.

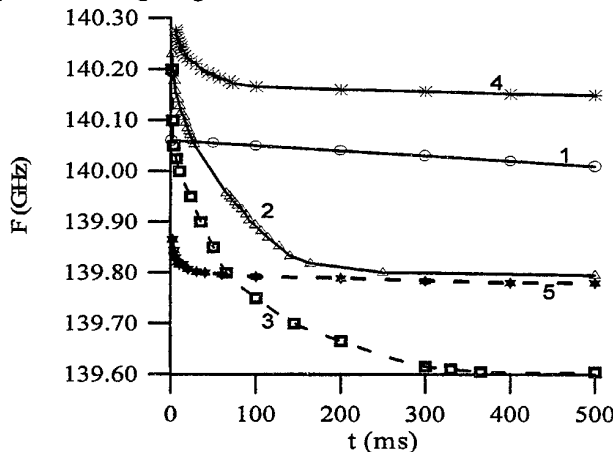


Figure 3. Frequency evolution for gyrotrons: "AII" - 1; "CI" - 2; "CII" - 3; "EI" - 4; "EII" - 5

type with a special care may be used also in a short pulse operation regime.

Another point important for CTS application is frequency variation during RF pulse and shot-to-shot stability of operating regime. Minimum frequency drift and the best reproducibility of the operation regime are obtained from the tube with inertial cathode cooling ("AI", "AII" and "AIII"). After few millisecond of transient regime all of these tube demonstrate very high shot-to-shot repetition stability varying in the generated RF frequency by less than 5 MHz in the corresponding parts of the pulse. The frequency variation during the pulse generated by "AI" tube is shown in Fig.2. It can be clearly seen that the total frequency is varied by not more than 25 MHz during 0.5 sec RF pulse.

To provide opportunity of short pulse operation of «CII» tube in a short pulse operation a specific regime was found with a programmed variation of output power. Corresponding frequency characteristics in such a pulse were suitable but in reality this pulse was not used in a real CTS experiment.

Frequency drift during RF pulse measured for 140 GHz gyrotrons designed for ECRH at W7-AS put some limitations to the fraction of generated RF pulse which may be used in CTS measurements. Gyrotrons of "A"-type are quite suitable for such experiments both in short and long pulse operation regimes. A quasi-steady-state fraction of RF pulse from gyrotrons of «C» and «E» types can be used in CTS, but additional limitations from conditions of W7-AS operation put severe restrictions for such measurement procedure. Gyrotrons of «E»

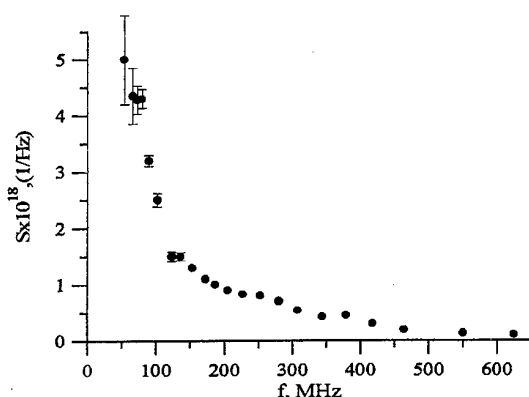


Figure 4. The spectrum of eigen noise of gyrotron "EI".

A serious problem for CTS in a moderate size installations is the stray radiation which couples from emitting antenna to the receiving one via side lobes and multiple reflections from the chamber walls. This radiation can disturb the operation or even destroy the detection system; this problem can be treated, in principle, by introducing the notch-filter at the receiver input. But the other problem is intrinsic noise generated by the gyrotron outside the central frequency in the same frequency range as expected scattered signal. The level of this noise is defined by the gyrotron and decoupling between emitting and receiving antennas only; the ratio of the signal to this noise is practically impossible to improve by some additional procedure. The measurements of gyrotron noise spectrum were also performed with the same detection system calibrated

by ECE at the second harmonics. As an example the spectrum of eigen noise of "EI" tube is presented in Fig.4. The specific noise intensity drops approximately as $1/f$ being of order of $\sim 10^{-18} \text{ Hz}^{-1}$ at the frequency shifted by 200 MHz from the line centre. Other tubes demonstrate similar behavior with the absolute values differing by the factor 2-3. With the expected level of scattered signal in the range few tens eV such noise characteristics allow to perform CTS measurements if decoupling between emitting and receiving antennas not less than 40 dB is provided. Such a possibility was successfully demonstrated in a proof-of-principle experiments at W7-AS, both thermal and nonthermal CTS spectra were registered gyrotrons "AII" "EI" and "EII" [1, 2].

So even gyrotrons designed for ECRH and ECCD can be successfully used for Collective Thomson Scattering experiments. Nevertheless the quality of CTS measurements can be essentially improved with using a specially designed gyrotron which should possess not extreme RF power and the pulse length but instead provides negligibly small frequency variation during RF pulse and high shot-to-shot reproducibility of operating regime. Besides, in order to perform CTS measurements in ECRH regimes the frequency of diagnostic gyrotron should be different from the frequency of radiation delivered by ECRH system. At present all the gyrotrons have slightly different frequencies (with the spread $\Delta f/f \approx 10^{-3}$) and if one of them is used in CTS measurements stray radiation from other tubes produce enormous strong disturbances in the measured spectra. A compromise could be the construction of a step-tunable tube which in the heating mode provides powerful long pulse radiation and in a second operating regime provides output power at a different (by 10-15 %) frequency with the power and pulse duration ensuring a sufficient signal-to-noise ratio for CTS.

References

1. E.V.Suvorov, V.Erckmann, E.Holzhauer, et. al. Ion temperature and beam-driven plasma waves from collective scattering of gyrotron radiation in W7-AS. *Plasma Phys. & Control. Fusion*, v. 37, pp. 1207-1213, 1995.
2. E.V.Suvorov, E. Holzhauer, W.Kasperek, et. al. *Plasma Phys. & Control. Fusion*, v. 39, N 12B, pp. B337-B351, 1997.

RELATIVISTIC GYROTRON AT THE 5th CYCLOTRON HARMONIC

V.L. Bratman, Yu.D. Grom, Yu.K. Kalynov, V.N. Manuilov, M.M. Ofitserov, and S.V. Samsonov
 Institute of Applied Physics, Russian Academy of Sciences
 46 Ulyanov St., Nizhny Novgorod, 603600, Russia
 Tel. (8312)384575, Fax: (8312)362061, E-mail: samsonov@appl.sci-nnov.ru

Abstract

A moderately relativistic high-harmonic Large Orbit Gyrotron (LOG) has been considered as a source of high power radiation in the millimeter/submillimeter wavelength range. The experiments on a LOG designed to operate at 5th cyclotron harmonic at the wavelength of 2 mm with output power of 50-100 kW are in progress. The LOG electron-optical system with a thermionic cathode is constructed and checked experimentally. It produces a thin rectilinear electron beam with an energy of 250 keV, current of 18 A, pulse duration of 10 μ s and diameter of 0.6 mm in an axial magnetic field of 16 kG. A pumping system transforms the straight beam into a beam of electrons gyrating around the axis with a velocity ratio of 1.5 and sufficiently small velocity spread. A possibility of selective excitation of the 5th cyclotron harmonic at the wavelength of 4 mm has been proved in a short-pulse experiment on LOG driven by 300 keV/30 A/20 ns electron beam.

Introduction

A gyrotron is usually the most natural solution for production of coherent radiation at millimeter waves with high averaged power. But for submillimeter waves, in spite of impressive gyrotron achievements [1-3], the preference is given to construction of rather expensive Free Electron Lasers with electron energies at least of several MeV. Meanwhile conventional gyrotrons with a strong magnetic field and electron energy of a few tens of keV has provided a power up to 100 kW at a wavelength of 0.46 mm (fundamental resonance [1]) and several tens W at 0.35 mm wavelength (second cyclotron harmonic [3]). Of course, when realizing such gyrotrons, difficult and non-completely solved new electron-optical and mode selection problems arise. These problems are especially complicated for operation at higher cyclotron harmonics whose excitation at low relativistic particle energy is not sufficiently effective. It is well-known that the excitation of the harmonics is significantly simplified at moderately relativistic energies of a few hundred keV. In order to provide a single-mode operation at higher harmonics, along with the electron energy increase a gyrotron selectivity should be enhanced. One of the possible ways is the use of a Large Orbit Gyrotron (LOG) configuration [4, 5] where a thin electron beam encircling the axis of an axi-symmetric electrodynamic system is utilized. Such a beam excites only co-rotating modes with azimuthal indices equal to the resonant harmonic number. A theoretical analysis and modeling experiments in millimeter wavelength band with a short-pulse LOG proved a possibility of selective excitation of higher harmonics.

Selective excitation of harmonics

According to the theory in a gyrotron with a traditional cavity for pitch factors, $g = v_{\perp}/v_{\parallel}$, ($v_{\perp, \parallel}$ are the transverse and axial electron velocities respectively) of order of 1-1.5 and electron energies of several hundred kilovolts, the starting currents for first few harmonics are of the same order of magnitude. A significant mode selection is achieved in a LOG, where electrons excite only co-rotating modes which azimuthal indices are equal to the resonant harmonic number. Due to non-equidistant spectrum of gyrotron modes, resonant values of magnetic field for different harmonics can be separated by the magnitude of order of the corresponding resonance lines (Fig. 1). In this case, one can hope for selective excitation of a higher cyclotron harmonic, at least for a small excess of the operating current over the starting current. The latter is confirmed by numerical simulations based on a time-domain multi-mode code.

A possibility of separate excitation of harmonics from 1st to 5th in a LOG was proved also experimentally [5]. The experiment was performed on the basis of high-current direct-action "Sinus-6" accelerator with the use of an explosive-emission cathode. The electron-optical system produced a 300 keV/30 A/20 ns thin rectilinear electron beam with a diameter of 1.5 mm, which was then transformed into a beam of electrons gyrating around the axis with a pitch factor up to 1.2 by means of a kicker. A few different LOG cavities were checked in the experiment. As a result, when decreasing the magnetic field from 12 kG down to 8 kG, we clearly observed successive excitation of the $TE_{s,1}$ modes at the harmonics $s=1-5$ with wavelength from 14 mm to 4 mm

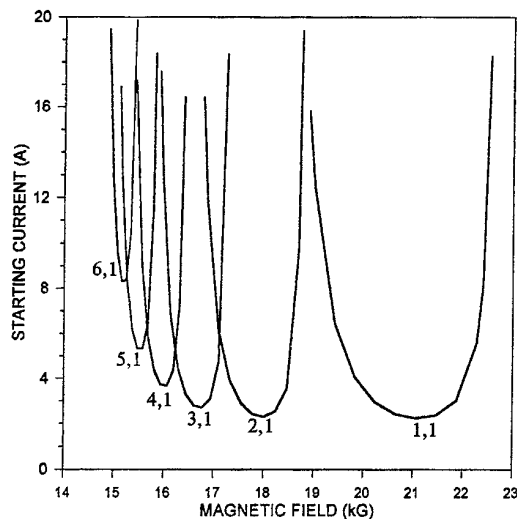


Fig. 1. Starting current of modes $TE_{p,1}$ for the LOG.

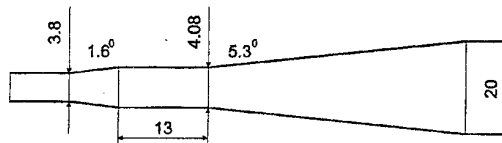


Fig. 2. Cavity of the LOG (sizes are given in mm).

Assuming a conventional current density for thermionic cathodes, 5 A/cm^2 , one obtains a very strong compression, over 1000, for the beam cross-section. To achieve such a compression without parasitic transverse velocities before the kicker a system providing particle trajectories parallel to the guiding magnetic field lines has been designed and constructed.

Following the chosen concept we find that the magnetic field at the cathode should have a very low magnitude of 0.015 kG, which corresponds to about 8 m Larmor period. The adiabatic magnetic compression in this situation is very inefficient. Therefore, the electron-optical system has been designed such that particle motion in the near-cathode region is mainly determined by fields of the quasi-Pierce gun and the space charge, while a system of coils provides the matching of axial magnetic field profile to the particle trajectories. After achieving a sufficiently strong magnetic field a conventional adiabatic compression is used for decreasing beam diameter to required level (Fig. 3).

The kicker is located in a region of adiabatic compression, in a relatively weak field, of about 5 kG. After the kicker, the electron transverse velocity is further increased in the tapered guiding field (Fig. 4). The kicker was optimized to pump the beam up to necessary pitch factor with minimum displacement of electron guiding centers from the axis and minimum sensitivity to electron position spread. For the operating parameters, simulations predict a transverse velocity spread, $(\delta v_\perp/v_\perp)_{\text{rms}} \approx 7\%$, which is sufficiently small for an effective operation of the 5th harmonic LOG. The kicker can effectively pump the beam within a very wide range, about 50%, of the axial field.

The operation of the electron-optical system was checked experimentally. The gun volt/ampere characteristics showed that at the cathode temperature of 1600 °C the designed space-charge limited regime of the operation with 18 A beam current at 250 kV voltage was achieved. The beam compression was checked by measuring of a straight beam diameter for a few points along the system in a modeling regime with a low voltage and current (22 kV/0.3 A/10 μs). Imprints produced by the beam on a perpendicular scintillator plate were observed. Results of the measurements are in a good agreement with the corresponding simulations.

respectively. The most selective excitation of the 5th harmonic with the power of 100 kW was obtained at the 2-3 time excess of the beam current over the starting one.

Basing upon theoretical and experimental results a LOG for operation at the 5th cyclotron harmonic ($TE_{5,1}$ mode) at 2 mm wavelength was designed (Fig. 2).

System of electron beam formation

Taking into account parameters of an existing high-voltage power supply [6] the following requirements for the electron beam for the LOG were determined: energy of 250 keV, current of 15-20 A, beam diameter of 0.6 mm, electrons should gyrate around the axis with minimum displacement of guiding centers and a pitch factor $g=1.5$ in a magnetic field of 16 kG.

In order to produce such a beam, a two-stage electron-optical system similar to that for the short-pulse LOG has been designed. First, a thin rectilinear beam is formed, and then the electrons acquire the necessary transverse velocity passing through a kicker. The use of a thermionic cathode, the necessity of utilizing the whole electron gun current and decrease of a beam diameter (because of double reduction of an operating wavelength) make a problem of the rectilinear beam formation for the long-pulse LOG significantly more complicated in comparison with the short-pulse one.

Assuming a conventional current density for thermionic cathodes, 5 A/cm^2 , one obtains a very strong compression, over 1000, for the beam cross-section. To achieve such a compression without parasitic transverse velocities before the kicker a system providing particle trajectories parallel to the guiding magnetic field lines has been designed and constructed.

Following the chosen concept we find that the magnetic field at the cathode should have a very low magnitude of 0.015 kG, which corresponds to about 8 m Larmor period. The adiabatic magnetic compression in this situation is very inefficient. Therefore, the electron-optical system has been designed such that particle motion in the near-cathode region is mainly determined by fields of the quasi-Pierce gun and the space charge, while a system of coils provides the matching of axial magnetic field profile to the particle trajectories. After achieving a sufficiently strong magnetic field a conventional adiabatic compression is used for decreasing beam diameter to required level (Fig. 3).

The kicker is located in a region of adiabatic compression, in a relatively weak field, of about 5 kG. After the kicker, the electron transverse velocity is further increased in the tapered guiding field (Fig. 4). The kicker was optimized to pump the beam up to necessary pitch factor with minimum displacement of electron guiding centers from the axis and minimum sensitivity to electron position spread. For the operating parameters, simulations predict a transverse velocity spread, $(\delta v_\perp/v_\perp)_{\text{rms}} \approx 7\%$, which is sufficiently small for an effective operation of the 5th harmonic LOG. The kicker can effectively pump the beam within a very wide range, about 50%, of the axial field.

The operation of the electron-optical system was checked experimentally. The gun volt/ampere characteristics showed that at the cathode temperature of 1600 °C the designed space-charge limited regime of the operation with 18 A beam current at 250 kV voltage was achieved. The beam compression was checked by measuring of a straight beam diameter for a few points along the system in a modeling regime with a low voltage and current (22 kV/0.3 A/10 μs). Imprints produced by the beam on a perpendicular scintillator plate were observed. Results of the measurements are in a good agreement with the corresponding simulations.

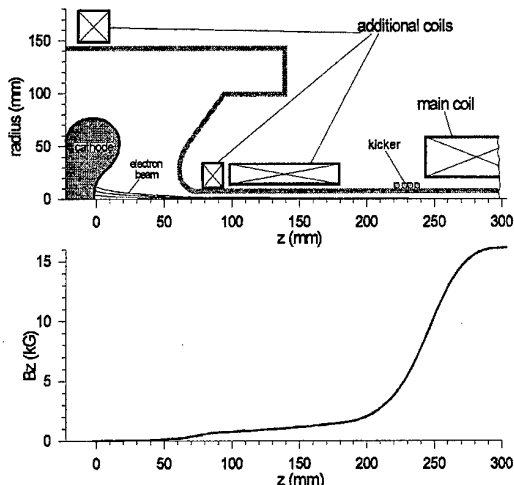


Fig. 3. Schematic of the electron-optical system and spatial profile of the axial guiding magnetic field.

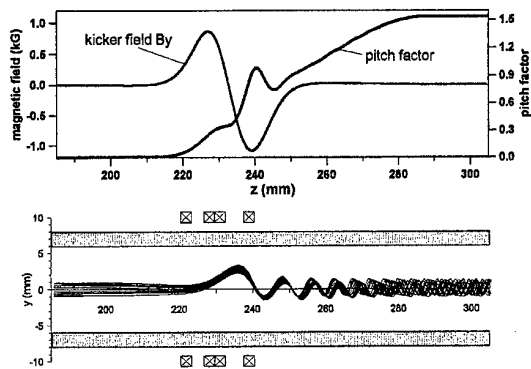


Fig. 4. Magnetic field of the kicker, pitch factor for the near-axis electrons, and particle trajectories in the helical beam formation region.

The operation of the kicker was checked at the beam voltage of 250 kV and a very low beam current (low temperature of the emitter surface). The measured mean diameter of more than 2 mm and the thickness of 0.5-0.8 mm of the observed axially centered Larmor rings in the field of 16 kG proved the correspondence of the obtained beam parameters to the designed ones.

Conclusion

A high-harmonic gyrotron with a strong magnetic field is one of the simplest candidates for development of powerful sources in the whole submillimeter wavelength range. The developed concept allows elaboration of relatively compact powerful sources in millimeter/submillimeter wavelength band. According to simulations and modeling experiments the use of moderately relativistic electron energies of order of several hundred kilovolts allows an effective generation of higher cyclotron harmonics at the wavelengths down to 0.1 mm. The experiments on the 5th harmonic LOG at the wavelength of 2 mm with an unique electron beam are in progress.

Acknowledgment

This work was supported by the Russian Interdisciplinary Scientific and Technological Program "Physics of Microwaves" and the Russian Foundation for Basic Research, Grant No. 96-02-18971.

References

1. V.A. Flyagin, A.G. Luchinin, G.S. Nusinovich, "A submillimeter-wave gyrotrons - theory and experiment," Int. J. Infrared Millimeter Waves, vol. 4, pp. 629-637, 1983.
2. S. Spira-Hakkilainen, K.E. Kreischer, R.J. Temkin, "Submillimeter-wave harmonic gyrotron experiment," IEEE Trans. Plasma Sci., vol.18, p. 334-342, 1990.
3. T. Idehara, T. Tatsukawa, I. Ogawa, Y. Shimizu, N. Nishida and K. Yoshida, "Development and applications of submillimeter wave gyrotrons," in Proc. Int. Wkshp. Strong Microwaves in Plasmas, Nizhny Novgorod, Russia, A.G. Litvak, Ed., 1996, vol.2, pp.634-659.
4. W. Lawson, W.W. Destler, and C.D. Striffler, "High-power microwave generation from a large-orbit gyrotron in vane and hole-and-slot conducting wall geometries," IEEE Trans. Plasma Sci., vol.13, p. 444-453, 1985.
5. V.L. Bratman, Yu.K. Kalynov, M.M. Ofitserov, S.V. Samsonov, and A.V. Savilov, "CARMS and relativistic gyrotrons as effective sources of millimeter and submillimeter waves," in Proc. of 22nd Int. Conf. on Infrared and Millimeter Waves, Wintergreen, Virginia, H.P. Freund, Ed., 1997, pp.58-60.
6. V.L. Bratman, I.E. Botvinnik, Yu.D. Grom, Yu.K. Kalynov, M.M. Ofitserov, "Relativistic pulse-periodic mm-wavelength cyclotron masers with hot cathodes," Proc. SPIE of the 16th Int. Symp. on Discharges and Electr. Insulation in Vacuum, Moscow - St. Petersburg, Russia, 1994, pp.538-541.

SIMULATION OF EXCITATION MECHANISMS OF OSCILLATION IN DIFFRACTION ELECTRONICS DEVICES ON COUPLED OPEN RESONATORS

G.S. Vorobjov, A.I. Ruban

Sumy State University, 2, Rymski-Korsakov St., Sumy, Ukraine, 244007

Tel. (0542) 39-23-72, fax 38.0542.33-40-58, E-mail kpe@ssu.sumy.ua

A.I. Tsvyk

Institute of radiophysics and electronics of NASU, 12, Ac. Proscura St., Kharkov, Ukraine, 310085

Tel. (0572) 44-85-48, E-mail a tsvyk @ rocketmail

Diffractive electronics devices of millimetric wave band on coupled open resonators (OR) in comparison with single-resonator diffractive emission generators (DEG) have a number of advantages: they have a wider band of electronic frequency change, may be effectively used as power amplifiers and frequency multipliers. Figure 1 shows schematically two possible versions of arrangement of such devices on coupled OR [1].

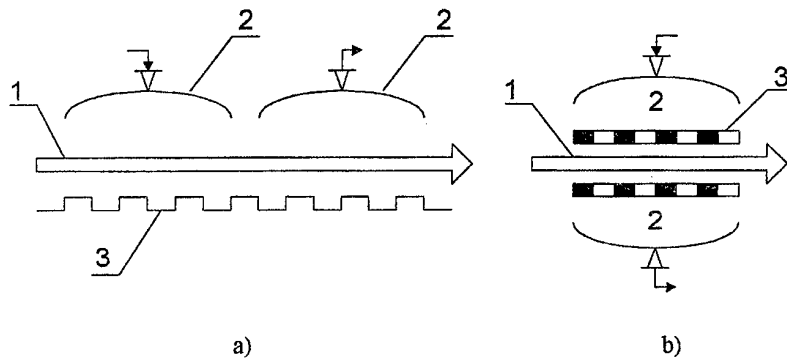


Figure 1.

In case of series connection of open resonators relative to axis of electron beam (EB) 1 (Figure 1a) electrodynamic system of generator consists of a number of spherical (or other form) mirrors 2 and a common mirror 3 with diffraction grating (DG). Electron flow, being focused in interaction field by magnetic field, is transmitted near the grating. A scheme at parallel connection of OR relative to axis EB 1 is given in Figure 1b, where open electrodynamic system is arranged as two coupled spheroidal resonators 2. Electron beam is moving here between two mirrors, on which strip DG 3 are located. In both cases, when the beam current exceeds the starting value, electromagnetic oscillations are excited in the device. If a signal from outside source is fed to input of one of the resonators and self-excitation condition is not provided, then the device operates as an amplifier. Besides, these devices can fulfill functions of frequency multipliers due to availability of two coupled OR.

Investigations of identical systems on coupled OR were carried out for the described schemes by simulation method within the frequency band of 45-49 GHz. In this case EB 1 (Figure 1) was replaced by a planar dielectric waveguide which was energized by microwave oscillator. Extraction of power from the system was carried out through coupling slots of spherical mirrors. Vibration and frequency spectra of OR were investigated at different distances between mirrors and parameters of DR. Also measurements of similar characteristics for single hemispherical and spheroidal OR were carried out, which were considered basic ones for the systems being investigated.

Comparative analysis of spectral characteristics and resonance curves given in Figure 1, coupled OR with basic resonators allowed to find out both common and distinctive features. Similarity of the systems under consideration consists in the fact that axially-symmetrical oscillations, which by their structure qualitatively coincide with the fields formed by single OR, are excited in coupled OR as well. But introduction into OR of surface wave scatters as reflecting and semi-transparent DG and also availability of coupling between the

resonators results in a significant change of frequency spectrum and resonance curves of oscillations for the systems being investigated: rarefaction of frequency spectrum, variation of steeples of frequency mechanical change, convergence and overlap of resonance curves take place. In particular, oscillation spectra of single spferoidal (plot 1) and two coupled through strip DG (plot 2) OR with fixed distance between the mirrors are given in Figure 2.

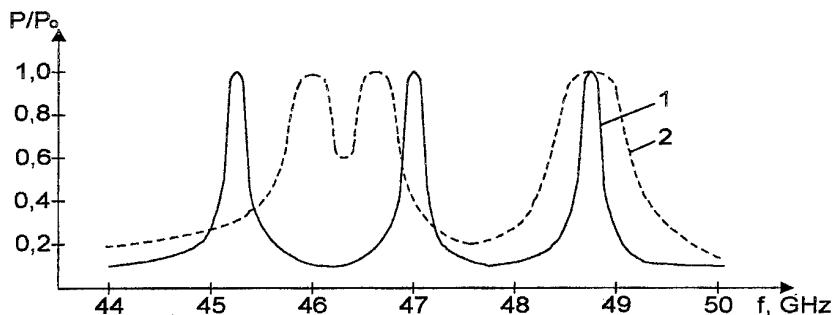


Figure 2.

The plots demonstrate that when a coupling is introduced between the resonators convergence of resonance frequencies is observed. This effect was achieved due to frequency pulling of one resonator by another and can be used for extending the bandwidth of electrodynamic system in case of its use in amplifiers of millimetric wave band.

1. Генераторы дифракционного излучения / Под ред. В.П. Шестопалова; АН УССР. Институт радиофизики и электроники. — Киев: Наукова думка, 1991.

SIMULATION OF THE EXCITATION PROCESSES OF DIFFRACTION-CERENKOV RADIATION BY THE ELECTRON BEAM SPACE CHARGE WAVES ON METAL-DIELECTRIC PERIODIC STRUCTURES

G.S. Vorobjov, K.A. Pushkaryov, A.I. Ruban

Sumy State University, 2, Rymski-Korsakov St., Sumy, Ukraine, 244007

Tel. (0542) 39-23-72, fax 38.0542.33-40-58, E-mail kpe@ssu.sumy.ua

A.I. Tsvyk

Institute of radiophysics and electronics of NASU, 12, Ac. Proscra St., Kharkov, Ukraine, 310085

Tel. (0572) 44-85-48, E-mail a tsvyk @ rocketmail

One of the problems in the field of physics and engineering of and submillimeter wave ranges is the creation of high-efficient sources of electromagnetic oscillations and element base of radiosystems. The theoretical and experimental research indicates an opportunity of using Cerenkov radiation (CR) or a combination of diffraction and Cerenkov radiation in some schemes of EHF [1, 2]. Periodic metal-dielectric structures (MDS) of the dielectric layer (resonator) — band diffraction grating (DG)-type are user in such devices for converting EB surface waves into volume waves.

In a general case the energy characteristic of excited radiation is represented by the energy density determined by average value of Pointing vector stream:

$$S_n = \frac{c}{8\pi\sqrt{\epsilon}} [\mathbf{E} \times \mathbf{H}^*],$$

where n — number of radiation space harmonic, c — speed of light, ϵ — relative dielectric permeability of the medium; \mathbf{E} and \mathbf{H} — vectors of electromagnetic wave excited by a monochromatic current of the space charge. It is possible to separate various regimes of radiation excitation which are realized by changing o fthe such parameters of system as ϵ , l (period of DG), and $\beta = V/c$ (relative velocity of EB).

The numerical modeling carried out has provides for the investigation of the radiation properties in a wide interval of changing MDS and EB parameters used practically ($\epsilon = 2\div100$; $\beta = 0.1\div0.9$). The dependencies S_{0e} / S_e on ϵ and β for various values of DG filling factor $u = \cos\pi d/l$ (d — width of DG bands) were obtained and analysed. As the analysis has shown one of the main factors influencing the density of CR energy is the screening influence of DG deposited on the dielectric surface along which EB is moving.

The MCD experimental model investigated is presented in Figure 1. In this case monochromatic EB is

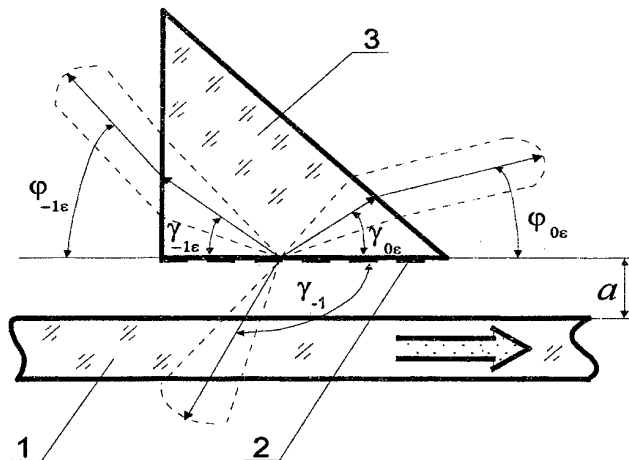


Figure 1. Experimental model of investigated MDS.

replaced by one-mode planar waveguide 1 locate along the band DG 2 deposited on the surface of the dielectric prism 3. The present model was used to realize the regime of simultaneous excitation of DR (radiation angles γ_1 and γ_2 in Figure 1) and CR (radiation angle γ_0 in Figure 1). In this case the electrodynamic system of MDS was investigated under the frequency range of $f=68\text{-}75$ GHz and it had the following parameters: $l=3$ mm, $\beta=0.9$; dielectric prism ($\epsilon=2.05$) with the basis sizes of $70 \times 70 \times 100$ mm and the hight of 40 mm; band diffraction gratings witch had various values of u were deposited onto the side of the prism 70×40 mm. Besides to identify of null diffraction harmonic with CR a prism without DG excited by the dielectric waveguide was investigated.

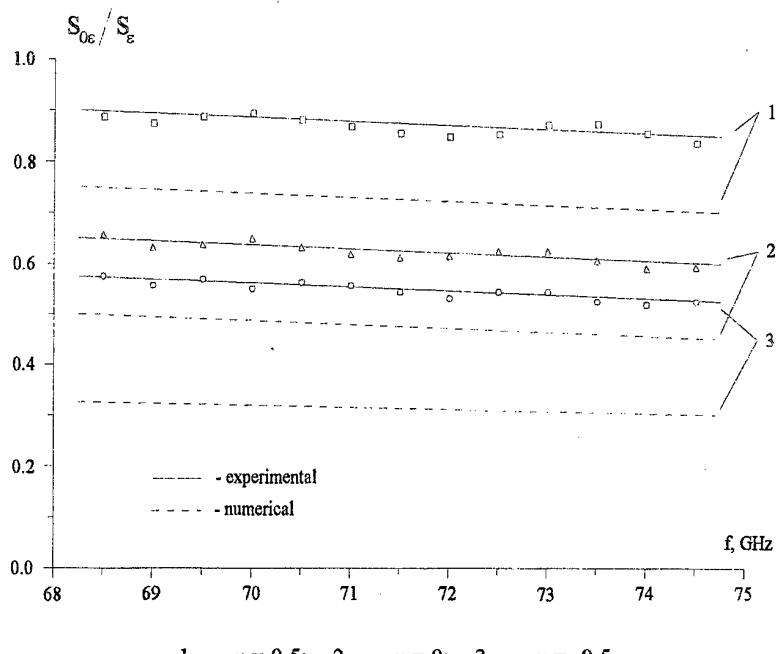


Figure 2. Effect of DG filling factor on the density of CR energy.

Figure 2 present the results of numerical analysis and experimental simulation in the form of dependencies S_{0e}/S_e related to the frequency at various u . The dependencies presented illustrate the screening influence of DG and demonstrate the qualitative conformity of theoretical and experimental results.

- Генераторы дифракционного излучения / Под ред. В.П. Шестопалова; АН УССР. Институт радиофизики и электроники. — Киев: Наукова думка, 1991.
- G.S. Vorobyov, A.I. Tzvyk, K.A. Pushkaryov, and O.S. Makeyev, "Scattering of electron stream waves on metal-dielectric periodic structures", Infrared and Millimeter Waves, Vol.17, No.10, pp.1761-1768, October 1996.

INSTALLATION FOR INVESTIGATION OF ELECTRON BEAMS OF VACUUM ELECTRONIC DEVICES OF MILLIMETER WAVE BAND

G.S. Vorobjov, D.A. Nagornyi, K.A. Pushkaryov

Sumy State University, 2, Rymski-Korsakov St., Sumy, Ukraine, 244007

Tel. (0542) 39-23-72, fax 38.0542.33-40-58, E-mail kpe@ssu.sumy.ua

Ye.V. Belousov, V.G. Korzh,

Institute of radiophysics and electronics of NASU, 12, Ac. Proscura St., Kharkov, Ukraine, 310085

Tel. (0572) 44-85-48

During the last years attention of investigators has been attracted by transient radiation which can be used effectively enough for diagnostics of EB [1,2].

Block diagram of the installation implementing this method is given in Fig1. Electron beam 1 is formed by gun 2 installed in such a way as to provide the possibility of angular movement relative to plane of movable target 3. For present mode of currents on it and on stationary target 4 that indicates to arrangement of lower boundary of target 3 on beam axis. During installation of movable target for preset cross-section of EB recording of optical radiation shall be performed which is taken out through peephole 5 and optical system 6 to radiation detector 7. Recording of currents on both targets is carried out simultaneously by indicators 8 and 9.

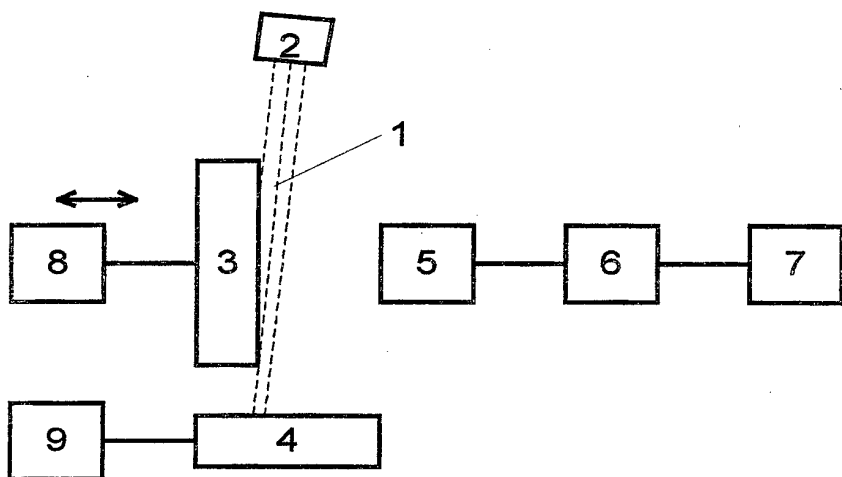


Fig 1.

Photographic camera, television camera, photomultiplier tube or devices with solid-state image probes for example, charge-coupled devices may be used as radiation detectors. Radiation detector shall be chosen in accordance with requirements to electron beam analysis: accuracy of measurements, data processing rate, evidence of information, etc. Processing procedure of beam glow trail on the target in the course of carrying out a series of measurements for determination of geometric dimensions of beam cross-section and current density distribution depends on the type of radiation detector. So, for example, determination of relative intensity of beam radiation on target in the main task during measurement of EB parameters by photographic method.

Particularly, Fig.2 presents current density distribution over the length of strip beam in minimum (curve 1) and maximum (curve 2) of static pulsation of EB being formed by diode gun with plane with plane geometry applied in devices of millimeter - wave band like diffraction radiation generator and backward wave tube.

It clear from the plots present that in case of cathode use with no defects current density is rather inhomogeneous which is especially evident in maximum of static pulsation. A similar phenomenon observed both at operation of current limitation by a space charge and at the mode of complete current take-off.

The current density of axially symmetric EB is less inhomogeneous, which connected with specificity of forming of such beams: axially symmetric optics, absence of magnetic field in the area of EB forming. Thus, Fig.3 present distribution of current density in relative units for three cross-section of the beam formed by three-electrode electron gun with axial symmetry applied in traveling wave tubes of millimeter-wave band. Plot 1 corresponds to cross-section of EB arranged at the distance of 4.4 mm from second anode, the rest two characteristics have been formed for cross-section arranged at 5.5 mm interval from the first cross-section.

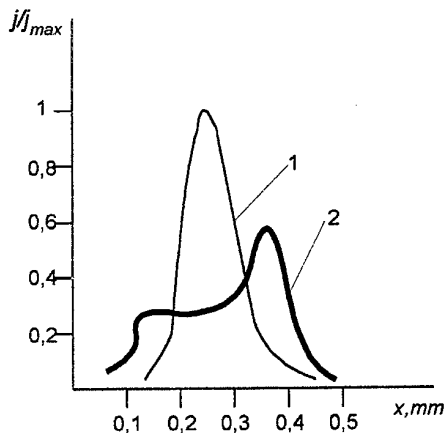


Fig.2

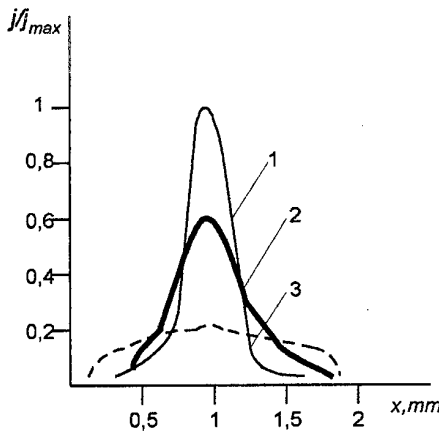


Fig.3

The plots show that in spite of availability of local and common inhomogeneities at distribution of current density over the EB diameter they develop to a sufficiently lesser extent than for strip beams.

1. Patent 4086 of Ukraine, International Classifier №6 - 1/94 of 27.12.94, published in Bulletin of Ukraine «Industrial property»

2. G.S. Vorobyov, A.A. Borisenco, Ye.V. Belousov, V.G. Korzh, I.A. Kulik, and K.A. Pushkaryov, "Method for Measurement of Static Parameters of Axially Symmetric Beams in Devices of Millimeter Wave Band", Infrared and Millimeter Waves, Vol.19, No.2, pp.243-250, February 1998.

INVESTIGATION OF PHASE-LOCKED DIFFRACTION RADIATION GENERATOR

M.Yu. Demchenko, G.P. Ermak, I.D. Revin

Institute of Radiophysics and Electronics NAS of Ukraine 12 Ak. Proskura Str., 310085 Kharkov, Ukraine, e-mail: ermak@ire.kharkov.ua

A number of millimeter-wave measuring systems require high stability, high-power sources. New opportunities for the plasma diagnostics, high-resolution spectroscopy and coherent radars can provide a new type of high-stability medium-power electromagnetic oscillator: the Diffraction Radiation Generator (DRGs).

The operation of the DRG is based on the phenomenon of diffraction radiation (Smith-Purcell effect), in which an electron beam passing over a periodic structure (e.g. diffraction grating) radiates as a result of interaction with the grating. The emitted radiation is collected by a high-Q open resonator that encloses the grating. To provide the frequency returning in a wide range the second mirror of the open resonator is made movable.

At this time, DRGs that operate over the 30-250 GHz frequency range are available with power levels from 50 down to 0.3 Watt at input voltage of about 3 kV and cathode current of about 0.12 A. The relative long-term frequency instability of the DRGs is about 5×10^{-6} [1].

There are two methods of improving the long-term frequency stability of the source without reducing of the output power. The first method is injection-locking, the second one is PLL-locking. The results of development and investigation of a PLL-locked V-band 10 Watt DRG are presented in this paper. The scheme of the PLL-locked source is presented in Figure 1.

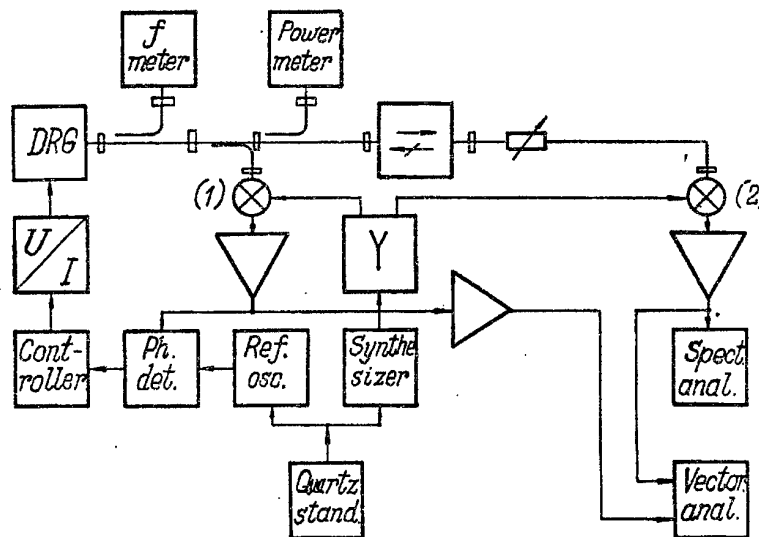


Fig.1

The PLL of the DRG consists of two loops, which are coupled by the harmonic-mixer(1). The first loop contains the components which are necessary to stabilize the DRG operating in the V-band. The second loop stabilizes a frequency synthesizer operating in C-band and the reference oscillator to the 5 or 10 MHz frequency standard. One part of the DRG power coupled to a harmonic-mixer(1), is downconverted by the output signal of the frequency synthesizer. The output signal of the mixer is fed to the phase detector, where it is compared in phase to a stable signal of the reference oscillator to generate a phase error signal, which controls the power supply of the DRG.

The investigation of the long-term frequency stability of phase-locked DRG provides by V-band high-resolution frequency meter 'RCh-3-72' with measurement error 5×10^{-10} . Figure 2 presents the long-term frequency stability of 10 Watt 60 GHz DRG measured at locked (****) and unlocked (*****) mode of operation. In the locked regime the long-term error of +/- 10 Hz was achieved.

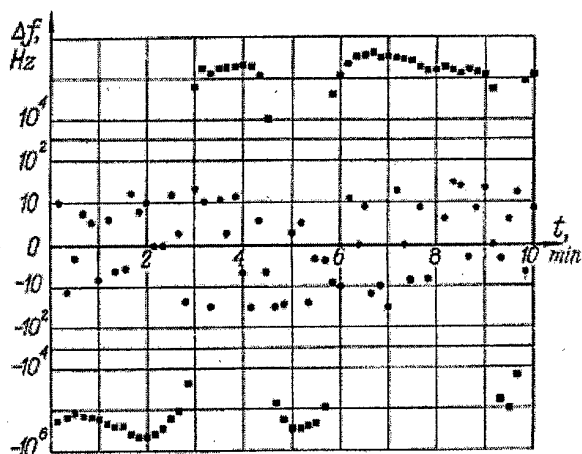


Fig. 2

The investigation of phase-locked spectrum of the DRG was realized by high-resolution receiving system. The operation of the high-resolution receiving system can be described as follows. The output signal of DRG passed through attenuator is mixed in the receiving mixer (2) with the signal coming from the coherent heterodyne. The measurement of the probing signal is carried out at an intermediate frequency by spectrum analyzer. The receiving system can measure the transmitted and reflected signals by a simultaneous analysis of amplitude and phase of the probing signal.

In figure 3 the phase-locked spectrum of the DRG measured with an audio spectrum analyzer with a transmission band of 3 Hz is presented. It demonstrates a good spectral purity of the DRG. The noise level is -80 dB in the band of +/-60 kHz.

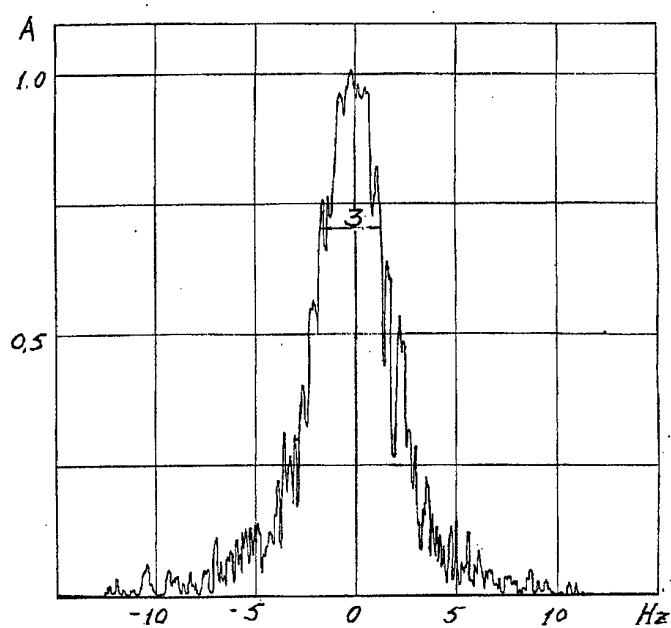


Fig. 3

The PLL locked DRG can be mechanically and electrically frequency tuned. The frequency tuning with the minimal frequency steps of 1 Hz is possible within the electrical tuning band of about +/- 15 MHz at any frequencies within the mechanical tuning operating band of the source. So the source can be used as frequency synthesizer with frequency step up to 1 Hz. The receiving system operates in the 55-75 GHz frequency band. The changing of the frequency band of the source and receiving system up to 150 GHz can be realized by replacing the DRG, waveguid components and harmonic mixers with the components of the required band. The main specifications of the locked DRG and the receiving system are as following:

-operating band of the DRG	60+/-5 GHz;
-output power	< 10 Watt;
min. frequency step	1 Hz;
-operating frequency band of the receiving system	55-75 GHz;
-dynamic range	120 dB;
-frequency resolution	<3 Hz

The phase-locked DRGs well suited for plasma diagnostics, for investigations of the substances with great losses, for radar remote sensing of the atmospheric pollution and high-resolution spectroscopy.

References:

1. V.P. Shestopalov, A.A. Vertij, G.P. Ermak, B.K. Skrynnik, G.I. Khlopov, A.A. Cvyk Diffraction Radiation Generators; Academy of Science of Ukraine; Institute of Radiophysics and Electronics. - Kiev: Naukova Dumka, 1991.-320 p

On Mechanism for Oscillation Excitation by Electron Beam in Cavity.

Buts V.A. Kovalchuk I.K.

NSC 'Kharkov Physical and Technical Institute', Bild.1, Academiceskaya street, 310108, Kharkov, Ukraine.
Tel (0572)404-414, E-mail: kovalchuk_ik@kipt.kharkov.ua

The study of mechanisms for the development of the beam instability, which causes the oscillation excitation in various electrodynamics systems, is necessary for the effective control of the process of the instability development. The understanding of the mechanisms itself is based on the following: the elementary mechanism of the radiation emission of the beam single particles, the number of bunch particles emitting coherently and the number of bunches emitting coherent radiation. The letter two components may be combined into the one—the total number of particles emitting coherently.

As it has been shown in [1,2] the correct employment of these three (two) components allows to describe not only the process of the beam instability development, but to obtain just correct analytical expression for the instability increment.

In the presented report, the physical mechanisms for the electromagnetic wave excitation by the electron beam in the cavity (monotron) are investigated. It is reaching basing on the simple physical consideration by the above mentioned principles. Monotron is one of the simple and interesting system. It was proposed long ago for the excitation of the electromagnetic oscillation and is enough studied in the present time.

Vavilov had been shown in work [3] that radiation can be generated in the matter by charged particle moving with constant velocity, which is less then light velocity in this matter, when one is limited in longitudinal direction. In first, probably, this radiation was considered quantitatively in [4]. It was named Vavilov radiation by authors. The article is difficult of access. The energy losses of the one charged particle in the rectangular cavity was obtained only in this work. The expressions for the electromagnetic field components are necessary for us.

In the presented work we define the increment of the beam instability in the monotron basing on the elementary Vavilov mechanism radiation emission of the one charged particle and the mechanisms of the beam bunching. In this case we use simple physical consideration. The obtained expression differs from exact one in the factor of the order of unit.

Let's consider a cylindrical cavity with radius R , length L and ideally conducting inner surface. At the moment $t=0$ an electron flies into the cavity through one of the butt-ends and is moving with constant velocity V along cavity axis. We consider only axially symmetric field of the E-type (E_r, E_z, H_ϕ). The field components expression are defined from Maxwell equations using Laplace transformation and Fourier series. When electron has flown through the cavity, the electromagnetic field in them is the superposition of the natural one. The expressions for the field components are employed for the definition increment, using simple physical consideration. These components are obtained with help of the Mellin transform, as functions of time.

To obtain the exact increment we consider the linear self-consistent theory of the oscillation excitation in monotron by the uniform in the cavity cross section electron beam, which fully fills cavity and moves with constant velocity V along the cavity axis. The constant external magnetic field which provides $\omega_h^2 \gg \omega^2$ is applied along the cavity axis. This allows to consider the electron movement as one dimensional. In order to describe this process we consider Maxwell equations for the electromagnetic fields and hydrodynamic equations for the small disturbances of density π and velocity V of the beam. This set, besides electric field boundary condition, must be supplemented with condition for beam: the disturbances of the beam density and velocity are equal to zero on the input butt-end. The expressions for disturbances of the density and velocity of the electron beam was obtained from hydrodynamics equations. It substitute to the Maxwell equations. After that we obtained integrodifferential equations for longitudinal electric field component. Using the boundary conditions we can obtain exact increment for the beam instability of the electron beam in the cylindrical cavity. Analogous problem was obtained in [5].

The increment of the beam instability may be obtained on the base simple physical consideration too. The expressions for the radiation emission of the one electron and beam density disturbance can be used in this case. The letter may be obtained from movement and continuity equations and is following:

$$\tilde{n} = -\frac{en_0}{\gamma^3 m V^2} \frac{\partial}{\partial z} \int_0^z dz' \int_0^{z'} E_z \left(z'', t - \frac{z-z''}{V} \right) dz''$$

Where \tilde{n} —the beam density disturbance, n_0 —the nondisturbed density of the beam, γ —relativistic factor, V —beam velocity, m, e —mass and charge of the electron, E_z —longitudinal component of the electric field in the cavity. In other hand, it can be obtained as sum of radiation fields of the individual electrons which are in the density disturbances:

$$E_z(z) = \int_0^R J_0(\alpha_m r) r dr \int E_z^{(0)}(z, z') \tilde{n}(z') dz'$$

where α —radial wave number, $J_0(x)$ —Bessel function of the zero order, $E_z^{(0)}(z, z')$ —radiation field in the point z generated by electron which is in the point z' . As a result, $E_z(z)$ may be expressed itself in the algebraic equation. From letter the expression may be obtained for the frequency imaginary part, which is increment. One differs from the exact increment in the factor of the order of unit.

Thus it may be conclude that the monotron instability is based on the elementary effect of the Vavilov radiation emission, and the beam particles bunching is the result of the linear collective processes. It take place in the 'dense' beam, when $\lambda^3 \gamma^2 n_0 >> 1$ (λ —wavelength of the radiation)

Another mechanism which provides the bunching and coherence of radiation emitted by single particles has been studied as well. This mechanism exists in the 'rare' beam. It's conditioned by a specificity of the nonlinear dynamics of the individual particles in the radiation wave field. The essence of this mechanism of the particle interaction with the electromagnetic field is the particle nonlinear dynamics asymmetry with respect to the accelerating and moderating phases. The approximation of the given field may be used in this case. In the simplest one it can be obtained the set of the ordinary differential equations for the beam particle motion and the phases of the wave interacting with the particle. This is following:

$$\begin{aligned} \frac{d\epsilon}{d\xi} &= \mu \left[\cos \Phi + \cos \left(\Phi + \frac{2\xi}{V_{ph}} \right) \right] \\ \frac{d\Phi}{d\xi} &= \frac{1}{\sqrt{\epsilon}} - \frac{1}{V_{ph}} \end{aligned}$$

where $\epsilon = V^2 / V_0^2$, V_0 —the initial particle velocity, $\mu = 2E / m\omega V_0$, E electric field amplitude, $\Phi = \omega t - kz$, $\xi = z\omega / V_0$, $\omega(k)$ is determined by the solution of the dispersion equation for the corresponding electromagnetic structure. This set can be solved by the method of the disturbance theory when $|\mu| \ll 1$. The efficiency which being defined as a ratio of the beam average energy density variation to the initial energy density, is the most important characteristic of the field excitation by an electron beam, which is following:

$$\eta = 1 - \langle \epsilon \rangle; \quad \langle \epsilon \rangle = \frac{1}{2\pi} \int_0^{2\pi} \epsilon d\varphi_0$$

Hear averaging is fulfilled over the initial phases φ_0 of the particles inlet into the cavity. The case $\langle \epsilon \rangle < 1$ corresponds to the oscillation mode of operation, if $\langle \epsilon \rangle > 1$ the beam is on the average accelerated.

The energy losses for one charged particle was calculated earlier. The energy losses formula and increment one contain the identical principal expressions. Thus it may confirm that elementary effect — Vavilov radiation dominates at the nonlinear stage.

References

1. Ginzburg V.L. "On The Utilization Of The Vavilov-Cherenkov Effect For The Radiowaves Radiation Emission", Report Of Academy Of Sciences Of USSR, Vol.56, No.3, pp.253-254, 1947.

2. Ginzburg V.L. "On The Emission Of Microwaves And Their Absorption In The Air", The Proceeding of Academy of Sciences of USSR, Vol.11, No.2, pp.165-182, 1947.
3. Vavilov S.I. "The Light Microstructure", Nauka, Moskow, pp.198, 1950.
4. Sineinikov K.D., Akhiezer A.I., Fainberg Ya.B., "The Particle Charged Radiation In The Region Which Bounded By The Metallic Surfaces". Proceeding of Science of Art. Acad, No.127, pp.1-8, 1953.
5. Rukhadze A.A., Sever'janov V.V. "The Physical Nature Of The Instability Of The Monotron Type", Journal Of The Technical Physics, Vol.62, No.12, pp.99-113, 1992.

THE PENIOMAGNETRON WITH BARREL-SHAPED RESONATOR

Victor D. Yeremka, Oleg P. Kulagin

Usikov Institute of Radiophysics & Electronics of National Academy of Sciences of Ukraine, 12, Acad.

Proskura st., 310085, Kharkiv, Ukraine. Tel.: 38-0572-448-519. Fax: 38-0572-441-105. E-mail:

eremka@ire.kharkov.ua

ABSTRACT

A source of millimeter (mm) waves with a peniotron mechanism of electron-wave interaction on high harmonics of cyclotron frequency for generation of high stability coherent radiation is suggested. An adiabatic electronic-optical system (EOS) is applied in the generator design. The EOS produces a large helical-orbit axis-encircling electron beam (EB), which gives up power to a high-frequency field in the interaction space of a generator electrodynamic system (GES). GES is constituted of the field-coupled resonator systems based on the gridwork cylinder waveguide with an azimuthally periodic structure of cutting slots and coaxially arranged barrel-shaped open resonator. The generated power is extracted from the barrel-shape cavity by a standard waveguide.

1. INTRODUCTION

At present, the problem of design of the mm-wave source that meets the requirements of the frequency high stability $\Delta f/f \sim 10^{-6}$, the opportunity of synchronous work of several sources with a phase spread of about 1° , remains actual. In this paper the first results of development of the mm-wave source with a peniotron mechanism of electron-wave interaction on high harmonics of cyclotron frequency for generation of high stability coherent radiation is suggested. The results are obtained at the Usikov Institute of Radiophysics & Electronics of the National Academy of Sciences of Ukraine.

2. DESIGN OF AN OSCILLATOR

The large-orbit EB are not sufficiently investigated, but attract attention due to their use in gyrode-vices operating on high gyro-harmonics. In this paper we present results of simulation and experimental breadboarding of the EOS three-electrode design producing a large-orbit EB for pulsed peniotron-diffratron, operating in a through-gyroresonance mode at a frequency of about 100 GHz on the 10-th cyclotron harmonic (Yeremka et al.[1]).

The selection of modes and the predominant extraction of an operating harmonic having m azimuthal variations in an oscillator peniomagnetron - diffratron can be ensured by using the coupled electrody-namics systems based on the waveguide with an azimuthally periodic structure of two types and a coaxially arranged barrel-shaped open resonator with respect to the waveguide. The electromagnetic coupling between them is provided by the slots. An electric component of the HF-field in the above listed magnetron-type waveguides is large near the cavity vanes and is exponentially decreasing in an axial direction of the resonator system. A large helical-orbit axis encircling EB formed by the adiabatic EOS is passed as close to the tops of the vanes as possible to effectively interact with the RF-waves. The interaction with 2π -mode on the 10-th cy-clotron harmonic requires the 22-vane cylindrical magnetron-type cavity.

The coupling slots are cut into an external wave of the magnetron-type cavity with the barrel-shaped open resonator which makes it possible to bring out the HF energy generated on the $TE_{11,1,1}$ mode into the load through an open resonator. In the barrel-shaped cavity a spectrum is produced with the same functional dependence as in a circular cylindrical cavity in radial and circular directions, but this spectrum is Gaussian in an axial direction. The field attenuation in an axial direction, caused by the walls curvature makes it possible to use the end walls to install the resonance frequency change systems.

The output of the microwave energy from the barrel-shaped cavity in a load is realized through the coupling slot and the standard waveguide with a vacuum-dense ceramic window on the $TE_{1,0}$.

Electromagnetic coupling between the resonators is provided by the slots. The electric component of the HF field in a magnetron waveguide is high near the vane tops and is exponentially decreasing exponentially in an axial direction of the EOS. The large-orbit EB, formed by the adiabatic EOS, travels as close to the tops of vanes of electrodynamics system as possible to interact effectively with HF field. The interaction with the 2π -

mode on the 10-th harmonic of a cyclotron frequency requires a magnetron cylindrical resonator with 22 vanes. There are 11 coupling slots in an external wall of the resonator which allow one to remove the HF energy of a $TE_{11,1}$ type in a load through an opened resonator. The analysis of the oscillation spectrum in the barrel-shaped resonator indicates that the spectrum of the resonator is similar to that of a cylinder resonator in radial and circular directions, but is Gaussian in EOS the axial direction of EOS.. The attenuation of the field in an axial direction, caused by the curvature of walls, allow to use the end walls for the placement of the resonance frequency change systems. The output of the HF energy from the barrel-shaped resonator in a load is carried out through the coupling slot and the standard waveguide with a vacuum-dense ceramic window on $TE_{1,0}$ mode. A quarter-wave transformer is installed between the barrel-shaped open resonator and a standard rectangular waveguide.

Of peculiar interest is the use of small-slot-cavity waveguides in a resonance oscillator acting as an interaction space of electrons and RF-waves. This waveguides ensure the T-wave propagation and autoresonance mode (Yeremka et al.[1,2]). In order to find the optimal efficiency operating modes of such a peniomagnetron-diffratron a study has been made into the interaction of a large-orbit magneto-directed EB with a standing field of the coaxial resonator under the initial conditions corresponding to the peniotron resonance mode with a forward-traveling partial wave T_{mnp} -oscillation. In the resonance mode the condition of gyroresonance with the backward and forward-traveling waves is simultaneously met, which are not necessarily ones of the same order:

$$\begin{cases} \omega \cdot (1 + \beta_z) = -\frac{s\Omega}{\gamma} \\ \omega \cdot (1 - \beta_z) = -\frac{n\Omega}{\gamma} \end{cases} \quad (1)$$

where ω is the circular frequency of the electromagnetic field, β is the longitudinal electron velocity normalized to the velocity c of light, Ω is the electron cyclotron frequency, γ is the relativist factor, $s, n=1,2,3,\dots$

Of greatest practical interest is the case when the peniotron resonance with the forward-traveling wave and the gyrotron resonance with the backward wave are achieved, thereby resulting in the dependence of power characteristics of the electron motion upon an initial phase. The influence of the backward wave brings about the substantial change in the electron efficiency. In the case of the nonsynchronous mode along with the effects caused by the nonsynchronous interactions in the electron power exchange with forward wave the effects which are only typical of the backward wave can be clearly observed. In order demonstrate this phenomenon consider an equation describing the time-varying dynamic factor γ included in the gyroresonance condition (1):

$$[\gamma(1 - \beta_z)]^* = 2\epsilon f(z)(\Omega a/\gamma_0 c)^2 \operatorname{Re}(w^{*m-1} \bar{w}^* e^{ip^*}) \quad (2)$$

где $p^* = \alpha r + kz$; $w = (\rho/a)e^{i\varphi}$; $k = \omega/c$; $\epsilon = (eA\gamma_0^2)/(m_e\Omega^2 a)$; $f(z)$ is the function describing an profile of the amplitude A of the standing wave field; ρ, φ are polar coordinates; \bullet - is the sign of differentiation over the fast time $t = \Omega t / \gamma_0$; $*$ - is the sign of the complex conjugation; 0 - is the index of initial conditions.

In the case where the backward wave does not exit, the right-side of equation (2) goes to zero, thus describing the autoresonance process. Otherwise, if the process of the resonance power exchange is considered to be slowly changing, the approximate solution of the equation can be obtained. As the solution shows, the initial value of the dynamic factor $\gamma(1 - \beta_z)_0$ averaged over the fast oscillations differs from the undisturbed value $\gamma_0(1 - \beta_{z0})$ by the magnitude

$$\overline{\gamma(1 - \beta_z)}_0 - \gamma_0(1 - \beta_{z0}) = -\frac{2eA\Omega a(\rho_0/a)^m \cos(m\varphi_0)}{m_e c^2 (\omega(1 + \beta_{z0}) + m\Omega/\gamma_0)\gamma_0} f(z_0) \quad (3)$$

This is equivalent to the frequency drift by $\Delta\omega$ from the precise gyroresonance, which is proportional to the magnitude of the phase of electron coming into the interaction space. The magnitude $\Delta\omega$ depends on the am-

plitude of the backward wave non-resonance field. As follows from the (3), the action of the backward wave can be substantially reduced by using the resonators as an electromagnetic system in which the profile of the HF field amplitude is equal to zero or a minimum at the beginning of electron and wave interaction space. The above-mentioned requirement are met by the barrel-shaped resonator we have used in the oscillator design.

Fig.1 shows the dependencies of the electronic efficiency η_e upon the number of electron orbits $N=10$ which were obtained by solving the non-averaged integration equations for the two variants of the HF amplitude distribution function along the resonator system $f(z)$ for $q=1,3$; $r/R = 0.8$; $\omega = 2\pi \cdot 6 \cdot 10^{10}$ GHz; the pitch-angle of 60° ; the operating voltage of 20 kV, and the field strength amplitude of the standing wave $A = 9 \cdot 10^5$ V/m for the cyclotron harmonic $n=10$. The figure 1 suggests that the use of the sinusoidal (or near-sinusoidal) distribution of the HF field amplitude along the interaction space allows one to eliminate the dependence of the electron power exchange with an electromagnetic wave upon the phase of the particle coming into the interaction space. It is hoped that neutralization of the distributive effect of the electron interacting with the backward wave will ensure that the operating autoresonance mode is maintained in the peniotron oscillator system with a barrel-shaped resonator on the high cyclotron harmonic with a relative high efficiency.

3. CONCLUSIONS

In this paper we have presented the first results of the studies on the novel type of the mm-wave source, which is expected to be widely used as a millimeter wave oscillator in the different areas of science and engineering. The high efficiency (nearly 40%) with the peniotron oscillator operating on the 10-th harmonic with a frequency about 100 GHz was predicted theoretically (Yeremka et al. [3,4]) and confirmed experimentally (Ishihara et al.[5]). Specifically, we are planning to construct a pulse resonance oscillator that could be operated at a frequency of 100 GHz with a power output of about 40 kW and a higher stability of the signal frequency in small-size resonance linear electron accelerators (linacs).

References

1. V.D.Yeremka ,I.I.Golenitskiy, B.Ch.Djubua., e.a. «Production and study of axis-encircling electron beams for peniotrons», ICMWFT'92. Sapl. Conf. Dig., Beijing, China, pp. 351-354, 1992.
2. V.D.Yeremka, V.A.Zhurakhovskij, «Generator and amplifier regimes of autoresonance peniomagnets» Proc. SPIE Vol.1929, pp. 520-521, 1992.
3. V.D.Yeremka, V.A.Zhurakhovskij, V.P.Shestopalov, «High-orbit through gyroresonane peniotron», J. of Communications Technology and Electronics, Vol..33 , No.9, pp.1900-1907,1989.
4. V.D.Yeremka, V.A.Zhurakhovskij, A.M.Kovalenko, «Peniomagnetron amplifier theory», ICMWFT'90. Sapl. Conf. Dig., Beijing, China, pp. 52-56,1990.
5. T.Ishihara, H.Tadano, H.Shimawaki, e.a., «Space harmonic peniotron in a magnetron waveguide resonator», IEEE Trans. on Electron Devices, Vol.43 No.5, pp.827-833,1996.

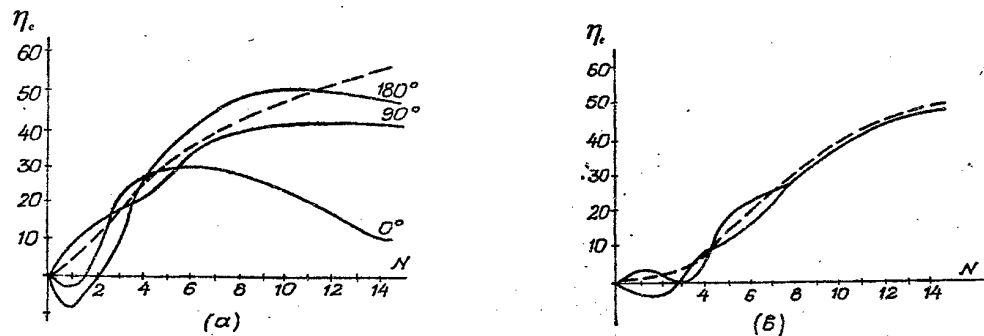


Figure 1. Electron efficiency versus the number of electron turns in the case $q=1,3$ for two types of the profile of RF field (taking into account the backward wave (solid curve) and without taking into account one (dotted curve)):

a) $f(z) = 1;$

b) $f(z) = \sin\left(\pi \frac{z}{z_{out}}\right) \quad (A = 9 \times 10^5 \text{ V/m}, \quad N=6)$

AUTOSOLITON MODE OF THE OSCILLATIONS IN THE SMOOTH ANODE MAGNETRON

O. P. Kulagin

*Usikov Institute of radiophysics and electronics of National Academy of Sciences of Ukraine, 310085,
Kharkov, Ac. Proscra St., 12,
fax: 0572-441105, e-mail: eremka@ire.kharkov.ua.*

ABSTRACT

The processes in the cylindrical magnetron with smooth anode have been considered. The investigation shows that the space charge in the system is the active nonlinear medium. The equations describing the excitation of oscillations in this medium have been derived. The autosoliton solution for the system is obtained. The results allow to take a new look into the mechanism of generation of mm-oscillations in the magnetron with a surface wave.

1. INTRODUCTION.

The conventional (classical) magnetrons generate with the operating magnetic field $H > H_k$. (where H_k is the critical magnetic field). At the same time, oscillations of the cyclotron-frequency type are described. These oscillations take place in the magnetrons with smoothbore anode with $H \sim H_k$. It is noted in the literature that this type is of no practical interest [1,2,3]. The reason for that is the noticeable lower efficiency compared with the traveling wave type oscillations which are used in the conventional multiresonator magnetrons.

On the other hand, over the last decades significant results were obtained on the millimeter wave generators - the surface wave magnetrons (SWM) which operate directly with $H \sim H_k$ and with the very high experimentally confirmed values of efficiency [4]. Unlike conventional magnetrons, the SWM operate not with a π -mode of oscillations. Probably, in these devices some other mechanism of electron-wave interaction is realized, which differs from the traveling wave type oscillations.

In order to understand this mechanism, it is seems necessary to analyze in more detail the processes in a magnetron with $H \sim H_k$ under static condition of the slow-wave system (there exist no oscillations caused by the multiresonator anode block). Just this topic is the aim of the work.

2. THE EQUIVALENT DISTRIBUTED LINE.

The experiment conducted on the cylindrical magnetron with slots cutted in the cavity [5] showed the following: in the case, where the disturbing potential $\Delta\phi$ is applied to one of the anode segments, the difference in current between the segments may be approximate as (here S_1, S_2 are the coefficients of approximation):

$$\Delta I = -S_1\Delta\phi + S_2\Delta\phi^3 \quad (1)$$

Thus, the space charge in a region between the cathode and anode is the active nonlinear medium. With low disturbances, the medium is characterized by a negative conductivity, as a disturbance increases it is characterized by a nonlinear absorption.

It is necessary to note that these results were obtained under the condition that was static for the anode slow-wave system, i.e., when the generation of usual magnetron oscillations of resonance type does not arise. Basically, this case is equivalent to the cylindrical magnetron with a smoothbore anode in which the space charge is exposed to some disturbance. Therefore, the origin of negative conductivity is not directly associated with the peculiarities of slow-wave system and is fully determined by the properties of a magnetron space charge.

During investigating the inter-electrode interval conductivity, real averaging of this parameter take place because a measurement time multiply exceed the period of cyclotron frequency oscillations occurred in the system. The value of the conductivity $G(U)$ calculated from experiments characterize, in fact, the static component of the conductivity. For full system analysis it is necessary to take into consideration additional

resistance R , which caused by high-frequency oscillation processes and become apparent as varied in sign additions to measured anode current (during the measurement process these additions are mutually annihilated as result of averaging and not included in the value ΔI determined from these experiments).

As follows from said, when $H \sim H_k$ and the electron cloud border (virtual cathode) is in vicinity of positive electrode, magnetron with smooth cylindrical anode may be presented by the equivalent distributed line which is schematically showed in fig.1:

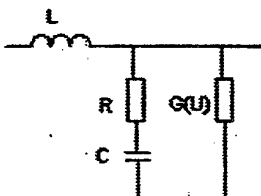


Figure 1. Equivalent distributed line

Here following designations are introduced: $G(U)$ is the nonlinear conductivity of the medium between the anode and the virtual cathode of the magnetron, C - is the capacity of this medium, L - is the inductivity of the anode, R - are the high frequency losses (all above-mentioned values are related to the unit of length).

3. ANALYSIS OF THE THEORETICAL MODEL

The system of equations describing propagation of the oscillations in the above-noted line, has the following form:

$$\frac{\partial U}{\partial x} + L \frac{\partial I}{\partial t} = 0; \quad \frac{\partial I}{\partial x} + \frac{\partial Q}{\partial t} + G(U)U = 0; \quad \frac{\partial U}{\partial t} = \frac{1}{C} \frac{\partial Q}{\partial t} + R \Delta x^2 \frac{\partial^2 Q}{\partial t^2} \quad (2)$$

where x is the direction of the electron drift, Δx is the characteristic length of disturbance, Q is the charge, related to the unit of length, U is the potential of disturbance, I is the current of disturbance, $G(U) = -g + g\gamma U^2$ (we designate $\frac{S_1}{\Delta x} = g$; $\frac{S_2}{\Delta x} = g\gamma$).

We will seek for the solution of the system in the form of the wave, for which the correlation is justified:

$$I \approx \sqrt{\frac{C}{L}} U; \quad \frac{\partial}{\partial t} = -\frac{1}{\sqrt{LC}} \frac{\partial}{\partial x} \quad (3)$$

(we assume that nonlinearity caused by the conductivity $G(U)$ is compensated by the dissipation processes) In the case, which is of some interest for us, the dissipation is completely compensated by the positive feedback. Proceeding from this, one can obtain the solution of the initial system of equations (2), having the form of the stationary solitary wave relating to the separatrix on a phase plane. This is kink:

$$U = \sqrt{\frac{1}{\gamma}} \operatorname{th} \left[\sqrt{\frac{gL}{2RC}} \frac{1}{\Delta x} \left(x - V_0 t + \frac{\Delta x}{2} \right) \right] \quad (4)$$

or antikink:

$$U = -\sqrt{\frac{1}{\gamma}} \operatorname{th} \left[\sqrt{\frac{gL}{2RC}} \frac{1}{\Delta x} \left(x - V_0 t - \frac{\Delta x}{2} \right) \right] \quad (5)$$

The case corresponding to the kink-antikink combination is the topologic advantageous (fig.2) (the stability of such bound state for equations of the type (14) is proved by numerical methods [6])

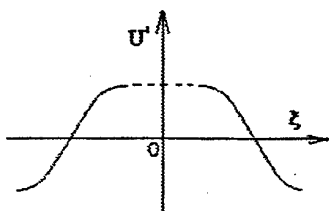


Figure 2. Kink-antikink combination

The wave presented at fig.3 is the autosoliton, which is the disturbance auto-supported by the system positive feedback [7]. The autosoliton parameters are completely defined by the system parameters and are not dependent upon the character of some externally produced disturbance.

At first sight, such solution seems to be one of the particular solutions. However, the essential peculiarity of this solution is that different nonstationary disturbances in the analyzed system, as they are being evolved, are closely approximate to the autosoliton shape.

The quantity of emerging autosolitons is determined from the condition of a complete compensation of losses by the feedback.

4. CONCLUSION

Are the obtained solutions of any practical interest? As we previously noted, there are some experimental data on the low efficiency of generation in the smoothbore anode magnetrons [3]. However, all these data were obtained when the conditions of the two-flow state of an electron cloud were realized in the magnetron. At the same time, in the SWM which also operate with $H \sim H_k$, but demonstrate a very high efficiency in the mm-wave band, the one-flow state occurs. This state is characterized by the relatively higher space charge density and by the negligible dispersion of electron velocity, which, to a large extend, is inherent to the two-flow state (the electron cloud is the current tube rotating around the cathode and the electron flow is approximate to the laminar type) [4,8]. It goes without saying that in this case a higher efficiency of the autosoliton regime is available.

The high efficiency of the SWM should be directly attributed to the fact that the nonlinear system constituted by the space charge and the anode resonator system, which are equally important to these mm-band generators, do not appear to be competing with each other during the oscillation generation process, but, on the contrary, successfully interact. So, one is led to the conclusion that the subsequent investigations in this field may be useful for improving the generation mechanisms for mm and sub-mm bands.

References

1. V.N.Shevchik, G.N.Shvedov, A.V.Soboleva. «The wave and oscillating phenomena in electron flows on the super high frequencies», Published by Saratov university, Saratov, pp. 335, 1962
2. W.H. Louisell. «Coupled mode and parametric electronics», Wiley, New York-London, pp.351
3. I.V.Lebedev. «Technics and devices of super-high frequencies. v.II The electron vacuum devices of super-high frequencies», Vissshaya shkola, Moscow, pp.376, 1972
4. A.Ya.Uistikov, E.A.Kaner, I.D.Truten and others. «Electronics and radiophysics of millimeter and submillimeter waves», Naukova dumka, Kiyev, pp.368,1986.
5. G.Ya.Levin, A.Ya.Uistikov, S.N.Terekhin, O.P.Kulagin, «Solitons and autosolitons in magnetrons», //Preprint of IRE NAS of Ukraine, №94-1, Kharkov, pp.16,1994.
6. R.K.Dodd, J.C.Eilbeck, J.D.Gibbon, H.C.Morris. «Solitons and Nonlinear Wave Equations», Academic Press, London, pp.696,1984.
7. B.Kerner, V.Osipov, «Autosolitons», Nauka, Moskow, pp.200,1991.
8. G.Ya.Levin, «The theory of the surface wave magnetron», Preprint of IRE NAS of Ukraine, №240, Kharkov, pp.40,1984.

EFFECT OF LOAD ON CHARACTERISTICS OF A MAGNETRON CAVITY

A. E. Serebryannikov

Institute of Radio Astronomy, National Academy of Sciences of Ukraine
4 Chervonopraporna Street, 310002 Kharkov, Ukraine

A. V. Sova

Kharkov Technical University of Radio Electronics
14 Lenin Ave., 310166 Kharkov, Ukraine

The effect of the mode index on the electromagnetic characteristics of a loaded magnetron cavity with the side resonators of sectorial geometry is studied. Some features which are peculiar for the complex natural frequency spectrum are revealed and analyzed.

1. Introduction

A choice of the operating mode is the problem of great practical importance at designing the cavity for millimeter-wave magnetron. Although $\pi/2$ -mode is of the most frequent use [1], the other modes can also be used in practice. A value of the cathode radius is usually determined by taking into account its emission properties. Choosing geometry of the anode block and the operating mode, one must provide the required values of the working frequency, rarefaction of the frequency spectrum and slow-wave characteristics. Therefore the modes corresponding to the first resonance and the cavities with sufficiently deep side resonators are usually used, so that the operating mode is one of the groove modes [2].

In the present paper we study the effect of the mode index and geometrical parameters of the anode block on the natural frequencies and external Q . The ohmic losses are not taken into account in our study. Besides, we suppose that asymmetry due to the loading does not lead to a strong variation of the real part of the corresponding natural frequency of azimuthally-periodic cavity, as it usually occurs in practice [3].

2. Formulation

Consider the case when the cavity has N side resonators (grooves) of sectorial geometry, so that the walls coincide with coordinate surfaces in the polar coordinates. The minimum and maximum radii of the anode block are denoted by ρ_1 and ρ_2 , respectively, the radius of cathode by ρ_0 . The aperture opening of each resonator is φ_0 . The considered cavity is supposed to be axially-homogeneous, with perfectly magnetic wall at end-faces. We analyze the external loading through a coupling hole in the back wall of one of the side resonators. Supposing that the real part of the natural frequency slightly varies with taking into account the external load, one can consider the eigenvalue modal problem for azimuthally-periodic lossless cavity as the key one. Then we search for the natural frequencies as for the eigenvalues of the Helmholtz equation with the Neumann or Dirichlet boundary condition. In the case of TE-modes, the use of the mode-matching technique leads to the following infinite-matrix equation [4, 5]:

$$A_p - \sum_{s=-\infty}^{\infty} \delta_{s+qN}^p A_s a_{ps} = 0, \quad p=0, \pm 1, \pm 2, \dots, \quad q=0, \pm 1, \dots, \pm (N/2-1), N/2. \quad (1)$$

Here δ_{s+qN}^p is the Kronecker delta, the coefficients a_{ps} are given as $a_{ps} = N(2\pi\varphi_0)^{-1} * b_s(k\rho_1, k\rho_0) \sum_{n=0}^{\infty} b_v^{-1}(k\rho_1, k\rho_2) c_{psn}$ where $v = \pi n / \varphi_0$, $b_m(x_1, x_2) = Z_m(x_1, x_2) \tilde{Z}_m^{-1}(x_1, x_2)$ with $Z_m(x_1, x_2) = J_m(x_1) Y'_m(x_2) - Y_m(x_1) J'_m(x_2)$, $\tilde{Z}_m(x_1, x_2) = \frac{d}{dx} Z_m(x_1, x_2) \Big|_{x=x_1}$, and $c_{psn} = 4psT$ with $T = \psi_n(s\varphi_0/2) \psi_n(p\varphi_0/2) (\nu^2 - s^2)^{-1} (\nu^2 - p^2)^{-1}$, $\psi_n(x) = \sin x$ if n is even and $\cos x$ if n is odd. In the formula for Z_m , the Bessel functions of the first and second kinds are denoted by J_m , Y_m , respectively. For definite sake, we search for the eigenvalues of $k\rho_1$ for a given geometry of the cavity.

To simplify a study of the loading effect, one should invoke the equivalent impedance approach. In line with this approach, the wall having a coupling hole is replaced by the homogeneous impedance wall while a rigorous representation of the field is used in both the regular coaxial region and the region with corrugations, including the loaded resonator. In this paper we consider the case of ideal matching with the load when there is no wave in the loaded resonator, which is travelling in the direction of decreasing ρ . Rigorous formulae for the external Q are given in [6] but omitted here. The use of the fundamental-harmonic approximation of the field leads to the following estimation:

$$Q_{ext} = (k\rho_0)^2 (\pi N S_0 / 2) e_q^{(1)} U_q^{-1} b_0^{-1}(k\rho_1, k\rho_2) + e_0^{(2)} Z_0^{-2}(k\rho_1, k\rho_2) \quad (2)$$

with $S_0 = J_0^2(k\rho_1) + Y_0^2(k\rho_1)$, $U_q = Z_q(k\rho_1, k\rho_2) \tilde{Z}_q(k\rho_1, k\rho_2)$, $e_q^{(1)} = \int_1^{\rho_1/\rho_0} x Z_q^2(k\rho_0 x, k\rho_0) dx$, $e_0^{(2)} = \int_{\rho_1/\rho_0}^{\rho_2/\rho_0} x Z_0^2(k\rho_0 x, k\rho_2) dx$.

Although Eq.(2) allows us to estimate Q_{ext} only at sufficiently large value of $\vartheta = N\varphi_0 / (2\pi)$ [7], it gives a possibility of qualitative analysis of the effect of geometrical parameters on Q_{ext} , that is carried out in the next Section.

3. Results

As it follows from (2), Q_{ext} does not depend on ϑ , and N is the only parameter taking into account the angular geometry of the cavity. Thus if there is a pair of the values of ϑ , at which the eigenvalues of $k\rho_1$ are the same, the corresponding values of Q_{ext} are equal to each other. Furthermore if the energy stored in the interaction space ($\sim e_q^{(1)}$) is small compared to that stored in the resonators ($\sim e_0^{(2)}$), Q_{ext} does not depend on q , so that a peculiar degeneracy can appear. It occurs for the groove modes, i.e., just for the modes of the most practical interest. The first $k\rho_1$ -eigenvalues are always limited by the first pole of the characteristic determinant, z_0 , which is equal to the first root of the equation $Z_0(z_0, z_0\rho_2/\rho_1) = 0$. The z_0 -value is decreasing with ρ_2/ρ_1 . As is shown in [2], the difference between z_0 and $k\rho_1$ -eigenvalue at $q \rightarrow N/2$ can be made as small as desired by increasing N , so that the eigenvalue of $k\rho_1$ becomes weakly sensitive to the variation of q . Since the $k\rho_1$ -eigenvalue can differ from z_0 by a small value, one should expect that the steep increase of Q_{ext} occurs with increasing q in this case, in line with (2). As for the modes with comparatively small q , their Q_{ext} is much smaller than that at $q \rightarrow N/2$. It is so due to the fact that since the $k\rho_1$ -eigenvalue is increased with q , at least for the first resonance, the value of Z_0^2 steeply increases when $k\rho_1$ is decreasing from z_0 . Then the second term in (2) gives the main contribution to Q_{ext} . Contrary to the case when ϑ varies, no degeneracy is expected when ρ_2/ρ_1 varies.

Numerical results obtained by using rigorous field expansions confirm the predictions obtained by the use of (2), which are related to the steep variation of Q_{ext} as a function of q and to the degeneracy appearing at varying ϑ . Figures 1 (a), (b), 2 (a), (b) show the eigenvalues of $k\rho_1$ and the corresponding values of $\Gamma = 1/(2Q_{ext})$ for the cavities with realistic geometrical parameters. Each circle on the plane $(k\rho_1, \Gamma)$ represents the complex normalized natural frequency. Each frequency is marked by a twin index, (q, j) , $j=1$. The frequencies corresponding to the same value of ϑ (Figs. 1(a), (b)) or ρ_2/ρ_1 (Figs. 2(a), (b)) are connected by a line. One can see that the dependencies shown in Figs. 1(a), (b) only differ in the values of q and ϑ starting from which the connecting lines superimpose each other, that is due to the fact that the number of the modes whose $k\rho_1$ -eigenvalue is located in the vicinity of z_0 is larger in the case of deeper grooves. Comparing Figures 2 (a), (b), one should notice that Γ can strongly depend on ρ_2/ρ_1 . The Γ -value shows a steep decrease with q even at sufficiently small ρ_2/ρ_1 . As an example, the modes with $q=1$ and $N/2$ differ in the value of Q_{ext} by the factor of 7 when $\rho_2/\rho_1 = 1.5$. Although the simplest model of the load was used here, the same behavior of Γ and Q_{ext} versus q also occurs for millimeter-wave magnetrons with more realistic kinds of loading [3] so that the modes with $q=N/4$ and $N/4+1$ which are frequently used in practice can differ in Q_{ext} by the factor of 2.

4. Conclusions

The effect of geometrical parameters on the natural frequencies and external Q has been studied for ideally-matched magnetron cavity. We found that the degeneracy appearing with varying ϑ is caused by

groove nature of the modes with $q \rightarrow N/2$. The same reason results in the fact that the mode index exerts a strong effect on Q_{ext} , even though the $k\rho_1$ -eigenvalue is weakly sensitive to the variation of q . These peculiar features must be taken into account at the stage of design of the output circuit, since the output characteristics can substantially vary if one uses the other mode than that, for which the output circuit was originally designed.

References

1. I. D. Truten, I. G. Krupatkin, O. N. Baranov, N. N. Galushko and V. E. Ignatov, "Pulse magnetrons of millimeter wavelength operating the mode of space harmonic", *Ukr. Phys. J.*, **20**, 1170-1176 (1975) (in Russian).
2. A. E. Serebryannikov, A. I. Nosich and D. M. Vavriv, "Limiting parameters for groove modes of a magnetron-type cavity", *J. Electromagn. Waves Appl.*, **12**, 1203-1216 (1998).
3. V. D. Naumenko, private communication.
4. Yu. A. Prokophchuk and V. G. Sologub, "Natural oscillations of a magnetron oscillatory system", *Radiotekhnika*, **10**, 216-221, University Publ., Kharkov (1969) (in Russian).
5. K. Schuenemann, A. E. Serebryannikov and D. M. Vavriv, "Analysis of the complex natural frequency spectrum of the azimuthally-periodic coaxial cavity", *Microwave Opt. Tech. Lett.*, **17**, 308-313 (1998).
6. A. E. Serebryannikov, "Analysis of the complex natural frequency spectrum of the loaded cavity with azimuthal corrugation", *Int. J. Infrared and Millimeter Waves*, **18**, 1037-1052 (1997).
7. D. M. Vavriv and A. E. Serebryannikov, "Calculation of Q-factor of a magnetron resonator system", *Radiotekhnika i Elektronika*, **42**, 472-478 (1997) (in Russian).

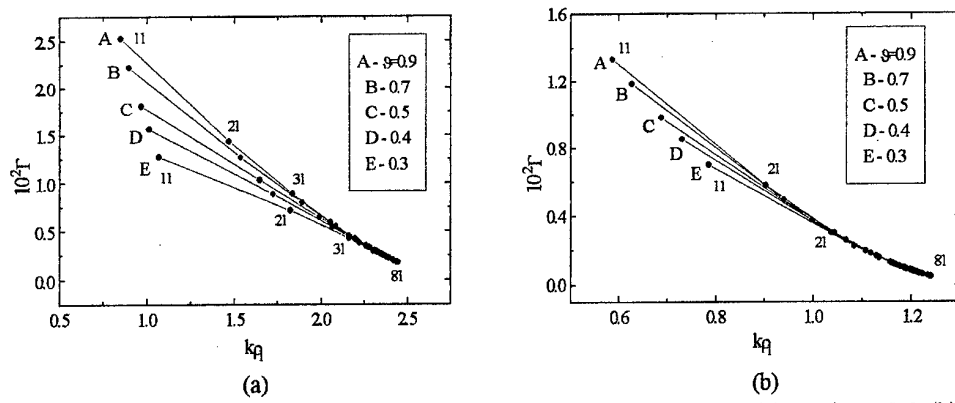


Figure 1. Eigenvalues of $k\rho_1$ and Γ at $N = 16$, $\rho_0/\rho_1 = 0.5$, $\rho_2/\rho_1 = 1.5$ (a), $\rho_2/\rho_1 = 2.0$ (b).

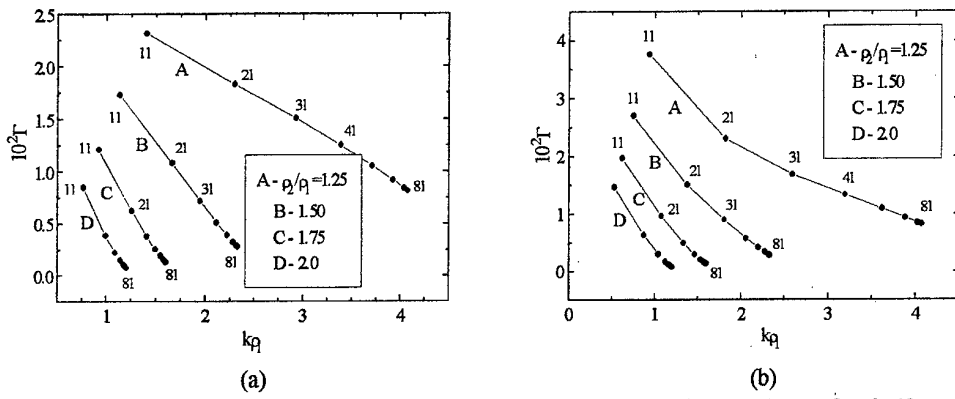


Figure 2. Eigenvalues of $k\rho_1$ and Γ at $N = 16$, $\rho_0/\rho_1 = 0.2$ (a), $\rho_0/\rho_1 = 0.7$ (b), $\vartheta = 0.62$.

HCN-LASER WITH COMBINED PUMPING OF ACTIVE MEDIUM.

Y.E.Kamenev

Institute of Radiophysics and Electronics of the National Academy of Sciences of Ukraine

12, Acad. Proskura st., Kharkov, 310085, Ukraine

phone:38(0572)448-568, Fax: 38(0572) 441-105, E-mail: kiseliov@ire.kharkov.ua

The paper presents the results of experiments with a HCN-laser. The design of a radiator of the laser allowed simultaneous pumping by the direct contained an anode and a cathode for connection to the direct current sources, that were placed on special branch pieces [1]. Between these branch pieces, external electrodes for connecting HF pumping were established [2]. The length active medium was equaled to 1m. HF generator (13,5 MHz), a source of the direct current supply, a source of the alternative current supply (50 Hz) and a 100 Hz pumping source were used as the sources of pumping. Combined pumping consisted in simultaneous switching-on of the HF discharge, on the one hand, and direct current or 50 Hz alternative, current, or pulse current, on the other hand.

The investigations have shown that when one type of pumping is used, pumping by HF radiation appears to be most preferable with respect to the temperature-energy characteristics. It is worthy to note that at pumping by 50 Hz alternative current, positive pulses of discharge current of pumping have been about 20% less by the amplitude than the negative ones. In compliance with this, the pulses of a laser radiation signal have also been less, what is, obviously, connected with the direction of pumping of the working mixture of gases [3].

At pumping by the pulse current, in case of inverted medium, the discharge current pulses have been distorted. This distortion was reflected in emergence of a bend on the current pulse at the moment when the generation pulse appeared. Probably, this phenomenon is connected with a cathode shape, since no sign of this effect has been observed when a hot hollow cathode [1] was replaced by a rod-shaped one having a disk on its end.

Investigation of the laser with combined pumping at every regime have been carried out on the levels of amplitude power quantity ~ 2 mW. It is necessary to point out, that at pumping in the form "HF + direct current", one observed the decrease of energy contribution to the discharge as compared with the contribution on the direct current, however, it appeared to be greater than at HF discharge. At combined pumping in the form "HF + 50 Hz alternative current", the total energy contribution appeared to be slightly less than in each separate case of pumping by HF radiation or alternative current. Using pumping in the form "HF + pulse current", a regime has been discovered, at which the total energy contribution decreased 1,5 times as compared with the energy contribution at one HF pumping. It should be emphasized that regimes with combined pumping at which a threshold regime of HF pumping is used (on the level when generation appears) are of great interest too. In this case, the minimum energy contribution from the second type of pumping is required.

The given results could apparently be applied to investigations of the regimes in the form of HF pumping with different duration and (pulse period-to-pulse duration ratio; relative pulse duration) of pulses, as well as the regimes in the form of "HF + LF".

References

1. Yu.E. Kamenev, E.M. Kuleshov, Compact waveguide continuous wave HCN-laser, Physics and Technology of milli- and submilliwaves, Naukova Dumka, Kiev, pp. 157-162, 1986.
2. Yu.E. Kamenev, E.M. Kuleshov, Characteristics of the application of retroreflectors in submillimetre lasers cavities, Kvantovaja Electronica (Moscow), v. 22, N8, pp. 847-848, 1995
3. D.N. Yundev, Compact HCN-laser, Prib. & Tekh. Eksp. (USSR), N2, pp. 182-185, 1997.

SUBMILLIMETRE DISCHARGE HCN LASER WITH THE INSIDE FILM ELECTRODES

N.F.Dachov, Yu.E.Kamenev, V.K.Kiseliov, E.M.Kuleshov, V.P.Radionov

IRE NAS of Ukraine, 12 Ac. Proskura st., Kharkov, 310085, Ukraine

Tel: 38(0572) 448-335, E-mail: kiseliov @ire.kharkov.ua

Submillimetre HCN lasers are used in physical investigations of plasma and for other special scientific purposes[1,2]. At a last time they are used in biologics and medicine too [3-6]. We designed the submillimetre discharge HCN laser with low frequency (LF) alternating current pumping. The frequency of the pumping current is 50 Hz. This laser is specially adjusted for laboratory and clinical biomedical investigations [7]. Carried out with its help the experimental investigations of the irradiated biomedical objects have corroborated biological efficiency of laser submillimetre radiation. The further improvement of consumer qualities of such lasers it is necessary for their broader introducing in the medical practice. The increasing of reliability, reduction of cost and reduction of size of lasers are some of the main problems.

One of the most high-priced elements of the HCN laser is its resonator. Size of the laser is basically conditioned by size of resonator. The resonator of the LF pumping laser used in medical studies include a glass discharge tube with two soldered-in glass branch pipe to which are installed electrodes of excitation. Similar discharge tube is used in lasers with direct current pumping. Using a soldering when making the glass discharge tube is a shortcoming of these lasers since it raises a resonator cost and reduces its reliability because destruction of the discharge tube is most likely in places of soldering. Besides electrodes installed on the branch pipe of the tube enlarge size of the laser. The lasers with high frequency (HF) pumping have a vastly more simply and reliable design of resonator as far as a continuous section of glass tube with installed outside cylindrical electrodes is used us discharge tube. However high-priced HF generator is used for pumping such lasers. It creates the powerful radio-frequency radiation, which can mask an effect from submillimetre radiating under biomedical studies, that is, of course, inadmissible. To eliminate the above-mentioned shortcoming we used the section of glass tube without the branch pipes as a resonator. To excite the gas discharge the internal film electrodes with defensive layer were applying. They were not use earlier in HCN lasers. Resonator of such laser is shown on Fig.1. Two cylindrical electrodes 2,3 made from the metallic foil 0,1 mm thick and 120 mm width are installed inside the glass discharge tube 1. This electrodes tightly adjoin to its internal surface. The electrodes cover with thin (thickness near 1 mm) self-repair protective layer which prevent from corosions and not preventing excitation of discharge. Sufficiently efficient cooling of electrodes is realized owing to the big area of contact of electrodes with the discharge tube. The feed of electrodes is realized by means of the film conductors 4,5 with the dielectric covering, which are entered inside resonator through the admittance and pumping out branch pipes 6,7. Conductors are connected to contact junctions 8,9 joined with the power source 10. Step-up transformer working from network of single-phase alternating current with voltage of 220V and frequency of 50 Gz serves us power source of laser. Output voltage of transformer is 1500 V when the pumping current is 0,4 A. Two mirrors 11,12 installed in adjusting units 13,14 on opposite ends of discharge tube form the resonator of laser. Mirror 11 is supply by the mechanism 15 for translational movement along the axis of the resonator when adjusting the laser. Mirror 12 represents a partly-transparent one-dimensional wire grating used to take out the radiation from the resonator. In adjusting units there are the branch pipe 6,7 through which the working mixture is pumped. The mixture composition is adjust with the help of two needle-shaped regulators 16,17. An air enters into the resonator through the regulator 16 and the methane is given from the reservoir 18. Mixture pumps by the vacuum pump 19, checking of a vacuum is realized by the thermocouple vacuummeter 20. The radiation go out from the resonator through the teflon window 21. Check of the laser radiating is produced by means of the optical-acoustic receiver or crystalline detector with the amplifier

Single-line-polarized laser radiation represents the periodical sequence of bell-shaped pulses with 100Hz repetition rate when relative pulse duration is near 5. When shortening the resonator by moving a mirror from optimum tuning, a gradual bifurcation of top of pulse is observed from the distance near 5mm (0,14l). This may leads to appearance of two separate pulses which are approximately quarter of pumping period apart. This effect is stipulated by changing density of active medium during flowing through it alternating current of the pumping. This cause change of resonance length of radiating way in the resonator,

and the conditions of the laser generation occur twice (during an increasing and during decreasing a pumping current). For instance this effect possible to use for the reduplication of modulation frequency of laser radiation without some constructive or circuital complicating. Average power of laser radiation is 3mW when the wavelength is 337 mkm and irradiated area is about 1 mm² when the power level is 3dB. Changing of radiating power caused by thermal disalignment of the resonator does not exceed 25% during 8 hours of continuous work. In the laser it is provided installing a remote control system, semiautomatic system of a cleaning resonator from the polymeric raid and automatic system of feed of a methane. Admission of laser radiation to irradiated objects as well as checking and control of parameters of radiation are realized by means of specially developed quasioptical tract made on the basis of a hollow dielectric waveguide [8].

In the laser there are constructive and technological decisions which are not earlier used in similar devices. They allows substantially to simplify and to reduce the price of process of laser resonator making. This results to higher reliability and electrosafety of laser. This decisions permit to use the processes of evaporation and chemical precipitation for making of electrodes of resonator. It may be useful under the serial making of such lasers.

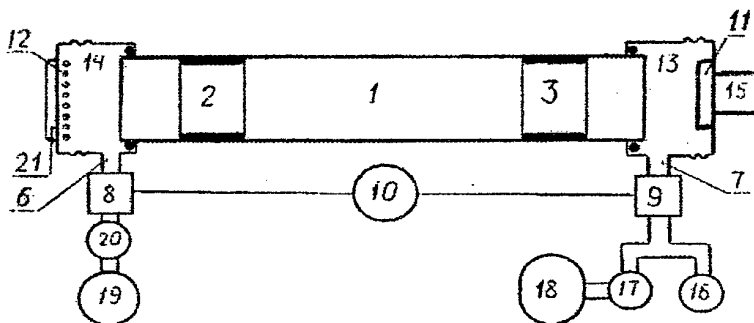


Figure 1.

References

1. E.P.Gorbunov, Ye.M.Kuleshov, P.K.Nesterov and others. Nine-channel Laser interferometer of submillimetre range for Ø-15 mounting // Diagnostics of plasma - M : Energomashizdat, 1989, pp. 135-137. (in Russian)
2. V.I.Bezborodov, Yu.E.Kamenev, V.K.Kiseliov et al. A set of Quasioptic Submillimeter-wave Devices for Thermonuclear Plasma Diagnostics.// 23rd European Physical Society Conference on Controlled Fusion and Plasma Physics, Kiev, June ,24-28, 1996. Abstracts of Invited and Contributed Papers, 1996. P. 328.
3. V.K.Kiseliov, Ye.M.Kuleshov, Yu.E.Kamenev and others. About possibility of using coherent hyper-high frequency radiation for the regulation of intensity of exchanged reactions in the organism. Using the radiowaves of millimetre, submillimetre range - Kharkov : Institute of Radiophysics and Electronics NAS of Ukraine , 1994, pp. 117-120. (in Russian)
4. V.K.Kiseliov, Ye.M.Kuleshov, Yu.E.Kamenev and others. Influence of hyper-high frequency laser radiation of submillimetre range on processes of bone tissue regeneration.// Techniques of millimetre and submillimetre range. - Kharkov : Institute of Radiophysics and Electronics NAS of Ukraine, 1993, pp. 73-78. (in Russian)
5. V.K.Kiseliov, Ye.M.Kuleshov, Yu.E.Kamenev and others. Using an submillimetre laser techniques in immunology investigations. Radiotechnical systems of millimetre and submillimetre ranges. - Kharkov : Institute of Radiophysics and Electronics NAS of Ukraine, 1991, pp. 176-181. (in Russian)
6. V.K.Kiseliov, Ye.M.Kuleshov, Yu.E.Kamenev and others. Influence of hyper-high frequency radiation on biochemical indices under process of dystrophy in tissue of vertebral of white rats.// 6th Republic Science-Practical Conference "Using lasers in medicine and biology", Kharkov, Apr, 8-13, 1996, pp. 24-25 (in Russian)
7. Dachov N.F., Kamenev Yu.E., Kiseliov V.K., Kuleshov Ye.M., Radionov V.P. "Hyperhigh-frequency laser for biomedical investigations", Proceedings of 7th International Crimean Microwave Conference CriMiCo'97. Vol.1, pp.187, 15-18 September 1997,Sevastopol, Crimea, Ukraine. (in Russian)
8. V.K.Kiseliov, E.M.Kuleshov, Yu.E.Kamenev, V.I.Makolinetz, O.P.Timoshenco, B.N.Shevitzov, "The biological effect of the coherent hyperhigh frequency radiation, when the parts of a body surface with the different density of the biologically active points being irradiated." Proceedings of 5th Crimean Microwave Conference Vol.2, pp.545-546, Sevastopol, Ukraine 1995. (in Russian)

QUANTUM CHAOS IN THE 3D ELECTRODYNAMIC SISTEMS OF MILLIMETER WAVE RANGE

E.M.Ganapolskii

Institute for Radiophysics and Electronics of NAS of Ukraine
310085, Kharkov, Ac. Proskura St. 12
Tel.(0572)448553, E-mail:ire@kharkov.ua

Quantum chaos (QC) effect consists in the manifestation of stochasticity in the quantum properties of dynamic system. The investigation of this effect which attracts a great attention at present time is of principal interest. This is associated with the following. Firstly, the investigation of QC effect gives the possibilities to study practically the relation between the classic and quantum description of dynamic system and to realize in such way the conformity principle. Secondly, the macroscopic systems which permit to model and to study experimentally the many unknown early properties of QC effect have been found at last time. The specially constructed quasi-optic closed electromagnetic resonators billiard type having the locally and total instability are belonged to the such systems. Earlier in [1] the QC effects in the two dimensional (2D) electromagnetic resonators were studied. The description of the electromagnetic field distribution in these resonators and natural frequency spectrum is reduced to the solving of Maxwell equations which is similar in this case to the Schrodinger equation with the corresponding boundary conditions. Therefore the problem about the studied stochastic phenomena of 2D resonator systems belong to QC does not arise. It is more complicated problem in the case of the three dimensional (3D) electromagnetic systems described by means of Helmholtz equation which can not reduce to the scalar Schrodinger equation. As it was demonstrated early [2,3] the stochastically effects are also observed in the such systems but in order to establish the implement of these effects to QC it is necessary to choose as an object for investigation the qualitative definite system and to study how the characteristics of stochastic phenomena in it satisfy to the QC criterion's [4].

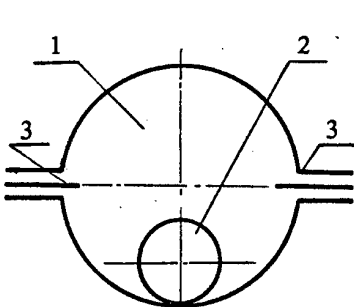


Figure 1. Schematic of S-system similar to the Sinai's billiard. 1 - the copper sphere cavity, 2 - the metal sphere, 3 - antenna.

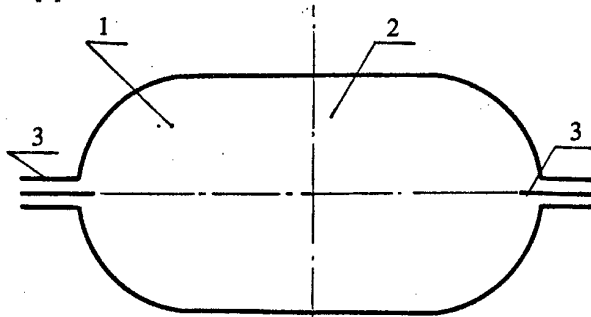


Figure 2. Schematic of B-system similar to the Bunimovich billiard. 1- the sphere-cavity part, 2- cylindrical part, 3 - antenna

With this aim the two quasi-optic electrodynamic 3D systems were chosen for the experimental investigation of the QC effects. The propagation of electromagnetic wave in the first system take place in the conditions of locally instability similar to the particle instability in the scattering Sinai's billiard (S-system). The second system is an analogy to the focusing Bunimovich billiard (B-system). The study of the QC effect in B-system is stimulated by the recent Bunimovich's work [5], where it has been theoretically shown that in the 3D systems similar to the focusing billiard the conditions when the Lapunov's coefficients are positive can realized. Due to this the effects of instability resulting to the field stochasticization can be observed in the such systems. The hypothesis was proposed in [6] and consisted in that the degree of quantum stochasticity of system has significant depended on the Kolmogorov-Sinai's (KS) entropy h . With the aim of the verification of this hypothesis the value of h for the chosen S-system exceeded the KS entropy for the B-system. It will be emphasized one more significant moment in the choose of objects for the QC effects investigation. For the purpose of the instability conditions in electrodynamic system would be similar to the same conditions of the particles moving in the appropriate billiard it is necessary to provide the ray character of wave propagation. In connection with this the

characteristic dimension D of the system was chosen satisfying to the inequality $D \gg \lambda$, where λ is the length of electromagnetic wave in the free space. The QC effect investigations were carried in the eight millimeter wave range at the frequencies 35GHz - 37 GHz where the ratio $D/\lambda \geq 10$.

The electrodynamic S-system represents the closed spherically cavity having the inner surface made from copper and polished. The metal sphere with the surface covered by the silver layer which thickness significantly exceed the value of skin layer was placed into the cavity. The diameter of the copper sphere cavity is of 95 mm and the diameter of metal sphere is of 30 mm. The antenna has served for the exciting and receiving of electromagnetic oscillations in cavity. It was built in the cavity wall and represented as a thin dipole on the end of coaxial line connected this cavity with the standard waveguide and matched over the wide band. The two identical antennas were mounted in the wall of spherical cavity for the measuring of cavity electromagnetic characteristics in two regimes «on reflection» and «on transmitting». The B-system is installed similar and for its excitation the same antennas as in the case of S-system were used. The B-system was represented the copper cavity consisted of two half-spherical parts of diameter 95 mm. The copper cylindrical section of 100 mm long is placed between them. In accordance to [6] one can estimate the values of the reduced KS entropy for the S and B systems.

$$h_S = \ln \frac{D}{\rho} \quad h_B = \ln \left(\frac{16lb}{a^2} \right) \quad (1)$$

where h_S and h_B are reduced KS entropy for S and B systems, D and ρ are the diameter of spherical surface and diameter of metal sphere placed inside the cavity, $2l$ is the cylindrical section length in cavity of B-system, a is the diameter of cylindrical section, b is the height of spherical part in B-system. As it was estimated the values of reduced KS entropy for the S and B systems are 1.8 and 1.4 respectively. The spectrums of natural oscillations of two systems were measured in the pointed frequency range. The standard apparatus in the form of the VSWR panning meter of P-65 type was used for these measurements. This VSWR panning meter permits to record in the automatic regime the spectral characteristics of electrodynamic system in the given frequency range.

The stochastically character spectrum takes place both in S and B systems. The 504 and 416 resonant lines are observed in frequency range of 35 GHz - 37 GHz in the S and B systems correspondingly. The quality of observed resonant lines was change in the wide range. The greatest value of quality of these resonance's is the order of 10^4 . The evaluation of the stochastic spectrum data has held a prominent place in the work. The spectrum processing deals with the relative interval between the neighboring resonance's

$$S_n = (\nu_n - \nu_{n-1}) \rho(\nu_n) \quad (2)$$

where $\rho(\nu_n)$ is the density of frequency spectrum. The distribution functions of the relative intervals for the S and B systems are represented on the Fig. 3. As it is shown from given data the both functions have nonmonotonic character with the maximums by $S < 1$.

In this case for the S system the maximum takes place by the smaller values of S in comparison with B system. The both functions differ qualitative from the Poisson function distribution $P(S) \sim \exp(-S)$ which is peculiar to the frequency spectrum with the noncorrelated accidental frequency distribution. As it follows from $P(0) = 0$ the effect of frequency repulsion which is characteristic for the system with QC takes place. The quantum character of stochastic processes in the measured S and B systems is manifested also in that the distribution functions have the same character as the Wigner distribution

$$P(S) = \frac{\pi}{2} S \exp\left(-\frac{\pi}{4} S^2\right) \quad (3)$$

which characterizes the distribution function of interlevel intervals in the spectrum of stochastic ensemble of real symmetrical matrixes invariant under orthogonal transformations - Gaussian orthogonal ensemble (GOA). In this manner the both system satisfy to the QC criterion concerned to the distribution functions of the interfrequency intervals.

The investigation of these systems were carried in the relation to the second QC criterion concerning of the orderliness of the spectrum frequencies. The characteristic of such orderliness serves the spectral rigidity which is determined by following expression

$$\Delta_3(z, L) = \frac{1}{L} \min_{A, B} \int_z^{z+L} (n(\nu) - A\nu - B)^2 d\nu \quad (4)$$

where $n(\nu)$ is staircase function which is equal to the frequency number in the spectrum with $\nu_n < \nu$. The function $\Delta_3(z, L)$ is determined as a minimum of square-law deflection of spectral distribution from the straight line. The value of $\langle \Delta_3(z, L) \rangle$ averaged on the z from the measured spectrum area depends on L only and designated $\Delta_3(L)$. For the chaotically distributed noncorrelated frequencies with the Poisson distribution

$\Delta_3(L) = L/15$, whereas for GOA incidental to QC by $L \gg 1$, $\Delta_3(L) \approx \frac{1}{\pi^2} \ln L$ [4]

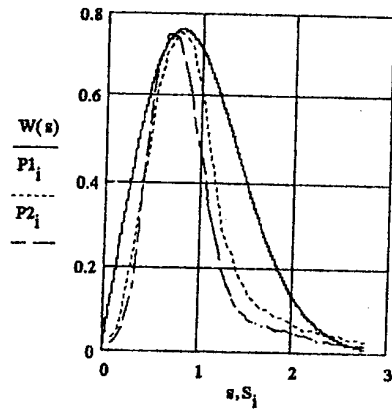


Figure 3. Distribution functions $P(S)$
 $W(s)$ - Wigner function, P_1 - for B-system,
 P_2 for S-system.

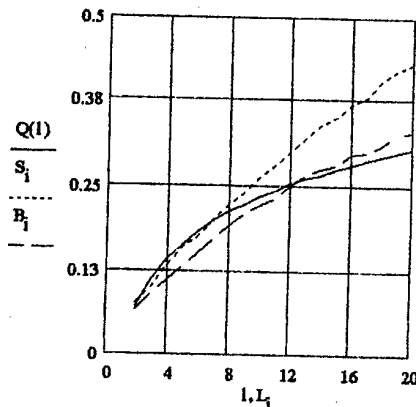


Figure 4. Spectral rigidity
 $Q(l)$ - for GOA system, S - for S-system
 B - for B-system

As is shown on the curves presented on the Fig. 4 for the both systems the spectral rigidity curve is close to the GOA curve in the reasonably degree. The spectral rigidity curve for the B system is more close to the GOA curve in comparison with one for the S system.

Thus in the result of the investigations of electrodynamic 3D systems similar to the scattering and focusing billiards it was established that in the stochastic spectrum of both systems the QC effects are manifested. They show the closing of the distribution function of interfrequency intervals and the function of spectral rigidity to the appropriate relationships for GOA. It is essential to note that the proposed in [6] hypothesis about the dependence of quantum stochastically degree on value of KS entropy does not find the confirmation. In spite of the fact the KS entropy in B system is smaller in the comparison with the S system the B system is closer on its properties to GOA.

References

- 1.H.-J.Stockman, J.Stein «Quantum» Chaos in billiards studied by microwave absorption. Phys.Rev.Lett.Vol.64,#19,pp.2215-2218, 1990.
- 2.H.Alt, H.-D.Graf, R.Hofferbert et al., Chaotic dynamics in a three-dimensional superconducting microwave billiard. Phys.Rev.E Vol.54,#3,pp.2303-2311,1996.
- 3.S.Deus,P.M.Koch,L.Sirko. Statistical properties of the eigenfrequency distribution of three-dimensional microwave cavities. Phys.Rev.E. Vol.52, #1, pp.1146-1155,1995.
- 4.P.V.Elutin. Problema kvantovogo chaosa. Uspechi Fizicheskikh Nauk. v. 155, #. 3, p. 397-442. 1988.
- 5.L.Bunimovich, G. Casati, I.Guarneri. Chaotic Focusing Billiards in Higher imensions. Phys.Rev.Lett.v.77,#14, pp.2941-2944,1996.
6. G.M. Zaslavsky. Stochastichnost' dynamitcheskich system. M.: Nauka. 271 p.1984.

INVESTIGATION OF CRITICAL REGIMES IN PERIODICAL STRUCTURE OF FEL, FORMED BY COUPLED GROOVED WAVEGUIDES

V.S. Miroshnichenko

Institute of Radiophysics and Electronics, Ukrainian Academy of Science

Address: 12, Akad. Proskury Street, Kharkov, 310085, Ukraine

Tel. (0572) 44-84-22, Fax (0572) 44-11-05, E-mail ire@ire.kharkov.ua

The vacuum generators and amplifiers for millimeter and submillimeter wavebands such as FEL, DRO, orotron etc. [1] are based on interaction of an electron beam with a fast electromagnetic wave. The angle between the directions of propagation of an electron beam and a fast electromagnetic wave constitutes usually $\sim 90^\circ$. For a nonrelativistic electron beam, the phase synchronism is provided by the use of a periodical structure with period $L < \lambda$. The periodical structure guides a fast wave, while the electron beam interacts with spatial harmonics of a field concentrated near to a surface of a periodical structure. It is natural, that the correct information on characteristics of propagation and critical regimes of fast waves in periodical structure is necessary for reaching of optimum conditions of such interaction.

In the given report, the new approach to consideration of a periodical structure of FEL is offered. We assumed, that the periodical structure is formed by coupled grooved waveguides, that are located parallel each other with period L , and the common gap between planes of waveguides forms a channel for an electron beam flowing (see. Figure 1). In such electrodynamic system, the directions of propagation of fast wave and electron beam are orthogonal, while the phase synchronism is provided by equality of velocity of an electron beam and phase velocity of one of spatial harmonics of fast wave. So, the electron beam flows along an axis OX in a channel of periodical structure, while the fast wave propagates along an axis OZ through the coupled grooved waveguides, that are formed by opposite slots of a periodical structure (see Figure 1). The insertion of a periodical structure in an open resonant system of FEL results in the analysis of a standing wave in coupled grooved waveguides and, therefore, the correct information on modes and critical regimes of the fast waves in coupled grooved waveguides is necessary for maintenance of an electron beam in a maximum of an electrical field of a standing wave.

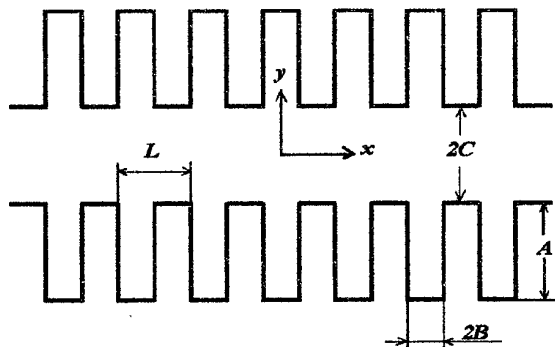


Figure 1. The periodic structure of FEL, formed by coupled grooved waveguides.

For one-grooved waveguide with rectangular form of groove, the wave modes and their characteristics nowadays in details are investigated [2]. So, for a wave with a structure of a field similar to H_{01} -mode in the closed waveguide, an increase of a gap between planes leads to a decrease of critical wavelength λ_{cr} in comparison with the geometric sizes of the groove region ($4A + 4C$). The further increase of width of a gap provides a penetration of a significant part of energy of a wave in lateral areas, and the characteristic of propagation for H_{01} -mode comes nearer to the asymptote $\lambda_{cr} = 4C$ (see Figure 2). It is necessary to mark, that the greatest drop of λ_{cr} in comparison with the geometric sizes is observed for one-grooved waveguide with narrow width of slots and for a small gap between planes. This case is of interest at the analysis of an electrodynamic system of FEL, where the width of slots is small $2B \ll \lambda$, and the depth of slots comes nearer to the resonant value $A \approx \lambda / 4$.

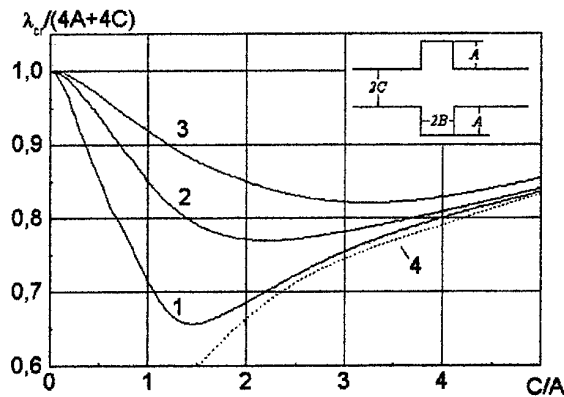


Figure 2. Characteristics of propagation of H_{01} -wave in one-grooved waveguide:
1 - $B/A = 0,25$; 2 - $B/A = 0,75$; 3 - $B/A = 1,5$; 4 - asymptote $\lambda_{cr} = 4C$.

For the analysis of critical modes of fast waves in a periodical structure consisting from coupled grooved waveguides with any cross section of grooves, the experimental method for measurement of λ_{cr} was used. For this purpose a section of a periodical structure was closed on two ends along an axis OZ (see Figure 1) and was transformed into a resonator. The resonator was excited through a variable slot of coupling, that is located in parallel and symmetrically to a channel for an electron beam. The resonant frequencies f_r were determined for several values of coupling σ inside the range $0 < \sigma < 0,5$, and the own resonant frequency of a section of a periodic structure was determined by a linear regression of $f_r(\sigma)$ for $\sigma = 0$. The given method provides high accuracy of measurement of λ_{cr} in coupled grooved waveguides: $\Delta f_r/f_r \sim 0,1\%$.

The testing of a method of measurement of λ_{cr} was carried out for the one-grooved waveguide with rectangular groove. The obtained experimental data and the data of theoretical calculations were compared. The all measurements were carried out in 8-mm waveband. The geometric parameters of the one-grooved waveguide are the next: $2B = 0,51$ mm; $A = 2,71$ mm; the width of a channel can be changed within the range $0 \leq 2C \leq 3,0$ mm. The good agreement of experimental and theoretical data for λ_{cr} is observed (see Figure 3).

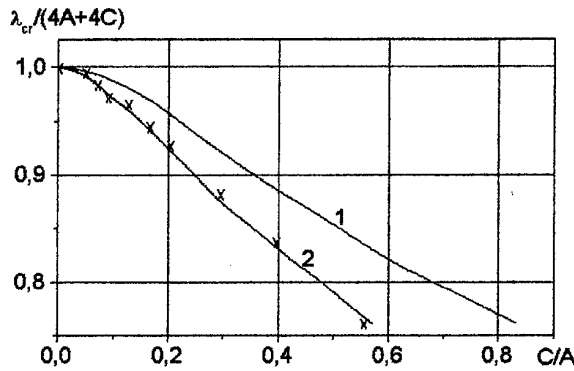


Figure 3. Critical wavelength of H_{01} -wave for the one-grooved waveguide:
1 - $B/A = 0,25$; 2 - $B/A = 0,095$; x - experiment ($B/A = 0,095$).

The experimental data obtained for λ_{cr} of H_{01} -wave in a periodical structure are shown on Figure 4. The periodical structure was formed by coupled grooved waveguides with the rectangular form of grooves ($L = 1,00$ mm; $A = 2,71$ mm; $2B = 0,51$ mm). For small width of a channel ($0 < C/A < 0,15$), the values of λ_{cr} of H_{01} -

wave in a periodical structure are slightly less than for the one-grooved waveguide because of field coupling of adjacent grooves. The further increase of a width of channel leads to the exceeding of λ_{cr} for a periodic structure in comparison with the one-grooved waveguide, and for a large value of channel width the critical wavelength comes nearer to the asymptote $\lambda_{cr} = 4[C + A(2B/L)]$.

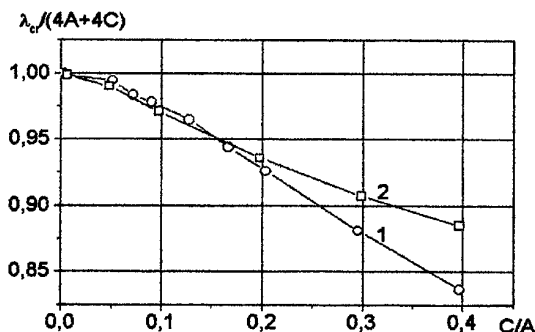


Figure 4. Critical wavelength of H_{01} -wave for the periodical structure, formed of coupled grooved waveguides:
1 - one-grooved waveguide; 2 - periodical structure.

The experimental data for the critical regimes in a periodical structure formed of H-waveguides are shown on Figure 5. Here are used the following designations: λ_{cr} - critical wavelength of H_{01} -mode measured in experiment, λ_H - calculated value of a critical wavelength for the closed H-waveguide. The geometrical parameters of a periodical structure were selected the following: period of a structure $L = 3,00$ mm; $A = 1,56$ mm; $a = 1,18$ mm; $2B = 0,97$ MM; $2b = 0,21$ MM. The width of a channel can be changed within the range $0 \leq 2C \leq 0,70$ mm.

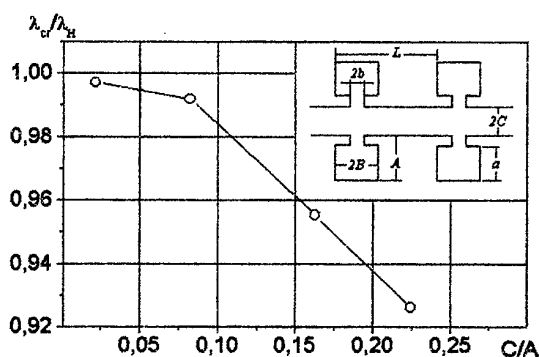


Figure 5. Critical wavelength of H_{01} -wave for periodical structure, formed of coupled H-waveguides

In summary we shall mark, that the offered experimental method of the analysis of critical modes of fast waves is applicable to periodical structures, that are formed of coupled grooved waveguides with any form of cross section of grooves.

References

- 1.O.I. Belous, A.I. Fisun, A.A. Kirilenko, V.K. Korneenkov, V.S. Miroshnichenko, "Research on orotron oscillator with dispersive open resonant system" Int. J. of Infrared and Millimeter Waves, vol.18, No.2, pp. 445-461, 1997.
- 2.R.A. Silin "Computation of characteristics of transmission lines for microwaves". Electron. Tekh. SVCh-teck., (in Russian), No. 5(449), pp.41-49, 1992.

“BUSH” OSCILLATIONS IN A DIFFRACTION RADIATION OSCILLATOR

I.K.Kuz'michev and B.K.Skrynnik

Institute of Radiophysics and Electronics
of the National Academy of Sciences of Ukraine
12, Ac.Proskury st., Kharkov, Ukraine, 310085
Tel: (0572)-448-393, Fax: (0572)-441105, E-mail: ire@ire.kharkov.ua

The oscillatory circuit of a diffraction radiation oscillator (DRO) represents a composite two-level hemispherical open resonator (OR) whose plane mirror is partially covered with a periodic structure in the form of reflection grating. The latter much changes the original OR field.

This communication presents the field distribution and the mode structure of the DRO oscillatory circuit depending on the reflection grating lifting above the plane mirror.

Measurements are performed in the 4mm wave range. The aperture and the curvature radius of the spherical mirror are 60mm . A reflection grating 10mm wide occupies the central area of the plane mirror. The grating period is 0.4mm , the grating grooves are of width 0.14mm and of depth 0.86mm . Measured with accuracy 0.01mm , the grating lifting is varied within $\Delta = 0 \div 0.9\text{mm}$. The OR is fed by a klystron oscillator through a slot coupler $3.6 \times 0.16\text{mm}^2$ placed at the spherical mirror center. The circuit is tuned to resonance in any change of the grating location. The OR signal is extracted with the aid of the other coupler which is offset by 7mm from the first one. A quite large mirror spacing serves to derive the most stable quasi - TEM_{20q} and quasi - TEM_{40q} oscillations and describe the field distribution near the plane mirror in maximum accuracy.

The resonance mirror spacing D_{OR} measured for quasi - TEM_{20q} and quasi - TEM_{40q} oscillations is shown versus the grating lifting Δ in Fig.1. The field distribution is displayed for typical (characteristic) points $1 \div 4$ with curves $1 \div 4$ in Fig.2. As the grating rises, complex quasi - TEM_{20q} oscillation gradually changes into fundamental oscillation TEM_{00q} (see curves 1,2, and 3). When the mirror surface is level with the grating equivalent plane which is at a distance Z_0 from the grating upper boundary, i.e. when $\Delta = Z_0$, TEM_{00q} exists in the nearly uncombined form. In the present context $Z_0 = 0.55$ for $\lambda_0 = 4.07\text{mm}$ [1]. The farther lifting causes the side spots in the field distribution, and the fundamental oscillation TEM_{00q} gradually changes into quasi - TEM_{20q} (see curve 4). The dotted lines in Fig.2 plot the field strength square of TEM_{00q} and quasi - TEM_{20q} oscillations calculated using normalized Hermite polynomials [2]. A good agreement between the calculations and measurements is evident.

The change of the resonance spacing caused by the grating lifting above the mirror and calculated with the constraint $\delta D_{OR} \cong \delta \Delta$ implying that the power of the desired mode is almost completely reflected from the grating is shown with the dotted, tilted 45 degrees lines in Fig.1. This situation occurs when the grating width is twice as large as the diameter of the field major spot, but it is impossible in the discussed OR. So the angular position of the measured dependences is off $\delta D_{OR} \cong \delta \Delta$. The relationship σ between the power reflected from the grating and the total power reflected from the whole composite mirror depends essentially on the field distribution: as can be easily found from the measured dependences, $\sigma = 0.9$ for quasi - TEM_{20q} and $\sigma = 0.25$ for quasi - TEM_{40q} . These values fit the relationships between the areas enclosed by the corresponding experimental curves in Fig.2 and they also fit the dependences calculated using normalized Hermite polynomials [2].

As far as the DRO oscillations, except for the fundamental oscillation TEM_{00q} , cannot be identified with the calculation results for the basic (without grating) OR [1], every mode excited in the composite OR may be regarded as a «bush» consisting of two and more oscillation types. These oscillations progressively change as the grating is lifted or the wavelength is varied. In this case, any field distribution in

the composite OR may be considered as a superposition of the basic OR modes with different coefficients. Thus the field distribution of the most common DRO oscillation that is quasi - TEM_{20q} is interpreted to be a half-sum of the fundamental oscillation TEM_{00q} and classic TEM_{20q} described by the Gaussian function multiplied by a Hermite polynomial. In this case, the width of the central spot increases 1.4 times, and the amplitude of the side spots grows smaller than the central spot amplitude.

Thus in the same fashion that a complex (modulated) signal can be decomposed into the sinusoidal components of different frequency and amplitude, the complex «bush» oscillations can be represented via the basic OR oscillations of common frequency but different amplitude. It follows from that any oscillation of the composite OR represents the interference picture of the OR steady-state field.

The similar situation takes place for the higher modes, e.g. quasi - TEM_{40q} (see Fig.1). The dispersion dependence becomes much more complex when two "bush" oscillations turn into coupling, which occurs as used here at $\Delta \approx 0.8mm$. This phenomenon is interpreted with the special theory [3] of the Morse critical points of dispersion equations. The MCP vicinity is characterized by the intensive power exchange, and as soon as the MCP is passed, one can see the mutual transformation of the modes. In the passage through the critical points, the "bush" composition changes but this "bush" remains as a unit. The modes replace one another, and their total number in the "bush" may change.

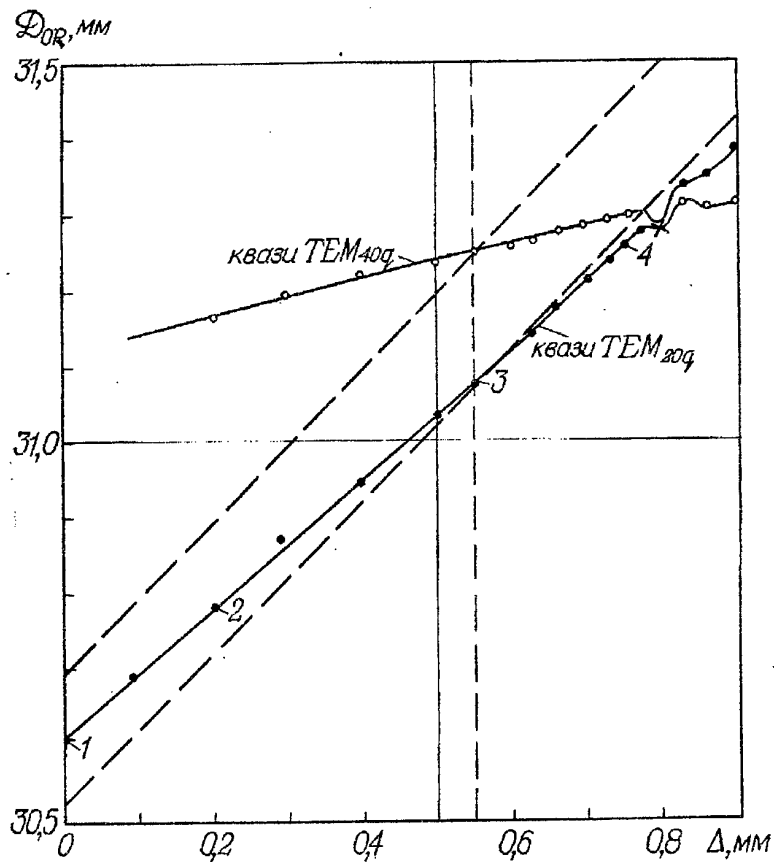


Figure 1. Resonance spacing D_{OR} measured for two oscillation types in a composite two-level open resonator versus the grating lifting Δ above the plane mirror. The dotted lines comply with $\delta D_{OR} \cong \delta \Delta$.

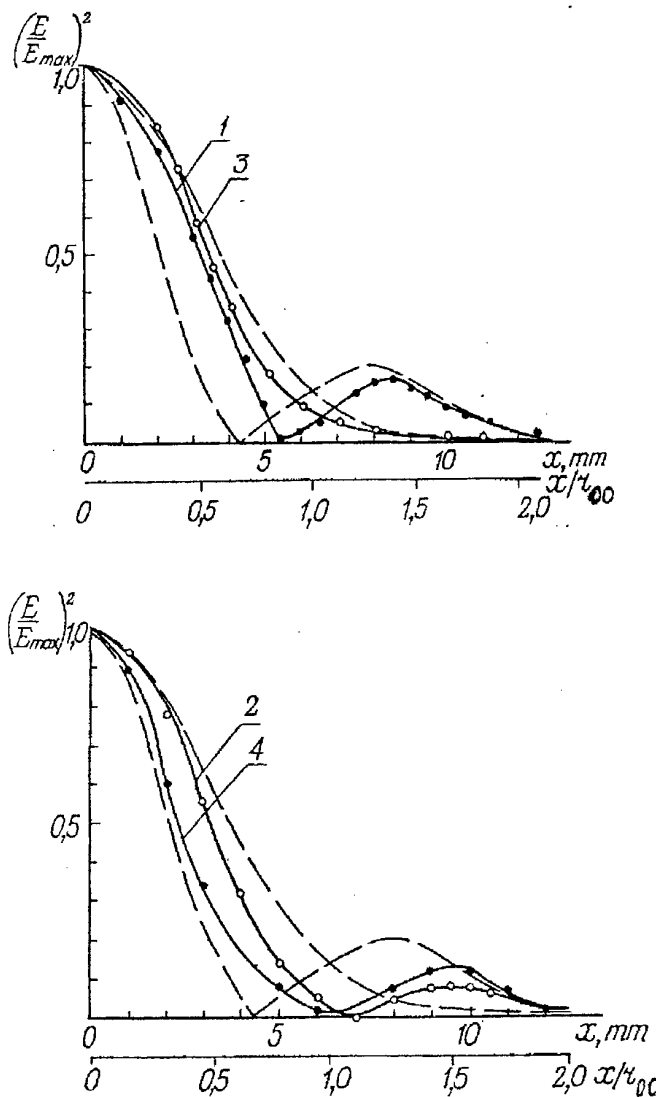


Figure 2. The distributions of the field strength square over the cross section of a composite two-level open resonator. Curves 1,2,3, and 4 are plotted for typical points 1÷4 indicated in Fig.1 and corresponding to $\Delta_1 = 0mm$, $\Delta_2 = 0.20mm$, $\Delta_3 = 0.55mm$, and $\Delta_4 = 0.75mm$; the fundamental oscillation TEM_{00q} and for quasi - TEM_{20q} oscillation are displayed with the solid lines, the dotted lines are for the calculation results.

References (all in Russian)

1. V.P.Shestopalov, "Diffraction Electronics", Kharkov State University, Kharkov, 232p., 1976.
2. A.G.Pivovarova and B.K.Skrynnik, "A Quite Realistic Description of High-Order Oscillations in a Diffraction Radiation Oscillator", Radiofizika i Elektronika, vol.2, No.1, pp.53-59, 1997.
3. V.P.Shestopalov, "Nonlinear Evolution Processes in a Diffraction Radiation Oscillator as a Free Electron Laser", J.Experim. i Teor. Fiziki, vol.3, No.6, pp.2243-2262, 1997.

**EXPERIMENTAL DETECTION AND ANALYSIS OF THE MORSE CRITICAL
POINT OF OPEN ELECTRODYNAMICAL STRUCTURE INVOLVED IN
DIFFRACTION RADIATION OSCILLATOR**

I.K.Kuz'michev

Institute of Radiophysics and Electronics
of the National Academy of Sciences of Ukraine,
12, Ac. Proskura st., Kharkov, Ukraine 310085

Tel: (0572) - 448-421, Fax: (0572)-441105, E-mail: ire@ire.kharkov.ua

Until the present time the direct experimental detection of the Morse critical points (MCP) of dispersion equations of open electrodynamical structures has been lacking. In the millimeter wave region , this is because the proper theoretical analysis [1] performed for H_{03} and H_{41} oscillations of a simplest open structure like a confocal resonator calls for impractical geometrical dimensions . This disadvantage has been overcome through the use of a suitable electrodynamical structure like an open resonator involved in a diffraction radiation oscillator The constructional feature providing the experiment feasibility is the reflecting diffraction grating which is embedded in one of the resonator mirrors and much changes the spectral characteristics of the canonical structure .

The considered open resonator consists of a plane mirror with aperture 60 mm and a spherical focusing mirror whose curvature radius and aperture are both 60 mm . The reflecting diffraction grating of width 10 mm occupies the central area of the plane mirror . The grating period is 0.4 mm , the grating grooves are 0.14 mm in width and 0.86 mm in depth . The excitation is realized through a slot coupler which is embedded in the spherical mirror centre and measures 3.6 mm x 0.16 mm . The other similar - sized coupler is placed some distance apart to extract the resonator signal .

The measured resonance transmission factor K_r of the three first oscillation types is shown in Fig. 1 as a function of the mirror spacing L/R . Since the lowest oscillation TEM_{00q} (where q is a number of the half

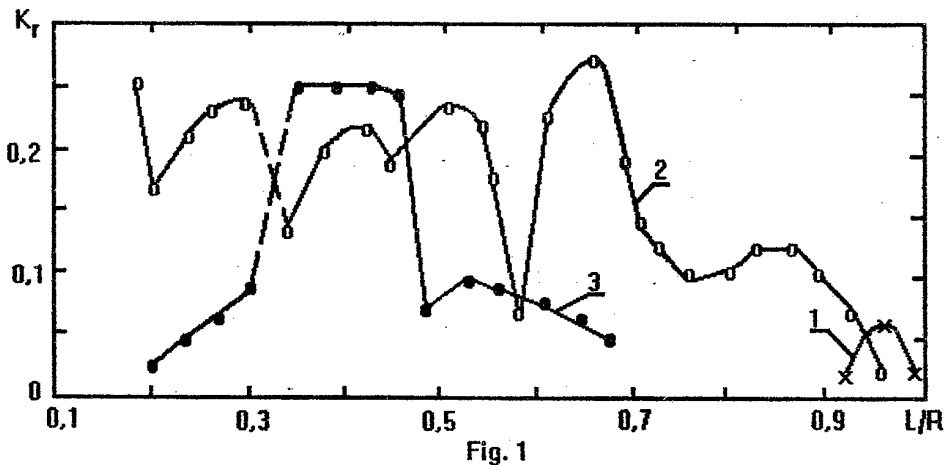


Fig. 1

Resonance transmission of TEM_{00q} (curve 1), TEM_{20q} (curve 2) and TEM_{40q} (curve 3)
oscillations as a function of the mirror spacing of the open resonator involving the
reflecting diffraction grating .

wavelengths which are present along the length of the mirror spacing) is maintained only within the narrow limits $L/R = 0.992 \dots 0.923$ (curve 1), it is quasi - TEM_{20q} oscillation (curve 2) that is recognized as dominant . The first high oscillation TEM_{40q} (curve 3) is illustrated for comparison . As seen , a sharp K_r change occurs in the vicinity of the point $L/R = 0.324$ for all these oscillations . When this point is approached from large mirror spacings the dominant oscillation is TEM_{40q} as it features the higher transmission factor K_r and , consequently , higher loaded Q . Once the coincidence point has been passed , the oscillations turn into

coupling of the two high - Q oscillations of the open electrodynamic system of a diffraction radiation oscillator was experimentally observed for the first time . Indicative of the event is the MCP appearance characterized by certain spectral parameter λ / L and nonspectral parameter L / R .

Fig. 2 shows the loaded - Q logarithm as a function of the mirror spacing L / R for quasi - TEM_{20q} (curve 1) and quasi - TEM_{40q} (curve 2) oscillations . As L / R is decreased , the loaded - Q factors of both

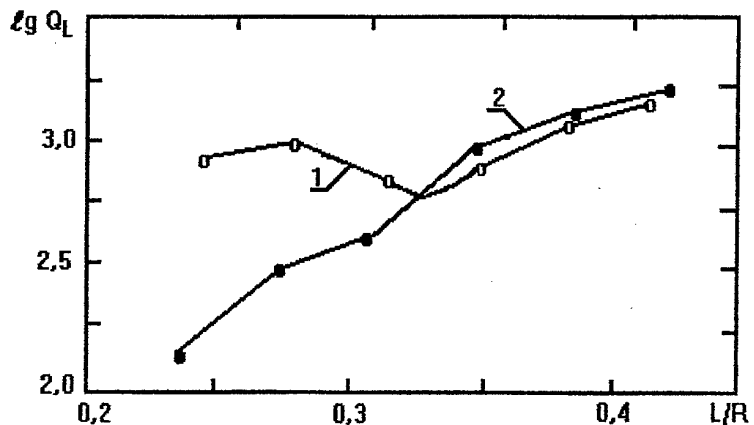


Fig. 2

Loaded Q factor of quasi - TEM_{20q} (curve 1) and quasi - TEM_{40q} (curve 2) oscillations in the condition of the resonator retuning near the MCP.

oscillations do the same until they are comparable at $L / R = 0.324$. The further decrease of L / R makes the loaded Q of quasi - TEM_{20q} oscillation 1.5 times greater , whereas the loaded Q of quasi - TEM_{40q} keeps its falling .

Dispersion curves (Fig . 3) of the analyzed oscillations were measured in the MCP vicinity where parameter L / R exerts influence on the resonance wavelength (frequency) of the system ; here λ_0 is a fixed

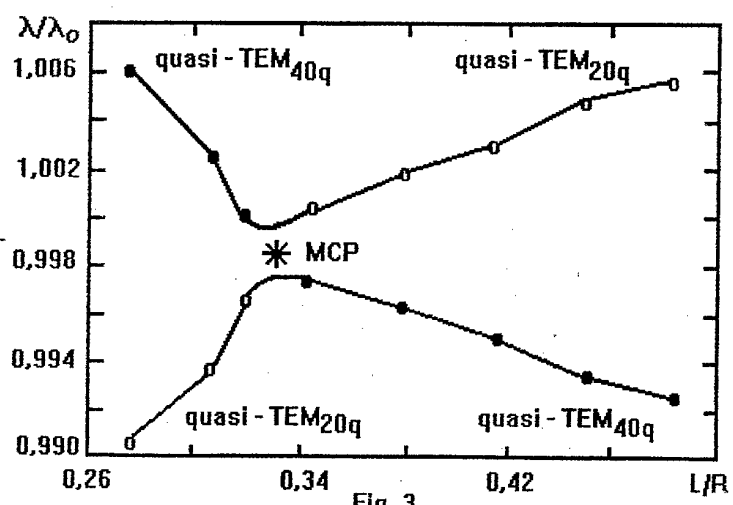
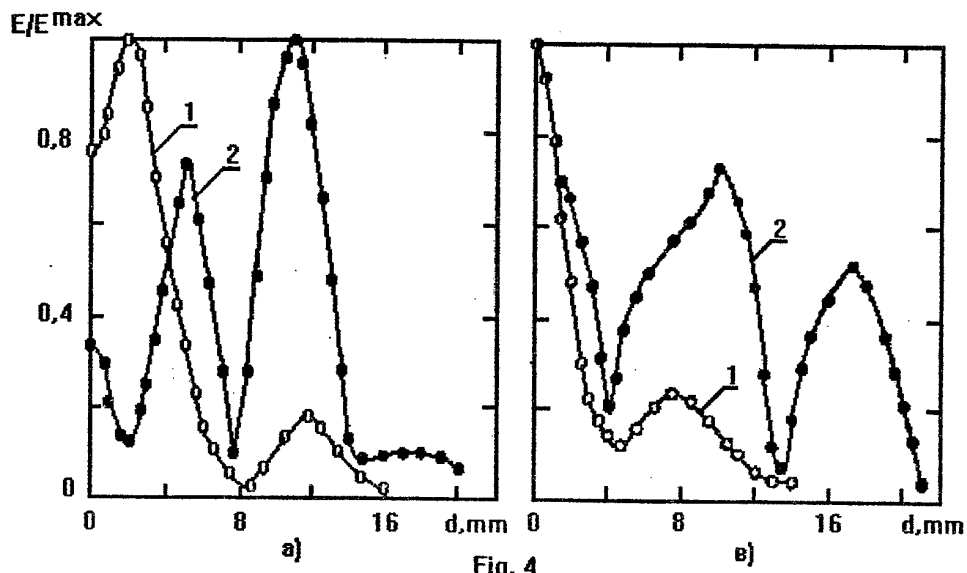


Fig. 3

Relative change of the operation wavelength of the examined oscillations in the MCP vicinity versus the mirror spacing.

wavelength of the preceding measurements. The examined oscillations are interconverted and they exchange energy when passing through the MCP. With the further L/R decrease, the oscillations take sharp turns along different branches of the dispersion characteristic.

Of practical interest is the field structure of the considered quasi-TEM_{20q} and quasi-TEM_{40q} oscillations near the MCP. For this purpose, the test body method [2] was used. The field distributions (Fig. 4) of quasi-TEM_{20q} and quasi-TEM_{40q} oscillations were measured in the plane of the \vec{H} vector of the



The field structure of the examined oscillations near the MCP.

dominant wave of the feeding waveguide. Away from the MCP, the examined oscillations do not couple and exist in uncombined form of quasi-TEM_{4,0,11} ($L/R = 0.413$; Fig. 4, a, curve 2) and quasi-TEM_{2,0,12} ($L/R = 0.41$; Fig. 4, b, curve 1) oscillations. Once the MCP has been passed, the interconversion of the oscillations occurs. Namely, quasi-TEM_{4,0,11} converts into quasi-TEM_{2,0,9} ($L/R = 0.307$; Fig. 4, a, curve 1) and quasi-TEM_{2,0,12} becomes quasi-TEM_{4,0,8} ($L/R = 0.304$; Fig. 4, b, curve 2).

Thus the mutual coupling of the two high-Q oscillations has been experimentally observed in the conditions of the resonator retuning due to the presence of the reflecting diffraction grating embedded in one of the resonator mirrors. The grating essentially changes the spectral characteristics of the open electrodynamical system, which eventually allows the MCP detection.

References

1. V.P.Shestopalov, "Morse Critical Points of Dispersion Equations", Naukova Dumka, Kiev, 1992, pp. 42-45.
2. "Submillimetre Wave Engineering", ed. By R.A.Valitov, Sov. Radio, Moscow, 1969, pp. 219-223.

ANALYSIS OF THE STEADY-STATE MODE OF THE ORMOTRON

G. A. Alexeev

Institute of Radiophysics and Electronics of NAS of Ukraine

12 Acad. Proscura str., Kharkov, 310085, Ukraine

Tel: 380 572 448 340; Fax 380 572 441 105; E-mail: homenko@ire.kharkov.ua

Ormotron is the microwave M-type generator with an injected electron beam and an open resonator [1, 2]. The simplified scheme of the ormotron is represented in Fig. 1. The solid line in Fig. 1 represents the snapshot of the infinite-thin electron beam in the interaction space, which is formed by the plane mirror of the open resonator and the transparent (for the fast spatial harmonics of the field) ladder-type diffractive lattice. In this paper the analysis has been made in the framework of the approximate analytical nonlinear theory to carry out analysis of the ormotron mode of the stationary oscillations. The analysis based on the using of the quasilinear and asymptotic expansions for the evaluation of the interaction integral [3]. It is shown that the ormotron is a generator with the hard self-excitation.

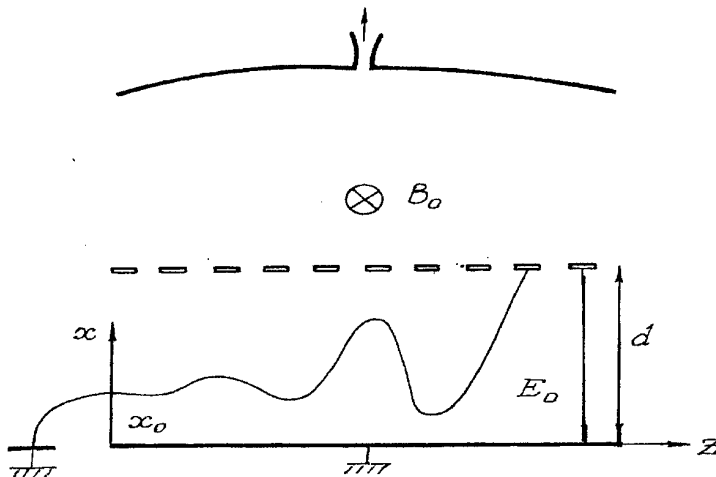


Fig.1.

One may suppose, that the field of the following synchronous surface harmonic, interacting with the electron beam, has the form:

$$E_x = -R \cdot \exp [\beta (x - x_0)] \cdot \sin (\omega t - \beta z); \quad (1)$$

$$E_z = R \cdot \exp [\beta (x - x_0)] \cdot \cos (\omega t - \beta z);$$

Here R is the amplitude on the level of the aimed distance x_0 of the electron ray, which is to be determined (in accordance with the method of the predetermined field); $\beta = \omega B_0 / E_0 = 2\pi/\ell$; E_0 and B_0 are the intensity and the induction of the crossed static fields, ℓ is the period of the diffractive structure.

The expressions for active P_a and reactive P_r of the components of the interaction power of the infinite-thin electron beam with the field (1) and the expressions for the amplitude $\xi = R / E_0$, the electron efficiency η_e and the frequency shift $\Delta\omega_0$ in the steady-state mode resulting from the shortened equations of the resonance systems excitation then have the form:

$$P_a = -I_0 E_0 \int_0^F G(F) dF / \beta = -I_0 E_0 F \cdot f(F) / \beta; \quad (2)$$

$$P_r = I_0 E_0 \int_0^F [\cos \varphi_1(F) + 1] dF / \pi \beta; \quad (3)$$

$$\xi_0 = D \cdot f(F_0); \quad (4)$$

$$\eta_e = F_0 \cdot f(F_0) / \beta d = \frac{L}{d} \cdot \frac{\xi_0^2}{D}; \quad (5)$$

$$\Delta\omega_0 = \frac{\omega'}{2Q} \cdot \frac{1}{\pi} \cdot \int_0^{F_0} [\cos \varphi_1(F) + 1] dF / \int_0^{F_0} G(F) dF; \quad (6)$$

Here $f(F_0) = \int_0^{F_0} G(F) dF / F_0$ is the oscillatory performance of the generator,

$D = 2QI_0 L / \omega' N E_0$ is the feed-back parameter, Q , N , ω' are the loaded quality, the norm and the own frequency of the working oscillation, $I_0 = \rho_0 \cdot E_0 / B_0$ is the full static current of the electron beam, L and d are the length and the width of the interaction channel,

$$G(F) = \frac{1}{\pi} \cdot \int_{\varphi_1(F)}^{\pi} \sin \varphi \cdot \operatorname{ctg}(\varphi - F \sin \varphi) d\varphi; \quad (7)$$

$F = \xi \beta z$; $F_0 = \xi_0 \beta L$ are the parameters of the electron beam grouping [4]. The initial phase of the electrons φ_1 , settling on the periodic structure, is determined by the solution of the transcendental equation:

$$h \cdot \sin \varphi_1 = \sin(\varphi_1 - F \sin \varphi_1); \quad F > F^* = 1 - h; \quad (8)$$

where $h = \exp[-\beta(d - x_0)] \ll 1$ is the small parameter of the theory, F^* is the point of the break of the curve $G(F)$. The electron settling on the negative electrode (flat mirror of the open resonator) is not taken into account (it is supposed that $\beta x_0 \gg 1$).

The analytical solution of the problem can be obtained, using the approximate expressions for the interaction integral $G(F)$ on the various sites of the representation area, which have the form [3]:

$G(F) = F + \frac{2}{3} F^3$; ($0 \leq F \leq F^0$) in the area of the quasilinear expansions in the Taylor series on the parameter of the grouping;

$G(F) = \alpha_1 / \sqrt{1-F}$; ($F^0 \leq F \leq F^*$) in the area of the asymptotic evaluation, which uses (according to the Laplace method) the expansions of the integrand functions near the singular point of the denominator $\varphi = 0$;

$G(F) = G^*(1 - \alpha_3 \sqrt{F - F^*})$; $G^* = \alpha_1 / \sqrt{h}$; ($F^* \leq F \leq 1$) in the area of the expansions in the Taylor series on the parameter $\sqrt{F - F^*}$;

$G(F) = \alpha_5 / F^2$; ($F \geq 1$) in the area of the asymptotic expansions near the point $\varphi = \varphi_1$, determined (when $h \ll 1$) by the simplified equation $\varphi_1 = (F + h) \sin \varphi_1$.

The coefficients α_1 , α_3 , α_5 is the result of the slow factors averaging [3]. For example when $\beta(d - x_0) = 3$; ($h = 0.05$); $F^0 = 0.7$ they are equal: $\alpha_1 \approx 1$, $\alpha_3 \approx 2.2$, $\alpha_5 \approx 2.27$. The exact (7) and approximate dependencies $G(F)$ for this case are reduced in Fig. 2 (continuous curves).

For the oscillatory performance of the orotron shall receive:

$$f(F) = \frac{1}{2} F + \frac{1}{6} F^3; \quad 0 \leq F \leq F^0;$$

$$f(F) = [F^0 \cdot f(F^0) - 2\alpha_1(\sqrt{1-F} - \sqrt{1-F^0})]/F; \quad F^0 \leq F \leq F^*; \quad (9)$$

$$f(F) = [F^* \cdot f(F^*) + G^* \cdot (F - F^*) - \frac{2}{3}\alpha_3 G^* \cdot (F - F^*)^{3/2}]/F; \quad F^* \leq F \leq 1;$$

$$f(F) = [f(1) + \alpha_5 - \alpha_5/F]/F; \quad F \geq 1.$$

This performance is represented (for the case $h=0,05$; $F^0=0,7$) in Fig. 2 by the dashed curve. One can see, that she describes the hard excitation mode.

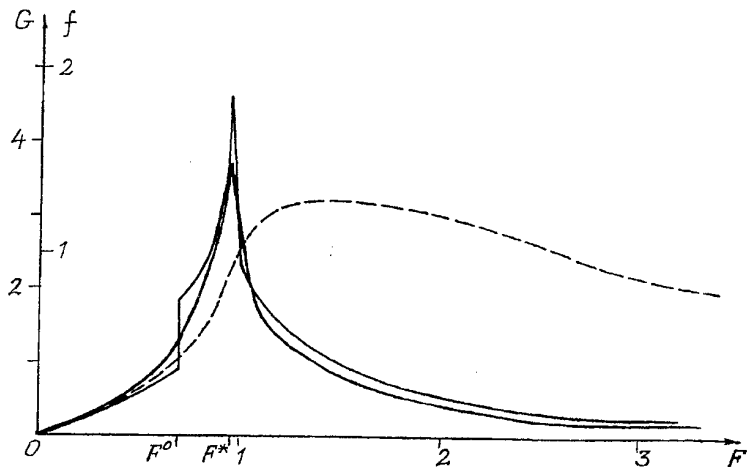


Fig.2.

From (4), (9) the cubic equation for the steady-state amplitude ξ_0 follows. From the conditions of the self-excitation and the stability of the oscillations it is possible to find the bifurcation values of the feed-back parameter, at which happen the excitation and the failure of the oscillations (for example, at current retuning of the generator):

$$\begin{aligned} D_{start} &= 2/\beta L; \\ D_{failure} &= (\beta L)^2 \xi_0^3 / \{ 2\alpha_5 - \beta L [f(1) + \alpha_5] \xi_0 \}. \end{aligned} \quad (10)$$

The maximum electron efficiecy and the frequency shift, accordingly, are equal:

$$\eta_{e \max} = C_m / \beta D; \quad (11)$$

$$\Delta\omega_0 = \frac{\omega'}{2Q} \cdot \int_{1-h}^{F_0 \gg 1} (\cos\varphi_1 + 1) dF / \pi C_m \leq \frac{\omega'}{2Q} \cdot \pi / 2 C_m; \quad (12)$$

$$\text{where } C_m = [\frac{1}{2} (F^0)^2 + \frac{1}{6} (F^0)^4 + \alpha_1 (2\sqrt{1-F^0} - \sqrt{h}) - \frac{2}{3} \alpha_1 \alpha_3 h + \alpha_5]. \quad (13)$$

For the case $\beta(d-x_0)=3$ from (13) follows $C_m \approx 3,37$ and, for example, if $\beta d=5$ we shall receive $\eta_{e \max} \approx 67\%$.

Thus, the analysis shows that the orotron can be a highly effective coherent microwave source, having both the high efficiency and the high stability of the oscillations.

References

1. L.A.Pospelov. "On the nonlinear theory of the M-type generator with an open resonator", Tes. of the reports of the VIII Intercollegiate Conf. on the Microwave Electronics, pp. 29-30, Rostov-na-Donu, Sept. 1976.
2. L.A.Pospelov, S.A. Cherenshikov. "On the excitation of the M-type generator with an open resonator", Radiotekhnika, (Kharkov), No. 45, pp. 80-83, 1978.
3. G.A.Alexeev, L.A. Pospelov. "Use of the asymptotic expansions in the nonlinear theory of the M-type devices with an injected electron beam", Reports of the VII All - Union Conf. "Electron microwave devices and their application", Vol.2, pp. 4-11, Tomsk, 1972.
4. J. Feinstein, G. Kino. "The Large-Signal behavior of Crossed-Field Traveling-Wave Devices", Proc. IRE, Vol. 45, No. 10, pp. 1364-1373, 1957.

ANALYSIS OF ELECTRON-WAVE INTERACTION IN CATHODE DRIVEN CROSSED-FIELD AMPLIFIERS BY COUPLED-MODE METHOD

G.I. Ghuryumov, T.I. Frolova

The Usikov¹ Institute for Radiophysics and Electronics

of the Academy of Science of Ukraine

12 Ac. Proscra St., Kharkov, 310085, Ukraine

Tel. +38 0572 448518, Fax: +38 0572 441105

Kharkov State Technical University of Radioelectronics

14 Lenin Av., Kharkov, 310726, Ukraine

Tel. +38 0572 409362, Fax: +38 0572 409113,

E-mail: et@kture.kharkov.ua

Increasing a gain of the crossed-field amplifiers is one of the most important problems [1]. To solve of this problem the various approaches are used. The main attention has been given to the advancement of the existing tubes and improvements in use of new technological processes and new materials. However, the theory of the tubes with improved characteristics is not sufficient advanced to evaluate in full measure their limited opportunities.

In present paper the processes of electron-wave interaction in the cathode driven crossed-field amplifiers are studied. These tubes have a higher gain due to the use of the weakly coupled delay lines placed on the anode and negative electrode (cathode). As a result the r.f. signal of same frequency is applied to the input of a cathode delay line (or to the inputs of the anode and cathode delay lines) and after an amplification the signal is coming to the output of the anode delay line (the mode of cathode excitation).

The interaction space of a classical crossed-field amplifier and cathode driven amplifier is schematically shown in Figure 1. As can be seen the areas of the input of r.f. wave ($y = d$) and the injection of electron beam ($y = y_0$) at the classical tubes are spatially separated (Figure 1, a). The use of the cathode excitation permits maximally to bring together these areas and hence to increase the value of r.f. field at the point in which the electron beam is. As a result we can decrease the power of input signal without deteriorating of the bunching and thus to increase the gain of the tube.

To analyze the physical processes in the cathode driven amplifiers let us use by coupled-mode method [2]. According to given method the system of differential equations will be written in the following form:

$$\frac{d A_i}{d z} = - jC_{ii} A_i - j \sum_{k=1}^N C_{ik} A_k, \quad i = 1, 2, 3, \dots, N, \quad (1)$$

where $C_{ii} = \beta_i$ is the phased constant of the i -th wave propagating in a delay line without the electron beam;

C_{ik} is the coupling factors between i -th and k -th normal waves ($i \neq k$); N is the number of the coupled waves. As was shown by Sasaki and Van Druzer [3], in the classical crossed-field tubes the electron-wave processes with consideration for the effects of space-charge are described by six normal waves ($N = 6$): two cyclotron-waves (fast and slow), two space-charge waves (growing and decaying) and two waves propagating

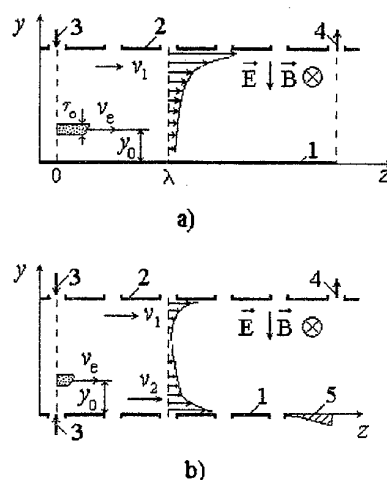


Figure 1. Schematic diagram of cathode driven crossed-field amplifier:
1,2-cathode and anode delay lines; 3 - r.f. input; 4 - r.f. output, 5 - matched load

to the positive and negative direction of the circuit, respectively. To simplify the problem let us suppose that the coupling factor between the cyclotron-waves in a beam and the waves in the circuit is weak (their coupling factors are less than to unit [2]). In this case we can take into account only four waves ($N = 4$): two waves in the circuit (the main waves on cathode A_1 and anode A_2 , delay lines) and two waves in the electron beam (growing A_3 and decaying A_4 waves). As a result the complete solution of the equations system (1) is given by the expression:

$$A(z) = \sum_{i=1}^4 A^i(0) \exp(-j\gamma_i z), \quad (2)$$

where $A^i(0)$ and $\gamma_i = \beta_i + j\alpha_i$ are the initial amplitude and complex propagation factor of the i -th normal wave. For a determination of the phase constants of the normalized waves and coupling factors C_{ik} the results of the reference [3] were used. The expressions for these constants are indicated in Appendix.

To find the propagation factor of the normal waves γ_i ($i = 1, 2, 3, 4$) we can use the non-trivial solution of the system of equations (1) (compatibility condition). As a result the dispersion equation for the propagation factor can be written in the following form:

$$(\beta_e - \gamma)^2 (\beta_1 - \gamma)(\beta_2 - \gamma) + \beta_e^2 (\beta_1 - \gamma)(\beta_2 - \gamma)S^2 + \\ + (\beta_e - \gamma)(\beta_1 - \gamma)\beta_1^2 D_1^2 + (\beta_e - \gamma)(\beta_2 - \gamma)\beta_2^2 D_2^2 = 0. \quad (3)$$

To define the initial amplitudes of a normal waves $A^i(0)$ it is necessary to use the initial conditions on the input (or output) of the forward (backward) wave amplifier as the following system of the equations:

$$\sum_{i=1}^4 A_i^i(0) = E^2(0); \quad \sum_{i=1}^4 A_2^i(0) = E^1(0); \quad \sum_{i=1}^4 A_3^i(0) = 0; \quad \sum_{i=1}^4 A_4^i(0) = 0, \quad (4)$$

where $E^{1,2}(0)$ are the r.f. amplitudes of the waves on the input of the cathode and anode delay lines of the forward-wave amplifier (or on the output of the backward-wave amplifier).

Figure 2 shows the gain as the function of the mismatch parameter b_1 for the case, when $D_1^2 = 0.03$, $D_2^2 = 0.01$, $S = 0.1$, $b_2 = 0$ (curves 1 - 4). For comparison in this figure the similar dependence is submitted for the classical crossed-field amplifier, when $D^2 = 0.03$, $S = 0.1$ (curve 5). As can be seen the gain of the tube with the cathode excitation exceeds its value, received for the classical amplifier in cases, when the interaction of the electron beam takes place with forward waves of the cathode and anode delay lines (the case positive dispersion) (Figure 2, curves 1 and 2). The use of the delay lines with negative dispersion in these tubes deteriorates the process of interaction between the electron beam and r.f. waves. As result the gain reduces and does not exceed the gain of the classical crossed-field amplifier (Figure 2, curves 3, 4 and 5).

On the other hand it should be noted that non-monotonous nature of a variation is specific for the dependence $K = K(b_1)$. The gaps on this dependence the most strongly present themselves in the cases when the cathode and anode delay lines have the negative dispersion (backward wave interaction). It is connected with the amplifying influence of the interference phenomena when the normal waves propagating in the

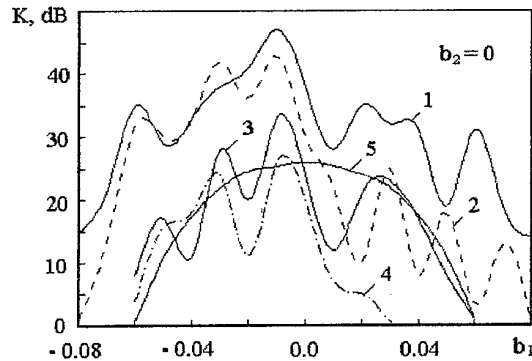


Figure 2. Gain versus the parameter of mismatch

electron-wave system with the different phase velocities are either in the phase or in the antiphase. This effect manifests stronger itself in the area of the positive values of the parameter b_1 , i.e. when the electron beam is ahead of the waves, propagating on the anode and cathode structures on condition that $b_2 = 0$. Variation of the parameter b_2 offers a shift of the dependence $K = K(b_1)$ according to the behavior of roots of the dispersion equation (3). The analysis shows that the gain depends on the mismatch parameter b_2 and decreases with its growth ($|b_2| > 0$). As a result the maximum gain of the tubes with the cathode excitation takes place in the case of a synchronous movement of the waves on the anode and cathode delay lines, when $v_1 = v_2$. Thus the use of the cathode delay lines with the positive dispersion permits to increase the influence of r.f. field on the bunching. As a result the gain of the tubes with the cathode excitation increases and the anode voltage zone, corresponding the stable gain, expands. The negative influence of r.f. wave, propagating in the cathode delay line, to the electron-wave interaction process exists and connects with a grow of wave interference phenomenon.

Appendix

Expressions for the coupling factors:

$$\begin{aligned} C_{13} &= jK_1 \sqrt{\alpha_1} (1+j); & C_{14} &= jK_1 \sqrt{\alpha_1} (1-j); \\ C_{23} &= jK_2 \sqrt{\alpha_2} (1+j); & C_{24} &= jK_2 \sqrt{\alpha_2} (1-j); \\ C_{31} &= -jK_1 \sqrt{\alpha_1} (1-j); & C_{32} &= -jK_2 \sqrt{\alpha_2} (1-j); \\ C_{41} &= -jK_1 \sqrt{\alpha_1} (1+j); & C_{42} &= jK_2 \sqrt{\alpha_2} (1+j), \end{aligned}$$

$$\text{where } K_1 = \frac{\beta_1}{2} \sqrt{\frac{\omega}{\omega_c} \frac{I_0 Z_1}{2U_a}}, \quad K_2 = \frac{\beta_2}{2} \sqrt{\frac{\omega}{\omega_c} \frac{I_0 Z_2}{2U_a}}, \quad D_1 = \frac{2K_1 \sqrt{\alpha_1}}{\beta_e}, \quad D_2 = \frac{2K_2 \sqrt{\alpha_2}}{\beta_e},$$

$$\beta_e = \frac{\omega}{v_e}, \quad \beta_1 = \frac{\omega}{v_1}, \quad \beta_2 = \frac{\omega}{v_2}, \quad \beta_3 = j\beta_e - \beta_s, \quad \beta_4 = j\beta_e + \beta_s.$$

$S = \frac{\beta_s}{\beta_e}$ is the space-charge parameter; $\beta_s = \frac{\beta_e}{\omega_c \epsilon_0 \tau_0} \left[\frac{I_0}{2U_0} \right]$ is the growth (or decay) factor for the space-charge waves; $\alpha_1 = cth(\beta_e y_0)$ and $\alpha_2 = cth[\beta_e(d - y_0)]$ are the circuit parameters; $b_1 = \frac{\beta_e - \beta_1}{\beta_1}$ and $b_2 = \frac{\beta_2 - \beta_1}{\beta_1}$ are the parameters of mismatch of the electron beam and waves in the cathode and anode delay lines; $\omega_c = \eta B$ is a angular cyclotron frequency; U_a is a dc anode voltage; I_0 is a dc beam current; $Z_{1,2}$ is a coupling impedance of the anode and cathode delay lines; d is a distance between anode and cathode.

References

1. Skowron J.F.: "The continuous-cathode (emitting-sole) crossed-field amplifier" *Proc. IEEE*, 1973, v. 61, 3, p. p. 330-356.
2. Louisell W.H.: "Coupled mode and parametric electronics", New York: Wiley, 1960.
3. Sasaki A. and Van Druzer T.: "Coupled-mode analysis of interactions in crossed fields", *IEEE Trans.*, 1966, ED - 13, 5, p. 494-501.

SIMULATION OF AN INVERTED COLD SECONDARY EMISSION MAGNETRON GUN

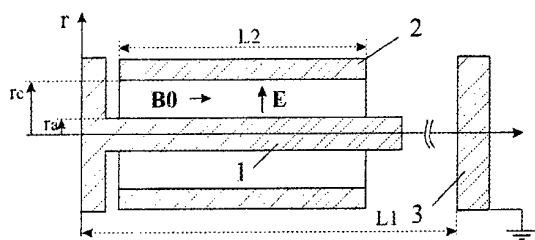
D.B. Eremeev & G.I. Churyumov
 Kharkov State Technical University of Radio Electronics
 14 Lenin Av., 310726, Kharkov, Ukraine
 tel.: +38 0572 40 93 62, fax: +38 0572 40 91 13
 E-mail: churyumov@kture.kharkov.ua
 N.I. Aizatsky, A.N. Dovbnya, V.V. Zakutin & N.G. Reshetniak
 National Science Center K I P T, Kharkov, Ukraine.

The processes of forming and transporting electron beams calls for further investigation of two independent problems. In the former case the problem of selection of efficient emitter, which possesses required emission capabilities and life are solved. The problem complicated considerably in the case when axially symmetric electron beams are used. For forming such beams thermionic cathodes are commonly used as emitters. Along with it there are works in which the autoelectronic emission were used for forming linear beams [1]. The use of these emitters allows significantly to increase a life of the cathodes and to go to crucially new methods forming of the electron beams. However, unstable character of autoelectronic emission and problems connected with unsolved questions of technologies of cold cathode production does not permit to go to their wider use.

Solution of the second problem is connected with calculation of the configuration of system of the driving electrodes, creating the distribution of the electrostatic field which is necessary to form of an electron beam. Under these conditions the complicated configuration of electrodes, which forms the axially symmetric electron beam, is the reason which makes necessary the search for more simple and technologically effective designs of guns.

In this paper a simulation of secondary electron emission in inverted cold cathode magnetron gun are presented. These investigations are considered as continuation of work which was begun from [2] and carried out for the usual cold cathode magnetron gun.

Schematically the interaction space of an axially symmetric magnetron gun and its geometric and electric parameters are shown in Fig. 1. Cathode is made of copper.



1 - anode; 2 - cathode;
 3 - collector $L_1 = 133 \text{ mm}; L_2 = 90 \text{ mm};$
 $r_c = 6.5 \text{ mm}; r_a = 1.25 \text{ mm}$
 $B_0 = 0.2 \text{ Tl}$

Fig. 1

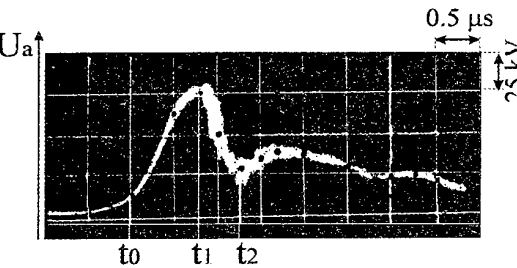


Fig. 2

For operation of gun the pulse of anode voltage, that is represented in Fig. 2, is fed to its anode at moment of time $t=0$. The process of secondary emission takes place when this pulse decays away in moment of the time $t_1 < t < t_2$. In order to form the sequence of electron bunches it is necessary to feed sequence of these pulses. To simulate the magnetron gun the mathematical model in two-dimensional and non-relativistic approximations is used. The self-consistent system of equation forms the basis of this model and in the normalized form in the case of inverted system can be written as:

$$\frac{du_r}{dT} = -G \left\{ \hat{\epsilon}_r^* - \frac{\zeta^*}{\chi + R} + G^* (\chi + R)(1 + \Theta) [1 - \gamma^*(1 + \Theta)] \right\} \quad (1)$$

$$\frac{d\Theta}{dT} = -\left\{\hat{\varepsilon}_\varphi - u_r G [1 - 2\gamma^*(1 + \Theta)]\right\} \times \frac{G\zeta}{\chi + R} \quad (2)$$

$$\frac{d\Phi}{dT} = \frac{\omega}{\omega_c} \Theta \quad (3)$$

$$\frac{dR}{dT} = \frac{\omega}{\omega_c} \frac{\zeta^*}{\gamma} u_r \quad (4)$$

$$\frac{\partial^2 V}{\partial Y^2} + \gamma \frac{\partial^2 V}{\partial \Phi^2} = r^2 \frac{1}{\varepsilon U_a} \rho \quad (5)$$

where $\varepsilon = r_c/r_a$, $\zeta = 1 - \varepsilon$, $G = E_0^a/(v_e^k B_0)$, $\chi = \varepsilon/\zeta$, $\zeta^* = \frac{1}{\zeta}$, $G^* = \frac{\zeta}{G}$,

$$\hat{\varepsilon}_{r,\varphi} = \hat{E}_{r,\varphi}/E_0^a, \quad \gamma^* = \omega/(\omega_c \gamma), \quad E_0^a = U_a/(r_a \ln(1/\varepsilon)) \quad \omega_c = \eta B_0$$

$$v_e^k = \frac{Ua}{r_c \ln \frac{r_c}{r_a}} - \text{non-exited drift velocity of beam t at the level of cathode.}$$

Solution of these equations carries out with moment of the time $t=t_0$ (see Fig. 2), with the proviso that by this moment a formed electron cloud with uniform distribution of particles exists in the interaction space.

To solve the Poisson's equation the Hockney method and FFT are used [4, 5]. The results of a solution of this equation are the values of space charge potential at each point of the space grid. These digital values of the potentials are approximated in the region $(i-1, i+1; j-1, j+1)$ by the analytical polynomial

$$V(x', y') = a_1 + a_2 x' + a_3 y' + a_4 x' y' + a_5 x'^2 + a_6 y'^2 \quad (6)$$

where

$x' = \frac{\Phi - \Phi_{ij}}{\Delta\Phi}$, and $y' = \frac{R - R_{ij}}{\Delta R}$ are normalized variables of coordinate system connected with point (i,j) . R_{ij} and Φ_{ij} are the coordinates of the point, nearest to the place where is the particle with the coordinates R and Φ . a_1, a_2, \dots, a_6 are the polynomial factors which are calculated by a least-squares method.

Finally, the expressions for the components of space charge field can be written as:

$$\hat{\varepsilon}_r = -\frac{(M-1)}{\zeta(\chi+R)} \frac{\partial V}{\partial y'}, \quad (7)$$

$$\hat{\varepsilon}_\varphi = -\frac{\ln(1/\varepsilon)}{2\pi} \frac{\gamma(N-1)}{\zeta(\chi+R)} \frac{\partial V}{\partial x'} \quad (8)$$

To solve the motion equation the forth-order Runge-Kutta method is used. The initial coordinates and velocities of particles $v_e = E_0/B_0$, $E_0 = U_0/(r \ln(r_c/r_a))$ are determined from the following expressions for the coordinates:

$$R_{i,j} = \frac{\Delta R}{L_e} i_j \quad (9)$$

$$\Phi_{i,j} = \frac{2\pi}{P_e} (j_i - 1) \quad (10)$$

where $i_j = 1, 2, 3, \dots$, - are number of layers for every particle $j = 1, 2, 3, \dots Pe$, and velocities of particles

$$(u_r^o)_{i,j} = \frac{(\tilde{v}_r^o)_{i,j}}{v_\phi^a} = \sin \xi \quad (11)$$

$$(\Theta^o)_{i,j} = \frac{(\tilde{\Omega}^o)_{i,j}}{\Omega} = \cos(1 - \xi) \quad (12)$$

respectively, where x is a random number having equally probable distribution from 0 to 1.

Hereinafter, when $t > t_0$ additional insertion of particles from cathode (secondary electron emission) is considered. As a model of secondary electron emission we take the model which is described before in [3]. The scheme of realization of the self-consistent system of equations is presented in Fig. 3

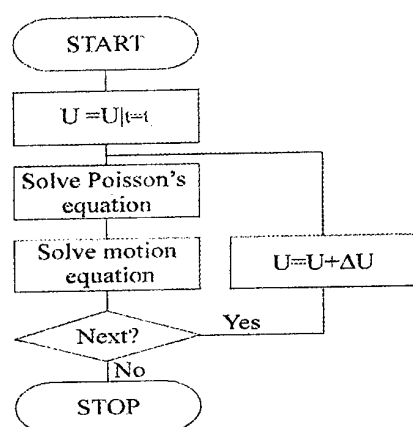


Fig. 3

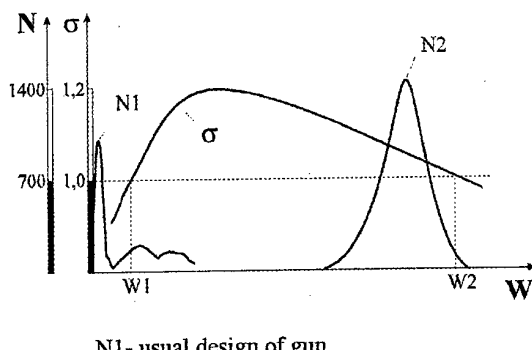


Fig. 4

The energetic distributions of primary electrons impacting the cathode of the inverted gun is a result of simulation. These results are depicted in Fig. 4. The similar distribution for the case of usual design [2] are shown in Fig. 4. for comparison.

The carried model experiments demonstrates that the process of electron beam forming in the inverted magnetron gun goes on in more effective way, comparing to the same in usual one, providing larger number of electrons in interaction space. In doing so, maximal quantity of electrons getting cathode has the energy which is matched by the value of coefficient of secondary electron emission more than 1 (see Fig. 4).

Therefore the application of the inverted design is promising way for solving problem of forming dense axis-symmetrical beams.

References

1. "Non - thermionic cathodes", ed. M.M Elinson, Sov. Radio, Moscow, 1974.
2. G.I. Churumov and others, "Simulation and modeling of secondary emission process in the cold cathode crossed-field gun", In: Proceedings 15-th International Symposium on Charged Particles Linear Accelerated. Kharkov, vol. 2, pp.24-26, 1997.
3. G.I. Churumov "Simulation of electron bombardment of the cathode and anode in amplitron", Electronnaya technika. Ser. 1. Electronica SVCH, no. 3 (457), pp. 23-26, 1993.
4. J.W. Cooly, J.W. Takey, "An algorithm for the machine calculation of complex Fourier series", Math. Comput., № 19, p. 161-175, 1965.
5. R.W. Hockney, "A fast direct solution of Poisson's equation using Fourier analysis", J. of the ACM. vol. 12, № 1, p.95-113, 1965.

THE MM-WAVE COLD CATHODE PENIOMAGNETRON

Victor D. Yeremka

Usikov Institute of Radiophysics & Electronics of National Academy of Sciences of Ukraine,
 12, Acad. Proskura st., 310085, Kharkiv, Ukraine.
 Tel.: 38-0572-448-519. Fax: 38-0572-441-105.
 E-mail: eremka@ire.kharkov.ua

ABSTRACT

The distinctive features of the peniotron device - a millimeter wave source with a peniotron mechanism of the electron-wave interaction on the high harmonics of the cyclotron frequency are considered. This device uses an adiabatic electronic-optical system (EOS) with a cold cathode. The EOS generates a large-orbit helical electron beam which releases the energy to the high frequency (HF) field in the space interaction of the source electrodynamic system (EDS). The EDS represents a coaxial cavity based on the round-shaped waveguide with an azimuthal periodic vane structure and slot-type resonators (magnetron waveguide). The scheme of the source makes it possible to operate in the modes of through gyroresonance or autoresonance. The first results of the investigation into the cold-cathode electron gun holds a greater promise for the devices based on such a system.

1. INTRODUCTION

The high performance of the peniotron mechanism of the electron-wave interaction of the high harmonics of the cyclotron frequency has been theoretically and experimentally demonstrated [1-3]. As part of an experiment the scheme of the highly efficient giroresonance device has exhibited a good advantage offered by following three attributes:

- a) a magnetron waveguide with an axially directed rod (which provides the mode selection with a required azimuthal index);
- b) a peniotron interaction mechanism (which makes for the equality of all beam electrons);
- c) the mode of through gyroresonance (which helps achieve a high electronic efficiency). We have called this type of the device a «peniomagnetron» [2].

A possibility of developing the peniomagnetron with an EOS comprising a non-heated («cold») cathode is discussed below. This paper is the result of the conceptual evolution in [4].

2. ADIABATIC ELECTRON-OPTICAL SYSTEM

The results of the studies on the EOS with a termionic cathode for peniotrons have been previously presented in [5]. We have utilized them in the development of the triode construction (Fig.1), of the cold-cathode EOS that forms a monohelical, tubular EB for a pulse oscillator peniomagnetron operating in a through-gyroresonance mode at a frequency of 100 GHz on a 10-th cyclotron harmonic. The expression

$$D_k^2 = 4,55 \cdot 10^{-11} \cdot \frac{U \cdot W_\phi}{|B \cdot B_k|}$$

was derived, which established the relation between an average diameter (D_k),

the induction of the magnetic field on the cathode (B_k), the potential of the interaction space (U) and a relative value of the EB rotational energy ($W_\phi = \frac{v_\phi^2}{v_z^2 + v_\phi^2}$). The average balanced diameter of the EB in the

interaction space is determined by the known relation $D = D_k \left(\frac{B_k}{B} \right)^{1/2}$. In order to obtain a small spread of the EB energy rotation and the required cathode current density the width of the ring-type emitter should be significantly less compared to the average diameter of the cathode ($\Delta / D_k \ll 1$) [5].

The analytical relations given in [5] were the main criteria for selecting the parameters of a tree-electrode cold-cathode gun. These criteria were implemented by the computer simulation of the EOS and the magnetic focusing system (MFS) and by matching the gun with the magnetic field in the interaction space to reduce the radial EB pulsations. The construction of the gun (Fig.1) incorporates a cathode assembly with the ring-type emitting surface (RTES) 1, the focusing electrodes 2,3, the accelerating electrode 4, the matching

electrode 5 and the anode 6. The matching electrode 5 ensures that the tubular EB is electrostatically focused to a certain degree and consistent with the magnetic field when there is a slight rise in the field (around 0.5 T/mm) in a transition region. The accelerating electrode 4 provides the prescribed magnitude of perveance. The focusing electrode 2 is combined with a field disc edge emitter (FDEE) made from refractory metal. The ring-type emitting surface is manufactured from the material having a high secondary electron emission factor $\delta > 1$. With a voltage pulse being fed across the electrodes 1 and 2 there occurred the pulse of the field emission current. The secondary electron emission process proceeded at the beginning of each anode voltage pulse with a duration of 0.5 to 3 μ s between the electrodes 1 and 4. The main current of the monohelical EB is set up by the secondary-emission electrons. A possibility of utilizing the chemically pure metals Pt, Mo, Ni, etc. as the materials for the ring-type emitting surface (RTES) has been examined. A comparison of the primary-emission electrons current to the FDEE and the secondary-electron emission current to the RTES indicates that their multiplication factor is on the order of 10^3 . To form the FDEE a technique for low-temperature metal evaporation has been employed. A study on the FDEE made from Mo, Cr, W, Nb is currently being performed.

3. PENIOTRON INTERACTION MECHANISM IN STATIC CROSSED FIELD

The peniotron mechanism may probably occur in static electric and magnetic crossed fields [4]. Consider the electron-wave interaction in a coaxial waveguide with a longitudinal rib-type periodical structure in which the field of the electromagnetic wave, having azimuthal variations, is rotating counter clockwise (fig.2). The central coaxial is integrated with a secondary-emission cathode. The EOS forming the tubular EB is mounted at one end of the coaxial waveguide whereas the electron collector is placed at the other end. The central EOS pin has a galvanic connection with a secondary-emission cathode. The thin tubular EB formed by the EOS receives the cyclotron rotation by the static magnetic field reverse, placed at the input to the coaxial waveguide [4]. The EB also rotates counter clockwise under the action of the radial electric, E , and the axial magnetic, B , static fields. The particles outrun the wave for one period of its azimuthal variations for one revolution about the axis of the system. In this case the electric high frequency (HF) field is sensed by electrons as the complementary static electric field E of linear orientation.

Now let us see how the preliminary circular path of electrons is influenced by the disturbing HF field ηE . We presented the non-relativistic system of equations for the electron motion in the fields E_0, B_0, E , but we will simplify the problem in such a way that the inhomogeneous stationary field will be approximately replaced by a field value corresponding to the stationary trajectory:

$$\begin{aligned} \ddot{x} + \Omega \dot{y} - Cx &= -\eta E \\ \ddot{y} - \Omega \dot{x} - Cy &= 0. \end{aligned} \quad (1)$$

Instead of the system (5) one equation can be written for the complex variable $z = x + jy$ [7].

$$\ddot{z} - j\Omega z - Cz = -\eta E. \quad (2)$$

The general solution of linear equation (1) with constant coefficients takes the form:

$$z = \alpha e^{j\nu_1 t} + \beta e^{j\nu_2 t} + \eta E / C, \quad (3)$$

where α, β are the complex random constants, $\nu_{1,2}$ is the angular rotational speed.

We select the initial conditions as the ones corresponding to the case where the V_2 electrons (which rotate at a great speed) receive the rotating HF field as being constant with an axially oriented electric vector (fig.2):

$$z(0) = \rho, \quad \dot{z}(0) = j\nu_2 \rho_0. \quad (4)$$

$$\text{Then } \ddot{z} = -\frac{\nu_2 \eta E / C}{\nu_2 - \nu_1} e^{j\nu_1 t} + \left(\rho_0 + \frac{\nu_1 \eta E / C}{\nu_2 - \nu_1} \right) e^{j\nu_2 t} + \frac{\eta E}{C}, \quad \text{or at } \nu_1 \ll \nu_2 :$$

$$z \approx \frac{\eta E}{C} \left(1 - e^{j\nu_1 t} \right) + \rho_0 e^{j\nu_2 t}. \quad (5)$$

Here, the second expression describes the fast rotation of the circle of the radius ρ_0 , whereas the first one describes the slow drift of the driving center of this circle.. It is easy to follow the drift direction by showing

the curve $\zeta = 1 - je^{j\eta t}$ on a complex plane (Fig.3). The center of an electron orbit is seen to be moving around a certain circle. The commencement of the drift occurs as the electrons become displaced towards the brake HF-field, thereby specifying the positive energy balance sign. This is a good indication that even in crossed fields the electron-wave and related peniotron interactions can be observed. A study into the possibility of integrating the positive features of magnetron - and peniotron-type interactions in the above-described device (peniotron) has been made. A large-orbit EB is injected into the peniomagnetron interaction space, and in this case the beam tube thickness is chosen as sufficient for its electrons to be involved in both of the parallel processes. A layer of electrons adjacent to the periodic structure provides an effective electron - wave interaction which is characteristic for the peniotron. In the region close to the system axis the drift of the electron-orbit driving centers is conducive to the electron bombardment of the secondary-emission cathode and the formation of the secondary-electron beam interacting with the HF-field in peniotron and magnetron modes. In this case by selecting the parameters of the electric and magnetic fields the secondary electrons can be phase-sorted in such a way as to get the latter involved in the effective energy exchange with the HF-field.

The design pulse of the devices output power is equal to 50 KW with an efficiency of 40% at a frequency of 100 GHz with a pulse operating voltage amplitude of 14 KV and a magnetic field strength of 0.36 T on a 10-th cyclotron harmonic.

4. CONCLUSION

The combined peniotron and magnetron interaction mechanisms in a single system may appear beneficial in developing the efficient oscillators and amplifiers that are operated in short-wave bands.

References

- 1 V. D Yeremka, V. A. Zhurakhovsky, V. P Shestopalov. «A large-orbit peniotron profiled from the law of through gyroresonance» Journal of Communications Technology and Electronics, N9, V.33, pp. 1900-1907, 1989.
2. V.D Yeremka, V.A Zhurakhovskij, A.M.Kovalenko. «Peniomagnetron amplifier theory» ICMWFT'90. Sapl. Conf. Dig.- Beijing, China. pp.52-56. 1990
3. T.Ishihara, H.Tadano, H. Shimawaki, e.a. «Space harmonic peniotron in a magnetron waveguide resonator» IEEE Trans. on Electron Devices, Vol.43 No.5, pp.827-833, 1996
4. V.D Yeremka , V.A Zhurakhovskij, O.P.Kulagin. «The peniotron with crossed static electric and magnetic fields in the space of interaction» APMC'96, Cjnf.Dig., New Delhi, India, pp.282-285. 1996.
5. V.D Yeremka, I.I.Golenitskiy, B.Ch.Djubua , e.a. «Production and study of axis-encircling electron beams for peniotrons» ICMWFT'92. Sapl. Conf. Dig.1992. Beijing, China. pp..351-354. 1992
6. Zh.I.Dranova., V.D Yeremka, T.I.Mazilova, LM Mikhailovskij, O.A Velikodnaya. «Forming of field emitter surface by gas induced field evaporation» Conf.Dig. 9-th Int.Vaccum Microelectronics Conf. St.Petersburg.- pp.169-173. 1996.
- 7 P. L.Kapitsa. Scientific Works. High-power electronics and plasma physics, M., Nauka, 403 p. 1991.

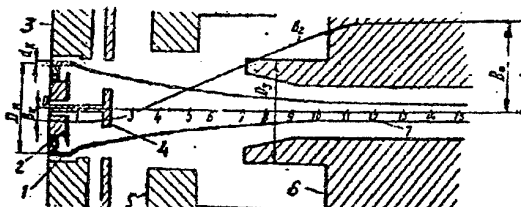


Fig.1. A scheme of the EOS.
1-secondary-electron emission cathode;
2,3-focusing electrodes; 4-accelerating electrode;
5-matching electrode; 6-anode.

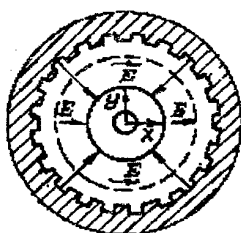


Fig.2

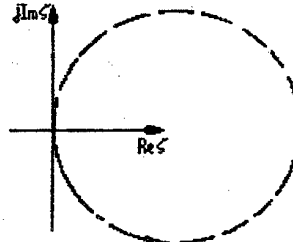


Fig.3

SLOW-WAVE STRUCTURE HIGH-POWER MM-BAND TWT

Victor D.Yeremka, Maxim O.Khorunzhiiy, Vladimir N.Koshparenok

The Usikov Institute of Radiophysics & Electronics of the National Academy
of Sciences, 12, Acad. Proskura st., 310085, Kharkiv, Ukraine

ABSTRACT

A description is given of the power millimeter-band TWT system comprising a slow-wave structure (SWS) (formed by spiraling two, coaxially arranged, slotted circular cylinders into a helix). The results of the investigation into the dispersion characteristics of the above system are presented. They were obtained by numerical simulation using the equivalent - circuit method.

INTRODUCTION

The development of the medium and high-power millimeter-band TWT continues to be an imperative issue of the up-to-date microwave electronics. An increase in the average power of the millimeter-wave TWT output signal is limited by the thermal dissipation capability of the SWS and the impedance of the interaction between the EB and the slow-wave field. This work is aimed at designing and developing the SWS of the millimeter-band TWT, which ensures a sufficient heat removal and an effective interaction between the powerful EB and traveling wave.

SLOW-WAVE STRUCTURE

The helical SWS for the high power TWT based on a standard rectangular waveguide are sufficiently known devices. The merits and limitations of the standard waveguide spiraled into a helix and utilized in the TWT as a SWS were first positively assessed by V.Valterson [1]. In the modified helical waveguide which was used as the SWS of the microwave amplifier the circular slot for the tubular electron beam was provided in its wide wall [2,3]. The findings of investigations into this SWS in the TWT suggest that an effective amplification can be achieved in a limited frequency range due to the backward wave excitation. The electron-backward wave interaction occurs with the TWT self-excitation and the deterioration of its amplifying properties. One of the major shortcomings of the SWS is the low coupling impedance. Therefore, we had to make an extensive search for a suitable SWS circuit design incorporating a spiraled waveguide built on a new concept.

We have utilized two round-shaped, slotted helical and coaxialy arranged waveguides placed opposite each other (Fig.1), which served the purpose of the SWS of the mm-wave TWT [4]. The frequency range at which the wave-guiding properties of such an electrodynamic system remain unchanged is on a par with that of the standard rectangular waveguide. The input and output of the signal being amplified in the SWS of the experimental TWT breadboard are provided by the standard rectangular waveguide with transitions to a round - shaped waveguide. The amplifier signal input and output are matched to the load.

Now write the lateral resonance frequency of a slotted cylinder:

$$f_0 = \frac{1}{2\pi\sqrt{C_1 L}}; \quad c = \frac{1}{\sqrt{\epsilon_0 \mu_0}}; \quad (1)$$

where c is the light velocity in a vacuum; C_1 is the slot capacity; L is the inductivity of a cylinder surface

$$C_1^{(1)} + C_1^{(2)} = \left[\frac{q}{d_l} + \frac{1}{\pi} \ln \left(\frac{2d_l}{d_l} \right) \right] \epsilon_0; \quad L = \left[\frac{\pi d_l^2}{4} + \frac{qd_l}{2} \right] \mu_0; \quad C_1^{(3)} = \frac{2\epsilon_0}{\pi} \ln \left| \frac{\sqrt{l} + \sqrt{l-d_l}}{\sqrt{d_l}} \right|; \quad (2)$$

where c is the light velocity in a vacuum; C_1 is the slot capacity; L is the inductivity of a cylinder surface turn. The capacity C_1 constitutes a capacity sum: the end slot capacity $C_1^{(1)}$, the interior cylinder surface capacity $C_1^{(2)}$ and the exterior flat cylinder surface capacity $C_1^{(3)}$ (which is defined as a half the capacity of the TWO parallel plate lying in a single plane).

$$C_1 = \epsilon_0 \left\{ \frac{q}{d_l} + \frac{2}{\pi} \ln \left| \frac{\sqrt{2d_l} (\sqrt{l} + \sqrt{l-d_l})}{d_l} \right| \right\} \quad (3)$$

The capacity of coupling between the slotted cylinders has this form: $C_2 = \frac{l-d_l}{2s}$.
(4)

The coefficient of coupling between the slotted cylinders is equal to $K = \frac{C_2}{2C_1 + C_2}$

(5) The coupling frequencies are $f_1 = f_0 \sqrt{1-K}$; $f_2 = f_0 \sqrt{1+K}$.

(6) For the system spiraled into a helix of the diameter D with the pitch l, we find the relation between the phase velocity of the wave propagation along the axis of the spiral and the velocity of light:

$$\frac{v_{ph}}{c} = \frac{fl}{\sqrt{(l^2 + D^2)(f^2 - f_2^2)}}, \quad (7)$$

where f is the operating frequency.

The latter formula is derived allowing for the fact that the wave velocity along the helical axis is related to the phase wave velocity in a spiral turn by the formula

$$v_{ph} = \frac{v_p l}{\sqrt{l^2 + D^2}}, \text{ where } v_p = \frac{cf}{\sqrt{f^2 - f_2^2}} \quad (8)$$

The form of the dispersion SWS characteristic calculated by the MATLAB system in a quasi-static approximation are shown in Fig.3.

In the 5-millimeter band the electromagnetic fields in spirals was excited by a probe antenna, and the SWR measurement was performed by a panoramic analyzer of P2-69 type. The wavy form of the SWR dependence $f(f/f_0)$ results from having the waveguides coiled into the helices. The attenuation magnitude of the circular ($\varnothing 4$ mm) copper spiral, slot-free waveguide is about 2 dB/m away from the critical frequency.

In selecting the size of the interaction gap we proceeded from the fact that the electron transit angle in it way equal to $2\beta \bar{v}_z < \pi/2$. All the coils of the coaxial spiraled waveguides are assumed to be identical and in the helical interaction gap 2ϑ the electrons meet with the waves in one and the same phase. The relation for the electron transit angle Θ between the gap of the two coils is given as

$$\Theta = 2\pi m, \quad (9)$$

where m is the number wavelengths being laid along the coil. Using (1) we find that the pitch L of the helical waveguides is determined from the relation:

$$L/\lambda = m \frac{\sqrt{U_o}}{505} \quad (10)$$

CONCLUSION

It is shown, that 10-50% of the power radiated by a probe antenna may be transferred to the SWS. It is assumed that a tube electron beam will transfer the same quantity of power to the above motioned helix SWS as well. The 3-mm-wave TWT parameters were calculated by using the techniques described in [3] for the width of the electron beam channel $dl = 0.6$ mm with the channel occupations coefficient 0.6 and the electron beam current $0.8A$, $m=19$ for the average frequency of the amplification band being equal to 10%. The design value of the output signal average power was $2kW$ at an operating voltage of 10kV with an amplification coefficient of .18 dB.

REFERENCES

- [1] Valtersson B. "Phase velocity in helical waveguides"// in Numero Special du Congres Tubes Hyperfrequences (Paris, France). (1956).
- [2] Ahn S., Ganguly A. K. Analisis of helical waveguides.// IEEE Trans. on Electron Devices. Vol.ED-33, N9. -P.1348-1355(1986).
- [3] Man'kin I. A., Usheronich B.L. To theory TWT with helical waveguide electrodynamical system..// J. of Communications and technology & Electronics. V34, N11, -P.2366, (1989).
- [4] Yeremka V.D. Coaxial TWT of mm wave region// Proc. SPIE. Vol.1929.-P.446-447(1994).

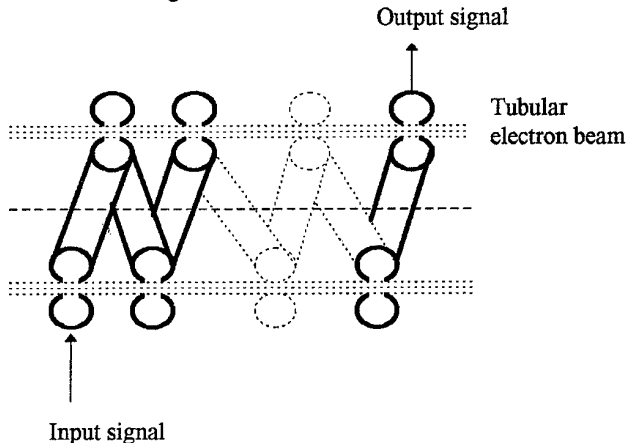


Fig.1. Diagrammatic representation of slow-wave structure.

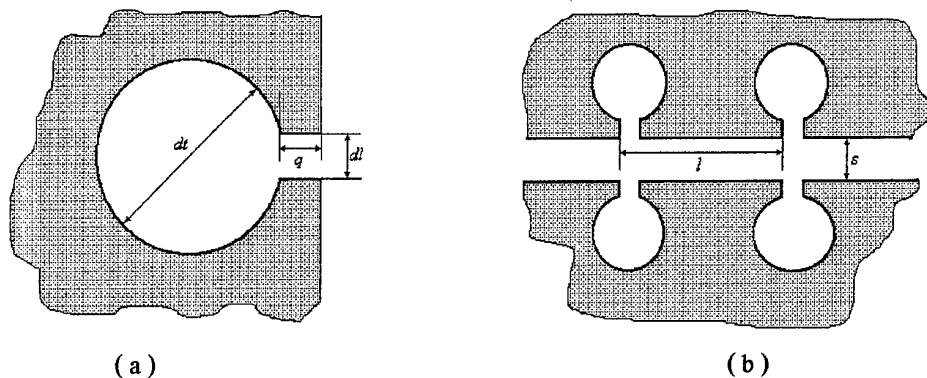


Fig.2. Geometric parameters of the SWS: (a) - cross-sections of slotted cylinder;
(b)- relative position of slotted cylinders

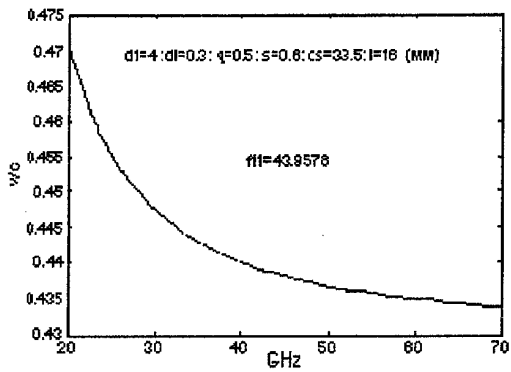


Fig.3 Dispersion characteristic of the SWS

MILLIMETER BAND MAGNETRON TRIODES WITH LENS OPTICS

Victor D.Yeremka, Gregory Ya.Levin,
Sergey N.Teryokhin, Oleg P.Kulagin

*Usikov Institute of radiophysics and electronics of National Academy of Sciences of Ukraine, 310085,
Kharkov, Ac.Proscura St., 12,
fax: 0572-441105, e-mail: eremka@ire.kharkov.ua.*

Abstract

To enable the output signal frequency of surface wave magnetrons to be controlled within a pulse length with no power consumption in the control circuit, we suggest that the lens optic facilities with no metal obstacles to the electron movement should be applied. It is shown that using the electrostatic lenses one can regulate the geometric and electric parameters of that electron cloud part which is responsible for the effective interaction between the particles and the high-frequency field of a slow-wave structure.

By investigating the electron lens behavior in the crossed electric and magnetic fields, we determine and explore the ways of using such facilities for the non-power control of the surface wave magnetrons (SWM) output signal frequency without transit-time effects.

Introduction

In the field of millimeter wave electronics, much attention is paid to the pulse electromagnetic generators - the miniature SWM, which have some positive peculiarities: relatively good power characteristics in the millimeter wave band [1] with not high accelerating voltages[2] and operating magnetic fields. Due to such circumstances, these devices have small-size dimensions and low weight. On the other hand, the inability to control the amplitude and frequency of an output signal without power being consumed in the control circuit, which is inherent in such generators, is the limitation for the SWM use in the information systems.

Attempts to design the centimeter - band magnetrons with electromagnetic oscillation parameters being controlled without power consumption in the control circuit have already been made. But the scale modeling method shows that the possibility to develop the millimeter wave grid-controlled magnetrons is very limited.

Experiments demonstrate impossibility to use grids in this case because of phenomena, caused by an electron bombardment: with the positive grid potential the grid is deformed; with the negative grid potential the deformation occurs in the anode block bars arranged above metal grid parts, where a magnetic field for electrons in the grid-anode gap is below the critical field.

In this paper the search activity and investigation results are briefly described.

The control of the SWM output signal parameters without transit-time effects

One of searching investigations results is the realization in experiments the method to control the SWM output signal parameters without transit-time effects. This method is based on the use of the lens electron-optics system (EOS) to control the electron flow in a magnetron interaction space [4]. The magnetron oscillators of the new class were named «magnetron triodes with lens optics» (MTLO). In the magnetron triode with electron lens optics (Fig.1) the electric field $V(z,y,V_{contr})$ is inhomogeneous along a device axis and. Therefore, consequently the electron motion is three-dimensional. Here the following designation introduced: z is the distance along cathode, V_{contr} is voltage on control electrode; $y = y(z,x, V_{contr}, H)$. By analyzing the potential distribution $V(z,y,V_{contr})$ in the interelectrode interval of the MTLO, we introduce concept of the limiting potential surface, for which $y = y(z,x, V_{contr}, H)$. The potential distribution on this surface is limiting in that: if the potential in a space point is below the limit potential, then electrons emitted by cathode cannot reach this point. Analysis of the limiting potential surface shape and its location allows the electron flow to be qualitatively determined in a static mode as the function of a control electrode voltage and to obtain information about the MTLO geometry and modes which are required for practical application.

With a negative lens potential that is below the natural potential, the system operated as a focusing lens, with a positive potential in the symmetry plane at the lens center the minimum of potential occurs and the system is a scattering lens. We designate as natural the potential of a given point in the inter electrode space of

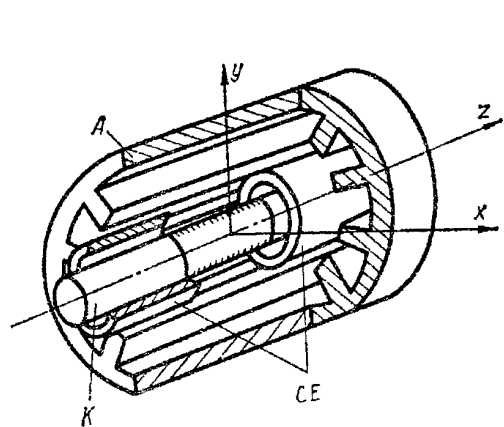
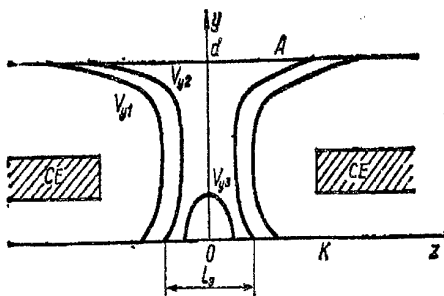


Fig.1. The circuit of a magnetron triode with lens optics:
A - anode; K - cathode; CE - control electrode



$$H = H_K = \text{const}; \quad 0 > V_{y1} > V_{y2} > V_{y3}.$$

Fig.2. The surface of the potential at different voltages on a control electrode

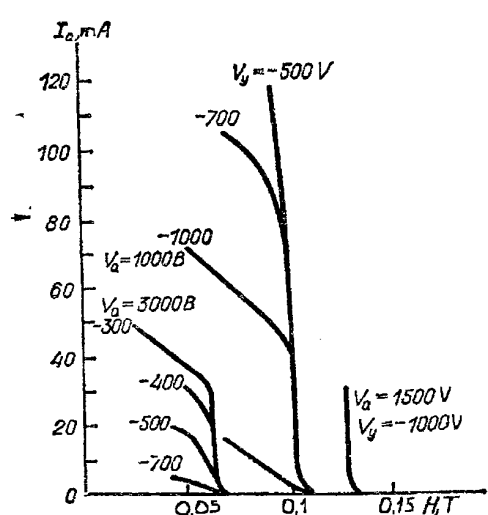


Fig.3. Function $I_a(H)$ at different negative voltages on a control electrode.

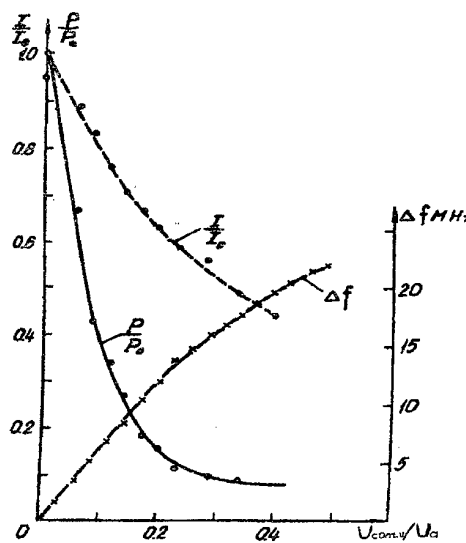


Fig.4. Amplitude and frequency of MTLO characteristics.

the idealized model of the magnetron diode with infinitely extending electrodes. For practical purposes a focusing lens is of certain interest.

The electron motion near a cathode surface is specified basically by the electron potential distribution in a region close to a cathode. As the control electrode voltage decreases, the line, where the limiting potential surface crosses the cathode, is shifted to the symmetric plane running through the device center perpendicularly to the cathode axis. At the same time the cathode effective (emitting) length l_e decreases (Fig.2). The electron escaped from the cathode near the limiting potential surface electrons are able to arrive at the anode only after they were specularly reflected from this surface, many times over that results in a decrease in their contribution to the anode current. Fig.2 show that the limiting potential surface are mirror symmetrical about the plane running trough the device center perpendicularly to the cathode axis. In the critical mode the limiting potential surface (LPS) are drawn as a tangent to the anode and the anode surface is their extension.

The dependence of an anode current upon a magnetic field is presented in Fig.3. One can see that with the constant lens control voltage when the magnetic field H increases up to a critical mode, the anode current I_a decreases (because of increasing the transit time of electrons and changing in the position of the LPS). The derivative dI_a/dH is maximum with $H=H_c$ (here H_c is the critical magnetic field) and is not dependent upon the control electron voltage. Within limits of measurement accuracy the calculated and experimental values of critical magnetic field are in agreement irrespective of voltage V_{cont} on the control electrode, though an upper bend on the cut-off characteristics is shifted towards the lower magnetic fields.

In the regime after a critical mode the LPS is separated from the anode and shifted to the cathode. Crossed dimensions of the electron occupied region decrease although the value of the emitting cathode part is not changed (with a growth of H , the peripheral electrons contribution to the anode current decreases and the complete emission current becomes more non-uniform). By changing the control lens voltage, one can provide the effective control on the lens optic SWM parameters with no current to the control electrode and without power being consumed in the control circuit.

The electromagnetic generation by the MTLO is realized in the 8-millimeter wave band in a continuous and pulsed operating mode. Amplitude and frequency characteristics were investigated by experiment. The power P_y/P_0 and the frequency change Δf in generated oscillations as functions of the control voltage value $|V_y/V_a|$ are given in Fig.4. It is seen that when a negative potential on the control lens grows, the output signal power decreases, but the frequency increases. With the 80%-amplitude modulation of output signal the frequency change was about 20MHz. And up to modulating voltage frequencies about 10 MHz the transit-time effects have not observed in the amplitude control. In an other MTLO model when the device operates in a pulse mode, with a slight (about 10%) amplitude change one can to vary the output signal frequency within the voltage pulse duration without power being consumed in the control circuit. In the latter case the pulse-to-pulse frequency change is provided.

Specifically, in a 8-mm wave band with an anode voltage amplitude of 5 kV, an output power of 2 kW (efficiency of 10%) and the pulse duration of 0.3 μ s, pulse-to-pulse variations in the output signal frequency varied are in the range of 60 MHz when the lens voltage did not exceed 50 % of the anode voltage.

Conclusion

The millimeter band surface wave magnetrons of with the frequency output signal modulation without power consumption in the control circuit have opened up new prospects for their to practical application in the pulsed generator mode. We plan to pursue on investigations aimed at designing of this type of pulsed magnetrons.

References

1. G.Ya.Levin, A.V.Atlasman, V.I.Vigdorchik, V.D.Sahatskiy, S.N.Teryokhin. «About estimation of cathode operating conditions in surface wave magnetrons.» J. of Communications Technology and Electronics. V. 19, №10 ,p..2116 (1974).
2. A.Ya.Usikov, E.A.Kaner, I.D.Truten end others «Electronics and radiophysics of millimeter and sub-millimeter waves» - Kiev: Naukova dumka. 368 p. (1986).
3. S.Ya.Braude, A.I.Ivanchenko «Magnetron with grid control» - J. of Techn. Phys., V.14, №10, pp.611-614 (1944).
4. Invent. sertificate. №286781 (USSR). «Magnetron triode». Discovery, inventory, manufacturing specimens, trade marks. №31, -p..185, (1975).

DIFFRACTION RADIATION GENERATOR WITH LOCAL INHOMOGENEITY OF MAGNETOSTATICAL FIELD IN THE INTERACTION SPACE

A.I.Tsvyk, A.V.Nesterenko, V.N.Zhelov

Institute of Radiophysics and Electronics of NATIONAL Academy of Sciences of Ukraine,
12, Acad. Proskura st., Kharkov, 310085, Ukraine
tel. 138 (0572) 44-85-48 fax:138 (0572) 44-11-05 E-mail: ire@ire.kharkov.ua

Abstract

We experimental show that output characteristics of non-relativistic Diffraction Radiation Generator (DRG) are greatly perfected when we create a local inhomogeneity of focusing magnetostatical field in the interaction space of electronic beam. We conclude that it is perspective to use a thick electron beams in the DRG of SubMM frequency range.

1. Introduction

The Smith – Purcell effect^{1,2} stimulated a progress in the electronics of MM and SubMM band range in different countries. In Ukraine the possibility of Smith – Purcell effect utilization in the electronics have been studied since 1963. Currently in IRE NASU on this principle there is proposed, created and explored a complex of new non-relativistic sources of electromagnetic oscillations, named by the Diffraction Radiation Generator (DRG)³. These types of generators include a passed DRG, a reflective DRG, a pulsed DRG and other devices. Some types of those generators were named "Orotron" and "Free-electron laser" in some countries⁴⁻⁸. DRG works in 30 - 370 GHz frequency range and has a number of improved output characteristics in comparison with known classical device. However when the generation wavelength of λ is decreased, an efficient thickness of electron beam is decreased as $\Delta_{\text{eff}} = l/\pi$, where $l = v\lambda/c$ is a period of diffraction grating, v is the velocity of electron beam, c is a velocity of light. So actual problem is to study the possibilities of using a thick electron beams ($\Delta > \Delta_{\text{eff}}$) in DRG. We offer to decide this problem creating a specific inhomogeneous magneto-static field in the interaction space of DRG.

2. Experiment

Here we show the results of experimental study for DRG, that has a magnetic inhomogeneity of focusing magneto-static field created in the interaction space of fine ferromagnetic cylindrical stem. This set named DRG-MI uses a well-known DRG with spheric-cylindrical open oscillator, in which stem is located under diffractional grating in region of electromagnetic field pot on the surface of cylindrical mirror of open resonator. A stem diameter is 3 mm, its length is 10 mm; a width of grating is 10 mm, a length of grating is 34 mm. An electron beam of section $5 \times 0.2 \text{ mm}^2$ is created by the diode electronic gun and is focused in the interaction space by uniform magneto-static field. Studies are conducted within the 50÷78 GHz frequency range.

We obtained that output characteristics of DRG-MI are greatly perfected. In particular, a start current I_s decreases in two times, an output power P increases in 1.5 times, a spectrum width ΔF of generation signal being observed during $0.3 \div 5$ s decreases in 1.5-2 times and approximately comes to $5 \div 20 \text{ kHz}$; a long instability is perfected and comes to 10^{-7} (fig. 1, 2).

The figure 1 shows the dependencies of start current (I_s) from the generation wavelength (λ) (or accelerating voltage U) and the output power (P) from the value of induction (B) of focusing magneto-static field. The graphs 1 - 4 correspond to values $B=0.4, 0.25, 0.16, 0.1 \text{ T}$. A dotted line (5) characterizes the DRG without magnetic inhomogeneity for $B=0.4 \text{ T}$. From these graphs we may conclude that DRG-MI can work under smaller focusing magnetic fields.

The figure 2(a) shows the dependencies of DRG-MI output power from the frequency of main type oscillation arisen in the open resonator under the current of electron beam is 130 mA. There is seen that the range of continuous realignment of frequency, that we take by changing a distance between mirrors of resonator and accelerating voltage, approximately comes to 20%. The figure 2(b) shows the particularities of changing the DRG-MI output characteristics within one range of generations ($f=65.5 \text{ GHz}$). The graphs 1-3 correspond to the currents $I=70, 110, 170 \text{ mA}$. The shaded area corresponds to values of spectrum widths ΔF of generation signal. We obtain besides this generator keeps the characteristics on deposition relative to the focusing magnetic field axis that improves exploitation properties of DRG.

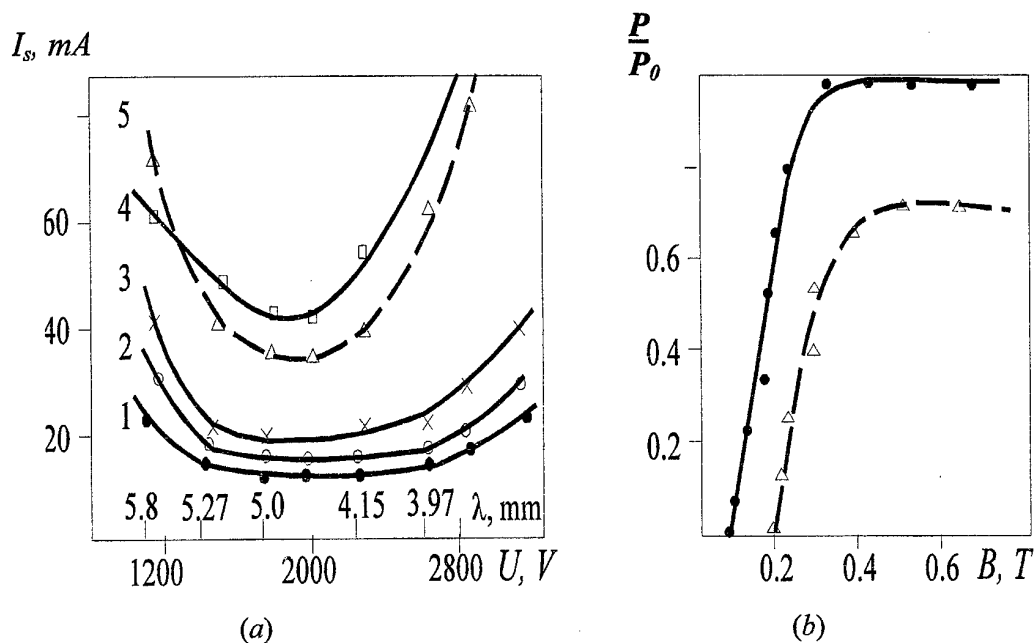


Fig.1 Particularities for changing (a) the start current from the generation wavelength and (b) the output power from a value of focusing magnetic field for DRG (dotted line) and DRG-MI (solid line).

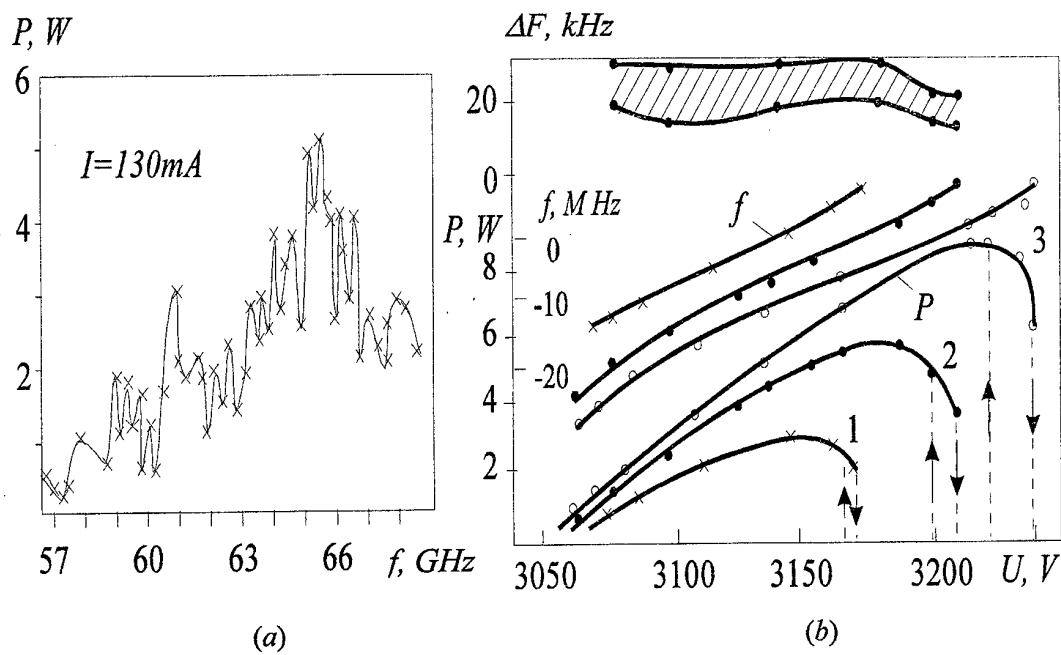


Fig 2. (a) Dependency of DRG-MI output power from the generation frequency; (b) DRG-MI characteristics changing within one generation band.

In the table1 we show the comparative output parameters of known GDR and GDR-MI being investigated (under equal standard specifications) on the frequency of 67 HHZ. Here I_s is activate current, P is output power, ΔF and $\Delta F/f_0$ are width of spectrum to generations and long instability of frequency within a time 0,3 with respectively; a current is 160 mA, voltage is 3,2 kV. There is used diode electronic gun creating the band electronic flow of section $5 \times 0,2 \text{ mm}^2$ and we use a constant focusing magnetic field of 0,4 T.

Table 1. Characteristics of generators.

Generator	I_s , mA	P, W	ΔF , kHz	$\Delta F/f_0$
GDR	36	5.2	40	$5 \cdot 10^{-7}$
GDR-MI	18	8	10	10^{-7}

From these and other results it follows that DRG-MI is highly perspective to use for getting the electromagnetic oscillations in short-wave band of MM and SubMM ranges.

These results come satisfactorily to the agreement with the first of experimental investigation on influence of local disturbance of focusing manetostatical field on excitement of oscillations in DRG and with the next of theoretical investigations reported in papers ⁹⁻¹¹.

3. References

1. G.J.Smith and E.M.Purcell, "Visible light localization surface changes moving across a grating," Phys.Rev., v.92, 4, pp.1069-1073, 1953.
2. K.Ishiguro, T.Tako, "An estimation of Smith-Purcell effect as a light source in the infrared region," Optica Acta, v.8, 1, pp. 25-32, 1961.
3. V.P.Shestopalov, A.A.Verdyi, G.P.Yermak, B.K.Skrynnik, G.I.Hlopov and A.I.Tsvyk, Diffraction radiation generators, Naukova Dumka Press, Kiev, 1991.
4. F.S.Rusin, G.D.Bogomolov, "The generation of electromagnetic waves in open resonator," Pis'ma JETF, v.4, 6, pp. 236-239, 1966.
5. V.V.Nerubenko, A.I.Tsvyk, "The investigation of diffraction radiation generator in MM-wave band," Radiotekhnika, Kharkov University Press, v.19, 107-113, 1971.
6. R.R. Leavitt, D.E. Wortman and H.Dropkin, "Wave orotron oscillation," IEEE J. of Quantum Electronics, v.17, 8, 1333-1348, 1981.
7. Zou, Wen - lu, International Conference on Millimeter Wave and Far-infrared Technology, China, pp.92-95, June 1989.
8. E.Price, J.Wolsh, Proceeding SPTE, v.1514, p.135, 1990.
9. I.M. Balaklytsky, G.S. Vorob'ov, A.I.Tsvyk, V.P. Shestopalov. "The increasing of work efficiency of GDR with magnetic focusing of electron beam", Izvestia vus'ov, Radioelektronika, 20, 10, pp. 93-95, 1977.
10. A.I.Tsvyk. "The influence of dynamical and static shifts of electrons upon the start current," Izvestia vus'ov, Radiofizika, v.21, 8, pp.1216-1219, 1978.
11. Ye.I. Odarenko, A.A. Shmat'ko. "The influence of magnetic local inhomogeneity upon the start characteristics of resonance devises of O-types," Radiotecknika i elektronika, v.37, No.5, pp. 901-908, 1997.

LOW-NOISE MM TRAVELING-WAVE MASER WITH INSTANTANEOUS BANDWIDTH OF 470 MHz

N.T.Cherpak, A.A. Lavrinovich, T.A. Smirnova

Usikov Institute for Radiophysics and Electronics, National Academy of Science of Ukraine
12, Proskura str., Kharkov, 310085, Ukraine
Tel.: 380 572 448 363; Fax: 380 572 441 105; E-mail : cherpak@ire.kharkov.ua

Quantum paramagnetic amplifiers (solid - state masers) which are regarded as the most sensitive microwave - devices remain to be characterized by a relatively narrow passband [1]. The bandwidth Δf is primarily determined by the electron paramagnetic resonance (EPR) line of an active crystal $\Delta f_L = 60$ to 150 MHz. The above - mentioned characteristic in the millimeter - wave range compares unfavorably with the amplification band of other types of low - noise amplifiers, particularly, of paramagnetic ones.

The aim of the present paper is to describe the quantum amplifiers operating in a bandwidth which exceeds the EPR line width $\Delta f > \Delta f_L$ due to the improved efficiency of interaction between an electromagnetic wave and an active crystal in the periodic slow - wave structure (SWS) with the use of the non - uniformity of the static magnetic field and disorientation of magnetic complexes in an active crystal. This paper is an advanced addition to the investigation that had been previously carried out [2,3]. The amplifiers employ the same number of our traditional maser elements [1-3].

A traveling wave maser (TWM) was developed on the basis of a comb - type slow - wave structure (SWS) with an active andalusite crystal doped with Fe^{3+} ions ($Al_2SiO_5: Fe^{3+}$) and a nonreciprocal element made of textured hexagonal ferrites for the frequency range 40 - 46,5 GHz. The nonreciprocal element, i. e. isolator, which is an integral part of the TWM brings about the inhomogeneity of the static magnetic field in the active crystal volume. This phenomenon in combination with the microwave magnetic field distribution plays an important part in forming the amplitude - frequency characteristic (AFC) of the amplifier. This type of influence is dependent upon the shape and position the ferrite isolator (FI) in the SWS. The investigations of different FI configurations from perpendicular to tangent orientation of the magnetic field in relation to a magnetized ferrite plate indicate that the EPR line of the active crystal can be broadened 2 to 3 times. The effect appears to increase if the ferrite plate is arranged on the dielectric one having a large value ϵ . The reasonable restriction of Δf is determined by the disturbance of AFC smoothness or prohibitively low meaning of the net gain of the TWM.

The presence of magnetic complexes in the andalusite crystal [4] enables the amplification band to be further broadened. In this work a three - level pumping scheme with the magnetic field being oriented at 90° to the axes z_1 and z_2 of the two magnetic complexes in the crystal has been employed. The axis z_1 of one of the complexes was lying parallel to the longitudinal SWS axis whereas the field B_o was perpendicular to the axis z_1 and could be rotated with respect to the plane of the axes z_1 and z_2 . And in this case the line was seen to be additionally broadened. However, it should be born in mind that as the angle rotates by $\alpha > 6^\circ$ a trough in the amplitude - frequency characteristic is clearly visible. This is due to the fact that the quantum transition frequencies of the signal f_s and the pumping f_p of the second complex tend to change their magnitude with the variation in the angle of rotation about the axis z_2 , and the frequencies of the transition of the first complexes remain unchanged. The broadened line of the signal transition 1 - 2 falls into the trough between the lines of the pumping transitions 1 - 3 (1 - 4) of the complexes z_1 and z_2 , thereby causing the difficulties over the inversion of the transition line 1 - 2. Therefore, in order to obtain the limit values Δf it is necessary to be provided with additional pump sources or the frequency pumping modulation.

The most important problem one has to deal with in developing the TWM is to ensure that the pumping source power is reduced. The basic pumping losses tend to occur in the input channel and the SWS.

Apart from the technological improvement of the above elements an E - polarised wire grid at the SWS output was employed. This grid allowed a signal at a frequency f_s to be easily conducted, and it reflected the pumping radiation at a frequency f_p , thereby creating in the SWS the condition

of a standing (instead of traveling one) wave and providing for a more effective interaction between the pumping and the active crystal. The electrical field vectors at signal and pumping frequencies are mutually perpendicular. The rotation of the pumping - wave polarisation plane resulted in an power decrease of 7 to 10 dB.

Thus, the studies that had been performed in this work and earlier made it possible to develop the TWM based on the andalusite natural crystals featured by the following characteristics:

TRAVELING-WAVE MASER	TWM -1	TWM -2
Gain Factor (Net Gain) G, dB	20	27-30
Amplification Band Δf , GHz	470	300
Frequency Range f_s , GHz	41-44	40-43
Pumping Power P, mW	400	270
Noise Temperature T_N , K	<25	<25
Pumping Frequency f_p , GHz	141-142	140-142
Operating Temperature T, K	1.7-2.0	1.7-2.0
Overall Losses *	L_Σ dB	≤ 10
Crystal Length l,	20	13

*) The overall losses in the amplifier, L_Σ , include such in the SWS, the waveguide with transitions to the SWS, the filter and also the signal and pump powers combiner .

The frequency change interval was determined by the SWS passband. The pumping power source did not exceed 400 mW. We hope using the pumping modulation of this source enables the amplification band to be broadened up to 1 GHz. Moreover, it has been shown that there is an additional possibility to improve the AFC form by means of the auxiliary superconducting plate, arranged near the active crystal [5].

The fluctuation sensitivity of the radiometer with a maser at the output with $G = 20$ dB, $\Delta f = 470$ MHz, $T_N = 25$ K, a noise temperature of the intermediate - frequency amplifier $T_{IF} < 1000$ K and a time constant $\tau = 1$ s is expected to be at the level $8T \cong 10^{-3}$ K.

Thus, the findings of the above investigations show that the broadbandness of the mm-wave masers may be close on principle to that of semiconductor amplifiers. The developed TWM amplifiers can be used for radioastronomy measurements and specific microwave extralow-noise laboratory investigations (see for example [6]).

References

1. N.T.Cherpak, «The distributed type quantum amplifiers (masers) in millimeters wavelength», Kiev, Naukova dumka, 212 p., 1996 (in Russian).
2. N.T.Cherpak, T.A.Smirnova, V.V.Mishenko, S.A.Peskovatskii, A.A.Lavrinovich, «A traveling-wave quantum amplifiers in mm wavelength band», Radiotekhnika i Electronika, vol. 27, No. 9, 1804 - 1812 pp., 1982 (in Russian).
3. N.T.Cherpak, T.A.Smirnova «A broad-band traveling-wave maser for the range 40-46,5 GHz», IEEE Trans. Microwave Theory and Tech., Vol. MTT-31, No.3, pp. 306 - 309, 1986.
4. I.I.Eru, V.D.Korolyov, V.V.Mishenko, S.A.Peskovatskii, V.M.Shul'ga «Iron doped andalusite as an active crystal for maser», Preprint No.46, Kharkov, IRE AN Ukr.SSR, 45p., 1975 (in Russian).
5. A.A.Lavrinovich, T.A.Smirnova, N.T.Cherpak, «Performance improvement of traveling-wave masers for millimeter waves », Abstracts, I Ukr. Symposium «Physics and Engineering of MM and SubMM Waves», Kharkov, Oct. 15-18,1991, Kharkov, IRE AN Ukr SSR, p.242-243, 1991 (in Russian).
6. A.Ainsaar, «Cyclotron frequency technique of the measurement of beta decay spectra», Proc. Estonian Acad. Sci. Phys. Math., Vol.44, No.4, pp.466-475, 1995.

C



**WAVE PROCESSES IN FINITE-SIZE
SEMICONDUCTORS, SOLID-STATE
STRUCTURES AND HTSC MATERIALS**

**CONNECTION OF RESIDUAL LOSSES OF A MICROWAVE ENERGY IN
SUPERCONDUCTIVE STATE OF $\text{YBa}_2\text{Cu}_3\text{O}_{7-\delta}$ FILMS ON SAPPHIRE
SUBSTRATES WITH THEIR RESISTANCE IN A NORMAL STATE**

O.D.Poustynik

The State Research Center "Fonon", 37, Peremogy Ave., KPI - 3240, Kyiv, Ukraine.
E-mail: oleg@fonon.kiev.ua

Abstract. The results of research of temperature dependence of surface resistance $R_s(T)$ of epitaxial films $\text{YBa}_2\text{Cu}_3\text{O}_{7-\delta}$ deposited onto sapphire substrates are presented. The measurements were made at a frequency 135 GHz. It is shown that the obtained results in a low temperature range can be satisfactorily explained by means of existing theoretical model of losses in high-temperature superconductor films connected with a presence of normal domains like spherical inclusions.

Introduction

It is shown in a number of works that one of directions of practical use of high-temperature superconductor films is the creation of ultra low noise receiving devices of a millimeter wave range [1]. Thus, the small own losses of passive elements based on high-temperature superconductor films are realized, in comparison with the films of normal metals. Basic phenomenological model which is used for calculating surface resistance of a high-temperature superconductor at microwave frequencies is the two-liquid model. Under this, the following dependence of current on field takes place [2]

$$j = \tilde{\sigma} E \quad (1)$$

Where $\tilde{\sigma} = \sigma_N = i(\omega\mu_0\lambda_L^2)^{-1}$,

$$\sigma_N = n_N e^2 \tau_N / m \lambda_L^2 = m / (n_s e^2 \mu_0)^2; \quad (2)$$

n_N and n_s are concentrations of charge carriers at $T < T_C$. For fields possessing the harmonical temporal dependence, the utilization of the equations (1), (2) gives a possibility to introduce the effective dielectric permittivity of superconductive film:

$$\epsilon_{\text{eff}} = \epsilon_0 \epsilon' + \frac{\sigma_N}{i\omega} - (\omega^2 \mu_0 \lambda_L^2)^{-1} \quad (3)$$

Here ϵ' is a dielectric permittivity of a crystal lattice of a superconductor, λ_L is Londons' penetration depth of a field. For the analysis of losses of energy of a microwave in a film, suppose that the plane wave propagates in it. Under this, the surface impedance $R_s = \sqrt{\mu_0/\epsilon_0}$ of vacuum and wave number $k = \omega/\sqrt{\mu_0\epsilon_0}$ are taken into account. Substituting the value of ϵ_0 from expression (3), we can determine a surface impedance R_s and wave number k for a defectless film of a high-temperature superconductor [2]

$$R_s = i\omega\mu_0\delta; \quad k = i/\delta \quad (4)$$

$$\delta = (\lambda_L^{-2} + 2i\delta_N^{-2})^{-1/2}, \quad \delta_N = \sqrt{\frac{2}{\omega\mu_0\sigma_N}} \quad (5)$$

The technology of deposition of HTSC films affects on properties of produced films [4]. So, in dependence on frequency and duration of a laser pulse under deposition a HTSC film, the normal domains are formed in a film which make an influence on losses of microwave energy by this film. Taking into account that the sizes of normal domains and distance between them are less than Londons' penetration depth of a field, it is possible to determine the effective concentration of normal domains of spherical form in a HTSC film [5]:

$$\epsilon_{\text{eff}} = \epsilon_{\text{ext}} + \eta \frac{\epsilon_{\text{ext}}(\epsilon_{\text{in}} + \epsilon_{\text{ext}})}{\epsilon_{\text{in}} + \chi(\epsilon_{\text{in}} - \epsilon_{\text{ext}})} \quad (6)$$

Where $\epsilon_{\text{ext}} = \frac{\sigma}{i\omega}$ is dielectric permittivity of a HTSC film; $\epsilon_{\text{in}} = \frac{\sigma_d}{i\omega}$ is dielectric permittivity of the normal domain; σ_d - is conductivity of the domain; χ - is form-factor equal to 1/3 for spherical normal domains.

Therefore, the effective dielectric permittivity of a HTSC film with spherical domains is equal to:

$$\varepsilon_{\text{eff}} = \frac{\sigma_{\text{eff}}}{i\omega} - \frac{1}{\lambda_{\text{eff}} \omega^2 \mu_0} \quad (7)$$

The substitution of values of ε_{ext} and ε_{in} into the expression (6) allows to get the values of effective conductivity σ_{eff} and penetration depth of a field into the composite film with spherical normal inclusions. These results allow to determine a surface impedance of a composite film with a thickness h :

$$Z = \frac{i\omega \mu_0 \delta}{h/\delta} \quad (8)$$

$$\text{under } \frac{h}{\delta} \ll 1, Z = \frac{i\omega \mu_0}{h}, \delta^2 = -\frac{c^2}{\omega^2 \varepsilon_{\text{eff}}} \quad (9)$$

The substitution of values of effective conductivity σ_{eff} and effective penetration depth λ_{eff} gives a possibility to get an expression for a surface impedance of a composite film:

$$Z_s = \frac{1}{h\omega} I_m \left(\frac{1}{\varepsilon_{\text{eff}}} \right) = -\frac{1}{h\omega} \frac{\varepsilon''}{\varepsilon'^2 + \varepsilon''}, \quad (10)$$

$$\varepsilon' = -\frac{1}{\lambda_{\text{eff}} \omega^2 \mu_0}, \quad \varepsilon'' = -\frac{\sigma_{\text{eff}}}{\omega}$$

$$R_s = \frac{\sigma_{\text{eff}}}{h} \frac{\lambda_{\text{eff}}^4 \omega^2 \mu_0^2}{1 + (\sigma_{\text{eff}} \lambda_{\text{eff}} \omega \mu_0)^2}$$

Near the superconductive transition $T=T_c$ under $\lambda_{\text{eff}} \rightarrow \infty$, $R_s = \frac{1}{h\sigma_{\text{eff}}}$,

$$\text{In the low temperatures region, the surface is equal to: } R_s \approx \frac{\sigma_{\text{eff}}}{h} \lambda_{\text{eff}}^4 \omega^2 \mu_0 \quad (11)$$

Results of measurements and their discussion

The samples $\text{YBa}_2\text{Cu}_3\text{O}_{7-\delta}$ films were produced by a method of pulse laser sputtering onto sapphire substrates with a sub-layer $\text{GdBa}_2\text{Cu}_3\text{O}_{7-\delta}$ - with a thickness 200 Å, to prevent mutual thermodiffusion of components of a film and a substrate during the synthesis of a film $\text{YBa}_2\text{Cu}_3\text{O}_{7-\delta}$ [4]. The critical parameters of investigated films, their geometrical sizes, conductivities of films and normal spherical clusters are given in a Table 1.

Table 1. Parameters of investigated HTSC films

Sample	T_c, K	$\Delta T, \text{K}$	$J_c, \times 10^6 \text{ A/m}^2 (77 \text{ K})$	ρ_{300}/ρ_{100}	Thickness of film h, nm	Specific conductivity of film σ_n $T=100 \text{ K}, (\text{Ohm}\cdot\text{m})^{-1}$	Specific conductivity of film σ_n $T=300 \text{ K}, (\text{Ohm}\cdot\text{m})^{-1}$	Conductivity of normal spherical clusters σ_{in} $(\text{Ohm}\cdot\text{m})^{-1}$
1523	89,3	1,0	$\sim 10^6$	3,2	110	$2,5 \cdot 10^7$	$8 \cdot 10^7$	$6 \cdot 10^7$
1526	89,3	0,5	$> 10^6$	3,0	100	$4,3 \cdot 10^7$	$1,3 \cdot 10^6$	$6 \cdot 10^7$
1529	90,0	0,5	$> 10^6$	3,0	150	$1,4 \cdot 10^7$	$4,2 \cdot 10^7$	$6 \cdot 10^7$
1535	90,0	0,25	$> 10^6$	3,5	150	$2 \cdot 10^7$	$7,0 \cdot 10^7$	$6 \cdot 10^7$
1539	88,8	0,3	$> 10^6$	3,3	150	$1,6 \cdot 10^7$	$5,3 \cdot 10^7$	$6 \cdot 10^7$

The investigated samples had a high critical density of a current at a temperature of $T_c = 77 \text{ K}$, high values of a critical temperature and small temperature interval of transition of into superconductive state. The high level of

the used technology of producing film is specified by high value of parameter $\gamma = \rho_{300}/\rho_{100}$ characterizing the efficiency of scattering of normal charge carriers by defects of a crystalline lattice and impurities within a film of a high-temperature superconductor.

The measurements of surface resistance of samples were carried out at frequency 135 GHz in a temperature range 10...90 K using a technique described in [4]. The results of these measurements are presented in a Fig. 1. It

is shown that the value of temperature dependence of a surface impedance of all samples has a minimum which magnitude is determined by conductivity of investigated films measured at a temperature 300 K, that fact is in good agreement with known dependence given in expression (4). Besides, the absolute values of a surface impedance of measured films in the low temperatures region pointed out in expression (11) agree with values of specific resistance of measured films, as it is shown in a Fig. 2.

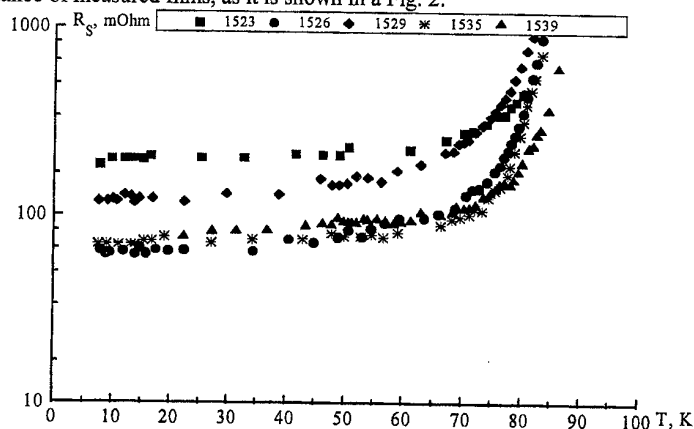


Fig. 1 Temperature dependence of surface resistance R_{eff} for samples No 1523, 1526, 1529, 1535, 1539.

Mismatch of the obtained experimental results with theoretical representations near T_c , accordingly to expression (11), can be connected with a character of penetration of a field into normal domains and its inhomogeneity in an environment of normal domains in high-temperature superconductive film.

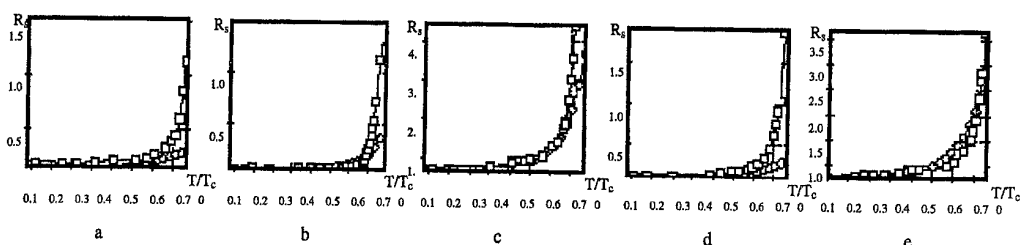


Fig. 2 Temperature dependences of a surface impedance of films $\text{YBa}_2\text{Cu}_3\text{O}_{7-\delta}$ at frequency 135 GHz; a) - sample №1523, b) - sample №1526; c) - sample №1529; d) - sample №1535; e) - sample №1539; □ - experimental results; O - theoretical representations).

Conclusion. The comparative analysis of temperature dependence of surface resistance of $\text{YBa}_2\text{Cu}_3\text{O}_{7-\delta}$ films on sapphire substrates is carried out. It is shown that the measured level of a surface impedance of films in the field of low temperatures is described by a specific resistance of a film and it is connected with an existence of normal spherical domains in a film.

References

1. Newman N., Lyons W.G., "High-temperature superconducting Microwave devices: Fundamental Issues in Materials, Physics, and Engineering", Journal of Superconductivity, 1993, v.6, № 3, pp.119-160.
2. O.G.Vendik, M.M.Gaidukov, A.P.Karpluk, "Waveguide Switch of Millimeter Band on a base of Superconductive Films", Pisma Zh. Tekn. Fiz., 1990, v.60, № 13, pp.78-82.
3. G.Korn, A.Gupta, R.F.Baseman, "Laser Wavelength dependent properties of $\text{YBa}_2\text{Cu}_3\text{O}_{7-\delta}$ (Thin Films Deposited by Laser Ablation)", Appl. Lett., 1989, v.55, № 23, pp. 2450-2452.
4. O.Pustynnik, V.Vratskikh, S.Vasiliev, A.Dymnikov, I.Voinovsky, O.Khimenko, "The Millimeter Wave Surface Resistance Measurements of Y-Ba-Cu-O Films Epitaxially Grown on Non-buffered Sapphire Substrates", Cryogenics, 1992, v.32, pp.620-625.

PHENOMENOLOGICAL APPROACH TO RADIOFREQUENCY RESPONSE OF HTS THIN SAMPLES TO MICROWAVE IRRADIATION

N.T.Cherpak, E.V.Izhyk, A.Ya.Kirichenko, A.V.Velichko

Usikov Institute for Radiophysics and Electronics, National Academy of Sciences, Ukraine
12, acad. Proskura str., Kharkov, 310085, Ukraine
Tel.: 38 0572 448 363; Fax: 38 0572 441 105; E-mail : cherpak@ire.kharkov.ua

The first observation of radiofrequency (rf) response (RRSMI) of high-temperature superconductors (HTS) to microwave (mw), including millimeter-wave, irradiation one has been reported in [1]. The effect consists in that the response of the HTS sample to mw irradiation is registered with a help of weak probing radiation with frequency Ω which belongs to radiofrequency band (i.e. MHz-band) and differs from the mw field frequency ω some orders, $\omega \gg \Omega$. Of course, the samples must be quit thin (the sample thickness and the field penetration depth are approximately equal) because the rf and mw fields act on opposite sides of the sample.

Further investigations have shown that RRSMI consists of two components, bolometric and nonbolometric. The nonbolometric component was found to cause by microwave-induced motion of magnetic vortices in the HTS sample [2]. Evidently the nonbolometric component can be conditioned also by the other physical mechanisms of dissipating mw energy in dependence on the experiment conditions and the sample properties. Particularly, the effect of heating electron system in both LTS and HTS films is known (see for example the review [3]). However there is no any analytical approach to description of RRSMI which gives rise to certain difficulties at both analyzing measurement results and comparing them with the another experimental data. The work proposes the phenomenological approach to description of the discovered phenomenon.

A traditional bolometric effect when variation ΔR of dc ohmic resistance R at influence of electromagnetic irradiation of the sample is registered can be presented as

$$\Delta R(P_\omega) = \frac{dR}{dT_L} \frac{dT_L}{dP_\omega} P_\omega,$$

where P_ω is the mw power absorbed by the sample; T_L is the sample lattice temperature depending on P_ω . Evidently the bolometric component of RRSMI may be described in a similar fashion

$$\Delta R_{\Omega}(P_\omega) = \frac{dR_{\Omega}}{dT_L} \frac{dT_L}{dP_\omega} P_\omega. \quad (1)$$

Here R_{Ω} is the surface resistance of the HTS sample at the Ω radiofrequency.

Consider the nonbolometric component of RRSMI caused by microwave-induced movement of magnetic vortices. In addition we characterize state of the vortices structure by temperature T_v which in general case differs from temperature T_P of the system of the pinning centers. As far as the latter is connected with the basic HTS lattice one may think that $T_P = T_{lo}$. Then average temperature of the vortices structure under conditions of interaction with the mw field can be written as

$$T_v = T_P + T_{v\omega}, \quad (2)$$

where $T_{v\omega}$ is increase in the vortex system temperature due to the microwave irradiation. Suppose, T_P does not

depends on P_ω . Then energy balance for one vortex obtains a form by analogy with energy balance for one electron in semiconductor [4]

$$\frac{d\varepsilon(T_v)}{dt} = \frac{P_\omega(t)}{n_v V_s} - P(T_v, T_p), \quad (3)$$

where ε is the average energy of the vortex; P_ω is the average rate at which power is absorbed by the sample; n_v is a number of vortices per unit volume of the sample; V_s is the sample volume; $P(T_v, T_p)$ is the average rate at which a vortex loses energy to the lattice.

Expansion of $P(T_v, T_p)$ into Taylor series in the vicinity of T_p point with retention of only the first order term yields

$$\frac{d\varepsilon}{dT_v} \frac{dT_v}{dt} = \frac{P_\omega(t)}{n_v V_s} - \frac{\partial P(T_v, T_p)}{\partial T_v} T_{v\omega}. \quad (4)$$

In the no-signal condition ($P_\omega = 0$) $T_{v\omega} = 0$ and $dT_v/dt = 0$. Bearing in mind that $d\varepsilon/dT_v = C_v$, where C_v is the vortex specific heat we obtain from (4)

$$\frac{dT_{v\omega}}{dt} + \frac{1}{C_v} \frac{\partial P(T_v, T_p)}{\partial T_v} T_{v\omega} - \frac{P_\omega(t)}{n_v V_s C_v} = 0. \quad (5)$$

Here the equality (2) has been used from which $dT_v = dT_{v\omega}$ follows. In stationary case the equation (5) yields

$$T_{v\omega} = \frac{1}{n_v V_s} \left(\frac{\partial P(T_v, T_p)}{\partial T_v} \right)^{-1} P_\omega. \quad (6)$$

If to use a definition of the energy relaxation of the vortices as

$$\tau_v = C_v \left(\frac{\partial P(T_v, T_p)}{\partial T_v} \right)^{-1},$$

then it is convenient to rewrite (6) in a form

$$T_{v\omega} = \frac{\tau_v}{n_v V_s C_v} P_\omega. \quad (6a)$$

The dependence $R_{S\Omega}(T_{v\omega})$ follows from experimental data, therefore one can write

$$R_{S\Omega}(T_{v\omega}) = R_{S\Omega}(T_p) + \frac{\partial R_{S\Omega}}{\partial T_v} T_{v\omega} + \frac{1}{2} \frac{\partial^2 R_{S\Omega}}{\partial T_v^2} T_{v\omega}^2 + \dots \quad (7)$$

from which

$$\Delta R_{S\Omega}(T_{v\omega}) = \frac{\partial R_{S\Omega}}{\partial T_v} T_{v\omega} + \frac{1}{2} \frac{\partial^2 R_{S\Omega}}{\partial T_v^2} T_{v\omega}^2$$

or

$$\Delta R_{S\Omega}(P_\omega) = \alpha P_\omega + \frac{1}{2} \alpha^2 P_\omega^2, \quad (8)$$

where

$$\alpha = \tau_v / (n_v V_s C_v).$$

Thus, the phenomenological approach to the description of RRSMI allows to obtain the dependence of variation $\Delta R_{S\Omega}(T_{v\omega})$ against the mw energy absorbed by the sample. There are experimental indications that magnitude $\Delta R_{S\Omega}(T_{v\omega})$ at small levels of P_ω can be changed proportionally to $H_\omega \sim P_\omega^{1/2}$. Evidently, in this case a term with $P_\omega^{1/2}$ in (8) can arise if the second-order term in Taylor expansion of P is kept. In addition, it is worthily of note we supposed here that n_v was independent value on P_ω which is generally speaking incorrect. In order to be more rigorous we must determine what part of P_ω is expended for generation of vortices. Though this aspect must be studied else, by now one can see that it can change the dependence of $\Delta R_{S\Omega}$ versus P_ω noticeably.

Presence of the vortex finite mass (see for example [5]) can be in our opinion a justice ground of introducing temperature T_v of the vortices structure. The concept of temperature of the vortices system may be applicable when the average temperature of the vortices will increase above the lattice temperature due to the fact that the rate at which the energy is redistributed among the vortices is much higher than the rate of transfer of energy from the vortices to the pinning centers in the lattice.

Notice that analogous approach can be used for considering nonbolometric component of the response conditioned by heating of normal electrons. Herewith it can be to use dependence of the sample resistance $R_{S\Omega}$ against rf conductivity σ which in its turn depends on interaction of electrons with mw field.

Assuming that HTS crystal lattice has close contact with a thermostat (i.e. cryocoolant), average temperature of electrons can be written as

$$T_e = T_{lo} + T_{e\omega},$$

where $T_{e\omega}$ is increase of electron temperature caused by the mw irradiation. The approach is analogous to one in [4] for semiconductor detectors with mw bias.

Experimental details of studying RRSMI were given in [2]. The experimental set-up could be divided into three parts: microwave and radiofrequency (radiowave) monitoring circuits and a cryogenic part. The mw circuit makes use of the quasioptical dielectric resonator (QDR) which allows to use two different resonances for mw pump application and for the additional mw response registration. It should be mentioned, that despite a relatively small mw magnetic field amplitude ($H_\omega^{\max} \approx 10 \text{ O}$) we easily obtain the mixed state (at least at the edges of the film) due to a special field distribution in the resonator.

The rf part makes use of an inductance coil included in a resonance circuit. This coil is attached to the other side of the sample in the form of a disk shaped plate. When the losses of the sample change due to interaction with the radiation, it leads to changing the quality and frequency of the resonance circuit. The rf response is monitored with the help of a Q-factor meter.

The YBaCuO films and ceramic RRSMI was studied by means of QDR of Al_2O_3 single crystal for application of radiation (at about 34.9 GHz) and probe mw signal (at 37.6 GHz) and inductance coil included in a rf resonance circuit for the response measuring at a frequency of 9MHz. QDR with HTS samples was excited with mw signal from the pump generator with output power to 5W in 8mm wave band.

Taking into account that a purely bolometric response is given by $\Delta R_{SO} = (dR_{SO}/dt)\Delta T$ one can note that RRSMI has a mixed nature including a strong enough non-bolometric component. It is seen [2] that peak of the response is shifted to lower temperature relative to T_c by about 1K, while the maximum of purely bolometric component is closer to T_c . A shift between the maxima is about 0.5-0.7K. The quantity $\Delta T = \Delta R_{SO} / (dR_{SO}/dt)$ is an effective temperature rise in the case of purely bolometric effect. ΔT increases sharply below T_c while the thermal properties of the substrate, film and interface between the film and the substrate are not expected to vary noticeably in the relevant temperature range. The latter fact also confirms the presence of a nonbolometric component in the response.

Calculation from experimental data yields values of ΔT which equal to several kelvins [2]. Certain part of these values is $T_{v\omega}$ of our approach. We cannot say that $\Delta T = T_{v\omega}$ in accord with the abovementioned remark concerning the possible dependence of the vortices number on the microwave power.

References

1. N.T.Cherpak, E.V.Izhyk, A.Ya.Kirichenko, A.V.Velichko and I.N.Chukanova, Microwave Radiation Effect
on High-Frequency Properties of YBaCuO Thin Films, In: Int. Conf. on High-Temperature Superconductivity and Localization Phenomena, 11-15 May 1991, Moscow, p.M47, 1991.
2. A.V.Velichko, N.T.Cherpak, E.V.Izhyk, A.Ya.Kirichenko and I.N.Chukanova, High-Frequency Response to
Millimeter Wave Irradiation of YBaCuO Thin Films and Ceramic, Physica C, Vol.C277, pp.101-112,
1997.
3. A.V.Velichko and N.T.Cherpak, Response of High-Temperature Superconductors to Electromagnetic
Radiation, Fizika Nizkikh Temperatur, Vol.23, No.5, pp. 395-428, 1998 (in Russian).
4. I.I.Eldumiahi and G.I.Haddad, A Microwave-Biased Millimeter and Submillimeter-Wave Detector Using
InSb, IEEE Trans. On Electron Devices, Vol.ED-19, No.2, pp.257-267, 1972.
5. G.E.Volovik, Vortex Mass in BCS Systems Kopnin and Baym-Chandler Contributions, Pis'ma ZhETF,
vol. 67, pp.502-504, 1998.

INTERACTION OF MAGNETOSTATIC SURFACE WAVES WITH FILM GRANULAR HTSC STRUCTURE

V. A. Krakovskiy

University of Control Systems and Radioelectronics

40 Lenin Avenue , Tomsk 634050, Russia, Phone: 007 - (3822) - 496223, Fax: 007 - (3822) - 223262.

E - mail: - kes@rk.tasur.edu.ru.

Interest shown in surface magnetostatic waves (SMSV) is aroused due to their practical application [1,2]. Nowadays various elements and devices are created on the basis of surface magnetostatic waves: tunable filters,

nonreciprocal, delay lines and so on. An important property of surface magnetostatic is the dependence of their dispersion characteristics on the state of the impedance layer deposited on the surface of the magnetic film. Considering the later structure HTSC - magnetic films it is possible to define more accurate definition the electrodynamics characteristics granular HTSC media and to consider the possibility of creation control devices. We shall now derive the dispersion for a SMSV propagation in a ferrite film of thickness d , bounded a semi-infinite HTSC layer (Fig. 1). Let the surface MSV propagate perpendicular to a magnetic field H_0 in the direction of the y axis. The magnetic potential of the wave is written as

$$\Psi(x, y) = \Psi(x)\exp[-i(\omega t - ky)] \quad (1)$$

where ω and k – angular frequency and wave vector SMSV. Potential in a magnetized ferrite, in this case, satisfies the Laplace equation. The magnetic field of the superconductor loses its potential nature and is defined instead by the wave equation.

$$\Delta^2 \vec{H} + k_s^2 \vec{H} = 0, \quad k_s^2 = i\mu_0 \omega \delta_{sn}, \quad \delta_{sn} = \delta_n + \frac{i}{\omega \Lambda_s} \quad (2)$$

where k_s is the transverse wave vector superconductor, μ_0 is the vacuum magnetic permeability, δ_{sn} – complex conductivity of the HTSC layer δ_n – normal conductivity of HTSC ceramic. In a granular film the contacts between the granules play an important role, and it is absolutely necessary that the induction of these contacts be taken into account [5,6]. If a contact is regarded as a Josephson junction with a critical current j_c , then the specific induction due to the contact is [7].

$$\Lambda_s = \mu_0 \lambda_s^2 \quad \lambda_s^2 = \frac{\hbar}{2e j_c \mu_0 S} \quad (3)$$

where S is the size of the HTSC granular, e is the electron charge, \hbar is the Plank's constant. For HTSC materials the values are $j_c = 10^2 \div 10^4$ A/cm², $S = 0.1 \div 0.5$ μm. Using the standard boundary conditions we obtain dispersion equation for a surface MSV propagation in a layer structure of a YIG film in a semi-infinite HTSC layer.

$$\operatorname{cth}(kd) = \frac{p(\mu_a^2 - \mu^2 - \xi\mu_a) + (\xi\mu_a - 1)}{\mu(p+1)} \quad (4)$$

where $p = \frac{k_x}{k}$, $k_x = \sqrt{k^2 + k_s^2}$, $\xi = \operatorname{sgn}(k)$ μ_a and μ component of the magnetization tensor. When $k_s \rightarrow 0$ and $|k_s| \gg |k|$ an Eq. 5 gives the Damon – Eshbach dispersion from a free film and for an ideal metal. The dispersion Eq. 5 describes nonreciprocal propagation of SMSW: for forward waves $k > 0$, $\xi = 1$ and for reverse waves $k < 0$, $\xi = -1$. If the infinite HTSC layer is replaced with one of thickness h , then the dispersion equation becomes

$$\operatorname{cth}(kd) = \frac{p \operatorname{cth}(k_x h)(\mu_a^2 - \mu^2 - 1) + p^2(\mu_a^2 - \mu^2 - \xi\mu_a) + (\xi\mu_a - 1)}{\mu(2p \operatorname{cth}(k_x h) + 1 + p^2)} \quad (5)$$

From this solution we can obtain all the cases considered, by using the limits. We shall now calculate the temperature dependence surface waves velocity and damping, using Eq. 5 close to the critical temperature, where we assume that close to $T = T_c$ we can represent the critical current as a linear function temperature and the conductivity, due to the normal electrons, is written in the Kasimir – Gorter approximation

$$j_c(T) = J_c \left(\frac{T_c - T}{T_c - 77} \right) \quad \sigma_n = \sigma_n \left(\frac{T}{T_c} \right)^4 \quad \text{при } T < T_c \quad (6)$$

The calculation were done for $H_0 = 270$ G and $d = 10$ μm and $4\pi M_0 = 1000$ G and for HTSC film having the following parameters: $h = 0.1$ μm and $S = 0.1$ μm, $j_c = 10^3$ A/cm², $T_c = 86^\circ$ K, $\sigma_n = 3.3 \cdot 10^4$ cm/m. In Fig. 2,3 we show the

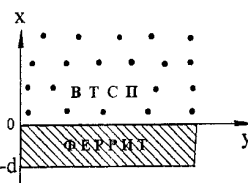


Fig.1

temperature dependence of the phase velocity and the linear damping of SMSW in a structure containing a magnetic film and HTSC film. The curves correspond to various frequencies (curves 1,2,3,4 - $f = 1665, 1675, 1690, 1700$ MHz).

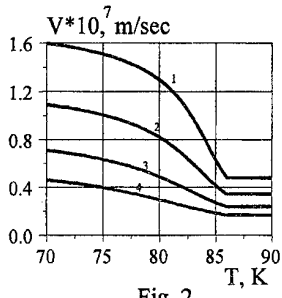


Fig. 2

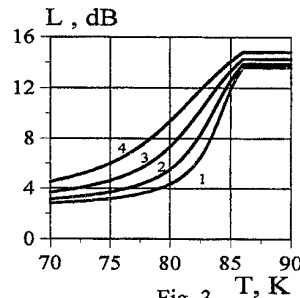


Fig. 3

As a rule in designing the devices the film structures with finite size are used. Consider the reflection from SMSW strip of HTSC. We shall assume that on the surface of a ferrite plate 1 thickness d (Fig. 4) there is a layer of a granular high-temperature superconductor 2, whose thickness is described by the equation

$$t(y) = \gamma d \quad (7)$$

where $f_{\max}(0)=1$ and $\gamma = h/d \ll 1$. SMSW propagate along the y axis and constant magnetic field H_0 lies along the z axis. We will assume the layer of HTSC ceramic to be thin $h \ll \Lambda \ll \lambda$, where Λ is the penetration depth of the

field into the granular superconductor. In the approximation of a thin layer of HTSC ceramic, the boundary condition at $x=0$ can be written in the form.

$$B_{1x} = B_{2x}, \quad H_{1y} = H_{2y} + t(y)[\sigma_n + i/(w\mu_0\lambda_j^2)]E_z, \quad (8)$$

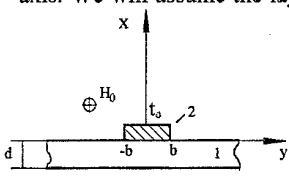


Fig. 4

Here B_x is the normal component of the magnetic induction vector, which to the first order remains continuous, H_y is the tangential component of the magnetic field which undergoes a jump due to the currents induced by the SMSW in the superconducting film, E_z is the component of the electric field which induces a conduction current (first term) and a Josephson current (second term). In the boundary condition (8), index 1 refers to the region of the ferrite, and index 2 to the vacuum region $x>0$. At the smooth boundary $x=-d$, the boundary condition takes the usual form. The solution will be sought by the method of indagation. The scattered field of potential will be represented in the form of integrals Fourier.

$$\Psi_{1,2,3}^P(x,y) = \int \Psi_{1,2,3}(k) \exp(iky) dk, \quad (9)$$

$$\Psi_1(k) = A(k) \exp(-kx), \quad \Psi_2(x,y) = B(k) \exp(kx) + C(k) \exp[-k(x+d)], \quad \Psi_3(k) = D(k) \exp[k(x+d)].$$

Using the boundary condition Fourier's transforms, $B(k)$, $C(k)$, and $D(k)$ is obtained. We substitute the transforms in the Eq. 9 to get the scattered field of potential

$$\Psi_2^P(x,y) = \frac{i\hbar\mu_0\omega}{2\pi} \sigma_{sn} \int_{-\infty}^{\infty} \frac{[(\mu - \mu_a + 1)e^{|k|x} + (\mu + \mu_a - 1)e^{-|k|d} e^{-|k|(x+d)}]}{kD(|k|)} F_2(k) e^{iky} dk, \quad (10)$$

$$\text{where } F_2(k) = A(e^{-qd} + \frac{\mu - \mu_a + 1}{\mu + \mu_a - 1} e^{qd}) \int_{-\infty}^{\infty} f(y) e^{-i(k_+ - k)y} dy,$$

and $D(|k|) = 0$ the Damon – Eshbach dispersion and $|k| = k_+, k_-$ corresponds to the forward wave which propagates along the y axis, k_- corresponds to the reverse wave which runs opposite to the y axis. The coefficient reflection of the wave is written as

$$P = \frac{\Psi_2^P(-d,0)}{\Psi_2(0,0)} = \frac{h\mu_0\omega \sigma_{sn} F(k \rightarrow k_-) \exp(dk_-) \mu}{dk_- [(\mu - 1)^2 - \mu_a^2]}. \quad (11)$$

$$\text{where } F(k \rightarrow k_-) = \lim_{k \rightarrow k_-} \int_{-b}^b f(y) \exp[i(k_+ - k)] dy.$$

At the rectangular distribution $f(y)$ we have

$$P = -\frac{hb^2\omega\mu_0 \sigma_{sn} \exp(-k_+ d) \mu \sin(2bk_+)}{dk_- [(\mu - 1)^2 - \mu_a^2](2bk_+)}. \quad (12)$$

We calculate the electronic waste SMSW for their propagation through the granular film. The resistance of waste in film is defined as follows

$$R = \frac{\sigma_n}{4bh|\sigma_{sn}|^2 \frac{\sin^2(k_+ b)}{(k_+ b)^2}} \quad (13)$$

We shall now calculate the frequency and temperature dependence of coefficient reflection modules, using Eq. 12. The calculation were done for $H_0 = 270$ G and $d = 10$ μm and $4\pi M_0 = 1000$ G and for HTSC film having the following parameters: $h = 0.1$ μm and $S = 0.1$ μm , $j_c = 10^3$ A/cm 2 , $T_c = 86^\circ\text{K}$, $\sigma_n = 3.3 \cdot 10^4$ cm/m, $2b = 100$ μm . In Fig. 5 we show the frequency dependence of the coefficient reflection modules. The curves correspond to different temperatures (curves 1,2,3,4 - $T = 88^\circ, 84.5^\circ, 83.5^\circ, 77.5^\circ\text{K}$). From the graphs it can be seen that the strip of the HTSC ceramic in the high temperature region $T > T_c$ (curve 4) has properties of the conductor with low conductivity. In the low temperature region $T < T_c$ there is substantial reflection of SMSW from HTSC strip. In Fig. 6 we show temperature dependence of the (модуля) coefficient reflection calculated in frequency $f = 1.64$ GHz, with different meaning critical current granular HTSC film.

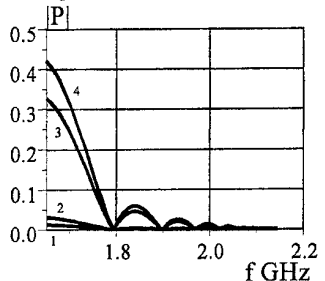


Fig. 5.

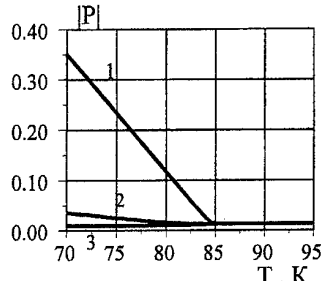


Fig. 6.

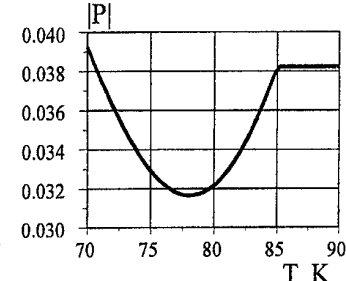


Fig. 7

Curves 1,2,3 correspond to the critical current $J_c = 5 \cdot 10^6, 10^6, 10^5$ A/m 2 . As if evident from Fig. 6 at $J_c = 5 \cdot 10^6$ A/m 2 (curve 1) the film posseses blunt expressed superconductor properties, $J_c = 5 \cdot 10^5$ A/m 2 (curve 3) actually it loses its properties and behaves itself as a common conductor. In the intermediate regime (curve 2, $J_c = 10^6$ A/m 2) HTSC film posses the minimum coefficient of deflection. This property has more expressed the character at the following parameters of the film: $\sigma_o = 2.1 \cdot 10^4$ Cm/m, $J_c = 5.5 \cdot 10^5$ A/m 2 , $S = 0.8$ μm (Fig. 7). The present effect can also be used for constructing the specific devices, for example, bolometric photodetectors.

The high frequency-selective properties can show themselves at the reflection of SMSW from the periodical structures. The analysis of MSMW propagation in periodic planar structure of granular high-temperature superconductors formed on the surface of a magnetic film which have been carried out showed that in the region of the N-S transition there is a resonant dependence of the MSMW parameters on the frequency and temperature [9]. In the region low temperature with propagation of SMSW into the depth of the lattice substantial resonant absorption. The studies done have both practical and purely physical significance. By studying the propagation of SMSW allows a granular HTSC structures, one can obtain additional information about the nature of granular superconductor, which allows one to construct a more precise electrodynamic model granular media. The results found can also be used for constructing frequency – selective structures such as filters and resonators. The high sensitivity of the damping with respect to temperature allows one to the use these structures to make fast bolometric photodetectors.

In conclusion, the authors would like the thank Prof. E. S. Kovalenko for detailed discussion of these results.

References

1. G. A. Vugalter and I. A. Gelinskii, Izv. Vyssh. Uchebn. Zaved., Radiofiz., 32, №. 10. 1187-1220 (1989)
2. Microelectronics and Semiconductor Devises [in Russian], A. A. Vasenkov and Ya. A. Fedotov (eds.), Radio i Svyaz, Moscow (1989), pp. 83-85.
3. V. A. Krakovskii and E. S. Kovalenko, Izv. Vyssh. Uchebn. Zaved., Fiz., №. 3. 50-55 (1995)
4. V. A. Krakovskii and E. S. Kovalenko, Izv. Vyssh. Uchebn. Zaved., Fiz., №. 6. 72-77 (1996)
5. M. G. Gershenson and M. A. Tarasov, Itogi Nauk. Tekh. Elektronika, 2, 38-75 (1990)
6. E. M. Gershenson and G. N. Goltsman A. L. Dzardinova, et al., Sverkhprov: Fiz. Khim. Tekh., 5, № 12 2386 (1992)
7. E. S. Kovalenko, Izv. Vyssh. Uchebn. Zaved., Fiz., №. 8. 32-41 (1996)
8. R. W. Damon, J. R. Eshbach //J. Phys. Chem. Sol., -1961. - V. 19. - N 3 - 4. - P. 308.
9. V. A. Krakovskii, Izv. Vyssh. Uchebn. Zaved., Fiz., №. 10. 94-98 (1997)

EVOLUTION OF OSCILLATIONS OF SEMIBOUNDED ELECTRON PLASMA

V.L.Falko, S.I.Khankina, V.M.Yakovenko

Institute for Radiophysics and Electronics of National Academy of Sciences of Ukraine,
12 Acad. Proscura St., Kharkov, 310085, Ukraine
Tel. (380)572-448474, Fax. (380)572-441105, E-mail: yakovenko@ire.kharkov.ua

1. For the most comprehensive study of electromagnetic oscillations in confined plasma-like media, it is necessary to solve a general problem on an evolution of an initial disturbance in it. Such problem for an unbounded homogeneous plasma was formulated and settled by L.D.Landau [1]: a nonequilibrium electron distribution in the entire plasma volume was given at the initial instant and the electron distribution function and electric fields were determined at subsequent instants of time; the dependencies of frequencies and a damping decrement of the oscillations on a wave vector were found. The oscillations of a semibounded plasma were considered in lots of papers (see the monography [2]), but the initial conditions were not taken into account and, in consequence of this, the obtained spectrum of the natural oscillations could not be accepted as comprehensive.

2. Let us consider an heterogeneous structure, consisting of two semibounded media: a solid-state or gas plasma and nonabsorbing nondispersive medium (dielectric or vacuum). At the initial instant $t = 0$ the nonequilibrium distribution function of the electrons $f^{(0)}(\vec{r}, \vec{p})$ is given (\vec{p} is the momentum of the electrons). We study the evolutions of the electron distribution function $f(t, \vec{r}, \vec{p})$ and electric fields $\vec{E}(t, \vec{r})$ in such structure at all subsequent instants of time. We shall restrict our consideration to Coulomb plasma when one can neglect by delay effects of electromagnetic interactions. Electromagnetic properties of the plasma (the medium "1", $y > 0$) are described by the set of the Maxwell's equations and the linearizing kinetic equation for the nonequilibrium distribution $f(t, \vec{r}, \vec{p})$.

The electric fields in the dielectric (the medium "2", $y < 0$) are determined by the equations of the electrostatics. The boundary conditions are the continuity conditions for the tangential components of the electric fields and for the normal components of the complete (displacement and conduction) currents at the interface $y = 0$, and also the irradiation conditions at $y \rightarrow \pm\infty$. We suppose the conduction electrons are specularly scattered by the surface $y = 0$.

All the function of the x -coordinate in the equation set depend on x as $\exp(iq_x x)$ and their dependences on time t may be expanded into Fourier integrals for $t > 0$ with integration on the complex plane of frequency $\omega(\vec{q})$ (the wave vector). As a result, the Fourier transform of the equation set contains the values of the electric fields and electron distribution function at the initial instant $t = 0$.

Owing to the symmetry of this task, the E -wave and the H - wave propagate independently. We shall study the E -wave as it only makes possible a solution associated with the surface plasma waves.

We have obtained expressions for the electric fields in the both media from the boundary conditions in the form of the Fourier integrals over variables ω and q_y . The peculiarities of the evolution of the function $\vec{E}(\vec{r}, t)$ are determined by the singularities of the integrands on the complex plane ω which are connected, in their turn, with the properties of the semiconductor longitudinal permittivity $\epsilon^l(\omega, \vec{q})$. The function $\epsilon^l(\omega, \vec{q})$ essentially depends on the concrete form of the equilibrium distribution function of the electrons, $f_0(\vec{p})$, and the conditions of the spatial dispersion. The results for the cold, Maxwellian and degenerate plasma are given below.

3. The cold plasma

First we shall consider the most simple case of a cold plasma (a spatial dispersion is absent). The electric field in the semiconductor has the form:

$$E_{1x}(t, q_x, y) = -\frac{2ieq_x}{\varepsilon_0} \cos \omega_p t e^{-\frac{\nu}{2}t} \int_{-\infty}^{\infty} dq_y \frac{n^{(0)}(\vec{q})}{q^2} (e^{iq_y y} - e^{-q_y y}) - \\ \frac{2ieq_x}{\varepsilon_0 + \varepsilon_d} \cos \omega_s t e^{-\frac{\nu}{2}t - q_x y} \int_{-\infty}^{\infty} \frac{n^{(0)}(\vec{q})}{q^2} dq_y \quad (y > 0) \quad (1)$$

Here $\omega_p = \frac{\omega_0}{\sqrt{\varepsilon_0}}$ is the frequency of the volume Langmuir oscillations; $\omega_0^2 = \frac{4\pi e^2 n_0}{m}$; n_0 and $n^{(0)}(y)$ are the equilibrium and disturbed at the point $t = 0$ concentrations of the electrons; e, m are the charge and the mass of the electrons; ε_0 and ε_d are the dielectric constants of the semiconductor lattice and the dielectric, correspondingly; $q^2 = q_x^2 + q_y^2$.

It follows from the formula (1), that in the plasma, along with the volume Langmuir oscillations of the frequency ω_p , two surface modes of the different frequencies ω_s and

$$\omega_s = \frac{\omega_0}{\sqrt{\epsilon_0 + \epsilon_d}}, \quad (2)$$

exist (ω_s is the surface plasmon frequency). The compensation of the electric fields of the volume and surface oscillations at the frequency $\omega = \omega_p$ takes place near the boundary $y = 0$. As a result, in the dielectric only the field of the surface plasmons with the frequency ω_s (2) is formed. The damping of the fields in the both media are due to the electron relaxation frequency ν .

4. The Maxwellian plasma

Inclusion of the spatial dispersion of the dielectric permeability brings to appearance of additional modes (in comparison with the cold plasma). When the conditions of the weak spatial dispersion are fulfilled:

$$\omega_p \gg q_x v_T \gg \nu, \quad (3)$$

the field is the superposition of the oscillations of the different frequencies: $\omega_n(q)$ and Ω_s :

$$\operatorname{Re} \omega_n = \omega_p \left(1 + \frac{3}{2} q^2 r_d^2\right) \quad \operatorname{Im} \omega_n = -\omega_p \sqrt{\frac{\pi}{8}} \frac{e^{-\frac{1}{2q^2 r_d^2}}}{q^2 r_d^2} \quad (4)$$

$$\operatorname{Re} \Omega_s = \omega_s \left[1 + \frac{\epsilon_d^2}{2\epsilon_0(\epsilon_0 + \epsilon_d)} q_x r_d\right] \quad \operatorname{Im} \Omega_s = -\gamma_s = -\sqrt{\frac{2}{\pi}} \frac{\epsilon_d^2}{\epsilon_0^2} q_x v_T \quad (5)$$

(v_T is the thermal velocity of the electrons; $r_d = \frac{v_T}{\omega_p}$). It should be mentioned that in the plasma there are the volume as well as the surface oscillations of the frequency ω_n (4). Here we do not write the expression of the volume oscillations because its analytic formula can be obtain only for the concrete form of the initial function $f^{(0)}(\vec{q}, \vec{p})$. The field of the surface oscillations of the frequency ω_n (4) in the plasma, $E_{1x}^{(n)}(t, q_x, y)$, is equal

$$E_{1x}^{(n)}(t, q_x, y) = \frac{2ieq_x r_d}{\epsilon_0} e^{-q_x y} \int_{-1}^1 d\xi \frac{\cos [\omega_p t + \frac{3}{2}\omega_p t \xi^2] e^{-\operatorname{Im} \omega_n(\xi)t}}{\xi^2 + q_x^2 r_d^2} \\ \oint d\vec{p} \frac{f^{(0)}(\xi, \vec{p})}{1 - \xi \frac{v_y}{v_T}} \quad (6)$$

(\oint signs the main value of the integral; $\xi = q_y r_d$)

The field of the surface oscillations of the frequency Ω_s (5) in the plasma may be written as

$$E_{1x}^{(s)}(t, q_x, y) = E^{(s)}(t, q_x) G(\Omega_s, q_x, y) \quad (7)$$

$$E^{(s)}(t, q_x) = 2ieq_x \cos \Omega_s t e^{-\gamma_s t} \frac{\epsilon_d \Omega_s}{\epsilon_0 + \epsilon_d} \int_{-\infty}^{\infty} \frac{dq_y}{q^2 \epsilon^l(\Omega_s, \vec{q})} \int d\vec{p} \frac{f^{(0)}(\vec{q}, \vec{p})}{\Omega_s - \vec{q} \vec{v}} \quad (8)$$

The Green's function $G(\omega, q_x, y)$ describes the spatial distribution of the field:

$$G(\omega, q_x, y) = \frac{q_x}{\pi} \int_{-\infty}^{\infty} \frac{dq_y e^{iq_y y}}{q^2 \epsilon^l(\omega, \vec{q})} \quad (9)$$

Taking into account, that at $\nu \rightarrow 0$ the contribution to $\epsilon^l(\omega, \vec{q})$ from the resonance particles, for which $\vec{q} \vec{v} = \omega$ (the Landau damping), $\operatorname{Im} \epsilon^l$, is small in comparison with the contribution from nonresonance ones, $\operatorname{Re} \epsilon^l$, we can represent $G(\omega, q_x, y)$ as the expansion in terms of the small parameter $|\frac{\operatorname{Im} \epsilon^l(\omega, \vec{q})}{(\omega, \vec{q})}|$. Then we obtain in the case of the weak spatial dispersion (3):

$$G(\Omega_s, q_x, y) = \frac{1}{\epsilon(\Omega_s)} e^{-q_x y} + \frac{q_x r_d}{\epsilon_0} e^{-\frac{y}{r_d}} - \frac{i\omega_0^2 q_x}{\sqrt{2\pi} \epsilon^2(\Omega_s) v_T^3 \Omega_s^3} \int_{-\infty}^{\infty} dv_y |v_y|^3 e^{-\frac{v_y^2}{2v_T^2} + i \frac{\Omega_s}{v_y} y} \quad (10)$$

The first term in (10) is the contribution of the pole $q^2 = 0$ to the integral (9), and as in the cold plasma, it describes the penetration of the longitudinal-transverse field which is due to the collective behaviour

of the electrons. The second term is a result of taking into account of the pole $\varepsilon^l(\omega, \vec{q}) = 0$ at the large values q_y ($q_y \gg \frac{1}{r_d}$). The third term, G_3 , defines a ballistic transfer of the field along the y -axis by the charged particles (the waves of Van Kampen [3]). We can estimate it at large y

$$y \gg 1/q_x \gg 1/r_d \quad (11)$$

using the steepest descent method

$$G_3(\Omega_s, q_x, y) = i \frac{\omega_0^2 q_x y}{\sqrt{3} \Omega_s^2 c^2(\Omega_s)} e^{-3/4(\Omega_s y/v_T)^{2/3}} \cos \left[\frac{3\sqrt{3}}{4} \left(\frac{\Omega_s y}{v_T} \right)^{2/3} - \frac{2\pi}{3} \right] \quad (12)$$

As Eq (12) indicates, the electrons form the field which falls off at the distances (11) according to the exponential law with $y^{2/3}$ in the index and involves the oscillating multiplier, along with the damping factor. This field component exceeds the first term in Eq (10) at the distances $y > (\frac{3}{4})^{3/2} \frac{\Omega_s}{q_x v_T}$, and we shall denote it as the field of the anomalous penetration at the surface plasmon frequency Ω_s . The smallness of its amplitude is due to the small quantity of the dissipative part of the dielectric permeability, $\text{Im } \varepsilon^l$.

A comparison between the expressions for the fields and the damping decrements of the surface oscillations of the different frequencies ω_n and Ω_s (with the same penetration depth equal to $1/q_x$) shows that the amplitude $E_{1x}^{(n)}$ is smaller than $E_{1x}^{(s)}$ one, but the field $E_{1x}^{(n)}$ exists longer.

The surface oscillation field in the dielectric ($y < 0$) is the sum of the oscillations of the different frequencies, ω_n and Ω_s , which damp at the length $\frac{1}{q_x}$ along the y -axis.

5. The degenerate plasma

In the case of the degenerate plasma with the Fermi distribution function, the dielectric permeability $\varepsilon^l(\omega, \vec{q})$ has the branch points $\omega = \pm qv_F$ on the plane of the complex variable ω (v_F is the Fermi velocity of the electron). They bring to a new term $E_{1x}^{(p)}(t, q_x, y)$ in the field expression in addition to the contributions of the poles (4) $E_{1x}^{(n)}$ and (5) $E_{1x}^{(s)}$. In the component $E_{1x}^{(s)}$ the imaginary part of $G(\omega, q_x, y)$ (9) is negligibly small in comparison with the real part.

The field $E_{1x}^{(p)}(t, q_x, y)$ at large distances y , but less than the electron path in time t :

$$tv_F > y \gg \frac{1}{q_x} \quad (13)$$

has an oscillating nature

$$E_{1x}^{(p)}(t, q_x, y) = i \frac{4\sqrt{2}}{3^{3/4} \pi \sqrt{\pi}} \frac{\omega^{(0)} E_x(\omega_0, q_x, 0)}{(\omega_p t)^{3/2}} \cos[q_x \sqrt{t^2 v_F^2 - y^2} + \frac{\pi}{4}] \quad (14)$$

$$\omega^{(0)} = q_0(t, y) v_F \ll \omega_p \quad q_0(t, y) = q_x \frac{tv_F}{\sqrt{t^2 v_F^2 - y^2}}$$

At the greater depths, $y > tv_F$, the field $E_{1x}^{(p)}$ exponentially damps ($E_{1x}^{(p)} \sim \exp[-q_x \sqrt{y^2 - t^2 v_F^2}]$).

It should be mentioned that the field of the anomalous penetration (14) has another physical nature than the oscillating component in the Maxwell plasma (12), since it is connected with the nondissipative part of the dielectric permeability, $\text{Re } \varepsilon^l$. All the electrons, drifting from the boundary into the plasma depth, perform the ballistic transfer of the field energy, interacting with a large set of spatial-time harmonics of the field. Owing to the abrupt boundary by velocities in the Fermi distribution of the electrons, the group of the particles from the vicinity of the maximum value $v_y \simeq v_F$ are separated out (contributions of the rest ones are mutually compensated). The smallness of the amplitude $E_{1x}^{(p)}$ has the power character and is determined by the small quantity of the separated group.

References

- [1] Landau L.D. J.Phys. USSR, v.10, p.25, 1946.
- [2] Alexanrov A.F., Bogdankevich L.S., Rukhadze A.A. Oscillations and Waves in Plasma Media. Moscow, Izd. MGU, 1990.
- [3] Van Kampen N.G. Physica, v.21, p. 949, 1955.

SEMIQUANTAL DYNAMICS OF THE ELECTRONS IN A PERIODIC POTENTIAL UNDER THE MICROWAVE EXCITATION

L. V. Yurchenko¹ and V. B. Yurchenko^{1,2}

¹ Institute of Radiophysics and Electronics, National Academy of Sciences
12 Proskura St., Kharkov 310085, Ukraine

Tel. 380 572 44 8349, Fax 380 572 44 1105, E-mail: yurchenk@ire.ire.kharkov.ua

² Electrical and Electronics Engineering Department, Bilkent University
Bilkent, Ankara 06533, Turkey

Tel. 90 312 266 4307 Fax 90 312 266 4126 E-mail: yur@ee.bilkent.edu.tr

Nonlinear dynamics of the ballistic electrons in classical and semiquantal superlattices (SL) excited by a strong microwave field of the frequency f have been studied. Although the problem of microwave excitation of different kinds of SL has been treated by many authors, we consider some new effects possible, supposedly, in a special kind of lateral SL created in 2D electron gas of extremely high mobility.

The classical dynamics of the electrons in the cosine SL potential are shown to be chaotic when the electrons are excited by a strong microwave field. Quantum effects, generally, destroy the chaos when the electrons are delocalized either in the real space (for two or more periods of SL) or in the energy (when they are localized in the real space within a region small as compared to the SL period L).

However, if the electrons are properly localized in both the energy and the real space, i.e. their thermal or Fermi energy ε is within the range $(2\pi\hbar)^2/(2mL^2) \ll \varepsilon \ll V_0$ where \hbar is the Planck's constant, m is the electron effective mass, and V_0 is the amplitude of the SL potential $V(x)$, some time τ is required for the transition from irregular quasi-classical motion to the regular quasi-quantum one. So, if $\tau \gg 1/f$ and both the energy and momentum relaxation times, τ_e and τ_i , respectively, are comparable to the transition time τ , the electron dynamics are mainly classical, ballistic, and chaotic.

To simulate the electron motion in SL, we apply the concept of semiquantal dynamics [1] which is an advanced approximation accounting for the effect of spatial delocalization of quantum particles. It is based on considering the evolution of generalized Gaussian wavepackets

$$\Psi(q, t) = (2\pi\rho^2)^{-1/4} \exp [ip(q - x) - (q - x)^2 / \sigma^2(\rho, \Pi)] \quad (1)$$

where x and p are the 'average' coordinate and momentum, respectively, ρ and Π are the 'fluctuation' coordinate and momentum, and $\sigma^2(\rho, \Pi) = 4\rho^2/(1 - 2i\rho\Pi)$ is the squared complex width of the wavepacket evolving in time.

The evolution of the wavepacket is reduced to the dynamics of four variables x , p , ρ and Π which form the Hamiltonian system with the motion equations [1]

$$\frac{dx}{dt} = p, \quad \frac{dp}{dt} = -\sum_{k=0}^{\infty} \frac{\rho^{2k}}{k!2^k} V^{(2k+1)}(x) \quad (2)$$

$$\frac{d\rho}{dt} = \Pi, \quad \frac{d\Pi}{dt} = \frac{\hbar^2}{4\rho^3} - \sum_{k=1}^{\infty} \frac{\rho^{2k-1}}{(k-1)!2^{k-1}} V^{(2k)}(x) \quad (3)$$

where the particle of unit mass is assumed.

For the purpose of our research, we transformed Eqs. (2) and (3) into the form which is more suitable for the analysis of the electron dynamics in a periodic potential.

When $V(x)$ is expanded in the sine and cosine series as

$$\tilde{V}(\tilde{x}) = \sum_{n=0}^{\infty} [\tilde{V}_{Cn} \cos(n\tilde{x}) + \tilde{V}_{Sn} \sin(n\tilde{x})], \quad (4)$$

the summation in Eqs. (2) and (3) can be done explicitly, and we obtain

$$\frac{d^2\tilde{x}}{dt^2} = \sum_{n=1}^{\infty} [\tilde{V}_{Cn} \sin(n\tilde{x}) - \tilde{V}_{Sn} \cos(n\tilde{x})] n \exp(-n^2 \tilde{\rho}^2/2) \quad (5)$$

$$\frac{d^2\tilde{\rho}}{dt^2} = \frac{\tilde{\hbar}^2}{4\tilde{\rho}^3} + \tilde{\rho} \sum_{n=1}^{\infty} [\tilde{V}_{Cn} \cos(n\tilde{x}) + \tilde{V}_{Sn} \sin(n\tilde{x})] n^2 \exp(-n^2 \tilde{\rho}^2/2) \quad (6)$$

where $\tilde{x} = 2\pi x/L$, $\tilde{\rho} = 2\pi\rho/L$, $\tilde{t} = 2\pi ft$, $\tilde{\hbar} = 2\pi\hbar/(mL^2f)$, and $\tilde{V} = V/(mL^2f^2)$.

Further, we assume the cosine SL potential and harmonic microwave excitation so that $\tilde{V}(\tilde{x}, \tilde{t}) = -\tilde{V}_0 \cos(\tilde{x}) - \tilde{\epsilon}\tilde{x} \cos(\tilde{t})$ where $\tilde{\epsilon} = E_0/(2\pi m L f^2)$ and E_0 is the amplitude of the electric field. In this case, Eqs. (5) and (6) take the closed form as follows

$$\frac{d^2\tilde{x}}{dt^2} = -\tilde{V}_0 \sin(\tilde{x}) \exp(-\tilde{\rho}^2/2) + \tilde{\epsilon} \cos(\tilde{t}) \quad (7)$$

$$\frac{d^2\tilde{\rho}}{dt^2} = \frac{\tilde{\hbar}^2}{4\tilde{\rho}^3} - \tilde{V}_0 \cos(\tilde{x}) \tilde{\rho} \exp(-\tilde{\rho}^2/2). \quad (8)$$

Notice that in the classical limit ($\tilde{\hbar} \rightarrow 0$, $\tilde{\rho} \rightarrow 0$), Eqs. (7) and (8) are reduced to the equation of nonlinear pendulum driven with an external force,

$$\frac{d^2\tilde{x}}{dt^2} + \tilde{V}_0 \sin(\tilde{x}) = \tilde{\epsilon} \cos(\tilde{t}). \quad (9)$$

Equations (7)–(8) were solved by the Dormand-Prince method [2] with automatic choice of integration step providing the local accuracy of a solution up to $\epsilon = 10^{-12}$. Some results of the computations are shown in Figures 1 and 2.

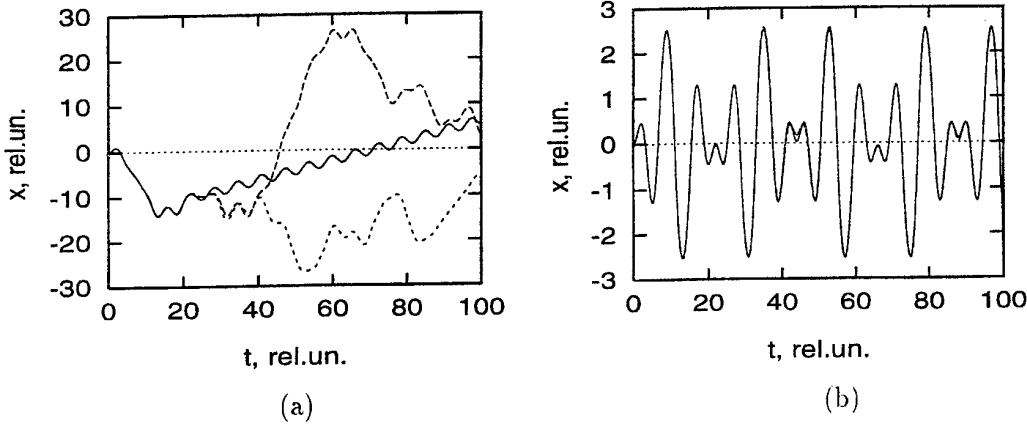


Figure 1: (a) The trajectories of semiquantal (solid curve) and classical electron when the initial conditions are $\tilde{x} = 0$, $\tilde{\rho} = 0$, $\tilde{\rho} = 0.1$, $\tilde{\Pi} = 0$ and the accuracy of a solution is $\epsilon = 10^{-10}$ (dashed curve) and $\epsilon = 10^{-9}$ (dotted curve). The model parameters are $L = 1\mu m$, $V_0 = 20meV$, $E_0 = 1.2kV/cm$ and $f = 60GHz$ that corresponds to $\tilde{V}_0 = 1$, $\tilde{\epsilon} = 1$ and $\tilde{\hbar} = 10^{-3}$. (b) The same for the case of $E_0 = 0.6kV/cm$ ($\tilde{\epsilon} = 0.5$).

Numerical simulation has shown a possibility of the chaotic dynamics of classical and, partly, semiquantal electrons in ballistic superlattices under the strong microwave excitation.

Figure 1 shows the chaotic trajectory of the classical electron and illustrates the importance of using microwave field of high power. The latter is essential since the electrons at equilibrium have to be excited properly to achieve the regions of the chaotic dynamics in the phase space of the system.

Figure 1 shows also that semiquantal electron follows the classical trajectory initially but deviates from it later and propagates further in its own way. Semiquantal motion is, however, rather regular as compared to the classical one.

In Figures 1 and 2, one can see an example of sensitive dependence of the electron trajectories on accuracy of solution and on initial conditions. The effect is recognized as a signature of the dynamical chaos in the system.

Semiquantal electron reveals some sensitive dependence on initial conditions, too. It is similar to the classical particle since semiquantal electron follows the classical trajectory initially for some time τ .

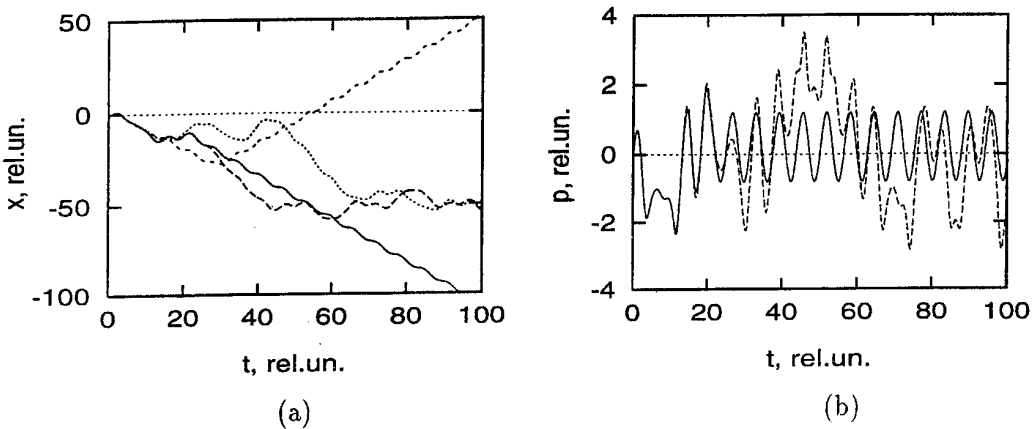


Figure 2: (a) Comparing the trajectories of semiquantal and classical electrons when the initial position is $\tilde{x} = -0.2$ (solid and long-dashed curves, respectively) and $\tilde{x} = 0.2$ (short-dashed and dotted curves). Other parameters are the same as in Figure 1, a ($\epsilon = 10^{-10}$). The value of $\tilde{x} = 0.2$ is the halfwidth of the ensemble of nondegenerate electrons in a valley of SL at the temperature $T = 4K$. (b) Momentum variations of semiquantal (solid curve) and classical electron (dashed curve) in the case of Figure 1, a ($\epsilon = 10^{-10}$).

The requirements for the chaos to appear are rather restrictive (in particular, a strong microwave field of high frequency $f \gg \tau^{-1}, \tau_i^{-1}, \tau^{-1}$ is needed), although they could be satisfied in some structures, e.g., in a lateral SL with 2D electron gas at very low temperatures when the electron mobility can reach $10^7 cm^2 V^{-1} s^{-1}$ and ballistic motion up to $100\mu m$ is possible [3].

In experiment, the dynamical chaos of this kind could be observed as the current fluctuations of abnormally high level, and the structure could be used as a noise generator operating by means of conversion of a coherent microwave field into the chaotic current of the ensemble of ballistic electrons.

References

1. A. K. Pattanayak and C. Schieve, "Gaussian Wavepacket Dynamics: Semiquantal and Semiclassical Phase Space Formalism", Phys. Rev. E, Vol. 50, pp. 3601–3614, 1994.
2. E. Hairer, S. P. Norsett, and G. Wanner, "Solving Ordinary Differential Equations. I. Nonstiff Problems", Springer-Verlag, Berlin, pp. , 1987.
3. C. Weisbuch and B. Vinter, "Quantum Semiconductor Structures. Fundamentals and Applications", Academic Press, New York, pp. 252, 1991.

Influence of Microcorrugated Surface on Electron States in 2D Quantum Well

V.A.Pogrebnyak

Institute of Radiophysics and Electronics NASU
12 Acad. Proskura St. Kharkov 310085 Ukraine
vpog@ire.kharkov.ua

Analysis of electronic states in a periodic potential is the central problem of the theory of solids. However except of solids physics wave processes in periodic structures occur in many areas of physics and technology: quantum- and nanoelectronics, acoustoelectronics, optics and integrated optics, low-dimensional systems and many others.

The problem is often analyzed in the cases of unbounded or layered media [1-3]. The theoretical studies of bounded periodic media reported in the literature are usually based on the coupled-wave equations [4]. In this connection we should like to note the coupled-wave model is a good approximation while we are not interesting by the harmonic interaction. The interaction is initially fell out from the consideration.

We show in the Report that the more exact approximation let to take into account the interaction of harmonics. The approach used in this paper let to reveal electron resonances in a bounded periodic medium.

Let us study electron states in an infinitely deep potential well in which one of walls has one-dimensional periodically irregular form $y_0(x) = \xi \cos(qx)$, where $q = 2\pi/a$, ξ and a are an amplitude and a period of irregularity. So an electron moves in the potential well $U(x, y)$

$$U(x, y) = \begin{cases} 0, & d > y > y_0(x) \\ \infty, & y \geq y_0(x), y \geq d. \end{cases} \quad (1)$$

Where d is the quantum well width.

The electronic eigenfunctions $\Psi(x, y, z)$ and eigenvalues E can be found from the three-dimensional Schrodinger equation

$$\Delta\Psi + \frac{2m}{\hbar^2}[E - U(x, y, z)]\Psi = 0 \quad (2)$$

with the usual boundary conditions

$$\Psi(x, y_0, z) = \Psi(x, d, z) = 0. \quad (3)$$

Since the potential and the boundary conditions do not depend on the variable z , one can separate the variables in the Schrodinger equation. Then, because of the periodicity

of the boundary relief, Ψ must be invariant for the translation $x \rightarrow (x + a)$. Therefore, Ψ may be represented as

$$\Psi = \sum_n (a_n \cos(k_y y) + b_n \sin(k_y y)) \exp[i(k_x + nq_x)x + ik_z z]. \quad (4)$$

Where \mathbf{k} is the electron wave vector. Substituting (3) into the Schrodinger Eq. (2) gives the relation between E and \mathbf{k}

$$k_{y,n}^2 = \frac{2mE}{\hbar^2} - (k_x + nq_x)^2 - k_z^2, \quad (5)$$

and the boundary conditions (3) impose a relation on k_x , k_z and defining allowed values $k_{y,n}$, hence, the dispersion law $E(k)$.

Substituting $\Psi(y_0)$ and $\Psi(d)$ into (3) we obtain the system of linear algebraic equations for coefficients a_n and b_n , the determinant of the system yields the allowed eigenvalues $k_{y,n}$. In the case of small values of the irregularity $\xi/d \ll 1$ it is easy to obtain an analytical solution.

Expanding (3) into a series with respect to the small parameters we obtain (further we omit the index y in the wave numbers $k_{y,n}$)

$$\tan(dk_0) = \frac{\xi^2}{4} k_0 [k_{-1} \cot(dk_{-1}) + k_{+1} \cot(dk_{+1})]. \quad (6)$$

We shall solve (6) by means of successive approximations about ξ : $k_0 = k_0^{(0)} + \delta k + \dots$ If $\xi = 0$ we have $\tan(k_0^{(0)} d) = 0$ therefore

$$k_0^{(0)} = \frac{p\pi}{d}, \quad p = 1, 2, 3, \dots \quad (7)$$

The solution (7) describes 2D energy subbands in a smooth quantum well [5].

$$E_p = \frac{\hbar^2 p^2 \pi^2}{2md^2} + \frac{\hbar^2 (k_x^2 + k_z^2)}{2m}. \quad (8)$$

The next approximation gives δk which defines a desired solution. In the paper we will give the main attention to analysis only of resonance cases, and the energy level shifts will be described in a separate paper.

In zero approximation the wave numbers $k_{\pm 1}$ can be written as

$$k_{\pm 1} = \sqrt{\frac{p^2 \pi^2}{d^2} \mp 2k_x q - q^2}. \quad (9)$$

From Eq.(9) we see that at $k_x = \pm q/2$ the Bragg resonances occur in all 2D subbands. It gives the usual zone structure of the electron energy spectrum in the quantum well. However we will analyse resonances which are caused by the electron movement in the y -direction.

From Eq.(6) and (9) we see that the general resonance condition is

$$k_{\pm 1} = k_0^{(0)} + \frac{l\pi}{d}, \quad k_{\pm 1} > 0, \quad l = 0, \pm 1, \pm 2, \pm 3 \dots \quad (10)$$

The case $l = 0$ corresponds the Bragg resonance. It is seen that the relations (10) and (7) correspond the electron wave resonances. From Eq.(10) we can find resonant values $k_x^{\pm}(p, l)$, e.d. the values of the wave numbers k_x at which electron resonances for the k_{+1} and k_{-1} harmonics take place correspondingly

$$k_x^{\pm}(p, l) = \mp \frac{q}{2}(1 + \beta_{p,l}), \quad \beta_{p,l} = \frac{l(2p + l)\pi^2}{(dq)^2}, \quad l + p > 0. \quad (11)$$

Combining Eq.(11) and (8) gives resonance energies $E_{p,l}^r$

$$E_{p,l}^r = E_p + E_B(1 + \beta_{p,l})^2 + \frac{\hbar^2 k_z^2}{2m}. \quad (12)$$

In Eqs.(11) and (12) l denotes the number of the resonance for the p -2D subband in the quantum well; $E_B = \hbar^2 q^2 / 8m$.

It is easy to see from Eq.(13) that at $l < 0$ and $\beta_{p,l} \rightarrow -1$ the resonance electron energy in the p -2D subband $(E_{p,l}^r - E_p) \rightarrow 0$, e.d. the resonances occur in all energy range starting from zero.

In a vicinity of the resonances the Eq.(6) reduces to the quadratic algebraic equation which describes the spectrum splitting and appearance of the forbidden gaps $\delta E_{p,l}$

$$\delta E_{p,l} = \frac{2\xi}{d} E_p \frac{l+p}{p}. \quad (13)$$

The energy range $\Delta E_{p,l,l+1}$ between l and $l + 1$ resonances in the p -2D subband can be derived from (12). It has a more simple view in the case of the wide quantum well $\beta_{p,l} \ll 1$

$$\Delta E_{p,l,l+1} = \frac{2(2p + 2l + 1)\pi^2}{(qd)^2} E_B. \quad (14)$$

Two last equations show that the electron energy spectrum takes miniband character.

In the above analysis we have shown the periodic boundary essentially effects on electronic states in 2D quantum well. Resonant interaction of different harmonics results in appearance of forbidden gaps in the electron energy spectrum.

References

1. L.Brillouin, Wave propagation in Periodic Structures, Dover, N.Y. (1953).
2. L.M.Brekovskih, Waves in Layered Media, Academic Prewss, N.Y. (1960).
3. V.A.Pogrebnyak, V.M.Yakovenko, I.V.Yakovenko, Fizika Tverdogo Tela **39**, 1875 (1997).
4. H.Kogelnik, C.V.Shank, J. Appl. Phys. **43**, 2327 (1972).
5. T.Ando, A.Fowler, F.Stern, Review of Modern Physics **54**, 437 (1982).

RESONANT FIELD EMISSION IN MULTILAYER CATHODES WITH QUANTUM WELL

N.M. Goncharuk, V.E.Chayka, V. G. Litovchenko*, A. A. Evtukh*, Yu.M. Litvin*
 Research Institute «Orion», 8a Egena Potie; Kiev, 252053, Ukraine. Tel.: /Fax (380-44) 228 22 09,
 E-mail: DVORNICH@BLIZZARD.SABBO.KIEV.UA
 *Institute of Semiconductor Physics, 45 Prospekt Nauki, Kiev, 252650, Ukraine. Tel. / Fax: (380-44)
 265 62 90, E-mail: Lvg@div9.semicond.kiev.ua

In some works a resonant tunneling phenomenon application in the semiconductor field emitters have been considered ^{1,2}. The higher field emission efficiency at definite fields has been shown in these investigations. We present more thorough theoretical and experimental analysis of the field emission processes in Si-SiO₂-Si-SiO₂ multilayer cathodes (MLC) with quantum well (QW). The tunneling processes only from the three-dimensional emitter conductive band electron states have been accounted disregarding tunneling processes from localized in space charge region two-dimensional electron states. One analized the influence of the external electric field value (E), temperature (T), MLC layers parameters, emitter and QW doping level (N_e, N_w) on the field emission current. MLC was modeled, as two SiO₂ trapezoidal barriers with QW layer between them and vacuum tringular potential barrier. Stationary Shredinger equation with boundary conditions of wave function and its derivative continuity has been solved. MLC field emission density current has been calculated as a sum of resonant and nonresonant components.

$$J_{t,n} = \sum_i (4\pi q m_i K T / h^3) \int D_{t,n}^i(\epsilon) \times \ln[1 + \exp((\epsilon_f - \epsilon)/KT)] \times d\epsilon$$

where m_i - longital electron mass in i-th valley of emitter conductive band; q - electron charge; h and K - Plank and Boltzman constants; ϵ_f and ϵ - emitter Fermi energy and tunneling electron energy; $D_{t,n}^i$, $D_{t,n}^i$ - resonant and nonresonant MLC transmission coefficient of conductive band i-th valley electrons.

Investigations have shown that MLC current on field dependences of MLC with QW have current resonant maxima (CRM). Decreasing of N_e from 5×10^{19} to 5.6×10^{17} cm⁻³ (Fig.1, curves 1,2) of MLC with $b_1=b_2=0.5$, $w=1$ nm and $N_w=5.6 \times 10^{17}$ cm⁻³ leads to considerable decreasing (about 10^2) of as the resonant as the nonresonant current, narrowing and shift of CRM to aside smaller electric field values about 7×10^6 V/cm without changing of current resonance overfall. It is stipulated by the less free electron states band width and less dependence of states density on the energy in nondegenerated semiconductor conduction band, than in degenerated one. That is why for nondegenerate emitter electron gas CRM has place under the greatest overlapping two-dimensional electron states miniband in QW with three-dimensional states density tail of emitter free electron. And for degenerate emitter electron gas CRM has place under coincidence two-dimensional electron states miniband in QW with emitter conductive band bottom.

An amount of CRM increases with the width of QW (w) increase. They are shifted towards the lower electric field values with increasing both widths of QW and potential barriers (b_1, b_2). Width of CRM is less under less resonant electric field value and greater width of potential barriers. For every MLC parameters set there is optimum number of resonant level in QW, resonant tunneling through that corresponds to greatest CRM value and resonant current overfall in CRM and following minimum. The greatest values of CRM 10^5 - 10^6 A/cm² and current resonant overfall 10^2 take place with $T = 300$ K and E in the interval from 4.5×10^7 before 8.5×10^7 V/cm for MLC with $b_1=b_2=0.5$ nm (Fig.2, curves 2-5) , N_e and N_w 1.5×10^{19} cm⁻³ and 5.6×10^{17} cm⁻³ correspondingly. With increasing b_1 and b_2 current resonant overfall and CRM are decreased.

The resonant current density of MLC with quite thin potential barrier layers (0.5nm) and QW width 1-3nm for resonant electric field values more than 3.5×10^7 V/cm⁻³ is a few times higher, than current density general cathodes (Fig.2, curve 1) under the same electric field values. It is stipulated by the resonant tunneling electron nonperceptibility as potential SiO₂-barriers as insulator-vacuum energy barrier. In contradiction to that in general cathodes emitting electrons must overcome Si-vacuum output work potential barrier. It points on the possibility of work function reduction when using MLC with optimum parameters.

Calculations for $T = 300$, 77, and 40K were conducted supposing that electron impulse relaxation time constant in Si equals 5×10^{-13} , 1.8×10^{-12} , 2.5×10^{-12} s. The resonant current temperature dependence decrease with increasing resonant level number or resonant electric field value. This is stipulated by increase of resonant level natural broadening contribution in comparison with its relaxative broadening contribution. With temperature lowering from 300 to 77K nonresonant current level reduces and resonant current overfall increases

in three times and CRM narrows (in 1,5 times) because of the electron mobility increasing and redistribution of electron state density in emitter conduction band. For $T = 40K$ CRM is narrower in comparison with $T = 77K$ because of the higher electron mobility.

Dependence of current-voltage characteristic MLC on N_w has been calculated. Conduction band bottom in QW layer rises with comparison on that in emitter layer under decreasing N_w . It leads to rising of resonant electric field value for every resonant level in QW. For MLC with $b_1=b_2=0.5\text{nm}$ and intrinsic QW layer with width $w=1\text{nm}$ resonant level in QW is at field $8.3 \times 10^7 \text{V/cm}$ and for QW doping level $5.6 \times 10^{17} \text{cm}^{-3}$ its value is at field $5.75 \times 10^7 \text{V/cm}$ and CRM is a some narrowed, because less electron dwell time constant.

Experimental investigations of electron field emission from MLC have been performed using silicon tip emitters. Silicon tips were prepared with wet etching of silicon and following sharpening by thermal oxidation³. The ultrathin SiO_2 and Si layers in MLC structures were formed using low pressure chemical vapor deposition technique (LP CVD) and measured with ellipsometer. The thickness of separate layers in MLC structures were varied. The measurements of emission current from MLC structures were performed in the vacuum system which could be pumped to the stable pressure of 10^{-6} Torr. The emission current was measured in the diode structure. The emitter-anode spacing was constant and equals to $20 \mu\text{m}$. We fabricated a test diode construction by the sandwiching of anode and cathode plates. A silicon wafer with MLC structure was used as the cathode and a quartz plate coated with ITO (indium-tin oxides) as an anode. $20 \mu\text{m}$ high fluoroplast film spacer are used to keep the two plates separated. The field emission was obtained from tips in the drive voltage range from 100 to 1500 V and in the current range from 5 nA to above 20 μA . A $0.56 \text{M}\Omega$ resistor was placed in series with the cathode to provide a short-circuit protection.

During the electron field emission into vacuum measurements the resonant tunneling have been observed for some MLC structures. Fig.3 shows the measured current-voltage characteristics and corresponding Fowler-Nordheim plots. To compare with theory the electric field strength have been calculated. For this the field enhancement coefficients obtained from Fowler-Nordheim plots according to procedure described in⁴ have been used. The two separate resonant peaks can be seen in experimental curves (Fig.3).

As a result of theoretical calculations and experimental investigations the resonant current peaks in Si-base MLC structures have been revealed. Resonant tunneling process over n-th resonant level in QW is characterized by own time constant value of electron dwell in QW τ_n . The value of τ_n increases with increasing QW width because of lowering electron resonant energy and mostly with decreasing potential barrier permeability. For MLC under research and electric field value in interval $3 \times 10^7 - 8.5 \times 10^7 \text{V/cm}$ value τ_n is within the range $10^{-9}-10^{-14} \text{c}$ depending on parameters of MLC and resonant level number. Finite delay time of electrons in QW and sufficiently large average negative conductivity value on the falling interval of current resonant dependency, witnesses on perspective use MLC with the QW for the electromagnetic oscillation amplification or generations within the millimeter and submillimeter wave lengths range.

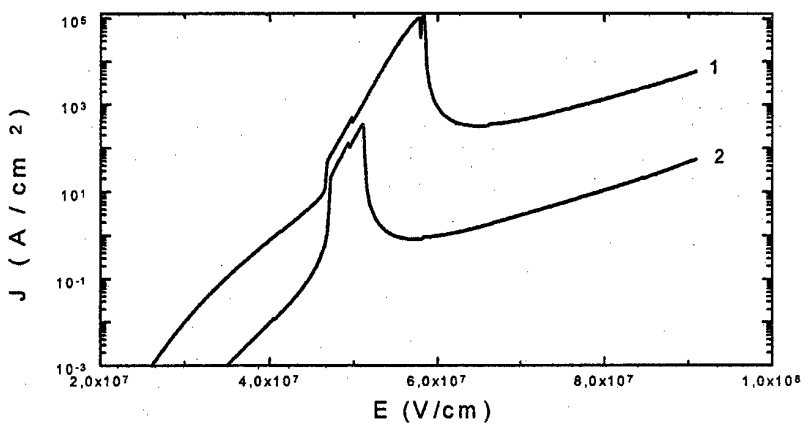


Figure 1. Theoretical current density on electric field dependences: 1 - $N_e = 5 \times 10^{19} \text{cm}^{-3}$; 2 - $N_e = 5.6 \times 10^{17} \text{cm}^{-3}$, $w=1\text{nm}$, $b_1=b_2=0.5\text{nm}$, $N_w = 5.6 \times 10^{17} \text{cm}^{-3}$, $T = 300\text{K}$.

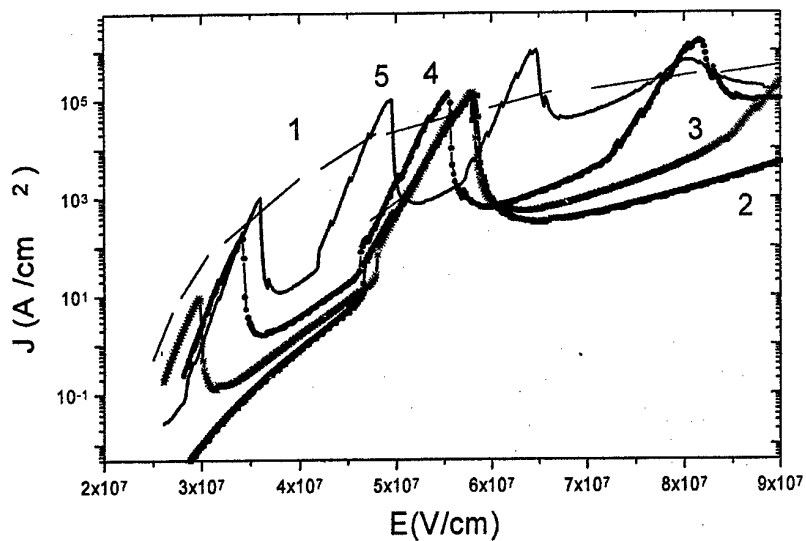


Figure 2. Theoretical current density on electric field dependences: 1 - $w = b_1 = b_2 = 0$; 2, 3, 4, 5 - $w=1$, 1.5, 2, 3nm, $b_1 = b_2 = 0.5$ nm, $N_e = 5 \times 10^{19} \text{ cm}^{-3}$, $N_w = 5.6 \times 10^{17} \text{ cm}^{-3}$, T = 300K.

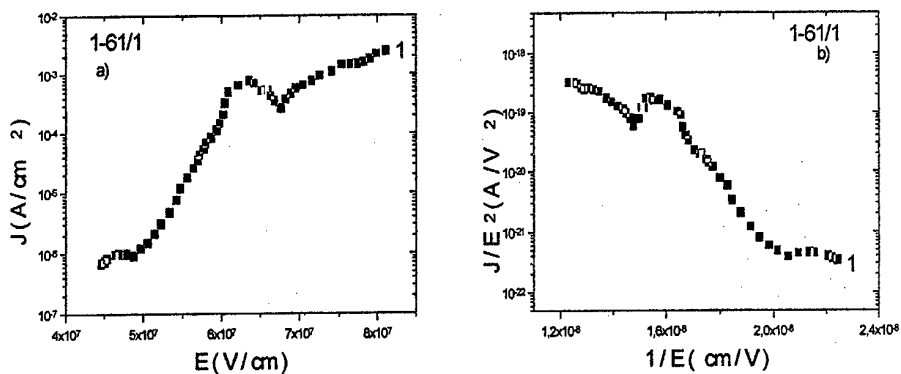


Figure 3. Experimental current density on electric field dependence (a) and corresponding Fowler-Nordheim plot (b) $w=2$ nm, $b_1 = b_2 = 2$ nm, $N_e = N_w = 5.6 \times 10^{17} \text{ cm}^{-3}$, T = 300K.

References

1. V.G. Litovchenko, Yu.V. Kryuchenko "Field emission from structures with quantum wells", J. Vac. Sci. Technol. B11(2), pp.362-365, 1993.
2. V.G. Litovchenko, Yu.V. Kryuchenko "The Dynamic Characteristics of the Field Emission from the Structures with Quantum Wells", J. de Physique IV, V.6, pp.C5-141-C5-146, 1996.
3. A.A. Evtukh, V.G. Litovchenko, R.I. Marchenko, N.I. Klyui, V.G. Popov and V.A. Semenovich. "Peculiarities of the Field Emission with Porous Si Surfaces, Covered by Ultrathin DLC Films", J. de Physique III, V 6, pp.C5-119-C5-124, 1996.
4. D.W. Branston and D. Stephani "Field Emission from Metal-Coated Silicon Tips", IEEE Trans. Electron Dev., V.38, N.10, pp.2329-2333, 1991.

NEGATIVE DYNAMIC CONDUCTIVITY IN DIODE STRUCTURE WITH THE CONE CATHODE.

V.E.Chayka, N.M. Goncharuk, D.V. Mironov

Research Institute «Orion», 8a Egena Potie; Kiev, 252053, Ukraine. Tel.: /Fax (380-44) 228 22 09,
E-mail: DVORNICH@BLIZZARD.SABBO.KIEV.UA

Recently, an interest to high-frequency oscillations generation and amplification in matrix cone structures on base of autoelectron emission has risen¹. Mostly the solid-state structures permitting to receive oscillation amplification and generation up to a middle part of the millimeter range up to 100 GHz frequencies are used as the sources of oscillations. In the given work the possibility of diode structures with cone cathode application for obtaining negative dynamic conductivity and consequently of high-frequency oscillations generation in a short-wave part of the millimeter range and in submillimeter is investigated. The principle of such diode operation is similar to that of the solid-state injection-transit diode, where to provide oscillations generation or to obtain negative conductivity it is necessary that the time of electron transit between the cathode and the anode was approximately 0.75 oscillation period.

However in contradiction to semiconductor injection-transit diodes, where the carriers velocity is equal to the saturation velocity, in vacuum diodes carrier motion velocity is much higher because of absence of scattering mechanisms. Therefore the standard cathode - anode electron transit time in autoemission structures is 0.1-1ps. Hence it is difficult to receive negative dynamic conductivity and high-frequency oscillations generation out of 0.75-7.5THz frequency band in diode cone structures. So the possibility to obtain negative dynamic conductivity of the cone cathode structures with a quantum well in a broad frequency interval of 200MHz -100THz was studied. In this case, resonant character of tunneling allows to obtain electron delay time from 10fs to 1ns and depending on well parameters and applied voltage. That allows in optimum to phase an inducted current and the applied voltage. Here the maximum of the inducted circuit current will be biased relatively to the applied voltage one. That allows to receive negative conductivity in a broad band of frequencies by selection of parameters of multilayer cathode.

On the fig.1 the curves 1 and 2 shows typical statical field emission current on the field dependences of the Si-SiO₂-Si-SiO₂ flat cathode with quantum well, the width of that and of the alike potential barriers are 3nm and 0.5nm (curve 1) and 1nm and 1nm (curve 2) accordingly. As it is visible from fig.1, in the presence of resonant tunneling the current has several maxima appropriate to electron tunneling through 5-th, 6-th, 7-th, 8-th (1-th, 2-th, 3-th, 4-th maxima of the curve 1 in the fig.1) and through 2-th, 3-th (1-th, 2-th maxima of the curve 2 in the fig.1) resonant levels in the quantum well with width 3nm and 1nm accordingly. The own dwell time of an electron in the quantum well corresponds to each resonant level. The dwell time 12ps corresponds to the most low-voltage level, and consequently 3.35ps, 0.15ps, and 7.5fs do to the next ones in quantum well with the width 3nm. And the electron dwell time on 2-th and 3-th resonant level in quantum well with the width 1nm is 2.5ns and 40fs. If such structure is applied with alternative voltage with frequency, which period is equal to the double dwell time, the induced circuit current will have a sharp peak shifted on 0.5 period relatively to the maximum of the alternative voltage. The first harmonic of that current will be in opposition with the applied voltage, and this causes negative conductivity.

The calculations of statical the emission current on the field dependences were performed by the solution of the stationary Shredinger equation with appropriate boundary conditions and of dinamical that by the combined solution of the Poisson equation and continuity equation with necessary boundary conditions. The Poisson equation was solved by the numerical method on base of the fifty-point difference scheme, and the continuity equation was done by Euler method. The cathode was approximated by a hyperboloid of revolution. Carriers diffusion was neglected. Peculiarity of cone cathode field emission in comparison with the flat case shown on the fig.1 is that, under change voltage, the resonant field value corresponds to various cathode segments. Under small voltage the resonant field emission has place from an cathode edge, and under voltage increase it does from a lateral area of the cathode. Thus static current on the field dependence of the cone cathode with the quantum well is a little smoother in comparison with the flat cathode with the quantum well.

On the fig.2 the dependences between applied voltage phase and induced electron emission current through the sixth resonant level in the quantum well (the second maximum of the curve 1 in fig.1) with the width 3nm and the barrier width 0.5nm is shown. The voltage $U(t) = U_0 + U_1 \times \sin(2\pi ft)$ is applied, where U_0 , U_1 - applied direct and alternative voltage, f - frequency, t - time, $U_0 = 240V$, $U_1 = 40V$. The curve 1 corresponds to the frequency ($f = 149GHz$), which period two times as much as the electron dwell time on the sixth level in the

quantum well. As it is visible from the fig.2, in this case the sharp current peak is opposite to the applied voltage, that causes high value of negative differential conductivity with efficiency 10%. Curves 2 and 3 correspond to frequencies accordingly on 25% below and above than that of the curve 1. As it is visible from the figure 2, in these cases the peak of the induced current is also in the part of a negative halfcycle of applied voltage, that also provides negative differential conductivity, though with smaller values of the efficiency (7% and 6% accordingly).

In case of the resonant field emission through the seventh level in the quantum well with the width 3nm and barrier width 0.5nm maximum negative differential conductivity has place on the frequency 3.3THz with efficiency 7%. Generation frequencies 42GHz and 67THz correspond resonant emission through the 5-th and the 8-th levels in this quantum well. And 250MHz and 12.5THz correspond resonant emission through the 2-th and 3-th levels in quantum well with barrier and well width 1nm. It is necessary to mark, that the peak width of the induced current is determined by the time of electron transit from the cathode to the anode, that leads to efficiency change at different resonant levels owing to changing of the first harmonic value relative to the direct current value.

The least and the greatest frequency of negative conductivity region is 1.5 times less and more consequently, than the maximum negative conductivity frequency. In the case of the resonant field emission through the 8-th resonant level in the quantum well with the width 3nm and barrier width 0.5nm the greatest frequency of the negative differential conductivity region is near 100THz. And the minimum frequency of negative conductivity region under the resonant emission through the 2-th level in quantum well with barrier and well width 1nm is less 200MHz. Therefore, it is possible by change of the quantum well and barrier parameters of multilayer cone cathode to obtain negative dynamic conductivity and oscillation generation in wide frequency band from 200MHz up to 100THz in the diode structure on the base of cone cathodes with resonant field emission through the quantum well.

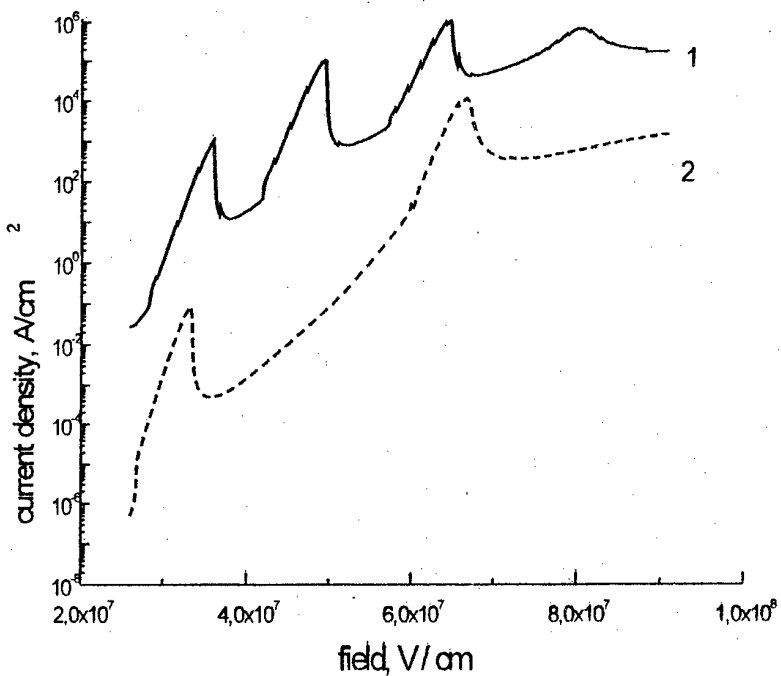


Figure 1. Current on the field dependences of the Si-SiO₂-Si-SiO₂ flat cathode with the quantum well. The width of the well and of the alike potential barriers are 3nm and 0.5nm (curve 1); 1nm and 1nm (curve 2).

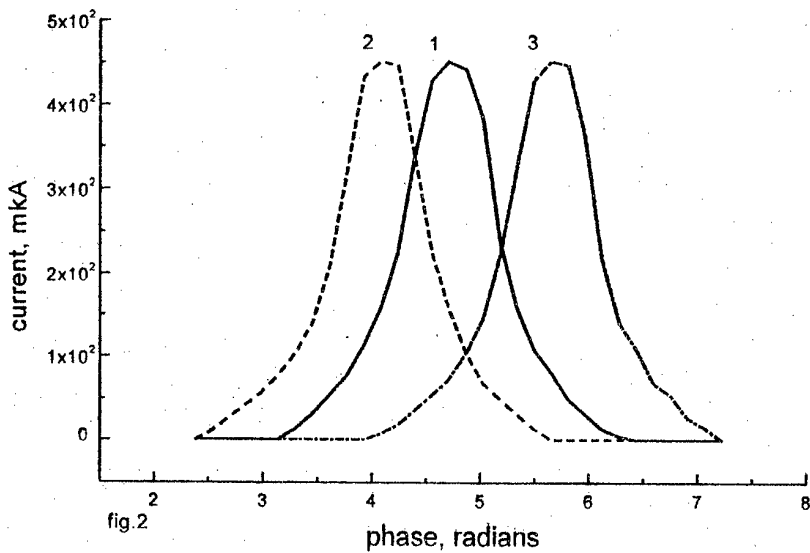


Figure 2. The dependence between phase of applied voltage and induced current through the sixth resonant level in quantum well with the width that and barrier 3 and 0.5nm. The direct voltage is 240V and alternative voltage amplitude and frequency are 40V and 149, 112, 186Ghz (curves 1, 2, 3).

References

1. W. I. Orwiss, C. S. Maconadhy, D. R. Ciarko, «Modeling and fabrication microcavity integrated vacuum tube», IEEE Electron Devices, Vol. ED-36, No. 11, pp. 2651-2657, 1989.

LOSSES IN DIAMONDS AT MILLIMETER RANGE

B.M. Garin, A.N. Kopnin, M.P. Parkhomenko, E.E. Chigryai
 Institute of Radio Engineering & Electronics of Russian Academy of Sciences,
 1 Vvedensky Sq., Fryazino, Moscow Region 141120, Russia
 Tel.: +007-095-526-9266; Fax: +007-095-702-9572; E-mail: ask@ms.ire.rssi.ru

V.V. Parshin, A.B. Mazur
 Institute of Applied Physics of Russian Academy of Sciences,
 ul. Ulyanova 46, N.Novgorod 603600, Russia
 Tel.: +007-8312-38-4566; Fax: +007-8312-36-2061; E-mail: parsh@appl.sci-nnov.ru

V.G. Ralchenko, V.I. Konov
 General Physics Institute of Russian Academy of Sciences,
 ul. Vavilova 38, Moscow 117942, Russia
 Tel.: +007-095- 132-8229; Fax: +007-095-234-9022; E-mail: ralchen@ran.gpi.ru

Introduction

In various low loss materials the theoretical lower limit of lattice loss (absorption) at millimeter (MM) and submillimeter (SMM) wavelength ranges is determined by the multiphonon (mainly two-phonon) absorption in corresponding ideal crystal [1,2]. This type of loss may be referred to as the "intrinsic" lattice loss (ILL). In practice an additional lower bound on the loss may be imposed by absorption on lattice disorder, defects and impurities or free charge carriers [3-5]. It had been predicted theoretically [1,3,4] that in the crystals of diamond-type lattice (diamond, Si, Ge) extremely low ILL values at MM and SMM ranges can be expected. Furthermore the diamond is characterized by the lowest limits both for lattice and free charge carriers induced losses among various diamond-type crystals [3-5]. The progress in the synthesis of polycrystalline diamond films by the method of chemical vapor deposition (CVD) made available the diamond plates of large diameter (5–10 cm) and thickness (up to 1–2 mm). This allows to measure low loss diamonds in MM range and opens opportunities for design of diamond windows for the most powerful MM waves sources (gyrotrons). The results of the loss measurements in CVD diamond in MM range [6-9] and also at lower frequencies [10] are available in literature. But the temperature and frequency dependences of the loss, the effect of synthesis conditions on the loss value were not practically researched. The loss nature was not revealed, and the possibilities of significant loss reduction were not studied. The present work is devoted to these problems. The lower loss limit in diamond have been considered and series of low loss synthetic diamonds at 1.75–6.8 mm range and T = 20–500 °C have been researched.

Theoretical estimations of intrinsic lattice loss in diamond

In [4,5] the rough theoretical estimations of absolute loss tangent $\tan\delta$ values have been obtained for the ILL in diamond, silicon, germanium, respectively: $\tan\delta \sim 10^{-9}$, $3 \cdot 10^{-8}$ and $2 \cdot 10^{-7}$ at the wavelength $\lambda = 2$ mm and room temperature. Up to date the lowest losses among solid state materials at those conditions have been observed in the gold-doped silicon (Si:Au) [5,11]. These losses, including the record breaking lowest loss ($\tan\delta \sim 3 \cdot 10^{-6}$ at $\lambda = 2$ mm and temperature T = 20 C [11]), are due to free carriers of charges as it follows from the measured temperature and frequency dependences. Hence in silicon the ILL $\tan\delta \leq 10^{-6}$. From the theoretical estimations, it follows that the ILL in diamond is approximately 1/30 of that in silicon. From the comparison with the mentioned experimental data it follows that $\tan\delta$ value for the ILL in diamond should be $\leq 3 \cdot 10^{-8}$ at the same conditions.

Experimental results

At the present work the series of low loss synthetic diamond polycrystal plates have been grown at GPI from the $\text{CH}_4\text{-H}_2\text{-O}_2$ mixtures in a microwave plasma as described elsewhere [12]. The diamond deposition rates were 2–5 $\mu\text{m}/\text{hour}$, nitrogen impurity concentrations was varied in the range of $(2\text{--}30) \cdot 10^{17} \text{ cm}^{-3}$. The

specimens, separated from Si substrate, had the form of disks of 55–60 mm diameter and thickness of up to 1.3 mm. The macroscopic dc resistivity of the diamond plates was in the range of 10^{12} – 10^{14} Ω·cm. The loss measurements in the series of plates (as-grown, ungrounded) were carried out at IREE using an open resonators [5] in the wavelength range of 2.15–6.8 mm. The results presented in Tables 1 and 2 show that the losses in this diamond samples are in the range of $\tan\delta = (1-10) \cdot 10^{-4}$. The tendency have been observed of the loss decrease with the decrease of deposition rate and nitrogen impurity concentration. In addition, a considerable reduction of loss after annealing in air at $T = 550^\circ\text{C}$ has been found, in particular $\tan\delta$ decreased from $\sim 1.5 \cdot 10^{-4}$ to $\sim 5 \cdot 10^{-5}$ for specimen No. 111.

The lowest loss have been observed in the specimen No. 113 (deposition rate 2.4 μm/hour, nitrogen concentration $2 \cdot 10^{17} \text{ cm}^{-3}$) that was measured at IAP (see Figure 1). In order to improve the measurement precision in connection with low loss, this disk has been grinded on both sides, which have made parallel to the accuracy of 5 μm on diameter of 55 mm. During the grinding its thickness has been reduced from 1.05 mm to 0.74 mm. At the final thickness the measurement frequency 170 GHz was "resonance" one (the thickness was a multiple of one half of wavelength in material). After mechanical treatment the disc had been annealed in air. The measurement technique [13] have been modified to reduce the $\tan\delta$ measurement error down to $\pm 10^{-6}$. The loss determined for this specimen, $\tan\delta \sim 8 \cdot 10^{-6}$ (170 GHz; 20°C), is on the level of the lowest value among known in literature for diamond [9] and approaches the lowest value observed among various materials to date ($\tan\delta \sim 3 \cdot 10^{-6}$ in Si:Au, see above). The estimation of transmission power shows that the best investigated diamonds are applicable for windows of gyrotrons at power ~ 3 MW and higher in continuous wave regime.

Interpretation and conclusions

The loss dependence on frequency f (see Table 2) can be approximated by the $1/f$ law. The observed loss in CVD diamond can be explained by the loss on the electric conductance in the inclusions of nondiamond phases containing amorphous carbon and nanographite. The spatial distribution of those inclusions with enhanced local conductivity σ is assumed to be very inhomogeneous. Based on Raman spectroscopy data the relative volume concentration of nondiamond phases is less than 10^{-3} . According to the proposed loss mechanism the more weak frequency dependence (compared with the $1/f$ law) at $f \ll 10$ GHz [10] is due to decrease of a number of local regions that satisfy the condition $\tau_M^{-1} \ll \omega$ (where: $\tau_M = \epsilon\epsilon_0/\sigma$ and ϵ are the local values of the Maxwell's electric relaxation time and dielectric permittivity, respectively; ϵ_0 is the dielectric constant; $\omega = 2\pi f$). The relatively weak loss dependence on temperature at $T < 400^\circ\text{C}$ can be naturally explained by the weak dependence of the conductivity in the nondiamond inclusions.

The observed losses differ by its temperature and frequency dependences from the ILL (the latter must considerably increase with rise in frequency and temperature [1-4]) and significantly exceeds the estimated values for ideal crystal (see above). So the intrinsic lattice loss in diamond, as well as in other diamond-type crystals including silicon [5,11] are not experimentally revealed to the present time. From the obtained data and consideration and also from the ILL estimations it follows that there are possibilities of further significant loss reduction in diamond and achievement of lowest losses compared with other materials in MM and SMM ranges.

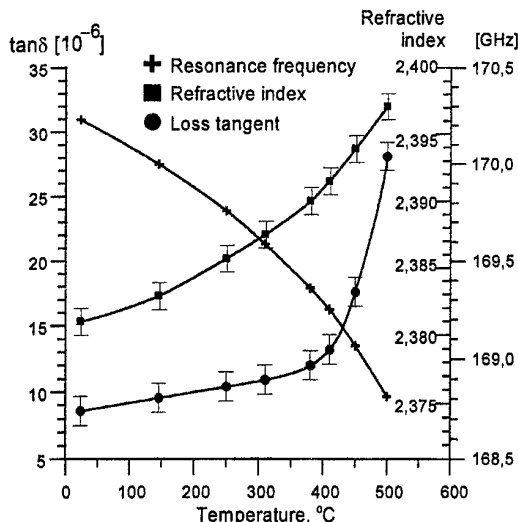
This work was supported in a part by the Russian Foundation of Fundamental Researchs (Grant No. 96-03-32798) and Russian Scientific-Technical Program "Microwave Physics" (Projects No. 3.3 and 3.19).

Table 1. Losses $\tan\delta$ at $\lambda = 2.15$ mm and room temperature in unpolished CVD diamonds.

Specimen number	Mean Thickness [μm]	Deposition rate [μm/hour]	$\tan\delta [10^{-4}]$
92	1280	5.0	8
83	190	4.6	10
79	490	4.5	1.5±3
70	230	3.9	<5
111	490	3.7	1±2
93	430	3.2	2
56	270	2.7	2
100	640	2.6	1.5±3.5
AST	180	2.5	<2

Table 2. Losses at $\lambda = 2.15\text{--}6.8 \text{ mm}$ in specimen No.79.

$\lambda [\text{mm}]$	2,15	3,9	6,0	6,8
$\tan\delta [10^{-4}]$	1,5±3	4	5	9,5

Fig. 1. Temperature dependences of $\tan\delta$, refractive index and resonance frequency for grinded diamond disc of 0.74 mm thickness.

References

1. A.V. Galdetskii, B.M. Garin, "On the multiphonon absorption of IR radiation in crystals due to optical unharmonicity", Preprint No.17(320). Moscow, Inst. of Radio Engineering & Electronics of the USSR Academy of Sci., 1981; the same, Digest of All-Union Conf. "Designing and Applications of Radio-electronic Devices on dielectric waveguides and resonators", Saratov, Russia, pp.98-99 (1983) [in Russian].
2. B.M. Garin, Digest of 18th Int. Conf. on IR & MM Waves, Colchester, England, vol.1, pp.509-510 (1993).
3. B.M. Garin, A.N. Kopnin, M.P. Parkhomenko, et al, Digest of 1st Ukrainian Symp. "Physics and Technology of MM and SubMM Radio Waves", Khar'kov, Ukraine, vol.1, pp.86-87 (1991) [in Russian].
4. B.M. Garin, Russian Conf. "Dielectrics-93", St.-Petersburg, 1993. Digest, vol.1, pp.98-99 [in Russian]; Digest of Third Int. Conf. on Millimeter-wave and Far-Infrared Sci. and Technol., Guangzhou, China, pp.275-277 (1994).
5. B.M. Garin, A.N. Kopnin, M.P. Parkhomenko, et al, Technical Phys. Lett., vol.20, pp.878-879 (1994); B.M. Garin, A.N. Kopnin, M.P. Parkhomenko, et al, Digest of 21st Int. Conf. on IR & MM Waves, Berlin, paper CT15 (1996).
6. R. Heidinger, Digest of 19th Int. Conf. on IR & MM Waves, Japan, pp.277-278 (1994).
7. R.S. Sussman, J.R. Brandon, G.A. Scarsbrook, et al, Diamond Related Materials, vol.3, p.303 (1994).
8. V.V. Parshin, V.A. Khmara, V.I. Mankeev, et al, 9th Joint Russian-German Meeting on ECRH and Gyrotrons, pp.143-144 (1997).
9. R. Sporl, R. Schwab, R. Heidinger, ibid, pp.167-174.
10. A. Ibarra, M. Gonzalez, R. Vila, et al, Diamond Related Materials, vol.6, pp.856-859 (1997).
11. R. Heidinger, J. Molla, V.V. Parshin, Digest of 21st Int. Conf. on IR & MM Waves. Berlin, paper AW8 (1996).
12. V.G. Ralchenko, A.A. Smolin, V.I. Konov, et al, Diamond Related Materials, vol.6, pp.417-421 (1997).
13. Yu. A. Dryagin, V.V. Parshin, Int. J. on IR & MM Waves, vol.13, pp.1023-1032 (1992).

POLARITON EXCITATIONS IN TWO-DIMENSIONAL ELECTRON MAGNETOPLASMA

V.V. Popov, T.V. Teperik, G.M. Thymbalov

Institute of Radioengineering and Electronics, Saratov Branch
Saratov Research Centre of the Russian Academy of Sciences

P.O. Box 286, Saratov 410002, Russia

Tel: (8452)264510, Fax: (8452)519104, E-mail: popov@ire.saratov.su

In this paper, the polariton excitations associated with magnetoplasma and cyclotron oscillations in a homogeneous two-dimensional (2D) electron layer surrounded by two dielectric half-spaces with different dielectric constants ϵ_1 and ϵ_2 are theoretically studied. As it follows from previous works of the others [1,2], the 2D magnetoplasmon-polariton frequency goes to zero as its wave vector goes to zero for both cases $\epsilon_1 = \epsilon_2$ and $\epsilon_1 \neq \epsilon_2$. It is shown below that, contrary to the conclusions of Ref.[2], a low-frequency band gap exists in the 2D magnetoplasmon-polariton spectrum when $\epsilon_1 \neq \epsilon_2$ and the dc magnetic field is nonzero.

The 2D magnetoplasmon-polaritons are in essence the surface non-radiative electromagnetic waves. Unlike them the homogeneous cyclotron oscillations in the plane of 2D system are accompanied by electromagnetic radiation into surrounding media. The frequency and radiative damping of homogeneous cyclotron oscillations have been calculated in Ref.[3]. In present paper, nonhomogeneous radiative cyclotron oscillations (radiative cyclotron-polaritons) are studied for the first time.

Let us consider the 2D electron layer placed in the plane $z = 0$ between two dielectric half-spaces 1 and 2 (for definiteness sake, we assume $\epsilon_1 > \epsilon_2$). The dc magnetic field H_0 is directed along the z -axis into medium 2. The time and space dependence for the polariton fields is taken in the form of $\exp(-i\omega t - ikx \pm \alpha_{1,2}z)$, where upper and lower signs before the transverse wave numbers $\alpha_{1,2}$ refer to media 1 and 2, respectively. The fields are assumed as uniform ones in y -direction.

One can obtain the dispersion relation for the polariton excitations in the structure under consideration from self-consistent solution of the Maxwell equations in media 1 and 2 with the boundary conditions in the plane $z = 0$ which account for the response of the 2D electron magnetoplasma. Neglecting the electron scattering in the 2D system, the dispersion relation can be written as

$$\left(\omega^2 - \frac{\alpha_1 \alpha_2 \eta_0}{\alpha_1 \epsilon_2 + \alpha_2 \epsilon_1} \right) \left(1 + \frac{\eta_0}{(\alpha_1 + \alpha_2)c^2} \right) - \omega_c^2 = 0, \quad (1)$$

where $\eta_0 = 4\pi N_s e^2 / m^*$, N_s is the areal density of electrons in the 2D layer, e and m^* are the electron charge and effective mass, c is the light velocity, $\omega_c = |e|H_0/(m^*c)$ is the cyclotron frequency.

The relationship between the transverse wave numbers $\alpha_{1,2}$ and in-plane wave vector k is given by

$$\begin{aligned} \alpha_1 &= \pm \sqrt{k^2 - \left(\frac{\omega}{c}\right)^2 \epsilon_1}, \\ \alpha_2 &= \pm \sqrt{k^2 - \left(\frac{\omega}{c}\right)^2 \epsilon_2}. \end{aligned} \quad (2)$$

It should be noted that the dispersion relations obtained in Ref.[1,2] can be brought into the form of Eq.(1). However a solution $\omega(k)$ of the set of simultaneous equations (1), (2) crucially depends on the signs chosen before the radicals in Eqs.(2). Just this point was not received adequate attention in Ref.[1,2].

Let us start with the non-radiative 2D magnetoplasmon-polaritons. In this case one should look for the real solutions $\omega(k)$. For the surface non-radiative electromagnetic wave, both transverse wave numbers α_1 and α_2 have to be real and positive. These conditions can be met only when $k > \omega\sqrt{\epsilon_1}/c$ and while positive signs are chosen before the radicals in Eqs.(2). Hence it follows that for any positive value of k the magnetoplasmon-polariton frequency falls into the interval $0 \leq \omega \leq \omega_1$, where $\omega_1 = ck/\sqrt{\epsilon_1}$. If the

real unique solution $\omega(k)$ exists for a given k , the left side of Eq.(1) has to have different signs at $\omega = 0$ and $\omega = \omega_1$. Denoting the left side of Eq.(1) by $f(k, \omega)$, one has, for $\alpha_{1,2} > 0$, from Eqs.(1), (2) that

$$f(k, 0) = - \left[\omega_c^2 + \frac{\eta_0 k}{\epsilon_1 + \epsilon_2} \left(1 + \frac{\eta_0}{2kc^2} \right) \right] < 0$$

for any values of $k \geq 0$. From the other hand

$$f(k, \omega_1) = \left[\frac{k^2 c^2}{\epsilon_1} \left(1 + \frac{\eta_0}{c^2 k} \sqrt{\frac{\epsilon_1}{\epsilon_1 - \epsilon_2}} \right) - \omega_c^2 \right] > 0$$

only for $k \geq k_0$, where

$$k_0 = \frac{1}{2} \left[\sqrt{a^2 + \frac{4\omega_c^2 \epsilon_1}{c^2}} - a \right] \quad (3)$$

with

$$a = \frac{\eta_0}{c^2} \sqrt{\frac{\epsilon_1}{\epsilon_1 - \epsilon_2}}.$$

In Fig.1, the 2D magnetoplasmon-polariton dispersion (curve 1) terminates at the point (k_0, ω_0) , where $\omega_0 = ck_0/\sqrt{\epsilon_1} < \omega_c$. It follows from Eq.(3) that $k_0 = 0$ and hence $\omega_0 = 0$ only when $\omega_c = 0$ or/and $\epsilon_1 = \epsilon_2$ ($\lim_{\epsilon_1 \rightarrow \epsilon_2} k_0 = 0$).

Note that one can find a solution $\omega(k)$ for $0 < k < k_0$ (curve 2 in Fig.1) but only when α_1 is negative. Obviously, such a solution has no physical meaning since it is infinitely growing away from the surface $z = 0$ into medium 1. Perhaps just this solution was mistaken by the author of Ref.[2] for an extension of the surface 2D magnetoplasmon-polariton dispersion into the low frequency band $0 < \omega < \omega_0$.

The cyclotron-polariton dispersion dependencies (curve 3 and 4 in Fig.1) are obtained upon transition to the complex-valued frequencies $\omega \rightarrow \tilde{\omega}$, where $\tilde{\omega} = \omega + i\gamma$ in Eqs.(1), (2) in deciding on negative signs before radicals in Eqs.(2). Dispersion curves $\omega(k)$ almost entirely reside inside the region $\omega > kc/\sqrt{\epsilon_1}$. The imaginary part γ of the complex-valued frequency refers to the radiative damping of the cyclotron oscillations. For the radiative polaritons, the transverse wave numbers $\alpha_{1,2}$ are the complex-valued quantities with $\text{Re}\alpha_{1,2} < 0$ and $\text{Im}\alpha_{1,2} < 0$ which correspond to the outgoing electromagnetic waves with growing amplitudes away from the 2D electron layer into media 1 and 2. Such amplitude-phase pattern is a common one for the radiative eigenmodes in open electromagnetic resonant systems [4].

It follows from Fig.1 that the cyclotron-polariton radiative damping increases roughly as N_s . When N_s grows, the cyclotron-polariton dispersion curve progressively penetrates into the region $k > \omega\sqrt{\epsilon_1}/c$. At smaller N_s , a well-defined dip on the radiative damping curve appears as the dispersion curve $\omega(k)$ intersects the light line $\omega = ck/\sqrt{\epsilon_2}$. The depth of the dip increases when N_s grows smaller. The physical reason for the dip in the radiative damping may be clarified as follows. At a sufficiently small 2D electron density, the radiative damping is much less than the cyclotron-polariton eigenfrequency. It follows from Eq.(2) that in this case $\text{Re}\alpha_2 \ll \text{Im}\alpha_2$ which means that a nearly uniform plane electromagnetic wave is emitted into medium 2 at an angle of $-\arctg(\text{Im}\alpha_2/k)$ to the plane of the 2D system. One can see from Eq.(2) that $\arctg(\text{Im}\alpha_2/k) \approx 0$ as $k = \omega\sqrt{\epsilon_2}/c$. In this situation the electromagnetic wave is emitted along x -direction, i. e. along the axes of dipoles resulting from nonhomogeneous cyclotron oscillations in the plane of 2D system. Clearly the emission intensity (it is proportional to the radiative damping) is vastly reduced at such angles.

Using the term introduced in Ref.[5], one can relate the radiative cyclotron oscillations to the virtual excitations. These excitations can not exist in the system for long since they are subjected to radiative decay. However, such excitations may reveal themselves as absorption resonances when an external electromagnetic wave is transmitted through the 2D electron layer. In order to excite the nonhomogeneous 2D cyclotron oscillations one has to use the oblique incidence of the electromagnetic wave.

This work has been supported by the Russian National Foundation for Basic Research through grant No. 96-02-19211.

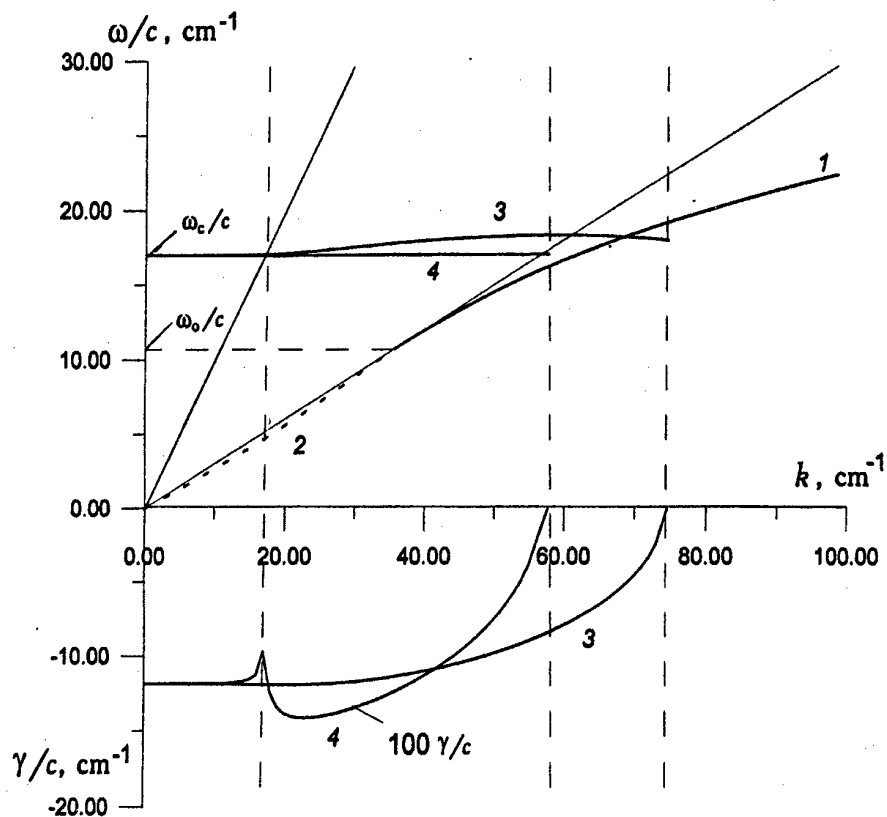


Fig. 1. The frequencies (ω) and radiative damping (γ) for the non-radiative surface magnetoplasmon-polaritons (curve 1) and for the cyclotron-polaritons (curves 3, 4). Curve 2 refers to the "non-physical" branch. $N_s = 10^{12} \text{ cm}^{-2}$ for curves 1, 2 and 3, and $N_s = 10^{10} \text{ cm}^{-2}$ for curves 4

References.

1. K.W.Chiu, J.J.Quinn, Plasma oscillations of a two-dimensional electron gas in a strong magnetic field, Phys. Rev. B, Vol.9, No.11, pp.4724-4732, 1974.
2. M.S.Kushwaha, Interface excitations associated with double inversion layers in SIS heterostructures in a transverse magnetic field, Solid State Commun., Vol.67, No.10, pp.933-997, 1988.
3. O.R.Matov, O.F.Meshkov, O.V.Polishchuk, V.V.Popov, A theory of electromagnetic emission of two-dimensional magnetoplasma and cyclotron oscillations in a semiconductor heterostructure with a periodic screen, JETP, Vol.82, No.3, pp.471-478, 1996 (Zh. Eksp. Teor. Fiz., Vol.109, No.3, pp.876-890, 1996).
4. L.A.Vainstein, Otkrytye resonatory i otkrytye volnovody (Open resonators and open waveguides), Sovetskoe Radio, Moscow, pp.319-324, 1966.
5. A.Harstein, E.Burstein, J.J.Brion, R.F.Wallis, Virtual excitation type surface polaritons on anisotropic media, Solid State Commun., Vol.12, No.10, pp.1083-1086, 1973.

PERTURBATION OF QUASIOPTICAL DIELECTRIC RESONATOR BY A RADIAL SLOT WITH ANISOTROPIC SUBSTRATE

N.T.Cherpak, E.V.Izhyk, A.Ya.Kirichenko, A.Ya.Dan'ko¹, A.T.Budnikov¹ and V.G.Pedyash²
 Usikov Institute for Radiophysics and Electronics, National Academy of Sciences, Ukraine
 12, acad. Proskura str., Kharkov, 310085, Ukraine
 Tel.: 38 0572 448 363; Fax: 38 0572 441 105; E-mail : cherpak@ire.kharkov.ua

¹⁾ Institute of Single Crystals, National Academy of Sciences, Ukraine
 60, Lenin av., Kharkov, 310001, Ukraine
²⁾ Kharkov State Polytechnical University
 21, Frunze str., Kharkov, 310002, Ukraine

Dielectric resonators with waves (or oscillations) of whispering gallery type, which are named as the quasioptical dielectric resonators (QDR or WGR), initiate stable interest from a point of view of both electrodynamic study and various applications [1]. The perturbed QDR is special interest, because its properties manifest themselves in real physical systems. The QDR perturbation can be local or distributed. The local perturbation with a narrow radial slot have been studied and used for quality monitoring of dielectric films [2]. Details of QDR with two radial slots studied in [3]. It was shown by experiment that QDR with one or two slots can be used for isotropic dielectric permittivity measurements of large-area substrates including single crystal ones for HTS films [4].

Low dielectric losses, moderate value of dielectric permittivity, low temperature coefficients of dielectric constant and linear expansion along with high thermal conductivity make sapphire (Al_2O_3) substrate more attractive for HTS microwave devices in comparison with the others [5]. However anisotropy of dielectric constant leads to complex design problems, limiting application of sapphire-based HTS devices. Thus nondestructive methods necessity of monitoring the anisotropic substrate characteristics arises.

This work describes study results of QDR with narrow radial slot containing thin sapphire substrate with arbitrary orientation of optical axis relative to the substrate plane. Resonance frequency was measured as a function of both C -axis orientation angle, α , with respect to the substrate and angle, φ , of substrate rotation about substrate geometric axis in the slot.

Measurements were carried out at 8mm waveband by means of teflon QDR with diameter of 75 mm and hight of 5 mm. EH_{11n} -mode of the higher-order azimuthal oscillations was used ($n=14-16$). The slot width was equal to 0.5 mm. The sapphire substrate diameter was ≈ 50 mm. Herewith C -axis and the plane substrate made the angle, α , of: 0° (parallel orientation), 34° (tilted orientation) and 90° (normal orientation). At substrate rotation about geometric axis of the substrate the resonant frequency was changed and at that trend of the dependence of frequency f against φ -angle was influenced by the α -angle (Fig.1).

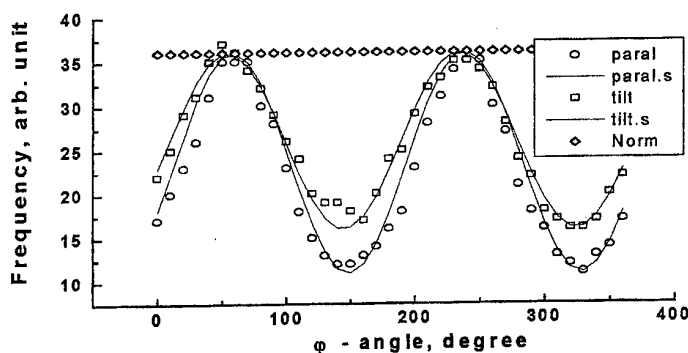


Fig.1. Dependence of the resonance frequency of QDR versus φ -angle at three meanings of α -angle as a parameter.

Analysis of the data on the Fig.1 allowed to have noted a number of points. Firstly, as we waited, the frequency, f , did not depend on rotation φ -angle for normal C -axis orientation. Secondly, f as function of φ was sine, and the sine amplitude

$$\Delta f = f_{\max} - f_{\min}$$

depended on the α -angle i.e. on C -axis orientation in the substrate. Thirdly, at some values of the φ -angle the frequency, f , did not depend on α -angle.

The latter must be commented. The matter is that in the general case of radial, E_r , and azimuthal, E_φ , components presence, relative position of the curves on the Fig.1 must be another. Analysis of obtained experimental data on Fig.1 gives a cause to state that, at the last at the slot area, $E_r >> E_\varphi$. Only in this case we can to understand wonderful, at the first sight, independence of the frequency, f , on C -axis orientation, when magnitude of dielectric permittivity along the E_φ -component varies between ϵ_\parallel and ϵ_\perp .

Fig.2 shows δf as a function of α -angle. Experimental data have been obtained for the substrates with three different C -axis orientations. As analytical expression for dependence $\delta f(\alpha)$ is unknown yet we have

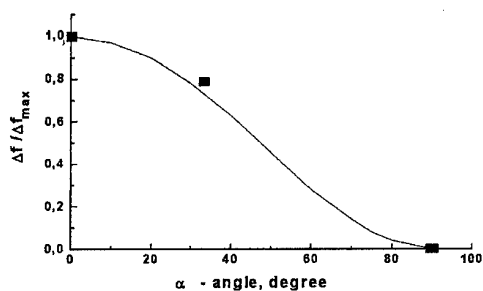


Fig.2. Dependence of normalized frequency maximal variation for QDR with sapphire substrate in radial slot versus α -angle between C -axes and the substrate plane.

used some functional dependences for effective dielectric permittivity, ϵ_{eff} . On the Fig.2 solid line corresponds to expression

$$\epsilon_{eff} = \epsilon_\perp \sin^2 \alpha + \epsilon_\parallel \cos^2 \alpha.$$

Although total validity of above approximation now can be established only by the more detailed experiment, this circumstance does not obstruct to use experimental dependence $\delta f(\alpha)$ for microwave measurements of C -axis orientation in the sapphire substrates and the other analogous single crystal ones. The obtained results show an evident procedure of determining the substrate optical-axes orientation. The minimal (maximal) frequency corresponds to position of the substrate cross-section plane with optical axes that is parallel (normal) to the QDR plane. The average of these two measurement results identifies the plane with the optical axes. At last, the C -axes orientation with respect to a plane or geometric axes of the QDR is determined after difference of $\Delta f = f_{\max} - f_{\min}$. An average derivative, $d\alpha/df$, equals to $\approx 0.4^\circ$ per MHz and somewhat decreases at $\alpha < 20^\circ$ and at $\alpha > 70^\circ$.

References

1. N.T.Cherpak, Yu.F.Filipov, S.N.Kharkovsky, A.Ya.Kirichenko, Quasioptical Dielectric Resonators in Millimeter Waves, The International Journal of Infrared and Millimeter Waves, Vol.14, No.3, pp.617-627, 1993.
2. Ye.V.Bykov, A.P.Geppe, V.S.Dobromyslov, V.V.Kostromin, Measurement of Polimeric Film Dielectric Permittivity Using Disc Dielectric Resonators, Elektronnaya Tehnika. Elektronika SVCh, Vol.61, No.6, pp. 61-65, 1986 (in Russian).
3. Yu.F.Filipov, S.N.Kharkovsky, Resonant Frequency Spectra of Nonhomogeneous Disc Dielectric Resonator, Izv. VUZ'ov. Radiofizika, Vol.33, No.11, pp.1304-1306, 1990 (in Russian).
4. N.T.Cherpak, E.V.Izhyk, A.Ya.Kirichenko, M.B.Kosmyna, A.V.Velichko, Dielectric Constant Characterization of Large-Area Substrates in Millimeter Wave Band, The International Journal of Infrared and Millimeter Waves, Vol.17, No.5, pp.819-831, 1996.
5. Z-Y. Shen, High-Temperature Superconducting Microwave Circuits, Artech House, Boston, London, 1994.

ON COLLISIOLESS DAMPING OF SURFACE PLASMONS

V.M. Yakovenko, I.V. Yakovenko*

Institute of Radiophysics and Electronics, National Academy of Sciences
of Ukraine, 12, Acad. Proskura st., 310085, Kharkov, Ukraine

*Research and Design Institute "Molniya", Ministry of Education of Ukraine,
47, Shevchenko st., 310013, Kharkov, Ukraine
Tel.: 380 572 448 317; Fax: 380 572 441 105; E-mail: yakovenko@ire.kharkov.ua

In papers [1,2] the investigation of the surface wave properties in the plasma like media has been carried out taking into account the spatial dispersion of permittivity under condition of the specular reflection from the media interface. Here it was shown that the spatial dispersion leads to the collisionless damping (the Landau damping) of the surface plasmons whose decrement differs from that for Langmuir oscillations in the infinite medium. Collisionless damping of plasmons in the quantum case when electrons are specularly reflected from the boundary and plasmon energy exceeds the temperature of the electron gas was considered in papers [3,4]. In spite of the fact that collisionless wave damping was discovered more than 50 years ago this interesting phenomenon calls attention of physicists as before [5].

The paper proposed is devoted to studying the mechanism of collisionless damping of the surface plasma oscillations at an arbitrary character of the electron reflection from the media interface. It was found the dependence of the decrement on a parameter characterizing the electron scattering process at the boundary. It is shown that the damping of the surface plasmons is caused by their transformation into Van Kampen waves [6,7] propagating from the interface with particle velocity.

Let region $y > 0$ be occupied by the plasma medium. The situation when the waves are slow and the delay effect can be neglected is of the most interest here. In this case the properties of the medium are described by the following system:

$$\text{rot} \vec{E}(x, y, t) = 0; \quad \epsilon_0 \text{div} \vec{E} = 4\pi en; \quad e \frac{\partial n}{\partial t} + \text{div} \vec{j} = 0; \quad (1)$$

$$\vec{j} = e \int \vec{v} f(x, y, t, \vec{p}) d\vec{p}; \quad (2)$$

$$\frac{\partial f}{\partial t} + \vec{v} \frac{\partial f}{\partial \vec{r}} + e \vec{E} \vec{v} f'_0 = -\nu f, \quad (3)$$

where ϵ_0 is the lattice permittivity, $f_0(\vec{p})$ is the equilibrium function of the electron distribution, f'_0 is its derivative with respect to energy, f is a small addition to the distribution function in a perturbed state, ν is the electron collision frequency.

Hereafter the dependence of all values appearing in equations (1)-(3) on coordinates and time will be represented as:

$$\vec{E}(x, y, t) = \vec{E}(\omega, q_x, y) \exp[i(q_x x - \omega t)].$$

Here axis x is parallel to the boundary and for the definiteness we suppose: $\omega > 0, q_x > 0$.

The general solution of kinetic equation 3) can be written as

$$f = -\frac{e f'_0}{v_y} \int_c^y \vec{E} \vec{v} \exp[i \frac{\tilde{\omega}}{v_y} (y - y')] dy', \quad (4)$$

where $\tilde{\omega} = \omega - q_x v_x + i\nu$.

Constant C is determined from the boundary conditions for the distribution function at $y = 0$ and $y = \infty$. Let us denote the distribution functions by f^- and f^+ for the particles with $v_y < 0$ and $v_y > 0$, correspondingly. Then we obtain from the condition that f^- is the finite quantity at $y = \infty$

$$f^- = \frac{e f'_0}{v_y} \int_y^\infty \vec{E} \vec{v} \exp[i \frac{\tilde{\omega}}{v_y} (y - y')] dy', \quad (5)$$

Taking into account the fact that the surface oscillations exist under conditions of a cold plasma and their damping caused by the thermal movement of the particles is small [1-3], one can restrict oneself to the approximation of a weak space dispersion. Here $\omega \gg q_x v_x$, the depth of the field penetration into medium is large as compared with the scale characterizing the spatial dispersion, and coupling between $f(y)$ and $\vec{E}(y)$ can be made local. Then expression (5) can be simplified. Changing variables $y' - y = z$ and expanding the field $\vec{E}(y + z)$ in z series we obtain

$$f^- = \frac{ef'_0}{i\omega} \vec{E} \vec{v}; \quad \omega \gg \nu.$$

In order to find C at $v_y > 0$, let us formulate the condition at the surface $y = 0$. If we denote the fraction of particles reflected from the boundary specularly by δ and diffusely by $1 - \delta$ then can be written [7]

$$f^+(v_x, v_y, y = 0) = \delta f^-(v_x, -v_y, y = 0). \quad (6)$$

Hence we find:

$$f^+ = -\frac{ef'_0}{v_y} \int_0^y \vec{E} \vec{v} \exp[i\frac{\omega}{v_y}(y - y')] dy' + \delta \frac{ef'_0}{i\omega} [E_x(0)v_x - E_y(0)v_y] \exp(i\frac{\omega}{v_y}y). \quad (7)$$

Having performed the corresponding change of variable in formula (7) and holding the largest terms of the field expansion we finally obtain for f^+

$$f^+ = \frac{ef'_0}{i\omega} \vec{v} \vec{E}(y) + F(\omega, q_x, y, \vec{p}) \exp(i\frac{\omega}{v_y}y), \quad (8)$$

where

$$F(\omega, q_x, y, \vec{p}) = \frac{ef'_0}{i\omega} \left\{ \delta[v_x E_x(0) - v_y E_y(0)] - \vec{v} \vec{E}(y) \right\}.$$

In expression (8) the additive containing the multiplier $\exp i\frac{\omega}{v_y}y$, described the Van Kampen waves excited and propagating along the positive direction of the axis y near the plasma boundary.

As a result the conductivity current and electric induction of medium $\vec{D} = \epsilon_0 \vec{E} + \frac{4\pi i}{\omega} \vec{j}$ take the form

$$\vec{j}(\omega, q_x, y) = \frac{i\omega_0^2}{4\pi\omega} \vec{E}(\omega, q_x, y) + e \int \vec{v} F(\omega, q_x, y, \vec{p}) \exp(i\frac{\omega}{v_y}y) d\vec{p} \quad (9)$$

$$\vec{D}(\omega, q_x, y) = \epsilon(\omega) \vec{E}(\omega, q_x, y) + \frac{4\pi i}{\omega} \int \vec{v} F(\omega, q_x, y, \vec{p}) \exp(i\frac{\omega}{v_y}y) d\vec{p} \quad (10)$$

where $\epsilon(\omega) = \epsilon_0 - \frac{\omega_0^2}{\omega^2}$, ω_0 is the Langmuir electron frequency, integration is performed with respect to positive values v_y .

The system of equations (1) is transformed to equation

$$\frac{\partial^2 E_x}{\partial y^2} - q_x^2 E_x = \frac{4\pi i e q_x}{\epsilon(\omega)} \int F(\omega, q_x, y, \vec{p}) \exp(i\frac{\omega}{v_y}y) d\vec{p} \quad (11)$$

where $E_y = -\frac{i}{q_x} \frac{\partial E_x}{\partial y}$.

As far as the oscillation decrement is small as compared with frequency this equation can be solved by the method of successive approximations. Supposing the right part to be small we obtain at $\frac{\omega^2}{v_y^2} \gg q_x^2$

$$E_x = A \{ \exp(-q_x y) + \frac{4\pi i e^2 q_x (1 + \delta)}{\omega^3 \epsilon(\omega)} \int_{v_y > 0} v_y^3 f'_0 \exp(i\frac{\omega}{v_y}y) d\vec{p} \} \quad (12)$$

This solution is worth only near the boundary when $0 \leq y \leq \frac{1}{q_x}$

In this approximation the normal vector component of electrical induction appears to be equal to $D_y(\omega, q_x, y) = i\epsilon(\omega)A \exp(-q_x y)$, that is for Van Kampen waves bias currents $\epsilon_0 \frac{\partial \vec{E}}{\partial t}$ and conductivity \vec{j} along axis y compensate each other.

In the domain $y < 0$ (with non-dissipative media with permittivity ϵ_d) $F(\omega, q_x, y, \vec{p}) = 0$, the fields take form

$$E_x = B \exp(q_x y); E_y = -iB \exp(q_x y) \quad (13)$$

By using further the continuity conditions of the tangential component \vec{E} and the normal component \vec{D} at the boundary $y = 0$, we find the following dispersion equation for surface plasmons

$$\epsilon(\omega) + \epsilon_d = -\frac{4\pi ie^2 q_x (1 + \delta)}{\omega^3 \epsilon(\omega)} \epsilon_d \int_{v_y > 0} v_y^3 f'_0 d\vec{p} \quad (14)$$

Thus we obtain the natural frequency of the surface plasmons and their decrement

$$\omega = \frac{\omega_0}{\sqrt{\epsilon_0 + \epsilon_d}} + i\gamma \quad (15)$$

where

$$\gamma = \frac{2\pi e^2 q_x}{\omega_0^2} (1 + \delta) \int_{v_y > 0} v_y^3 f'_0 d\vec{p}.$$

It appears to be equal to $\gamma_M = -\frac{(1 + \delta)}{\sqrt{2\pi}} q_x v_T$ in the case of the Maxwell particle distribution with the average thermal velocity v_T or $\gamma_F = -\frac{(1 + \delta) q_x v_F}{16}$ for the degenerated gas with fermi velocity v_F . In the case of the specular reflection of particles these formula go to the known results [1-3]. The decrement of the surface plasmons is reduced in two times at the diffusion reflection $\delta = 0$.

In conclusion the authors express their gratitude to Dr. V.L. Falko and Dr. Yampolsky for discussing the results of the paper.

References

1. Yu.A. Romanov, "Electromagnetic waves in a half space plasma", Izv. VUZ, Radiophysics, Vol. 7, pp. 242-254, 1964.
2. A.F. Alekandrov, L.S. Bogdankevitch, and A.A. Rukhadze, "Principles of electrodynamics of plasma", Vysshaya shkola, M., 407 p., 1978.
3. V.M. Yakovenko, I.V. Yakovenko, "Interaction of surface plasmons with charge carries at media interface", Phys. Let. A, Vol. 196, pp. 290-294, 1994.
4. V.L. Falko, S.I. Khankina, and V.M. Yakovenko, "Collisionless damping of surface plasmons", Low Temp. Phys., Vol. 22, No.10, pp. 877-881, 1996.
5. Yu.L. Klimontovich, "Physics of collisionless plasma", Uspekhi Fiz. Nauk., Vol.167, No 1, pp. 23-55, 1997.
6. B.B. Kadomtsev, "Collective phenomena in plasma", Nauka, M., 238 p., 1976.
7. V.P. Silin, A.A. Rukhadze, "Electromagnetic properties of plasma and plasma-like media", Atomizdat, M., 244 p., 1961.

Quantizing of transition radiation of the surface polaritons by the charge, intersecting two-layer two-dimensional electron system, placed into strong magnetic field.

Yu.O.Averkov, N.N.Beletskii, V.M.Yakovenko

Institute for Radiophysics and Electronics National Academy of Sciences of Ukraine,
12 Acad. Proskura str, 310085, Kharkov, Ukraine. Tel.: 38 (0572) 448-474,
Fax: 38 (0572) 441-105, E-mail: averkov@online.kharkiv.net

Recently close attention has been paid to the two-dimensional electron systems (2DES), the fundamental properties of which have a number of interesting peculiarities (phase transitions, electron localization effects, surface polaritons (SP) and others). It is evident that some of them will be revealed while investigating the losses of energy by the charged particles, going through the 2DES, for instance, their transition radiation.

In the present paper [1] the transition radiation of SP is theoretically investigated, which appears when the charge is moving through the homogeneous isotropic medium with the dielectric constant ϵ , into which the two-layer 2DES, placed in the transversal quantizing magnetic field \tilde{B} (i.e. $\hbar\Omega \gg T$, where \hbar is Plank's constant, Ω is the cyclotron frequency of the electron, T is the temperature in energy units), is implanted. The two-layer 2DES consists of two GaAs infinitely deep quantum wells separated by a AlGaAs potential barrier of finite width and height. The quantizing magnetic field and the direction of the charge movement are perpendicular to the 2DES. The energy spectrum of the electrons in such system is fully discrete, and this leads to stepwise dependencies of Landau level filling factor N and Hall's conductivity of the two-layer 2DES σ_H on the magnetic field B . In its turn, as it is shown in the paper, the stepwise character of the dependency $N(B)$ (see the dash curve on Fig.2) leads to the quantizing of the spectrum density of the SP transition radiation energy flow (see Fig.1) and to the non-monotonous (saw-like) dependency of the SP energy flow (see Fig.2) on the magnetic field.

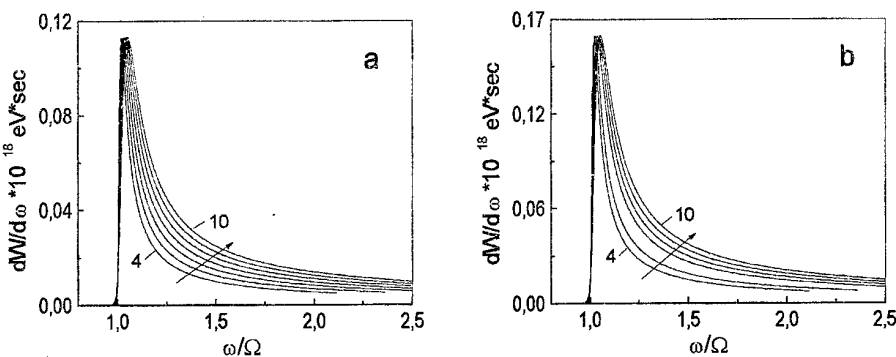


Fig.1. The spectrum density of the SP transition radiation energy flow $dW / d\omega$. Fig.1a is the case of presence the all Hall's plateaux on dependency $N(B)$. Fig.1b is the case of absence the Hall's plateau with $N=6$. Arrow indicates the direction of increasing of filling factor N .

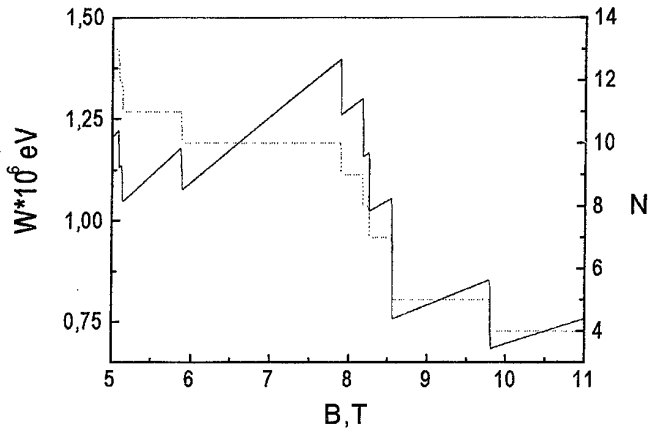


Fig.2. The dependency of the SP energy flow W on the magnetic field (solid curve). The dependency of $N(B)$ is shown by the dash curve. The case of absence the Hall's plateau with $N=6$ is considered.

As it has been discovered by the authors, some values of the geometric dimensions of the 2DES can lead to the situation when the point of intersection of two spin-splitting Landau levels will lie at the Fermi level. This will lead to the disappearance of the plateau on the dependency $N(B)$ with a certain value of Landau level filling factor N (both with even and odd values) and to the disappearance of the plateau on the dependency $\sigma_H(B)$ as the Hall's conductivity $\sigma_H(B)$ is proportional to N :

$$\sigma_H = \frac{e^2}{h} \frac{N}{1 + \xi^2}, \quad (1)$$

where $\xi = (v - i\omega)/\Omega$, v is the momentum relaxation frequency. Let us note that the effect of the Hall's plateau disappearance with odd value of N was observed in [2].

The absence of the Hall's plateau with a certain value of N is shown to be the reason of the disappearance of the spectrum density curve (see Fig.1b) with the same value of N as well as the step of maximum value on the dependency $W(B)$ (see Fig.2).

The spectrum density of the SP transition radiation energy flow was found to be described by following expression:

$$\frac{dW}{d\omega} = \frac{q_0^2 \beta^3 \omega}{8 \epsilon v_0^2 c^2 \gamma^2 [\beta^2 + \omega^2 / v_0^2]^2} [\epsilon \Omega^2 + (\alpha \Omega N + c \beta)^2], \quad (2)$$

where $\beta^2 = \gamma^2 - \epsilon \omega^2 / c^2$, γ is the solution of the dispersion equation describing the SP propagation [3].

In the case of slow SP (when $v_{ph} \ll c$, where v_{ph} is the phase velocity of the SP, c is the light velocity in vacuum) in high magnetic fields ($N \leq 10$) the transition radiation energy W is described by the following equation:

$$W = \frac{\alpha q_0^2 v_d \Omega}{8 \epsilon^{3/2} v_0^2} N \ln \left(\frac{v_0}{\Omega l} \right), \quad (3)$$

where $\alpha = e^2/(c\hbar)$ is the fine structure constant, e is the electron charge, q_0 is the charge of the particle intersecting the two-layer 2DES, v_0 is the velocity of the charge, $v_d = c / \sqrt{\epsilon}$ is the light velocity in the dielectric, $l = (c\hbar / eB)^{1/2}$ is the magnetic length.

From (3) it is seen that the dependency of W on the magnetic field B is practically linear and it experiences steps, conditioned by the stepwise dependency $N(B)$. To each of the linear sections of the dependency $W(B)$ corresponds its value of N .

The value of N of the disappearing plateau can be easily found from (3). From the condition of the spin-splitting Landau levels intersection at Fermi level the authors have found the relation between the width of the potential barrier, the value of the electrons g-factor in the 2DES and the value of the N filling factor for the disappearing plateau on the dependency $\sigma_H(B)$ (see Fig.3). With the help of this relation, the value of the electrons g-factor in the 2DES can be found from the known values of the system geometric dimensions and the N value of the disappearing plateau.

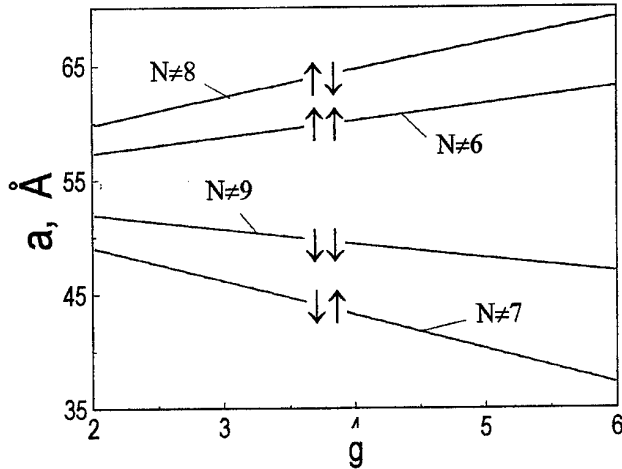


Fig.3. The relation between the half-width of the potential barrier (a), the value of the electrons g-factor in the 2DES and the value of the N filling factor for the disappearing plateau on the dependency $\sigma_H(B)$. The symbols \downarrow and \uparrow shows the electrons spin orientations of intersecting energy levels.

Thus, the authors the effect of disappearing of some Hall's plateau on the dependency $\sigma_H(B)$ (both with even and odd values) have been predicted. Besides, the effect of quantizing of the SP transition radiation energy flow have been predicted too. A new contactless method for determining the electron g-factor in the 2DES has been proposed. This method is based on the properties of the slow SP energy, radiated by the charge, intersecting the two-layer 2DES.

References

1. Yu. O. Averkov, N.N. Beletskii, "Transition radiation of the surface polaritons by the charge, intersecting a two-layer two-dimensional electron system placed into strong magnetic field" (in Russian), Doklady NANU, No. 1, pp. 96-102, 1998.
2. G.S. Boebinger, H.W. Jiang, L.N. Pfeiffer, and K.W. West, "Magnetic-field-driven destruction of quantum Hall states in a double quantum well", Phys. Rev. Lett., Vol. 64, No. 15, pp. 1793-1796, 1990.
3. I.E. Aronov and N.N. Beletskii, "Fundamental steps of the group velocity for slow surface polaritons in the two-dimensional electron gas in a high magnetic field", J. Phys. Condens. Matter, Vol. 8, pp. 4919-4936, 1996.

NON-RADIATIVE POLARITONS IN A GaAs/AlGaAs HETEROSTRUCTURES UNDER QUANTUM HALL EFFECT CONDITIONS

N.N.Beletskii, S.A.Borisenko

Institute for Radiophysics and Electronics National Academy of Sciences of Ukraine,

12 Acad. Proskura St., Kharkov, 310085, Ukraine

Tel.: (380)572-448474, Fax: (380)572-441105, E-mail: beletski@ire.kharkov.ua

Surface polaritons on the boundaries of the two-dimensional electron systems (2DES), in the external magnetic field, attract close attention [1-3]. The case of high magnetic field, when there is the integer quantum Hall effect (IQHE) in 2DES, is of particular interest [2,3]. Under the IQHE conditions the components of 2DES high-frequency conductivity tensor are quantized, i.e. they exhibit step-wise behavior with the change of magnetic field. As the result all the characteristics of the SP are becoming quantized, too. The properties of the SP under IQHE conditions have been investigated in detail for two cases: a single 2DES [2] and a double 2DES [3]. In these papers it has been shown that the SP group velocity under IQHE conditions experiences steps, which are proportional to the fine-structure constant, $\alpha = e^2 / c\hbar$, where e is the electron charge, c is the light velocity, $\hbar = h/2\pi$, h is Plank's constant.

The properties of the SP have been investigated in [2] under the assumption that the surface taken by 2DES is placed into homogeneous medium with dielectric constant ε . In reality, the actual structure of GaAs/Al_xGa_{1-x}As heterojunction, which is modeling the 2DES, is more complex. Actually, the doped Al_xGa_{1-x}As layer has finite thickness. As the result, the electrons forming the 2DES, lie between the GaAs layer (this layer forms substrate and its thickness can be considered to be infinite) and the Al_xGa_{1-x}As layer, which has a boundary with vacuum/air. Besides, in [2] it has been pointed out that dielectric constants Al_xGa_{1-x}As and GaAs are different. In these papers the ratio of Al_xGa_{1-x}As dielectric constant to that of GaAs was equal to 0.95. These circumstances can lead to new qualitative peculiarities in the propagation of surface polaritons along the real GaAs/Al_xGa_{1-x}As heterojunction. Besides, in real situation the dissipation in 2DES must be taken into account. It can lead not only to quantitative change in SP spectrum, but also to the emergence of new types of non-radiative polaritons (both surface and bulk types), electromagnetic field of which exponentially decreases from both boundaries of Al_xGa_{1-x}As layer.

In this paper, we investigate the non-radiative polaritons in real GaAs/Al_xGa_{1-x}As heterojunction under IQHE conditions. The influence of Al_xGa_{1-x}As layer thickness and the degree of energy dissipation in 2DES over the existence conditions, the spectrum and damping of non-radiative polaritons is investigated. It is shown that in addition to SP, which are localized at GaAs/Al_xGa_{1-x}As boundary, another type of SP can exist in the heterojunction, and they are localized at Al_xGa_{1-x}As-vacuum/air boundary (Brewster's modes). It is found that in addition to these two types of SP, bulk polaritons of various orders can propagate in GaAs/Al_xGa_{1-x}As heterojunction, which possess one or several maximums of energy flow in Al_xGa_{1-x}As layer. It is pointed out that under IQHE conditions all the characteristics of surface and bulk polaritons are quantized. It is determined that if the wave number changes, surface and bulk polaritons can continuously transform one into another.

As a model for GaAs/Al_xGa_{1-x}As heterojunction we consider the structure shown in Fig.1. It consists of two semi-infinite media: 1 ($z > d$) and 3 ($z < 0$) with dielectric constants ε_1 and ε_2 , accordingly. Between these media there is a semiconductor layer of d thickness (medium 2) with dielectric constant ε_2 . Let medium 2 represent the Al_xGa_{1-x}As semiconductor, and medium 3 represent the GaAs semiconductor. These two semiconductors form a 2DES at the boundary $z = 0$. The external quantizing magnetic field \vec{B} is directed along z axis, perpendicularly to the 2DES. We assume that the polaritons in the structure considered are non-radiative, i.e. their electromagnetic field in media 1 and 3 decrease exponentially with the increase of the distance from layer 2 boundaries. We consider that non-radiative polaritons propagate along x axis. The dependence of all electromagnetic fields on x co-ordinate and time t we describe by the expression $\exp[i(kx - \omega t)]$, where k is the wave number, ω is the wave frequency.

In order to obtain the dispersion equation, describing the propagation of non-radiative polaritons in GaAs/Al_xGa_{1-x}As heterojunction, two wave types must be considered: TE- and TM-waves. This is conditioned by the existence of surface electric current at the 2DES boundary $z = 0$, which mixes both TE- and TM-waves. We believe that at the boundary $z = d$ the tangential components of electric field \vec{E} and magnetic field \vec{H} of the non-radiative waves are continuous, and at the boundary $z = 0$ the tangential components of magnetic field experience a break:

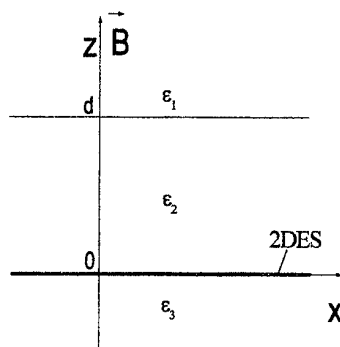


Figure 1. Geometry of problem

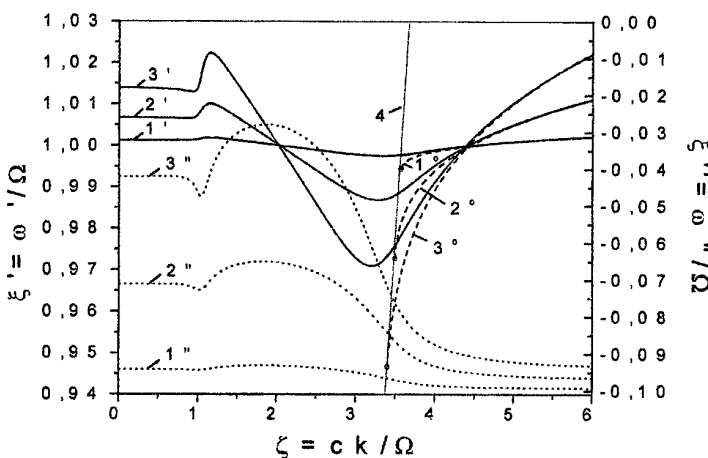
ordinate axis, in the case $\delta = 0.1$, $\Gamma = 0.1$ for three values of the Landau-level filling factor N : 1 - $N = 1$; 2 -

$N = 5$; 3 - $N = 10$.

Dashed line 4 corresponds to light line for GaAs ($\xi' = \zeta / \sqrt{\epsilon_3}$).

In the absence of dissipation ($\Gamma = 0$) this line serves as a boundary between the regions of radiative and non-radiative polaritons. Dispersion curves with $''$ index (dashed lines in Fig. 2) correspond just to the case of the absence of dissipation. For N values mentioned above all of them start at light line 4.

In Fig. 2 it is seen that the presence of dissipation in 2DES leads to broadening of the existence area of the non-radiative polaritons: they exist for all values of ζ . To the right of the light line 4,

Figure 2. Spectrum and damping of non-radiative polaritons for different values of N .

dispersion curves change slightly in comparison to the non-dissipative case. In this region electromagnetic field of the non-radiative polaritons decreases exponentially from the 2DES boundary ($z = 0$), i.e. here we deal with surface polaritons. With the approach to light line 4, dispersion curves $\xi'(\zeta)$ shift up in comparison to the non-dissipative ones and they continue non-monotonously up to the ordinate line $\zeta = 0$. In papers [2,3] it has been pointed out that in the vicinity of cyclotron resonance ($\zeta \approx 1$) dispersion curves intersect, in the first approximation, in one point. In Fig. 2 it is seen that taking into account the 2DES dissipation leads to the emergence of two points of dispersion curves intersection. One of them lies to the left of light line 4, the other one lies to the right of it. When going through these points, the dependence manner of non-radiative polaritons frequency ξ' on N (for fixed value of ζ) changes into the opposite. Thus, to the left of the first intersection point of the dispersion curves, polaritons frequency ξ' increases with the increase of N ; in the region of wave numbers ζ , lying between the two points of dispersion curves intersection, polaritons frequency decreases with the increase of N . Finally, to the right of the second intersection point of the dispersion curves, wave frequency ξ' , once more increases with the increase of N . We point out that in region of wave numbers ζ , lying to the left of the first in-

tersection point of the dispersion curves, there is a region on the curve $\xi'(\zeta)$ in which $\partial\xi'/\partial\zeta > 0$. The length of this region increases with the increase of N . We assume that the dispersion curve region with $\partial\xi'/\partial\zeta > 0$ is connected with the emergence of surface polaritons of Brewster mode type at the boundary $z = d$. The possibility for Brewster mode emergence of TM polarization at the boundary of 2 dissipative media, the real parts of dielectric constants of which are positive has been pointed out in scientific literature. The particularity of our case is that the polarization of the SP of Brewster mode type, considered by us, is mixed, and their «attachment» to the $z = d$ boundary appears due to the dissipation of in the 2DES, located at $z = 0$ boundary. It is shown in Fig.2 that Brewster modes emerge if $\zeta \approx \sqrt{\varepsilon_1} = 1$.

Fig. 3 shows for the case $N = 5, \delta = 0.1$ the change of the spectrum $\xi'(\zeta)$ (solid lines with ' index) and the damping $\xi''(\zeta)$ (dotted lines with " index) of non-radiative polaritons for a number of Γ values: 1 -

$$\Gamma = 0.01; 2 - \Gamma = 0.03; 3 -$$

$$\Gamma = 0.05; 4 - \Gamma = 0.1.$$

Dashed lines represents the

$$\text{light line } \xi' = \zeta / \sqrt{\varepsilon_3}$$

for GaAs (medium 3). It follows from Fig. 3 that for low values of Γ ($\Gamma = 0.01-0.03$) dispersion curves $\xi'(\zeta)$ have the of spectrum

start $p_3 = 0$, located to the left of light line 5. In this point electromagnetic field of nonradiative polaritons becomes delocalized, and their damping turns into zero: $\xi'' = 0$. For further increase of Γ the point of spectrum start of nonradiative polaritons shifts to the left and at $\Gamma = 0.05$ it reaches the coordinate axis $\zeta = 0$. At point $\zeta = 0$ we observe surface electro-

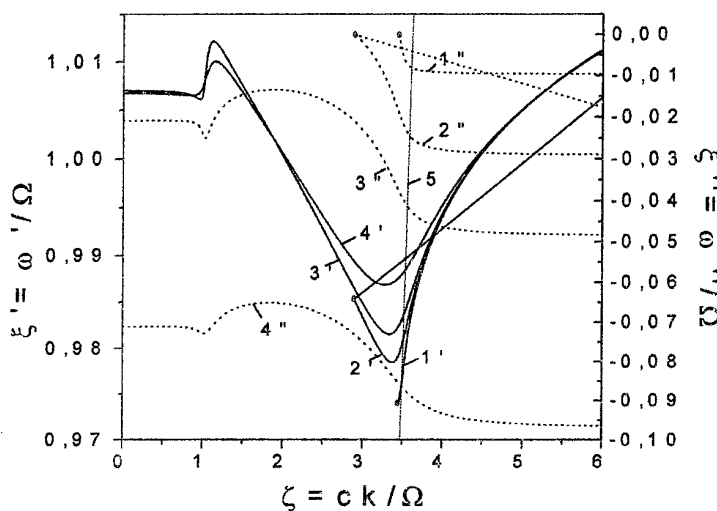


Figure 3. Spectrum and damping of non-radiative polaritons for different values of Γ .

magnetic oscillations, which are circularly polarized in 2DES surface ($E_{x2}/E_{y2} = i$, $H_{x2}/H_{y2} = i$) and the frequency of which depends on the values of δ .

Thus, in the GaAs/Al_xGa_{1-x}As heterojunctions various types of rapid and slow non-radiative polaritons can exist. They can be used for contactless diagnostics of heterojunction parameters: determining the value of Landau-level filling factor, the thickness of the Al_xGa_{1-x}As layer, and the frequency of electron momentum relaxation. Besides, due to the step-like change of non-radiative polaritons properties, they can be used for creating various nanoelectronics devices.

Finally, we point out that experimental investigation of non-radiative polaritons in semiconductors can be carried out by various methods. For instance, with the help of attenuated total reflection method, as well as inelastic light scattering method. The latter method allows to conduct SP investigation for higher values of wave number $k \sim 2 \cdot 10^5 \text{ cm}^{-1}$, which correspond to slow polaritons with phase velocity of the order of 0.01c.

References

1. Yu.A.Kosevich, A.M.Kosevich, J.C.Granada, Phys. Lett., Vol.127A, No1, pp.52-56, 1988.
2. I.E.Aronov, N.N.Beletskii, J.Phys.: Condens. Matter, Vol.8, No.27, pp.4919-4936, 1996.
3. I.E.Aronov, N.N.Beletskii, G.P.Berman, A.R.Bishop, Phys. Rev., Vol.B56, No.8, pp.10392-10403, 1997.

FEATURES OF A SPECTRUM OF MAGNETO-PLASMA WAVES IN PERIODIC SEMICONDUCTING LATTICE

A. A. Bulgakov, O. V. Shramkova

Institute of Radiophysics and Electronics of the NAS of Ukraine

12 Ac. Proskura St, Kharkov, 310085, Ukraine

Tel:+380 (572) 448-323, Fax:+380 (572) 441105, E-mail:<bulgakov@ire.kharkov.ua>

The research of stratified - periodic mediums has been rousing constant interest for scientific literature [1-6] for many years. Quoted papers apply to various materials and various frequency ranges, but the availability of a transmitting symmetry in researched structures is common in these papers. The interest for such researches is due to the fact that the periodic structures represent a new type of artificially created materials. The properties of such structures are easy for operating while changing structure of layers or their dimensions.

The specific pass-band zone arising in stratified - periodic semiconductor - dielectric structure located in a magnetic field is being examined in the paper. The existence of this zone is conditioned by the distribution of surface magneto-plasma waves along the boundaries of a structure, by percolation (or tunneling) of the fields of these waves through layers of a structure and by formation of a "collective" mode.

Let's consider the stratified - periodic structure, that was derived by a periodic recurring of a semiconductor layer of a thickness d_1 and of a dielectric layer with a thickness d_2 . Let's direct an axis Z perpendicularly to boundaries of strata. The external magnetic field is supposed to have applied in a direction of an axis OY. Let's examine the distribution of magneto-plasma waves in a plane XOZ, that is perpendicularly to the magnetic field.

Then, in consequence of homogeneity of a medium in a direction OY, it is supposed, that $\frac{\partial}{\partial y} = 0$. The result is that the Maxwell's equations disintegrate on the equations for two polarizations: first — with components of fields E_x, E_z, H_y , second — with components H_x, H_z, E_y . The first polarization is investigated hereinafter.

From the Maxwell's equations with allowance of continuity of a tangential components of electromagnetic field on the boundaries of a structure with the help of Floquet's theorem we shall receive a dispersion relation :

$$\cos \bar{k}d = \cos k_{z1}d_1 \cos k_{z2}d_2 - \frac{\epsilon_{f1}\epsilon_2}{2k_{z1}k_{z2}} \left[\left(\frac{k_{z1}}{\epsilon_{f1}} \right)^2 + \left(\frac{k_{z2}}{\epsilon_2} \right)^2 - k_x^2 \left(\frac{\epsilon_{\perp 1}}{\epsilon_{II1}\epsilon_{f1}} \right)^2 \right] \sin k_{z1}d_1 \sin k_{z2}d_2, \quad (1)$$

$$k_{z1} = \left[\frac{\omega^2 \epsilon_{f1}}{c^2} - k_x^2 \right]^{\frac{1}{2}},$$

$$k_{z2} = \left[\frac{\omega^2 \epsilon_2}{c^2} - k_x^2 \right]^{\frac{1}{2}}$$

$$\epsilon_{f1} = \epsilon_{II1} + \epsilon_{\perp 1}^2 / \epsilon_{II1},$$

$$\epsilon_{\perp} = -i\epsilon_0 * \frac{\omega_p^2 \omega_H}{\omega \left[(\omega + i\nu)^2 - \omega_H^2 \right]}, \quad \epsilon_{II} = \epsilon_0 * \left(1 - \frac{\omega_p^2 (\omega + i\nu)}{\omega \left[(\omega + i\nu)^2 - \omega_H^2 \right]} \right),$$

k_{z1}, k_{z2} — wave numbers in a direction Z,

ϵ_f — voigt's permeability,

ω_H — cyclotron frequency,

ω_p — plasma frequency,

ν — collision frequency.

To investigate the equation (1) it is necessary to take into account, that this equation can have a solution both by real and by imaginary significances k_{z1} and k_{z2} . If the dielectric permeability of layers is positive, the solution (1) is possible only, when k_{z1} and k_{z2} are real numbers. For existence of a solution by imaginary k_{z1} and k_{z2} it is necessary that ε_f (or ε_{II} by $H_0 = 0$) should be negative. It is possible to analytically prove [4], that in this case there are solutions, when surface magneto- plasma waves are distributed along the boundaries of a structure. Thus, there are pass-band zones that are bound up with surface waves, the fields of the latter "percolating" through layers of a structure.

In this research work we pay attention to the fact that the appearance of a feature in a spectrum is possible close by the frequency of a hybrid resonance $\omega_\infty = \sqrt{\omega_H^2 + \omega_p^2}$, by which ε_f turns into infinity. As can be seen from the equation (1), in this case $k_{z1}d \gg 1$ and the correspondent trigonometrical functions oscillate fast. As a result, numerous pass-band zones and stop-band zones arise. Close by the frequency ω_∞ the breadth of these zones tends to zero.

To make it visual, we carried out a numerical solution of the equation (1). In the work the accounts were made for a structure with parameters: the first layer— semiconductor of a type InSb ($\varepsilon_{01} = 17.8$), second layer — dielectric ($\varepsilon_2 = 2$).

Zonal structure of a spectrum with allowance for finiteness of speed of light is shown in figure. The pass-band zones are marked out by line drawing. A sloping direct line — $k_{z2} = 0$, to the left of this line the fields in the second layer having waveguide character; k_{z2} is a real number, to the right of the line — $k_{z2}^2 < 0$, k_{z2} is an imaginary number, and the field "tunneling" through the second layer.

The kind of dispersing curves depends on the character of distribution of waves through a structure. If the distribution of waves in layers of a semiconductor and dielectric goes on as it does on a waveguide ($k_{z1,2}^2 > 0$), the formation of pass-band zones and stop-band zones is determined by the number of half-waves, packing across layers. Consequently, the condition of a geometric resonance takes place, the integer of half-waves stacking across each of the layers.

The second characteristic area of dispersing dependences relates to the "collective" surface magnetoplasmons area, when the wave numbers in both layers are imaginary magnitudes, that is in each layer the field of a wave falls down exponentially in a depth of a layer from both boundaries. In this case the surface polaritons fields "tunnel" through the both of a layers of a structure, and $\varepsilon_f < 0$. With increase of longitudinal wave number k_x the frequency of magneto- plasma waves tends to frequency of surface magnetoplasmon ω_{ps} . On a picture of dispersing zones it shows clearly that the breadth of pass-band zones tends to zero with growing k_x , and the frequencies tend to frequency ω_{ps} . In this area the delaying can be neglected.

The changing of magnitude of an external magnetic field allows to control the process of zones formation, as H_0 determines all characteristic frequencies of a spectrum.

In the real structure the forming of zones are to be under the influence of collisions. It can be assumed, that the narrowest stop-band or pass-band zone may appear to be a kind of an effective collision frequency. The breadth of pass-bands, as to the frequency, cannot exceed an effective collision frequency ν , therefore, close to ω_∞ , the band with a ν breadth is formed, the damping of waves being great.

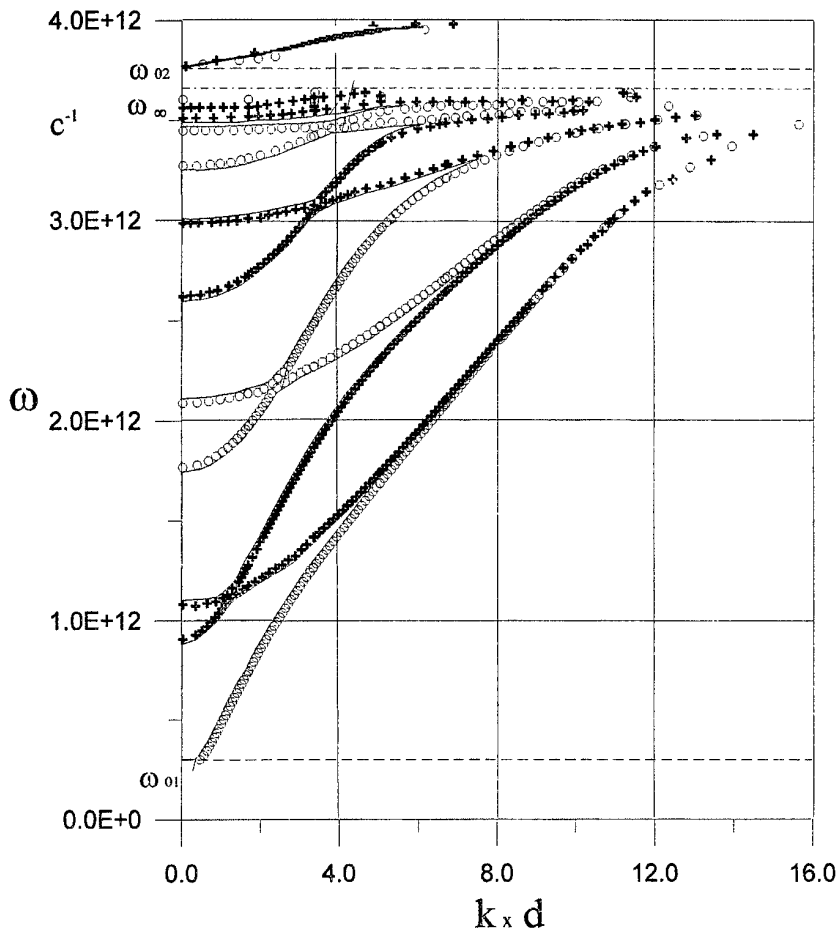


Figure. Dispersing dependence

($d_1 = 5 \times 10^{-3} \text{ cm}$, $d_2 = 2 \times 10^{-2} \text{ cm}$, $H_0 = 2000 \text{ A/cm}$, $\epsilon_{01} = 17.8$, $\epsilon_2 = 2$, $+ — \vec{k}d = \pi$, $\circ — \vec{k}d = 0$,

$$\omega_{01,02} = \pm \frac{\omega_H}{2} + \left(\frac{\omega_H^2}{4} + \omega_{ps}^2 \right)^{1/2}; \quad \omega_{ps} = \omega_p \sqrt{\frac{\epsilon_{01}}{\epsilon_{01} + \epsilon_2}} \quad \text{(frequency of surface plasmon)}$$

References

- 1 C. Elachi , "Waves in active and passive periodic structures", IEEE Trans. Antennas Propagat., Vol.64, No. 12, pp.22 ,1976.
- 2 A. Yariv, P. Yeh, "Optical waves in crystals", M., The world, pp. 616, 1987.
- 3 E. L. Albuquerque, M. G. Cottam, "Superlattice plasmon-polaritons", Physics Reports, Vol.233, No. 2, pp. 67-135,1993.
- 4 F.G.Bass, A.A.Bulgakov, "Kinetic and electrodynamic phenomena in classical and quantum semiconductor superlattices", New-York, Nova Science Publisher, Inc., pp. 498, 1997,
- 5 E. Yablonovich, "Photonic band-gap structures", Optical Society of America, Vol.10, No. 2, pp. 283-295, 1993.
- 6 A.C Baynham, A.D. Boardman, "Transverse magneto-plasma wave propagation in a periodic structure", J. Phys. C., Vol.2, No. 2, pp. 619-628, 1969.

Surface polaritons in the finite superlattice placed into the quantizing magnetic field

J.V. Bludov

Institute for Radiophysics and Electronics National Academy of Sciences of Ukraine,
12 Acad. Proskura str., 310085, Kharkov, Ukraine
Tel: 448593; E-mail: beletski@ire.kharkov.ua

Surface polaritons (SP) in semiconductors with superlattice (SL), consisting of two-dimensional electron systems (2DES), are the object of great interest of physicists [1,2,4]. Earlier the SP in finite SL have been theoretically considered both in absence [1] and in presence [2] of external constant classical magnetic field. Besides, in papers [3,4] the SP in the isolated 2DES [3] and the SP in the system, consisting of two 2DES [4], placed into the high quantizing magnetic field, have been investigated. This paper deals with the theoretical investigation of surface polaritons (SP) in the finite superlattice (SL). We consider the SL, consisting of a finite number M of infinitely extended 2DES, arranged on the equal distance d from each other at planes $z = 0, d, \dots, (M-1)d$. The constant quantizing magnetic field \vec{B} is directed perpendicularly to the 2DES along the axis z (the axis of SL). We suppose, that the space $0 < z < (M-1)d$ is occupied by the dielectric with the dielectric constant ϵ , the space $z < 0$ is occupied by the dielectric with the dielectric constant ϵ_1 and the space $z > (M-1)d$ is occupied by the dielectric with the dielectric constant ϵ_2 (geometry $\epsilon_1 - \epsilon - \epsilon_2$). We admit that the Landau-level filling factor N is equal in all 2DES ($N = \pi l^2 n$, $l = (\hbar/eB)^{1/2}$ is the magnetic length, n is the electron density in 2DES).

The solutions of Maxwell's equations in such structure for TE- and TM-waves take the form:

a) TM-wave

$$0 < z < (M-1)d$$

$$H_y(k, \omega, z) = B_+^m e^{p(z-md)} + B_-^m e^{-p(z-md)},$$

$$E_x(k, \omega, z) = -i \frac{cp}{\omega \epsilon} [B_+^m e^{p(z-md)} - B_-^m e^{-p(z-md)}],$$

$$z < 0$$

$$H_y(k, \omega, z) = A_1 e^{p_1 z}, \quad E_x(k, \omega, z) = -i \frac{cp_1}{\omega \epsilon_1} A_1 e^{p_1 z},$$

$$z > (M-1)d$$

$$H_y(k, \omega, z) = A_2 e^{-p_2(z-(M-1)d)}, \quad E_x(k, \omega, z) = i \frac{cp_2}{\omega \epsilon_2} A_2 e^{-p_2(z-(M-1)d)},$$

b) TE-wave

$$0 < z < (M-1)d$$

$$E_y(k, \omega, z) = D_+^m e^{p(z-md)} + D_-^m e^{-p(z-md)},$$

$$H_x(k, \omega, z) = i \frac{cp}{\omega} [D_+^m e^{p(z-md)} - D_-^m e^{-p(z-md)}],$$

$$z < 0$$

$$E_y(k, \omega, z) = C_1 e^{p_1 z}, \quad H_x(z) = i \frac{cp_1}{\omega} C_1 e^{p_1 z},$$

$$z > (M-1)d$$

$$E_y(k, \omega, z) = C_2 e^{-p_2(z-(M-1)d)}, \quad H_x(z) = -i \frac{cp_2}{\omega} C_2 e^{-p_2(z-(M-1)d)},$$

$$\text{where } p = \sqrt{k^2 - \frac{\omega^2}{c^2} \epsilon}, \quad p_i = \sqrt{k^2 - \frac{\omega^2}{c^2} \epsilon_i}, \quad i = 1, 2, m = 0, 1, \dots, M-2.$$

To obtain the dispersion relation we used the standard boundary conditions. The tangential components of the electric field E_x, E_y were considered to be continuous across the interface and the tangential components of the magnetic field H_x, H_y are considered to be discontinuous across the interface and the values of discontinuity are equal to $H_{x2} - H_{x1} = \frac{4\pi}{c} j_{ys} = \frac{4\pi}{c} (\sigma_{yx} E_x + \sigma_{yy} E_y)$ и $H_{y2} - H_{y1} = -\frac{4\pi}{c} j_{xs} = -\frac{4\pi}{c} (\sigma_{xx} E_x + \sigma_{xy} E_y)$.

The application of above-mentioned boundary conditions gives the following equations in unknowns $D_+^m, D_-^m, B_+^m, B_-^m, A_1, A_2, C_1, C_2$:
at the interface $z = md$

$$B_+^m - B_-^m - (B_+^{m-1} e^{pd} - B_-^{m-1} e^{-pd}) = 0, \quad (1)$$

$$D_+^m + D_-^m - (D_+^{m-1} e^{pd} + D_-^{m-1} e^{-pd}) = 0, \quad (2)$$

$$D_+^m - D_-^m - (D_+^{m-1} e^{pd} - D_-^{m-1} e^{-pd}) = -i \frac{4\pi\omega}{c^2 p} \sigma_{yy} (D_+^m + D_-^m) - \frac{4\pi}{\epsilon c} \sigma_{yx} (B_+^m - B_-^m), \quad (3)$$

$$B_+^m + B_-^m - (B_+^{m-1} e^{pd} + B_-^{m-1} e^{-pd}) = i \frac{4\pi p}{\omega \epsilon} \sigma_{xx} (B_+^m - B_-^m) - \frac{4\pi}{c} \sigma_{xy} (D_+^m + D_-^m), \quad (4)$$

at the interface $z = 0$

$$A_1 = \frac{\epsilon_1 p}{p_1 \epsilon} (B_+^0 - B_-^0), \quad C_0 = D_+^0 + D_-^0, \quad (5)$$

$$D_+^0 - D_-^0 - \frac{p_1}{p} C_0 = -i \frac{4\pi\omega}{c^2 p} \sigma_{yy} (D_+^0 + D_-^0) - \frac{4\pi}{\epsilon c} \sigma_{yx} (B_+^0 - B_-^0), \quad (6)$$

$$B_+^0 + B_-^0 - A_1 = i \frac{4\pi p}{\omega \epsilon} \sigma_{xx} (B_+^0 - B_-^0) - \frac{4\pi}{c} \sigma_{xy} (D_+^0 + D_-^0), \quad (7)$$

at the interface $z = (M-1)d$

$$A_2 = -\frac{\epsilon_2 p}{p_2 \epsilon} (B_+^{M-1} e^{pd} - B_-^{M-1} e^{-pd}), \quad C_1 = D_+^{M-1} e^{pd} + D_-^{M-1} e^{-pd}, \quad (8)$$

$$\begin{aligned} D_+^{M-1} e^{pd} - D_-^{M-1} e^{-pd} + \frac{p_2}{p} C_2 = & i \frac{4\pi\omega}{c^2 p} \sigma_{yy} (D_+^{M-1} e^{pd} + D_-^{M-1} e^{-pd}) + \\ & + \frac{4\pi}{\epsilon c} \sigma_{yx} (B_+^{M-1} e^{pd} - B_-^{M-1} e^{-pd}), \end{aligned} \quad (9)$$

$$\begin{aligned} B_+^{M-1} e^{pd} + B_-^{M-1} e^{-pd} - A_2 = & -i \frac{4\pi p}{\omega \epsilon} \sigma_{xx} (B_+^{M-1} e^{pd} - B_-^{M-1} e^{-pd}) + \\ & + \frac{4\pi}{c} \sigma_{xy} (D_+^{M-1} e^{pd} + D_-^{M-1} e^{-pd}). \end{aligned} \quad (10)$$

The analysis of SP dispersion properties in the finite SL we will carry out, using the formula for $\sigma_{\alpha\beta}(\omega)$, obtained in [3,4] using the Wigner distribution function formalism. Since all effects we are interested in take place under the condition $kl \ll 1$, the spatial dispersion of the 2DES conductivity tensor can be neglected. In this case the non-zero components of the 2DES conductivity tensor $\sigma_{\alpha\beta}(\omega)$ will take the form [3,4]:

$$\sigma_{xx}(\omega) = \sigma_{yy}(\omega) = \frac{2e^2}{h} \frac{\aleph \gamma}{1 + \gamma^2}, \quad \sigma_{xy}(\omega) = -\sigma_{yx}(\omega) = \frac{2e^2}{h} \frac{\aleph}{1 + \gamma^2}, \quad (11)$$

where $\gamma = \frac{\nu - i\omega}{\Omega}$, $\Omega = \frac{eB}{m^* c}$ is the cyclotron frequency, m^* and ν are the effective mass and the electron relaxation frequency, \aleph is the Landau level filling factor, which value is to be the integer only ($\aleph=1, 2, \dots$).

From equations (1)–(4) it follows, that the coefficients $B_+^{m-1}, B_-^{m-1}, D_+^{m-1}, D_-^{m-1}$ and $B_+^m, B_-^m, D_+^m, D_-^m$ are connected by such matrix relation:

$$\begin{pmatrix} B_+^{m-1} \\ B_-^{m-1} \\ D_+^{m-1} \\ D_-^{m-1} \end{pmatrix} = \begin{pmatrix} e^{-pd}(1-a) & ae^{-pd} & \epsilon be^{-pd} & \epsilon be^{-pd} \\ -ae^{pd} & e^{pd}(1+a) & \epsilon be^{pd} & \epsilon be^{pd} \\ -be^{-pd} & be^{-pd} & e^{-pd}(1+s) & se^{-pd} \\ be^{pd} & -be^{pd} & -se^{pd} & e^{pd}(1-s) \end{pmatrix} \begin{pmatrix} B_+^m \\ B_-^m \\ D_+^m \\ D_-^m \end{pmatrix} = \hat{T} \begin{pmatrix} B_+^m \\ B_-^m \\ D_+^m \\ D_-^m \end{pmatrix}, \quad (12)$$

where \hat{T} is the transfer-matrix, $a = i \frac{2\pi p}{\omega \epsilon} \sigma_{xx}$, $s = i \frac{2\pi \omega}{c^2 p} \sigma_{xx}$, $b = \frac{2\pi}{\epsilon c} \sigma_{xy}$.

So, the relation, which connects the coefficients $B_+^0, B_-^0, D_+^0, D_-^0$ and $B_+^{M-1}, B_-^{M-1}, D_+^{M-1}, D_-^{M-1}$ using (12) can be written in the form:

$$\begin{pmatrix} B_+^0 \\ B_-^0 \\ D_+^0 \\ D_-^0 \end{pmatrix} = \hat{F} \begin{pmatrix} B_+^{M-1} \\ B_-^{M-1} \\ D_+^{M-1} \\ D_-^{M-1} \end{pmatrix}, \quad (13)$$

where the general transfer-matrix $\hat{F} = (\hat{T})^{M-2}$. The transfer-matrix \hat{T} can be raised to the $M-2$ power using Abeles theorem [5].

The linear uniform system of equations (1-10) have a solution only in the case, when it's determinant is equal to zero. So the dispersion relation, describing the SP propagation in SL, formed of the finite number of 2DES, can be deduced to the form:

$$\det \begin{vmatrix} G_1 & G_2 & G_3 & G_4 \\ P_1 & P_2 & P_3 & P_4 \\ e^{pd}(1+\theta_2+2a) & e^{-pd}(1-\theta_2-2a) & -2\epsilon b e^{pd} & -2\epsilon b e^{-pd} \\ 2b e^{pd} & -2b e^{-pd} & e^{pd}(1+\mu_2-2s) & -e^{-pd}(1-\mu_2+2s) \end{vmatrix} = 0. \quad (14)$$

Here

$$G_i = (1-\theta_1-2a)F_{1i} + (1+\theta_1+2a)F_{2i} + 2\epsilon b(F_{3i} + F_{4i}),$$

$$P_i = 2b(F_{2i} - F_{1i}) + (1-\mu_1+2s)F_{3i} - (1+\mu_1-2s)F_{4i},$$

$\theta_1 = \frac{\epsilon_1 p}{p_1 \epsilon}, \theta_2 = \frac{\epsilon_2 p}{p_2 \epsilon}, \mu_1 = \frac{p_1}{p}, \mu_2 = \frac{p_2}{p}$. In the case when SL consists of two 2DES ($M = 2$) and $\epsilon_1 = \epsilon_2 = \epsilon$ (geometry $\epsilon - \epsilon - \epsilon$), the dispersion relation (14) coincides with the dispersion relation, obtained in [4].

The properties of SP in the finite SL are characterized by the below-mentioned features. Firstly, under the integer quantum Hall effect conditions all characteristics of SP are represented by the quantized values. Secondly, the SP spectrum in the finite SL consists of the number of modes which is equal to the number of 2DES in SL. At the same time in the vicinity of the CR the phase velocity of the SP decreases and the group velocity is quantized into fundamental steps, defined by the fine-structure constant α , the values of the dielectric constants $\epsilon, \epsilon_1, \epsilon_2$ and the distance between 2DES d .

We considered two cases: the case, when the dielectric constants of the media inside the SL and outside it are equal (geometry $\epsilon - \epsilon - \epsilon$) and the case, when they are different (geometry $\epsilon_1 - \epsilon - \epsilon_1$). In the case of geometry $\epsilon - \epsilon - \epsilon$ all the SP modes lie inside the zone of the SP propagation in the infinite SL. Also the SP spectrum in such SL has no the low-frequency non-propagating gap. In the case of geometry $\epsilon_1 - \epsilon - \epsilon_1$ the SP spectrum contains two particular modes lying outside the zone of the SP propagation in the infinite SL. These particular modes lie above (in the case $\epsilon_1 < \epsilon$) or below (in the case $\epsilon_1 > \epsilon$) the zone of the SP propagation in the infinite SL. Consequently, the phase velocity of the SP in the finite SL can be considerably less (in the case $\epsilon_1 > \epsilon$) than the phase velocity of the SP in the infinite SL.

In conclusion the author expresses his gratitude to Dr. N.N. Beletskii for discussing the results of the paper.

References

1. J.K. Jain, P.B. Allen, "Plasmons in layered films", Phys. Rev. Lett., Vol. 54, No. 22, pp. 2437-2440, 1985.
2. E.L. Albuquerque, P. Fulco, G.A. Farias, M.M. Auto, D.R. Tilley, "Magnetoplasmon polaritons in finite n-i-p-i superlattices", Phys. Rev. B, Vol. 43, No. 3, pp. 2032-2041, 1991.
3. I.E. Aronov, N.N. Beletskii, "Fundamental steps of the group velocity for slow surface polaritons in the two-dimensional electron gas in a high magnetic field", J. Phys. Condens. Matter, No. 8, pp. 4919-4936, 1996.
4. I.E. Aronov, N.N. Beletskii, G.P. Berman and A.R. Bishop, "Collective electromagnetic excitations in a double-layer two-dimensional electron system in a high magnetic field", Phys. Rev. B, Vol. 56, No. 16, pp. 10392-10402, 1997.
5. F.G. Bass, A.A. Bulgakov, A.P. Teterov, "High-frequency properties of semiconductors with superlattices", Nauka, Moscow, p. 288, 1989.

Non-linear magnetoplasma excitations in compensated metals: periodic and solitary waves

N. M. Makarov, G. B. Tkachev and V. E. Vekslerchik

*Institute for Radiophysics and Electronics NASU,
12 Academician Proskura Str., Kharkov 310085, Ukraine*

It is known [1] that in compensated metals (or semi-metals) in the presence of an external magnetic field H_0 there exist linear electromagnetic excitations – so-called magnetoplasma waves. Their frequency ω is much larger than the electrons and holes relaxation frequency ν ,

$$\omega \gg \nu. \quad (1)$$

If the magnetoplasma wave propagates transversely to the external magnetic field vector H_0 , its magnetic field is parallel to H_0 . In this geometry the wave spectrum is determined by the conductivity in the plane perpendicular to H_0 . In the case when the phase wave velocity V is much larger than the Fermi velocities of electrons v_F^e and holes v_F^h ,

$$V \gg v_F^{e,h}, \quad (2)$$

the spatial dispersion effects are negligible, and the transverse part of the conductivity tensor in the Cartesian coordinate frame $x, y, z \parallel H_0$ is of the form [1]:

$$\begin{aligned} \sigma_{zz} = \sigma_{yy} &= (Ne c / H_0) [\gamma_e (1 + \gamma_e^2)^{-1} + \gamma_h (1 + \gamma_h^2)^{-1}] \\ \sigma_{xy} = -\sigma_{yx} &= (Ne c / H_0) [(1 + \gamma_h^2)^{-1} - (1 + \gamma_e^2)^{-1}] \\ \gamma_{e,h} &= (\nu - i\omega) (eH_0 / m_{e,h} c)^{-1}. \end{aligned} \quad (3)$$

Here c is the light velocity, e is the elementary charge, the quantities m_e and m_h are effective electron and hole masses correspondingly and N is the concentration of either electrons or holes. Using (3) and Maxwell equations, one can deduce the following dispersion relation between the frequency ω and wavevector q of the magnetoplasma wave [1] (for definiteness the vector q is chosen to be parallel to the x -axis):

$$q = (\omega / V_A) (1 - \omega^2 / \Omega_0^2)^{-1/2}, \quad V_A = H_0 / [4\pi N(m_e + m_h)]^{1/2}, \quad \Omega_0 = eH_0 / (m_e m_h)^{1/2} c. \quad (4)$$

According to (4) the phase velocity $V = \omega / q$ of the wave is always less than the Alfvén velocity V_A . From this result and the inequality (2) one can conclude that the magnetoplasma waves can be observed in such strong external fields H_0 that the Alfvén velocity is much larger than the Fermi velocities, both electron and hole, $V_A \gg v_F^{e,h}$.

The results for the transverse magnetoplasma wave described above have been obtained in the limit of infinitesimal amplitudes, i.e. in the linear case. The question arises of what kind of magnetoplasma oscillations will take place in the non-linear regime. It is already known that metals possess rather peculiar non-linear electrodynamic properties (see, e.g., review [2]). Usually, in plasma or semi-conductors, a non-linear response to electromagnetic perturbation is achieved owing to the considerable departure of the electron system from equilibrium. In metals, because of the high concentration, electrons are always in a near-equilibrium state. Nevertheless, it is easy to observe a non-linear regime there, which is due to the fact that in metals sources of non-equilibrium and non-linearity are different. The former is caused by a weak electric field, while the latter is caused by a strong magnetic field of an electromagnetic wave. The Lorentz force, determined by the magnetic wave component, affects the dynamics of charge carriers. Hence, the conductivity of a metal depends on the configuration of the magnetic field. Such a magnetodynamic mechanism of non-linearity is typical for pure metals under low temperatures. On the base of the work [3] in the present paper we study the propagation of the transverse magnetoplasma waves taking into account the magnetodynamic non-linearity.

We have solved the Boltzmann kinetic equation in the case of a high-frequency finite-amplitude electromagnetic wave and calculate the current density in the plane perpendicular to the magnetic field $H(x, t)$ which is the sum of the external magnetic field H_0 and the magnetic field of the wave. The expressions for the components of the non-linear conductivity turn out to be similar to the formulae (3). However, in the non-linear tensor, instead of the constant H_0 , the total magnetic field $H(x, t)$ appears. Moreover, in the

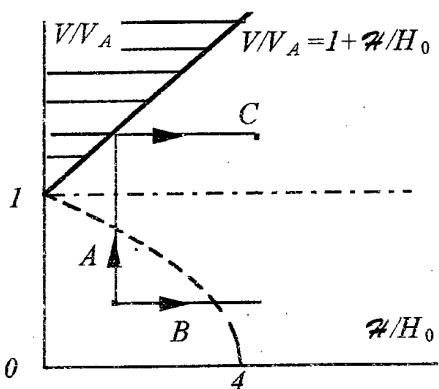


Fig.1 The range of admissible values of the amplitude and velocity of the magnetoplasma wave (the unshaded part of the H - V plane). The dashed curve is the boundary of the quasilinear excitation region. Line $V/V_A = 1 + H/H_0$ corresponds to the soliton.

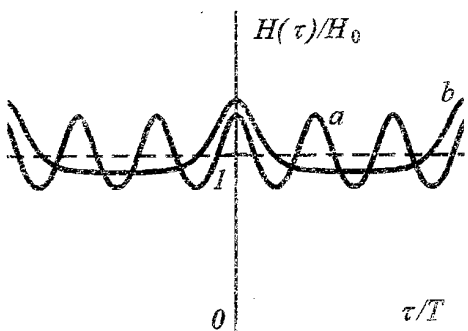


Fig.2 The shape of the magnetoplasma wave at the fixed amplitude $\mathcal{H}=2H_0$ and different values of the velocity: (a) $V=0.7V_A$, (b) $V=1.1V_A$.

In Fig.2 the dependence of the dimensionless total magnetic field H/H_0 on τ/T , when the amplitude is fixed, $\mathcal{H}=0.2H_0$, is presented for two different values of the velocity V . Curve "a" corresponds to quasi-harmonic oscillations. Curve "b" represents the wave profile in the non-linear regime. One can see that the non-linear wave is a series of separated pulses, and its period T increases infinitely with growth of the velocity V . The aperiodic regime occurs when the phase velocity V takes a maximal – for a given amplitude \mathcal{H} – value (see (5)). At this moment the point (\mathcal{H}, V) in Fig. 1 reaches the line $V/V_A = 1 + \mathcal{H}/H_0$ along the path "A", and the magnetoplasma wave transforms into a solitary pulse, i.e. a soliton,

$$H(x, t) = H_0 + 2H_0 \left[\frac{V^2}{V_A^2} - 1 \right] \left\{ 1 + \frac{V}{V_A} \operatorname{ch} \left[\Omega_0 \left(\frac{V^2}{V_A^2} - 1 \right)^{1/2} \left(t - \frac{x}{V} \right) \right] \right\}^{-1}. \quad (7)$$

From this expression one can see that the soliton propagates against the external magnetic field H_0 . Its typical width $\Delta\tau$ is, in order of magnitude, equal to $2\pi\Omega_0^{-1}(V^2/V_A^2 - 1)^{-1/2}$. The phase velocity V is larger than the Alfvén one, V_A , and depends linearly on the amplitude \mathcal{H} according to law $V = V_A(1 + \mathcal{H}/H_0)$. Thus, the solitary wave (7) is a distinguished single-parameter solution.

expression for $\gamma_{e,h}$ the quantity $-i\omega$ is replaced with the operator for differentiating with respect to time, $\partial/\partial t$. This takes into account temporal dispersion effects in non-linear, and hence non-monochromatic, wave fields. These distinctions lead to qualitatively new properties of $\sigma_{xx}, \sigma_{yy}, \sigma_{xy}, \sigma_{yx}$. They are not the operators for multiplying any more, but differential operators acting on the electric field of the wave. This theory of the non-linear high-frequency conductivity enables one to perform self-consistent analysis of the dynamics of the transverse finite-amplitude magnetoplasma waves.

We have obtained and analyzed analytical solution for the travelling non-linear magnetoplasma wave in the case in which the total magnetic field is of constant sign. It has been shown that the wave profile – the dependence of the wave magnetic field on the running variable $\tau = t - x/V$ – is specified by two parameters, namely the amplitude \mathcal{H} of the wave magnetic field and the phase velocity V . Besides, the wave period T depends on \mathcal{H} and V as well. Therewith the range of admissible values of the amplitude and velocity is given by the inequalities (Fig. 1)

$$0 \leq \mathcal{H} \leq \infty, \quad 0 \leq V \leq V_A(1 + \mathcal{H}/H_0). \quad (5)$$

We see that the velocity of the non-linear magnetoplasma wave can be either less or larger than that the Alfvén one, V_A . In other words, the domain of existence of the magnetoplasma waves is wider in the non-linear case than in the linear one, in which electromagnetic waves propagate only when $V \leq V_A$ (see (4)).

In the case of sufficiently small amplitudes

$$\mathcal{H} \ll 4H_0 [1 - (V/V_A)^2] \quad (6)$$

and $V \leq V_A$ our solution is reduced to the linear magnetoplasma wave which described by the dispersion law (4). The range (6) of existence of the linear excitation is situated under the dashed curve in the Fig 1. The condition (6) is broken when the amplitude \mathcal{H} increases, as well as the velocity V increases. In both cases the higher harmonics begin to play a significant role in forming the wave shape.

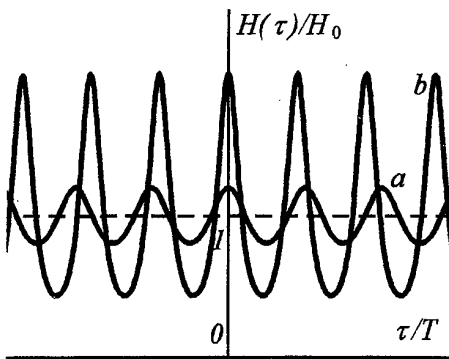


Fig. 3 The shape of the magnetoplasma wave at the fixed velocity $V=0.7V_A$ and different values of the amplitude: (a) $\eta=0.2H_0$, (b) $\eta=0.8H_0$

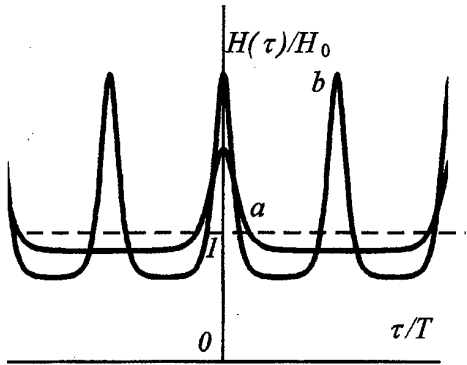


Fig. 4 The shape of the magnetoplasma wave at the fixed velocity $V=1.2V_A$ and different values of the amplitude: (a) $\eta=0.3H_0$, (b) $\eta=0.8H_0$.

We pay special attention to the fact that the strongly non-linear regime can occur even in the case in which the wave amplitude is small in comparison with the external magnetic field. This enables experimental observation of the predicted non-linear excitations to be achieved. Indeed, the non-linear waves with small amplitudes have the phase velocity V close to V_A (see Fig. 1). In such a case, the condition (2), which allows one to neglect the spatial dispersion effects, is reduced to the inequality $V_A \gg v_F^{sh}$. Therefore the non-linear excitations can be observed in the same range of the external magnetic fields H_0 as the linear waves exist in. In the bismuth-like semi-metals the Alfvén velocity V_A exceeds considerably the Fermi velocities v_F^{sh} , if the external magnetic field H_0 is of the order of few thousands oersteds (or higher). At the same time, the amplitudes of the alternating signal in today's experiments attain values of tens or hundreds oersteds (see, e.g., review [2]). For just this reason, it is important that the non-linear effects discussed in our paper take place also in the case where $\eta \ll H_0$.

For growing η and fixed V one can observe transformations of the wave shape which are inverse to the ones described above. As follows from Fig. 1 it is necessary to analyze two distinct cases: $V \leq V_A$ (path "B") and $V \geq V_A$ (path "C"). In the first case the point (η, V) in Fig. 1 moves away from the quasilinear region, located under the dashed curve. Fig. 3 demonstrates a crossover from the harmonic wave (curve "a") to the non-linear one (curve "b") for $V=0.7V_A$. We can see that with η growing, the maxima of the function $H(\tau T)$ become sharper, and the wave period decreases.

Consider now the magnetoplasma wave with a velocity larger than the Alfvén one, $V \geq V_A$. This case differs from the previous one, since the point (η, V) in Fig. 1 starts from the line $V/V_A = 1 + \eta/H_0$ corresponding to the soliton (7), and does not leave the non-linear region. Such a wave for $V=1.2V_A$ and two values of the amplitude η is depicted in Fig. 4. It is seen that for any η magnetoplasma oscillations have the essentially non-linear form of isolated pulses. Their period decreases with growth of the amplitude.

Like the soliton, the periodic magnetoplasma wave with a velocity larger than V_A has no analogue in the linear case. It is formed exceptionally due to the self-action, caused by the magnetodynamic mechanism of non-linearity. Fig. 4 convincingly demonstrates the fact that in the non-linear case the magnetoplasma wave possesses two characteristic scales of τ . The first one is the wave period T , while the second one is the interval $\Delta\tau$, during which the wave field changes by a quantity of the order of the amplitude. Naturally, in the linear limit the two scales, T and $\Delta\tau$, coincide.

- [1]. Kaner E. A. and Skobov V. G. Electromagnetic waves in metals in a magnetic field // Adv. Phys. – 1968. – 17, N 69. – P. 605.
- [2] Makarov N. M. and Yampol'skii V. A. Nonlinear electrodynamics of metals at low temperatures // Fiz. Nizk. Temp. – 1991. – 17, N 5. – P. 547. (Engl. Transl.: Sov. J. Low Temp. Phys. – 1991. – 17. – P. 285.)
- [3]. Makarov N. M., Tkachev G. B. and Vekslerchik V. E. Non-linear conductivity and magnetoplasma waves in compensated metals and semi-metals // J. Phys.: Condens. Matter. – 1998. – 10. – P. 1033.

Acoustic Wave Resonances in a Solid Layer with a Periodically Irregular Boundary

A.S.Bugaev, V.V.Pogrebnyak

Moscow Institute of Physics and Technology, Moscow, Dolgoprudny
141700, Russia, seva@oscar.kharkov.ua

Abstract. Interaction of acoustic wave harmonics in a solid layer with one-dimensional periodically irregular boundary is studied in detail. Resonances between different modes of the harmonics has been predicted in such structure. Due to the resonances the acoustic spectrum of the layer takes miniband character with densely spaced forbidden gaps.

There are a lot of papers devoted to the investigation of wave propagation in bounded periodic structures. In the case of the plane acoustic waveguide the problem is usually analysed in the coupled-wave approximation [1,2]. This method is applied to many cases of wave propagation in waveguide geometries with a periodic perturbation [3-6]. However the coupled-wave model describes behaviour of the system only near the Bragg resonances and it does not describe the mode interaction in the frequency range far from the Bragg resonances.

In the Report we show solving the problem in the multimode approximation let to analyze this interaction and to reveal resonances between different modes in a waveguide with a periodically irregular boundary.

Consider an isotropic solid layer with free boundaries one of which has the one-dimensional periodically irregular form $y_0 = \xi \cos(qx)$, where $q = 2\pi/l$, ξ and l are an amplitude and a period of the irregularity. The layer occupies the space of $y_0 \leq y \leq d$, $-\infty < x, z < \infty$. The mean thickness of the layer is d .

It is known that the acoustic shear wave with the single displacement component u_z can propagate in the layer. The elastic displacement amplitude $u_z(x, y, t) \equiv u$ satisfies the wave equation

$$\frac{\partial^2 u}{\partial t^2} - s^2 \left(\frac{\partial^2 u}{\partial x^2} + \frac{\partial^2 u}{\partial y^2} \right) u = 0 \quad (1)$$

Where s is the transverse sound velocity. It is necessary to supplement Eq.(1) with the boundary conditions: an equality to zero of a pressure at the both boundaries of the layer

$$\sigma_{i,k} n_k \Big|_{y=d} = \sigma_{i,k} n_k \Big|_{y=y_0(x)} = 0 \quad (2)$$

Where \mathbf{n} is the normal to the surface of the layer, $\sigma_{i,k}$ is the stress tensor.

Since the boundary has a periodic form one may seek the desired quantity u as the Fourier series

$$u = \sum_n \{a_n \cos(k_{y,n}y) + b_n \sin(k_{y,n}y)\} \exp\{\imath[(k_x + nq_x)]x - \omega t\} \quad (3)$$

Where coefficients a_n, b_n , wave numbers $k_{y,n}$ and the frequency ω are subjected to be determined from the input equations.

Substituting (3) into the wave equation (1) and boundary conditions (2) we obtain the system of linear algebraic equations for the coefficients a_n and b_n . In the case of small irregularities, $\xi/d \ll 1$, we can restrict ourselves to the approximation of the main three harmonics with the wave numbers $k_{y,0}$ and $k_{y,\pm 1}$. This simplifications let to derive the dispersion equation in an implicit form

$$k_0 \tan(dk_0) = \frac{\xi^2}{4} \left\{ \frac{(k_{-1}^2 + q^2 - k_x q)(k_0^2 + k_x q)}{k_{-1} \tan(dk_{-1})} + \frac{(k_{+1}^2 + q^2 + k_x q)(k_0^2 - k_x q)}{k_{+1} \tan(dk_{+1})} \right\}. \quad (4)$$

Here we have denoted $k_{y,n} \equiv k_n$. In the right-hand side of (4) we have neglected by more small order terms which contain the second harmonic wave numbers $k_{\pm 2}$, since in the short Report we restrict ourselves only by analysis of resonance cases which depend on the first three main harmonic contribution.

The relation between the wave vector components and ω follows from (1) and (3)

$$k_n^2 = \frac{\omega^2}{s^2} - (k_x + nq)^2 \quad (5)$$

Eq.(4) can be solved by means of successive approximations about ξ [7]: $k_0 = k_0^{(0)} + \delta k + \dots$. If $\xi = 0$ then $\tan(k_0^{(0)}d) = 0$ and we obtain the known solution for a layer with smooth boundaries

$$k_0^{(0)} = \frac{m\pi}{d}, \quad k_x = \sqrt{\frac{\omega^2}{s^2} - \frac{m^2\pi^2}{d^2}} \quad m = 0, 1, 2, \dots \quad (6)$$

Substituting zero solution in the right-hand side of Eq.(4) we obtain in the next approximation the correction δk which describes the effect of the periodic boundary.

From Eqs.(4) and (5) we see that the general resonance condition is

$$k_{\pm 1} = k_0^{(0)} + \frac{l\pi}{d}, \quad k_{\pm 1} > \frac{\pi}{d}, \quad l = 0, \pm 1, \pm 2, \pm 3, \dots \quad (7)$$

At these values of $k_{\pm 1}$ the tangen in the right-hand side of Eq.(4) vanishes. It is obvious Eqs.(7) and (6) express the condition of a resonance between different modes of zero and first harmonics of the acoustic wave in the layer. Substituting (7) into (5) we find the resonant values of k_x at which the resonances occur

$$k_x^{\pm}(m, l) = \mp \frac{q}{2}(1 + \theta_{m,l}), \quad \theta_{m,l} = \frac{l(2m + l)\pi^2}{(dq)^2}, \quad m + l > 0. \quad (8)$$

The particular case $m = l = 0$ corresponds to the Bragg resonance.

The resonant frequencies we obtain from Eq.(5) and (8)

$$\omega_{m,l} = \sqrt{\omega_m^2 + \omega_B^2(1 + \theta_{m,l})^2}, \quad \omega_B = \frac{sq}{2}. \quad (9)$$

From Eq.(9) we can see that at $l < 0$ and $\theta_{m,l} \rightarrow -1$ the resonant frequency $\omega_{m,l} \rightarrow \omega_m$. Thus, we come to the important conclusion the mode resonances occur in all frequency range starting from zero.

Near the resonance Eq.(4) reduces to the quadratic algebraic equation which gives two roots

$$\delta k(1, 2) = \pm \frac{\xi}{2\pi ms^2} [\omega_m^2 + 2\omega_B^2(1 + \theta_{m,l})]. \quad (10)$$

which describe, just as in the case of the Bragg resonance, spectrum splitting and appearance of the forbidden gap (stop band) $\delta\omega$. The expression for $\delta\omega$ takes a more simple view in the case of the thick layer $\theta_{m,l} \ll 1$

$$\delta\omega = \frac{\xi}{d} \frac{\omega_{m,l}^2 + \omega_B^2}{\omega_{m,l}}. \quad (11)$$

The frequency range $\Delta\omega$ between two sequential resonances l and $l + 1$ (pass band) of the m -mode of the thick layer may be derived from Eq.(9)

$$\Delta\omega = \frac{(2m + 2l + 1)\pi^2\omega_B^2}{(qd)^2\omega_{m,l}}, \quad \theta_{m,l} \ll 1. \quad (12)$$

In the important for acousto- and quantum electronics cases, $\omega_B \gg \omega_m$, Eqs.(11) and (12) become quite simple and suitable for experimental verification

$$\delta\omega = 2\frac{\xi}{d}\omega_B, \quad \Delta\omega = \frac{(2m + 2l + 1)\pi^2\omega_B}{(qd)^2}. \quad (13)$$

These equations show the acoustic spectrum of the layer takes miniband character with densely spaced stop bands, since $\Delta\omega \ll \omega_B$. In connection with it acoustic properties of the layer will change in accordance with the new features of the spectrum.

References

1. S.E.Miller, Bell System Techn. Journ, **33**, 661 (1954).
2. H.Kogelnik, Bell System Techn. Journ, **48**, 2909 (1969).
3. D.Marcuse, Light Transmission Optics, Van Nostrand Reinhold Comp., N.Y. (1972).
4. Integrated Optics, Ed. T.Tamir, Springer-Verlag, Berlin (1975).
5. G.S.Kino, Acoustic Waves: Devices, Imaging and Analog Signal Processing. Prentice-Hall, Inc (1987). [Translation in Russian: Mir, 1990].
6. S.Solimeno, B.Crognani, P.DiPorto, Diffraction, and Confinement of Optical Radiation. Acad. Press, Inc (1986). [Translation in Russian: Mir, 1989].
7. V.A.Pogrebnyak, V.M.Yakovenko, I.V.Yakovenko, Phys. Lett., A **209**, 103 (1995).

OPTICAL SURFACE MODES IN A RANDOM SYSTEM OF SMALL METALLIC PARTICLES

A. Ya. Blank, L. V. Garanina, and L. G. Grechko*

Institute of Radio Astronomy, NASU
4, Krasnoznamennaya St., Kharkov, 310002, Ukraine
*Institute of Chemistry of Surface, NASU
31, Nauki Av., Kiev, 252028, Ukraine

1. The absorption of electromagnetic radiation (EMR) in a system of small metal particles reveals the characteristic resonance caused by existence of surface mode (SM) of a single particle on a frequency $\omega_s = \omega_p / \sqrt{3}$ [1]. This mode corresponds to dipole electron oscillation in a metal particle. This absorption turns out to be sensitive to the value and features of direct multipole interaction between particles even though their concentrations are quite small [2].

Interaction mechanism consists in changing the acting electrical field in particle's location place due to polarization of neighboring particles. Account of the direct dipole interaction between particles leads to appearance of two different SM – longitudinal and transverse – shifted in opposite frequency sides, which calls some definite peculiarities in absorption in a system of metal particles [3].

Here, we consider changes in the spectrum of SM caused by particles interaction in a system of non-equivalent particles, differing by their sizes and dielectrical properties (permittivities).

In our previous paper [4] we developed rather general approachment starting from Maxwell-Garnett approximation for finding the system effective dielectric function with account of direct multipole interaction between particles. The principal point of our treatment consists in using quasistatic approach together with the account only pair interaction between particles whereas this interaction is accounted exactly in all the orders of the perturbation theory.

By that the effective dielectric function as well as the mean dipole moment are presented through two-particle polarization found from the solution of a problem of two metallic spheres in alternating electric field.

For dipole moment \vec{P} of a single particle in the presence of the other particle we find limiting ourselves with only dipole interaction

$$\vec{P}\vec{m} = X_{\perp}n_zm_z + X_{\parallel}(n_xm_x + n_ym_y), \quad (1)$$

where $\vec{m} = \vec{r}/r$, \vec{n} is the unit vector in the external field \vec{E}_0 direction, r_1 , r_2 are spherical particles radii, R is a distance between spheres centers, X_{\perp} and X_{\parallel} are transverse and longitudinal components of the dipole moment, correspondently. Geometry of location of two particles in an external field is shown in a Fig. 1.

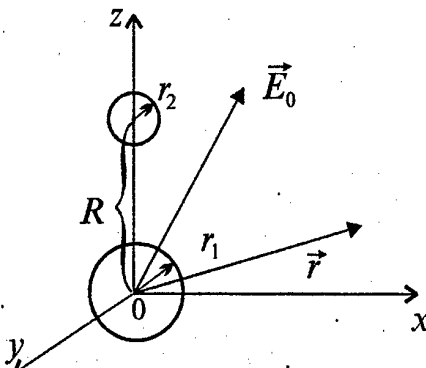


Fig. 1. Two spheres in external electric field \vec{E}_0

Under account of only dipole interaction we have [4]

$$X_{\perp} = \frac{\alpha_2^{-1} + 2R^{-3}}{(\alpha_1\alpha_2)^{-1} - 4R^{-6}}, \quad (2)$$

$$X_{\parallel} = \frac{\alpha_2^{-1} - R^{-3}}{(\alpha_1\alpha_2)^{-1} - 4R^{-6}}, \quad (3)$$

where $\alpha_i = \frac{\epsilon_i - \epsilon_0}{\epsilon_i + 2\epsilon_0} r_i^3$, ($i=1,2$) is polarizability of a single particle (when $R \rightarrow \infty$, $X_{\perp} = X_{\parallel} = \alpha_1$); ϵ_i is dielectric permittivity of particles, ϵ_0 is permittivity of dielectric matrix, r_i is a radius of a particle. The value α_2 accounts for the other particle's influence on the magnitude of the dipole moment of the first one.

2. Surface modes spectrum is defined by polarizability singularities, that is

$$A_1(\omega)A_2(\omega) - a \cdot \Delta^3 \sigma^6 = 0, \quad (4)$$

where $A_i(\omega) = \frac{\epsilon_i(\omega) + 2\epsilon_0}{\epsilon_i(\omega) - \epsilon_0}$ ($i=1,2$); $\Delta = \frac{r_2}{r_1}$; $\sigma = \frac{r_1}{R}$; $a = \begin{cases} 4 & \text{for longitudinal and transverse modes,} \\ 1 & \text{correspondently.} \end{cases}$

These relations determine frequencies of electron homogeneous oscillations in particles with different sizes and permittivities.

In following we use the simplest Drude kind of metal permittivity $\epsilon(\omega) = 1 - \frac{\omega_p^2}{\omega^2}$, where ω_p is a plasma frequency.

2.1. In a case of equal particles ($r_1 = r_2 = r$, $\epsilon_1 = \epsilon_2 = \epsilon$) we find known result [3] for longitudinal and transverse SM:

$$\omega_{\parallel}^2 = \omega_s^2 \frac{1 - 2(r/R)^3}{1 - 2(r/R)^3 \alpha_{\infty}}, \quad (5)$$

$$\omega_{\perp}^2 = \omega_s^2 \frac{1 + (r/R)^3}{1 + (r/R)^3 \alpha_{\infty}}, \quad (6)$$

where $\alpha_{\infty} = \frac{\epsilon_{\infty} - \epsilon_0}{\epsilon_{\infty} + 2\epsilon_0}$ is Clausius-Mosotti factor, $\omega_s = \frac{\omega_p}{\sqrt{\epsilon_{\infty} + 2\epsilon_0}}$ is Fröhlich's mode of a single particle.

Dipole interaction between particles leads, first, to doubling of SM, and, second, to their non-symmetric shifting to different frequency sides.

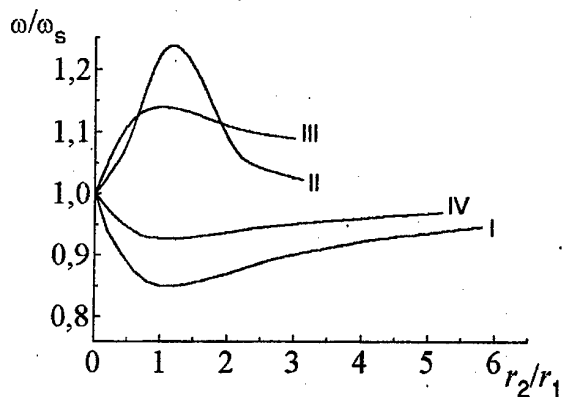


Fig. 2. Surface modes in a system of two non-equivalent particles with account of dipole interaction ($R = r_1 + r_2$):

I. $\omega_{\parallel,-}$; II. $\omega_{\parallel,+}$; III. $\omega_{\perp,+}$; IV. $\omega_{\perp,-}$

2.2. For particles of different sizes and equal dielectric properties equations (4) give in distinction from case of equal particles not two, but four SM:

$$\omega_{\parallel,\pm}^2 = \omega_s^2 \frac{1 \mp 2\Delta^{3/2}(r_1/R)^3}{1 \mp 2\Delta^{3/2}(r_1/R)^3 \alpha_{\infty}} \quad (7)$$

$$\omega_{\perp,\pm}^2 = \omega_s^2 \frac{1 \pm \Delta^{3/2}(r_1/R)^3}{1 \pm \Delta^{3/2}(r_1/R)^3 \alpha_{\infty}} \quad (8)$$

As seen, interaction between particles turns to splitting of transverse and longitudinal frequencies and to their shifting to different frequency sides. The situation is very like to the appearance of optical modes in one-dimensional infinite ring of two kinds of atoms with different masses in the same cell. The dependence of SM for different size particles on their radii ratio is shown at Fig. 2.

2.3. In the case of particles of equal sizes but with different dielectric functions, $\epsilon_1 \neq \epsilon_2$, we find equation for SM:

$$\frac{\epsilon_1(\omega) + 2\epsilon_0}{\epsilon_1(\omega) - \epsilon_0} \cdot \frac{\epsilon_2(\omega) + 2\epsilon_0}{\epsilon_2(\omega) - \epsilon_0} = a \left(\frac{r}{R} \right)^6, \quad (9)$$

which in non-dimensional variables $x = \frac{\omega^2}{\omega_{sl}^2}$ transforms to a kind

$$(x-1)(\Gamma x - 1) = \gamma \left(\frac{r}{R} \right)^6, \quad (10)$$

where $\Gamma = \left(\frac{\omega_{p1}}{\omega_{p2}} \right)^2$, and we put $\epsilon_0 = \epsilon_\infty = 1$.

Analysis of this equation shows that region between SM of single particles ω_{sl} and ω_{s2} creates a "forbidden zone". There is analogy also with the appearance of forbidden zones in one-dimensional bound oscillator rings.

Thus, we see that symmetry breaking, connected with particles non-equivalence, leads to the increase of the number of proper modes in a system. Correspondently, the dipole moment of a system of two non-equivalent particles is presented as a sum of inputs of dipole momenta of four independent oscillators with frequencies found above. It gives evidence in appearance of fine structure in EM absorption.

References

1. C. F. Bohren, D. R. Huffman. Absorption and Scattering of Light by Small Particles. Wiley & Sons, 1983, 680 p.
2. U. Kreibig, A. Althoff, H. Pressmen. Surf. Sci. 1981, v. 106, p. 308.
3. M. Inoue, K. Ohtaka. J. Phys. Soc. Jap. 52, 3853, 1983.
4. L. G. Grechko, A. Ya. Blank, V. V. Motrich, A. A. Pinchuk, and L. V. Garanina. Dielectric Function of Matrix Disperse Systems with Metallic Inclusions. Account of Multipole Interaction between Inclusions. Radio Phys. and Radio Astron., vol. 2, No.1, pp.19-27, 1997.

INTERACTION OF SUBMILLIMETER ELECTROMAGNETIC WAVES WITH FERROELASTIC SOLID-STATE STRUCTURES

Ya. O. Shablovsky

Gomel polytechnical institute
Address: 48, October prosp., 246746, Belorussia
Tel. (0232) 480406

I. Introduction.

The practical application of many solid compounds is based on changing their physical properties under the action of external fields. From this viewpoint solid-state structures possessing ferroelastic properties are very promising materials for the SubMM wave electronics. The characteristic feature of ferroelastics is the presence of spontaneously strained domains that build the bulk of a crystal. Such a peculiar domain structure exists only at temperatures $T < T_c$, where T_c is a Curie temperature, and therefore ferroelastics can be regarded as the mechanic analogues of ferroelectrics [1]. The compounds on the base of $\text{KH}_3(\text{SeO}_3)_2$, $\text{KD}_3(\text{SeO}_3)_2$, DyVO_4 , BiVO_4 , Nb_3Sn , V_3Si , RbMnCl_3 can serve as the examples of materials of this kind.

Dielectric properties of ferroelastics in the SubMM range are not determined by a reaction of the electron subsystem. Unlike the majority of "traditional" radioelectronic materials ferroelastic solid-state structures display anomalously sharp susceptibility to the external action if the latter changes with frequencies of the SubMM range. This is due to the fact that the energies of structural transformations (ST) at ferroelastic phase transitions exactly correspond to the SubMM frequencies. Therefore the processes of propagation and refraction of the SubMM waves in ferroelastics depend very strongly not only on the frequency ω of the wave but also on the temperature of a solid. The subject of this paper is the theoretical study of the nature of these dependences. Here we choose the complex dynamic dielectric susceptibility $k(\omega) = k' + ik''$ as the principal quantitative characteristic of the wave propagation in ferroelastics.

II. Thermodynamic aspects of ferroelastic transformations in solids.

Any ST in a solid can be regarded as a certain "distortion" of the crystal lattice. The most convenient way of describing distortions of this kind is based on the use of the so-called ordering parameter [2]. Its concrete meaning is determined by a demand that it must describe the peculiarities of a ST as completely as possible. Here we choose the spontaneous strain x as the ordering parameter.

We suppose that the change of state at the ST is continuous. Then we can represent the change of the free energy F of the solid in the form

$$F = F_o + ax^2/2 + bx^4/4 + \dots + F^* \quad (1)$$

F_o is a regular part of F and is not susceptible of ST; b is a positive constant; F^* corresponds to the additional energy of a solid due to its interaction with external fields. In the vicinity of T_c the coefficient $a = a_T(T-T_c)$ changes its sign. This temperature region corresponds to a metastable intermediate state of a ferroelastic and is characterized by strong fluctuations of x . For the SubMM waves the reverse time of relaxation of x exceeds strongly the frequency of the wave field. Therefore we can consider the interaction of x with the field E as quasistatic and describe it within the classic quasi-equilibrium thermodynamics. Within the scope of a quasi-equilibrium approximation the interaction of x and E can be interpreted as electrostrictive (a model of a quasi-equilibrium electrostrictive coupling). Then

$$F^* = -Z_{ij}x E_i E_j - (k_\infty)_{ij} E_i E_j,$$

where k_∞ is a constant dielectric susceptibility for hyperhigh frequencies, and we obtain the final form

$$F = F_0 + ax^2/2 + bx^4/4 - Z_{ij}x E_i E_j - (k_\infty)_{ij} E_i E_j \quad (2)$$

Z_{ij} are the constants which determine the interaction of x with the SubMM wave field and are independent on frequency and temperature.

III. Fluctuations and Landau-Khalatnikov kinetic equation.

From (2) we find the fluctuation of polarization :

$$\delta P_j = -\partial F / \partial E_j = (\partial^2 F / \partial E_j^2) \delta E_j + (\partial^2 F / \partial E_j \partial x) \delta x^E. \quad (3)$$

If the changes of δE are harmonic then $\delta P(t)$ is harmonic too, but its phase won't coincide with the phase of δE . This will result in fading of the SubMM wave, and this fading will depend both on the frequency of the wave and on the temperature of a solid it passes through. According to the adopted model we consider that fluctuations δx^E follow the oscillations of the field :

$$\delta E_j, \delta x^E \sim \exp(i\omega t). \quad (4)$$

Then we can write (3) in the form :

$$\delta P_j = ((k_\infty)_{jj} + \Delta k_{jj}) \delta E_j \quad (5)$$

where Δk arises due to the interaction of relaxational and fluctuational processes developing in the ST region. To find the expression for $\delta x^E(\omega, T)$ we use the Landau-Khalatnikov equation [3]

$$\partial x / \partial t = -L^{-1} \partial F / \partial x. \quad (6)$$

L is a kinetic coefficient independent on frequency and temperature. Further we can approximately write :

$$\partial F / \partial x = (\partial^2 F / \partial x \partial E_j) \delta E_j + (\partial^2 F / \partial x^2) \delta x \quad (7)$$

Then from (5) - (7) we have :

$$\delta x^E = -Z_j E_j \tau L^{-1} (1 + i\omega\tau)^{-1}. \quad (8)$$

Here

$$\tau = L(a + 3bx_o^2)^{-1} \quad (9)$$

is the relaxation time of the spontaneous strain, x_o - its equilibrium value :

$$x_o = [a_T(T_c - T)/b]^{1/2}, \quad T \leq T_c \\ x_o = 0, \quad T > T_c \quad (10)$$

IV. Frequency dispersion in ferroelastics.

From (3), (5), (8) we have

$$\Delta k_{jj} = Z_j^2 (1 + i\omega\tau)^{-1} (a + 3bx_o^2)^{-1} E_j. \quad (11)$$

Then, if we write

$$\Delta k_{jj} = \Delta k'_{jj} + i\Delta k''_{jj},$$

from (9) - (11) it follows :

$$\Delta k'_{jj} = Z_j^2 \tau (1 + \omega^2 \tau^2)^{-1} L^{-1}, \quad (12)$$

$$\Delta k''_{jj} = -Z_j^2 (1 + \omega^2 \tau^2)^{-1} L^{-1} \omega \tau^2.$$

Since τ depends strongly on the temperature (see (9) , (10)) we obtain an opportunity to control the SubMM response of a ferroelastic material by a simple change of its temperature . If $\omega\tau \ll L$ (millimeter waves) then

$$\Delta k' \sim |T - T_c|^{-1}, \Delta k'' \sim |T - T_c|^{-2}.$$

With account of a coupling between k and complex refractive index $n = m + ih$

$$m = [(\sqrt{\Delta k'_{jj}^2 + \Delta k''_{jj}^2} + \Delta k'_{jj})/2]^{1/2},$$

$$h = [(\sqrt{\Delta k'_{jj}^2 + \Delta k''_{jj}^2} - \Delta k'_{jj})/2]^{1/2},$$

we can also briefly analyze the peculiarities of the SubMM wave refraction in the region of ferroelastic ST . The formulas (9) , (10) , (12) yield that due to ST in the region $T < T_c$ $n(\omega)$ acquires an additional anomalous part with a strong temperature dependence . The influence of ST manifests itself not only in a sharp response of $m(\omega)$ and $h(\omega)$ on petty changes of the temperature at $T < T_c$ but also in abrupt kinks of temperature dependences of $m(\omega)$ and $h(\omega)$ at $T = T_c$ since in the region $T > T_c$ no significant temperature dependences of $m(\omega)$ and $h(\omega)$ are expected . For higher frequencies these kinks tend to blur due to the increase of the dispersion factor $(1 + \omega^2 \tau^2)^{-1}$. For hyperlow frequencies ST-induced relaxational fading of the SubMM waves is negligible :

$$\Delta k'' \rightarrow 0 \text{ and } h \rightarrow 0 \text{ when } \omega \rightarrow 0.$$

Author thanks to Dr. S.V. Shalupayev for attention and support.

References

1. Aizu K. "Possible species of ferromagnetic, ferroelectric, and ferroelastic crystals" , Phys. Rev. B , Vol. 2, № 3, pp.754 - 772, 1970.
2. Гуфан Ю. М. Структурные фазовые переходы , Наука , Москва, с. 8 - 12 , 1982 .
3. Ландау Л. Д., Лифшиц Е. М. "Об аномальном поглощении звука вблизи точек фазовых переходов" , Докл . АН СССР, Т. 96, № 3, с. 469 - 472.

PECULIARITIES OF ELECTRON-WAVE INTERACTIONS IN THE RESONANCE SYSTEM WITH A SEMICONDUCTOR

V.A.Abdulkadyrov

Institute of Radiophysics and Electronics

Academy of Sciences of the Ukraine,

12, Acad. Proskura St., Kharkov 310085

Fax: (0572)441105, E-mail: ire@ire.kharkov.ua

The way of the multifunctional scheme creation using wave phenomena in, semiconductors and a search of new physical principles of generation, amplification, electromagnetic wave transformation is the development of mm and submm ranges with the semiconducting devices.

This report deals with electron-wave interactions in an active spatial-periodical semiconducting system placed in longitudinal electrical and strong magnetic fields. The key element of the electrodynamical model of the system under consideration is an h thickness semiconducting sample with a spatial-periodical structure having the period 1. By virtue of system nonequilibrium the spatial charge disturbances arising in the semiconductor propagate in the form of electrokinetic waves which are transformed, in their turn, into electromagnetic radiation, a part of which interacts again with the carriers and so on.

1. Within the framework of general electrodynamical formalism of spatially bounded plasma media, on the basis of quasi-hydrodynamical model of a drifting electron beam in a semiconductor and the rigorous solution of the boundary problem using the method (1) there has been obtained a characteristic equation of the system under investigation

$$\det \left\{ \frac{|n|}{n} T_n \Psi_m^n - \delta_{mn} \right\} = 0, \quad (1)$$

$$\text{where } T_n = 1 + i \frac{|n|}{n} \frac{g_{n1}}{k_{nz}} Q_{n1} A_n; \quad m, n = 0, \pm 1, \pm 2, \dots$$

$$Q_{n1,2} = B_{n1} e^{-ig_{n1}b} \pm B_{n2} e^{ig_{n1}b}; \quad g_{ns} = \frac{\omega^2}{c^2} \epsilon_s - k_{nz}^2;$$

$$\delta_{mn} = \begin{cases} 0 & m \neq n \\ 1 & m = n \end{cases}; \quad \delta = 0, 1, 2, 3.$$

$$A_n^{-1} = Q_{n2} - \frac{Z_{n2} e^{2ig_{n2}a} - 1}{Z_{n2} e^{2ig_{n2}a} + 1} \cdot \frac{\epsilon_2 g_{n1}}{\epsilon_1 g_{n2}} Q_{n1}; \quad k_n = g_{n3}^2 \frac{\epsilon_{zz}}{\epsilon_3}$$

$$B_{n1,2} = \frac{1}{2} (L_{n1} S_{n1,2}^2 e^{-ik_n h} + L_{n2} S_{n2,1}^2 e^{ik_n h});$$

$$L_{n1,2} = \frac{g_{n0}}{2k_n g_{n3}^2} [Z_n (\epsilon_n g_{n0} k_n \pm g_{n3}^2) e^{-ig_{n0}f} + (\epsilon_3 g_{n0} k_n \mp g_{n3}^2) e^{ig_{n0}f}];$$

$$S_{n12} = \frac{\epsilon_1 g_{n0} \pm \epsilon_3 g_{n1} k_n}{g_{n1}^2 \epsilon_{zz}}; \quad \epsilon_{zz} = \epsilon_3 - \frac{\omega_p^2}{\omega^1 (\omega^1 + i\nu) - v_T^2 k_{nz}^2};$$

$$z_{n1,2} = \frac{\xi_{1,2} \frac{\omega}{c} \pm g_{n0,2}}{\xi_{1,2} \mp g_{n0,2}}; \quad \omega_n^1 = \omega - v_d k_{nz},$$

k_{nz} - is the wave propagation constant along the system, ω_p and ω the frequencies of plasma and electromagnetic oscillations, $\epsilon_0=1$, ϵ_3 is the static semiconductor permeability, $\epsilon_{1,2}$ is the permeability of substrates placed under a semiconductor film and a periodical structure, correspondingly, f and a , f and a , f are the distances from a semiconductor to screens with the impedances ξ_1 and ξ_2 , b is the distance from the film to the structure, v is an effective

frequency or collisions with the pulse transfer, v_d is the carriers' drifting velocity, V_T is the heat velocity. The values $V_m^n, V_\delta^n, R_m, R_\delta$ are defined in [1]. The equation (1) has been obtained supposing a cyclotron frequency to be considerably greater than all the characteristics of system frequencies. The characteristic equation allows to study a spectrum of volume and surface waves supported by the system.

From the asymptotic solution (1) when $m, n = 0, -1, -2$ in the first approximation of the perturbation theory we obtain the complex constants of wave propagation in the case of plasma and relaxation mechanisms of oscillation swing in a drifting beam of charge carriers in the semiconductor. Note, that depending on geometrical, dynamical and electrophysical parameters of the system the growth and attenuation of waves is possible as they are propagating. The presence of growing waves of a spatial charge in the semiconductor indicates the formation of modulation of the drifting charge carriers and the appearance of coherent radiation. Under the influence of the radiation field the carriers' modulation increases (in virtue of an inverse effect of the radiation on medium) along with the increase of the coherent radiation in the system. As far as radiating "bunches" are formed by the field itself the radiation is the induced one. However, the system in which there appear the induced radiation possesses a fundamental property, i.e. a possibility to obtain amplification. The spatial amplification coefficient is determined from the solution (1). It is shown that based on InSb samples where the highest drifting velocity is achieved at $T = 77$ K, a considerable spatial signal amplification is possible, when $V_d \sim \omega l / 2\pi$, $\nu \sim 10^{11} \text{ c}^{-1}$.

2. Any mechanism of the inverse feedback (interior inverse feedback, external inverse feedback, boundary inverse feedback) in the system leads to the regime of self-excitation.

The drifting flow is described in the frames of a quasi-hydrodynamic model in a semiconductor. Determine the complex power of the interaction in the form

$$P = \frac{i w \theta_n B_n g a_T}{16 \pi h_p \gamma} \sum_{j=0}^{\infty} (1)^j \int_{-\infty}^{\infty} \frac{|\tilde{E}(K)|^2}{h_j - K} dK \quad (2)$$

here θ_n is the coefficient of using the drifting flow; B_n is the amplitude of average of the cross-section of flow of the synchronous harmonic's field, $\tilde{E}(K)$ is the spectral density of the synchronous field, K - is the spectral wave number:

$$h_j = \left[h_0 \left(1 + i \frac{\nu}{2w} \right) + (-1)^j h_p \gamma \right] a_T - \text{is the propagation constant of waves of the space charge (WSC):}$$

$$h_0 = \frac{w}{V_0}; \quad h_p = \frac{w_p}{V_0}; \quad \gamma = \left\{ a_T - \frac{\omega^2}{\omega_p^2} \left[a_T \left(1 + i \frac{\nu}{\omega} \right) - \left(1 + i \frac{\nu}{2\omega} \right) \right] \right\}^{1/2};$$

w, w_p are the electromagnetic and plasma frequencies, correspondingly. The first addend (2) determines the efficiency of the power-exchange of slow WSC with space-inhomogeneous fields of OR, the second one is the quick WSC. To separate a real and imaginary parts of the expression (2) and an imaginary part of the expression (2) one may by means of the expansion of its analytical function determined by the catch integral along the real axis on degrees h_j'' [2] and using the integral Gilbert transformation.

A complex power of the interaction of the drifting carriers flow in a semiconductor with a wave beam of OR at $\nu \sim 2 w_p$ one may represent in the following form

$$\begin{aligned} P &= P_0 F_m(\varphi, \varphi_\nu), \\ P_0 &= \frac{w g \theta_n B_n^2 d^2 y}{8}, \quad \varphi_\nu = \frac{\nu}{2V_0} dy, \\ F_m(\varphi, \varphi_\nu) &= \frac{\sqrt{\pi}}{2^{m+2} m!} \left\{ \frac{2mH_{m-1}(z)}{H_m(z)} T_m(z) - \frac{H_m(z)}{H_{m+1}(z)} T_{m+1}(z) \right\}; \quad z = \frac{\varphi + i\varphi_\nu}{2\sqrt{2}}; \\ T_m &= H_m^2(z) w(z) + \frac{2}{\sqrt{\pi}} H_m(z) \sum (-1)^s C_m^s \cdot H_{m-s}(z) \cdot H_{s-1}(-iz); \quad C_m^s = \frac{m!}{(m-s)!}. \end{aligned}$$

$\varphi = \left(\frac{2\pi s}{e} - \frac{h_0}{a_T} \right)$ - the parameter of missynchronism; d_y - is the diameter of the field's spot of the main oscillation type; $\nu = \sum_i \nu_i$, ν_i are the frequencies of collisions corresponding to the concrete mechanism of carriers scattering in a semiconductor; V_T - is the heat velocity; $w(z)$ - is the complex integral of probability.

In the case of the given field distribution in the system under investigation with plane mirrors from the condition of self-excitation we find a value of the threshold current, necessary for the support of the autooscillation regime.

$$I \approx \frac{m^* s_0}{e \varepsilon_3} \cdot \frac{A_0^4}{A_n^4} s_v^2 s_p^2;$$

$$s_v = \frac{\nu_p^2}{\nu_p - 1 + \exp(-\nu_p)}; \quad s_p = \frac{DV_d^{3/2} g_{n0}}{Ql[1 - \exp(-2g_{n0}h)]};$$

where $\nu_p = \frac{\nu L}{2V_d}$; L is a length of the sample in which the interaction of waves and carriers takes place; A_n - is the harmonics of the field spectrum of the resonance system; s_0 - is a simple cross-section; Q - is a loaded of the system; D - is the spacing between mirrors; m^* - is an effective mass of the conductivity electron.

3. If a complex information signal with the frequency difference $\omega_{i+1} - \omega \approx \Delta\omega \sim 10^{11}-10^{12} \text{c}^{-1}$ comes to the input of the system performed on the samples with the non-linearity resulted from the non-paraboloidal character of energetic zones, it transforms into a signal on the $\Delta\omega$ frequency. After falling into the range of spatial system amplification the signal will be essentially intensified, as shown in T .

Thus, a semiconducting system having spatial periodicity and performed in the single technological cycle may amplify, generate and transform the oscillations in the submm range when matching the correspondent parameters. All the necessary pure semiconductor materials, high drifting velocities, small spacing of a periodical structure are obtained using an advanced technology.

Note, that the kind of a periodical structure (strip, reflecting ridge, echelle, V-type, mosaic, etc.) made of metal, dielectric or semiconductor is not important, however, it affects the system output characteristics.

References

1. V.P.Shestopalov. The method of the Riemann-Gilbert problem in the diffraction theory and wave propagation. Kharkov: Pub. Kharkov State Univ., 1971 (in Russian).
2. T.Stix. The theory of plasma waves. M. 1965 (in Russian).

**THE THEORY OF AN ELECTROMAGNETIC RADIATION BY A
SEMICONDUCTING HETEROSTRUCTURE WITH PERIODIC SCREENS**

V.A.Abdulkadyrov

Institute of Radiophysics and Electronics

Academy of Sciences of the Ukraine,

12, Acad. Proskura St., Kharkov 310085

Fax: (0572)441105, E-mail: ire@ire.kharkov.ua

Within the framework of general electrodynamical formalism of spatially bounded plasma media and the rigorous solution of the boundary problem using the method (1) there has been obtained a characteristic equation of the system (Fig.1) under investigation

$$\det \left\{ \frac{|n|}{n} L_m^n \xi_m - \delta_{mn} \right\} = 0$$

где $m, n = 0, \pm 1, \pm 2, \dots$

$$L_m^n = V_m^n - R_m \frac{V_\sigma^n}{R_\sigma}; \quad \delta_{mn} = \begin{cases} 0 & m \neq n \\ 1 & m = n \end{cases}$$

$$\text{где } \Psi_n = \frac{g_{n4}}{\varepsilon_4} \left(\Phi_{n2} - \frac{\Theta_{n2}}{\Theta_{n1}} \Phi_{n1} \right); \quad \Psi_{n1} = \frac{g_{n4}}{\varepsilon_4 g_{n5}} \frac{\Phi_{n1}}{\Theta_{n1}}, \quad \Phi_{n1,2} = \tau_{n1,2} e^{ig_{n4}\alpha} + \tau_{n3,4} e^{-ig_{n4}\alpha}$$

$$2Y_n = \frac{2\pi}{l} (\chi\alpha + n) (A_n \Theta_{n1} + \delta_{0n} \Theta_{n2} e^{-ig_{n1}(a+b+h)})$$

$$\xi_n = 1 + i \frac{|\chi\alpha + n|}{\chi\alpha + n} \cdot \frac{|n|}{n} \cdot \Psi_{n1} \sqrt{\frac{\chi^2}{(\chi\alpha + n)^2} - 1}; \quad \Theta_{n1,2} = \frac{g_{n4}}{\varepsilon_4 g_{n5}} [(g_{n4} - \varepsilon_4 g_{n5}) \tau_{n1,2} e^{ig_{n4}\alpha} + (g_{n4} + \varepsilon_4 g_{n5}) \tau_{n3,4} e^{-ig_{n4}\alpha}]; \quad \chi = \frac{l}{\lambda};$$

$$\tau_{n1} = M_{n1} \varphi_{n2}^{(-)} e^{-i\Gamma_{n1} h} + M_{n3} \varphi_{n2}^{(+)} e^{i\Gamma_{n1} h};$$

$$\tau_{n2} = M_{n2} \varphi_{n2}^{(-)} e^{-i\Gamma_{n2} h} + M_{n4} \varphi_{n2}^{(+)} e^{i\Gamma_{n2} h};$$

$$\tau_{n3} = M_{n1} \varphi_{n1}^{(+)} e^{-i\Gamma_{n3} h} + M_{n3} \varphi_{n2}^{(-)} e^{i\Gamma_{n3} h};$$

$$\tau_{n4} = M_{n2} \varphi_{n1}^{(+)} e^{-i\Gamma_{n4} h} + M_{n4} \varphi_{n2}^{(-)} e^{i\Gamma_{n4} h};$$

$$M_{n1} = z_{n1} \hat{\lambda}_{n1} + z_{n4} \hat{\lambda}_{n4};$$

$$M_{n2} = z_{n1} \hat{\lambda}_{n3} + z_{n2} \hat{\lambda}_{n4};$$

$$M_{n3} = z_{n3} \hat{\lambda}_{n4} + z_{n2} \hat{\lambda}_{n2}; \quad M_{n4} = z_{n3} \hat{\lambda}_{n3} + z_{n4} \hat{\lambda}_{n4};$$

$$\hat{\lambda}_{n1} = \lambda_n^{(+)} e^{-ig_{n1}b}; \quad \hat{\lambda}_{n2} = \lambda_n^{(-)} e^{ig_{n2}b};$$

$$\hat{\lambda}_{n3} = \lambda_n^{(-)} e^{-ig_{n3}b}; \quad \hat{\lambda}_{n4} = \lambda_n^{(+)} e^{ig_{n4}b};$$

$$\lambda_n^{(\pm)} = g_{n2}^{-2} (\varepsilon_2 g_{n1}^2 \pm g_{n1} g_{n2});$$

$$\varphi_{n1}^{(\pm)} = \varepsilon_3^{-1} g_{n4}^{-2} (\varepsilon_4 g_{n3}^2 + g_{n4} g_{n3}^2 \sigma_s^* \pm \Gamma_n g_{n4} \varepsilon_3);$$

$$\varphi_{n2}^{(\pm)} = \varepsilon_3^{-1} g_{n4}^{-2} (\varepsilon_4 g_{n3}^2 - g_{n4} g_{n3}^2 \sigma_s^* \pm \Gamma_n g_{n4} \varepsilon_3);$$

$$z_{n1,2} = \frac{\varepsilon_3 g_{n2}^2}{\varepsilon_2 g_{n3}^2} \pm T_n^{(\pm)}; \quad z_{n3,4} = \frac{\varepsilon_3 g_{n2}^2}{\varepsilon_2 g_{n3}^2} \mp T_n^{(\pm)}; \quad T_n^{(\pm)} = \frac{g_{n2} \varepsilon_2 \pm \sigma_s^* g_{n2}}{\varepsilon_2 \Gamma_n}; \quad \sigma_s^* = \frac{4\pi}{c K_0} \sigma_s;$$

$$\Gamma_n^2 = g_{n3}^2 \left(1 - \frac{\omega_p^2}{\omega'^2 + i\tau^{-1}\omega - V_T^2 K_{nz}^2} \right);$$

$$\omega' = \omega - V_0 K_{nz};$$

k_{nz} - is the wave propagation constant along the system, ω_p and ω the frequencies of plasma and electromagnetic oscillations, $\epsilon_0=1$, ϵ_3 is the static semiconductor permeability, $\epsilon_{1,2}$ is the permeability of substrates placed under a semiconductor film and a periodical structure, correspondingly, f. The values $V_m^n, V_\delta^n, R_m, R_\delta$ are defined in [1]. The equation (1) has been obtained supposing a cyclotron frequency to be considerably greater than all the characteristics of system frequencies. The characteristic equation allows to study a spectrum of volume and surface waves supported by the system.

In the local approximation, which is valid for plasmon wavelengths large as compared to the average interelectron spacing, σ_s does not depend on the subscript m and can be written in the Drude form

$$\sigma_s = \frac{e^2 N_S}{m^*} \frac{\tau}{1 + i\omega\tau},$$

where τ is a phenomenological electron scattering time.

In the long wavelength case the reflection coefficient is equal to...

$$A_0 = \frac{-i\varphi_0 D}{ig_{01}(\psi_0 D + R_0)} \frac{1}{\Theta_{01}} - e^{ig_{0n}(a+b+h)} \frac{\Theta_{02}}{\Theta_{01}}, \quad (6)$$

where $D = V_\delta R_0 - V_0^0 R_\delta$.

The structure under study is shown in Figure...

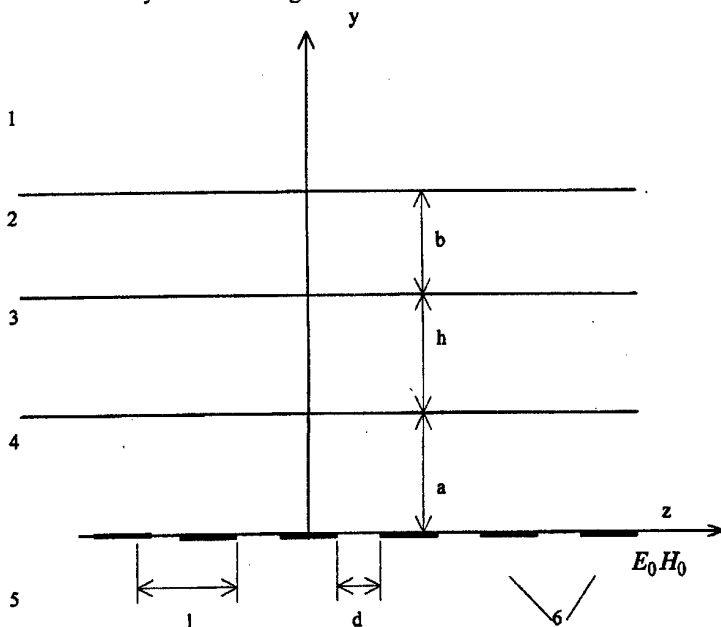


Fig. Structure under consideration. $\epsilon_1, \epsilon_2, \epsilon_4, \epsilon_5$ are the dielectric constants of the media; ϵ_3 - are the plasma layer; 6 - are the grating periodicity.

References

1. V.P.Shestopalov. The method of the Raman-Gilbert problem in the diffraction theory and wave propagation. Kharkov: Pub. Kharkov State Univ., 1971 (in Russian).



PROBLEMS OF THE THEORY OF WAVE DIFFRACTION

Preceding Page Blank

**A Regularization Method for a Class
of Dual Series Equations in Diffraction Theory**

Andrey V. Brovenko and Anatoly Ye. Poyedinchuk

Institute of Radiophysics and Electronics
of the National Academy of Sciences of Ukraine
12, Acad. Proskury st., Kharkov, 310085, Ukraine
Phone: (7-0572) 44 85 56, FAX: (7-0572) 44 11 05
e-mail: brove@ire.kharkov.ua

The paper is devoted to the development of a regularization technique for the following class of dual series equations

$$\sum_{n=-\infty}^{+\infty} x_n e^{in\varphi} = 0, \theta < |\varphi| \leq \pi, \quad (1)$$

$$\sum_{n=1}^{+\infty} n x_n e^{in\varphi} - a \sum_{n=-1}^{-\infty} n x_n e^{in\varphi} = \sum_{n=-\infty}^{+\infty} g_n e^{in\varphi}, |\varphi| < \theta \quad (2)$$

$$g_n = f_n + \sum_{m=-\infty}^{+\infty} V_{nm} x_m \quad (3)$$

The two-dimensional problems of electromagnetic wave diffraction on metal screens located on the interface between anisotropic dielectric media, some contact problems in the theory of elasticity, etc. are reduced to the equations of the form (1) - (3) or to the systems of the equations of this kind.

1. The solution $x = (x_n)_{n=-\infty}^{+\infty}$ of equations (1)-(3) is sought in the space $I_2(I) = \left\{ x = (x_n)_{n=-\infty}^{+\infty} : \sum_{n=-\infty}^{+\infty} |x_n|^2 (|n| + 1) < \infty \right\}$. The coefficients $f = (f_n)_{n=-\infty}^{+\infty}$ and matrix operator

$V = (V_{mn})_{m,n=-\infty}^{+\infty}$ are found under the following conditions: first, $f \in I_2(I)$ and the matrix operator $V: I_2 \rightarrow I_2$ is a compact one; second, series (1) is a Fourier series of a function which belongs to $L_2[-\pi, \pi]$ and series (2) is the Fourier series of the similar function which belongs to $\dot{L}_1[-\pi, \pi]$.

Note that the limitations imposed on the solutions of equations (1) - (3), on matrix operator V and coefficients f are usual for the considered problem. In any case, these limitations form the sufficient conditions of the existence of a unique solution of equations (1) - (3).

2. An idea of the equivalent reformulation of these equations in terms of the conjugation problem of analytic functions which is the Riemann-Hilbert problem for an unclosed contour forms the basis of the suggested method of the regularization of equations (1) - (3).

The formal scheme of the reduction of equations (1) - (3) to the Riemann-Hilbert problem is following. Once equation (1) has been differentiated with respect to φ , we denote $y_n = nx_n, n = \pm 1, \pm 2, \dots, y_0 = x_0$ and reduce (1) - (2) to the following equations

$$\sum_{n=-\infty, n \neq 0}^{+\infty} y_n e^{in\varphi} = 0, \theta < |\varphi| \leq \pi \quad (4)$$

$$\sum_{n=1}^{+\infty} y_n e^{in\varphi} - a \sum_{n=-1}^{-\infty} y_n e^{in\varphi} = \sum_{n=-\infty}^{+\infty} g_n e^{in\varphi}, |\varphi| < \theta \quad (5)$$

$$\sum_{n=-\infty, n \neq 0}^{+\infty} \frac{(-I)^n y_n}{n} = -y_0 . \quad (6)$$

Condition (6) is obtained from (1) at $\varphi = \pi$. Let us introduce the two functions of a complex variable Z

$$X^+(z) = \sum_{n=1}^{+\infty} y_n z^n, X^-(z) = - \sum_{n=1}^{+\infty} y_{-n} z^{-n}$$

which are analytical inside and outside the circle $|z| < 1$, respectively. Let an arc L_2 of circle $|z| = 1$ connect points $e^{-i\theta}$ and $e^{i\theta}$ and run through the point $z = -I$; L_1 is the rest of the circle. With the introduced functions, equations (4) - (5) can be rewritten in the form

$$X^+(e^{i\varphi}) - X^-(e^{i\varphi}) = 0, e^{i\varphi} \in L_2 \quad (7)$$

$$X^+(e^{i\varphi}) + \alpha X^-(e^{i\varphi}) = g(e^{i\varphi}), e^{i\varphi} \in L_1 , \quad (8)$$

where
$$g(e^{i\varphi}) = \sum_{n=-\infty}^{+\infty} g_n e^{in\varphi}.$$

From (7) it follows that

$$X(z) = \begin{cases} X^+(z), |z| < 1 \\ X^-(z), |z| > 1 \end{cases}$$

extends to the function analytical in a complex plane having a slit along arc L_1 . This function descends as

$$z \rightarrow \infty, \text{ i.e. } X(z) = -\frac{y_{-1}}{z} + O\left(\frac{1}{z^2}\right).$$

Once the limit values of this function on arc L_1 have been obtained from condition (8), equations (1) - (3) are reduced to the problem of reconstruction of function $X(z)$ which is analytical outside the arc L_1 .

3. Let constant $\alpha > 0$ and the right hand side of (2) be known. Then the solution of the Riemann- Hilbert problem (8) can be obtained in a closed form. That is

$$X(z) = K(z) \left[\frac{1}{2\pi i} \int_{L_1} \frac{y(t) dt}{K^+(t)(t-z)} + C \right], \quad (9)$$

where $K(z) = (z - e^{i\theta})^{-1} \exp\left((0.5 - i\beta) \int_{L_1} \frac{dt}{(t-z)}\right)$ is a canonical solution of the homogeneous problem

corresponding to (8), $\beta = \frac{\ln \alpha}{2\pi}$, C is an arbitrary constant, $K^+(t)$ is the limit of $K(z)$ when approached from the inside of the circle $|z| = 1$. Note that solution (8) is valid for a class of functions admitting an integrable singularity in the vicinity of the ends of arc L_1 . With the Plemel - Sokhotsky formulas for (9) and under condition (6) we obtain the solution of equations (1) - (2) in an analytical form

$$x_m = \sum_{n=-\infty}^{+\infty} a_{mn} g_n, \quad (10)$$

where

$$\begin{aligned}
a_{mn} &= \frac{1}{m} \left[P_n^m + W_n^m + e^{-2\beta\theta} R_m(P_n^0 + W_n^0) \right], m \neq 0; a_{0n} = P_n^\sigma + W_n^\sigma + e^{-2\beta\theta} R_\sigma(P_n^0 + W_n^0), \\
R_m &= \begin{cases} -e^{2\beta\theta} P_m(\beta, \theta), m \geq 0 \\ -P_{-m-1}(-\beta, \theta), m \leq -1 \end{cases} \quad W_n^\sigma = \sum_{m \neq 0} \frac{(-I)^m W_n^m}{m}, \quad R_\sigma = \sum_{m \neq 0} \frac{(-I)^m R_m}{m}. \\
P_n^m &= b \begin{cases} \frac{\theta}{\pi}, m = n \\ \frac{\sin(n-m)\theta}{\pi(n-m)}, m \neq n \end{cases} \quad P_n^\sigma = b \begin{cases} 0, n = 0 \\ \frac{\cos n\theta - (-I)^n}{\pi n}, n \neq 0 \end{cases} \\
W_n^m &= \frac{e^{-\pi\beta}}{2ch(\pi\beta)} \begin{cases} -\sum_{p=0}^{n+1} \mu_{n-p+1}(\beta, \theta) R_{m-p}, n \geq 0 \\ e^{-2\beta\theta} R_{m+1} - R_m, n = -1 \\ e^{-2\beta\theta} \sum_{p=0}^{-n-1} \mu_{-n-p-1}(-\beta, \theta) R_{m+p+1}, n < -1 \end{cases}
\end{aligned}$$

Here $P_m(\beta, \theta)$ are the Pollaczek polynomials (Pollaczek F. 1950, C.R. Acad. Sci. Paris 230, p. 1563-1565)

and $b = \frac{a-1}{2a}$. Coefficients $\mu_n(\beta, \theta)$ can be expressed in terms of the Pollaczek polynomials by the formulas

$$\mu_0 = 1, \mu_1 = -P_1(-\beta, \theta), \mu_n = P_n(\beta, \theta) - 2\cos\theta P_{n-1}(\beta, \theta) + P_{n-2}(\beta, \theta), n \geq 2.$$

Using the asymptotics of $P_n(\beta, \theta)$ for $n \rightarrow \infty$ one can prove that, first, the matrix $A = (a_{mn})_{m,n=-\infty}^{+\infty}$ defines the compact operator in the space l_2 and, second, if $g = (g_n)_{n=-\infty}^{+\infty} \in l_2(I)$, $x = (x_n)_{n=-\infty}^{+\infty} \in l_2(I)$. Then series (2) converges uniformly within $[-\pi, \pi]$ with the exception of an arbitrary small vicinity of the points $\varphi = -\theta, \theta$.

Notice: 1. If the constant $a < 0$, the solution (8) of the Reeman-Hilbert problem is written as

$$X(z) = \frac{\tilde{K}(z)}{2\pi i} \int_L \frac{g(t)dt}{\tilde{K}^+(t)(t-z)},$$

where $\tilde{K}(z) = \exp\left(i\tilde{\beta} \int_L \frac{dt}{t-z}\right)$ is a canonical solution, $\tilde{\beta} = \frac{\ln(-a)}{2\pi}$, and $\tilde{K}^+(t)$ is the limit of function

$\tilde{K}(t)$ when approached from the inside of the circle $|z| < 1$.

2. The Pollacheck polynomials $P_m(\beta, \theta)$ are replaced by elements $B_m(\tilde{\beta}, \theta)$ defined as follows

$$B_0(\tilde{\beta}, \theta) = 1, B_1(\tilde{\beta}, \theta) = 2\tilde{\beta}\sin(\theta), B_m(\tilde{\beta}, \theta) = \frac{2(m-1)\cos(\theta) + 2\tilde{\beta}\sin(\theta)}{m} B_{m-1}(\tilde{\beta}, \theta) - \frac{m-2}{m} B_{m-2}(\tilde{\beta}, \theta)$$

for $m \geq 2$.

4. Using the solution of equations (4)-(5) in an explicit form (see (10)) one can obtain $x + Hx = h$, where $H = AV: l_2 \rightarrow l_2$ is a compact operator, $h = Af$, and, consequently, (11) is a second-kind equation in l_2 .

HARMONIC FILTERS ON RIDGED WAVEGUIDES

A.A. Kirilenko, L.A. Rud', V.I.Tkachenko

Institute of Radiophysics and Electronics of the National Academy of Sciences of Ukraine
 12 Acad. Proskura St., Kharkov, 310085, Ukraine
 Tel. +38-0572-448518, Fax +38-0572-44105, E-mail: kirilenko@ire.kharkov.ua

The paper is devoted to the method and results of design and analysis of evanescent mode lowpass filters (LPF) that may be used as higher frequency harmonic filters (up to the fourth harmonic). Configuration of low-pass filter (LPF) is based on shorten ridged waveguide sections (resonators) with a ridge profile varying along the longitudinal axis (in a general case). Resonators may be performed on single- (see Figures 1, 2a, c) or double-ridge (Figures 2b, d) waveguide sections with a symmetrical (Figures 2a, b) or non-symmetrical (Figures 2c, d) distribution of their gaps along a filter longitudinal axis. Resonators are separated from each other by notches formed by other ridged waveguide sections (in a general case) or by rectangular waveguide sections (in a limiting case). The ended sections of LPFs are bounded at external sides by one-step transformers. The latter have the housing dimensions equal to the ones of main rectangular waveguide. These ended transformers are not conventional transitions from the main waveguide to the filter waveguide as they simultaneously play the double role of transitions and the ended K-invertors of LPF. Introduction of such a type of transformers does the proposed LPF configurations differ from the known ones [1-3] and leads to the significant decreasing of overall filter length and widening of the pass and stop bands. The exact full-wave models are used for the obtaining of generalized S-matrices of all components, and analysis of LPF as a whole structure is carried out on the base of the generalized S-matrix technique.

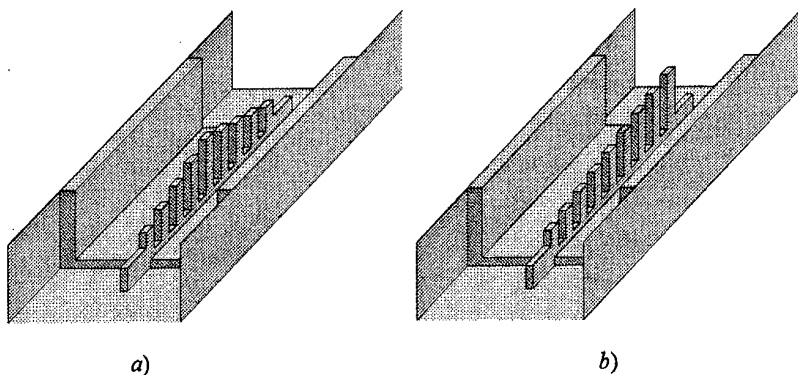


Figure 1. Low-pass (harmonic) filters on single-ridged waveguides with a symmetrical (a) and non-symmetrical (b) distribution of filter sections along longitudinal axis.

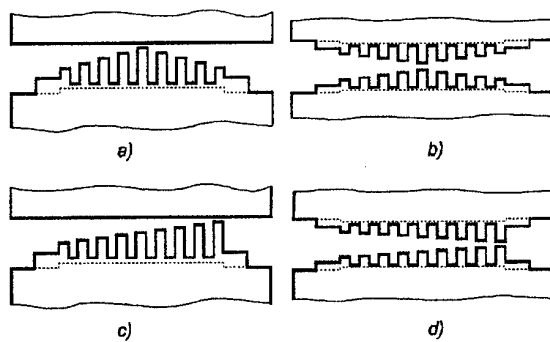


Figure 2. Longitudinal cross-sections of low-pass filters on single-ridged waveguide sections (a, c) and double-ridged ones (b, d).

The design algorithm has some stages. At the first stage the search of ridged waveguide housing is done according to the given values of ridge thickness t , minimal gap size w_{\min} , and the specified frequencies of pass band beginning F_b and stop band edge F_s . The selection of width a_r and height b_r of ridged waveguide housing is based on two following requirements: 1) the cutoff frequency of dominant mode for the ridged waveguide with the specified minimal gap w_{\min} must be below F_b ; 2) the next higher cutoff must be above the stop band upper limit F_s . The procedure of a_r and b_r definition is performed with the aid of preliminary calculated database and consists in the choice of these values, satisfying the conditions 1) and 2) simultaneously. At that, the geometry with maximal a_r is considered as the best one.

At the second step, the maximal gap size w_{\max} is found reasoning from the requirements that the ridged waveguide with dimensions a_r , b_r , t , and $w = w_{\max}$ must be above cutoff within pass band. The laws of section gap distribution along the filter may be assorted ones: from the uniform distribution with equal gaps $w = w_{\min} = w_{\max}$ to a non-uniform law, for example the exponential one. The notch depths, i.e. the values of notch ridged waveguide gaps are chosen according to the requirement that these waveguide sections should be cutoff ones above the filter pass band. However they need not be cutoff through the whole stop band. Simply removing the ridge from the notch sections, i.e. the choice of $w_{nt} = b_r$ is usually satisfactory. At that, the calculation time is essentially decreased, as instead of time-consuming calculation of junctions between two ridged waveguides we have to calculate the junctions between rectangular and ridged waveguides.

After that the initial filter synthesis is performed with the aid of scheme proposed by Levy [4] and then used in [5] to design lowpass filters on tapered corrugated rectangular waveguides. Levy's procedure provides the set of $n+1$ K -invertors (n is a number of filter sections that may be defined by prototype synthesis procedure or may be set as the fixed value) and electrical lengths of waveguide segments in between. Notches model the internal K -invertors of lowpass prototype if to consider the K -invertors as segments of evanescent mode waveguides between single-mode ridged waveguides. The external K -invertors have usually greater values than the internal ones, as they play a matching role. As a consequence, in the majority of cases the value of reflection coefficient for a junction between the main rectangular waveguide and the ridged waveguide of the first (last) filter section is too large. It has to be reduced by implementing an additional matching section of ridged waveguide with the cross-section of main rectangular waveguide. This matching section may be considered as a transformer and its ridge is fabricated in the same septum as internal part of the filter. The search of transformer dimensions is performed by two steps: 1) the first global minimum of reflection coefficient within the range $w_{\max} \leq w_r \leq b_r$ and different lengths $l_r \geq 0$ is roughly defined; 2) the final dimensions are being found by exact estimation of l_r to provide the required K -inverter value at the maximum possible transformer gap. The latter requirement is necessary to avoid some possible restrictions at the optimization. The initial synthesis is carried out at the given filter cutoff frequency $F = F_{cut}$.

If all elements, playing the role of K -invertors, are defined then the stage of searching filter section lengths is performed. It should be noted that obtained lengths are essentially less than $\lambda_g / 2$ where λ_g is the operating mode wavelength. That's why the lowpass filters as well as bandpass filters based on ridged waveguide sections are widely used today in the microwave and millimeter-wave technique.

More often than not, the characteristics obtained after the synthesis, based on the circuit theory, are not completely satisfactory mainly within the stop band. The reason consists in fringing field interaction within filter sections and some frequency dispersion of filter elements. To reach the specified response, the initial geometry is optimized on the base of full-wave exact model and the following goal function

$$G = W \sum_{q=1}^N \left(\frac{L(F_q)}{L_r} \right)^2 + \left(\frac{L_d}{L(F_a)} \right)^2 + \sum_{\substack{q=1 \\ F_c < F_q < F_d}}^{N_r} \left(\frac{L_{qr}}{L(F_q)} \right)^2$$

where W defines the relation between the role of pass band and stop band in goal function, N is the number of uniformly placed frequency points in a pass band, $L(F_q)$ is an insertion loss value at the frequency point F_q , N_r is number of points between the edge frequency of pass band F_c and the beginning frequency of stop band F_d . Value of L_{qr} is calculated at above points according to a linear law. Usually $N_r = 2 - 4$ is enough to reach the required steepness of filter response to be optimized.

The design algorithm was realized as the C++ source-code software with a possibility of operation in the media of BORLANDC 4.5, VISUALC++ 5.0, and GNU-LINUX SLACKWARE 3.4 compiler. The set of concepts and principles described in [6] were used at creating the software. Except of the above described design stages the software contains tools for creating and saving databases for the ridged waveguide mode bases and for the given order S-matrices of all filter components. It essentially decreases the CPU time on the optimization procedure operation and calculation of frequency response of the optimized filter. The latter is exposed to the additional analysis to obtain the information on possible parasitic resonances within the specified filter stop band. The output text file is provided for saving the results of filter design and calculated frequency response.

As an example of the created software possibilities, the characteristics of one designed lowpass filter with wide transmission and rejection bands are presented in Figure 3. The filter was designed for the 7.2×3.4 mm rectangular waveguide operating band 26 – 40 GHz (return loss >20dB) and the specified stop band 52 – 160 GHz (suppression >60, 50, 40 dB for the second, third, fourth harmonics, respectively). The filter topology is similar shown in Figure 2b and has eleven ridged resonators the gaps of which are varying from $w_{\max} = 0.2$ mm (edge sections) to $w_{\min} = 0.08$ mm (central section) according to the exponential law. At the ridged waveguide housing 2.6×1.6 mm, overall filter length including two transformers is 18.04 mm. As one can see, the designed filter satisfies the required specification in the whole frequency range practically. Breaks in the response curve within stop band are caused by appearance of new propagating modes in the input and output rectangular waveguides. The most depth spikes are observed at the end of stop band but their large Q-factors (more than 10000) allow saying that they will not appear on the response of the fabricated filter owing to ohmic loss.

It should be noted that other topologies, in particular based on single-ridged waveguides (see Figure 1a), are suitable for the design of harmonic filters with the narrower pass and stop bands.

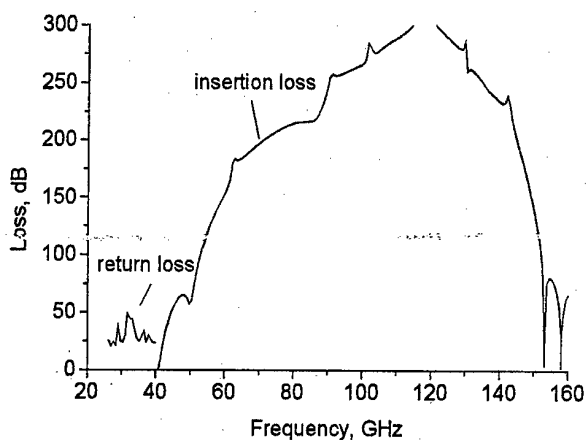


Figure 3. Frequency response of the optimized harmonic filter on double-ridged waveguide sections with a wide pass and stop bands.

References

1. H.F. Chappel, "Waveguide low pass filter using evanescent mode inductors", *Microwave Journal*, Vol. 21, No. 12, pp.71-72, 1978.
2. C. Nguyen, K. Chang, "Millimetre-wave low-loss finline lowpass filters", *Electronics Letters*, Vol. 20, No. 24, pp. 1010-1011, 1984.
3. J. Bornemann, F. Arndt, "Modal S-matrix design of metal finned waveguide components and its application to transformers and filters", *IEEE Trans. on MTT*, Vol. 40, No. 7, pp. 1528-1537, 1992.
4. R. Levy, "Tapered corrugated lowpass filters", *IEEE Trans. on MTT*, Vol. 21, No. 8, pp. 526-532, 1973.
5. A.A. Kirilenko, L.A. Rud', S.L. Senkevich, V.I. Tkachenko, "Synthesis and analysis of small-size low-pass filters (LPF) on corrugated rectangular waveguides", *Radiophysics and electronics*, Collected volume of IRE NASU, Vol. 1, No. 1, pp. 5-16, 1996 (in Russian).
6. A.A. Kirilenko, V.I. Tkachenko, "System of electromagnetic simulation of microwave – millimeter-wave devices", *Izv. Vuzov. Radioelektronika*, Vol. 39, No. 9, pp. 17-28, 1997 (in Russian).

WAVEGUIDE BAND PASS FILTERS WITH INCREASED STOP BAND ATTENUATION

M.E. Ilchenko^{*}, A.A. Kirilenko^{*}, A.G. Yushchenko^{**}, L.A. Rud^{*}, V.I. Tkachenko^{*}

^{*} - Institute of Radiophysics and Electronics of National Academy of Sciences
12 Ulitsa Acad. Proskury, Kharkov, 310085, Ukraine; tel.: 38-0572-44-85-95; email: yush@ire.kharkov.ua
^{**} - National Technical University of Ukraine "Kiev Polytechnic Institute",
37 Peremogy Prospect, Kiev, 252056, Ukraine; tel.: 38-044-441-12-20; email: yush@polytech.kiev.ua

Introduction

Band pass filters are base elements of receiving-transmitting systems for wireless telecommunications. Designing such systems in millimeter wave range greatly differs from standard approaches, developed for the technologically carefully studied centimeter range. Band pass filters based on the all-metal inserts placed in E-plane of rectangular waveguide (Fig. 1a) are the most technologically acceptable in the millimeter range, due to well reproducible planar technology of resonator fabrication. But, essential defect of such filters designing ideology is a restrain factor of their broad utilizing. At first, it is necessary to point to the presence in them of the closely situated parasite pass band that gives a problem of compacting and compatibility of some datapaths in their use.

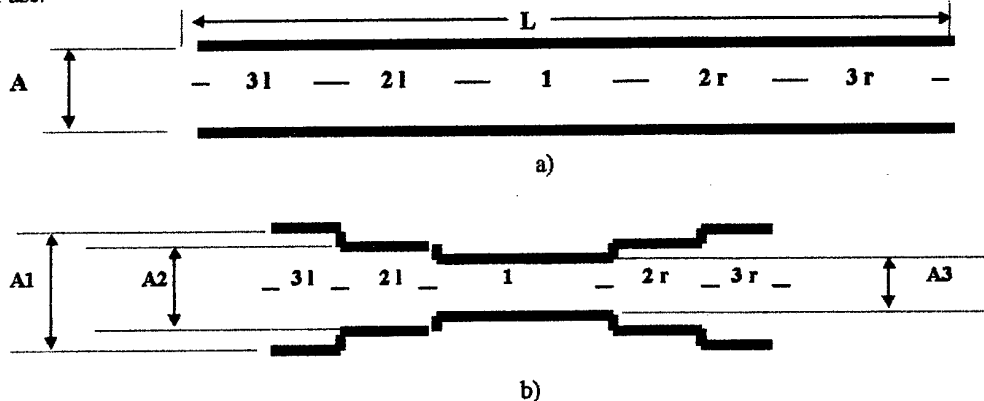


*Fig. 1. Band-pass filter designs based on E-plane longitudinal strip diaphragms:
a)- classical structure; b) - new structure*

Classical structure physics and new filters design

The frequency responses (FR) of the all-metal classical filters, based on strip diaphragms, are shown in Fig. 2. The big value of the parasite bandwidth is conditioned by "strong" modes coupling having two field variations on the length of the resonator, formed by two adjacent diaphragms. Coupling turns out to be strong as far as at the parasite mode frequency, the waveguide arms, formed by dividing of waveguide by the diaphragm, become non-cut-off. It is characteristic, that with increasing the thickness of diaphragm (t) a certain increase of maximum stop band attenuation level and some shift of close situated parasite resonance in the higher-frequency area and some diminution of parasite pass band occurs. However, it is impossible to develop given positive effect in classical designs, because in this case the length of input strip has already decreased twice. The above mentioned filters FR change are explained by the fact that when increasing a thickness of the strip, the sizes of the coupling waveguides decrease and they turn out to be more cut-off. Simple reduction of waveguide housing width, on

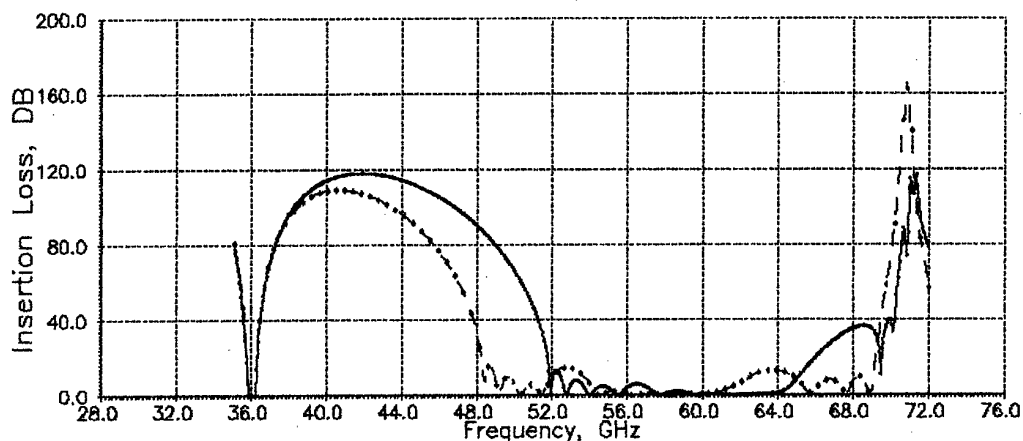


Fig. 2. $A_1 = A_3 = 7.2\text{mm}$, $t = 0.5\text{mm}$, $L = 30.48\text{mm}$ — dashed; $t = 1\text{mm}$, $L = 28.99\text{mm}$ — solid

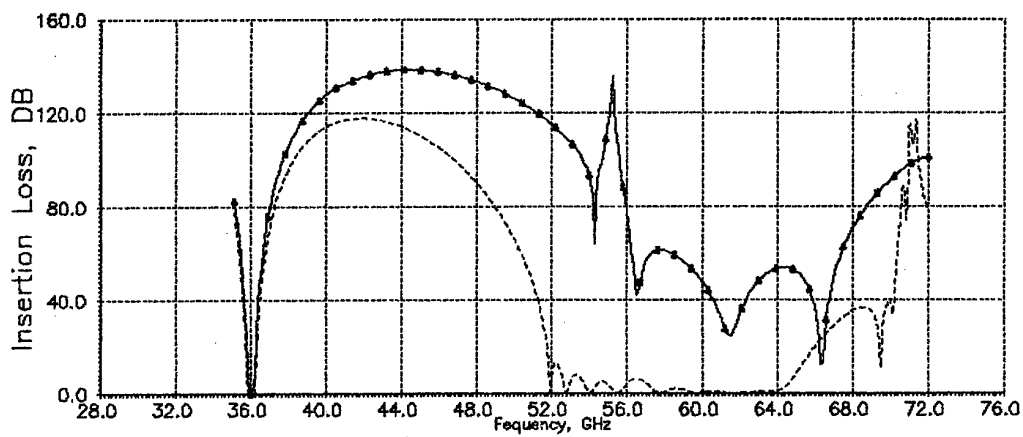


Fig. 3. $A_1 = A_2 = 7.2$, $t = 1$, $L = 29$ — dashed; $A_1 = 10$, $A_3 = 5$, $t = 2$, $L = 29$ (mm) — solid

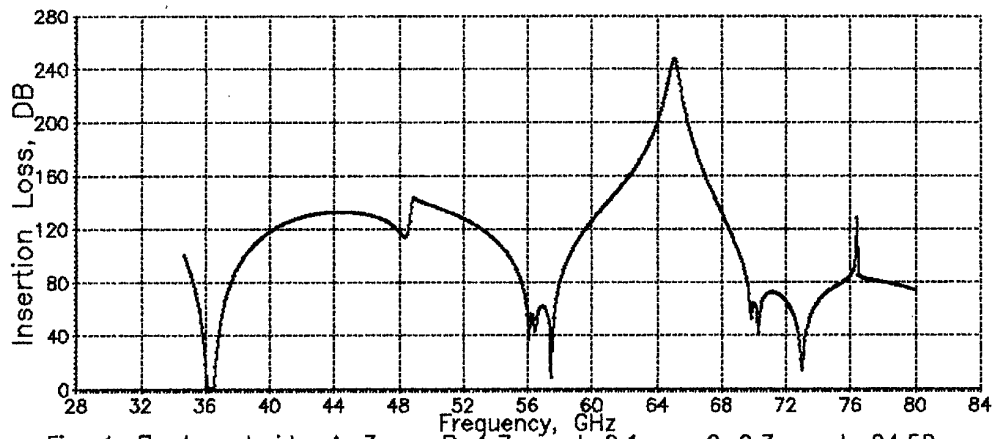


Fig. 4. II-shaped ridge; $A = 3\text{mm}$, $B = 1.7\text{mm}$, $t = 0.1\text{mm}$, $G = 0.3\text{mm}$, $L = 24.58\text{mm}$

which the filter is built and which can increase arms cut-off, is limited due to the fact that the length of input diaphragm turns out to be so little, that technologically it cannot be realized. For solving this research problem, *a new design, has shown in Fig. 1b, is offered here*. As one can see, *now adjacent resonators (3l and 2l; 2l and 1; 1 and 2r; 2r and 3r) have been placed in different waveguide screens*. Besides, *a possibility of essential increase of the central resonator cut-off appears*. In this filter parasite modes in adjacent resonators do not coincide in the frequency and are mutually suppressed. *In this work some efficient algorithms of rigorous analysis and exact synthesis of such structures have been proposed, that actually has created a possibility for the deep physical study of parasite modes suppression effects*.

In addition to this, the designs of presently popular filters, based on ridge waveguides have been analyzed and optimized [1]. Their high electrical parameters are conditioned by the unique possibility to form low-frequency resonances at the small phase retarding on the length of the resonator, due to the big value of phase of reflecting factor on metallic elements.

Physical analysis of the new structure parasite mode suppression effects

In Fig. 3 the typical FR (the solid line) of the new filter designs (Fig. 1b) is shown. In contrast with the preceding case (the dashed line) *the effect of mutual parasite mode suppression is graphically shown*. Here already the broad parasite pass band is not observed. Some areas with very narrow bands widths remain here, whose attenuation will be greatly increased in the real design due to the ohmic losses. Note that with thin diaphragms in this case, significant number of high order resonances, the dynamics of which weakly changes at variations of the strip thickness from 0.1 mm up to 0.25 mm are observe. At the end of the frequency range a rather broad parasite band, whose frequency is equal to the doubled working frequency is observed, while in the classical case it is removed only to 1/4 of its values. Increasing the thickness of the diaphragm up to 0.5 mm increases the number of "narrow" resonant areas at the expense of a more intensive transformation of waves on these inhomogeneities and enlarges the loaded-Qs of parasite modes. For increasing a length of an input strip, the variant with the increased input waveguides, has been calculated. The further increasing of the diaphragm thickness up to 2 mm intensifies an effect of increasing the loaded-Qs of parasite resonances and, therefore, their attenuation. The best suppression result is observed at the 3-mm strip thickness, however in this case we have to essentially increase the input waveguide size. It is important to note, *that besides the parasite mode suppressions, a big increase of the FR steepness is observed*. In Fig. 4 the FR of the ridge filters, based on the II-waveguides with the reduced height of housing waveguides is shown. Similar FRs for the filters based on H-shaped ridge have been received. The stop band attenuation's of the former are better when their height is reduced two times, but the latter one - on the contrary, is better when their height is equal to the height of the input waveguide. This is conditioned by specifics of wave transformation at the junction of the regular and ridge waveguides. It is important to note that *filter reliability on strip diaphragms is better, than on ridge waveguides, that especially manifests itself in millimeter range*. Consequently, the final choice of optimum designs must be done considering all these factors. Design technology development of original filter fabrication shows that is their mass production the most acceptable method is stamping or the method of molding of separate sections.

Conclusion

It has been shown that the new filters design can considerably improve the stop band attenuation up to double working frequency, that is why they have a good chance of being widely used in receiver - transmitter wireless telecommunication devices in centimeter and millimeter wave band. The described here effect of suppression parasite modes is similar in its physical nature to one found for the filters, based on resonators of different classes [2].

Acknowledgments

This work was supported by the grant from Ministry of Ukraine for Science and Technology under the contract N2/469-97.

References

1. A.A. Kirilenko, L.A. Rud', V.I. Tkachenko, "Low pass ridge filters", Private report in this Conference.
2. M.E. Ilchenko, A.G. Yushchenko, S.F. Shibalkin, V.V. Popov, "Frequency Selective Devices Based on Resonators of Different Classes", Conf. Proc. "MIKON-94", Krakow, Poland, 1994.

Investigation of different non-uniform grids in waveletbased planar circuit analysis

Karsten Bubke, Gerald Oberschmidt and Arne F. Jacob
 Institut für Hochfrequenztechnik, Technische Universität Braunschweig
 P.O. Box 3329, 38023 Braunschweig, FR Germany, Fax.: +49 531 391 5841
 E-mail: K.Bubke@tu-bs.de, G.Oberschmidt@tu-bs.de, A.Jacob@tu-bs.de

Abstract- Adapted, nonuniform meshes are introduced in a full wave analysis of planar microwave circuits. The meshes are designed for improved accuracy and conservative use of computer resources. The calculations are further accelerated by means of nonuniform wavelets. Several numerical examples are given.

I. INTRODUCTION – The method of moments in conjunction with a mixed potential integral equation is a well-established tool for the numerical analysis of planar microwave structures. Nevertheless, calculation of the reaction integrals and inversion of the impedance matrix is still a time-consuming task, in particular for large scale two-dimensional problems. As a possible relief, wavelets have been introduced as basis-functions for the unknown current distribution leading to very sparsely populated system matrices [1, 2]. With iterative equation solvers and advanced storing techniques both memory requirements and CPU time can be reduced. Furthermore, by employing a-priori estimates of the wavelet elements, only a small fraction of them needs to be calculated, thus reducing matrix fill-time.

In this work we report on the application of wavelets based on B-splines of second order and defined on non-uniform knot sequences. Because of the higher approximation order and the better suited mesh we achieve a much faster convergence as compared to the popular equidistant rooftops. The exclusive use of non-uniform instead of uniform wavelets increases the computational cost because of the lack of translational symmetry [3]. Therefore, we restrict non-equidistant meshes to small but important parts of the structure under investigation to benefit from the advantages of both discretization types. Several examples are presented to demonstrate use and advantage of the non-uniform wavelet method.

II. NON-UNIFORM WAVELETS – The wavelet property of vanishing moments is related to their good localization in both space and frequency domain. This allows for a better redundancy reduction in the system matrices as compared to conventional discretization schemes. As a consequence, a large number of matrix elements can be neglected [1, 2]. The basic steps for the construction of locally supported, piecewise linear wavelets are as follows [4, 5]:

1. Construct the linear B-spline basis (hat-functions) on the finest knot sequence.
2. Set up a coarse knot-sequence by omitting every other knot; keep the knot multiplicities.
3. Construct the scaling functions, i.e. coarse B-splines, from three adjacent fine hat functions.
4. The dimensions of the fine and the coarse spaces are (N_f) and (N_c). The difference (wavelet) space must have ($N_f - N_c$) dimensions.
5. The wavelets are the shortest fine B-spline sequences that are orthogonal to the coarse space.

The above scheme leads to a semiorthogonal wavelet basis. It can be applied recursively for additional levels of resolution. No further steps are required to realize inhomogeneous boundary wavelets as they are needed, for instance, to approximate the current at the edges of a strip. However, special care has to be taken, when vanishing functions are required at the bounds. In order to get the correct dimension of the wavelet space, shorter homogeneous boundary wavelets without vanishing mean but with a vanishing first order moment have to be introduced.

III. NUMERICAL EXPERIMENTS – As a first example, we consider a microstrip line of width $w = 0.635$ mm, substrate height $h = 0.635$ mm, and dielectric constant $\epsilon_r = 9.8$. The strip is divided into two parts, the first being discretized equidistantly with 5 basis-functions in the transverse direction, the second with n additional equidistant knots near the edges. Fig. 1a shows the reflection coefficient $|R|$ of the terminated line for (α) $n=0$, (β) $n=1$, (γ) $n=2$, (δ) $n=5$ additional knots in the outer cells. Deviations are observed between 5 and 15 GHz, where the reflection is barely detectable ($|R| \approx 46$ to -47.5 dB). Not shown here are the results for a quadratic and geometric (factor 2) mesh refinement towards the edges. Also here, the reflection remains below -45 dB. However, the value of the reflection coefficient for all cases considered has no practical significance and thus allows transverse refinement without meaningful errors. The influence of a matrix compression after a basis transformation with one

wavelet level in transverse and two in longitudinal direction is shown in Fig. 1b. Already a rather coarse discretization of 10 functions per effective wavelength in longitudinal direction leads to errors larger than 2 dB for sparsities above 50% in case (α). The effectiveness of the compression increases with the resolution in the transverse direction because of the higher redundancy in the moment matrix. In case (δ) one reaches a sparsity of up to 70% for an error less than 1 dB.

At next an open ended, 30 mm long microstrip line (parameters as above) was investigated. Fig. 2 shows the phase angle of the reflection coefficient for different grids. These consist of an equidistant part (I) and a nonuniformly refined mesh (II) at the end of the strip. For comparison, two completely uniform meshes are included. They have a longitudinal grid size of 0.25 mm (α) and 0.5 mm (β), respectively. In both cases 7 transverse functions are used. In cases (γ) and (δ) region I has the same longitudinal mesh as for (α) and (β), respectively, but with only three transverse functions. In region II, however, the grid is much finer and geometrically refined in both cases: 7 (9) functions and a refinement factor of 2 (1.2) are taken in the transverse (longitudinal) direction. In the latter, the minimum grid size is 0.0488 mm. Region II is 1 mm long. The results demonstrate that a finer discretization close to the discontinuity allows for a coarser mesh in the uniform portion without loosing accuracy. The primed curves in Fig. 2b show the effect of matrix compression via wavelets in the cases (α), (γ) and (δ) of Fig. 2a. The case (γ) is included for reference. Obviously, the errors introduced remain very small. A large number of matrix elements can be neglected, though: in (α) 693,889 elements have to be stored, whereas in (γ') 63,544 and in (δ') 37,072 suffice.

The last example is an end-coupled band-pass filter (Fig. 3a). The gaps measure 0.25 mm, the inner strip is 4 mm and the feed lines are approximately 20 mm long. The transmission characteristic is shown in Fig. 3a for different resolutions. Again, a uniform grid is chosen in regions I and various (non-)uniform ones in regions II. In the cases (α) and (β) the same grid is used in regions I and II. The longitudinal grid size is 0.25 mm; in transverse directions 7 (α) and 3 (β) functions are used. In the remaining cases the sections II are kept 0.5 mm long. In comparison to case (β) their mesh is modified as follows:

- Case (γ): 3 geometrically refined functions (factor: 1.2; minimum cell size: 0.138 mm) in longitudinal direction; 3 transverse functions.
- Case (δ): 5 geometrically refined functions (factor: 1.2, minimum cell size: 0.0672 mm) in longitudinal direction; 7 geometrically refined functions (factor: 2) in transverse direction.

With a finer grid at the ends a lower resonant frequency is predicted. The mesh size is much less critical further away from the discontinuities. In Fig. 3b we show the effects of wavelet thresholding. The number of significant matrix elements is reduced from 1,500,625 (α) to 180,501 (α'), from 204,543 (γ) to 55,890 elements in (γ'), and from 148,996 (δ) to 43,883 in (δ'). It is observed that wavelet transforms and impedance matrix compression may be applied without sacrificing much accuracy.

IV. CONCLUSION – Various planar microwave structures were analyzed with non-uniform wavelets as basis functions. It is found, that the transverse resolution can be refined almost without any numerical reflections at the junction. This encourages the use of a fine resolution close to discontinuities such as open circuits, gaps or filters. It is demonstrated that the prediction of the reflection in these cases is much more accurate with an adapted mesh close to the end of the strips. Furthermore, the computational effort can be reduced by the correct application of wavelets on non-uniform grids.

References

- [1] K. Sabetfahri, L. P. B. Katehi: *An Integral Transform Technique for Analysis of Planar Dielectric Structures*; IEEE Trans. Microwave Theory Tech.; **42**(6):1052–1062; June 1994.
- [2] G. Oberschmidt, K. Bubke, A. F. Jacob: *Two-Dimensional Wavelet-Analysis of a Microstrip Open*; To be published in IEEE Transactions on Microwave Theory and Techniques, May, 1998.
- [3] G. Oberschmidt, A. F. Jacob: *Non-Uniform Wavelets on Adapted Grids for Modelling Edge Singularities*; in *Proceedings of the European Microwave Conference*; volume 27; pp. 1258–1263; Jerusalem, Israel; September 1997.
- [4] M. D. Buhmann, C. A. Micchelli: *Spline Prewavelets for Non-uniform Knots*; Numerische Mathematik; **61**:455–474; 1992.
- [5] G. Oberschmidt, A. F. Jacob: *Non-Uniform Wavelets in Electromagnetic Scattering*; Electronics Letters; **33**(4):276–277; 1997.

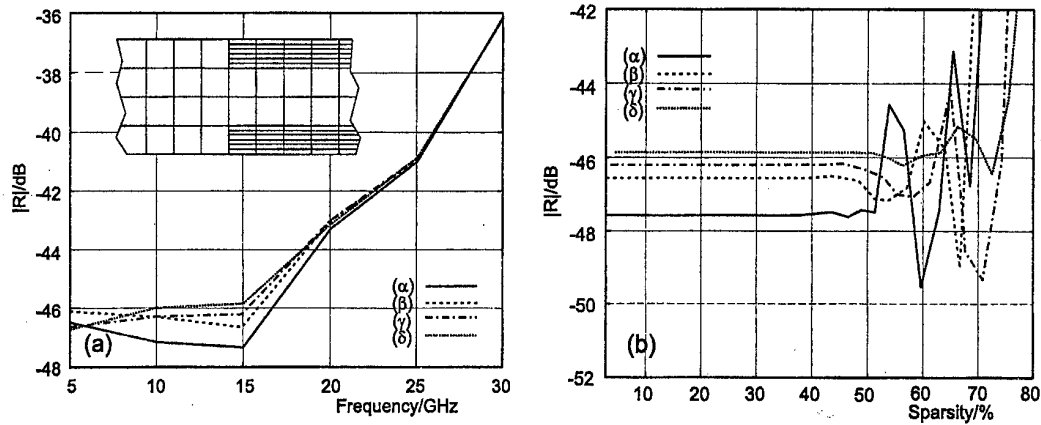


Figure 1: Reflection coefficient (magnitude) of a terminated transmission line with a numerical discontinuity. Effect of (a) different meshes, (b) sparsification with wavelets ($f=15 \text{ GHz}$)

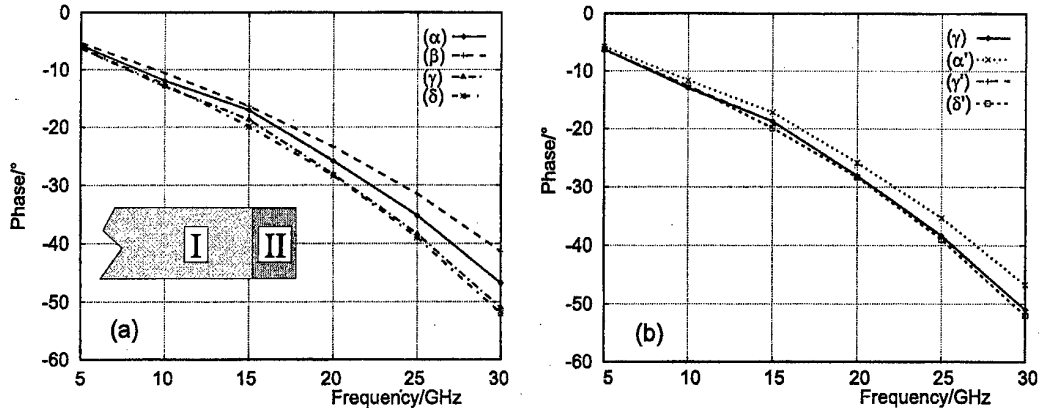


Figure 2: Reflection coefficient (phase) of a microstrip open. Effect of (a) different meshes, (b) non-uniform wavelets

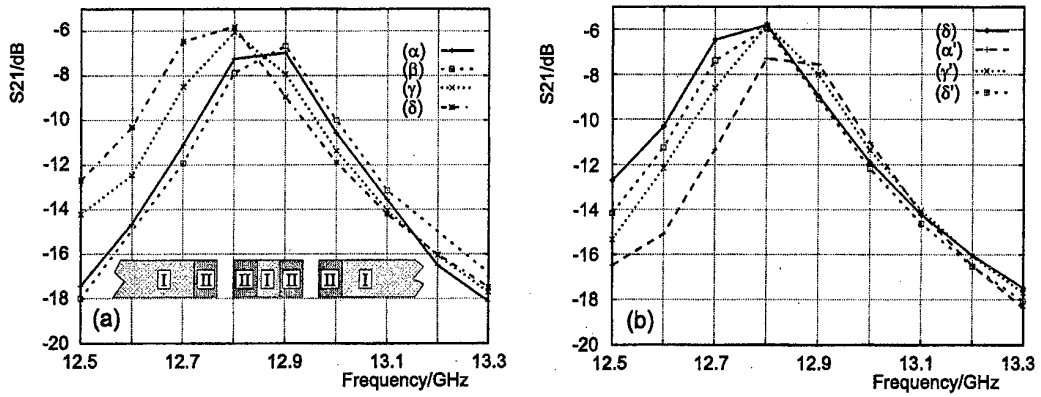


Figure 3: Transmission of a bandpass filter. Effect of (a) different meshes, (b) sparsification with wavelets

FUNDAMENTAL AND APPLIED SYNTHESIS PROBLEMS FOR PERIODIC STRUCTURES

L. G. Velychko

Institute of Radiophysics & Electronics, 12 Acad. Proskura St., Kharkov, 310085, Ukraine
Tel.: 38 0572 448 557, Fax: 38 0572 441 105, E-mail: sirenko@ire.kharkov.ua

This paper is devoted to the investigation of model synthesis problems for quasioptical systems with diffraction gratings as frequency selective elements. For some model structures (see Fig.1) we construct the electrodynamic models and optimize them in accordance with the operation requirements. For the model of efficiently absorbing coating (Fig.1,a) the reflected energy is minimized in various operating conditions of the system "dielectric layer - grating". For the plane pattern-forming structures (Fig.1,b) the periodic surfaces are synthesized that yield a desired radiation pattern of the grating illuminated by a beam of plane waves or placed in a field of point sources. In the construction of resonators with a considerably rarefied spectrum (Fig.1,c) and with a given electrodynamic characteristics at a basic operating frequency the prototype principle is used. The basis for this principle is the equivalent replacement of nonselective mirrors in selective gratings at a chosen operating frequency. As a result of the optimization process we get a set of requirements imposed on complex amplitudes of diffraction spectrum of gratings. By this means we reduce the model synthesis of the system involved to the solution of the inverse synthesis problem for a periodic grating.

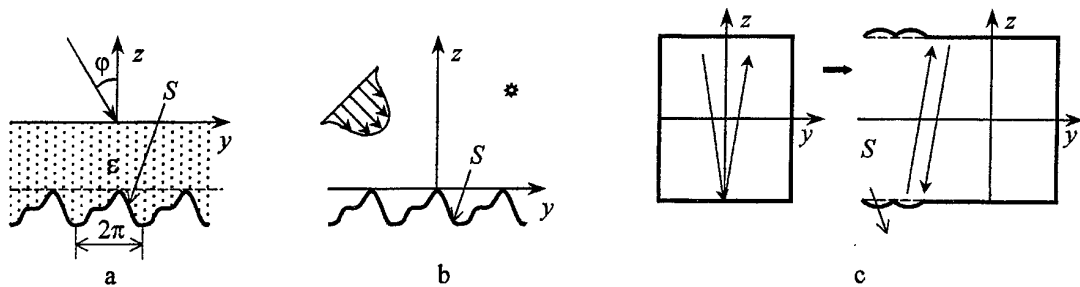


Figure 1. The examples of quasioptical systems with diffraction gratings

In this work we suggest two schemes for solving the inverse synthesis problem for perfectly conducting grating realizing given electrodynamic characteristics (complex amplitudes of a scattered field) for the frequencies κ contained in some interval $[\kappa_1, \kappa_2]$ [1]. These schemes are based on the integral representations relating the complex scattered amplitudes $a_{n,0}$ with the continuous current density $\eta(y)$ on the boundary S (see Fig.1):

$$\left\{ \begin{array}{l} a_{n,0} \\ \delta_n^0 \end{array} \right\} = \frac{i}{4\pi\Gamma_n} \int_0^{2\pi} \eta(y_0) e^{\{ \pm i\Gamma_n f(y_0) \}} e^{-iy_0} dy_0, \quad n = 0, \pm 1, \dots \quad (1)$$

Here, $\Gamma_n = \sqrt{\kappa^2 - \Phi_n^2}$, $\operatorname{Re}\Gamma_n \geq 0$, $\operatorname{Im}\Gamma_n \geq 0$, $\Phi_n = n + \kappa \sin \varphi$, φ is the angle of incidence of the plane wave $\exp(i(\Phi_0 y - \Gamma_0 z))$, κ is a dimensionless frequency parameter (the ratio of grating's period to the incident wavelength), Φ_n and Γ_n are the propagation constants of the scattered harmonic with a number n in y and z directions, respectively, the function $f(\cdot)$ describes a profile of the grating.

The first step is the same for both algorithms and consists in expanding the exponential functions under the integral sign in the second relation (1) in power series. Remaining only the highest terms in these series we obtain the approximation for the density $\eta(y, \kappa)$, which does not contain the information about scattered

amplitudes. Taking into account this approximation, we get the classical nonlinear problem for the unknown function $f(y)$, and we have to invert a Urysohn operator. The solution is obtained by the Newton-Kantorovich method with the help of Lavrent'ev α -regularization.

The second scheme is based on the use of the approximation for $\eta(y, \kappa)$ in a combination of both of the equations from system (1). In this case the integral equation of the first kind is reduced to the integral equation of the second kind by the method of Lavrent'ev α -regularization. The solution exists, it is unique, and it gives the desired profile $f(y)$ as $\alpha \rightarrow 0$.

If we have M amplitudes $a_{n_1,0}, a_{n_2,0}, \dots, a_{n_M,0}$ of the scattered field on the frequency interval $[\kappa_1, \kappa_2]$, then the solution takes the form:

$$f(y) = \operatorname{Re} \left(-\frac{i}{2\Gamma_0(\kappa_2 - \kappa_1)} \int_{\kappa_1}^{\kappa_2} \sum_{m=1}^M (a_{n_m,0} + \delta_{n_m}^0) e^{imy} d\kappa \right). \quad (2)$$

Numerical examples of the use of this algorithm for different M (a number of scattered amplitudes in the input data) are presented in Fig.2. The problem is to synthesize a periodic structure having scattered characteristics closely approximating the given complex amplitudes $a_{n_m,0}(\kappa)$ (curve 1 in Fig.2) at $0.652 < \kappa < 0.952$ and $\varphi = 10^\circ$. As input data for solving the inverse problem the solutions (complex amplitudes) of a direct problem for perfectly conducting grating from semicylinders (curve 1 in Fig.2,a) are used. The profiles of synthesized structures and their diffraction characteristics (by the example of “-1” scattered harmonic) are depicted in Fig.2,b,c by curves 2–4. The sets of input data $\{a_{-1,0}(\kappa), a_{0,0}(\kappa), M = 2\}$, $\{a_{\pm 1,0}(\kappa), a_{0,0}(\kappa), M = 3\}$, and $\{a_{-5,0}(\kappa), \dots, a_{5,0}(\kappa), M = 11\}$ correspond to curves 2, 3, and 4, respectively.

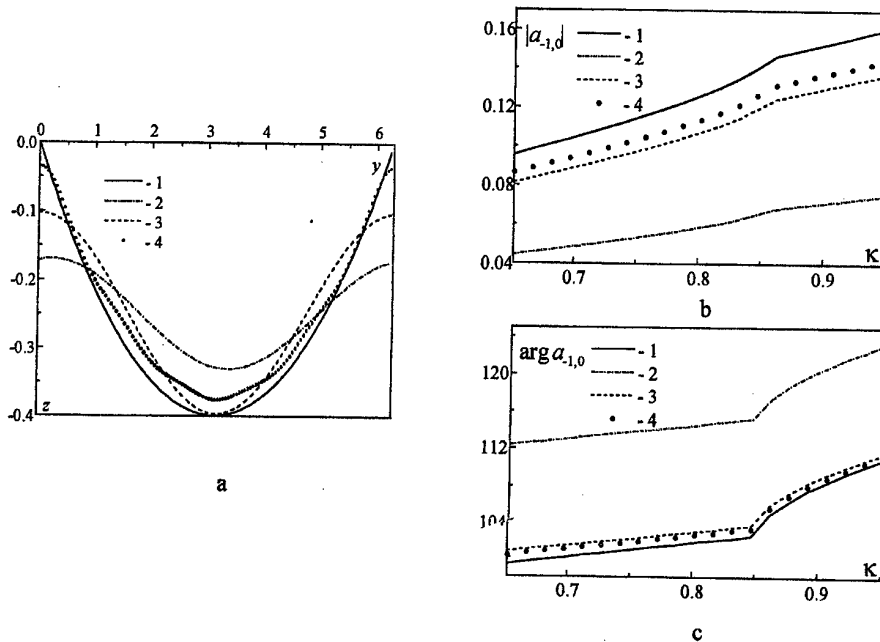


Figure 2. The profiles of synthesized gratings (a); absolute values (b) and arguments (in degrees) (c) of the corresponding scattered amplitudes

References

1. L.G.Velychko and Y.K.Sirenko, “Synthesis of the reflecting gratings with an arbitrary profile”, *Radiofizika i Radioastronomija*, Vol. 2, No. 2, pp. 214-219, 1997 (in Russian).

AN EFFICIENT EDUCATIONAL PROGRAM FOR A FIN LINE COUPLER ON SEMICONDUCTOR

Humberto César Chaves Fernandes

Department of Electrical Engineering - Technological Center
Federal University of Rio Grande do Norte - P. Box 1583
Tel/Fax: +55 84 2153731 / 32, E-mail: humbeccf@ct.ufrn.br
59.072-970 - Natal - RN - Brazil

Abstract - Computer programs are developed in FORTRAN 77 language, given the results in 3-D of the dispersion and of the coupling, as functions of the frequency, conductivity and permittivity for the unilateral fin lines coupler asymmetric in E-plane, on semiconductor substrate. The characteristic impedance and complex propagation constant, for the odd and even-modes excitation are obtained by Transverse Transmission Line method - TTL. These programs are easily used in graduate and undergraduate courses with good efficiency.

1. INTRODUCTION AND DEVELOPMENT

In this work are used computer programs to obtain the main characteristics parameters of structures with the finline and was developed for application in coupler structures.

The structure is basically a slotline inserted in the E-plane of a rectangular waveguide, shown in Fig.1. This report pertains to application of computer programs in design of directional coupler, most particularly the *Parallel-Coupled Fin-Line Coupler* shown in the Fig 2. This type of coupler offers forward wave coupling, i. e., if a signal is fed to port 1, port 3 is the coupled port and port 4 is the isolated port.

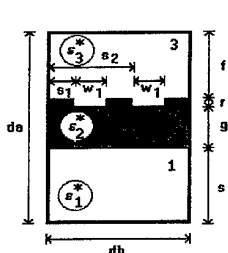


Fig. 1 - Cross section of arbitrary unilateral finline with coupled slots.

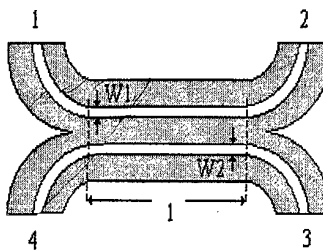


Fig. 2 - Top and internal view of the unilateral fin-line coupler.

In the direct and concise TTL method, the Maxwell's equations in Fourier transform domain, are firstly used to obtain the electromagnetic fields in terms of the transversal electromagnetic fields [1]. By applying the boundary conditions, the fields in all dielectric regions are determined as functions of the electric fields in the slots.

An inhomogeneous equation system is obtained, in which the current densities in the fins are related to the electric fields in the slots. By expanding these fields in terms of suitable basis functions and using the moment method and the Parseval's theorem, the current densities are eliminated, and an homogeneous equation system is obtained with two variables.

The complex propagation constant is obtained by setting the determinant of the system matrix equal to zero. The effective dielectric constant is determined by means of the relation between the phase constant and the wave number of the free space.

2. THEORY

For the unilateral fin-line with two coupled slots in the Fig 1, when used to be a parallel coupled fin-line coupler, the results obtained for even and odd modes of the phase constant using this TTL method, are used to given the coupling length L [2], where a complete transfer of power from port 1 to port 3 is present:

$$L = \pi / (\beta_{\text{even}} - \beta_{\text{odd}}) \quad (1)$$

The amplitude of the coupling coefficient between ports 1 and 3 is:

$$|S_{13}| = \sin(\pi L / 2L) \quad (2)$$

where the length of the coupling region L , for any L can be calculated by using (2). The expression for the coupling is defined as:

$$C_3 = 20 \cdot \log \left(\frac{1}{|S_{13}|} \right) \quad (3)$$

3. RESULTS

Computer programs were developed to give the numerical results of the planar structures analyzed.

In Fig. 3, curves for the two excitation modes of the characteristic impedance of the unilateral finline are showed. The structure is a WR-28, $da = 7.112$ mm and $db = 3.556$ mm, $g = 0.254$ mm, $s = 3.302$ mm, $x_1 = 0.789$ mm, $x_2 = 2.567$ mm, $w_1 = w_2 = 0.2$ mm. Was considered a dielectric substrate with relative permittivity $\epsilon_{r2} = 2.22$ and values of σ_2 between 0 S/m and 1 S/m. The range of frequency is 25 GHz until 40 GHz.

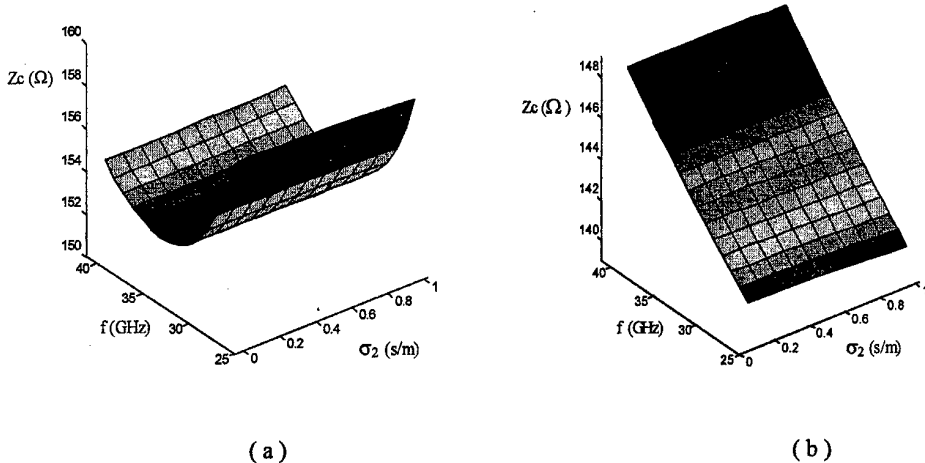


Fig. 3 - Results in 3-D of the characteristic impedance $Z_{c1} = Z_{c2} = Z_c$, as functions of the frequency and of the conductivity of the coupled unilateral finline for a) odd mode end b) even mode.

Results of the coupling in the port 3 as functions of the frequency and conductivity, in 3-D, are shown in Fig 4. In these results are considered, WR-28, $w_1 = w_2 = 0.2$ mm, relative permittivity in region 2, $\epsilon_{r2} = 12.0$, $L = 0.5$ mm, $g = 0.254$ mm e $s = 3.302$ mm.

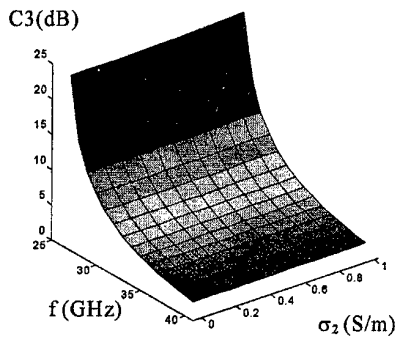


Fig. 4 - Coupling as functions of the frequency and conductivity.

4. CONCLUSIONS

Computer programs, with good appeal, are developed for to be used in graduate and under graduate courses. The theory and numerical results were presented to the unilateral fin lines and coupler with semiconductor substrate. The full wave analysis of the Transverse Transmission Line method - TTL in the FTD was used in determination of the electric and magnetic fields in all dielectric regions. Good results were presented and compared with that of the literature [3]. This work was supported by CNPq and CAPES.

REFERENCES

- [1] H. C. C. Fernandes, "Attenuation and propagation in various fin-line structures", International Journal of Infrared and Millimeter Waves, Vol. 17, N° 08, pp. 1419-1430, Aug. 1996.
- [2] B. Bhat, S. K. Koul, "Analysis, design and applications of fin lines", Artech House, Norwood, MA, 1987.
- [3] D. Mirshekar-Syahkal and J. B. Davies, "An Accurate , Unified Solution to Various Fin Lines Structures of Phase Constant, Characteristic Impedance and Attenuation ", IEEE Trans. on MTT-30, pp. 1854-1861 , Nov.1982.

MICROSTRIP LINE WITH SUPERCONDUCTIVITY IN MULTILAYER SEMICONDUCTOR

Humberto César Chaves Fernandes, Gustavo Adolfo de Brito Lima and Wellton Pires Pereira
 Department of Electrical Engineering - Technological Center - Federal University of Rio Grande Norte
 P.O.Box 1583, Tel/Fax: +55 84 215.37312, E-mail: humbeccf@ct.ufn.br 59.072-970 - Natal - RN - Brazil

Abstract - The theory of the multilayer shielded and open microstrip lines considering the superconductor strip on semiconductor regions is presented. The Transverse Transmission Line (TTL) is used in the analysis. The superconductor effect is included with the boundary condition of the surface impedance that is related to the complex conductivity of the material, calculated from the advanced two-fluid model. Applying the moment method the complex propagation constant of the structure, including the phase constant and the attenuation constant, is obtained. Results are presented for the complex propagation constant, versus the frequency and the temperature, of this multilayer superconducting microstrip line.

1. Introduction

The microstrip line is a structure normally utilized in Microwave Monolithic Integrated Circuits MMIC's. The utilization of high-Tc superconductor films in the structures has practical applications [1] and permits a reduction of ohmic losses and low dispersion. Different methods have been proposed in the Fourier transform domain (FTD) and others scheme [2]-[8], for the microstrip and stripline characterization. In this work is used the full wave analysis of the Transverse Transmission Line (TTL) method, developed by the author recently with success [2], [8]. This TTL method permits an exact and concise analysis to obtain the dyadic Green matrix impedance of the structure. For microstrip with the superconductor film thickness, as shown in the Fig. 1, much thinner than the effective penetration depth, the introduction of this superconductor can be analyzed by considering a Complex Resistive Boundary Condition [4]. The conductivity of the superconductor film is complex and is given by the Two Fluid Theory [4].

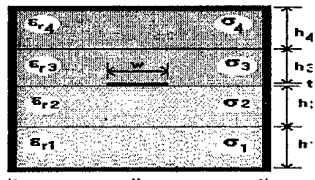


Fig.1. Cross section of the overlay shielded superconducting microstrip line on double substrate with losses.

The superconductor effect is included with the boundary condition of the surface impedance, that is related to the complex conductivity of the material, calculated from an advanced two-fluid model [2],[4]. In the TTL method the electromagnetic fields in \hat{x} and \hat{z} directions (\hat{z} is the direction of propagation with complex constant $\Gamma = \alpha + j\beta$) are obtained as functions of the transverse electromagnetic fields. Applying the magnetic boundary condition with the surface impedance is obtained a matrix system that relates the tangential electric fields with the surface current densities resulting the impedance matrix. In the sequence, the moment method is used conducting to a characteristic equation, such that their roots are numerically calculated to give the complex propagation constant, including the phase constant and the attenuation constant.

2. Theory

In the TTL method, applying the Maxwell equations, a set of equations that represent the electromagnetic fields, in the direction \hat{x} and \hat{z} , in the regions of the structure are given as a function of the fields in the direction \hat{y} , transverse to the interfaces, in the Fourier transform domain (FTD), as follow:

$$\vec{E}_T = \frac{1}{K^2 + K_y^2} \left[\frac{\partial}{\partial y} (\nabla_T \vec{E}_y) - j\omega \mu (\nabla_T \times \vec{H}_y) \right] \quad (1) \quad \vec{H}_T = \frac{1}{K^2 + K_y^2} \left[\frac{\partial}{\partial y} (\nabla_T \vec{H}_y) + j\omega \epsilon (\nabla_T \times \vec{E}_y) \right] \quad (2)$$

Applying the boundary conditions and the Helmholtz equations, the electromagnetic fields of the microstrip line are obtained. After application of the magnetic boundary conditions the matrix equation is obtained relating the fields and the current densities,

$$\begin{bmatrix} \tilde{Z}_{xx} & \tilde{Z}_{xz} \\ \tilde{Z}_{zx} & \tilde{Z}_{zz} \end{bmatrix} \begin{bmatrix} \tilde{J}_{xg} \\ \tilde{J}_{zg} \end{bmatrix} = \begin{bmatrix} \tilde{E}_{xg} \\ \tilde{E}_{zg} \end{bmatrix} \quad (3)$$

Where $\begin{bmatrix} \tilde{Z} \end{bmatrix}$ represent the dyadic Green impedance matrix in the FTD, obtained by the TTL method.

After to obtain this matrix, the Complex Resistive Boundary Conditions model [2-4] is applied to include the superconducting characteristic of the microstrip structure. The tangential components of the electric field on the plane $y = g$ ($h_1 + h_2$) are given as

$$\begin{cases} \tilde{E}_{xg} = \tilde{E}_{xg}^{in} + \tilde{E}_{xg}^o \\ \tilde{E}_{zg} = \tilde{E}_{zg}^{in} + \tilde{E}_{zg}^o \end{cases} \quad (4)$$

Where \tilde{E}_{xg}^o and \tilde{E}_{zg}^o are the electric fields out of the superconductor, and, \tilde{E}_{xg}^{in} and \tilde{E}_{zg}^{in} are the electric fields in the superconductor. These last fields are related with the current densities by the presence of the impedance surface, since the superconducting film thickness is much thinner than λ_{eff} [2], [4]. This impedance surface is given as

$$Z_s = \frac{1}{t_{sc} \sigma_{sc}} \quad (5)$$

where σ_{sc} is the conductivity of the superconductor and is obtained of the Two Fluid theory [4]:

$$\sigma_{sc} = \sigma_n \left(\frac{T}{T_c} \right)^4 - j \left(\frac{1}{\omega \mu \lambda_{eff}^2(0)} \right) \left[1 - (T/T_c)^4 \right] \quad (6)$$

σ_n Is the conductivity of the superconductor, T_c is the critical temperature of the superconductor; and, $\lambda_{eff}(0)$ is the penetration effective depth when $T = 0$ K. The Two Fluid theory is used for high-temperature materials with success at the present time, appears of the originally applied in low-temperature materials [4]. The «enhanced» Two Fluid theory is used by others authors for corrections in materials parameters obtained experimentally [7].

After the inclusion of the superconducting impedance, considering the algebraic modifications, the matrix equation (3) is changed for:

$$\begin{bmatrix} (\tilde{Z}_{xx} - Z_s) & \tilde{Z}_{xz} \\ \tilde{Z}_{zx} & (\tilde{Z}_{zz} - Z_s) \end{bmatrix} \begin{bmatrix} \tilde{J}_{xg} \\ \tilde{J}_{zg} \end{bmatrix} = \begin{bmatrix} \tilde{E}_{xg}^f \\ \tilde{E}_{zg}^f \end{bmatrix} \quad (7)$$

where $[J]$ is the surface current density in the superconductor strip, $[E]$ is the tangential electrical field in the lateral of the superconducting strip, and $[Z]$ is the impedance matrix. The Moment method is applied at the equation (7), resulting in the homogeneous matrix equation. In this matrix the surface current densities was expanded in terms of basis functions, The complex root of the determinant is the complex propagation constant, $\Gamma = \alpha + j\beta$, where α is the attenuation constant and β is the phase constant.

3. Results

Using a Pentium, 133 MHz microcomputer, programs in the FORTRAN 77 language were created to calculate the complex propagation constant of the shielded overlay superconducting microstrip line including multilayer substrates with losses. The numerical results are presented for the effective dielectric constant and attenuation constant as a function of the frequency to various temperatures and conductivity.

In all the figures the superconducting material used is the (YBCO), where the effective penetration depth at temperature of 0 K is $\lambda_{eff}(0) = 150$ nm, the conductivity at normal temperature ($T > T_c$) is $\sigma_n = 2 \times 10^5$ S/m and the critical temperature $T_c = 90$ K. In the fig. 2 are used a WR-28 (da = 7.112 mm, db = 3.556 mm), s=0.154mm, g= 0.1 mm, r =

10.0 nm and $w_1 = 0.4$ mm. The substrates used are the RT-duroid 5880TM where $\epsilon_r = 2.22$, and the $\epsilon_r=10.5$ to substrate with losses. The temperature used is T=70 K.

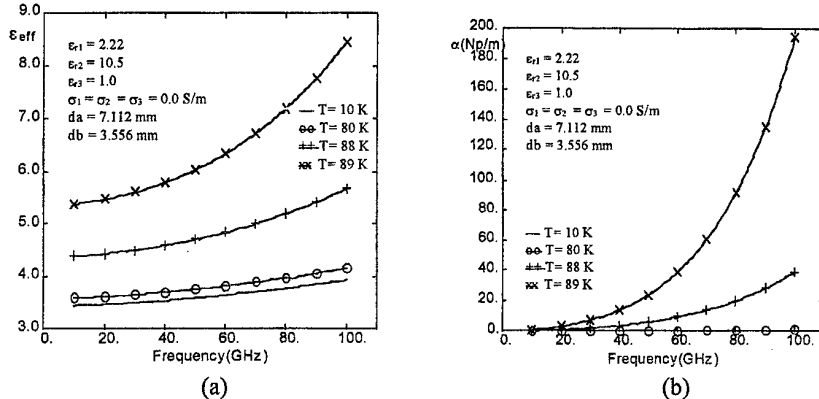


Fig.2. Temperature of the superconductor, to: (a) effective dielectric constant, and (b) attenuation constant, versus frequency of the shielded microstrip line with two layers.

4. Conclusions

In conclusions the utilization of superconducting film in microwave devices, as microstrip, open a variety of new applications. The advantages include low attenuation, low distortion and the propagation of slow waves. The comparisons realized shows this advantages. The inclusion of the semiconductor substrate with the complex variables, permit the use of these superconducting microstrip line in solid state devices. A new conjunction of methods is utilized for the characterization of these structures that use high-Tc superconducting : the TTL — Transverse Transmission Line, and the Complex Resistive Boundary Condition model. The analysis have been concise and objective, producing excellent results, that were compared with that obtained in another works. This work was supported by CNPq.

References

- [1] S. M. El-ghazaly, R. B. Hammond and T. Itoh, "Analysis of Superconducting Microwave Structures: Application to Microstrip Lines", IEEE Trans. Theory and Tech., vol. 40, n° 03, pp. 499-508, march 1992.
- [2] H.C.C.Fernandes, «Shielded and Open Two-layer Superconducting Microstrip Lines», SPIE's 1995 International Symposium on Optical Science, Engineering and Instrumentation, in the Conference, High-Temperature Microwave Superconductors and Applications, San Diego , CA, USA, Conf. Proc. pp. 22-29, Jul. 1995.
- [3] J.M.Schellenberg, «CAD Models for Suspended and Inverted Microstrip», IEEE Trans. Microwave Theory and Techniques, vol. 43, n° 6, pp. 1247-1252, June, 1995.
- [4] J.M.Pond, C.M.Crowne and W.L.Carter, "On the Application of Complex Resistive Boundary Conditions to Model Transmission Lines Consisting of Very Thin Superconductors", IEEE Trans. MTT, vol. 37, n° 1, pp. 181-190, Jan. 1989.
- [5] Z. Cai and J. Bornemann, "Generalized Spectral Domain Analysis for Multilayered Complex Media and High-Tc Superconductor Applications", IEEE Trans. Theory and Tech., vol. 40, n° 12, pp. 2251-2257, Dec. 1992.
- [6] D. Nghiem, J. T. Willians and D. R. Jackson, "A General Analysis of Propagation along Multiple-Layer Superconducting Stripline and Microstrip Transmission Lines", IEEE Trans. Theory and Tech., vol. 39, n° 9, pp. 1553-1565, Sept. 1991.
- [7] O. R. Baiocchi, K. Kong and T. Itoh, "Pulse Propagation in Superconducting Coplanar Striplines", IEEE Trans. Theory and Tech., vol. 40, n° 03, pp. 509-513, March, 1992.
- [8] H.C.C.Fernandes, E.A.M.Souza and I.S.Queiroz Jr., «High precision analysis of finlines on semiconductor substrate», International Journal of Infrared and Millimeter Waves, Vol. 16, N° 1 pp.185-200, Jan. 1995.

PROJECT AND ANALYSIS OF UNILATERAL FIN LINE POWER DIVIDERS

Humberto C.C. Fernandes, Robson L.M. Lima and Eduardo L. Freitas

Department of Electrical Engineering - Technological Center

Federal University of Rio Grande do Norte,

P. O. Box 1583 - Tel/Fax: +55 84 2153731 / 32 - E-mail: humbeccf@ct.ufrn.br
59.072-970 - Natal/RN - Brazil

Summary: The Transverse Transmission Line (TTL) Method in the Fourier transform domain is used to project and analyze unilateral power dividers with three-ports in millimeter wave by the first time. In addition, broadband power dividers have been analysed by using series connections of two fin lines, having essential applications to divide power and to work like an impedance transformer. Results of power at each output arm are obtained to different ratios of slot widths power dividers.

1. Introduction

This work presents an electromagnetic application to obtain the effective dielectric constant, the attenuation constant and the characteristic impedance of the arms of the power divide in millimeter wave frequencies, consisting of the unilateral fin lines with semiconductor substrate as shown in Fig. 1. The power in the output arms of this device to different ratios of slot widths utilizing the TTL [1] method, by first time, is also presented. In addition, broadband power dividers have been analysed by using series connections of two fin lines, having essential applications to divide power and to work like an impedance transformer [2]. Broadband power dividers having unequal power divisions can be designed by choosing different ratios of slot widths, corresponding to different line impedances.

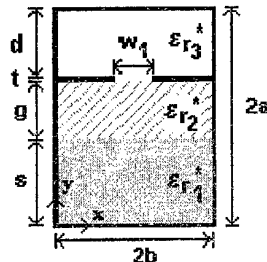


Fig. 1. Cross section of an arbitrary bilateral fin lines with semiconductor substrate.

The TTL method, the Maxwell's equations in Fourier transform domain, are used to obtain the electromagnetic fields in terms of the transversal electromagnetic fields.

By applying the boundary conditions to the tangential electric fields, the fields in all dielectric in all dielectric regions are determined as functions of the electric fields in the slots. Applying the boundary conditions to the magnetic fields at the interface, an inhomogeneous equations system is obtained, in which the current densities in the fins are related to the electric fields in the slots. Applying the boundary conditions to the magnetic fields at the interface, an inhomogeneous equations system is obtained, in which the current densities in the fins are related to the electric fields in the slots. By expanding these fields in terms of suitable basis functions and using the moment method and the Parseval's theorem, the current densities are eliminated, and an homogeneous equations system is obtained [3]. The LLUSSE.FOR and POWDIV.FOR computer programs, are developed in FORTRAN 77 language and the results obtained show rapid convergence and exactness.

2. Development

In the TTL method starting from the Maxwell's equations in Fourier transform domain, the tangential electromagnetic fields are obtained in terms of the transversal electromagnetic fields in the i-region of the structure [3].

$$\tilde{E}_i = \tilde{E}_{xi} + \tilde{E}_{yi} + \tilde{E}_{zi} \quad (1)$$

$$\tilde{H}_i = \tilde{H}_{xi} + \tilde{H}_{yi} + \tilde{H}_{zi} \quad (2)$$

Then are obtained the electromagnetic fields in the directions x and z, as function of the fields in the direction y.

By applying the boundary conditions to the tangential electric fields, the fields in all dielectric regions are determined as functions of the electric fields in the slots. An inhomogeneous equation system is obtained, by applying the boundary conditions to the magnetic fields at the dielectric interface, in which the current densities in the fins are related to the electric fields in the slots.

$$[Y] \cdot [\tilde{E}] = [\tilde{J}] \quad (3)$$

By expanding these fields in terms of suitable basis functions and using Galerkin's method and Parseval's theorem, it is possible to eliminate the current densities. Then an homogeneous equation system is obtained with two variables.

The characteristic equation for determining the complex propagation constant ($\Gamma = \alpha + j\beta$), is obtained by setting the determinant of the system matrix equal to zero. The effective dielectric constant is determined by means of the relation $\epsilon_{eff} = (\beta/k_0)^2$ [3].

The characteristic impedance is then determined

$$Z_c = \frac{V_s^2}{2P} \quad (4)$$

where the voltage in slot and the transmitted power are given by the expressions shown below:

$$V_x = \int_{-w_{1/2}}^{+w_{1/2}} \tilde{E}_{xt} dx \quad (5)$$

$$P = \frac{1}{8} \operatorname{Re} \sum_{-\infty}^{+\infty} \left[\int_0^{2a} (\tilde{E}_x \tilde{H}_y - \tilde{E}_y \tilde{H}_x) dy \right] \quad (6)$$

The powers in the output arms are obtained by analysing series connections of two fin lines [2].

3. Results

Computer programs are developed in FORTRAN 77 language, and the results obtained for the effective dielectric constant and of the attenuation constant are presented as a functions of the frequency, of the arbitrary dimension s (mm), and of the dimensions of the slots w_1 and w_2 (mm), in 3-D. The results were compared with references in 2-D, in which the substrate is a loss less material and for the symmetric not arbitrary structure [1], and the agreement was observed.

Results of the power at each output arm are obtained to different ratios of slot widths power dividers, in 2-D, also. It's important to note that such power dividers are reactive devices. For example, a 1:1 power divider that uses 300 Ohms input line and two 150 Ohms output lines is reported to a power division of 3.4 ± 0.2 dB at each output arm over entire Ka band, for comparison with the literature [2].

4. Conclusions

In conclusions, results in 3-D were presented, and compared with references in 2-D, for an unilateral finline on semiconductor substrate, using the TTL method and applied to results of power dividers. These results increase the possibility of application in millimeter wave devices [4]-[5]. This work was supported by CNPq.

References

- [1] H. C. C. Fernandes, E. A. M. Souza and I. S. Queiroz Jr, "High precision analysis of finlines on semiconductor substrate", International Journal of Infrared and Millimeter Waves, Vol. 16, Nº 1, pp.185-200, Jan. 1995.
- [2] Bharathi Bhat, and Shiban K. Koul, "Analysis, design and applications of fin lines", Artech House, 1987.
- [3] H. C. C. Fernandes, "A Direct Method (TTL) Applied To General Planar Devices And Structures Of Millimeter Waves", Int. Conf. on Millimeter and Submillimeter Waves and Applications III , part of the SPIE'96, Denver-Colorado Conf. Proc. pp. 5-10, USA, August 5 - 9, 1996 .
- [4] K. Ogius, "Dielectric waveguide and power divide with metallic reflector", IEEE Transaction Microwave Theory and Techniques, vol. MTT-32, pp113-116, January 1984.
- [5] L.C. Freitas Jr., H.C.C. Fernandes and S.A.P. Silva, "A Coupler with Losses in Millimeter Waves", 1997 SBMO/IEEE MTT-S International Microwave and Optoelectronics Conference, Natal, Brazil, pp. 59-64 , Aug. 1997.

HTC SUPERCONDUCTING PLANAR ANTENNAS DESIGN USING THE TTL METHOD IN THE FOURIER TRANSFORM DOMAIN

Humberto César Chaves Fernandes

Department of Electrical Engineering - Technological Center

Federal University of Rio Grande do Norte, P. O. Box 1583

Tel/Fax: +55 84 2153731 / 32 - E-mail: humbeccf@ct.ufrn.br 59.072-970 - Natal/RN - Brazil

Abstract - An analysis and design for HTc superconducting planar antenna, particularly microstrip patch antenna, is presented in this work. The rigorous Transverse Transmission Line (TTL) method in the Fourier Transform Domain (FTD) along with the Transmission Line Model are applied. However, the analysis can be extended to others planar structures using materials with losses, as semiconductor, or lossless dielectric substrate. Since the TTL is a concise full wave method and very much suitable on microwave and millimeter-wave components study, it gives accurate effective dielectric constant which contributes definitively to obtain all others antenna parameters with higher precision such as length, efficiency, bandwidth, quality factor, radiation patterns.

I. INTRODUCTION

Modern societies depend principally on an efficient communication system, capable to transmit, receive and handle information with reliability, precision and each time faster. As a consequence, devices and equipments are required to supply those needs, and must conciliate lightweight, to be highly efficient with low cost and reduced dimensions.

HTS Microstrip patch antenna holds these characteristics, can be used in many applications, including cellular, satellite and wireless communications, over the broad frequency range from microwave to millimeter-wave and HTS antenna shows a substantial improvement over an identical antenna made with normal metals, with a higher gain and radiation efficiency [1], especially when the number of radiating elements increases, due to superconducting thin-films have quite lower microwave surface resistance (R_s) compared to normal conducting films [2],[3].

A microstrip patch antenna consists of a very thin metallic patch or superconducting thin-film, placed a small fraction of a wavelength above a conducting ground-plane with a dielectric substrate between them. The radiating patch can assume any shape, but simple geometries are generally used in order to simplify the analysis and the performance prediction.

The applied theories are the Transverse Transmission Line (TTL) method [4] in conjunction with the theory of the rectangular-patch antenna [5] to design and analyze the related antenna. Various applications using the rigorous TTL method has been presented by H. C. C. Fernandes et al.[4],[6]. This complete and efficient method provides appropriate analysis for various others planar structures, giving precise effective dielectric constant (ϵ_{eff}) for these structures, which is quite important to design and to calculate antenna parameters with accuracy.

II. THEORY - TTL METHOD

Considering the microstrip patch antenna, as a section of a microstrip line, a set of equations that represent the electromagnetic fields in the x and z direction as function of the electric field in the y direction are obtained applying the TTL method. Starting from the Maxwell's equations, two components can be used to represent the electric and magnetic fields: the transverse (y) and tangential ($t = x$ and z) components to the patch antenna and after various algebraic manipulations the general equations for the structure in the FTD is obtained, for example for the x direction:

$$\tilde{E}_{xi} = \frac{-j}{k_i^2 + \gamma_i^2} \left(\alpha_n \frac{\partial}{\partial y} \tilde{E}_y + \omega \mu_0 \Gamma \tilde{H}_y \right) \quad (1)$$

$$\tilde{H}_{xi} = \frac{-j}{k_i^2 + \gamma_i^2} \left(\alpha_n \frac{\partial}{\partial y} \tilde{H}_y + \omega \epsilon_i \Gamma \tilde{E}_y \right) \quad (2)$$

where $\gamma^2 + k^2 = \alpha_i^2 - \Gamma^2$ and α_i is the spectral variable.

After the application of the boundary conditions, the Moment method is used to eliminate the electric fields and to obtain the homogeneous matrix equation for the calculation of the complex propagation constant. The roots of this matrix are the attenuation constant (α) and phase constant (β). The effective dielectric constant is obtained from $\epsilon_e = (\beta/k_0)^2$, where k_0 is the free space wave number.

III. RESULTS

A microstrip antenna can be fed by a coplanar microstrip line, which is the simplest method, or a coaxial cable. Coaxial feeds are widely used, where the inner conductor is connected to the patch while the outer conductor is connected to the ground plane. Other method is to use aperture or electromagnetic coupling. The matching between the supply line and the antenna is generally necessary and can be done by using several techniques. One method is to use a microstrip quarter-wave transformer section, a software was developed a theory and a computational program that provides a transformer sections number and its principal characteristics, being necessary the knowledge about the input and output impedance that are evaluated by a computational program that uses the TTL method also [6], or simply by adjusting the position of the probe feed.

The results are shown in 3-D, demonstrating the accuracy of the superconducting microstrip patch antenna parameters due to the dynamic method application.

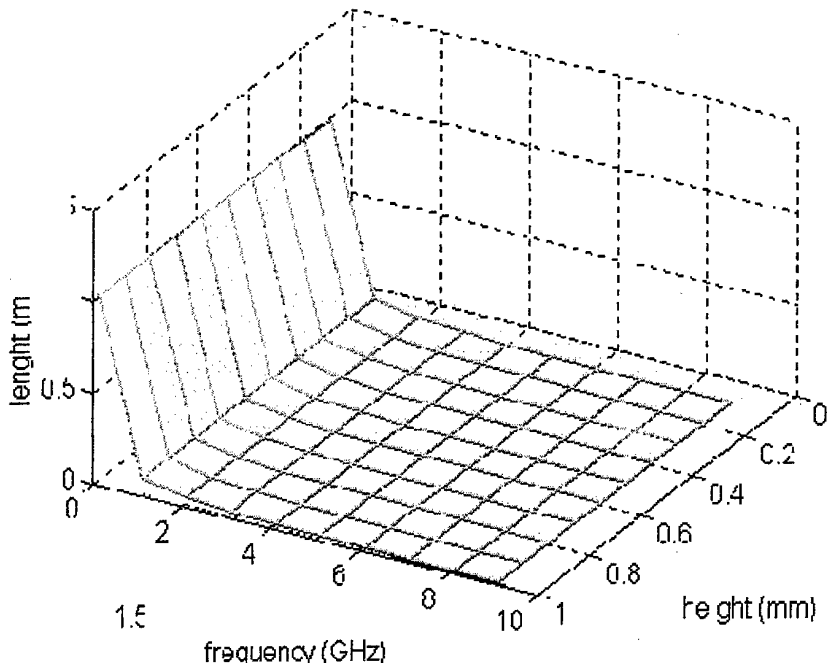


Fig. 1. Element length Comparison between HTS antenna (red) and metallic patch radiator (green). Details:
W=9.8 mm, $\epsilon_r = 2.32$, natural scale.

Notice that the difference raises mainly at higher frequencies.

The repeated and sequential usage of this rigorous method [2] contributes to design and to model such devices with higher precision.

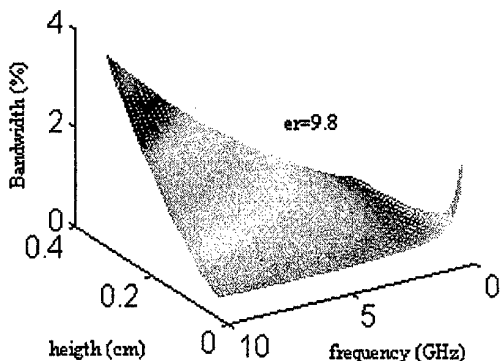


Fig. 2. 3-D presentation of Bandwidth as function of frequency and height

IV. CONCLUSION

The rectangular patch antenna are analyzed using The TTL Method. Results for the patch antenna design and bandwidth are presented, confirming the exactness of the TTL method applied to such devices. A more accurate value of the effective permittivity gives a better value for the element length which contributes definitively to all others parameters to achieve higher precision.

To sum up, The Transverse Transmission Line - TTL is an efficient and accurate method for rectangular microstrip antenna patch analysis and design. This is a very versatile method that can be used with a lossless or semiconductor substrate in various planar architectures. This work was supported by CNPq and CAPES.

REFERENCES

- [1] H. C. C. Fernandes and Geraldo F. da S. Filho, "Recent Advances on Superconducting Microstrip Patch Antennas", *Progress in Electromagnetics Research Symposium - PIERS*, Julho 1998.
- [2] M. A. Richard, K. B. Bhasin, P. C. Claspy, "Superconducting Microstrip Antennas: An Experimental Comparison of two Feeding Methods", *IEEE Transactions on Antennas and Propagation*, vol. 41, no. 7, pp. 967-974, July 1993.
- [3] Naobumi Suzuki, Keiichiro Itoh, Yasuhiro Nagai e Osamu Michikami, "Properties of an Electromagnetically Coupled Small Antenna with a Superconducting Thin-Film Radiator", *IEEE Transactions on Applied Superconductivity*, vol. 6, no. 1, pp. 13-17, March 1996.
- [4] H. C. C. Fernandes, "Attenuation And Propagation In Various Finline Structures", *International Journal of Infrared and Millimeter Waves*, Vol. 17, Nº 08, pp. 1419-1430, Aug. 1996.
- [5] I.J. Bahl and P. Bhartia, "Microstrip Antennas", Artech House, Inc., 1980.
- [6] H. C. C. Fernandes, A. J. Giarola and D. A. Rogers, "PACMO: A Comprehensive CAD Package for Microwave Devices", *IEEE Transactions on Education*, Vol. E-26, No. 4, pp. 162- 164, Nov. 1983.
- [7] S. A. Bokhari, Jean-François Z., J. R. Mosig and F. E. Gardiol, "A Small Microstrip Patch Antenna with a Convenient Tuning Option", *IEEE Transactions on Antennas Propagation*, Vol. 44, No. 11, pp. 1521-1528, Nov. 1996.
- [8] C. Balanis, "Antenna Theory", John Wiley & Sons, Inc., pp 487-496, 1982.

ANALYSIS OF WAVE DIFFRACTION ON THE SYSTEMS OF SCREENS BY THE METHOD OF THE PRODUCT OF PARABOLIC REGIONS

I.V.Petrusenko

Dniepropetrovsk State University

13 Naukovy lane, Dniepropetrovsk, 320625, Ukraine

Tel.: +38 (0562) 769-092, Fax: +38 (0562) 445-294, E-mail: petrus@rff.dsu.dp.ua

The analysis of physical phenomenon of waves interaction in complicated electrodynamics systems (in particular which working in a resonance range) requires application of strict methods of the mathematical theory of a diffraction.

The wide class of wave diffraction problems which have large importance for engineering is a non-coordinate problems. For such ones the boundary of field determination domain cannot be described by coordinate surfaces of one system of coordinates. Although sometimes it is possible to apply a method of partial overlapping regions, the non-coordinate character of region boundary is the reason for application the more difficult mathematical apparatus, which is connected to a way of introduction of the geometrical information at a stage of statement of the problem [1].

In this paper the new method of applied electrodynamics for solving the two-dimensional non-coordinate problems is described. This technique is a development of the method of the product of elliptical regions [2]. According to basic idea of the method the each of rectilinear parts, making a boundary of complex domain, is possible to cover by convex compact - a parabola. It allows to conceive the whole area of field determination as a common part of parabolic regions, which are external in relation to compact. It gives a possibility to construct the solution of a problem for the whole complex geometry domain.

The class of problems under consideration includes the exterior problems of wave diffraction on the systems of rectilinear semi-infinite screens and interior electrodynamics problems of computing of waveguide discontinuities, the geometry of which supposes description in some local Cartesian frames.

Theory

Let we have system of N ideally conducting half-infinite plane-surface screens, the part of which is represented on fig 1. Some screens can be joined with each other under a corner $0 < \alpha \leq \pi$.

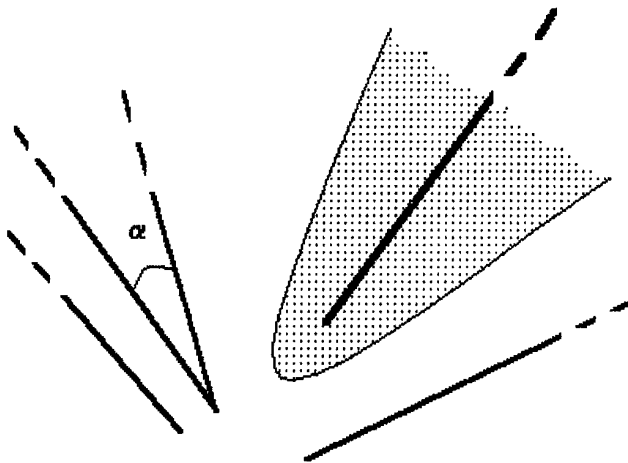


Figure 1. System of half - infinite plane - surface screens

We set each l -th screen the local systems of rectangular coordinates (x_l, y_l) and coordinates of the parabolic cylinder (ξ_l, η_l) , as it is shown in fig. 2. The centre of rectangular system of coordinates is on sharp edge of the

screen, along which axis OZ is directed. The coordinate surface $\eta_l = \eta_0^{(l)}$ forms parabola, the focus of which is located on edge of the screen. At $\eta_0^{(l)} \rightarrow 0$ the parabola degenerates in bilateral half-line.

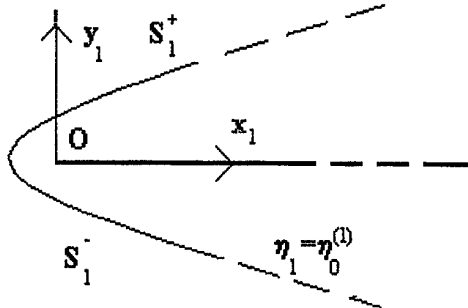


Figure 2. Local systems of rectangular and parabolic cylinder coordinates for screen

Each half-plane on fig.1 we consider as the degenerate parabolic cylinder, and area of wave diffraction is the product of external areas of degenerate parabolic cylinders. According to general idea of a product regions method [2] the desired solution is represented as a sum of the partial solutions

$$U(\xi, \eta) = U_s(\xi, \eta) + \sum_{l=1}^N U_l(\xi, \eta),$$

where U_s - is an inside source field.

Each partial solution is the solution of the homogeneous wave equation outside of l -th degenerate parabolic cylinder. In coordinates of the parabolic cylinder we have representation

$$U_l(\xi, \eta) = \begin{cases} \int_{-\infty}^{\infty} \left[U_l(\xi'_l, \eta'_l) \frac{\partial G_l^D}{\partial \eta'_l} \right]_{\eta'_l=\eta_0^{(l)}} d\xi'_l; & (D) \\ - \int_{-\infty}^{\infty} \left[G_l^N \frac{\partial U_l(\xi'_l, \eta'_l)}{\partial \eta'_l} \right]_{\eta'_l=\eta_0^{(l)}} d\xi'_l, & (N) \end{cases}$$

where G_l - the Green's function of the Helmholtz equation for infinite external area of l -th parabolic cylinder, the designation D and N corresponds to a Dirichlet or Neumann's boundary problem.

On the basis of a limiting absorption principle we come to representation for partial solution as

$$U_l(\xi, \eta) = \sum_{m=0}^{\infty} A_m^{(l)} D_m(\xi p) D_{-m-1}(\eta p), \quad p = \sqrt{2k},$$

where D_m, D_{-m-1} - wave functions of the parabolic cylinder. The representation of the solution is meaningful expansion on radiate waves, as at $|\xi|, |\eta| \gg \sqrt{m}$

$$D_m(\xi p) D_{-m-1}(\eta p) \propto V(\phi) \frac{e^{-ikR}}{\sqrt{kR}}, \quad R \rightarrow \infty,$$

that corresponds to Sommerfeld radiation condition.

To satisfying the boundary conditions on the system of screens we require the vanish a complete field

$$U_l + \sum_{j \neq l}^N U_j = -U_s, \quad \eta_l = 0, l = \overline{1, N};$$

for Dirichlet problem or its normal derivative

$$\frac{\partial U_l}{\partial \eta_l} + \sum_{j \neq l}^N \frac{\partial U_j}{\partial \eta_l} = -\frac{\partial U_s}{\partial \eta_l}, \quad \eta_l = 0, l = \overline{1, N};$$

for Neumann's problem.

Substituting this expansion for a field into integral equations, we receive infinite system of the linear algebraic equations

$$A_n^{(l)} + \sum_{j \neq l}^N \sum_{m=0}^{\infty} A_m^{(l)} d_{mn}^{jl} = f_n^{(l)}, \quad n = \overline{0, \infty}; j, l = \overline{1, N},$$

rather desired complex coefficients. Here we have

$$d_{mn}^{jl} = \frac{p}{\sqrt{\pi}} 2^{-n/2} \Gamma^{-1}\left(\frac{n+1}{2}\right) \int_{-\infty}^{\infty} [D_m(\xi_j p) D_{-m-1}(\eta_j p)] \Big|_{\eta_j=0} D_n(\xi_l p) d\xi_l;$$

$$f_n^{(l)} = -M_n \int_{-\infty}^{\infty} U_s \Big|_{\eta_l=0} D_n(\xi_l p) d\xi_l,$$

for Dirichlet problem and

$$d_{mn}^{jl} = -\frac{p}{\sqrt{2\pi}} 2^{-n/2} \Gamma^{-1}\left(\frac{n}{2} + 1\right) \int_{-\infty}^{\infty} \left\{ \frac{\partial}{p \partial \eta_l} [D_m(\xi_j p) D_{-m-1}(\eta_j p)] \right\} \Big|_{\eta_l=0} D_n(\xi_l p) d\xi_l;$$

$$f_n^{(l)} = -\tilde{M}_n \int_{-\infty}^{\infty} \frac{\partial U_s}{p \partial \eta_l} \Big|_{\eta_l=0} D_n(\xi_l p) d\xi_l,$$

for Neumann's problem.

The properties of the final matrix operator are investigated.

Notice, that for the method of product of the parabolic regions the each equation in final system is possible to interpret as a result of the inversion of a part of the operator of the diffraction problem, connected with a separate screen.

The problem of the electromagnetic wave diffraction on a system of two screens are solved.

Conclusion

The new effective technique for solving two-dimensional non-coordinate electrodynamics problems was developed and substantiated.

References

1. V.M.Onufrienko, V.P.Chumachenko, "Calculation of cut-off frequencies of waveguides of the complicated form of cross-section", In: Radiophysics and electronics of millimetre and submillimeter ranger, IRE NASU, Kharkov, pp. 55 - 59, 1991.
2. V.P.Chumachenko, "Application of the integral equation method for a solution of one class of the electrodynamics problems", Izvestiya vuzov. Radiophysika, v. 21, N 7, pp. 1004 - 1010, 1978.

METHOD OF ANALYSIS OF THE THIN-FILM DIELECTRIC PARAMETERS.

V.Derkach, A.Pojedinchuk, A.Brovenko and A.Vertij

The Usikov' Institute for Radiophysics and Electronics of the Academy of Sciences of Ukraine,

12 Ac Proskura St., Kharkov, 310085, Ukraine

Phone (0572) -44-85-94, Fax (0572) - 441-105, E-mail: derkach@ire.kharkov.ua

Introduction

The methods of the resonant quasioptical interferometry based on the use of open resonators (OR) can be effectively used in the non-destructive testing of dielectric materials. The investigated object can be placed both inside the OR and outside it [1]. The high measurement accuracy is necessary for testing the dielectric parameters of thin films. In this case it is advisable to place the object inside the resonator.

In permittivity the present paper the mathematics of the resonator method of analysis and reconstruction of permittivity function $\varepsilon = \varepsilon(r)$ of thin ($h \ll \lambda$) dielectric samples is considered (here h is a thickness of the film, λ is an operative wavelength. The results of the model experiments in the two-millimeter range of electromagnetic waves are presented.

Description of the method

The essence of the method consists in the use of the multimode millimeter-wave open resonator as the analyzer of the spectrum of spatial frequencies of the waves passing through the object. It is known that in an empty two-mirror resonator with square-law phase correction the axial-symmetric modes TEM_{lpq} (l, p and q is the indexes of modes) are excited. These modes are Gaussian wave beams [2]. In the infinite aperture mirror approximation they are described the Laguerre-Gaussian functions in a cylindrical coordinate system with sufficient accuracy. At a smooth change of frequency or distance between the reflectors at the certain geometrical parameters of the resonator, in the OR the set of modes TEM_{lpq} with different indexes l,p,q and corresponding configurations of fields in cross section are excited. The modes with different indexes represent the elementary linearly independent fields.

In the case when a thin dielectric film with the permittivity $\varepsilon = \varepsilon(r)$ is placed inside the resonator, its resonant properties change. The object presence changes only the mode resonant frequencies (w_{lpq}) provided the absorption and dispersion losses in the object are not taken into account. Thus the frequency shift Δw_{lpq} depends on the mode configuration and function $\varepsilon(r)$. With the experimentally measured Δw_{lpq} and using well known expressions of Laguerre-Gaussian functions the function $\varepsilon(r)$ is restored.

The action of the object on the OR properties, namely, on the resonant frequencies determined executed on the basis of the theory of small disturbance [3]. As the result we have the Fredholm-type integral equation of the first kind

$$\int_0^{\tau} K(p,s)Y(s)d(s) = g(p) \quad (1)$$

in the unknown function $Y(s) = \Delta\varepsilon(r) = \varepsilon(r) - 1$.

Here $K(p,s) = (L_p(s))^2 e^{-s}$; $L_p(s)$ is Laguerre's polynomials; $g(p) = -\frac{l_p}{h} M(\tau, p) (\frac{\Delta w}{w})_p$;

$M(\tau, p) = 2 \int_0^\tau L_p^2(s) e^{-s} ds$; τ and l_p are geometric parameters of the electrodynamics system "OR plus sample"; $\left(\frac{\Delta w}{w} \right)_p$ is comparative value of the mode frequency shifts measured experimentally. The reconstruction of the behavior of function $\varepsilon = \varepsilon(r)$ implies the solution of equation (1). It is necessary to note that the function $g(p)$ is a discrete function and it can be experimentally determined only at some of points p_i with limited accuracy. Therefore this integral equation represents a non-correct problem. The solution depends on the experimental data involving the measurement errors and the requirement of stability of the exact solution in relation to insignificant changes of the initial data is not carried out. Nevertheless, function $y(s)$ can be determined by the method of regularization with some accuracy [4]. Then we introduce a smoothing operator of type:

$$F_\alpha(y, g)_\tau = |\hat{A}y - \hat{g}|^2 + \alpha \int_0^\tau y^2(x) dx, \quad (2)$$

here

$$\hat{A}y = \int_0^\tau \hat{K}(p, s)y(s)ds;$$

$\hat{K}(p, s)$ and $\hat{g}(p)$ are approximate values accordingly $K(p, s)$ and $g(p)$, $\alpha \geq 0$ is a regularization parameter. Accordingly with [4] the next extremely problem was examined:

$$F_\alpha(y, g) \rightarrow \inf, \text{ when } y \in L_2(0, \tau) \quad (3)$$

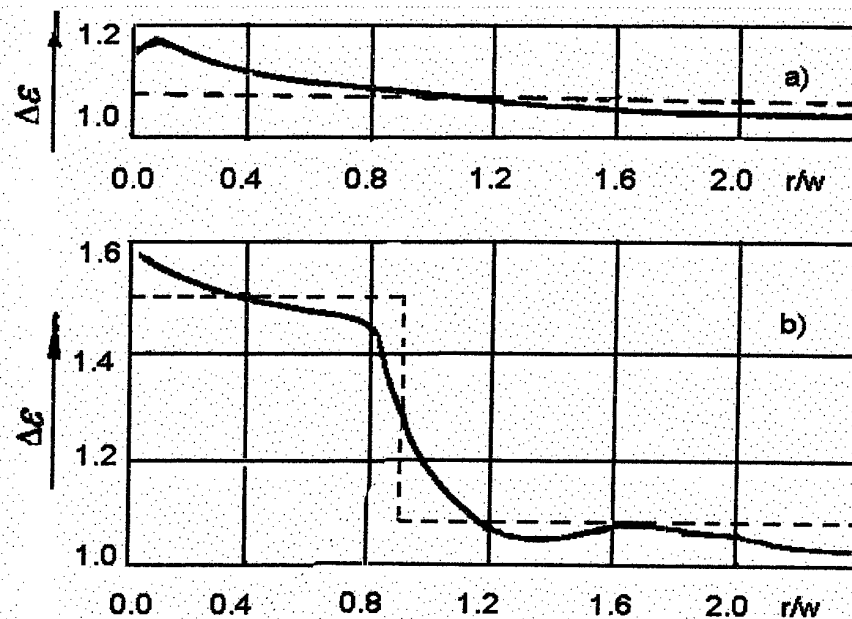


Figure 1.

It has a single solution ω satisfy the integral equation of the second kind:

$$y_\alpha(t)\alpha + \int_0^\tau \left\{ \int_c^d \hat{K}(p,t) \hat{K}(p,s) dp \right\} y_\alpha(s) ds = \alpha \int_c^d \hat{K}(p,t) \hat{g}(p) dp \quad (4)$$

Here $y'_\alpha(0) = y'_\alpha(\tau) = 0$, and regularization parameter α is defined by well-known method of generalized discrepancy [5]. The integral in (3) can be substituted by their discrete analogs obtained by the rectangle formula. And then we arrive at the system of linear algebraic equations of the form

$$(C\alpha + H)y_\alpha = z. \quad (5)$$

Here C is a diagonal unit matrix and H is a positively definite matrix. This system is solved by the method of a square root.

Model experiments

Based on the obtained formulas the calculation algorithm for function $\Delta\epsilon(r)$ was developed. Some model experiments in the two-millimeter wave range were carried out with the multimode two mirror open resonator as a gauge. The OR with mirror curvature $R_{1,2} = 30\lambda$, aperture size $2b = 30\lambda$, intermirror space $l_{ip} \approx 24\lambda$ was taken to work at wavelength $\lambda = 2.2mm$. Resonator was operated in a transmission mode, with transmission spectra obtained using CSW Analyzer. Input and output coupling to the OR was achieved with narrow slots in the center of the mirrors. The mirrors of the resonator were designed in adjustable headers and were placed on the stand to possibility of its smooth moving to tune the resonator. The space distribution of the resonance mode electromagnetic fields was mapped out using a perturbation technique.

The Teflon film of $h \approx 0.01mm$ was located at a maximum of the electric component of the resonance mode electromagnetic field and in the area of plane phase front. The frequency shifts of 10 axially symmetric modes with radial index $p = 0 - 9$ were measured.

Fig. 1a shows $\Delta\epsilon(r/w_0)$ for a homogeneous Teflon film with the uniform $\epsilon(r)$ distribution. The solid curve is for the restored function $\Delta\epsilon$, the dotted curve shows the Teflon permittivity $\Delta\epsilon = \epsilon_{ref} - 1$. The curve for $\Delta\epsilon(r/w_0)$ of an inhomogeneous Teflon film is in Fig 1b. The permittivity inhomogeneous Teflon film was modeled by varying the film thickness in the center of the film. The function restoration accuracy can be raised by increasing of the modes number.

References

1. A.A. Vertiy, I.V. Ivanchenko, V.N. Derkach, "Quasi optical instrument for thickness measurements", Proc. of Intern. Conf. San Diego. USA. Vol.2250, pp. 373-375, 1994.
2. H.Kogelnik, "Resonators and laser wavebeams", Foreign electronics, No3, pp.102-133, 1967.
3. V.V.Nikolsky, "Variation methods for internal tasks of electrodynamics", M.: Nauka, p.460, 1967.
4. A.N.Tikhonov, "Methods for solution of incorrect problems", M.: Nauka, p.288, 1986.
5. A.F.Verlan, A.N.Sizikov, "Integral equations, methods, algorithms, programs", Kiev: Naukova dumka, p.554, 1986.
6. N.S.Bakhvalov, "Numerical methods," M.: Nauka, p.632, 1975.

BANDPASS AND BANDSTOP MULTIAPERATURE IRISES FOR MILLIMETER AND CENTIMETER WAVE RANGE

A.A. Kirilenko, L.P. Mos'pan

Institute of Radiophysics and Electronics of National Academy of Sciences of Ukraine
12, Ac. Proskury Str., Kharkov, 310085, Ukraine,
phone (380572)448-442, fax: (380572)441-105, E-mail lyuda@ire.kharkov.ua

On the base of rigorous numerical models multiaperture irises in a rectangular waveguide have been investigated in order to obtain new electromagnetic features with the aim to use them in waveguide filter design. Rigorous models for a multiaperture iris has been developed on the base of the scattering matrix formulation. S-matrix of key-building block of the double-plane multifurcated discontinuity, has been obtained by solving appropriate diffraction problem by known mode-matching technique of the moments. The number of basis functions of the waveguides, providing required accuracy in numerical studies, has been chosen according to their cross-section dimensions.

Numerical investigations were carried out for multiaperture irises with both rectangular and complicated apertures. The irises with two, three and five rectangular apertures were considered (see Fig. 1).

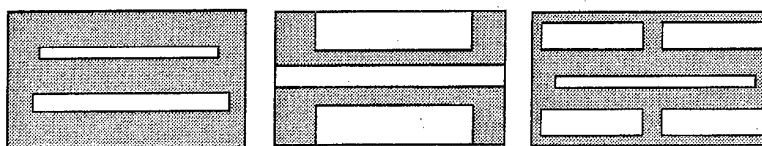


Figure 1. Multiaperture rectangular irises under consideration

Numerical studies were carried out for two-aperture iris, shown that iris frequency response has two resonances, corresponding to full transmission, resonant frequencies of which are defined by geometries of iris apertures. While studying an influence of mutual positioning the apertures of the iris it turns out changing the distance between apertures leads to a shift of both resonant frequencies but response character remains the same.

If lengths of iris aperture are essentially different, a rejection band is formed between two resonances of full transmission. On the base of obtained results a two-bandpass filter based on two-aperture irises has been designed. Frequency response of three-section two-passband filter is presented in Fig. 2.

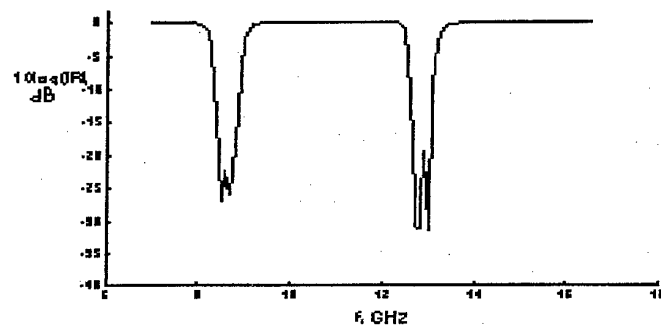


Figure 2. Frequency response of two-bandpass filter based on two-aperture irises

If iris aperture lengths are close the rejection band is transformed into rejection resonance. Numerical study for a lot of multiaperture irises was carried out in order to make clear a mechanism of forming such a rejection resonance. The salient feature of such an iris is following. Each aperture of the iris is not resonant by its nature because of its sufficiently large dimensions but all they together form sharp rejection response. This

resonance is formed by all the apertures of the iris. Varying aperture dimensions does not change the character of the response and results in changing resonant frequency and frequency band of the resonance. Studies of quality factor and bandwidth of such an iris depending on dimensions of iris apertures were carried out.

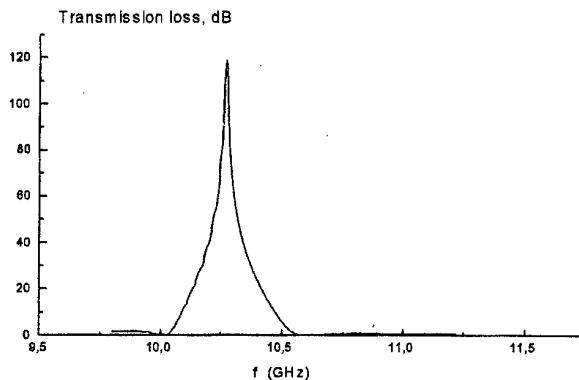


Figure 3. Frequency response of rejection filter based on three-aperture irises

For example it was turned out that three-aperture iris with relatively large aperture dimensions can provide sufficiently high quality factor (of order of 300 and more without ohmic loss accounting). As an example of practical application, three-section rejection filter on three-aperture irises was designed. It provides

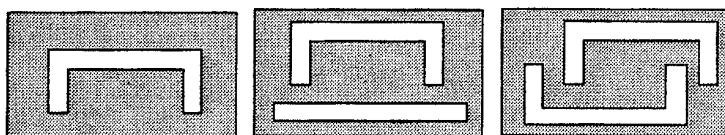


Figure 4. Multiaperture complicated irises under consideration

return loss of not less than 80 dB in the rejection band of 5%. Frequency response of the filter is presented in Figure 3.

All above-mentioned frequency-selective devices can find a wide application in the centimeter wavelength range. In order to broad an application area of such devices, complicated multiaperture irises were investigated (see Fig.4.). Ridged iris has been chosen as a special case of the iris with complicated cross-section. Studying electromagnetic features of such an iris shown that complication of shapes of iris aperture makes possible to develop the irises, quality factor of which is essentially higher than one of classic irises. It was appeared that the magnitude of iris quality factor is determined by the ratio of horizontal and vertical arms of the iris aperture. The smaller is the ratio, the higher is quality-factor of the iris (see. Fig.5). Such irises with complicated apertures have one more attractive feature. Complication of shapes of iris aperture makes possible to design frequency selective devices operating in shorter wavelength range. Operating range of both rectangular and complicated aperture irises is limited by aperture length. So the irises with complicated apertures have more wide operation range. For example, ridged iris, which resonant wavelength exceeds the resonant wavelength of classic iris at least in two times higher, can be easily designed. So bandpass and bandstop devices on the base of multiaperture irises, cross-section of which contains apertures of different shape for shorter wavelength range can be designed.

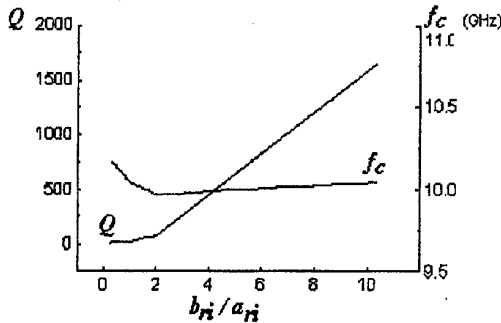


Figure 5. Q-factor and resonant frequency of a ridged iris versus the ratio of its vertical and horizontal arms

**THE ANALYTICAL AND NUMERICAL SOLUTION METHOD
OF THE WAVE DIFFRACTION PROBLEM FOR A ONE-DIMENSIONAL
PERIODIC GRATING WITH CHIRAL MEDIUM**

Sergey B. Panin and Anatoly Ye. Poyedinchuk

Institute of Radiophysics and Electronics
of National Academy of Sciences of Ukraine
12. Acad. Proskury st., Kharkov, 310085,
Ukraine, Phone: (7-0572) 44 85 56,
Fax: (7-0572) 44 11 05, E-mail: panin@ire.kharkov.ua

The present development of UHF-techniques is characterized by the widespread of composite materials, thereat the perspectives of the chiral media use is particularly interested[1].

The rigorous solution method is suggested for a number of problems dealing with the wave diffraction by systems incorporating diffraction grating with chiral medium.

1. Let us consider this method by the example of the following problem. Let the XOY plane separates chiral ($z < 0$) and nonchiral ($z > 0$) media. A periodical grating formed by infinitely thin and perfectly conducting elements parallel to the OX axis is located at $z = 0$, its period is 1 and element spacing is d .

The E-polarized plane wave $\mathbf{E} = \mathbf{E}_0 \exp(-ikz)$, where $\mathbf{E}_0 \parallel OX$, $|\mathbf{E}_0| = I$ (time factor $\exp(-i\omega t)$ is omitted), is normally incident perpendicularly on this grating. The problem is to find the scattered field.

Due to the symmetry property the desired fields are independent of the X coordinate, so the considered problem is two-dimensional.

2. An isotropic chiral medium is described by the following constitutive relations [2]

$$\mathbf{D} = \epsilon_0 \epsilon \mathbf{E} + i\gamma \sqrt{\epsilon_0 \mu_0} \mathbf{H},$$

$$\mathbf{B} = \mu_0 \mu \mathbf{H} - i\gamma \sqrt{\epsilon_0 \mu_0} \mathbf{E},$$

where ϵ and μ are, respectively, the permittivity and permeability, γ represents the chirality parameter which characterizes the magnetoelectric interaction.

For the problem under consideration, the following relations describing the field in a homo-geneous chiral medium have been obtained

$$\Delta_z U^\pm + k^2 U^\pm = 0$$

$$E_x^\pm = U^\pm(y, z), \quad E_y^\pm = \mp \frac{1}{k^\pm} \frac{\partial U^\pm}{\partial z}, \quad E_z^\pm = \pm \frac{1}{k^\pm} \frac{\partial U^\pm}{\partial y},$$

$$\mathbf{E} = \mathbf{E}^+ + \mathbf{E}^-, \quad \mathbf{H} = -i \frac{I}{\eta} (\mathbf{E}^+ - \mathbf{E}^-),$$

$$\text{where } k^\pm = k_0 (\sqrt{\epsilon \mu} \pm \gamma), \quad k_0 = \omega \sqrt{\epsilon_0 \mu_0}, \quad \eta = \sqrt{\mu_0 \mu / \epsilon_0 \epsilon}.$$

So the electric field is described by the sum of the so called "wave" fields \mathbf{E}^\pm . It is worth noting that notwithstanding the problem is two-dimensional, all the components of the required fields are kept. Thus the vector problem is considered.

3. Due to the periodicity of the grating along the OY axis, the solution can be expanded into the Fourier series. Therefore the problem is reduced to the finding of the Fourier coefficients.

Using the boundary conditions on the $z=0$ and $z=h$ surfaces one can obtain the two following systems of the dual series equations:

$$\begin{cases} \sum_{n=-\infty}^{n=+\infty} k_z \{x_n [A_{11} + A_{12}] + y_n [A_{21} + A_{22}]\} \exp(ik_y y) = 2k \exp(-ikh), & |y| < d/2 \\ \sum_{n=-\infty}^{n=+\infty} \{x_n [\Omega_n^+ A_{11} + \Omega_n^- A_{12}] + y_n [\Omega_n^+ A_{21} + \Omega_n^- A_{22}]\} \exp(ik_y y) = 0, & d/2 < |y| \leq l/2 \end{cases}$$

$$\begin{cases} \sum_{n=-\infty}^{n=+\infty} \{x_n [B_{11} + B_{12}] + y_n [B_{21} + B_{22}]\} \exp(ik_y y) = 0, & |y| < d/2 \\ \sum_{n=-\infty}^{n=+\infty} k_z \{x_n [\Omega_n^+ B_{11} + \Omega_n^- B_{12}] + y_n [\Omega_n^+ B_{21} + \Omega_n^- B_{22}]\} \exp(ik_y y) = 0, & d/2 < |y| \leq l/2 \end{cases}$$

where $A_{11} = I$, $A_{12} = -\frac{\omega \mu_1}{\eta k_z} \frac{\Delta k^+}{k^+}$, $A_{21} = I$, $A_{22} = -\frac{\omega \mu_1}{\eta k_z} \frac{\Delta k^-}{k^-}$;

$$B_{11} = \frac{\omega \varepsilon_1 \eta}{k_z} \frac{\Delta k^+}{k^+}, \quad B_{12} = -I, \quad B_{21} = -\frac{\omega \varepsilon_1 \eta}{k_z} \frac{\Delta k^-}{k^-}, \quad B_{22} = I;$$

$\Omega_n^\pm = I \pm \exp(2ik_z h)$, $k = \sqrt{\varepsilon_1 \mu_1} \omega$, $k_z = 2\pi n/l$, $k = \sqrt{k^2 - k_y^2}$, $\Delta k^\pm = \sqrt{k^2 - k_y^2}$, $\varepsilon_1/\varepsilon_0$ and μ_1/μ_0 are, respectively, the permittivity and permeability of the $z>0$ half space; x_n, y_n are the Fourier coefficients describing the field in the chiral medium and giving all the unknown values. The obtained systems show that the diffraction fields consist of both E- and H-polarized waves despite the fact that the only E-wave is incident.

4. It was proved that these systems can be simplified by the method of the Riemann-Hilbert boundary value problem [3]. Applying this method to each system separately, the following system is obtained

$$\begin{cases} X_m = \sum_{n=-\infty}^{n=+\infty} V_{mn}(u) \{ \alpha_n X_n + \beta_n Y_n \} + b_m, \\ Y_m = \sum_{n=-\infty}^{n=+\infty} \tilde{V}_{mn}(\tilde{u}) \{ \tilde{\alpha}_n X_n + \tilde{\beta}_n Y_n \}, \end{cases} \quad m = 0, \pm 1, \dots$$

where

$$\begin{aligned} X_n &= x_n [\Omega_n^+ A_{11} + \Omega_n^- A_{12}] + y_n [\Omega_n^+ A_{21} + \Omega_n^- A_{22}], \\ Y_n &= x_n [B_{11} + B_{12}] + y_n [B_{21} + B_{22}], \\ V_{00} &= -W_0(u), \quad V_{0n} = V_{n-1}^{-1}(u)/n, \quad V_{mn} = V_{m-1}^{n-1}(u)/m, \\ \tilde{V}_{00} &= -W_0(\tilde{u}), \quad \tilde{V}_{0n} = (-1)^n V_{n-1}^{-1}(\tilde{u})/n, \quad \tilde{V}_{mn} = (-1)^{m+n} V_{m-1}^{n-1}(\tilde{u})/m, \\ W_0 &= \ln((1+u)/2), \quad u = \cos(\pi d/l), \quad \tilde{u} = -u, \\ \alpha_0 &= i\chi R_0^+ / T_0^+, \quad \alpha_n = |n| \{ \varepsilon_n R_n^+ + R_n^- \exp(2ik_z h) \} / T_n^+, \\ \beta_0 &= 2i\chi A_0 \exp(2ikh) / T_0^+, \quad \beta_n = -2|n|(1-\varepsilon_n) A_n \exp(2ik_z h) / T_n^+, \\ b_0 &= 2i\chi W_0(u) \exp(-ikh), \quad b_m = -2i\chi V_{m-1}^{n-1} \exp(-ikh) / m, \end{aligned}$$

$$\begin{aligned}
\tilde{\alpha}_0 &= 2i\chi B_0 \exp(2ikh)/T_0^+, \quad \tilde{\alpha}_n = -2|n|(1-\varepsilon_n)B_n \exp(2ik_z h)/T_n^+, \\
\tilde{\beta}_0 &= i\chi C_n/T_n^+, \\
\tilde{\beta}_n &= |n|\{\varepsilon_n C_n - T_n^- \exp(2ik_z h)\}/T_n^+, \\
A_n &= A_{11}A_{22} - A_{12}A_{21}, B_n = B_{11}B_{22} - B_{12}B_{21}, \\
C_n &= [\Omega_n^+ A_{11} + \Omega_n^- A_{12}] [\Omega_n^+ B_{21} + \Omega_n^- B_{22}] - [\Omega_n^+ A_{21} + \Omega_n^- A_{22}] [\Omega_n^+ B_{11} + \Omega_n^- B_{12}], \\
R_n^\pm &= [A_{11} \pm A_{12}] [B_{21} + B_{22}] - [A_{21} \pm A_{22}] [B_{11} + B_{12}], \\
T_n^\pm &= [\Omega_n^+ A_{11} + \Omega_n^- A_{12}] [B_{21} \pm B_{22}] - [\Omega_n^+ A_{21} + \Omega_n^- A_{22}] [B_{11} \pm B_{12}], \\
\chi &= l/\lambda, \quad I + \varepsilon_n = \sqrt{1 - (\chi/n)^2}, \quad V_m^n \text{ were defined in [3].}
\end{aligned}$$

So, we have arrived to the infinite system of the linear inhomogeneous equations of the second kind (when $|n| \rightarrow \infty$; $\tilde{\alpha}_n, \beta_n \sim |n| \exp(-4\pi h/l |n| (I + (kl/2\sqrt{2}\pi n)^2))$; $\alpha_n, \tilde{\beta}_n \sim I/|n|$). This system gives X_n and Y_n and thus all the unknown coefficients.

Using this system, various diffraction values (reflection and propagation characteristics, etc.) can be calculated by the reduction method in any necessary accuracy. Having chosen the smallness parameter, for example γ , an analytical solution of the problem can be found by the method of successive approximations.

The given approach permits to consider a number of following problems: the wave oblique incidence; the involvement of optional layers, the more complicated grating geometry, etc.

References

- 1.B.Z.Kacelenbaum, E.N.Korsunova, A.N.Sivov, A.D.Satrov,"Chiral electrodynamical object", Uspehi Fizitceskikh Nauk, Vol.167, №11, p. 1202-1212, 1997. (In Russian)
- 2.S.A.Tretyakov,"Electrodynamics of the complex chiral medium", Radiotekhnika i Elektronika, Vol.39, №10, p.1457-1470, 1994. (In Russian)
- 3.V.P.Shestopalov,"The method of the Riemann-Hilbert boundary value problem in the diffraction theory and the electromagnetic wave propagation", Kharkov: Pub.KhSU, p.400, 1971. (In Russian)

FRACTAL ELECTRICAL AND MAGNETICAL RADIATORS

Eldar I. Veliev¹⁾, Vladimir M. Onufrienko²⁾

¹⁾Institute of Radiophysics and Electronics, National Academy of Sciences

Ulitsa Proskury, 12, Kharkov, 310085, Ukraine

E-mail veliev @ dut.kharkov.ua

²⁾State Technical University

Zhukovsky Str., 64, Zaporizhzhya, 330600, SP-39, Ukraine

In the present paper we apply the concept of fractional calculus to one of the basic problems in electromagnetics, the problem of radiation of the fractal radiators and their corresponding potentials.

The concept of a radiating contour fractal geometrical structure is the physical basis of our consideration. In this connection, we assume the occurrence of fractal distribution of the contour in current. In space such current forms the appropriate electromagnetic field.

The directional pattern of the fractal analogue of electrical Hertz dipole we have investigated. The features of our fractal model and its differences from classical Hertz dipole are discussed.

We make comments on the model of the fractal magnetic radiator. The numerical account of the directional patterns of fractal electrical and magnetic radiators is compared.

Introduction

The Hertz dipole is known as a variant of the circuit, which ensures an intensive radiation at a rather small-connected part of energy. For mathematical simulation of such dipole usually the idealized elementary electrical vibrator is used, which is located in an unlimited homogeneous isotropic nonconducting medium. The vibrator is presented as wire, short in comparison with wave's length, the amplitude and phase of a current being constant along its length. In inconsistency with this classical model there is a problem of practical creation of a vibrator with amplitude and phase of a current being constant along its length. Nor it is obviously possible to ensure the presence of a material medium with properties of a homogeneity, isotropy and non-conductivity.

The study of properties of an elementary vibrator is important for understanding the process of antennas' radiation even in such idealized statement of the problem, the antennas considered as consisting from a set of vibrators. The principle of superposition allows studying an emitted field as a sum of fields of elementary vibrators.

Hereby we try, proceeding from fractal conceptions of the current's structure in a conductor and the field in a semiconducting medium, to enter α -features of an electromagnetic field ([1], [2]) and to develop a differintegral model of an electrical vibrator.

Construction of differintegral model

As well as in a classical case, we shall assume, that an indirect current creates the monochromatic field

$$I_m^{in} e^{i\omega t}. \quad (1)$$

We shall place a vibrator so that at the beginning of a spherical frame r, θ, φ is in middle of its length l .

The polar axis coincides with axis of the vibrator $\theta = 0, \theta = \pi$.

Instead of a classical vectorial potential, used in such case,

$$\vec{z} \circ A_z(r, \theta, t) = \vec{z} \circ \frac{1}{4\pi} I_m^{in} \int_{-l/2}^{l/2} \mu \frac{e^{i(\omega t - kR)}}{R(r, \theta, \xi)} d\xi, \quad (2)$$

where μ - magnetic permeability of a medium, $k = 2\pi / \lambda$, λ - length of a wave,

$$R(r, \theta, \xi) = \sqrt{r^2 + \xi^2 - 2r\xi \cos\theta}, \quad -l/2 \leq \xi \leq l/2,$$

we consider α -features (differintegral, $0 < \alpha < 1$) till a θ (see [1], [2]):

$$A_z^\alpha(r, \theta, t) = \theta_0^\alpha {}_a D_\theta^\alpha A_z(r, \theta, t), \quad (3)$$

where

$${}_a D_\theta^\alpha f(x) \equiv \frac{1}{\Gamma(1-\alpha)} \frac{d}{d\theta} \int_a^\theta \frac{f(u)}{(\theta-u)^\alpha} du$$

is fractional derivative of the α -order (definition see in [3]), $\Gamma(x)$ – Gamma-function.

Thus,

$$\begin{aligned} A_z^\alpha(r, \theta, t) &= \theta_0^\alpha \frac{1}{\Gamma(1-\alpha)} \frac{\partial}{\partial \theta} \int_a^\theta \frac{A_z(r, \theta, t)}{(\theta-\theta')^\alpha} d\theta' = \\ &= \frac{\theta_0^\alpha}{4\pi} \frac{\partial}{\partial \theta} \int_a^\theta \frac{1}{\Gamma(1-\alpha)} \frac{\mu I_m^{in}}{(\theta-\theta')^\alpha} \left[\int_{-l/2}^{l/2} \frac{e^{i(\omega t-kR)}}{R(r, \theta', \xi)} d\xi \right] d\theta' . \end{aligned} \quad (4)$$

Potential (4) we call α -feature of potential $A_z(r, \theta, t)$. Obviously, at $\alpha = 0$ of (4) we obtain a classical potential.

The introduction of α -features can be proved through reviewing the two new physical and mathematical models corresponding with two statements of the problem of radiation of the Hertz dipole:

- 1) Electrical dipole has a geometric fractal structure. It implies modification of magnitude of current (1) in the direction of the angle θ under the law

$${}_a D_\theta^\alpha (\text{const}_\theta) = \theta_0^\alpha \frac{\text{const}_\theta}{\Gamma(1-\alpha)} \frac{1}{(\theta-\alpha)^\alpha}, \quad (5)$$

where $\text{const}_\theta = I_m^{in} e^{i\omega t}$, magnetic permeability μ - constant.

Here we use the formula of α -order fractional derivative for a constant. It is obvious, that fractality of the current distributions a on φ and r is necessary to take into account in models of a vibrator with a defined thickness ΔS .

- 2) Electrical dipole - ideal (thickness $\Delta S = 0$, current vary on (1)) and is in a medium with a permeability μ , which has a fractal structure of type (5) on cone to $\theta=\text{const}$.

α -features diagrams of a vibrator field

For determinancy, we shall consider the field of the vibrator in a distant (wave) zone ($r >> l, l << \lambda, 2\pi r >> \lambda$).

$$\text{In this case } \vec{z}_o A_z = \vec{z}_o \frac{\mu}{4\pi r} I_m^{in} e^{i(\omega t - kr)}. \quad (6)$$

$$\text{In view of that } \vec{E} = -\frac{i}{\omega \epsilon} \text{rot} \vec{H}, \quad \vec{H} = \frac{1}{\mu} \text{rot} \vec{A}, \quad (7)$$

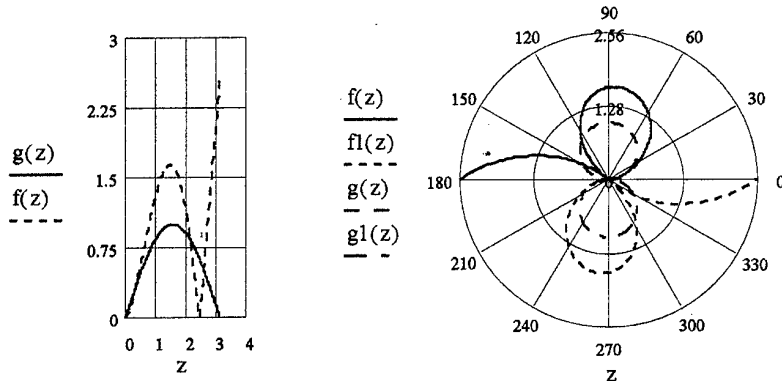
Having disregarded the addends $(1/kr)^2$ and $(1/kr)^3$, it becomes possible to obtain 0- and α -feature of θ -component of strength electrical vector [4]:

$$E_\theta = \frac{i I_m^{in} l}{2\pi r} \sqrt{\frac{\mu}{\epsilon}} \sin \theta e^{i(\omega t - kr)} \quad (8)$$

$$E_\theta^\alpha = \frac{iI_m^{in} l}{2\lambda r} \theta_0^\alpha \sqrt{\frac{\mu}{\epsilon}} \left[\frac{\theta^\alpha}{\Gamma(\alpha+1)} \left({}_1F_1(1; \alpha+1; i\theta) - {}_1F_1(1; \alpha+1; -i\theta) \right) \right] \quad (9)$$

(${}_1F_1(a; c; z)$ - hypergeometric function (Kummer)).

We have obtained the graphs of amplitudes of strength of a field, normalized to associations' maximum



value, from direction to the viewpoint (at $r=\text{const}$ in distant zone $2\pi >> \lambda$).

Figure 1. The θ -component of wave is shown as function of the $z=0$ in Cartesians and polar coordinates

In Fig., curves $g(z) = E_\theta^0$, $g_1(z) = -g(z)$ correspond to 0-feature; curves $f(z) = E_\theta^\alpha$, $f_1(z) = -f(z)$ correspond to 0.5 -feature. The graphs $|E_\theta^0|$ and $|E_\theta^\alpha|$ completely coincide when $\alpha = 0$. The stream of waves is noticed in direction $\theta = 0$ and $\theta = \pi$, when $\alpha \neq 0$ (this radiation is absent in a classical model).

Conclusion

For deriving differintegral models of the elementary magnetic vibrator, in the formula for E_θ^α we substitute I_m^{in} with I_m^{mg} , $\mu \leftrightarrow \epsilon$. Therefore, we obtain α -feature for a θ -component of a magnetic field.

Obtained in paper α -features can be used for development of differintegral model of Huygens element and for solution of such a diffraction problem, as [5].

References

1. V. Onufrienko, "On " α -features" of electrical wave above impedance plane", Conference Proceedings. 12 International Conference on Microwaves & Radar (MIKON-98), Poland, Krakow, May 20-22, 1998. Vol.1, pp. 212-215.
2. V. Onufrienko, "New Description of Spatial Harmonics of Surface Waves", Conference Proceedings. 1998 International Conference of Mathematical Methods in Electromagnetic Theory (MMET-98), Ukraine, Kharkov, June 2-5, 1998. Vol.1, pp. 219-221.
3. N. Engheta, "On the Role of Fractional Calculus in Electromagnetic Theory", IEEE Antennas and Propagation Magazine. Vol. 39, No. 4, pp. 35-46, August 1997.
4. V.I. Volman, Y.V. Pimenov, "Technical Electrodynamics", M.: Svyaz, 1971 (in Russian).
5. E.I. Veliev, K.Kobayashi, M. Ogata, S. Kosikawa, "Diffraction by a strip with different surface impedances: the case of H polarization", Conference Proceedings. 1998 International Conference of Mathematical Methods in Electromagnetic Theory (MMET-98), Ukraine, Kharkov, June 2-5, 1998. Vol. 2, pp. 727-729.

THE MORSE CRITICAL POINTS AND PROBLEMS OF SYNTHESIS AND ANALYSIS DIELECTRIC LAYER

V. V. Yatsik

Usikov Institute of Radiophysics and Electronics of the National Academy of Sciences of Ukraine

12, Ac. Proskura St., Kharkov, 310085, Ukraine

Tel.: +380 (572) 448421, Fax: +380 (572) 441105, E-mail: yatsik@ire.kharkov.ua

The spectral problem of a flat dielectric layer with ever varying permittivity is solved. The initial problem is equivalently reduced to the second-kind integral equation in the sought function. By applying quadrature method, we arrive at the homogeneous system of the second-kind linear algebraic equations with the nonlinear entrance of spectral parameters. The resulting dispersion equations yield not only the regular spectrum points but the Morse critical points (MCP) as well, here dispersion curves can be constructed providing effective algorithms of analysis and synthesis of the dielectric layer properties.

The problem is considered using a dimensionless space-time coordinate system, E-polarization case ($E_y = E_z = H_x = 0$). The layer thickness is $4\pi\delta$, $\varepsilon(z) = \{\varepsilon'(z) + i\varepsilon''(z), |z| \leq 2\pi\delta; 1, |z| > 2\pi\delta\}$ is a piecewise continuously differentiable function of z characterizing relative permittivity of the layer, in which $\varepsilon'(z) = \operatorname{Re}\varepsilon(z) > 0$, $\varepsilon''(z) = \operatorname{Im}\varepsilon(z)$, and $\operatorname{Im}\varepsilon(z)\operatorname{Re}\kappa \geq 0$. The time dependence is chosen to be $\exp(-i\omega t)$, where $\omega = \kappa c$ is the dimensionless circular frequency, κ is the dimensionless frequency parameter. The structure has no x -dependence, the layer quasihomogeneity is assumed to be y -directed.

If a semitransparent structure $\varepsilon(z)$ possesses a plane of symmetry $z = 0$, its eigenfields may be either symmetric or antisymmetric. The possibility of symmetric and antisymmetric quasieigenfields is caused by the symmetry of the considered dielectric structure (permittivity $\varepsilon(z)$) about plane $z = 0$. The analytical nature of a relationship between spectral parameters κ, ϕ , and (κ, ϕ) and nonspectral parameters τ_1, \dots, τ_M describing the structure geometry and/or physical characteristics provides an adequate investigation into dispersion properties of spectra $\kappa(\tau_1, \dots, \tau_M) \in \Omega_\kappa(\tau_1, \dots, \tau_M)$, $\phi(\tau_1, \dots, \tau_M) \in \Omega_\phi(\tau_1, \dots, \tau_M)$, and $(\kappa, \phi)[\tau_1, \dots, \tau_M] \in \Omega_{(\kappa, \phi)}(\tau_1, \dots, \tau_M)$ of both regular and anomalous wave-oscillation processes. It also provides the classification of quasieigenfields of dielectric structures with symmetric or antisymmetric permittivity $\varepsilon(z) = \varepsilon(z, \tau_1, \dots, \tau_M)$ depending on the possibility of a quasieigenfield formal reference to a specific class of symmetry (for example, in varying nonspectral parameters τ_1, \dots, τ_M , the relevant dispersion characteristic continuously approaches that corresponding to the eigenfield of one of possible classes of the structure symmetry).

Of particular interest is the analysis of quasieigenfields of open electrodynamical structures, effects of "interaction" and intertype coupling of eigenfields [1]. The considered dielectric layer with asymmetric about $z = 0$ permittivity $\varepsilon(z)$ represents a simplest scattered (spectral parameter is frequency $\kappa \in \Omega_\kappa$), a simplest waveguide (spectral parameter is quasihomogeneity constant $\phi \in \Omega_\phi$), or a simplest oscillating-guiding structure (with generalized spectral parameter $(\kappa, \phi) \in \Omega_{(\kappa, \phi)}$) that naturally fit this requirement [2]. The mathematical model to solve spectral problems

$$(E - B(\kappa, \phi))U = 0, \quad (1)$$

$$f(\kappa, \phi) = \det(E - B(\kappa, \phi)) = 0, \quad (2)$$

(nontrivial solutions U of problem (1) correspond to the isolate discrete points of spectra Ω_κ , Ω_ϕ , and $\Omega_{(\kappa, \phi)}$ obtained by the solution of the relevant characteristic equations (2)) is capable of analyzing structures with both symmetric and asymmetric about $z = 0$ permittivity $\varepsilon(z)$.

A solution of (1)-(2) as spectral problems of analysis implies the investigation of spectral properties of

the structure with permittivity $\varepsilon(z)$ given. On occasion a perittivity functional dependence is conveniently considered depending not only on the space coordinate z but also on a finite number of nonspectral parameters τ_1, \dots, τ_M describing a family of dielectric structures to approximate the examined $\varepsilon(z) = \varepsilon(z, \tau_1 = const, \dots, \tau_M = const)$, for example, $\varepsilon(z) \equiv \varepsilon(z, \tau_1 = const) = 2 + |\tau_1|(z + 2\pi\delta)$. The problems of synthesis and analysis of dielectric structures fitting certain anomalous conditions of electromagnetic field near the MCP center around the search for the permittivity $\varepsilon(z)$ and the appropriate dispersion relations describing spectral characteristics of oscillating, wave, and wave-oscillation processes near the MCP.

Permittivity $\varepsilon(z)$ is sought in the form $\varepsilon(z) = \varepsilon'(z) + i\varepsilon''(z)$, where

$$\begin{aligned}\varepsilon'(z) &= |\alpha_1\phi_1(z) + \alpha_2\phi_2(z) + \dots + \alpha_R\phi_R(z)|, \\ \varepsilon''(z) &= |\beta_1\psi_1(z) + \beta_2\psi_2(z) + \dots + \beta_I\psi_I(z)| \cdot sign(\operatorname{Re} \kappa),\end{aligned}\quad (3)$$

are in agreement with the physical requirements imposed on the permittivity. The real continuous functions within the modules symbols in (3) are given through their expansions in systems of the basis functions $\{\phi_i(z)\}_{i=1}^R$ and $\{\psi_i(z)\}_{i=1}^I$. As basis functions $\{\phi_i(z)\}_{i=1}^R$ and $\{\psi_i(z)\}_{i=1}^I$ for the approximation of the continuous functions on the interval $[-2\pi\delta, 2\pi\delta]$, the Chebyshev systems like $\{1, z, z^2, \dots, z^n, \dots\}$ or $\left\{1, \cos \frac{z}{2\delta}, \sin \frac{z}{2\delta}, \cos \frac{2z}{2\delta}, \sin \frac{2z}{2\delta}, \dots, \cos \frac{nz}{2\delta}, \sin \frac{nz}{2\delta}, \dots\right\}$ are most frequently used in numerical analysis.

The unknown coefficients $\{\alpha_i\}_{i=1}^R$ and $\{\beta_i\}_{i=1}^I$ are chosen so that the model given by (3) meets the physical requirements imposed on the permittivity. When the choice of the coefficients $\{\alpha_i\}_{i=1}^R$ and $\{\beta_i\}_{i=1}^I$ is identified with the search for nonspectral parameters $\tau_1, \tau_2, \dots, \tau_M \in C$ specifying the layer permittivity $\varepsilon(z) \equiv \varepsilon(z, \tau_1, \tau_2, \dots, \tau_M)$, coefficients $\{\alpha_i\}_{i=1}^R$ and $\{\beta_i\}_{i=1}^I$ in (3) may be related to nonspectral parameters τ_1, \dots, τ_M as follows: $\alpha_1 = \tau_1, \alpha_2 = \tau_2, \dots, \alpha_R = \tau_R, \beta_1 = \tau_{R+1}, \beta_2 = \tau_{R+2}, \dots, \beta_{I-1} = \tau_{R+I-1}, \beta_I = \tau_M$.

As a rule, the anomalous eigenfields of a dielectric layer with $\varepsilon(z) \equiv \varepsilon(z, \tau_1, \dots, \tau_M)$ are interpreted via singularities in the regular behavior of the dispersion characteristics $\kappa(\phi, \tau_1, \dots, \tau_M) \in \Omega_\kappa (\phi \in R, \tau_1, \dots, \tau_M)$, $\phi(\kappa, \tau_1, \dots, \tau_M) \in \Omega_\phi (\kappa \in R, \tau_1, \dots, \tau_M)$, and $(\kappa\phi)[\tau_1, \dots, \tau_M] \in \Omega_{(\kappa, \phi)}(\tau_1, \dots, \tau_M)$. This permits their descriptions in the vicinity of the mapping critical points

$$f(\kappa, \phi, \tau_1, \dots, \tau_M) = \det(E - B(\kappa, \phi, \tau_1, \dots, \tau_M)) : H \times \Phi \times C^M \rightarrow C \quad (4)$$

or, similarly, in the vicinities of the critical points of the complex hypersurface

$$\Omega(\kappa, \phi, \tau_1, \dots, \tau_M) = \{(\kappa, \phi, \tau_1, \dots, \tau_M) \in H \times \Phi \times C^M : f(\kappa, \phi, \tau_1, \dots, \tau_M) = 0\}. \quad (5)$$

Here R and C are sets of real and complex values; the consideration is given to the analytical continuation of function (2) to the domain of complex values $(\kappa, \phi, \tau_1, \tau_2, \dots, \tau_M) \in H \times \Phi \times C^M$.

Let change the variables $(\kappa, \phi, \tau_1, \tau_2, \dots, \tau_M) \equiv (x_1, x_2, \dots, x_{M+2})$ and expand $f(x_1, x_2, \dots, x_{M+2})$ (see (4)) into a multiple Taylor series in the vicinity of the isolated and nondegenerate point, i.e. near the MCP $(\kappa_{1,0}, \phi_{1,0}, \tau_{1,0}, \tau_{2,0}, \dots, \tau_{M,0}) \equiv (x_{1,0}, x_{2,0}, \dots, x_{M+2,0})$:

$$\left\{ \frac{\partial f}{\partial x_i} = 0 \right\}_{i=1}^{M+2}, (x_1, x_2, \dots, x_{M+2}) = (x_{1,0}, x_{2,0}, \dots, x_{M+2,0}); \quad (6)$$

$$\det J(x_1, x_2, \dots, x_{M+2}) \neq 0, (x_1, x_2, \dots, x_{M+2}) = (x_{1,0}, x_{2,0}, \dots, x_{M+2,0}). \quad (7)$$

Here $J(x_1, x_2, \dots, x_{M+2}) = \left[\begin{array}{c} j_{i,p} \end{array} \right]_{i,p=1}^{M+2} = \left[\begin{array}{c} \partial^2 f / \partial x_i \partial x_p \end{array} \right]_{i,p=1}^{M+2}$ is the Hessian matrix of mapping (4). Then the hypersurface $\Omega(x_1, x_2, \dots, x_{M+2})$ (see (5) and [3]) is represented with accuracy to the cubic-smallness terms in the form

$$\sum_{i=1}^{M+2} \sum_{p=1}^{M+2} \frac{\partial^2 f}{\partial x_i \partial x_p} \Big|_{(x_{1,0}, x_{2,0}, \dots, x_{M+2,0})} (x_i - x_{i,0})(x_p - x_{p,0}) + 2f(x_{1,0}, x_{2,0}, \dots, x_{M+2,0}) = 0. \quad (8)$$

Problem (6)-(8) involving the search for the MCP $(\kappa_0, \phi_0, \tau_{1,0}, \tau_{2,0}, \dots, \tau_{M,0})$ in whose vicinity the spectral characteristics of the corresponding structures can be represented in form (8) may be viewed as a problem of synthesis of the family of dielectric layers $\varepsilon(z) \equiv \varepsilon(z, \tau_1, \tau_2, \dots, \tau_M)$ specified by nonspectral parameters $\tau_1, \tau_2, \dots, \tau_M$ near the discovered MCP. In the domain of the anomalous behavior of dielectric layer eigenfields (in the MCP vicinity), the analytical representation of dispersion relations of the synthesized structures is given by (8).

For dielectric structures $\varepsilon(z) \equiv \varepsilon(z, \tau_{1,0}, \tau_{2,0}, \dots, \tau_{M,0})$ whose parameters $\tau_1, \tau_2, \dots, \tau_M$ coincide with coordinates of nonspectral values of the discovered MCP $(\kappa_0, \phi_0, \tau_{1,0}, \tau_{2,0}, \dots, \tau_{M,0})$ dispersion relation (8) becomes

$$\begin{aligned} & j_{11}(\kappa_0, \phi_0, \tau_{1,0}, \tau_{2,0}, \dots, \tau_{M,0}) \cdot (\kappa - \kappa_0)^2 + j_{22}(\kappa_0, \phi_0, \tau_{1,0}, \tau_{2,0}, \dots, \tau_{M,0}) \cdot (\phi - \phi_0)^2 + \\ & + 2 \cdot j_{12}(\kappa_0, \phi_0, \tau_{1,0}, \tau_{2,0}, \dots, \tau_{M,0}) \cdot (\kappa - \kappa_0) \cdot (\phi - \phi_0) + 2 \cdot f(\kappa_0, \phi_0, \tau_{1,0}, \tau_{2,0}, \dots, \tau_{M,0}) = 0. \end{aligned} \quad (9)$$

Note that equation (9) is common for both problems of synthesis and analysis of dielectric media. The problem of analysis of dispersion relations of a given dielectric layer $\varepsilon(z)$ is focused, with the aid of (6)-(8), on the search for the MCP (κ_0, ϕ_0) , where the anomalous dispersion behavior takes place. The problem of synthesis of the layer $\varepsilon(z, \tau_{1,0}, \tau_{2,0}, \dots, \tau_{M,0})$ may be viewed as a problem of medium diagnosis in some range of values of the spectral parameters in order to know how close is this medium to the "degenerate" condition, that is the medium whose eigenfields obey anomalous dispersion law (9) near the MCP $(\kappa_0, \phi_0, \tau_{1,0}, \tau_{2,0}, \dots, \tau_{M,0})$.

The above-stated approach solves both the problems of determinate synthesis for $\varepsilon(z)$ with the pre-assigned z -dependence and the problems of synthesis of the dielectric layer $\varepsilon(z)$ involving the search for the unknown coefficients in the $\varepsilon(z)$ expansion in a system of basis functions (3).

The obtained results can be useful in diagnosis problems, wave propagation problems for layered dielectric waveguides within the Kerr approximation, nonlinear dielectric, semiconductor superlattices.

References

1. V.P. Shestopalov, "Morse Critical Points of Dispersion Equations", Nauk. Dumka, Kiev, pp. 216, 1992.
2. V.P. Shestopalov, V.V. Yatsik, "Spectral Theory of a Dielectric Layer and the Morse Critical Points of Dispersion Equations", Ukrainian Journal of Physics, Vol. 42, No. 7, pp 861-869, 1997.
3. Morse M. "Relations between the critical points of a real function of n independent variables", Trans. Amer. Math. Soc., Vol. 27, pp 345-396, 1925.

**SCALAR WAVE DIFFRACTION BY AXIALLY SYMMETRICAL FLAT SYSTEM
OF INFINITELY THIN PERFECTLY CONDUCTING CIRCULAR RINGS**

Yury.A. Tuchkin ^{1,2}, Ertugrul Karacuha.², Fatih Dikmen.²

1. Institute of Radiophysics and Electronics, NAS of the Ukraine, 12 Ac. Proscura St., Kharkov 310085, Ukraine.
2. Gebze Institute of Technology, PK. 141, 41400 Gebze-Kocaeli, Turkey.

Abstract

A new strong mathematically rigorous and numerically efficient method for solving the boundary value problem of scalar wave diffraction by a flat system of infinitely thin circular ring shaped screens is proposed. The method is based on the combination of the Orthogonal Polynomials Approach and on the ideas of the methods of analytical regularization. The solution is generalization of the investigation done for one ring (see[6]). As a result of the suggested regularization procedure, the initial boundary value problem was equivalently reduced to the infinite system of the linear algebraic equations of the second kind, i.e. to an equation of the type $(I + H)x = b$, $x, b \in l_2$ - in the space l_2 of square summable sequences. This equation can be solved numerically by means of truncation method with, in principle, any required accuracy.

Axially symmetrical system considered consists of N infinitely thin rings on $z=0$ plane having the origin of the coordinate system as their center points and surface of that system can be represented like

$$S = \bigcup_{j=1}^N S_j, \quad S_j = \{(z, r, \varphi) : z = 0, r \in [a_j, b_j], \varphi \in [-\pi, \pi], b_{j+1} < a_j\}, j = 1, 2, \dots, N \quad (1)$$

in cylindrical coordinate system. A combination of Orthogonal Polynomials Method [1-2] and Analytical Regularization Method as used in [3-5], is applied to solve the problem. The following integral equation of the first kind is equivalent to the diffraction problem posed:

$$\int_S J_D(p) G(q, p) ds_p = -u^i(q); \quad q \in S \quad (2)$$

where, $u^i(q)$ is known incident wave, $J_D(p)$ is unknown function i.e. current density like,

$$J_D(p) = [d(p)]^{-1/2} H(p) \quad p \in S. \quad (3)$$

where $H(p)$ is a smooth function on surface S , $d(p)$ is the distance to the nearest edge of a ring, $G(q, p)$ is the Green's function of free space.

The axially symmetry of the system of obstacles leads to an infinite system of one dimensional, non-interacting integral equations of the first kind below,

$$2\pi \sum_{j=1}^N \int_{a_j}^{b_j} J_n^j(r_p) G_n^{j,l}(r_p, r_q) r_p dr_p = g_n^l(r_q), \quad r_q \in [a_l, b_l], \quad l=1, 2, 3, \dots, N \quad (4)$$

where, g_n^l is the Fourier coefficients of incident field on l -th ring, J_n^j is the Fourier coefficients of unknown function where (-) sign of the index originates from orthogonality requirements, $G_n^{j,l}$ is the Fourier coefficients of Green function of the j -th ring with respect to l -th ring.

It can be proved easily that kernels $G_n^{j,l}$ are infinitely smooth for $l \neq j$ and $G_n^{l,l}$ are kernels with singular behaviour of the kind $\ln|r_q - r_p|$.

Solving the system by means of orthogonal Chebyshev polynomials approach is done by introducing one-to-one mapping of all points in each of the intervals $[a_j, b_j]_{j=1}^N$, to the points in the interval $[-1, 1]$ that Chebyshev polynomials are valid in.

The singularity of the system kernels in eq.(4) originates from the ring that has both the integration and the observation points on itself. When integral for this ring is extracted from the system, the remaining integral equation kernels in the system are infinitely smooth ones. The final form of this system of integral equation for the considered problem can be written, extracting the singular integral from whole system and treat it in the same way as one can follow from the investigation in [6] held for just one ring:

$$\int_{-1}^1 \left\{ -\frac{1}{\pi} \ln|u - v| + K_n^{l,l}(u, v) \right\} x_n^l(v) dv + \sum_{j=1}^N \int_{-1}^1 K_n^{j,l}(u, v) x_n^j(v) dv = \tilde{g}_n^l(u), \quad j \neq l$$

$$u \in [-1, 1], \quad l = 1, 2, \dots, N \quad (5)$$

where $K_n^{l,l}$ are sufficiently and $K_n^{j,l}$ are infinitely smooth functions and it is possible to express those functions and the unknown function $x_n^j(v)$ using Fourier-Chebyshev series. Then eq.(6) can be reduced to the infinite algebraic system of the first kind, i.e.

$$\gamma_q^{-2} x_{nq}^l + \sum_{p=0}^{\infty} \left[k_{qp}^{l,l} x_{np}^l + \sum_{\substack{j=1 \\ j \neq l}}^N k_{qp}^{j,l} x_{np}^j \right] = b_q, \quad q = 1, 2, 3, \dots; \quad l = 1, 2, 3, \dots, N \quad (6)$$

where, $\gamma_0 = (\ln 2)^{-1/2}$; $\gamma_q = |q|^{1/2}$, $q \neq 0$, for every $n=0, \pm 1, \pm 2, \pm 3, \dots$; x_{nq}^l and x_{np}^j are the Fourier - Chebyshev coefficients of the unknown function, b_q is Fourier - Chebyshev coefficients of the excitation term, $k_{qp}^{j,l}$ and $k_{qp}^{l,l}$ are Fourier - Chebyshev coefficients of the smooth kernels in eq. (5).

Problem reaches to this point using the classical features from Orthogonal Polynomials Method (see Ref. [1,2]). In the next step, eq. (6) which is a linear algebraic equation system of the first kind is reduced to a linear algebraic equation system of the second kind by means of Analytical Regularization procedure similar to the ones in [6-7]. This procedure in the case under consideration can be done in a very easy way: by introducing new variables $y_{nq}^l = x_{nq}^l / \gamma_q$ and multiplying each term in eq.(7) by γ_q .

As a result, final algebraic system is obtained as an equation of the second kind in l_2 of the type $(I + H)x = b$, $x, b \in l_2$ where I is the identical operator and H is a compact operator. Problems of numerical implementation of the algorithm and numerical results will be presented.

- [1] G. Ya. Popov. On one approximate method for solving the integral equation of wave diffraction by finite width strip.-Zhurnel tekhnicheskoy fiziki, 1965, v. 35, n. 3, p.p. 381-389 (in Russian).
- [2] G. Ya. Popov. On Orthogonal Polynomials method in contact problem of the elasticity theory. - Prikladnaya matematika i. mekhanika, 1969, V. 33, N3 (in Russian)
- [3] Yu. A. Tuchkin. Wave scattering by unclosed cylindrical screen of arbitrary profile with Dirichlet boundary condition. - Soviet Physics Doklady, 1985, v. 30. p.p. 1027-1030
- [4] Yu. A. Tuchkin. Wave scattering by unclosed cylindrical screen of arbitrary profile with Neumann boundary condition. - Soviet Physics Doklady, 1987, v. 32, p.p. 213-216
- [5] Yu. A. Tuchkin. Regularization of boundary value problem of wave diffraction by toroidal screen of arbitrary profile. - in the book: Electrodynamics of open structure of millimeter and submillimeter wave range. - Publishing house of IRE Acad. Sci. The Ukr. SSR, Kharkov, 1990 (in Russian)
- [6] Yu. A. Tuchkin, E. Karacuba, F. Dikmen. Scalar Wave Diffraction from Infinitely Thin Circular Ring. Proc. of International Symposium on Mathematical Methods in Electromagnetic Theory - MMET'98, Kharkov, Ukraine.
- [7] Yu.A. Tuchkin. Scalar Wave Diffraction by Axially Symmetrical Toroidal Screens. Proc. of International Symposium on Electromagnetic Theory, URSI'98, Thessaloniki, Greece.

A RIGOROUS APPROACH TO THE ANALYSIS OF TRANSIENTS IN COMPLETE-PARAMETRIC PERIODIC STRUCTURES

A. O. Perov

Institute of Radiophysics and Electronics of National Academy of Sciences

Address: Bildg. 12, Ac. Proskura Str., Kharkov, 310085, Ukraine

Tel. 38 0572 448 557, Fax. 38 0572 441 105 E-mail sirenko@ire.kharkov.ua

Investigation of the E-polarized electromagnetic waves in periodic structures (Figure 1) is reduced to solution of the initial-boundary problem

$$\begin{cases} \left[-\varepsilon(g) \frac{\partial^2}{\partial t^2} - \sigma(g) \frac{\partial}{\partial t} + \frac{\partial^2}{\partial z^2} + \frac{\partial^2}{\partial y^2} \right] U(g, t) = F(g, t); \quad t > 0; \quad g = \{y, z\} \in Q \\ U(g, t)|_{t=0} = \varphi(g); \quad \frac{\partial}{\partial t} U(g, t)|_{t=0} = \psi(g); \\ U(g, t)|_{g \in S} = 0; \quad U \left(\frac{\partial U}{\partial y} \right) (2\pi, z, t) = e^{i\Phi} 2\pi U \left(\frac{\partial U}{\partial y} \right) (0, z, t), \quad t > 0 \end{cases} \quad (1)$$

in region $Q = R \setminus \overline{\text{int } S}$, $R = \{g \in R^2 : 0 < y < 2\pi, |z| < \infty\}$; S is a boundary of ideal metal generatrixes of the grating on the period $0 \leq y \leq 2\pi$; R^2 is the plane of the variables y, z ; Φ is the real parameter of the Floquet channel R ; $\varepsilon(g)$ is the relative dielectric permeability of the grating material; $\sigma(g) = (\mu_0 / \varepsilon_0)^{1/2} \sigma_0(g)$; ε_0 and μ_0 are the dielectric and magnetic permeability of vacuum, respectively; $\sigma_0(g)$ is the specific conductivity; $U(y, z, t) = E_x$; $E_y = E_z = H_x \equiv 0$; and nonzero components of the vector of magnetic intensity are given by expressions

$$\frac{\partial}{\partial t} H_y = -\left(\frac{\varepsilon_0}{\mu_0}\right)^{1/2} \frac{\partial}{\partial z} E_x, \quad \frac{\partial}{\partial t} H_z = \left(\frac{\varepsilon_0}{\mu_0}\right)^{1/2} \frac{\partial}{\partial y} E_x;$$

$F(g, t)$, $\varphi(g)$, and $\psi(g)$, are functions of sources of non-stationary waves. With certain restrictions on $F(g, t)$, $\varphi(g)$, $\psi(g)$, $\varepsilon(g) - 1$, and $\sigma(g)$ [1], the problem (1) is unique solvable with respect to $U(g, t)$ in Sobolev's space $W_2^1(Q_L^T)$, $Q_L^T = Q_L \times (0, T)$.

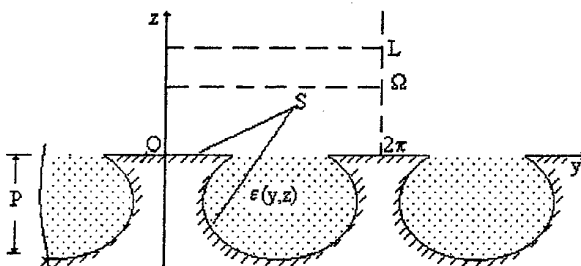


Figure 1.

Assuming that the carriers of functions of sources are located inside a limited area $Q_L = \{g \in Q : |g| < L\}$ in all times t , present the total field formed by the grating in the zone of reflection $z \geq 0$ as [2]

$$U(g, t) = U^i(g, t) + U^s(g, t),$$

where functions

$$\begin{aligned} U^i(g, t) &= \sum_n v_n(z, t) \mu_n(y); \\ U^s(g, t) &= \sum_n w_n(z, t) \mu_n(y); \end{aligned} \quad (2)$$

$$\mu_n(y) = \exp(i\Phi_n y), \quad \Phi_n = n + \Phi, \quad n = 0, \pm 1, \dots$$

describe the incident and reflected non-stationary wave, respectively.

Having employed the exact formula (see works [2,3])

$$w_n(z, t) = - \int_0^t J_0[\Phi_n((t-\tau)^2 - (z-\omega)^2)^{1/2}] \chi[(t-\tau) - (z-\omega)] \left[\frac{\partial}{\partial z} w_n(z, \tau) \right]_{z=\omega} d\tau, \quad z \geq \omega \geq 0 \quad (3)$$

representing general properties of elements $w_n(z, t)$ of the evolutionary basis [2] of non-stationary wave $U^s(g, t)$ "going away" from the scatterer, and representations (2), after simple transformations, the following expressions are obtained on fictitious boundary $z = L$:

$$\frac{\partial}{\partial t} U^s(y, L, t) + \frac{\partial}{\partial z} U^s(y, L, t) = \sum_n \left\{ \int_0^t J_1[\Phi_n(t-\tau)] w'_n(L, \tau) d\tau \right\} \mu_n(y) \Phi_n; \quad (4)$$

$$U^s(y, L, t) = - \sum_n \left\{ \int_0^{t-(L-\Omega)} J_0[\Phi_n((t-\tau)^2 - (L-\Omega)^2)^{1/2}] w'_n(\Omega, \tau) d\tau \right\} \mu_n(y), \quad 0 \leq \Omega < L; \quad (5)$$

Here $w'_n(z, t) = \int_0^{2\pi} \frac{\partial}{\partial z} U^s(y, z, t) \bar{\mu}_n(y) dy$, $J_m(\dots)$ is Bessel function; $\chi(\dots)$ is Heaviside's function; and the horizontal line means complex conjugation.

Application of conditions (4), (5) allows to reformulate problem (1) valid in the unlimited area Q into a problem in the limited area Q_L , which can be effectively solved with application of the method of the finite differences.

In some cases, representation of fields using (3) can allow to solve the problem (1) analytically. In the subsequent considerations, a wave of the type (2) incoming from above out of the region $z > 0$ having $v_n(0, t) = \delta_n^p \delta(t - \eta)$ is chosen as a wave of excitation $U^i(g, t)$. An integer p and $\eta > 0$ are both fixed quantities.

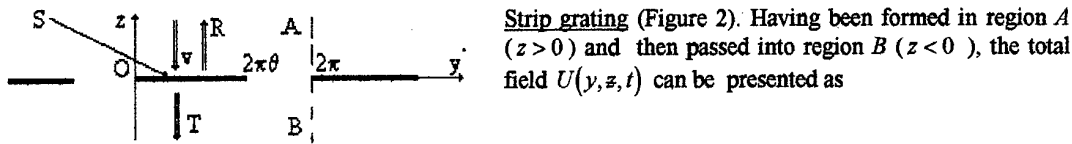


Figure 2.

Strip grating (Figure 2). Having been formed in region A ($z > 0$) and then passed into region B ($z < 0$), the total field $U(y, z, t)$ can be presented as

$$U(A) = - \sum_n \int_0^t J_0 \left[\lambda_n ((t-\tau)^2 - z^2)^{1/2} \right] \chi((t-\tau) \mp z) \begin{pmatrix} R_{np}^{AA} \\ T_{np}^{BA} \end{pmatrix} (\tau - \eta) d\tau \mu_n(y) + U^i;$$

where R^{AA} and T^{BA} are unknown functions of transformation of evolutionary basis of non-stationary wave coming from above (from region A), the transformation being on the boundary $z=0$ of the nonuniformity of the channel R . From both the boundary condition and the continuity condition of E_x component of electric intensity vector on the slot $2\pi\theta \leq y \leq 2\pi$, there follows

$$R_{np}^{AA}(t - \eta) - T_{np}^{BA}(t - \eta) = \delta_n^p v_p(0, t). \quad (6)$$

Substitution of (6) into the sewing-together conditions of the second tangential component of field vector results in

$$\sum_n R_{np}^{AA}(t - \eta) \mu_n(y) = 0, \quad 2\pi\theta \leq y \leq 2\pi.$$

The functional equality can be expanded up to the complete period by differentiating the boundary condition with respect to t .

$$\sum_n \int_0^t J_0 [\lambda_n(t-\tau)] \chi(t-\tau) R_{np}^{AA}(\tau - \eta) d\tau \mu_n(y) = \delta(t - \eta) \mu_p(y)$$

As a result, we can obtain

$$R_{np}^{AA}(t - \eta) = \frac{1}{2\pi i} \sum_m \frac{e^{i(m-n)2\pi\theta} - 1}{m - n} \left\{ \lambda_m \int_0^t J_1[\lambda_m(t-\tau)] \chi(t-\tau) R_{mp}^{AA}(\tau - \eta) d\tau + \delta_m^p \delta^{(1)}(t - \eta) \right\} \quad (7)$$

Included in the right-hand part of (7), the unknown vector-function elements influence the function value at the time t only by their values at the times τ that are strictly less than t . It allows us, by fixing t (the next step in moving along the time layers, start in a point $t = \eta$) to consider (7) as the exact solution of the problem of the non-stationary excitation of the strip grating.

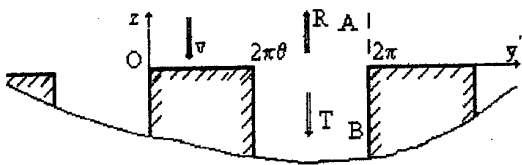


Figure 3.

Grating of thick half-planes (Figure 3). In the problem for a strip grating the fields on the boundary of two identical half-infinite Floquet channels were sewed together. Though the problem considered here is a little bit more complex, it can also be solved without basic changes in the approach used. In region A, we shall write down the total field as

$$U(A) = - \sum_{n=-\infty}^{\infty} \int J_0 \left[\lambda_n ((t-\tau)^2 - z^2)^{1/2} \right] \chi [(t-\tau) - z] R_{n p}^{AA}(\tau - \eta) d\tau \mu_n(y) + U^i$$

In the waveguiding channel B, the representation is true (see work [2])

$$U(B) = - \sum_{m=1}^{\infty} \int J_0 \left[\lambda_{ml} ((t-\tau)^2 - z^2)^{1/2} \right] \chi [(t-\tau) + z] T_{mp}^{BA}(\tau - \eta) d\tau \mu_{ml}(y),$$

where $\lambda_{ml} = m / 2(1-\theta)$, $\mu_{ml}(y) = (\pi(1-\theta))^{-1/2} \sin \frac{m}{2(1-\theta)}(y - 2\pi\theta)$, $m = 1, 2, \dots$

By both sewing the temporal derivatives of the tangential components of vectors of intensity of the complete field ($\partial U / \partial t$ and $\partial U / \partial z$) on the plane $z = 0$ and matching the boundary condition ($\partial U / \partial z = 0$) at the step $0 \leq y \leq 2\pi\theta$, we can obtain

$$\begin{aligned} R_{n p}^{AA}(t - \eta) &= \delta_n^p \delta^{(1)}(t - \eta) + \lambda_n \int_0^\infty J_1 [\lambda_n(t - \tau)] \chi(t - \tau) R_{n p}^{AA}(\tau - \eta) d\tau - \\ &- \frac{1}{2} \left\{ \sum_{n=-\infty}^{\infty} \left[\lambda_k \int_0^\infty J_1 [\lambda_k(t - \tau)] \chi(t - \tau) R_{k p}^{AA}(\tau - \eta) d\tau + \delta_k^p [\delta^{(1)}(t - \eta) + v_p'(0, t)] \right] \Psi_{n k} + \right. \\ &\left. + \sum_{m=1}^{\infty} \lambda_{ml} \int_0^\infty J_1 [\lambda_{ml}(t - \tau)] \chi(t - \tau) T_{mp}^{BA}(\tau - \eta) d\tau \Psi_{n ml} \right\}; \quad n = 0, \pm 1, \dots \end{aligned} \quad (8)$$

$$T_{mp}^{BA}(t - \eta) = - \sum_{n=-\infty}^{\infty} [R_{n p}^{AA}(t - \eta) + \delta_n^p v_p'(0, t)] \Psi_{n ml}; \quad m = 1, 2, \dots \quad (9)$$

$$\Psi_{n k} = \int_{2\pi\theta}^{2\pi} \mu_k(y) \cdot \bar{\mu}_n(y) dy \quad \Psi_{n ml} = \int_{2\pi\theta}^{2\pi} \mu_{ml}(y) \cdot \bar{\mu}_n(y) dy$$

Substitution of (9) into (8) results in exact solution of the problem within the framework of a scheme of consecutive moving along the time layers.

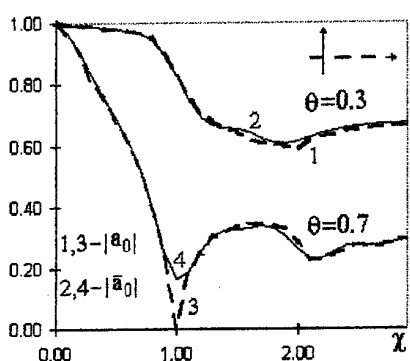


Figure 4.

The methods proposed are easily realized in numbers. Figure 4 shows results of testing of the algorithm for a strip grating. A result obtained at the time domain, with the help of Fourier transformation, was translated into the frequency domain, where the comparison was carried out. The solid lines represent frequency dependencies of the absolute value of reflection coefficient $|a_0(\chi)|$ of a plane wave $e^{-i\chi z}$, obtained by the most effective and reliable method of analysis of similar structures in frequency domain, i.e. by the method of the Riman-Gilbert problem. Dashed lines depict the solutions $|\tilde{a}_0(\chi)|$ obtained by transition from time domain. The different θ values ($\theta = 0.3$ и $\theta = 0.7$) determine the degree of filling of the structure period by metal.

Figure 5 shows reaction of the strip grating both having $\theta = 0.7$ on the plots of Figures 5.a and having $\theta = 0.3$ on the plots of Figures 5.b under excitation by a pulse

$$U^i(g, t) = \exp\left(-\frac{\tau^2}{T_0^2} - i\chi_0 \tau\right), \quad \tau = (t - t_0) + z, \quad t_0 = 0.6, \quad T_0 = 0.2, \quad \chi_0 = 0.$$

Recording the values $w_n(z,t)$ at different z values ($z=0$ and $z=3$) allows to look after the field transformation as it moves away from the grating in direction of increasing z .

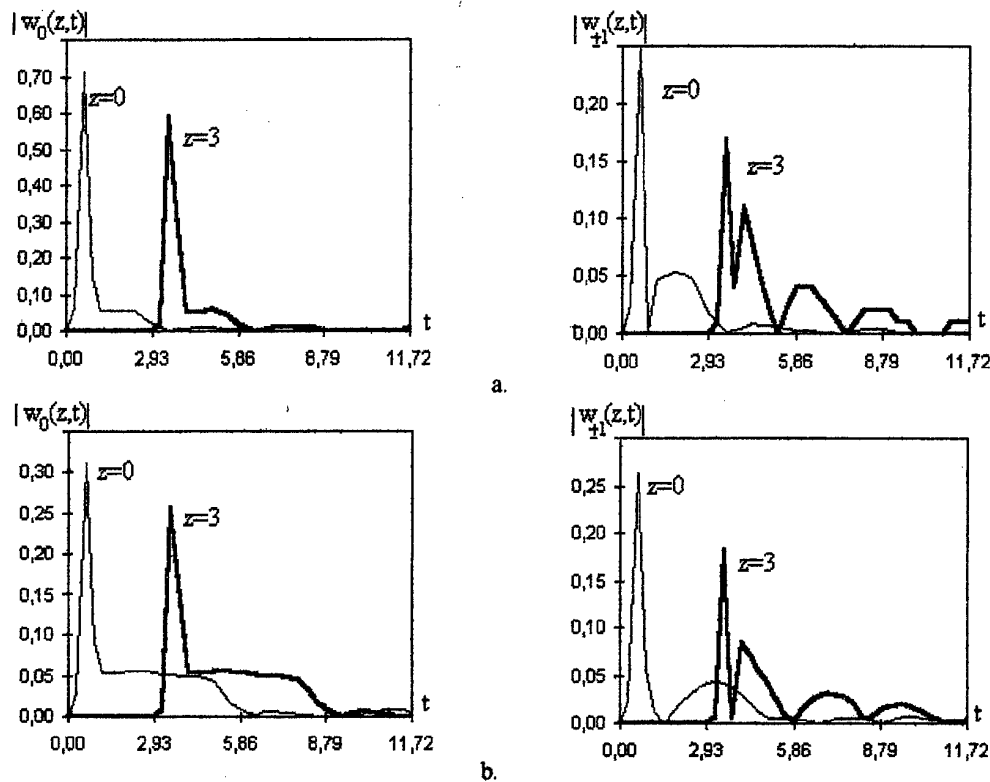


Figure 5.

References

1. O.A. Ladyzhenskaya, "Boundary problems of mathematical physics", Moscow: Nauka, pp. 408, 1973.
2. Yu.K. Sirenko, V.P. Shestopalov, N.P. Yashina, "New methods of the dynamic linear theory of opened waveguide resonators", J. Comput. Math. and Mathem. Physics, Vol. 37, No. 7, pp. 869-877, 1997.
3. A.R. Maikov, A.G. Sveshnikov, C.A. Yakunin, "Difference scheme for the non-stationary Maxwell equations in waveguide systems", J. Comput. Math. and Mathem. Physics, Vol. 26, No. 6, pp. 851-863, 1986.

RESONANCE EFFECTS IN ELECTROMAGNETIC WAVE DIFFRACTION BY A THIN STRIP WITH ANISOTROPIC CONDUCTIVITY

A. D. Shatrov, P. A. Malyshkin

Institute of Radio Engineering and Electronics, Russian Academy of Sciences,
1 Vvedenskii sq., Fryazino, Moscow region, 141120, Russia,
Tel. (095)5269266, Fax (095)7029572, E-mail vsolosin@ms.ire.rssi.ru

The problem of diffraction of a planar linearly polarized wave by a strip with anisotropic conductivity is considered. A strip of a width $2a$ is situated in plane $x = 0$. The unit vector $\tau = \{0, \sin \psi, \cos \psi\}$ (See Fig.1) indicates the direction in which the strip is perfectly conducting.

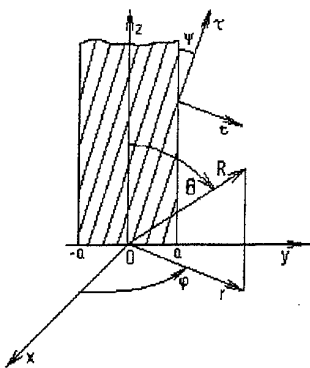


Fig.1. Strip with anisotropic conductivity.

The incident wave propagates in the specified direction which is determined by the angles θ_0, φ_0 :

$$\mathbf{E}^0 = \mathbf{n} \exp[-ik(x \sin \theta_0 \cos \varphi_0 + y \sin \theta_0 \sin \varphi_0 + z \cos \theta_0)]. \quad (1)$$

The unit vector \mathbf{n} specifies the electric field orientation in the incident wave.

Scattered field \mathbf{E}^s is induced by the strip surface current. When $r \rightarrow \infty$ this field behaves like cylindrical wave. For example, its E_z component is given by

$$E_z \approx \frac{\Phi(\varphi)}{\sqrt{\kappa r}} \exp(-i\kappa r - i\hbar z), \quad (2)$$

where $\hbar = k \cos \theta_0$, $\kappa = k \sin \theta_0$.

The surface current density in the strip $|y| < a$ is described by the function $f(\xi) \exp(-i\hbar z)$, $\xi = y/a$. Let

$$u = \frac{ka}{\sin \psi} \left(\frac{h}{k} \cos \psi + 1 \right), \quad v = \frac{ka}{\sin \psi} \left(\frac{h}{k} \cos \psi - 1 \right), \quad w = -\kappa a \sin \varphi_0. \quad (3)$$

Function $f(\xi)$ satisfies the integro-differential equation

$$\left(\frac{d}{d\xi} - iu \right) \left(\frac{d}{d\xi} - iv \right) \int_{-1}^1 G(\xi, \xi') f(\xi') d\xi' = \frac{1}{4} n_\tau (u-v)^2 \exp(iw\xi), \quad (4)$$

where

$$G(\xi, \xi') = \frac{i}{4} H_0^{(2)}(ka|\xi - \xi'|) \quad (5)$$

and n_τ is a scalar product of vectors \mathbf{n} and $\boldsymbol{\tau}$. Equation (4) should be supplemented with the condition that the surface current vanishes at the edges of the strip: $f(\pm 1) = 0$. In the case of narrow strips ($ka \ll 1$), one can use an asymptotic representation for the kernel (5):

$$G(\xi, \xi') \approx \frac{1}{2\pi} \ln \left(\frac{i\gamma ka |\xi - \xi'|}{2} \right), \text{ where } \gamma = 1.78. \quad (6)$$

Then, equation (4) has an explicit analytical solution, which is expressed in terms of Bessel functions. In particular, Fourier transformation of the surface current

$$F(s) = \int_{-1}^1 f(\xi) e^{is\xi} d\xi \quad (7)$$

is expressed by

$$F(s) = \frac{\pi}{2} \frac{(u-v)^2 n_\tau}{(u-w)(v-w) Q(u, v)} \{ Q(u, v) P(w, s) + Q(v, w) P(u, s) + Q(w, u) P(v, s) \}, \quad (8)$$

where

$$Q(u, v) = (u-v) J_0(u) J_0(v) + uv [J_0(u) J_1(v) - J_0(v) J_1(u)] \ln \left(\frac{i\gamma ka}{4} \right), \quad (9)$$

$$P(w, s) = \frac{w}{w+s} [w J_1(w) J_0(s) - s J_0(w) J_1(s)]. \quad (10)$$

When $Q(u, v) = 0$, expression (8) becomes infinite. This occurs when the frequency and the incidence angle θ_0 are determined by

$$ka = \frac{V_m + V_n}{2} \sin \psi, \cos \theta_0 = \frac{V_m - V_n}{(V_m + V_n) \cos \psi}, \quad (11)$$

where V_m are zeros of the Bessel function $J_0(V)$: $V_1 = 2.4$; $V_2 = 5.52$; $V_3 = 8.65$; etc. We assumed that $ka \ll 1$. Therefore, it follows from (11) that resonances occur only when $\psi \ll 1$. The fact that the currents become infinite under conditions (11) is due to approximation (6). Using the first two terms of the Taylor expansion of the Bessel function in representation (5) and applying a variation principle, we obtain more accurate solution in the neighbourhood of resonances. As a result, we obtain that the term

$$-\frac{i\pi}{4} (u-v) J_1(u) J_1(v) (ka)^2 \ln \left(\frac{i\gamma ka}{4} \right) \quad (12)$$

should be added to $Q(u, v)$ in the denominator in (8). Therefore, the resonance value of expression (8) becomes finite:

$$F(s) = -\frac{2in_\tau (u-v)^2 sw}{uv(ka)^2} \quad (13)$$

A vector diagram of scattered field can be expressed in terms of the function $F(ka \sin \varphi)$. For instance, when

$\theta_0 = \varphi_0 = \frac{\pi}{2}$, we obtain (See (2)):

$$\Phi(\varphi) = -\frac{2\sqrt{2}}{\sqrt{\pi}} e^{\frac{i\pi}{4}} \sin \varphi. \quad (14)$$

This means that in spite of the condition $ka \ll 1$ the total scattering cross section is not small: $\sigma = \frac{4}{\pi} \lambda$.

The problem of diffraction of a circularly polarized wave ($\mathbf{H}^0 = \pm i\mathbf{E}^0$) by a strip with perfect electric and magnetic conductance along the direction τ is considered similarly. In this case, surface currents of electric (f_e) and magnetic (f_m) types are induced in the strip. They are related by $f_m = \pm if_e$. Expression (8) obtained also gives a solution to this problem; in this case, $f_e = f$.

The numerical implementation of the analytical results obtained is illustrated in Fig. 2. This figure demonstrates the total scattering cross section versus frequency for $\psi = 0.1$, $\theta_0 = 1.16$ in two cases: $\varphi_0 = 0$ (dashed line) and $\varphi_0 = \pi/2$ (solid line). The resonance phenomena manifest themselves at the frequencies given by (11). The figure shows that there exists an additional resonance at the point $\frac{ka}{\sin \psi} < 1$, which is not described by (11). The amplitude of this resonance is close to those of others when $\theta_0 \ll 1$. Similar results were obtained in the case when $\theta_0 = \pi/2$.

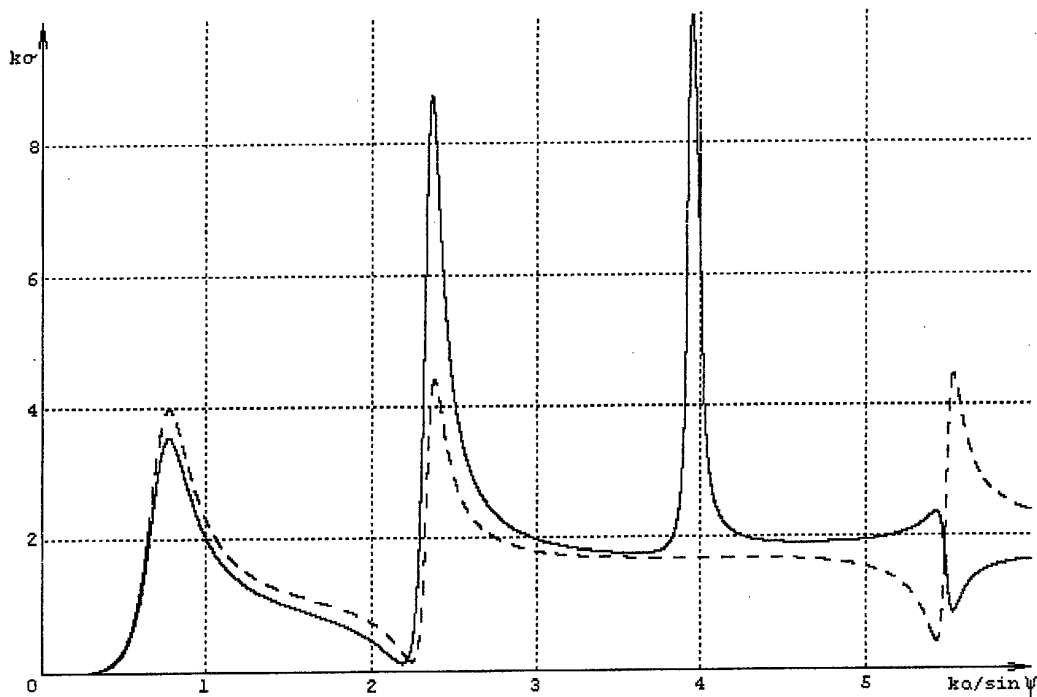


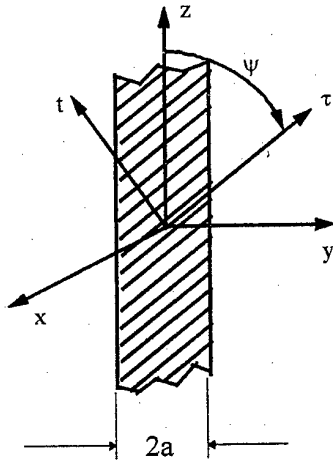
Fig. 2. Total scattering cross section vs frequency.

This work was supported in part by the Russian Foundation for Fundamental Research (project no. 98-02-16194).

PROPER AND IMPROPER WAVES OF STRIP WITH ANISOTROPIC CONDUCTIVITY

E. N. Korshunova, I. P. Korshunov, A. N. Sivov, A. D. Shatrov

Institute of Radio Engineering and Electronics, Russian Academy of Sciences,
1 Vvedenskii sq., Fryazino, Moscow region, 141120, Russia,
Tel. (095)5269266, Fax (095)7029572, E-mail vsolosin@ms.ire.rssi.ru



A wave-guiding structure in the form of a perfectly anisotropically conducting strip is investigated (see Fig. 1). The strip has a width of $2a$ and is located in the plane $x = 0$. The direction in which the structure is perfectly conducting makes an angle ψ with the z axis. Across the strip, the Vladimirskii boundary conditions are imposed, i.e.,

$$E_\tau^- = E_\tau^+ = 0, \quad H_\tau^- = H_\tau^+ \quad (1)$$

As is known, these boundary conditions are well justified for a small-period metal grating, provided that the values of the filling factor lie in a certain interval. Thus, an anisotropic strip can be implemented in the form of a system of parallel conductors of length $2l = 2a / \sin \psi$. The problem of the description of the waves [with the z -coordinate dependence $\exp(-ihz)$] guided by an anisotropic strip is reduced to the following homogeneous integral equation in a surface current f along the conducting direction τ :

Fig. 1.

$$\int_{-a}^a f(y') H_0^{(2)}(\kappa |y - y'|) d(ky') + A \exp(i\alpha y/a) + B \exp(-i\beta y/a) = 0, \quad (2)$$

where $k = 2\pi/\lambda$, λ is the free-space wavelength, $\kappa = \sqrt{k^2 - h^2}$ is a transverse wavenumber, and α and β are given by

$$\alpha = \frac{ka}{\sin \psi} \left(1 + \frac{h}{k} \cos \psi \right), \quad \beta = \frac{ka}{\sin \psi} \left(1 - \frac{h}{k} \cos \psi \right). \quad (3)$$

The constants A and B in equation (2) should be determined by the condition that the surface current vanishes at the edges of the strip, i.e., $f(\pm a) = 0$. The transverse wave number κ is purely imaginary for slow waves and is complex for leaky waves. In the case of narrow strips when $|ka| \ll 1$, we obtained an analytical solution to equation (2). The corresponding dispersion relation has the form

$$(\alpha + \beta) J_0(\alpha) J_0(\beta) + \alpha \beta (J_0(\alpha) J_1(\beta) + J_0(\beta) J_1(\alpha)) \ln\left(\frac{i\gamma\kappa a}{4}\right) = 0, \quad \gamma = 1.78... \quad (4)$$

We solved equations (2) and (4) numerically. We have experimentally studied a strip at wavelengths of about 4 cm. The experimental results are in a good agreement with the results of computations.

Figure 2 shows the normalized propagation constants of two lowest modes for $\psi = 5^\circ$, which are obtained from the rigorous equation (2) (solid curve) and by solving the approximate dispersion equation (4) (dashed curve). The fundamental mode exists at arbitrarily low frequencies; for this mode, $h \rightarrow k$ as $k \rightarrow 0$. The critical frequencies for the higher-order modes, i.e., the frequencies at which $h/k = 1$, can be determined from the equation

$$J_0(\alpha)J_1(\beta) + J_0(\beta)J_1(\alpha) = 0, \quad (5)$$

where $\alpha = kl(1 + \cos\psi)$ and $\beta = kl(1 - \cos\psi)$.

We experimentally investigated a strip with the parameters $2a = 0.8$ cm and $\psi = 30^\circ$. The strip has the form of a small-period grating (with a period of 0.2 mm) made of circular cross-section conductors of diameter 0.1 mm. Figure 3 demonstrates the measured values of h/k in the range of wavelengths λ from 3.6 to 4.5 cm (solid curve). The dashed curve in this figure represents the results of calculation by (2).

We solved the dispersion equation (4) for leaky waves ($\psi = 10^\circ$). Figures 4. and 5 represent the real and imaginary parts of the complex propagation constant $h = h' + ih''$ as a function of frequency for two modes.

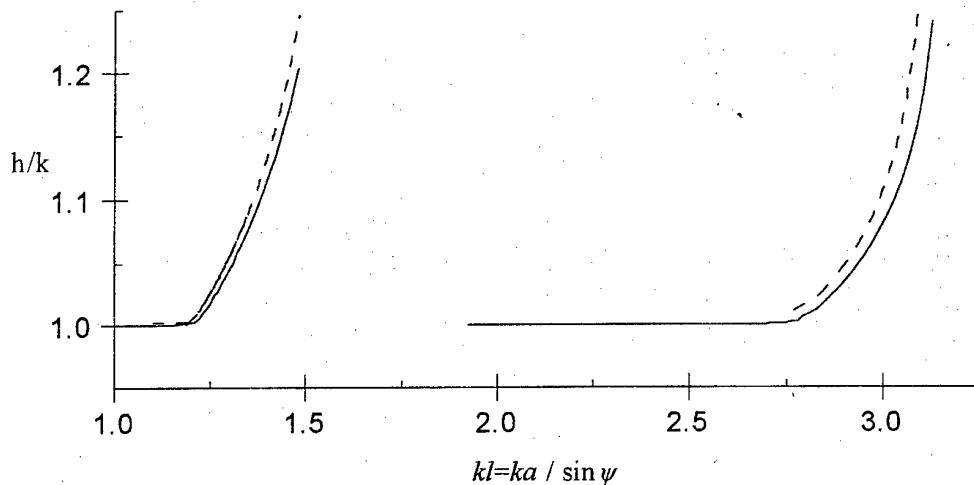


Fig.2

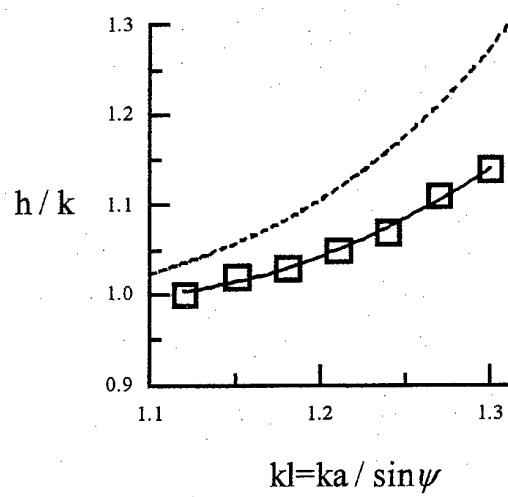


Fig.3.

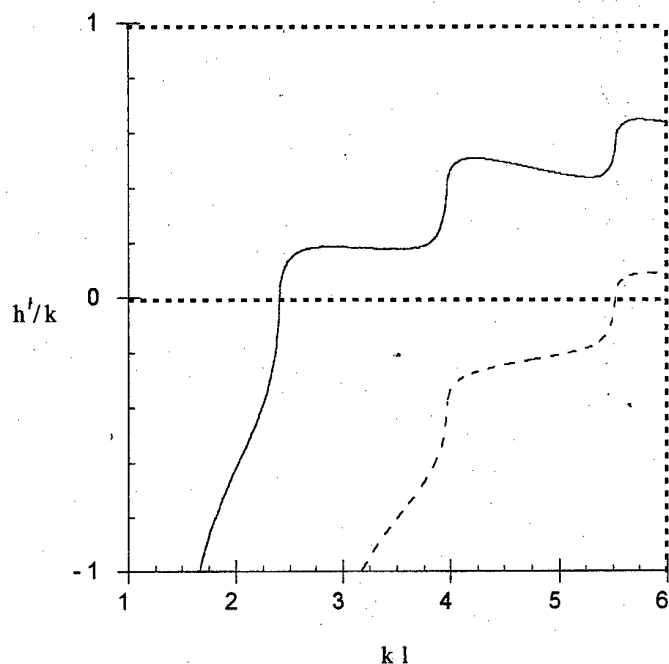


Fig.4.

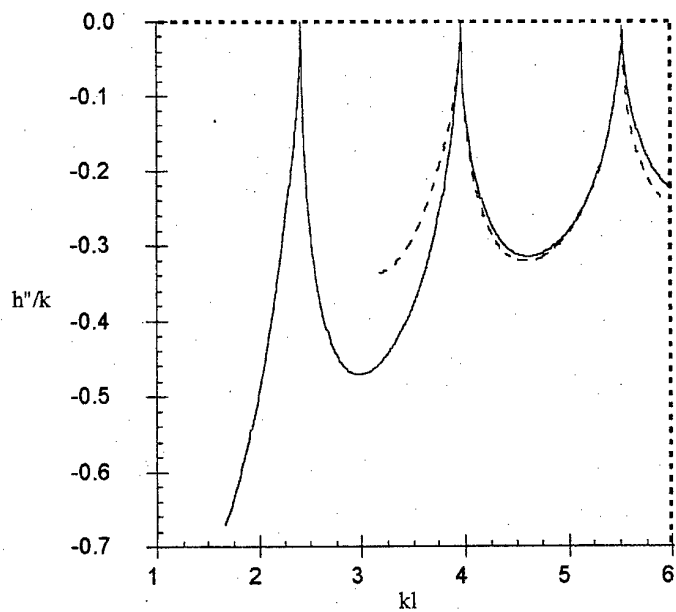


Fig.5.

This work supported in part by the Russian Foundation for Basic Research (project no. 98-02-16197).

THE DIFFRACTION OF NONSINUSOIDAL RADIO WAVES ON NATURAL MEDIA

S.O.Masalov, O.O.Puzanov and A.I.Timchenko

Usykov Institute for Radiophysics and Electronics of the National Academy of Sciences of Ukraine
12, Proscura St., Kharkiv-85, 310085, Ukraine

Tel. (0572) 44-84-34, 44-84-70, 44-86-36, Fax 7 0572 44-11-05

e-mails: masalov@ire.kharkov.ua, puzanov@ire.kharkov.ua, timchenko@ire.kharkov.ua

The use of the nonsinusoidal electromagnetic waves in subsurface sensing is increasing more and more. The efficiency of their application is governed by a possibility to achieve a high resolving capacity in attenuation which is far less than that of radio pulses of similar duration [1-4].

In some cases the analysis of diffraction phenomena can be performed in terms of the diffraction model for the lossless structures [5-9]. As far as these structures are concerned we have derived compact analytical expressions describing the fields of the nonsinusoidal radio wave diffraction; the transient processes have been revealed and examined [6-8]. Additionally, the limits of applicability of this model with various types of video pulses have been established [9]. In particular, it has been found that the diffraction model which does not allow for the attenuation in the media can be applied to the materials of the following two generalized groups (which have a common feature in terms of electromagnetic parameters) [10]:

- **Group III:** dry and moistened sands, limestones, shales, wet coals and granites, asphalt, concrete, brick (when sensing up to depth h_s not exceeding 0.5 m);
- **Group IV:** fresh water ice, marble, dry coals and granite, calcite, dolomite, gypsum, common salt, snow (when sensing up to depth h_s of 5 m; see the table 1 below).

Table 1. Allowed depths of the sounding and various pulses duration for the nondissipative model.

Allowed Δt and h_s	Pulse							
	Exponentially		$At e^{1-At}$		Triangular		Gaussian	
	Gr. III	Gr. IV	Gr. III	Gr. IV	Gr. III	Gr. IV	Gr. III	Gr. IV
Δt , ns	0,3	0,3-30	0,092-3,1	0,092-31	0,063-6,3	0,063-21	0,06-6	0,06-20
h_s , m	0,03	0,5-2,5	0,03-0,25	0,5-5	0,03-0,5	0,5-5	0,03-0,5	0,5-5

In cases where the quantities of specific conductivity cannot be neglected and a dispersion of specific conductivities and permittivities also occur with their variations in depth specified by the existing laws of moisture distribution within the rock, the processes that take place are simulated in terms of numerical analytical approach [11-14]. This approach consists in finding initially the solution in a frequency domain and in subsequent discrete Fourier transformation into a time domain.

The analysis of transient radio waves diffraction fields on different layered structures formed by the Earth's rocks has led to a conclusion that it would be appropriate to employ the outgoing pulses for which the time dependence in the antenna far-field region is close in waveform to the unipolar video pulses [13,14]. On the one hand, in this case it becomes easier to interpret the remotely sensed data when determining the permittivity relation of contiguous media. On the other hand, considering the specific features of the reflectance frequency dependence in a low-frequency region, where the unipolar pulses

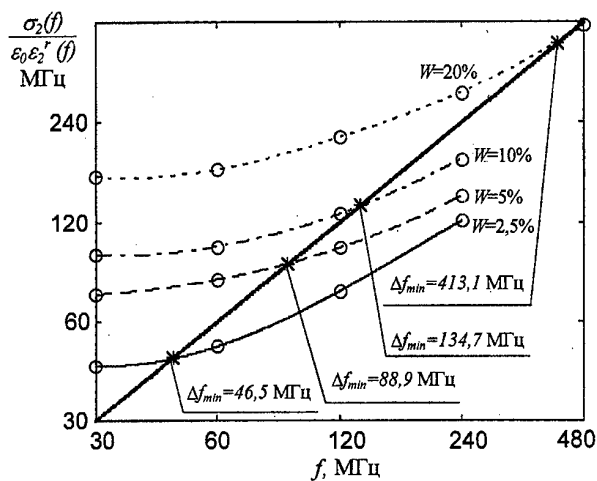


Figure 1. Dependence on frequency of the ratio $\sigma_2(f)/(\epsilon_0\epsilon_2'(f))$ for chestnut loam with various humidities W . The circles designate the calculated (node) values, and asterisks — the points corresponding to the frequencies $f=\Delta f_{min}$ that is the results of the graphic solution of the equation $f = \sigma_2(f)/(\epsilon_0\epsilon_2'(f))$. The heavy line shows the variations in Δf_{min} with varied humidity.

have maximum spectral density values, the typical change in the reflected pulses makes it possible to estimate the relations of the specific conductivities of these regions as well.

Canvassing the behavior of the reflectance in the low-frequency region, where it has a big values, one can determinate the limiting, minimal values of the frequencies $f=\Delta f_{min}$ that can bound spectra of the video pulses above. These frequencies correspond to the value $\tan\delta=0.2$ and they are determined as $\Delta f_{min} = \sigma_2 / (\epsilon_0\epsilon_2')$; here σ_2, ϵ_2' are the specific conductivity and permittivity of the medium, respectively; $\epsilon_0 = 8.85 \cdot 10^{-12}$ F/m is the permittivity of the vacuum. The example of the dependence on frequency of the ratio $\sigma_2(f)/(\epsilon_0\epsilon_2'(f))$ for chestnut loam with various humidities shows Figure 1. One can make a conclusion that for the purposes of the underground sounding, it is optimal that the main part of the pulse energy (against the ground humidity) would be concentrated above than 47-413 MHz.

The told imposes the restriction on the outgoing pulses duration from above. But a pulse duration cannot be too small, as it is not favorable from the power point of view. At an excessively wide spectrum only its insignificant part gets in the oscillating part (placed above the frequency Δf_{min}) of reflectance frequency dependence, where the specific conductivities of environments are minimum.

In addition, the peculiarities of the fields reflected from the multilayered

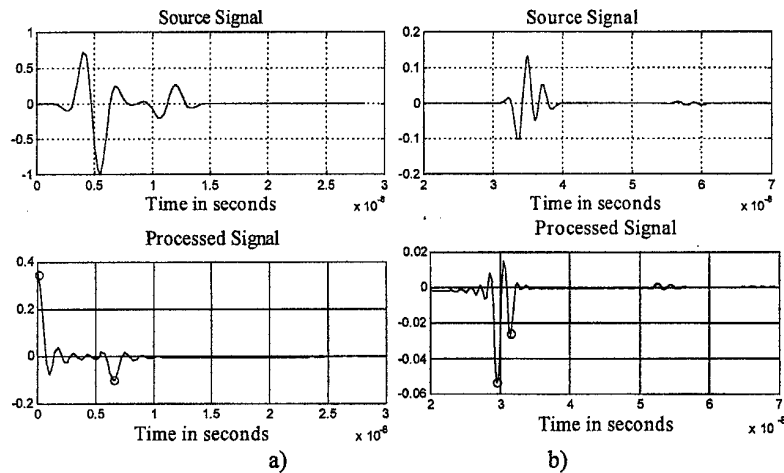


Figure 2. Time dependences of the diffraction fields for two layered structure with the layers of the thicknesses 2 and 0.1 m and the result of the processing after a inverse-conjugate filtration method. The circles denote the peaks of the processed signal corresponding to the moments: a) of the beginning of the outgoing pulse and the reflection from the upper boundary of the structure, b) of the occurrence of the reflections from the boundaries of the structure regions.

structures with a complicated law of the humidity change and also the cases where the spatial duration of a sensing video pulse considerably exceeds the thicknesses of the layers being sensed were considered. With this the efficiency of the subsequent processing of the signal [14] after the inverse conjugate filtration has been demonstrated (Figure 2).

A numerical algorithm that has been developed for simulating the interaction of transient radio waves with soils [15] is helpful in taking approaches to the analysis of radar data. It enables one to

optimise the algorithms to process the received signal and provides the basis for the solution an inverse radiolocation problem.

References

1. Harmuth. H.F., Nonsinusoidal Waves for Radar and Radio Communication, Radio i Svyaz, Moscow, 1985 (In Russian).
2. Cook J.C., Radar transparencies of mine and tunnel rocks. Geophysics, Vol. 40, 5, pp. 865-885, 1975.
3. Andreev G.A., Zaentsev L.V. and Yakovlev V.V., Radiowaves Underground Sounding Systems. Zarubezhnaya Radioelektronika, 2, pp. 3-22, 1991, (In Russian).
4. Astanin G.A., and Kostylev A.A., Principles of Ultrawideband Radar Measurements, Radio i Svyaz, Moscow, 1989. (In Russian).
5. Veselov G.I., Kirpa A.I. and Platonov N.I., On Transient Excitation Processes in Planar Dielectric Structures, Radiotekhnika i Elektronika, Vol. 30, 9, pp. 1702-1708, 1985, (In Russian).
6. S.O Masalov, O.O.Puzanov and A.I.Timchenko. Nonstationary excitation of layered dielectric structures, Rasprostranenie radiovoln v mm i submm diapazonakh, In-t radiofiziki i elektroniki NAN Ukrayny, 1995 r.
7. S.O Masalov, O.O.Puzanov and A.I.Timchenko. Non-Stationary Excitation of Layered Dielectric Structures, Telecommunications and Radio Engineering, 51(1), 1997.
8. S.O Masalov, O.O.Puzanov and A.I.Timchenko. The Diffraction Of Video Pulses On Dielectric Slabs, VIth International Conference on Mathematical Methods in Electromagnetic Theory (MMET'96), Lviv, Ukraine, pp. 108-111, 1996.
9. S.O Masalov and O.O.Puzanov, The diffraction of video-pulses by layered dielectric structures, Radiofizika i radioastronomiya, 2, №1, pp. 85-94, 1997 (in Russian).
10. M.I.Finkelstain, V.A.Kutev, and V.P.Zolotarev. Application of the Radar Underground Sounding in the Engineering Geology, Nedra, Moscow, 128 p., 1986 (in Russian).
11. L.M.Brekhovskikh, Waves in layered media, Akad. Nauk, Moscow, 1957 (in Russian).
12. K.Demarest, R.Plumb, and Z.Huang, FDTD Modeling of Scatterers in Stratified Media, IEEE Trans. Antennas and Propagations, Vol. 43., No 10, pp.1164-1168, 1995.
13. O.O.Puzanov, The Basic Physical Features of Interaction of Non-Sinusoidal Radio Waves with Lossy Layered Dielectrics, Radiofizika i elektronika, 3, №1, pp. 28-35, 1998.
14. N. Ossumi, K. Ueno, Microwave Holographic Imaging of Underground Objects, IEEE Trans. on Antennas and Propagation, Vol. 33, No 2, pp. 152-159, 1985.
15. S.O Masalov and O.O.Puzanov, Modelling Time-Dependent Radio Wave Scattering From Sub-Surface Ground Medium, VII International Conference on Mathematical Methods in Electromagnetic Theory (MMET'98), Kharkiv, Ukraine, Vol. 1, pp. 358-360, 1998.

This work is in part supported by the STCU fund. Project #366.

EXCITATION OF ELECTROMAGNETIC WAVES IN SPACE WITH SPHERICAL-LAYERD STRUCTURE

Yu.M.Penkin

Kharkov State University

4, Svoboda sq., Kharkov, 310077, Ukraine

Tel.(0572) 45-75-48, Fax (0572) 47-18-16, E-mail: Yu.M.Penkin @ univer. kharkov. ua

To insure connection, monitoring, investigation or diagnosis, aerials are placed in different material media, — such as soil, sea and fresh water, plazma, tissues, etc. Most oftent simple aerials are used: symmetric vibrators with small electric length or circular frame antennas which function separately or are grouped into directed arrays. Besides, in order to minimize or eliminate gas leak from antennas to medium, it is covered with isolating shell. Depending on its thickness, isolation can not only avert leak of free charges from antenna but reduce to a great extent dependence of current distribution on its surface from electrical properties of environment. In some cases it is most convenient to use spherical form of isolation, for instance — in the form of homogeneous dielectric ball or hollow spherical shell of dielectric [1]. When specifying electrodynamic characteristics of aerials with indicated types of spherical isolation there arises necessity of solution problems of excitation of heterogeneuos space having two-layer structure in one case (fig.1a) and three-layer structure in the other (fig.1b), where concentric spherical surfaces are boundaries between layers.

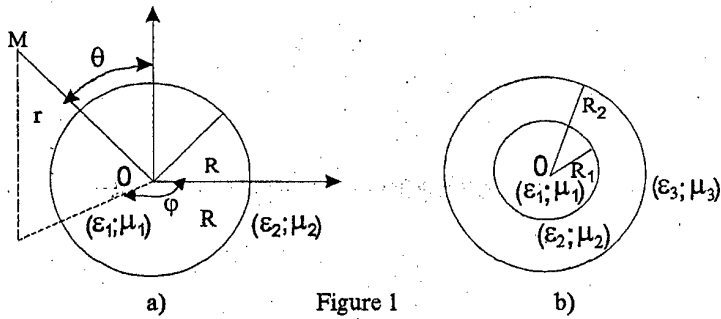


Figure 1

As known, the problem of excitation of volumes with coordinate boundaries can be solved the most conveniently with the help of Green tensor function for Hertz vector potential. For series of such electrodynamic volumes components of Green tensors are defined. For instance in the work [2] they are built for the volumes with spherical ideally conducting boundaries. It turns out that it is possible with the same method, not using more complicated apparatus of Green field functions [3] developed for planolaminated media, to solve the problem of excitation of laminated spherical structure in case of radially oriented extrinsic currents. It should be noted that known in literature Mi and Debai classic results as well as results, obtained in [4] by method of integral equations, describe scattering of outer electro-magnetic field on homogeneous dielectric ball without concretization of source geometry. Problem of excitation of dielectric spherical isolator by inner cur-rent is considered in [1] for case of single circular frame by eigen-wave method. Problem of excitation of three-layer spherical structure is not known to the author.

Let us introduce spherical coordinate system (fig.1a), beginning of which coincides with geometrical centres of spherical boundary surfaces. In this coordinate system radius-vector \vec{r} defines the point of observation with spherical coordinates $(r; \theta; \varphi)$ and \vec{r}' — the point of the source with coordinates $(r'; \theta'; \varphi')$. Expression for corresponding to the case of radial currents component of Green tensor function for Hertz vector potential from the work [2] is used as a key one:

$$G^{e(M)}(\vec{r}/\vec{r}') = - \sum_{n=0}^{\infty} \sum_{m=0}^n \frac{U^{e(M)}(2 - \delta_{om})}{2C_{nm}} \times P_n^m(\cos\theta) P_n^m(\cos\theta') \cos m(\varphi - \varphi'). \quad (1)$$

Here $C_{nm} = \frac{2\pi}{2n+1} \frac{(n+m)!}{(n-m)!}$, δ_{om} — is Kronecker symbol; $P_n^m(\cos\theta)$ — are Legendre associated functions of the first series; functions G^e, U^e —, are of electrical type and, G^M, U^M — are of magnetic type. It

should be noted that, if necessary, using Legendre polynomials addition theorem, expression for Green functions(1) can be presented in other form having made transition from double series to single one:

$$G^{e(M)}(\vec{r}, \vec{r}') = - \sum_{n=0}^{\infty} U_n^{e(M)} \frac{n+1/2}{2\pi} P_n(\cos \theta \cdot \cos \theta' + \sin \theta \cdot \sin \theta' \cos(\phi - \phi')). \quad (2)$$

Universality of expression (1) lies in the fact that in order to obtain it, only conditions of periodicity of Green functions for ϕ and field limitation for all angles θ were used, and dependences $U_n^{e(M)} = U_{ns}^{e(M)}(r, r')$ from radial coordinates this expression contains in implicit form. Functions $U_n^{e(M)}$ should be found from heterogeneous equation:

$$\frac{\partial}{\partial r} \left(r^2 \frac{\partial U_n^{e(M)}}{\partial r} \right) + \left[k_s^2 - \frac{n(n+1)}{r^2} \right] r^2 U_n^{e(M)} = 4\pi \delta(r - r') \quad (3)$$

in the layer, where sources of extrinsic currents are located, and from homogeneous equation analogous (3) in the rest regions of spherical-layered structure. In expression (3): $\delta(r - r')$ — is Dirak delta-function; $k_s = \omega \sqrt{\epsilon_s \mu_s}$ — is wave number (ω — is circular frequency; ϵ_s and μ_s — are dielectric and magnetic permeabilities of medium in the laeyr with number S). Solution of homogeneous equations are presented in the following form:

$$U_{ns}^{e(M)} = A_{ns}^{e(M)} j_n(k_s r) + B_{ns}^{e(M)} y_n(k_s r), \quad (4)$$

where $A_{ns}^{e(M)}$ and $B_{ns}^{e(M)}$ — are unknown coefficients. Here and further following symbols are accepted:

$$j_n(k_s r) = \sqrt{\frac{\pi}{2k_s r}} J_{n+1/2}(k_s r); \quad y_n(k_s r) = \sqrt{\frac{\pi}{2k_s r}} N_{n+1/2}(k_s r); \quad h_n^{(2)}(k_s r) = j_n(k_s r) - iy_n(k_s r),$$

in which $J_{n+1/2}(k_s r)$ — is Bessel function; $N_{n+1/2}(k_s r)$ — is Neiman function; $h_n^{(2)}(k_s r)$ — is Hankel function. Heterogeneous equation (3) is solved by method of variation of arbitrary constants. Unknown coefficients of representations are found from systems of equations, produced on the basis of demands of conditions' fulfilment for $U_{ns}^{e(M)}$ on boundary spherical surfaces. They are formulated in accordance with behaviour on layers' boundaries of normal and tangential components of unknown vector fields, which in case of U_{ns}^e are electro-magnetic fields of electrical type and in case of U_{ns}^M — are of magnetic type:

$$U_{n,s}^{e(M)} = U_{n,s+1}^{e(M)}; \quad a_s^{e(M)} \frac{\partial U_{n,s}^{e(M)}}{\partial r} = a_{s+1}^{e(M)} \frac{\partial U_{n,s+1}^{e(M)}}{\partial r}, \quad (5)$$

where $a_s^e = 1/\epsilon_s$ are for functions U_{ns}^e and $a_s^M = 1/\mu_s$ are for functions U_{ns}^M . In this case in inner layer condition of functions restriction in the point $r=0$ is superposed, and in case of outer layer — condition of radiation on infinity. The obtained expressions for functions $U_n^{e(M)}$ can be reduced in vivid form in case $r' < R$ (disposition of sources in inner layer):

a) for two-layer structure — dielectric ball with radius R (fig.1a)

$$U^{e(M)} = \begin{cases} 4\pi j_n(k_1 r) [k_1 y_n(k_1 r') + j_n(k_1 r') F_n], & r < r', \\ 4\pi j_n(k_1 r') [k_1 y_n(k_1 r) + j_n(k_1 r) F_n], & r' < r < R, \\ 4\pi j_n(k_1 r') h_n^{(2)}(k_2 r)/(R^2 Z_n), & r > R, \end{cases} \quad (6)$$

where:

$$Z_n = k_1 h_n^{(2)}(k_2 R) j_{n+1}(k_1 R) - j_n(k_1 R) \left[\frac{n}{R} \left(1 - \frac{a_2^{e(M)}}{a_1^{e(M)}} \right) h_n^{(2)}(k_2 R) + \frac{a_2^{e(M)}}{a_1^{e(M)}} h_{n+1}^{(2)}(k_2 R) \right];$$

$$F_n = \left[h_n^{(2)}(k_2 R) / (R^2 Z_n) - k_1 y_n(k_1 R) \right] / j_n(k_1 R);$$

b) for three-layer structure (fig. 1b)

$$U^{e(M)} = \begin{cases} 4\pi j_n(k_1 r) [k_1 y_n(k_1 r') - j_n(k_1 r') H_n], & r < r', \\ 4\pi j_n(k_1 r') [k_1 y_n(k_1 r) - j_n(k_1 r) H_n], & r' < r < R_1, \\ -4\pi j_n(k_1 r') [Q_n j_n(k_2 r) + \Phi_n y_n(k_2 r)] / (R_1^2 D_n), & R_1 < r < R_2, \\ -4\pi h_n^{(2)}(k_3 r) j_n(k_1 r') / [D_n(k_2 R_1 R_2)^2], & r > R_2, \end{cases} \quad (7)$$

where:

$$\begin{aligned} Q_n &= h_n^2(k_3 R_2) \left[\frac{n}{k_2 R_2} \left(1 - \frac{a_3^{e(M)}}{a_2^{e(M)}} \right) y_n(k_2 R_2) - y_{n+1}(k_2 R_2) \right] - \frac{a_3^{e(M)} k_3}{a_2^{e(M)} k_2} h_{n+1}^{(2)}(k_3 R_2) y_n(k_2 R_2); \\ \Phi_n &= h_n^{(2)}(k_3 R_2) \left[j_{n+1}(k_2 R_2) - \frac{n}{k_2 R_2} \left(1 - \frac{a_3^{e(M)}}{a_2^{e(M)}} \right) j_n(k_2 R_2) \right] - \frac{a_3^{e(M)} k_3}{a_2^{e(M)} k_2} h_{n+1}^{(2)}(k_3 R_2) j_n(k_2 R_2); \\ D_n &= \left[\frac{n}{R_1} \left(1 - \frac{a_2^{e(M)}}{a_1^{e(M)}} \right) j_n(k_1 R_1) - k_1 j_{n+1}(k_1 R_1) \right] [Q_n j_n(k_2 R_1) + \Phi_n y_n(k_2 R_1)] + \\ &\quad + k_2 \frac{a_2^{e(M)}}{a_1^{e(M)}} j_n(k_1 R_1) [Q_n j_{n+1}(k_2 R_1) + \Phi_n y_{n+1}(k_2 R_1)]; \\ H_n &= \frac{1}{j_n(k_1 R_1)} \left[k_1 y_n(k_1 R_1) + \frac{Q_n j_n(k_2 R_1) + \Phi_n y_n(k_2 R_1)}{R_1^2 D_n} \right]; \end{aligned}$$

Constructed by this method Green functions give opportunity to define radial components of electrical $\Pi_r^e(\vec{r})$ or magnetic $\Pi_r^M(\vec{r})$ Hertz vectors in every region of spherical-layered structures in the form of volumetric integral:

$$\Pi_r^{e(M)}(\vec{r}) = \frac{1}{4\pi i\omega \epsilon_s(\mu_s)} \int_V j^{e(M)}(\vec{r}') \cdot G^{e(M)}(\vec{r}/\vec{r}') dV, \quad (8)$$

where V — is electrodynamic volume from S -layer, in which extrinsic radial electrical $j^e(\vec{r}')$ or magnetic $j^M(\vec{r}')$ currents. Form of expression for $G^{e(M)}(\vec{r}/\vec{r}')$ is defined by the formula (1) and by concrete form of functions $U^{e(M)}$ from (6, 7) that depends on mutual disposition of sources points and observation in spherical-layered structure. Basing on known coefficients electromagnetic fields are defined with the help of $\Pi_r^{e(M)}(\vec{r})$. It should be noted that the obtained expressions for Green functions are convenient while making numerical investigations in cases of resonance spherical isolators, electrical diameters of which are about several waves lengths in boundary media. For spherical surfaces with larger electric diameters series in the adduced expressions converge not quick enough, that results in necessity of their modification.

Thus the constructed Green functions of spherical-layered structures in case of the excitation by radial currents allow to widen possibilities of mathematical simulation for solution of different electrodynamic problems, including determination of aerials' characteristics with spherical form of isolation.

References

1. R.King, G.Smith. Aerials in material media. — M: Mir, 1984. — 2 volumes. — 882 p.
2. Yu.M.Penkin, L.P.Yatsuk. Green tensor of Helmholtz vector equation for simple electrodynamic volumes with spherical boundaries // Radiotekhnika. — 1991. — No.94 pp. 83—91.
3. N.P.Zhuk, O.A.Tretyakov. Green functions of Maxwell equation for plane-layered medium // Radiotekhnika and electronics. — 1985. — vol.33. — No.5 pp. 869—875.
4. N.A.Khizhnyak. Integral equations of macroscopic electrodynamics. — Kiev: Nauk. dumka, 1986. — 280 p.

COHERENT BACKSCATTERING BY A MEDIUM OF RANDOMLY ORIENTED MULTIPLE-SPHERE CLUSTERS

V.P. Tishkovets, P.V. Litvinov
 Astronomical Observatory of Kharkov State University,
 Sumskaya St., 35, Kharkov 310022, Ukraine,
 Tel.: (0572)432428, E-mail: tishkovets@astron.kharkov.ua

The scattering of electromagnetic waves by the system of interacted scatters is a problem of significant importance to many areas of science such as radiophysics, optics and astrophysics. For such systems of scatters, collective effects are observed. They manifest themselves as the well known effect of enhanced backscattering and a specific behavior of linear polarization degree in the range of opposition scattering angles [e.g., Refs.1, 2 and references therein]. These phenomena are caused by constructive interference of multi-scattered waves. The interpretation of measurements of a signal reflected by the medium based on reliable theoretical models of these phenomena might define the structure of the medium and the properties of the scatters. The theoretical models of these effects are weakly developed now. The rigorous approach is realized only for rare media consisting of scatters with size much smaller than the wave length of incident radiation [e.g., Ref.3 and references therein]. In other cases the phase function for the medium particles is replaced by some approximate one. As a result additional free parameters are necessary.

In this work we use the theory of electromagnetic wave scattering by clusters of spherical particles in order to investigate the enhanced backscattering effect for a rare medium consisting of identical chaotically oriented clusters. The scattering characteristics of individual clusters are calculated precisely, whereas the coherent component of scattered radiation is considered as interference of second-order scattered waves between individual scatters of different clusters. The noncoherent component of scattered waves is calculated with help of the well known equation of scalar transfer theory.

We consider scattering by clusters in the circular polarization basis of the incident wave:

$$\mathbf{E}_n^0 = \mathbf{e}_n \exp(i\mathbf{k}\mathbf{r}), \quad (1)$$

where \mathbf{e}_n is the cyclic unit vector, $n = \pm 1$, \mathbf{k} is the wave vector.

The equation describing the scattering by a cluster in the wave zone is:

$$\begin{pmatrix} E_1 \\ E_{-1} \end{pmatrix} = \frac{\exp(i\mathbf{k}\mathbf{r})}{-i\mathbf{k}\mathbf{r}} \begin{pmatrix} t_{11} & t_{1-1} \\ t_{-11} & t_{-1-1} \end{pmatrix} \begin{pmatrix} E_1^0 \\ E_{-1}^0 \end{pmatrix}. \quad (2)$$

Here t_{np} are elements of the amplitude matrix of scattering, ($p = \pm 1$).

The scattering matrix elements which transform the Stockes parameters of the incident wave to those of the scattered wave are determined by square quantities of matrix (2). In particular the intensity of the scattered wave is proportional to the scattering matrix element

$$F_{II} = (|t_{11}|^2 + |t_{1-1}|^2 + |t_{-11}|^2 + |t_{-1-1}|^2) / 2. \quad (3)$$

In double scattering approximation the amplitude matrix (2) for J -th cluster may be written as

$$t_{np}^{(J)} = t_{np}^{(JJ)} + \sum_{\Delta \neq J} t_{np}^{(\Delta)}. \quad (4)$$

Here matrix $t_{np}^{(JJ)}$ corresponds to the single scattering of wave (1) by J -th cluster, $t_{np}^{(\Delta)}$ is the matrix corresponding to scattering waves travelling from Δ -th cluster. Having average square expressions of matrix (4) over clusters orientations and coordinates of Δ -th cluster regarding to J -th one, one can obtain

$$\langle t_{np}^{(J)} t_{\nu\mu}^{*(J)} \rangle = \langle t_{np}^{(JJ)} t_{\nu\mu}^{*(JJ)} \rangle + \langle t_{np}^{(\Delta)} t_{\nu\mu}^{*(\Delta)} \rangle. \quad (5)$$

This expression determines values $\langle F_{II} \rangle$ which may be considered as a characteristic of a singly scattered wave by a small-volume element. The scattering matrix for randomly oriented clusters has been done in [4]. The approximate expressions for the coherent part $\langle t_{np}^{(\Delta)} t_{\nu\mu}^{*(\Delta)} \rangle$ have the form [5]:

$$\langle t_{np}^{(J\Delta)} t_{\nu\mu}^{*(\Delta J)} \rangle = \sum_{s\delta} j_0(2kR_s \cos \frac{\theta}{2}) j_0(2kR_\delta \cos \frac{\theta}{2}) \sum_{LMlm} G_{lm}^{(s\delta np)} G_{LM}^{*(\delta sv\mu)} F_{lmLM}, \quad (6)$$

where

$$\begin{aligned} G_{LM}^{(s\delta np)} &= \sum_{lqm} (2l+1)(2q+1) Q_{lql}^{(s\delta np)} C_{l1q-1}^{L0} C_{lmq-n}^{LM} D_{mp}^{*l}(\phi, \theta, 0), \\ Q_{lql}^{(s\delta np)} &= (a_l^{(s)} a_q^{(\delta)} + np b_l^{(s)} b_q^{(\delta)}) I_{lql}^+ + (na_l^{(s)} b_q^{(\delta)} + pb_l^{(s)} a_q^{(\delta)}) I_{lql}^-, \\ F_{lmLM} &= \frac{\pi \tilde{n}}{k^3} (-1)^{L+M} \sum_{q\eta} i^q C_{l0L0}^{q0} C_{lmL-M}^{q\eta} D_{\eta 0}^q(\phi, \frac{\theta}{2}) \int_{2k\Lambda}^\infty \exp(-\tau) j_q(2x \cos \frac{\theta}{2}) dx, \\ I_{lql}^\pm &= (1 \pm (-1)^{L+q-l}) / 2, \\ \tau &= x \tilde{n} \langle C_{ext} \rangle / k. \end{aligned}$$

Here $s, \delta = 1..N$, N is the number of particles in a cluster, $j_L(x)$ being the Bessel spherical function, the symbols C and D denote the Clebsch-Gordan coefficients and Wigner function respectively, R_j is the distance between the center of the cluster and the center of the j -th particle, $a_L^{(j)}$ and $b_L^{(j)}$ are the Mie coefficients, \tilde{n} is the concentration of clusters in a medium, Λ is the radius of the sphere circumscribed around the cluster, $\langle C_{ext} \rangle$ is the extinction cross section of cluster [4], ϕ is the azimuthal angle of the spherical coordinate system, θ is the scattering angle.

As an example dependences of $\langle F_{II} \rangle$ on scattering angle for clusters containing three contacting identical components for some values of parameter $\xi = \frac{4}{3} \tilde{n} \pi \Lambda^3$ are given in Fig.1. The parameters of particles are following: $k\tilde{a} = 4$, $\varepsilon^2 = 1.32 + 0.05i$ (a is the particle radius, ε is the permittivity of particle). Fig.2 show the same for the co- and cross-polarized components $\langle |t_{xx}|^2 \rangle$, $\langle |t_{yy}|^2 \rangle$, $\langle |t_{xy}|^2 \rangle = \langle |t_{yx}|^2 \rangle$. Here t_{xx} , t_{yy} , t_{xy} , t_{yx} are the elements of the amplitude matrix (2) in the base of linear polarization.

For calculation of the effect of enhanced backscattering by a medium we use the scalar transfer theory. The intensity of radiation reflected by a plane-parallel medium layer is given by $I(\tau_0, \mu_0, \mu, \phi) \sim \rho(\tau_0, \mu_0, \mu, \phi) \mu_0$. Here τ_0 is the optical thickness of medium, μ_0 , μ are cosines of incident and reflected angles of radiation respectively, ϕ is difference between the azimuth angles of the incident and reflected radiation,

$$\rho(\tau_0, \mu_0, \mu, \phi) = \frac{\omega}{4(\mu_0 + \mu)} [\chi(\theta) (1 - \exp(-\tau_0 (\frac{1}{\mu_0} + \frac{1}{\mu}))) + \Delta\rho(\tau_0, \mu_0, \mu, \phi)],$$

$$\omega = \langle C_{sc} \rangle / \langle C_{ext} \rangle,$$

$$\frac{1}{k^2} \langle C_{sc} \rangle \int_0^{2\pi} \int_0^\pi \langle F_{II} \rangle \sin \theta d\theta d\phi = \frac{1}{2} \int_0^\pi \chi(\theta) \sin \theta d\theta = 1,$$

ω , $\chi(\theta)$ are the single-scattering albedo and the normalized to unity scattering phase function respectively, $\langle C_{sc} \rangle$ is the scattering cross section, $\Delta\rho(\tau_0, \mu_0, \mu, \phi)$ involve the multiple scattering in the medium.

Dependences of coefficient $\rho_1(\tau_0, \mu_0, \mu, \phi) = \frac{4(\mu_0 + \mu)}{\omega} \rho(\tau_0, \mu_0, \mu, \phi)$ for $\mu_0 = \mu$, $\phi = 0$ and for the same clusters on the scattering angle are given in Fig.3 and Fig.4 for $\tau_0 = 0.5$ and $\tau_0 = 5$ respectively. Coefficient $\Delta\rho(\tau_0, \mu_0, \mu, \phi)$ is calculated for approximate phase function $\chi(\theta) = 1 + x_1 \cos(\theta)$ with $x_1 = 1.5$.

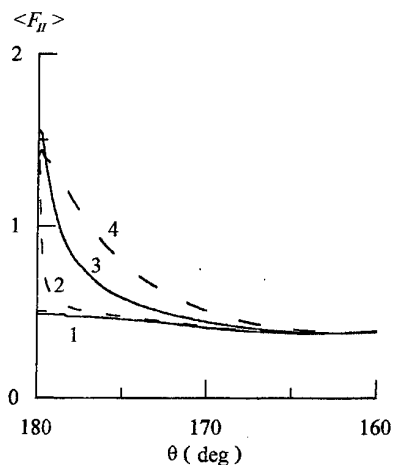


Fig.1. 1 is the isolated cluster, 2 - $\xi = 0.005$,
3 - $\xi = 0.05$, 4 - $\xi = 0.2$.

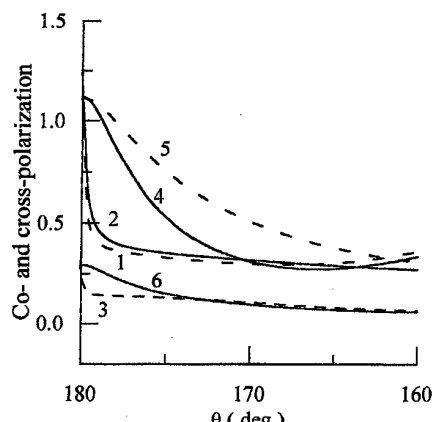


Fig.2. 1, 2, 3 denote $\langle |t_{xx}|^2 \rangle$, $\langle |t_{yy}|^2 \rangle$, $\langle |t_{xy}|^2 \rangle$
respectively for $\xi = 0.005$. 4, 5, 6 denote those
for $\xi = 0.2$.

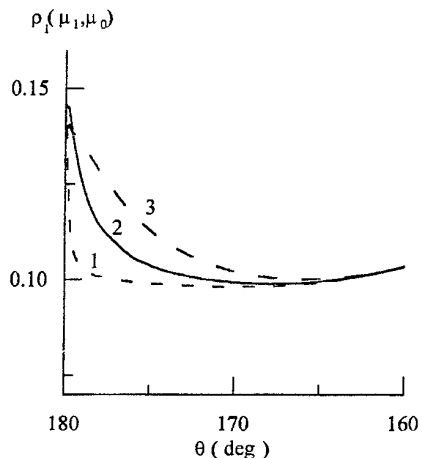


Fig.3. 1 - $\xi = 0.005$, 2 - $\xi = 0.05$, 3 - $\xi = 0.2$,
 $\tau_0 = 0.5$

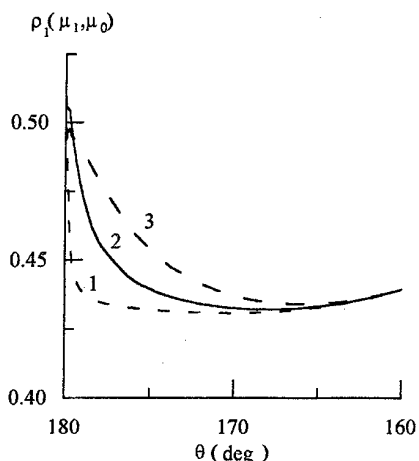


Fig 4. 1 - $\xi = 0.005$, 2 - $\xi = 0.05$, 3 - $\xi = 0.2$,
 $\tau_0 = 5$.

References

1. Kravtsov, Yu.A. and Saichev, A. I. "Effects of double passage of wave in randomly inhomogeneous media", Uspekhi Fizicheskikh Nauk, 1982, V.25, pp. 494-508 (in Russian).
2. Shkuratov Yu.G., Muinonen K. et al. "A critical review of theoretical models for the negative polarization of light scattered by atmosphereless solar system bodies", Earth, Moon and Planets, V.65, No 3, pp. 201-246.
3. Zubkov L.A., Kuz'min L.V. and Romanov V.P. "Coherent backscattering from fluctuations of anisotropy parameters", Optics and Spectroscopy, 1996, V.80, No 5, pp. 804-813 (in Russian).
4. Mackowski D.W., Mishchenko M.I. "Calculation of the T matrix and the scattering matrix for ensembles of spheres", J. Opt. Soc. Am. Ser. A., 1996, V.13, pp. 2266-2278.
5. Tishkovets V.P., Litvinov P.V. "Electromagnetic Scattering by system of chaotically oriented clusters of spherical particles", Radiophysics and Electronics, 1998, V.3, No 1, pp. 57-61 (in Russian).

MODELLING AND VISUALISATION OF THE ELECTROMAGNETIC FIELDS IN CHANNEL WAVEGUIDES

G. F. Zargano, K. V. Vdovenko, G. P. Sinyavskij
 Rostov State University, Physics Department
 Zargano Genadij F. Box 6505, Rostov-on-Don, 344004, Russia.
 E-mail: vkv@jeo.ru , sinyavsky@phys.rnd.runnet.ru

Channel waveguide is one of a group of waveguiding structures proposed 20 or more years ago for use at millimetre wavelength. Many advantages of channel waveguides are becoming increasingly appreciated. There is a great number of mm-wave devices employing channel waveguides. It is clear that an electromagnetic field solver is needed but it is also necessary for electromagnetic field-solver to give the mm-wave design engineer visualisation tools to attack his or her more difficult design problems. Besides providing valuable analytical data, the visualisation capabilities can lead to startling new insight into how millimetre wave components actually behave. Because of complexity of channel waveguides, 3D models of electromagnetic fields in these structures are actually required.

Three-dimensional EM field simulator for H- and E-waves in various channel waveguides with uniform dielectric filling is presented in this paper. The simulator is divided into two parts: the EM field-solver itself is the first part, and the visualisation tool is the second.

The EM field-solver implements a solution of Helmholtz's equation using the method of partial region taking into account singularities of the electromagnetic field at the edge [1,2]. This method is an improved field-matching method because it provides a rapid convergence. In computation of the components of electromagnetic fields and the cut-off wavenumbers we limited ourselves using the third approximation of the method and 50 members of the series of eigenfunctions of partial regions. The error of computation of the cut-off wavenumber was $1 \cdot 10^{-7}$ and maximum discrepancy of the field components on the line of partial region separation was 1.2%.

On the basis of computer modelling and visualisation of electromagnetic fields of any wave types there is the set of differential equations, which describes complex spatial structure of both electric and magnetic field lines and is presented in parametric form. As an independent parameter for modelling the length of electromagnetic field line $L[0, \infty]$ have been used.

$$\begin{cases} \frac{dx}{dL} = F(L)W_x(L) & F(L) = 1/\left(W_x^2 + W_y^2 + W_z^2\right)^{1/2} \\ \frac{dy}{dL} = F(L)W_y(L) \\ \frac{dz}{dL} = F(L)W_z(L) & \vec{W} = \begin{Bmatrix} \vec{H} \\ \vec{E} \end{Bmatrix} \end{cases}$$

The function $F(L)$ is arbitrary finite function, that does not equal zero for the whole range of definition. In realisation of the method of modelling we use vector model. Each point of a spatial structure is represented by a radius-vector, drawn from a centre. Picture of the spatial field structure is created with parallel projection of all vectors, which specify the structure, on an image plane. The set of equations was solved numerically by Runge-Kutt method of the fourth order.

The program for modelling, visualisation, and computation of the EM fields was written using the language C++. A number of pictures of the electromagnetic field of H- and E-waves in channel waveguides were produced. The density of the lines is proportional to field strength and their system reflects the field structure objectively. Some results of calculation and modelling of the electromagnetic field in plane and spatial projection are shown in Figure 1. The first H_{eo} -wave is the dominant mode of opened channel waveguide [Figure 1.a] and the first H_{oe} -wave is the dominant mode of closed channel waveguide [Figure 1.b] ($k_{oe(eo)}$, l is the normalised cut-off wavenumber of $H_{oe(eo)}$ -wave, kl is the wavenumber in free-space). It is clear from electromagnetic field structure of H_{eo} -wave that this mode is to be leaky in opened channel waveguide, but at the same time the H_{eo} -mode can be propagating. The electromagnetic field structure can be compared with the electromagnetic field

structure in ridged waveguide [Figure 1.c]. The ridges and channels distort the structure of the fields of all types of H- and E-waves very much, that is why it is not so simple to predict the EM field structure especially for higher modes.

This visualisation tool has been developed as a universal tool for analysis of different microwave and mm-wave structure and can be used in CAD-systems, because almost for every high frequency application it appears to be necessary to know the field distribution in complex waveguiding structures.

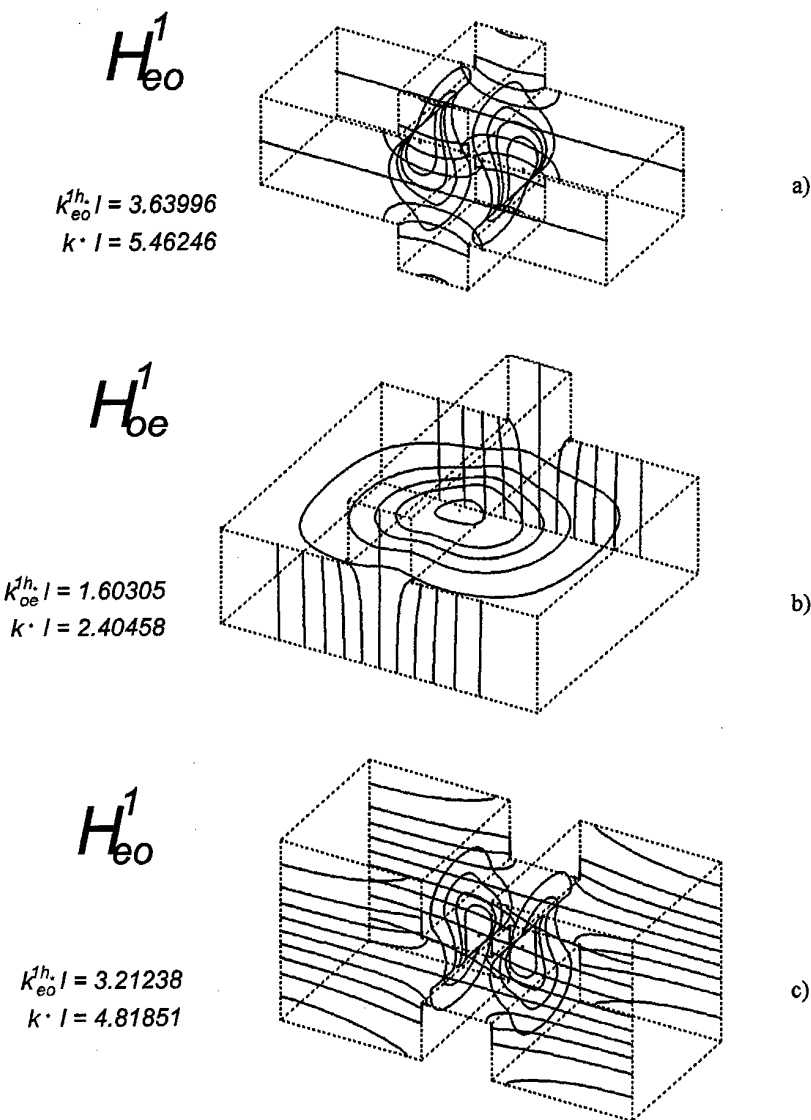


Figure 1. Spatial structures of EM fields in channel waveguide (a), in T-waveguide (b), and in H-waveguide (c).

References

1. G.F.Zargano, V.P.Lyapin, the others, "Waveguides of complex cross sections", Radio i Sviaz, Moscow, 1986.
2. G.F.Zargano, G.P.Sinyavskij, B.P.Tkachenko , "Research of the structure of the electromagnetic fields in ridged waveguides," Izv. VYZ, Radiofizika, V.30, 11, 1350-1357, 1987.

ANALYSIS OF LINE CURRENT WAVE DIFFRACTION FROM METAL-BACKED DIELECTRIC STRIP BY EXTENDED PO METHOD

Andrey S. Andrenko and Makoto Ando
 Dept. of Electrical and Electronic Engineering
 Tokyo Institute of Technology
 2-12-1 O-okayama, Meguro-ku, Tokyo 152-8552, Japan
 Tel: 81-3-5734-2563, Fax: 81-3-5734-2901, E-mail: andrey@antenna.pe.titech.ac.jp

1. Introduction

The modeling of wave scattering by compound metal-dielectric obstacles is both theoretically interesting and practically important for pattern analysis and radar scattering. Planar and curved metal-backed dielectric surfaces have been considered for modeling composite and radar absorbing materials developing the concept of approximate boundary conditions [1]. However, in the analysis of scattering by finite coated perfectly conducting strips there still exist some difficulties in the efficient implementation of the numerical solutions. Because of the complexity of scattering process, the method of moments and other numerical techniques become computationally intensive and often unsuitable especially to electrically large coated surfaces. This paper presents the Physical Optics (PO) analysis to effectively solve the problems of line current wave scattering from finite planar metal-backed dielectric strips.

As is well-known, classical PO method was formulated for calculating the field scattered by perfectly conducting surfaces and proved to be widely used in reflector antenna design. This work is a further development of the numerical PO approach to analyze the 2-dimensional wave diffraction from planar strips coated with a homogeneous dielectric layer. At first, we define the equivalent PO currents on the illuminated dielectric interface in terms of the reflection coefficients of an infinite grounded slab which have been derived for both E- and H-polarized scattering under the plane wave incidence. The reflection coefficients depend on slab's thickness and permittivity so that the present analysis allows a quantification of the effect of a coatings on the scattering properties of the strips. Next, to calculate the scattered field we integrate the derived equivalent PO currents over the actual width of coated strip along the dielectric interface. It is shown that the presence of a coatings not only affects the amplitude levels, as compared with that of perfectly conducting strips, but due to multiple reflection shifts the scattering lobes orientation. Numerical results have been obtained for different thickness and wide range of the scatterer's width, dielectric permittivities, and the line current positions demonstrating that one can substantially change the scattering properties of a coated strip by varying its geometrical and material parameters. To check the accuracy of proposed approach and the limits of its applicability, we have compared the numerical results with the measurement data for vertical electric dipole wave scattering by grounded dielectric disk. It is confirmed that good agreement is observed within a wide range of parameters but there exists a critical minimum source's distance to the scattering surface, of the order of one wavelength, when the accuracy of PO calculation degrades since the reflection coefficients are derived assuming locally plane wave incidence.

2. Formulation and PO Analysis

Consider a line current wave scattering by planar perfectly conducting strip coated with a homogeneous dielectric layer of the same width as depicted in Fig.1. The cases of both electric and magnetic line current wave incidence corresponding to E- and H-polarization have been analyzed. Denoting as U' the total field E_z -component for electric line current wave scattering or H_z -component for magnetic line current, we have

$$U' = U^i + U^{sc}, \quad (1)$$

where direct incident cylindrical wave field U^i is given by zero-order Hankel function of the first kind while the field scattered by a coated strip can be calculated by introducing the equivalent PO currents on the dielectric interface $\bar{I} = (1-R)\hat{n} \times \bar{H}^i$ and $\bar{M} = (1+R)\bar{E}^i \times \hat{n}$, where R is the exact reflection coefficient of an infinite grounded dielectric slab under the plane wave incidence, and integrating them over the strip's actual width. Satisfying boundary conditions on the dielectric-air interface and the perfectly conducting plane, the reflection coefficient is obtained as

$$R = \frac{R_1 \exp(j\beta) - \exp(-j\beta)}{\exp(j\beta) - R_1 \exp(-j\beta)}, \quad (2)$$

where $\beta = kw(\epsilon_{r1} - \sin^2 \theta_i)^{1/2}$, $R_1 = (Z_1 - 1)/(Z_1 + 1)$, and the parameter Z_1 is given by

$$Z_1 = \frac{\cos \theta_i}{(\epsilon_{r1} - \sin^2 \theta_i)^{1/2}}, \quad (3)$$

for the case of E-polarized plane wave scattering and

$$Z_1 = \frac{(\epsilon_{r1} - \sin^2 \theta_i)^{1/2}}{\epsilon_{r1} \cos \theta_i}, \quad (4)$$

for the case of H-polarized plane wave scattering where θ_i denotes the angle of incidence with respect to y -axis. Taking into account the latter assumption of plane wave incidence, in practical calculations the line source should be at least a wavelength away from the dielectric surface. Nevertheless, the reflection coefficients are the functions of the permittivity and thickness of the dielectric slab that provides a quantification of the effect of a coatings on the scattering properties of the strips within the framework of PO approximation.

Next, we present, for the sake of brevity, the scattered field expressions corresponding only to the electric line current wave scattering by a coated strip as follows [2]

$$E_z^{sc} = j\omega(\mu A_z - \epsilon B_\phi), \quad (5)$$

$$A_z = -\frac{j}{4} \int_L I_z H_0^{(2)}(kp') dl, \quad (6)$$

$$B_\phi = -\frac{j}{4} \int_L M_\phi H_0^{(2)*}(kp') dl, \quad (7)$$

where p' is the distance from integration point to an observer and the components of equivalent currents involving the reflection coefficient of grounded slab are defined as

$$I_z = |(1 - R)\hat{n} \times H_\phi \hat{\phi}|, \quad (8)$$

$$M_\phi = |(1 + R)E_z^i \hat{z} \times \hat{n}| \quad (9)$$

3. Numerical Results

The scattering properties of coated strips have been numerically studied by calculating the total far-field pattern functions $20 \log[(\Psi_z^i(\phi) + \Psi_z^{sc}(\phi)) / \Psi_z^i(\phi)]$ for various distances of a line current to the scatterer and variety of material and geometrical parameters of the coatings. The obtained results are compared with those calculated by conventional PO for the wave scattering by perfectly conducting strips of the same width. Fig.2 presents the pattern functions for the electric current source located on y -axis two wavelengths from wide planar strip. It is seen that the presence of coating essentially changes the main lobe shape though the position of pattern's null points remains the same. The corresponding results for alternative H-polarized cylindrical wave scattering are shown for comparison in Fig.3. In this case, the pattern's shape is less affected by dielectric coating but the lobes are shifted. Figs.4 and 5 demonstrate the total far-fields for the wave scattering by the same coated planar reflectors but when the line currents are placed far away from the scatterer. As before, there is a difference of scattering properties of planar coated reflectors for E- and H- polarization though the effects of coatings are observed only within the GO zone, since in the case of distant source the incident cylindrical wave front becomes quasi-planar at the scattering surface.

It is also been shown that thicker coatings have a stronger effect on the pattern forming due to multiple reflection within the dielectric layer. Such a numerical results will be presented in the symposium.

4. Conclusions

We have presented the modified PO analysis of wave scattering by planar coated reflectors. The effects of dielectric coatings on the reflecting properties of planar strips are analyzed in the detail including the differences of pattern shape and null points' shift in the cases of E- and H-polarized scattering. It is shown that changing the dielectric permittivity and thickness of a coating may result in substantial pattern shape transformation for the same width of a reflector aperture.

The robustness of proposed approach can also be used for studying the scattering properties of thin multi-layered and varying thickness coatings by applying the corresponding expressions for the reflection coefficient.

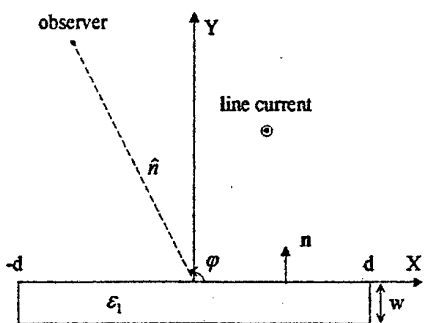


Fig. 1. Geometry of line current wave scattering by metal-backed dielectric strip

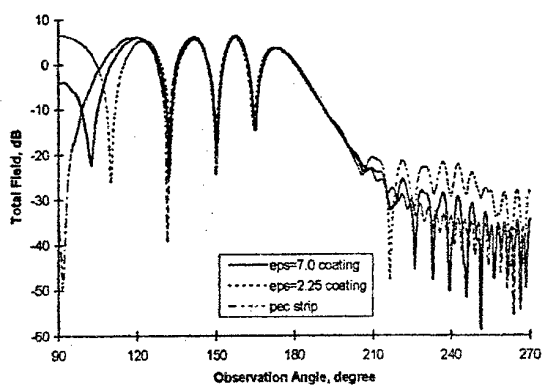


Fig. 2. Total field for electric line source 2λ from wide coated strip, $2d = 24\lambda$, $w = 0.8\lambda$

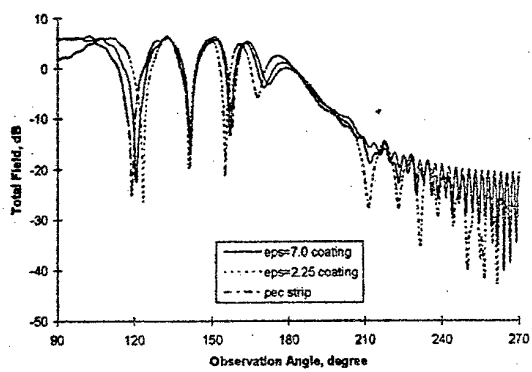


Fig. 3. The same as in Fig. 2 but for magnetic line source

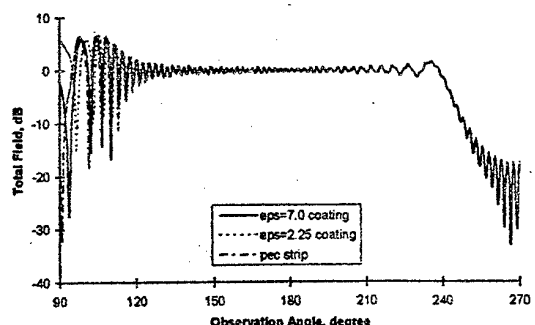


Fig. 4. Total field for electric line source 25λ from wide coated strip, $2d = 24\lambda$, $w = 0.8\lambda$

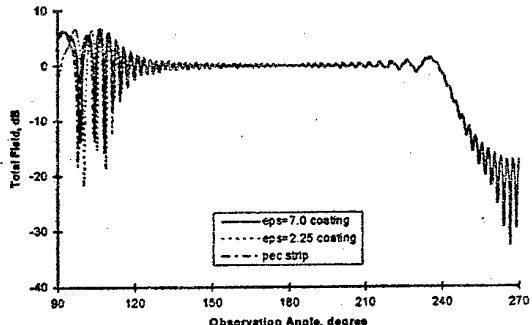


Fig. 5. The same as in Fig. 4 but for magnetic line source

References

1. T.B.A.Senior, J.L.Volakis, "Approximate Boundary Conditions In Electromagnetics", IEE Press, London, 1995.
2. M.Ando, "Physical Optics", in Analysis Methods For Electromagnetic Wave Problems, vol.2, Artech House, London, 1996.

THE EFFECTIVE MATHEMATICAL MODEL of a MICROSTRIP FREQUENCY SELECTIVE SURFACES

A.O. Kasyanov, V.A. Obukhovets
 Taganrog State University of Radio Engineering
 44 Nekrasovsky street, GSP-17A, Taganrog, Russia, 347928,
 Phone (86344) 61883. E-mail: decan@vao.rnd.su

THE PURPOSE of this work is the numerical analysis of frequency selective structures (FSS) scattering characteristics. We investigated electromagnetic structures, which look like arrays of metal patches or slots in the perforated screen. Besides the arrays with dielectric slabs as covers, and also as a cascading connection of arrays and dielectric slabs are investigated.

THE MATHEMATICAL MODEL. The mathematical model foundation for the microstrip electromagnetic structures under consideration is made in accordance with the concept of infinite periodic array. Such approach is reasonable because of consideration the multielement arrays with rather complicated element structure. An alternate way of modelling may be based on the basis of so called "element by element method" with taking into account mutual coupling between array elements. This way may become much more difficult because of necessity to solve large size system of integral equations.

The boundary problem is formulated as follows. Flat periodic element arrangement array consists of ideal conducting, infinitely thin microstrip elements of arbitrary shape, located in the unit cell of rectangular grid. From the direction determined by wave vector \vec{k}_0 , the plane electromagnetic wave of linear polarization incidents onto the array. It is denoted $k_0 = 2\pi / \lambda_0$, λ_0 - wavelength. It is necessary to determine the current distribution on the radiators of array, scattering frequency and angular characteristic of the array.

The problem under such consideration describes the arrays in free space. However in practice there are used arrays with elements placed on the dielectric substrates which change the scattering parameters of such arrays greatly. One of such problem solving methods is the research scattering parameters separately for array in free space and separately for dielectric slab scattering problem. The result is achieved by subsequent analysis of all structure on the basis of parameters of generalized scattering matrix, received for each case [1]. In this paper such approach is applied for analysis of microstrip arrays and perforated screens, reinforced by dielectrics. Such kind constructions are used for developing of rigid antenna radomes, as well as transfer type depolarizers of multireflector antennas. Coming back to statement of boundary problem, it's necessary to note, that there exists another approach to description of microstrip arrays with layers of dielectric. The main feature of this approach is the use of Green's function for dielectric layer. In this paper the approach is applied for analysis microstrip antenna and diffraction arrays. In antennas area such designs are used for conformal antennas, as well as reflector type depolarizers for multireflector antennas.

So, with reference to analysis of microstrip antenna arrays and microstrip diffraction arrays, in statement boundary problem the dielectric substrate of thickness d is considered. The permittivity of substrate is ϵ . The substrate represents the flat layer, on obverse surface of which (plane $z = 0$) there are printed the array elements. For shadow substrate surface (plane $z = -d$) adjoins the metal screen, serving as a reflector.

The delivered problem was solved by integral equation method. The equation is made on the basis of Lorentz's lemma in integral form. The application of periodicity condition has allowed to reduce the solution to search of currents within the limits of one Floquet channel. The integral equation solution is produced by moment method. The array aperture magnetic current surface density is approximated by set of subsectional current functions. In this case the rooftop functions are useful.

NUNERICAL EVALUATION of surface currents and reflection coefficients. This report section presents some numerical results, which show the application of described method to account of FSS scattering parameters. Let us consider the problem for conducting screen perforated by array of cross apertures. The perforations are located in units of square grid. The parameters of screen are: $d_1 = d_2 = 10 \text{ mm}$ - steps of array; $a = b = 7 \text{ mm}$

- slot length; $s_1 = s_2 = 1,4 \text{ mm}$ - slot width. The array is illuminated by normally incident plane wave polarized along unit vector \vec{i}_x . The frequency characteristics of this perforated screen, for the first time adduced in [2], was discussed early in [3]. It was shown, that while $k_0 = 4,15 \text{ sm}^{-1}$ the total passing through described FSS is observed. For the practice application the FSS should be reinforced by dielectrics. The reflection factor module frequency dependences for described perforated screen are shown in fig. 1. The array places in the middle of the layer. The curves,

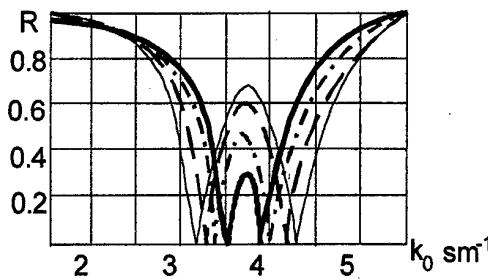


Fig. 1

accompanied by increasing of the interval between frequencies of total passing for perforated screen, reinforced by substrates.

Let's consider now the screen punched by slots, having the form of a Maltese cross. The apertures are arranged as a periodic grids. There are investigations of arrays having various unit cell shape. In this work the numerical results for arrays with square and triangular unit cells are discussed. The unit cells of slot array are represented on insertions of a fig. 2. They are quadrates,

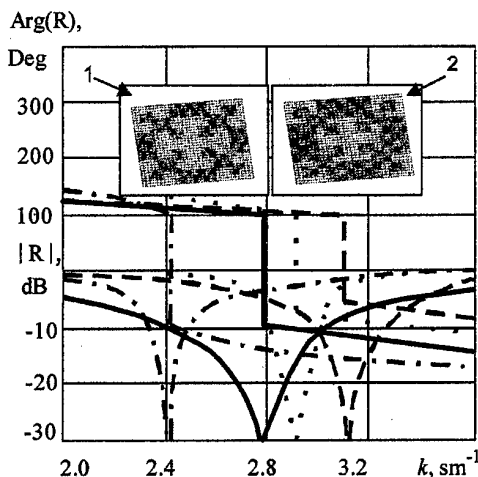


Fig. 2

screen. Let δf_{-20} is parameter, which is determined by expression $\delta f_{-20} = (\Delta f / f_0)_{-20}$, where Δf is bandwidth, in which reflection factor is reduced below than level -20 dB, f_0 is resonant frequency. The construction 1 in case of triangular grid has the greatest value $\delta f_{-20} = 7,1\%$. The least value $\delta f_{-20} = 2,1\%$ is observed for the same construction, but in case of a rectangular grid. Such kind of frequency selective arrays can be used in a number of construction of multifrequency reflector antennas. In this case flat microstrip frequency selective surface

shown in fig. 1, correspond to different layer relative permittivity ϵ . The layer thickness h is equal to $h_0 = 1,87 \text{ mm}$. The curve, represented by thick solid line, corresponds $\epsilon = 2$, dotted curve meets $\epsilon = 3$, point-dotted curve corresponds $\epsilon = 4$ and, at last, thin solid continuous curve shows the frequency characteristic, appropriate $\epsilon = 5$. It is shown, that perforated screen with dielectric layer has already not one, but two resonance frequencies (total transmission). The dependence $R(f)$ has the maximum at frequency f_0 , which value grows with growth ϵ of layer. Besides the growth ϵ is

In a fig. 2 the dependences, obtained for 4 various arrays are represented for normal incidence of an excited plane wave. These electromagnetic waves are linearly polarized along the edges of quadrates, which are represented on insertions 1 and 2. Scattering computations for a construction 1 are displayed by a solid and a prime-dashed curves in a fig. 2. The relationships for a construction 2 are shown by a dotted lines and points in a fig. 2. If the crosslike apertures in centers of the unit cells (insertions 1 and 2 of a fig. 2) are «metallized» scattering parameters computations are represented by a prime-dashed lines and curves, which are shown by points. These cases correspond to square grids. If the central apertures present, then scattering computations are represented by solid and dotted curves. These cases correspond to triangular grids. It is shown, that the resonance for the arrays, which have triangular grids, is observed at higher frequencies, than in cases of square grids. We define, that the resonance is the phenomenon, when electromagnetic wave pass through a perforated

allows to build the reflector antenna, which has multiple feeds.

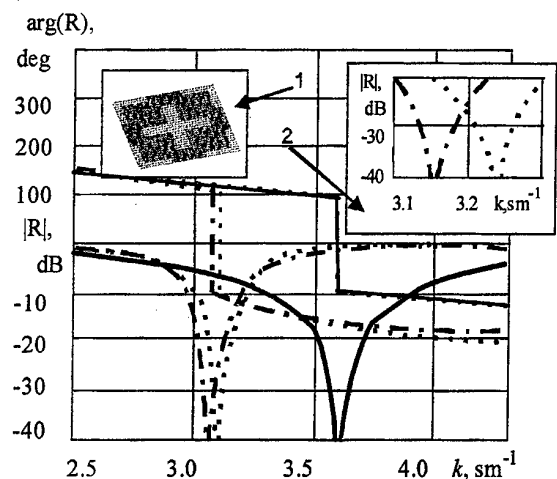


Fig. 3

characteristics control each crosslike aperture is supplied with $p-i-n$ diodes. The effective control of a scattering field is achieved in the case, when the diodes are included in the array scheme, which is shown in [3]. Thus if the $p-i-n$ diodes are open, then the array ceases to be transparent for single space mode. In this case the diodes can control the reflection wave polarization. If the $p-i-n$ diodes are included in slot, which is oriented along x axes, then electromagnetic wave should be polarized along axes y . It happens because of such polarized wave induces the greatest field in a slot containing diodes. Including diodes in a slot oriented in y direction, it is possible similarly to act on a x -polarized wave. If bias voltage is adjusted so that diodes are open in one crosslike slot and are closed in the others, thus the scattered field will be varied. In fig. 3 the graphs of the reflection factor module and phase frequency dependences are shown. The construction which unit cell is represented in insertion 1 of a fig. 3 is investigated. The crosslike slot radiators, which are located in centers of unit cells, contain diodes. Therefore these apertures can be at two electromagnetic conditions. If the diodes are open, they shunt a slot radiators. The graphs, which correspond to this condition, are represented by prime - dashed curves. When the diodes are closed those dependences are shown by solid curves. Besides the frequency characteristics of an array, which has the triangular unit cell, are shown in fig. 3. These results are plotted by points. It is shown, that a prime - dashed curves and the curves represented by points, differ rather unsignificantly. The difference is exhibited in a neighbourhood of resonance frequency. It is shown on insertion 2 of a fig. 3. Therefore, it appears possible to control the «arrangement» of slot radiators by means of diodes bias adjusting. In particular, it is possible to «convert» electronically an array with a triangular unit cell into a similar array with a square grid.

The received results can be used for choosing the most of rational FSS geometry variant at decision of particular problems by antennas engineering.

References

1. V.A.Kaplin, V.I.Fedin, S.M.Zakharov, «Electromagnetic waves diffraction on the perforated screen in the dielectrical slab» (in Russian) // Radioelectronika (Izvestiya Vysshikh uchebnykh zavedenii USSR).-1987.-N.2., pp.54-59.
2. B.J.Rubin, H.L.Bertoni, «Reflection from a periodically perforated plane using a subsectional current approximation» // IEEE Trans. Antennas and Propag., 1983.- Vol. AP-31, N 6, pp.829-836.
3. A.O.Kasyanov, V.A.Obukhovets, «Current control in a microstrip array with loaded elements» (in Russian) // Radiotekhnika 1995, N.12, pp.32-36.

The controllable electromagnetic structures may have additional advantages. Let's consider a microstrip diffraction array, which has the system of controlled loads [3]. In mathematical model loads can simulate such controlled elements as for example $p-i-n$ - diodes. When the computer accounts are performed, then the impedance strips are used for diodes description. The impedance values of these strips are known for open or closed diodes. In an outcome of a numerical researches it was established, that by means of tuned loads it is possible to control the scattering characteristics of a microstrip diffraction arrays.

In conclusion let's consider a screen punched by the controllable apertures. The unit cell of such screen is represented on insertion 1 of a fig. 3. The sizes of an array unit cell correspond to sizes of constructions 1 and 2 (insertion of fig. 2). With the purpose of an array scattering

ATOMIC FUNCTIONS AND WAVELET MATRIX TRANSFORM APPROACH FOR EFFICIENT SOLUTION OF ELECTROMAGNETIC INTEGRAL EQUATIONS IN THE BOUNDARY VALUE PROBLEMS OF MILLIMETER WAVE DIFFRACTION

Victor F. Kravchenko and Alexander A. Zamyatin

Institute of Radio Engineering and Electronics, Russian Academy of Sciences, ul.Mokhovaya 11, Moscow,
Center, GSP – 3, 103907 Russia.

Department of General and Applied Physics, Nonlinear Physics Laboratory, Moscow Institute of Physics and
Technology, Institutskii Pereulok 9, Dolgoprudnyi, Moscow Region, 141700 Russia.

Phone: +7(095) 9214837, 4086772, Fax: +7(095) 9259241.

E-mail: kvf@mx.rphys.mipt.ru, postmaster@nonlin.mipt.ru, zaoiprzh@glasnet.ru, alzam@aha.ru

Using Atomic Functions (AF) [1-3] and wavelet matrix transform produces highly sparse matrices, which can be solved efficiently. It has been found that using wavelet matrix transform, based on atomic function, one can obtain higher compression rate and better accuracy of approximate solutions than using spline wavelet transform and Daubechies' orthonormal wavelet transform [4]. A numerical example has been developed for the boundary value problems of millimeter wave diffraction on a perfectly conducting circular cylinder to show the validity and effectiveness of the method.

Currently AF are a topic of considerable interest in applied mathematics. Recently, AF have been used in signal processing and computer vision with great success. Those functions are the finite solutions to functional

different equations containing a linear argument transformation of the form $\hat{L}\varphi(x) = \sum_{k=1}^m c_k \varphi(ax - b_k)$, $|a| > 1$,

in which $\hat{L} = \sum_{k=0}^N A_k \frac{d^k}{dx^k}$ is a linear differential operator having constant coefficients. AF are used on the one hand because the operations with them are relatively simple (there are explicit formulas for the values of the moments, derivatives and Fourier transform, etc.), while on the other hand they have good approximating behavior, which is sometimes the best. These features are closely related to the scope for representing an algebraic polynomial as a linear combination of such functions. The functions have an advantage over polynomials in that they are locals (it is possible to truncate the approximating series near some point without altering it far from that point). AF are used in constructing Kalman-type filters, because they possess unique spatial-frequency features: finiteness in ordinary space and exponential localization in Fourier space.

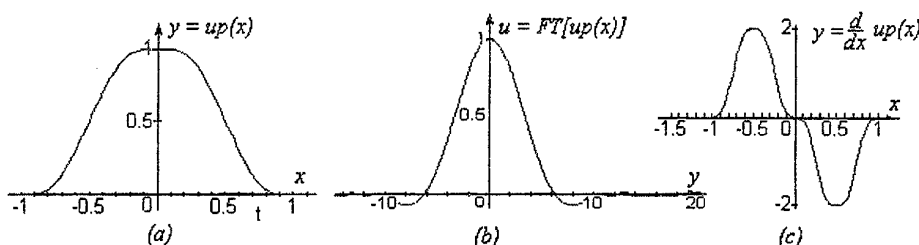


Figure 1. Based Atomic function $up(x)$ (a), its Fourier transform (b), and its derivative (c).

In this paper, we consider a new method of solving integral equations in the boundary value problems of millimeter waves diffraction by means of AF. In electromagnetics (EM) AF have been applied to the method of moments as basis and testing functions in the solving integral equations in the boundary value problems of millimeter waves diffraction.

Let us consider the scalar problem of computing the current J_z on the perfectly conducted Z-directed cylinder exited by a plane TM_z (transverse-magnetic to z -axis) wave. In order to solve this scattering problem, we resort to the E -field integral equation formulation. Using the well-known Method of Moments (MoM), the unknown current can be expanded in terms of N conventional pulse basis function. We have

$$J_z = \sum_{n=1}^N I_n P_n, \quad (1)$$

where P_n denotes the pulse function centered about the n th source point on the cylinder perimeter and I_n is an unknown coefficient. Applying the integral equation at each testing point on the cylinder perimeter, we derived

$$Z\vec{I} = \vec{V}, \quad (2)$$

where Z is the impedance matrix ($N \times N$), \vec{I} is the unknown current vector, and \vec{V} is the excitation vector. For large EM problems, the direct solution of (2) is at formidable cost $O(N^3)$ and often impossible to be realized even on supercomputers. To transform the pulse basis function into wavelet basis functions, we introduce an $N \times N$ transformation matrix W , which is assumed to be real and unitary. Carrying out the wavelet matrix transform (WMT), one can obtain

$$Z\vec{I}' = \vec{V}', \quad (3)$$

where $Z' = W Z W^T$, $\vec{I}' = (W^T)^{-1} \vec{I}$ and $\vec{V}' = W \vec{V}$. For a given threshold value, (3) becomes a sparse matrix equation which can be efficiently solved by a sparse solver. In wavelet bases current can be expressed as

$$J_z = \sum_{n=1}^N I'_n W_n, \quad (4)$$

where $\{W_n\}$, $n = 1..N$ denotes the wavelet functions. The result of wavelet matrix transform is shown in Figure 2.

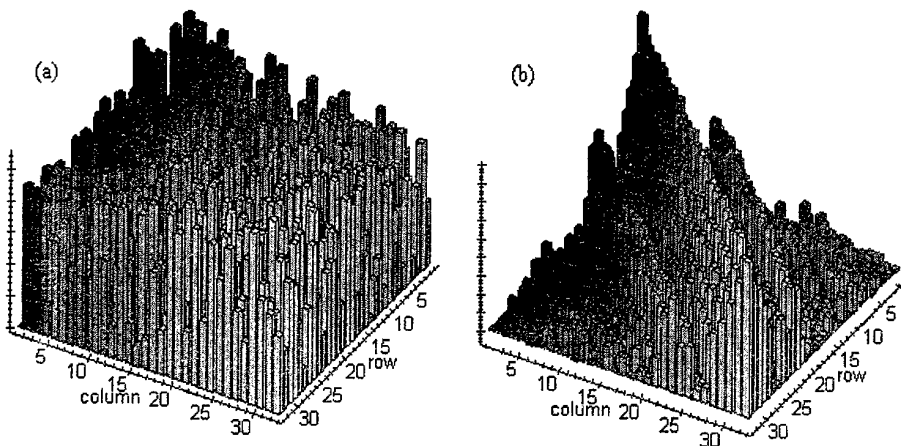


Figure 2. Magnitudes of the elements of random matrix before (a) and after (b) wavelet matrix transform using atomic functions with $N = 32$.

Now, we consider the algorithm for efficient wavelet matrix construction using AF. Wavelet function $\psi(x)$ are determined by

$$\psi(x) = \sum_{n=-m}^m 2(m-n)up(mx+n), \quad (5)$$

where m is defined by $m = M/2 + 1$, where M is the number of vanishing moments. The wavelet matrix is composed of translations and dilations coefficients of a single mother wavelet.

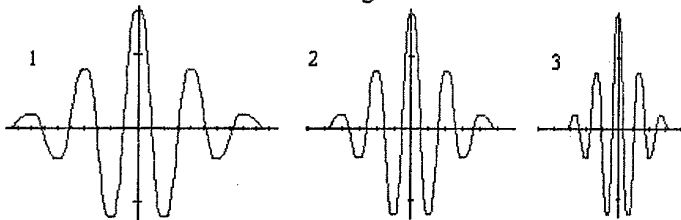


Figure 3. Sample basis vectors. Curves 1-3 show the rows 12, 48, and 96 of the wavelets, respectively ($M = 8$).

Translations of the lowest resolution wavelet comprise one half of the basis set; translations of the next better resolution wavelet make up one quarter of the set, and so on down the hierarchy to the finest resolution. Note that wavelets based on Atomic functions (**WAF**) are symmetrical, which is important to obtain a higher compression rate for EM problems. More details of the **WAF** basis matrix are shown in Figure 3.

Representative computations are given to show the validity of the proposed compression method and to demonstrate its merits. The first problem analyzed is that of TM_z plane wave scattering by a perfectly conducting circular cylinder with radius equal to the wavelength. The circular perimeter has been divided into N equally spaced pulses, which were, in turn, transformed into a wavelet basis using **AF**.

We will further illustrate some of the computational profits of the new method. In our case, a total of 128 pulse basis functions were originally used to expand the unknown current and the boundary condition was imposed in at least-square error sense at 128 testing points. Thus, if one had pursued the solution using a standard method of moments approach, the size of the resultant impedance matrix would have been 128×128 , which is a matrix comprising 16384 complex entries. If, instead of the pulse functions, symmetrical wavelets based on **AF** are used to expand the unknown current, the resulting matrix will also comprise 16384 entries, but the matrix will be more localized and a thresholding procedure can render the matrix sparse and without greatly degrading solution accuracy. Thus, applying a thresholding while allowing an average error level of $\varepsilon = 0.001\% (10^{-5})$ resulted in about 30% zero elements, which implies a good sparseness level.

By a selected threshold τ , the elements of Z' whose magnitudes are smaller than τ are set to zeroes, resulting in a sparse matrix equation. M stands for the largest magnitude of elements of the matrix Z' . R is defined as the ratio of the number of the remaining elements to the total number of elements. Results show that for the same threshold the **WAF** transform gives a higher compression rate than the nonsimilarity nonorthonormal cardinal spline wavelet (NS-NCSW) transform, and much higher than Daubechies' orthonormal wavelet (DOW) transform.

It should be emphasized that, unlike the wavelet expansion method, **WAF** transform can avoid a great number of wavelet integral computations by the wavelet matrix transform method, which can be easily realized by the proposed wavelet matrix construction method (5). The larger the size of EM problem, the more effective the wavelet matrix transform method.

To show the effectiveness of the proposed approach, we use two more practical examples. The first represents N infinitely long thin cylinders, placed parallel to the z axis, with the radius of the cylinder $r = 0.05\lambda$ and the array spacing $s = 1.0\lambda$. The second is the six-element Yagi-Uda antenna. We discretize the feeder and all the directors by n equal intervals and the reflector by n_0 equal intervals. If $n = 21$ and $n_0 = 23$, we obtain a moment matrix of order 128 ($128 = 21 \times 5 + 1 \times 23$). Comparisons with DOW and NS-NCSW transforms are given to show the validity and effectiveness of the method.

References

1. V.A.Rvachev, "Compactly Supported Solutions of Functional Differential Equations and Their Applications", *Uspekhi Mat. Nauk*, Vol.45, No.1, pp.77-103, 1990.
2. V.F.Kravchenko and V.A.Rvachev, "Application Atomic Functions for Solution Boundary Value Problems in Mathematical Physics", *Foreign Radioelectronics. Achievements in Modern Radioelectronics*, No. 8, pp. 6-22, 1996.
3. V.F.Kravchenko, "Approximation Diagram of Direction and Synthesis of Linear Radiator Based on Atomic Functions", *Foreign Radioelectronics. Achievements in Modern Radioelectronics*, No.8, pp. 23-28, 1996.
4. Ingrid Daubechies, "Orthonormal Bases of Compactly Supported Wavelets", *Communications on Pure and Applied Mathematics*, Vol. XLI, No.7, pp.909-996, October 1988.

OPTIMIZATION OF THE PROFILE OF THE ELECTRODYNAMIC SYSTEM OF A POWERFUL GYRO-TRAVELING-WAVE-TUBE (GYRO-TWT)

V.F.Kravchenko, A.A.Kuraev*, and S.V.Kolosov*.

Institute of Radio Engineering and Electronics, Russian Academy of Sciences, ul.Mokhovaya 11, Moscow,
Center, GSP - 3, 103907 Russia.

Department of General and Applied Physics, Nonlinear Physics Laboratory, Moscow Institute of Physics and
Technology, Institutskii Pereulok 9, Dolgoprudnyi, Moscow Region, 141700 Russia.

Phone: +7(095) 9214837, 4086772, 9024737(home), Fax:+7(095) 9259241.

E-mail: kvf@mx.rphys.mipt.ru, postmaster@nonlin.mipt.ru , zaoiprzh@glasnet.ru

*Belarus State University of Informatics and Radioelectronics, P.Brovka st. 6, Minsk,
220600 Republic of Belarus.

Phone: (375 -17) 239-84-98, 239-98-56, Fax:(375-17) 231-09-14.

E-mail:VMiPMail@gw.bsuir.unibel.by, kurayev@micro.rei.minsk.by

The three-dimensional self-consistent mathematical model of a relativistic Gyro-TWT with an irregular electrodynamic system (EDS) was described in [1,2].

The problem of the efficiency optimization of Gyro-TWTs over the frequency band was formulated by means of the following criterion function:

$$J_{np} = (1 - \bar{\eta})(1 + \sigma/G_1) + \frac{G_2}{M} \sum_{k=1}^{\tilde{M}} |\dot{\Gamma}_{2np}^{(M_k)}|, \quad (1)$$

where $\bar{\eta} = \frac{1}{\tilde{M}} \sum_{k=1}^{\tilde{M}} \eta_W^{(M_k)}$, \tilde{M} is the number of reference points over the frequency band, and

$\sigma = \sqrt{\frac{1}{\tilde{M}-1} \sum_{k=1}^{\tilde{M}} (\eta_W^{(M_k)} - \bar{\eta})^2}$ is the mean quadratic spread of wave efficiency $\eta_W^{(M_k)}$ by reference frequencies.

The following parameters were taken as prescribed: $\beta_0 = v_0/c = 0.476$, $S = \eta_0 I_0 / 2\pi^2 \epsilon_0 c^3 = 7 \cdot 10^{-4}$, $q = \beta_\perp/\beta_\parallel = 1.5$.

The optimized waveguide profile $g(z)$ and the magnetostatic field distribution $F(z)$ were represented by the following multi-parameter functions:

$$\left. \begin{aligned} g(z) &= g_0 + \sum_{i=1}^{n_g} A_{gi} up\left(\frac{T - T_{gi}}{\rho_{gi}}\right), \\ F(z) &= F_0 + \sum_{i=1}^{n_F} A_{Fi} up\left(\frac{T - T_{Fi}}{\rho_{Fi}}\right), \\ T &= z/z_0. \end{aligned} \right\} \quad (2)$$

The atomic function $up(z)$ is defined as a finite solution to the equations [3-5]

$$up'(z) = 2up(2z+1) - 2up(2z-1).$$

When optimizing gyro-TWT over the frequency band, the following three reference frequencies were used: $M_1 = \omega_1/\omega_0 = 1.025$, $M_2 = 1.0$, $M_3 = 0.975$. The current parameter end normalized source power was given: $r_0^0 = r_0 \omega_0/c = 0.7854$, $K_{in} = P_{in}/I_0 V_0 = 0.0143$.

For regular gyro-TWT, optimization of g_0 , F_0 , z_0 gave the following results: $g_0 = 1.0866$, $F_0 = 1.0066$, $z_0 = 50.2$, $\eta_1 = \eta(M_1) = 0.4$, $\eta_2 = 0.36$, $\eta_3 = 0.25$. The frequency characteristic of this variant is given in Fig.1 (curve 1).

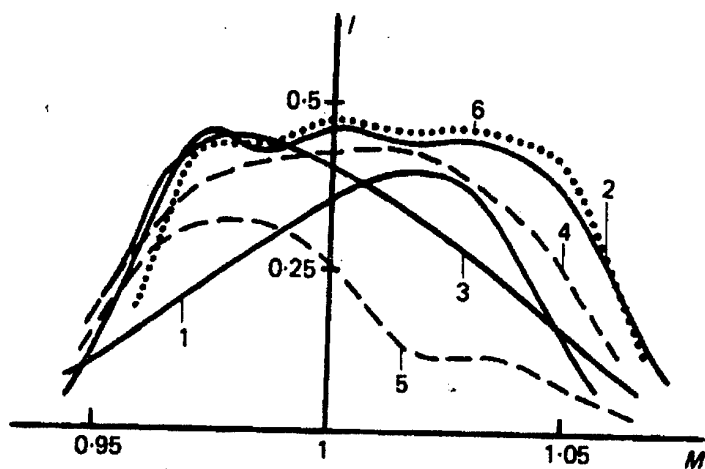


Figure 1. Frequency characteristics of gyro-TWT with operating H_{11} mode.

The optimization of the waveguide system profile $g(z)$ and of the magnetostatic field distribution $F(z)$ at $n=2$ in formula (2) has resulted in the following: $\eta_1=0.45$, $\eta_2=0.446$, $\eta_3=0.44$. The optimum distributions obtained, $g^{\text{opt}}(z)$ and $F^{\text{opt}}(z)$, are shown in Fig.2. Qualitatively, they are similar to those earlier obtained for a gyrotwistron wide band catcher [2]: the magnetostatic field increases initially, thus providing an optimum bunching regime, and then decreases, thereby promoting the displacement of electron phase bunch into the decelerating phase and, subsequently, the generation of a regime close to the isophase one. However, the waveguide profile $g^{\text{opt}}(z)$ corresponds to a low-quality resonator narrowing towards the end of the interaction region, which provides for an increase of the coupling impedance, improving the energy exchange between the bunched electron beam and the operating mode.

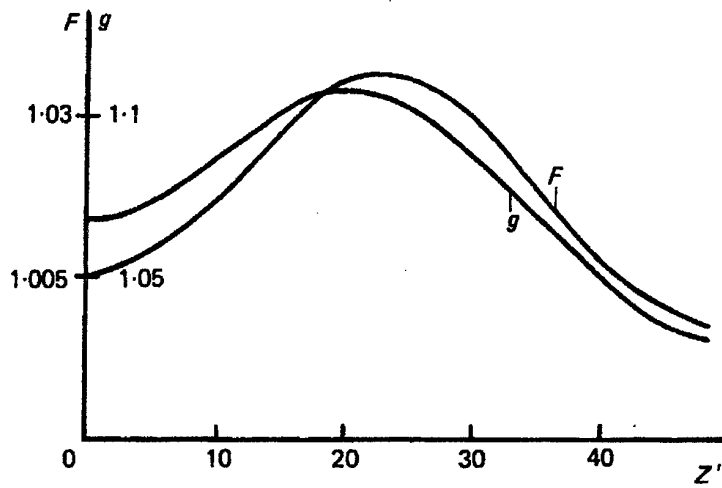


Figure 2. Optimum longitudinal distribution of the waveguide profile $g(z)$ and magnetostatic field $F(z)$ for the operating H_{11} mode at $K_m=0.0143$.

The frequency characteristic of this variant is found in Fig.1 (curve 2). The amplification band over the level of 0.5 from the maximum η_w amounts to 10.5% and is characterized by greater uniformity as compared to the case of a regular gyro-TWT (curve 1).

Figure 1 also shows the frequency characteristic graph of optimized gyro-TWT for $K_{in}=0.028$ (curve 3). This dependence shows, that, while the input power decreases, the amplification band of the gyro-TWT narrows, and the output maximum shifts into the lower frequency region. The dynamic deformation of the amplification band (the shifting of optimum η_w into low-frequency region, when the power input decreases) is accounted for by a strong frequency response of the coupling impedance in the vicinity of the cut-off frequency; at the optimum input level, the band equalization occurs at the expense of the low-frequency rebunching.

Considering the electron velocity angle spread in the flow, the parameter $q_s = \beta_{\perp s}/\beta_{\parallel s}$ for the s -th component of the beam was prescribed as follows:

$$q_s = q_0 \left(1 + \Delta q \left(\frac{N_s + 1}{2} - s \right) \right) / (N_s - 1), \quad s = \overline{1, N_s}. \quad (3)$$

Calculating $\eta_w^{(M)}$, the flow component distribution with q_s different in currents, was introduced with coefficients GG=(0.1, 0.24, 0.32, 0.24, 0.1) for $N_s=5$.

At $\Delta q=0.15$, the maximum efficiency decreases insignificantly: from 0.46 to 0.43 (Fig.1, curve 4). At $\Delta q=0.4$ this decrease is already substantial: down to 0.32, the maximum $\eta_w^{(M)}$ being displaced into the low-frequency region (Fig.1, curve 5).

Figure 1 (curve 6) illustrates the optimum variant frequency characteristic calculated without taking into account the angle spread and space charges. It demonstrates that the space charge reduces the efficiency by 2-3%. This is due to the specific features of the space-charge forces' formation in the case of an asymmetric operating H_{11} mode: the isophase electron tube, unlike the H_{01} mode, is not coaxial with the screen (waveguide wall), and, as a result, its field becomes partially compensated.

The application of atomic functions in approximation of the waveguide profile $g(z)$ and the magnetostatic field distribution $F(z)$ (1) makes it possible to predict new effective mechanisms of interaction in a gyro-TWT with an irregular electrodynamic systems and inhomogeneous magnetostatic fields.

References

1. A.A.Kuraev., "Excitation of longitudinal-irregular waveguides with circular cross section", Izv. Akad. Nauk, BSSR, seriya fiz.-teknh.nauk, pp.121-127, 1979.
2. A.A.Kuraev, S.V.Kolosov, A.F.Stekolnikov, G.Ya.Slepyan, and A.Ya.Slepyan, "TWT-gyrotrons: Non-linear theory, optimization and analysis", Int. J. Electronics, Vol.65, No.3, pp.437-462, 1988.
3. V.L.Rvachev and V.A.Rvachev, "Nonclassical Method of Approximation Theory in Boundary Value Problems", Kiev: Naukova Dumka, 1979.
4. V.F.Kravchenko, V.A.Rvachev, and V.L.Rvachev, "Mathematical Methods for Signal Processing Based on Atomic Functions", J. of Comm. Technology and Electronics, Vol.40, No.12, pp.118-137, 1995.
5. V.F.Kravchenko, A.A.Kuraev, and V.A.Rvachev, "Atomic Function in the Problems of Optimal Control of Dynamic Systems", Radiotekhnika, No.9, pp.4-8, 1997.

Applications of Atomic Functions to the Boundary Value Problems and Signal Processing Millimeter Band

V. F. Kravchenko, V. L. Rvachev*, and V. A. Rvachev**.

Institute of Radio Engineering and Electronics, Russian Academy of Sciences, ul. Mokhovaya 11, Moscow, Center,
GSP - 3, 103907 Russia.

Department of General and Applied Physics, Nonlinear Physics Laboratory, Moscow Institute of Physics and
Technology, Institutskii Pereulok 9, Dolgoprudnyi, Moscow Region, 141700 Russia.

Phone: +7 (095) 9214837, 4086772, 9024737(home). Fax: +7 (095) 9259241

E-mail: kvf@mx.rphys.mipt.ru, postmaster@nonlin.mipt.ru OR zaoiprzhr@glasnet.ru

*Institute of Machinery Problems, National Academy of Sciences of Ukraine,
ul. Pozharskogo 2/10, Kharkov, 310046 Ukraine.
E-mail: root@rvachev.kharkov.ua

**Zhukovskii Institute of Aviation, ul. Chkalova 15, Kharkov, 310085 Ukraine.

The Atomic Functions (AF) were discovered in early nineteen seventies by V.A.Rvachev and V.L.Rvachev[1]. The mathematical theory of AF has been developed mainly by V.A.Rvachev and his students. Applications to various subjects of mathematical physics, statistical analysis of random processes and fields, signal and image processing have been developed in collaboration with V.F.Kravchenko and V.A.Rvachev [2-6] and their students and colleagues. This paper is dedicated to the application of AF to boundary value problems for partial derivatives equations.

The methods to obtain approximations to the solutions of the boundary value problems depend heavily on the quality of the functions employed. What we desire to expect of these? Firstly, they must possess excellent approximation properties. If it is impossible to obtain good approximations of arbitrary functions by the basic functions, we can hardly hope for a good result from even an excellent numeric method with those bad basic functions. The best mill, if we put in stones instead of grain, will produce sand instead of flour. However, we need more than that. To obtain good accuracy even with the best possible basic function from the point of view of approximation theory, their number must be great enough, especially for 3D problems. However, then we have to solve large linear algebraic systems. There exist well-known difficulties in solving such large systems, to say nothing of the problem of computation of coefficients of those systems (as a rule, these coefficients are multiple integrals). From all those points the AF have advantages. They have best possible approximation properties. They are finite and so we can employ atomic basic functions with small supports. Moreover, the wavelet type orthogonal atomic basic functions have been constructed. So the algebraic linear systems in question have good qualities in particular they are sparse. The third point is the question of computations dealing with AF, for instance computations of the multiple integral mentioned earlier. The AF are convenient from this point of view too and that is because of the functional differential equation they satisfy.

AF are finite infinitely differentiable functions that satisfy some simple functional differential equations (FDE), e.g. linear with constant coefficients and with linear transformations of independent variable. The study of AF started in 1971 after the paper "On a finite function" by V.L.Rvachev and V.A.Rvachev in "Dopovidi AN USSR" (Reports of Ukrainian Academy of Sciences) in which the function $up(x)$ was introduced. This function satisfies the equation $y'(x) = 2y(2x+1) - 2y(2x-1)$ and has support $[-1, 1]$. Since then the number of papers dealing or mentioning the AF has grown exponentially to some two hundred, not to mention 4 to 6 monographs, the main directions of investigation being applications in the theory of functions of real variable, approximation theory, theory of FDE, numerical analysis particularly numerical analysis of boundary value problems for PDE of elliptic type (both in FEM and boundary integral equation method), signal and image processing, statistical spectral analysis of time series, wavelets, the generalized Taylor series (GTS), smooth splines, calculus of variations and control theory. Some topics of interest such as applications in computational geometry, fractals, non-parametric statistics, and mathematical economics are as yet barely touched in publications.

The main reason behind the introduction of the AF is the necessity of employment of smooth finite functions that are easy to handle. By handling a function we mean differentiation, integration, computation of the Fourier transform etc., to say nothing of computing values of the function. In turn, we need finite smooth functions in a great number of important fields of research comprising problems with smooth solutions to be solved by reduction to the local ones.

When we want to obtain an approximation to the true solution, the latter being very smooth function we need to employ smooth functions as approximation machinery in order to expect optimal or at least suboptimal rate of approximation. Certainly, one shouldn't expect that any smooth approximating functions will do. For instance, in approximation with spans of translates of $f(ax)$ when $a > 0$ the conditions of the Fix – Strang – Mikhlin theorem are to be satisfied. The trigonometric polynomials are well established in approximation of smooth periodic functions, algebraic polynomials though not optimal are quite satisfactory in the non-periodic case, to say nothing of rational algebraic functions. But all of them being analytic are naturally non-local. The AF (to be more exact, some AF, such as the above-mentioned $up(x)$ is a function and a vast scope of related AF) are both optimal for approximation purposes of a wide range of smooth function and local in the sense that there exist coherent flags of finite-dimensional spaces of spans of translates of appropriate AF $L(n)$ such that each $L(n)$ possesses a base of functions of supports, the length of which tends to 0 while $n \rightarrow \infty$. One of the main reasons behind the excellent approximation properties of spaces of spans of translates of the $up(x)$ function is its "polynomial representation" property. Namely, any algebraic polynomial of degree n is represented as locally finite sum of translates of $up(x)$ function. This means that the spaces $L(n)$ contain algebraic polynomials. The orthogonal bases in $L(n)$ include wavelet atomic bases of rather remarkable kind. The atomic wavelets are both exponentially localized and infinitely smooth. The AF are in a sense a generalization of algebraic and trigonometric polynomials. As each analytic function possesses the Taylor series expansion, the terms of which are powers of x , so infinitely differentiable but non-analytic (to be more exact not necessarily analytic) functions can be expanded into the Generalized Taylor Series expansion the terms of which being finite linear combinations of appropriate AF. The differential equations for linear polynomials with constant coefficients are similar to FDE for the AF. Of course the major distinctions are also conspicuous.

There are several currently active directions of research. In the domain of 'pure' mathematics one ought to mention further generalizations of the generalized Taylor series with the help of the AF and more deep and thorough investigation of the previously introduced GTS, studies of the function approximation properties of finite-dimensional spaces based on AF, studies of some classes of entire functions of exponential type and some classes of finite smooth functions with the employment of the AF technique, unveiling conditions responsible for existence of finite solutions of FDE, applications to the FDE theory of not necessarily finite solutions. The AF in a number of points present some new features, sometimes even rather startling, and pose or perhaps inspire problems to be solved. There is a lot to be said on AF of several independent variables. The scope of unsolved and appealing problems in one-dimensional case has moved the AF SIV to the background. As for 'applied' mathematics, many major activities are at present in the following fields:

(i) Developing methods for numerically treating the boundary value problems for PDE (partial derivatives equations) of (mainly) elliptic type (stationary problems) including variants of FEM (the finite element method), the boundary integral equation method, the structural method of V.L.Rvachev (R-functions Method, RFM), collocation method, etc.

(ii) Signal processing, including image processing in particular dirty image restoration, redundancy cutting, pattern recognition, etc.

(iii) Statistical analysis of random processes and fields (time series analysis in particular spectral analysis), construction of windows (weight functions) for those purposes.

(iv) Applications in computational geometry, surfaces design and related topics.

(v) Applications of mathematical programming, calculus of variations and theory of optimal control with AF as one of the tools employed.

(vi) Creation of multi-purpose program complexes for PC based on AF.

In short, where it is reasonable to apply splines or wavelets it is probable that for some cases or some purposes AF will do better than traditional splines or wavelets, AF being in a sense infinitely smooth splines and the tool to construct infinitely smooth and perfectly (as far as it is possible) systems of wavelets.

However, it would be wrong to restrict comparison of AF pleasant properties only to splines and wavelets (**SpW**). There are numerous instances of remarkable features of AF that have no direct counterpart in **SpW**. For instance, the $up(x)$ function which vanishes outside $[-1, 1]$ in every point of this interval has the Taylor series either with zero radius of convergence (for x not dyadic rational, hence for x belonging to the set of measure 2) or the Taylor series being polynomial (containing only finite number of terms). In neither case does the Taylor series of $up(x)$ converge to it. Nevertheless, this at first glance bad property is not really a flaw. A second glance (in fact, the time interval between the two glances took some time) discloses that there exist some strange but rapidly converging and easy to compute both by hand and computer series which have no analogues (as far as or maybe as near as our knowledge goes) in non-AF mathematics. Conversely there are points at which one is haunted by apparent similarities with well-established topics, but it is not obvious how to exploit them. One of them has been drawn to our attention by Micchelli, namely, the relation of AF to fractals, another by Y.V.Ostrovsky, namely, the relation of AF to oscillation reducing kernels. AF are related to splines and wavelets. They are best known candidates to the name of infinitely smooth splines. They had been introduced before the wavelets theory grew popular and were among the roots of the wavelet theory. Moreover, wavelets built with AF are in many points superior to any other wavelets known. They are infinitely differentiable, exponentially localized and easy to handle. It is possible to construct even finite atomic orthogonal wavelets. The main reasons behind the effectiveness of AF applications are excellent approximation properties plus the fact that they vanish outside small regions so that the corresponding matrices are sparse plus the fact that they are convenient to deal with. The main disadvantage or hurdle to their wide spread is the fact that they are as yet rather little known and nobody outside the narrow circle of initiated really knows their good qualities and how to manage them.

In such a brief summary it is impossible to consider the capabilities of the theory of AF. Attention here was focused primarily on the application of atomic to signal processing, image reconstruction, which is also the subject of the recent publications. However, the potential capabilities of this mathematical tool are quite diverse and they can find wide application in various boundary value problems in radio physics, thermal conductivity, diffraction of elastic waves, etc. They can be used as the basis functions for solving problems of electrodynamics, antenna analysis and synthesis, millimeter band, etc. Moreover, they can be used in signal processing problems in medical equipment in combination with other approaches.

References

1. V.A.Rvachev and V.L.Rvachev, "Nonclassical Methods of Approximation Theory in Boundary Value Problems", Naukova Dumka, Kiev, 1979.
2. V.F.Kravchenko, V.L. Rvachev, and V.A.Rvachev, "Mathematical Methods for Signal Processing Based on Atomic Functions", Journal of Communications Technology and Electronics, Vol.40(12), pp.118-137, 1995 [Originally published in Radiotekhnika i Electronica, No.9, pp.1385-1406, 1995.]
3. V.F.Kravchenko and V.A.Rvachev, "Applications of Atomic Functions for Solution Boundary Value Problems in Mathematical Physics", Zarubezhnaya Radioelectronics. Achievements in Modern Radioelectronics, No.8, pp.6-22, 1996.
4. V.F.Kravchenko, V.I. Pustovoit, and V.V.Timoshenko, "Atomic Functions in Processing of Signals of Simple and Complex Form", Radiotekhnika, No.1, pp.26-30, 1997.
5. V.F.Kravchenko, A.A.Kuraev, and V.A.Rvachev, "Atomic Functions in Problems of Operating on Dynamic Systems", Radiotekhnika, No.9, pp.4-13, 1997.
6. V.F.Kravchenko and A.M.Krot, "Methods and Microelectronic Facilities of the Digital Filtering of Signals and Images on the Basis of Number Theoretic", Zarubezhnaya Radioelectronics. Achievements in Modern Radioelectronics, No.6, pp.3-31, 1997.

**RELATIVISTIC TRAVELLING-WAVE-TUBE-O (TWT-O) WITH AN IRREGULAR
MODERATING SYSTEM**

V.F.Kravchenko, A.A.Kuraev*, and A.B.Zakalyukin*

Institute of Radio Engineering and Electronics, Russian Academy of Sciences, ul.Mokhovaya 11, Moscow,
Center, GSP -3 , 103907 Russia.

Department of General and Applied Physics, Nonlinear Physics Laboratory, Moscow Institute of Physics and
Technology, Institutskii Pereulok 9, Dolgoprudnyi, Moscow Region, 141700 Russia.

Phone: +7(095) 9214837, 4086772, Fax:+7(095) 9259241.

E-mail: kvf@mx.rphys.mipt.ru, postmaster@nonlin.mipt.ru , zaoiprzhr@glasnet.ru

*Belarus State University of Informatics and Radioelectronics, P.Brovka st. 6, Minsk,
220600 Republic of Belarus.

Phone: (375 -17) 239-84-98, 239-89-56, Fax:(375-17) 231-09-14.

E-mail: VMiPMail@qw.bsuir.unibel.by, kurayev@micro.rei.minsk.by

The optimization of the profile of the decelerating system (DS) of a relativistic O-type traveling-wave tube (O-TWT) is a very difficult nonlinear problem, which in addition is multidimensional (due to the necessity to apply the method of large particles). The form of the DS boundary surface under optimization is quasiperiodic and, as a rule, has a large number of periods (20–100). Obviously, the method of representation of the desired optimal boundary determines to a great degree the success of solving the optimization problem. As shown in [1-5], such problems can be rather efficiently solved with the use of atomic functions, which have the best approximating properties among other finitary infinitely differentiable functions. In the given work, atomic functions are used for approximating the profile of a nonregular DS of a relativistic O-TWT under optimization.

Let us use the general theory of interaction of a relativistic electron flow (REF) with the field of the E_{0r} -wave of an irregular waveguide, developed in [6]. Setting in the general equations the transverse velocities in the REF, v_r and v_φ , equal to zero, we obtain one-dimensional self-consistent equations of a relativistic O-TWT with an arbitrary nonregular DS in the following form:

$$\dot{C} = -\frac{1}{v_{01}g^2}\dot{V} - \frac{1}{L_0v_{01}g}\frac{dg}{dT}\dot{A} - \frac{j\sigma}{e_{011}v_{01}^2\pi g^2N}\sum_{i=1}^N J_o\left(\frac{r_o}{g}\right)e^{-j\omega t_i}, \quad (1)$$

$$\frac{d\dot{A}}{dT} = L_0\left(\dot{V} + v_{01}\dot{C}\right), \quad (2)$$

$$\frac{d\dot{V}}{dT} = -L_0\dot{A}\left[1 + \frac{1}{3L_0^2}\left(\frac{dg}{dT}\right)^2\left(4 + v_{01}^2\right)\right] - \dot{C}v_{01}g\frac{dg}{dT} - \frac{j\sigma}{e_{011}v_{01}\pi g N}\frac{dg}{dT}\sum_{i=1}^N \frac{r_o}{g}J_1\left(\frac{r_o}{g}\right)e^{-j\omega t_i}, \quad (3)$$

$$\frac{d\beta_i}{dT} = -\frac{L_0R_i^3}{\beta_i}\operatorname{Re}\left\{\left[J_0\left(\frac{r_o}{g}\right)\dot{C} + \frac{r_o}{L_0v_{01}g^2}\frac{dg}{dT}J_1\left(\frac{r_o}{g}\right)\dot{A}\right]e^{j\omega t_i}\right\}, \quad (4)$$

$$\frac{d\omega t_i}{dT} = \frac{L_0}{\beta_i}, \quad i = \overline{1, N}. \quad (5)$$

Here $T=z/L$, L is the length of the interaction domain, $L_0 = kL = \frac{\omega}{c}L$, $g=b(T)/2,405$, $b(T)=kb'(T)$, $b'(T)$ is

the internal radius of the waveguide, $\beta = v_{zi}/c$, i is the number of a large particle, $\dot{A} = \frac{\dot{E}_re}{m_0c^2}$, $\dot{C} = \frac{\dot{E}_ze}{\omega m_0c}$,

$R_i = (1 - \beta_i^2)^{1/2}$, $r_0 = kr'_0$ (r'_0 is the radius of the electron flow tube), $\sigma = \frac{e\mu_0}{m_0c}|I_0| = 0.73723 \cdot 10^{-3}|I_0|$, e and

m_e are the electron charge and mass, respectively, $e_{011} = \frac{1}{2} J_1^2(\nu_{01})$, and ν_{01} is the first root of the function $J_0(x)$.

The initial conditions can be stated as follows:

$$\beta_i(0) = \beta_0, \omega t_i(0) = 2\pi i/N, \frac{dg}{dT}(0) = 0 \text{ (the end of the waveguide's regular part),}$$

$$\operatorname{Re} \dot{A}(0) = \left(K_{in} \frac{(1-R_0)\chi}{R_0 \pi e_{01}} \right)^{1/2}, \operatorname{Im} \dot{A}(0) = 0,$$

$$K_{in} = \frac{P_m}{U_0 |I_0|}, \text{ where } P_m \text{ is the input power, } \operatorname{Re} \dot{V}(0) = 0, \operatorname{Im} \dot{V}(0) = -\frac{1}{\chi} \operatorname{Re} \dot{A}(0),$$

$$\chi = \sqrt{\left(1 - 1/g_0^2\right)}, R_i(0) = R_0, g_0 = g(0). \quad (6)$$

The electron efficiency (η_e) is determined as follows:

$$\eta_e(z) = \frac{1}{N} \sum_{i=1}^N \frac{1 - R_0/R_i(T)}{1 - R_0}. \quad (7)$$

The wave efficiency (η_v) is calculated by the formula

$$\eta_v(T) = \frac{\pi R_0 e_{011}}{(1-R_0)\sigma} \operatorname{Im} [\dot{A}(T)\dot{V}^*(T) - \dot{A}(0)\dot{V}^*(0)]. \quad (8)$$

The comparison of $\eta_e(T)$ and $\eta_v(T)$ in the absence of losses gives the estimation of the error of calculations.

Let us state the problem of optimization of the DS profile as follows: it is required to maximize $\eta_e(I)$ (7) defined on the solutions to (1)–(5) with the boundary conditions (6) by optimizing the function $g(T)$ and parameters K_{in} and β_0 with the given $|I_0|$ and L_0 . For solving this problem, introduce the multiparameter approximation of the function $g(T)$ by means of atomic functions as follows [1]:

$$g(T) = g_0 + \sum_{j=1}^n A_j \operatorname{up}\left(\frac{2T - (2j-1)h}{h}\right), \quad (9)$$

where $\operatorname{up}(x)$ is an atomic function, $h = 1/n$, and n is the number of the annular grooves of the DS.

By means of (9), after solving the problem (1)–(6), $\eta_e(I)$ becomes a function of the parameters g_0 , K_{in} , β_0 , and A_j , $j = j = \overline{1, n}$. In the given work, the maximum of this function was determined by the gradient method with the variable Goldfarb metric [7].

The optimization was performed for the following variant:

$$n = 67, L_0 = 62.8, |I_0| = 150 \text{ A}, \beta_{0opt} = 0.866, K_{inopt} = 0.07, \text{ and } \eta = 75\%.$$

The mechanism of the optimal interaction in the obtained variant substantially differs from those already known [8]. It can be treated as a mechanism of doubly strong focusing of an electron bunch and double intensive extraction of energy from it [8]. The first section of the extraction of energy is situated in the interval $T = 0.4-0.7$; here, the wave is decelerated (the grooves become deeper) and the bunch enters the decelerating wave phase. If the extraction continues, the bunch disintegrates [9] and the grouping function G is ready to grow again. To avoid this and focus the bunch, in the section $T = 0.6-0.8$ the wave is accelerated again and the bunch moves to the center of the focusing forces of the already sufficiently strong field. Due to this circumstance, the grouping improves again (G decreases) and, in a finite section $T = 0.8-1.0$, the bunch efficiently returns energy to the wave, decelerating in this segment (the grooves become deeper in this section again).

This variant has the character of the optimal interaction mechanism. It is expressed more distinctly due to a greater length of the interaction domain: in the section of the repeated focusing of the

bunch, $T = 0.7\text{--}0.8$, the center of the bunch so exactly coincides with the center of focusing forces that the interchange of energy is practically absent (the typical "shelf" of the function $\eta(T)$ appears).

Thus, results demonstrating the high efficiency of using the atomic functions in the problems of optimal control of the interaction process in the O-type devices are presented: not only have the efficiency-optimal DS profiles been found, but also a new mechanism of the optimal process of phase focusing and extraction of energy in relativistic O-TWTs, interesting from the physical point of view, has been discovered.

References

1. V.L.Rvachev and V.A.Rvachev, "Nonclassical Method of Approximation Theory in Boundary Value Problems", Kiev: Naukova Dumka, 1979.
2. V.F.Kravchenko, V.A.Rvachev, and V.L.Rvachev, "Mathematical Methods for Signal Processing Based on Atomic Functions", J. of Comm. Technology and Electronics, Vol.40, No.12, pp118-137, 1995.
3. V.F.Kravchenko and V.A.Rvachev, "Application Atomic Functions for Solution Boundary Value Problems in Matematical Physics", Foreign Radioelectronics. Achievements in Modern Radioelectronics, No. 8, pp.6-22, 1996.
4. V.F.Kravchenko, V.I.Pustovoit, and V.V.Timoshenko, "Atomic Function in Processing Simple and Compound Signals", Radio and Communications Technology, Vol. 2, No. 1, pp.25-31, 1997.
5. V.F.Kravchenko, A.A.Kuraev, and V.A.Rvachev, "Atomic Function in the Problems of Optimal Control of Dynamic Systems", Radiotekhnika, No.9, pp.4-8, 1997.
6. A.B.Zakalyukin and A.A.Kuraev, "Relativistic Cyclotron-Resonance Maser with E_{01} Operating Mode", Radiotekhnika i Elektronika, No. 8, Vol.34, pp. 1707-1714, 1989.
7. D.Gol'dfarb, "A Family of Variable-Metric Methods Derived by Variational Means", Mathematics of Computations, Vol. 24, No. 109, pp. 23-26, 1970.
8. A.A.Kuraev, T.L.Popkova, and A.K.Sinitsin, "Modeling and Optimization of a Relativistic O-TWT with a Decelerating System in the Form of a Nonregular Waveguide", Radiotekhnika, No. 9, pp.13-20, 1997.
9. A.A.Kuraev, Moshchnye pribory SVCh. Metody analiza i optimizatsii parametrov (High-Power Microwave Devices: Methods of Analysis and Optimization of Parameters), Moscow: Radio i Svyaz', 1986.

Optimization of the Variation of a Phase Velocity Wave in an Orotron of Millimeter Band Based on Atomic Functions.

V. F. Kravchenko, A. A. Kuraev*, A. K. Sinitsyn*, and A. I. Shakirin*.

Institute of Radio Engineering and Electronics, Russian Academy of Sciences, ul.
Mokhovaya 11, Moscow, Center, GSP-3, 103907 Russia

Department of General and Applied Physics, Nonlinear Physics Laboratory, Moscow
Institute for Physics and Technology, Institutskii 9, Dolgoprudnyi, Moscow Region,
141700 Russia

Phone: +7 (095) 921-4937, 408-6772, Fax: +7 (095) 925-9241

E-mail: kvf@mx.rphys.mipt.ru, postmaster@nonlin.mipt.ru OR zaoprzhr@glasnet.ru.

Belarus State University of Informatics and Radioelectronics, ul. P. Brovsky 6,
Minsk, 220600 Belarus

E-mail: vmipmail@gw.bsuir.unibel.by

The problem of optimal control of the detection of phase velocity changes in an orotron for which maximal efficiency is ensured has constantly attracted the attention of researchers. For its solution, different approaches and methods have been proposed. In [1], both the principle of Pontryagin's maximum and the method of interpolation of Lagrange polynomials is used. It is noted in particular that the successful realization of these methods requires both the application of an entire series of limits on the smoothness of the control functions sought, and knowledge of a priori information for setting the initial values of the polynomial coefficients. In [2] is suggested the synchronous electron method, making it possible to find the optimal laws ensuring an efficiency of up to 80%. However, the use of the given method is not acceptable when the influence of reverse waves or additional limits must be taken into account.

In work on the basis of the ideas in [3, 4] for the solution of the given optimization problem, a methodology based on the approximation of the sought-for control law $u(T)$ in the interval $0 \leq T \leq 1$

by the generalized series $u^M(T) = \sum_{k=1}^M a_k \varphi_k^{np}(T)$, the basis functions of which are a set of shifts of

Atomic Functions (AF) $up(x)$: $\varphi_k^{np}(T) = up\left(\frac{nT - k + p}{p}\right)$ [3]. Here, n is the number of sections into which the interval $[0,1]$ is divided, $2p$ is the number of intervals of overlapping finite functions $\varphi_k^{np}(T)$. It may be shown that the number of functions of the chosen basis are distinct from zero in the interval $[0,1]$ $M = (n-1) + 2p$. The uniqueness of this distribution lies in the fact that although the functions $\varphi_k^{np}(T)$ possess a finite carrier, the generalized series $u^M(T)$ is infinitely differentiable, since at the extremal points $x = \pm 1$ all produced functions $up(x)$ are equal to zero. The presence of p overlaps in such a concept makes it possible, in contrast to an ordinary spline and polynomial, to produce changes between the local and integral properties of control functions. Calculations show that in the approximation of two modal functions of the form $x = T \sin(2\pi T)$, an acceptable accuracy is achieved for $p = 3$ and $n = 2$.

The setting of boundary conditions for control at $T = 0$ and $T = 1$ is easy to take into account in the chosen distribution. For example, if a boundary condition of the first type $u(0) = u_0$ is given, the

relationship $u^M(0) = \sum_{k=1}^{2p-1} a_k \varphi_k^{np}(0) = u_0$ exists, and since $\varphi_p^{np}(0) = 1$, then

$$a_p = u_0 - \sum_{k=1, k \neq p}^{2p-1} a_k \varphi_k(0)$$

An analogous relationship is also obtained in setting boundary conditions of

the second or third type. The use of a generalized series leads from the problem of optimal control to the problem of the minimization of the function of M variables. The presence of additional boundary conditions makes it possible to decrease the number of optimized parameters. A methodology has been developed for obtaining the initial values of parameters a_k according to the method of least squares in the presence of some law of control adopted as an initial approximation.

The enumerated experiment has shown that the given method makes it possible to find effectively smooth optimal laws for the phase velocity of an orotron of the millimeter band ensuring an efficiency no lower than the laws obtained by the synchronous electron method ($\approx 70\%$). The optimal laws $v_\varphi(z)$ are defined with the help of AF, and the parameters of the orotron taking reverse waves into account are introduced as well. The presence of a reverse wave may lead to a decrease in efficiency in a millimeter band orotron by 15—20%.

REFERENCES

1. M.M.Tarasov, O.A. Tret'yakov, and A.A. Shmat'ko, "Optimization of Phase Velocity in Orottron-Type Generators", Radiotekhnika i Elektronika, Vol. 32, No. 6, p. 1286, 1987.
2. A.A. Kuraev, and A.K. Sinitsyn, "Study of an Autophase Regime in a Relativistic Orottron", Radiotekhnika i Elektronika, Vol. 32, No. 11, p. 2427, 1987.
3. V.F. Kravchenko, V.A. Rvachev, and V.L. Rvachev, "Mathematical Methods for Signal Processing Based on Atomic Functions", Radiotekhnika i Elektronika, Vol. 40, No. 9, p. 1385, 1995.
4. V.F. Kravchenko, A.A. Kuraev, and V.A. Rvachev, "Atomic Functions in the Problems of Optimal Control of Dynamic Systems", Radiotekhnika, no. 9, pp. 4—8, 1997.

Computation of Electrodynamical Characteristics of Arbitrarily Shaped Domains Based on R-functions Method.

V. F. Kravchenko, V. L. Rvachev*, and V. V. Torchinov.

Institute of Radio Engineering and Electronics, Russian Academy of Sciences,
ul. Mokhovaya 11, Moscow, Center, GSP-3, 103907 Russia.

Department of General and Applied Physics, Nonlinear Physics Laboratory, Moscow Institute for Physics and Technology, Institutskii Pereulok 9, Dolgoprudnyi, Moscow Region, 141700 Russia.

Phone: +7 (095) 9214837, 4086772. Fax: +7 (095) 9259241

E-mail: kvf@mx.rphys.mipt.ru, postmaster@nonlin.mipt.ru OR zaoprzhr@glasnet.ru

*Department of Applied Mathematics and Computational Sciences, Institute for Problems of Machinery,
Ukrainian National Academy of Sciences,
ul. Pozharskogo 2/10, Kharkov, 310046 Ukraine.

E-mail: root@rvachev.kharkov.ua

Modern radiophysics has recently been characterized by intensive development of millimeter and the submillimeter waves theory. Moreover, considered objects have arbitrary shape and their sizes are comparable with the wavelength or it exceeds them. It leads to the necessity of determining the eigenvalues (EV) and eigenfunctions (EF) of Laplacian within complicated shape bounded regions (for example, waveguides, open resonators, etc.) During the development of the algorithms and their numerical realization on a computer one should give particular attention to the procedure of analytical description of complicated shapes of real objects. In this respect, the R-functions theory [1] seems to be one of the most promising methods used for solving different inner and outer problems of electrodynamics. In this report, a method based on the R-functions theory and variational methods applied to the calculation of eigenvalues (EV) and eigenfunctions (EF) of complicated section shape waveguides is described. The application of this method for finding the eigenvalues and eigenfunctions of self-adjoint elliptic operators with any boundary conditions is illustrated. The estimation of the error is given, eigenvalues are shown and field maps for eigenfunctions are built.

Thus, the R-functions theory allows one to develop a mathematical apparatus which combines the possibilities of classical continuous analysis and Boolean algebra. This method (RFM) may be applied to the problems of electrodynamics of millimeter band for complicated shape bounded regions. It is well known that a procedure for analytic description of the complex geometric shapes of real objects is especially important for development of the appropriate algorithm and their numerical implementation in computers. The theory of R-functions (RFM), which is utilized in solving interior and exterior electrodynamic boundary value problems [1 – 5], is promising for this purpose.

The present paper describes a method based on RFM and variational difference methods that can be used to calculate the eigenvalues and eigenfunctions of waveguides with complicated cross sections (Fig. 1). The error level for the calculation is estimated, the field patterns are constructed, and the eigenvalues are determined. It should be remarked that, e.g., this approach and the overall formulation of the problem permit consideration of a broad class of interior electrodynamic problems for arbitrary regions. We will illustrate the foregoing by considering the problem of calculating the TE modes of a rectangular waveguide with two symmetrical grooves. The mathematical model of the problem of calculating the eigenvalues and eigenfunctions has the form

$$\begin{aligned} \Delta u + k^2 u &= 0, \\ \left. \frac{\partial u}{\partial n} \right|_{\Gamma} &= 0, \quad (\text{Neumann, corresponding to H-modes}). \end{aligned} \tag{1}$$

The operator of this problem is positive definite, so it can be solved by Ritz's method, minimizing the functional

$$J = \frac{\int_{\Omega} (\nabla u)^2 d\Omega}{\int_{\Omega} u^2 d\Omega} \quad (2)$$

on the class of functions from the domain of the boundary value problem operator (with solution structure $u = P - \omega D_1 P$ [1]) or from the energy space (solution structure $u = P$).

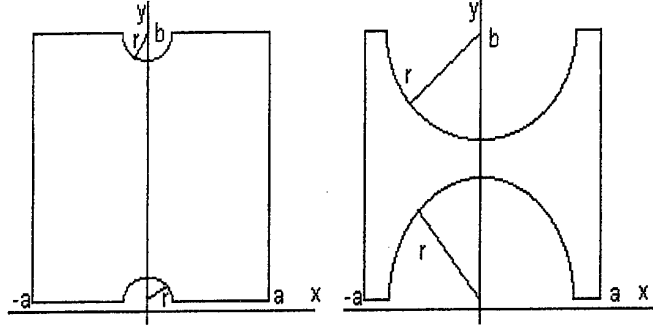
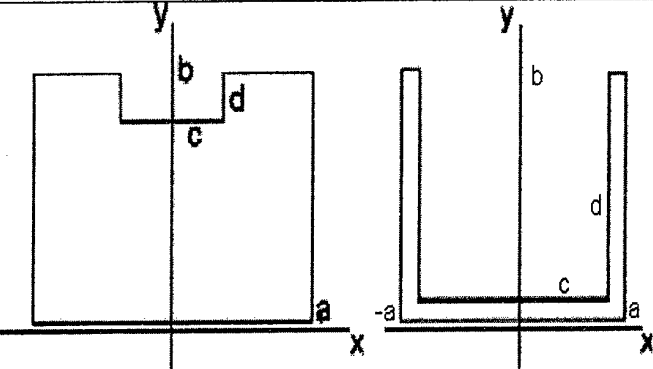
Domain geometry transformation	Analytic description
 a)	$\omega = (f_1 \Lambda f_2) \Lambda (f_3 \Lambda f_4)$ $F_1^D = a^2 - x^2;$ $f_1^N = \frac{1}{2a}(a^2 - x^2);$ $F_2^D = b - \sqrt{y^2 + (b-y)^2};$ $f_2^N = \frac{1}{\sqrt{2b}}(b - \sqrt{y^2 + (b-y)^2});$ $F_3^D = x^2 + y^2 - R^2;$ $f_3^N = \frac{1}{2R}(x^2 + y^2 - R^2);$ $F_4^D = x^2 + (b-y)^2 - R^2;$ $f_4^N = \frac{1}{2R}(x^2 + (b-y)^2 - R^2);$
 b)	$\omega = (f_1 \Lambda f_2) \Lambda (f_3 \vee f_4)$ $F_1^D = a^2 - x^2;$ $f_1^N = \frac{1}{2a}(a^2 - x^2);$ $F_2^D = b - \sqrt{y^2 + (b-y)^2};$ $f_2^N = \frac{1}{\sqrt{2b}}(b - \sqrt{y^2 + (b-y)^2});$ $F_3^D = x^2 - c^2; f_3^N = \frac{1}{2c}(x^2 - c^2);$ $F_4^D = d - x; f_4^N = \frac{1}{\sqrt{2d}}(d - x);$

Figure 1.

The equation for the boundary domain shown in Fig. 1a had the form

$$\Omega = (F_1 \Lambda F_2) \Lambda (F_3 \Lambda F_4),$$

where

$$F_1 = x^2 + y^2 - R^2, \quad (3)$$

$$\begin{aligned}F_2 &= x^2 + (b - y)^2 - R^2, \\F_3 &= a^2 - x^2, \\F_4 &= b - \sqrt{y^2 + (b - y)^2},\end{aligned}$$

at which $R < a$; $R < b/2$. Changing the R parameter leads to changes in the groove's depth. Changing the a and b parameters changes the main region's dimensions.

The numerical calculation was made for: $a = 0.64$, $b = 1$, $R = 0.3$.

References

1. V.L. Rvachev, "Theory of R-functions and Its Some Applications", Kiev: Naukova Dumka, 1982.
2. V.F. Kravchenko and V.L. Rvachev, "R-functions Theory and Its Applications for the Solution of Boundary Value Problems in Arbitrary Domains", Proceedings of the 3rd Workshop on Electromagnetic and Light Scattering, Theory and Applications, Eds. Th. Wright and Yu. Eremin, Universitat Bremen, Germany, pp.163-168, March 16 –17, 1998.
3. V.F. Kravchenko and V.L. Rvachev, "The Theory R-functions in Boundary Value Problems for Arbitrary Domains", First International Conference "Modern Trends in Computational Physics", Dubna, Russia, June 15 –20, Section 1: Numerical Algorithms, 1998.
4. V.F. Kravchenko and V.L. Rvachev, "R-functions Method (RFM) for Direct and Inverse Boundary Value Problems with Complex Domains in the Diffraction Theory", Progress in Electromagnetics Research Symposium, Nantes, France, Session B1: Mathematical Methods for Inverse Scattering Problems, July 13 – 17, 1998.
5. V.F. Kravchenko and V.L. Rvachev, "R-functions Theory and Methods of the Solution of Boundary Value Problems of Complex Domains", International Conference on Systems, Signals, Control, Computers (SSCC '98), Durban, South Africa, Invited Session R-functions and Atomic Functions, September 22 – 24, 1998.

CALCULATION OF A MILLIMETER WAVE ELECTROOPTICAL MODULATOR OF LASER BUNDLES BY A METHOD OF R-FUNCTIONS

V.F.Kravchenko, N.I.Kravchenko*, and N.D.Sizova **

Institute of a Radio Engineering and Electronics, Russian Academy of Sciences,
ul. Mohovaya 11, Moscow, Center, GSP-3, 103907 Russia.

*State Scientific - Production Joint "Metrology" of Ukraine,
ul. Mironositskaya 42, Kharkov, 310002 Ukraine.

** Institute of Machinery Problems, National Academy of Sciences of Ukraine,
ul. Dm. Pozharskogo 2/10, Kharkov, 310046 Ukraine.

In laser physics, optical communications systems, and fiber-optical transmitters, the cross-section electrooptical modulator of laser bundles on the basis of a biconical resonator loaded by crystal KDP is promising.

The biconical resonator (Fig.1), occupying area Ω_1 , consists of a cylindrical part of a radius R and length L , of two frustum of a cones forming which make an angle θ with an axes oz; a is radius of flat end faces of a resonator, d_1 is length of crystal, a_1 is radius of a flat end face of crystal, the crystal occupies area Ω_2 and can have the following form: circular ($r = a_1$), spherical convex ($r = a_2$) or spherical ($r = a_3$) cylinder.

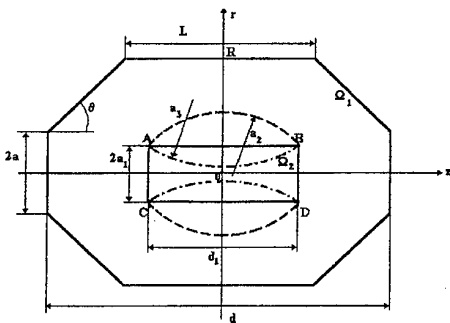


Figure 1.

Consider axially symmetric oscillation H_{011} , circumscribed by the two-dimensional boundary problem:

$$\Delta U(r,z) + k^2 U(r,z) = 0, \quad (1)$$

$$U(r,z)|_{\Gamma} = 0, \quad (2)$$

where Γ is the boundary of a resonator, $\Gamma = \Gamma_1 \cup \Gamma_2$, Γ_i is the boundary of area Ω_i ($i = 1, 2$); $k^2 = \omega_0^2 \epsilon \mu$, where $\epsilon_1 \mu_1$ and $\epsilon_2 \mu_2$ are dielectric and magnetic permeability of vacuum and crystal respectively.

Solution of a boundary value problem (1), (2) is discovered by a method of R-functions [1-3], by the construction of a coordinate sequence for a functional Releya-Ritza as follows:

$$u(r,z) = \omega(r,z)\Phi(r,z), \quad (3)$$

where $\omega(r, z)$ is equation of the boundary of area of a study, $\Phi = p(r)p(z)$ is selected to satisfy precisely the conditions on the boundary of a biconical resonator and on the boundary of a crystal, and also to precisely take into account a relation between ϵ_1 and ϵ_2 .

The generalized problem of eigenvalues is described by the equation

$$AX = k^2 BX, \quad (4)$$

where matrixes $A = \| a_{ij} \|$ and $B = \| b_{ij} \|$ are defined as follows:

$$a_{ij} = \left\{ \int_{\Omega} \frac{1}{r^2} \frac{\partial}{\partial r} (ru_i) \frac{\partial}{\partial r} (ru_j) + \frac{\partial u_i}{\partial z} \cdot \frac{\partial u_j}{\partial z} \right\} r dr dz, \quad (5)$$

$$b_{ij} = \int_{\Omega} u_i u_j r dr dz, \quad (6)$$

$$u_i = C_i \omega p_i(r) p_j(z), \quad (7)$$

$$u_j = C_j \omega p_i(r) p_j(z). \quad (8)$$

The numerical solution of a boundary value problem (1) and (2) is found with the help of programming system POLE [2] with use of Holetzki's expansion and Hausholder's method [3].

For checking the correctness of an obtained solution, the passages to the limit to outcomes of work [3,4] are investigated. The limit of a supposed error of the numerical definition of own frequencies and quality for a resonator [3] does not exceed 2 % and 3 % ($p = 0,95$) accordingly, and the structure of a field $U(r,z)$ for oscillation H_{011} (Fig.2) coincides with the outcome of work [3].

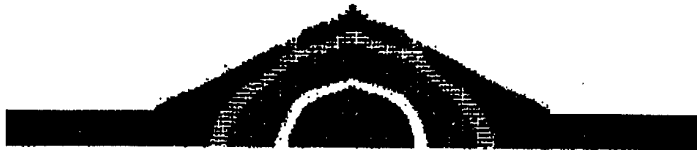


Figure 2.

For projection of cross-section electrooptical modulators of laser bundles, it is necessary to receive an association of resonance frequency of oscillation H_{011} from the geometric parameters of a resonator and crystal, physical parameters and form of monoaxial crystals of a type KDP, ADP, etc. [4].

In Fig.3a the distributions of an electrical component of a field on an axes of crystal are reduced at the following sizes of a resonator: $L = 2\text{mm}$, $\theta = 42^\circ$, $2a = 2\text{mm}$, $R = 2\text{mm}$, $d = 6\text{mm}$ and fixed ratio entering aperture of a resonator and diameter of crystal equal to one. For crystal KDP both in the form of the circular cylinder, and in the form of a solid of revolution convex (a_2) and concave (a_3) of curvilinear trapezoids with modification of crystal length, the electrical component of a field varied smoothly both on axes, and on volume of crystals.

It is necessary to note, that the electrical component of a resonance field has minimum longitudinal and transversal gradients at a geometric parameter of the modulator $d_1/d_2 = 0,4$.

In Fig.3b the outcomes of resonance frequency of the modulator for three ratios of diameters of crystal ($2a_1$) in the form of the circular cylinder to entering aperture of a resonator ($2a$) are reduced with modification of crystal length (d_1). In a passage to the limit $d_1/d_2 = 0$, resonance frequencies of modulators tend to the resonance frequency of a biconical resonator without crystal. The resonance frequencies of modulators are reduced with magnification of volume of crystal, both at magnification of its diameter, and at magnification of its length, which corresponds to the classical theory of resonators [5].

The offered and justified technique of calculating with the help of R-functions the basic performances of a biconical resonator with monoaxial crystal of KDP type can find application in the creation of resonance electrooptical modulators, deflectors, and switches of laser bundles with the help of cross-section waves.

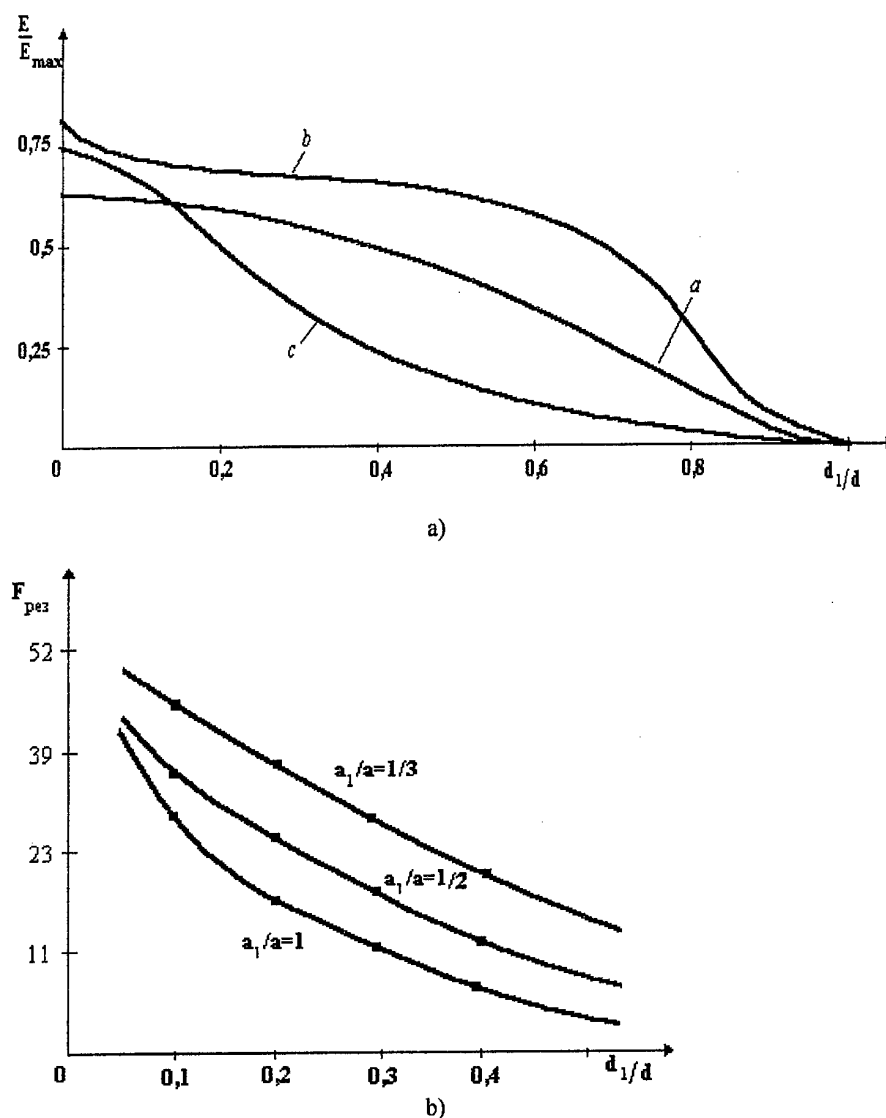


Figure 3.

References

1. V.L. Rvachev, "The Theory of R-functions and Some Its of Applications", Naukova Dumka, Kiev, 1982.
2. V.L.Rvachev and A.N.Shevchenko, "The Problem-oriented Languages and Systems for Engineering Calculations", Tekhnika, Kiev, 1988.
3. V.F.Kravchenko, V.V.Veretelnik, and V.L.Rvachev, "Calculation of electrodynamic characteristics of a biconical resonator", Izmeritel'naya Tekhnika, No. 3, pp.57-58, 1993.
4. A.Yariv and P. Yuh, "Optical Waves in Crystals", Mir, Moscow, 1987.
5. V.V.Nikolskii, "Variational Methods for Interior Problems of Electrodynamics", Nauka, Moscow, 1967.

**AN EFFECTIVE SOLUTION OF ELECTROMAGNETIC INTEGRAL EQUATIONS
IN THE BOUNDARY VALUE PROBLEMS OF MILLIMETER WAVE
DIFFRACTION BASED ON ATOMIC FUNCTIONS**

V. F. Kravchenko and A. A. Zamyatin

Institute of Radio Engineering and Electronics, Russian Academy of Science,
ul.Mokhovaya 11, Moscow, Center, GSP – 3, 103907 Russia.

Department of General and Applied Physics, Nonlinear Physics Laboratory, Moscow Institute of Physics and
Technology, Institutskii Pereulok 9, Dolgoprudnyi, Moscow Region, 141700 Russia.
Phone: +7(095) 4086772, 9024737(home), Fax:+7(095) 9259241.

E-mail: kvf@mx.rphys.mipt.ru, postmaster@nonlin.mipt.ru, zaoiprzhr@glasnet.ru, alzam@aha.ru

A great number of electromagnetic (EM) problems [1], can be formulated in the form of $L(\mathbf{J})=\mathbf{E}$, where L is a known linear operator, \mathbf{E} is a known excitation function, and \mathbf{J} is the unknown response function. L may be an integral operator or an integrodifferential operator depending on different EM problems. An appropriate tool, widely used to investigate EM problems, is the Green's functions technique. Once the Green's function for a given EM problem is known, the above-mentioned equation for this EM problem takes an integral form with its relevant Green's function as the integral kernel. The objective of study is to efficiently solve \mathbf{J} once L and \mathbf{E} are specified.

Using the Method of Moments (MoM) the unknown response function \mathbf{J} can be expanded in terms of N known basis functions $\{\varphi_n\}$ as $\mathbf{J} = \sum_n I_n \varphi_n$, with N unknown constants $\{I_n\}$. Then we derive mean

representation error $\varepsilon(x) = L\left(\sum_n I_n \varphi_n(x)\right) - \mathbf{E}(x)$, or, making use of linearity of the operator L : $\varepsilon(x) = \sum_n I_n L(\varphi_n(x)) - \mathbf{E}(x)$. To find the unknown coefficients $\{I_n\}$, N weighting functions are needed. After weighting procedure, we derive $\langle w_m, \varepsilon(x) \rangle \equiv \sum_n I_n \langle w_m, L(\varphi_n(x)) \rangle - \langle w_m, \mathbf{E} \rangle$. Setting to zero the projection of error vector to weighting function space, i.e., $\langle w_m, \varepsilon \rangle = 0$, yield the matrix equation: $Z \mathbf{I} = \mathbf{V}$, where $I_n = I_n$, $Z_{mn} = \langle w_m, L(\varphi_n(x)) \rangle$ are impedance matrix coefficients, $\mathbf{V}_m = \langle w_m, \mathbf{E} \rangle$, $m, n = 1, 2, \dots, N$. The symbol $\langle \cdot, \cdot \rangle$ stands for an inner product.

It is well known that the use of conventional basis and weighting functions in the MoM always results in a dense matrix equation. As the weighting function we choose delta function δ , to reduce the inner product computational complexity. Now, let us consider the main types of basis systems [1-4].

Atomic Functions (AF) interpolation $J(z) = I_j \text{up}(z - z')$.

Pulse functions
$$J(z) = \begin{cases} I_j, & z \in \Delta z_j, \\ 0, & \text{otherwise.} \end{cases}$$

Linear functions
$$J(z) = \begin{cases} \frac{I_j(z_{j+1} - z) + I_{j+1}(z - z_j)}{\Delta z_j}, & z \in \Delta z_j, \\ 0, & \text{otherwise.} \end{cases}$$

Sinusoidal functions
$$J(z) = \begin{cases} \frac{I_j \sin k(z_{j+1} - z) + I_{j+1} \sin k(z - z_j)}{\Delta z_j}, & z \in \Delta z_j, \\ 0, & \text{otherwise.} \end{cases}$$

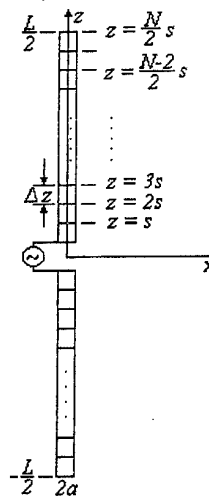
Square interpolation
$$J(z) = \begin{cases} A_j + B_j(z - z_j) + C_j(z - z_j)^2, & z \in \Delta z_j, \\ 0, & \text{otherwise.} \end{cases}$$

Sinusoidal interpolation

$$J(z) = \begin{cases} A_j + B_j \sin k(z - z_j) + C_j \sin k(z - z_j)^2, & z \in \Delta z_j, \\ 0, & \text{otherwise.} \end{cases}$$

The topic of interest of this paper is the first basis system.

Let us consider the scalar problem of computing the current J_z on the perfectly conducted Z -directed thin cylinders composing a dipole antenna, as shown in Figure 1, exited by a plane TM_z (transverse-magnetic to z -axis) wave.



The incident wave induces currents on the surface of cylinders and the induced currents have only z components. In order to solve this scattering problem, we resort to the E -field integral equation formulation. For perfectly conducted antenna we have $L(J) = E_z^s(0, z)$. The integral operator is defined by

$$L = -\frac{\lambda\sqrt{\mu/\epsilon}}{8\pi^2 i} \int_{-L/2}^{L/2} G(r, r') dz', \quad \text{where } r = \sqrt{a^2 + (z - z')^2},$$

and $G(r, r') = \frac{e^{-ikr}}{r^5} [(1 + ikr)(2r^3 - 3a^2) + k^2 a^2 r^2]$ is the Green's function.

$$\text{We derive } \int_{-L/2}^{L/2} I_s \mathbf{up}(z - z') \frac{\exp(-ikr)}{4\pi r^5} [(1 + ikr)(2r^2 - 3a^2) + (kar)^2] dz' = -iw\epsilon E_z^s.$$

$$\text{From } \sum_{j=1}^N Z_{js} I_s = E_z^s \text{ we obtain}$$

$$Z_i = \int_{-L/2}^{L/2} \mathbf{up}(z - z') \frac{\exp(-ikr)}{4\pi r^5} [(1 + ikr)(2r^2 - 3a^2) + (kar)^2] dz', \quad \text{where } z' \text{ is}$$

$$\text{defined as } z' = s \frac{L}{2} \frac{1}{N}.$$

Figure 1. Radiating dipole antenna.

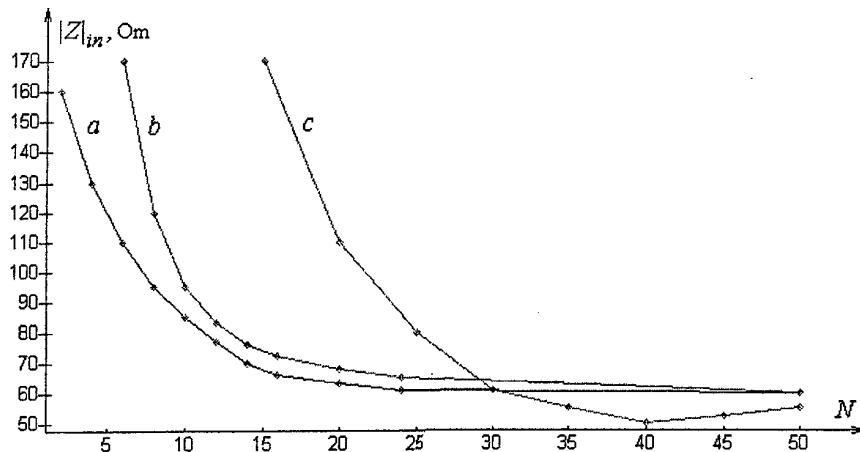


Figure 2. Curves illustrating the descending of the inner impedance of a dipole with increase in the number of considered basis functions ($L = 0.45\lambda$, $a = 0.007\lambda$).
(a) Atomic Functions interpolation. (b) Sinusoidal functions. (c) Pulse basis functions.

Table 1. Time dependence of number of interpolating basis function for different basis systems.

METHOD	NUMBER OF TESTING POINTS			
	$N = 8$	$N = 16$	$N = 64$	$N = 128$
Atomic Functions interpolation	3.7	7.7	37.8	83.1
Pulse functions	2.9	6.2	31.4	64.7
Sinusoidal interpolation	5.4	11.9	55.6	135.6

To show the effectiveness of the proposed approach, a practical Yagi-Uda antenna is used as another example. The main objective is to solve the current distribution and far-field radiation patterns. Generally, the thin cylinders are very thin, i.e., $a \ll \lambda$, so that all induced currents on the thin cylinders can be considered to flow in the z -axis direction. In our study we take $a = 0.05\lambda / 2\pi$, $s = 1.0 \lambda / 2\pi$. The induced current $I_z(z)$ on the thin cylinder by the point-matching technique (30) can be discretized into the matrix form. We discretize the feeder and all the directors by n equal intervals and the reflector by n_0 equal intervals. If $n = 21$ and $n_0 = 23$, we obtain a moment matrix of order 128 ($= 21 \times 5 + 1 \times 23$)

To solve the current distributions on all the thin cylinders, the excitation field E_z^i should be evaluated first.

Here, we use magnetic frill generator source modeling to evaluate E_z^i , which can be approximated by

$$E_z^i = -\frac{V_i}{2 \ln(b/a)} \left(\frac{\exp(-ikR_1)}{R_1} - \frac{\exp(-ikR_2)}{R_2} \right) \quad (\rho = 0, -l_f/2 \leq z \leq l_f/2),$$

where $R_1 = \sqrt{z^2 + a^2}$, $R_2 = \sqrt{z^2 + b^2}$, and V_i is the excitation voltage at the feeder terminal and l_f stands for the length of the feeder element. The inner radius a of the magnetic frill is chosen to be the radius of the feeder element, and the outer radius b of the magnetic frill is determined by the characteristics impedance of transmission line.

Once the current distributions on all the thin cylinders are solved, one can determine the far-field pattern by

$$E_\theta = \sum_{n=1}^N \frac{C_n \exp(-ikr)}{4\pi r} \int_{l_f/2}^{l_f/2} I_n \exp(ikz' \cos \theta) dz',$$

where $C_n = i\omega\mu \sin \theta \exp[ik(x_n \sin \theta \cos \phi + y_n \sin \theta \sin \phi)]$.

References

1. G.A.Thiele, "Wire Antennas", In: Computer Techniques for Electromagnetics, ed. R.Mittra, Pergamon Press, New York, Chapter 2, pp.17-105, 1973.
2. V.A.Rvachev, "Compactly Supported Solutions of Functional Differential Equations and Their Applications", Uspekhi Mat. Nauk, Vol.45, No.1, pp.77-103, 1990.
3. V.F.Kravchenko and V.A.Rvachev, "Application Atomic Functions for Solution Boundary Value Problems in Mathematical Physics", Foreign Radioelectronics. Achievements in Modern Radioelectronics, No. 8, pp. 6-22, 1996.
4. V.F.Kravchenko, "Approximation Diagram of Direction and Synthesis of Linear Radiator Based on Atomic Functions", Foreign Radioelectronics. Achievements in Modern Radioelectronics, No.8, pp. 23-28, 1996.

Application of R-functions Method to the Calculation of Microstrip Element of Pentagonal Shape.

V. F. Kravchenko, V. L. Rvachev*, and V. V. Torchinov.

Institute of Radio Engineering and Electronics, Russian Academy of Sciences,
ul. Mokhovaya 11, Moscow, Center, GSP-3, 103907 Russia.

Department of General and Applied Physics, Nonlinear Physics Laboratory, Moscow Institute for Physics and Technology, Institutskii Pereulok 9, Dolgoprudnyi, Moscow Region, 141700 Russia.

Phone: +7 (095) 9214837, 4086772. Fax: +7 (095) 9259241

E-mail: kvf@mx.rphys.mipt.ru, postmaster@nonlin.mipt.ru OR zaoiprzhr@glasnet.ru

*Department of Applied Mathematics and Computational Sciences, Institute for Problems of Machinery,
Ukrainian National Academy of Sciences,
ul. Pozharskogo 2/10, Kharkov, 310046 Ukraine.

E-mail: root@rvachev.kharkov.ua

In this paper using the **R**-functions method (**RFM**) is given the calculation of microstrip (**MS**) element of pentagonal shape. The comparison of experimental and theoretical resonance frequencies of first six eigenvalues of **MS** pentagonal element vibrations is made. This has shown the effectiveness of the method.

This paper consists of two parts.

In the first part, using the ideas, discussed in [1], a mathematical structure that enables the calculation of **MS** element eigenvalues, is suggested and validated. In some papers, such element of pentagonal shape was calculated using Green's functions method and conformal mapping method. In connection with that **R**-functions theory enables to describe the complex shape figures and bodies analytically, this method of approach has some practical advantages in comparison with methods been discussed before.

In the second part there is performed an numerical experiment.

We will illustrate the foregoing by considering the problem of calculating the **TE** modes of a **MS** pentagonal element. The mathematical model of the problem of calculating the eigenvalues and

eigenfunctions has the form

$$\begin{aligned} \Delta u + k^2 u &= 0, \\ \left. \frac{\partial u}{\partial n} \right|_{\Gamma} &= 0, \quad (\text{Neumann, corresponding to H-modes}). \end{aligned} \tag{1}$$

The operator of this problem is positive definite, so it can be solved by Ritz's method, minimizing the functional

$$J = \frac{\int_{\Omega} (\nabla u)^2 d\Omega}{\int_{\Omega} u^2 d\Omega} \tag{2}$$

on the class of functions from the domain of the boundary value problem operator (with solution structure $u = P - \omega D_1 P$ [1]) or from the energy space (solution structure $u = P$) [2].

In [1] are presented general structures that are used during solution of boundary value problems. For the structure $u = P - \omega D_1 P$ and also for the partial structure $u = P$ numerical calculations were performed.

Here

$$P(x, y) = \sum_{i=1}^n C_i \chi_i, \quad (3)$$

and below as $\{\chi_i\}$ basis functions are used Chebyshev polynomials and Atomic Functions (**AF**) [3, 4].

Domain geometry	Analytic description
	$\omega = ((f_1 \wedge f_2) \wedge (f_3 \wedge f_4)) \wedge f_5$ $f_1^N = y - x\sqrt{3} + a\sqrt{3};$ $f_2^N = y + x\sqrt{3} - a\sqrt{3};$ $f_3^N = -y + x\sqrt{3} + b;$ $f_4^N = -y - x\sqrt{3} + b;$

Figure 1. Pentagonal microstrip element and its boundary equation.

The equation for the boundary domain shown in Fig. 1 had the form

$$\Omega = ((F_1 \wedge F_2) \wedge (F_3 \wedge F_4)) \wedge y,$$

where

$$\begin{aligned}
 f_1 &= y - x\sqrt{3} + a\sqrt{3}, \\
 f_2 &= y + x\sqrt{3} - a\sqrt{3}, \\
 f_3 &= -y + x\sqrt{3} + b, \\
 f_4^N &= -y - x\sqrt{3} + b,
 \end{aligned} \quad (3)$$

at which $a < c$. Changing the a parameter leads to changes in the size of the cut off piece. Changing the b and c parameters changes the main region's dimensions.

The numerical calculation was made for: $a = 1.64$, $b = 11.258$, and $c = 6.63$.

References.

1. V.L. Rvachev, "Theory of R-functions and Its Some Applications", Naukova Dumka, Kiev, 1982.
2. S.G. Mikhlin, "Variational Methods in Mathematical Physics", Moscow, Nauka, 1970.
3. V.A. Rvachev and V.L. Rvachev, "Nonclassical Methods of Approximation Theory in Boundary Value Problems", Naukova Dumka, Kiev, 1979.
4. V.F. Kravchenko, V.L. Rvachev, and V.A. Rvachev, "Mathematical Methods for Signal Processing Based on Atomic Functions", Journal of Communications Technology and Electronics, Vol. 40(12), pp. 118-137, 1995.

Analytical and Numerical Methods in the Boundary Value Problems of Superconducting Electrodynamics of Structures in the Millimeter Band.

V. F. Kravchenko.

Institute of Radio Engineering and Electronics, Russian Academy of Sciences,
ul. Mokhovaya 11, Moscow, Center, GSP-3, 103907 Russia.

Department of General and Applied Physics, Nonlinear Physics Laboratory, Moscow Institute for Physics and Technology, Institutskii Pereulok 9, Dolgoprudnyi, Moscow Region, 141700 Russia.

Phone: +7 (095) 9214837, 4086772. Fax: +7 (095) 9259241

E-mail: kvf@mx.rphys.mipt.ru, postmaster@nonlin.mipt.ru OR zaoiprzhr@glasnet.ru

The aim of the paper consists in working out of rigorous methods of study and practical recommendations for the solution of external and internal boundary value problems of excitation, scattering, and propagation of electromagnetic waves on intricately shaped conducting bodies. This includes:

- (i) theoretical analysis and the substantiation and application of the non-self-adjoint operator theory to the solution of a broad class of external and internal boundary value problems associated with the excitation, scattering, and propagation of electromagnetic waves in various superconducting structures;
- (ii) development of the mathematical foundations for the electrodynamics of superconducting structures for superconducting impedances of the one or two kind;
- (iii) development of algorithms and computer programs for the calculating of the main electrodynamic characteristics of superconducting extremely narrow beam antennas, superconducting printed flat antennas for satellite communications and TV, superconducting SAR for remote sensing purposes as well as superconductor based integrated circuits and microelectronic devices;
- (iv) on the basis of the techniques developed, preliminary evaluations will be made for the further theoretical and experimental study of the problems;
- (v) on the basis of theoretical calculations, breadboard millimeter wave devices will be fabricated.
- (vi) open superconducting structures.

Preliminary results of the research team on the subject are presented in the following publications:

References

1. IEEE MTT, Special Issue on the Microwave and Millimeter Wave Applications of High Temperature Superconductivity, eds. M.Nisenoff and W.J.Meyers, Vol. 44, No. 7, 1996.
2. "Physical Properties of High Temperature Superconductors I", ed. D.M. Ginsberg, World Scientific, London, 1989.
3. A.S. Davydov, "High Temperature Superconductivity", Naukova Dumka, Kiev, 1990.
4. N.M. Plakida, "High-Temperature Superconductors", Moscow, 1996.
5. E.A. Andryushin, V.L. Ginzburg, and A.P. Silin, "On the Boundary Conditions in the Macroscopic Theory of Superconductivity", Uspekhi Physicheskikh Nauk, Vol. 163, No.9, pp. 105-108, 1993.
6. "Superconductivity, Superdiamagnetism, Superfluidity", ed. V.L. Ginzburg, Mir, Moscow, 1987.
7. F.F. Mende and A.I. Spitsyn, "Surface Impedance of Superconductors", Naukova Dumka, Kiev, 1985.

8. N. Newman and W.G. Lyons, "High-Temperature Superconducting Microwave Devices: Fundamental Issues in Materials, Physics, and Engineering", Journal of Superconductivity, Vol.6, No.3, pp.119-160, 1993.
9. M.A. Megahed and S.M. El.-Ghazaly, "Nonlinear Analysis of Microwave Superconductor Devices Using Full-Wave Electromagnetic Model", IEEE MTT, Vol.43, No.11, pp.2590-2599, 1995.
10. V.F. Kravchenko, "Application of Spectral Theory to the Internal and External Boundary Value Problems of Excitation, Scattering, and Propagation of Electromagnetic Waves in Various Superconducting Structures" Abstracts Sommerfeld'96 — Workshop, Modern Mathematical Methods in Diffraction Theory and Its Applications in Engineering, ed. E. Meister, Freudenstadt, Schwarzwald, Preprint-Nr. 1988, p.25, 30 September-4 October 1996.
11. Yu.V. Gandel', V.F. Kravchenko, and V.I. Pustovoit, "Scattering of Electromagnetic waves by a Thin Superconducting Band, Doklady Mathematics", Vol.54, No.3, pp.959-961, 1996. (Translated from Doklady Akademii Nauk, Vol.351, pp.462-464, 1996).
12. Yu.V. Gandel', V.F. Kravchenko, and N.N. Morozova, "Diffraction of Electromagnetic Waves on Superconducting Thin Stripes Grating, Electromagnetic Waves and Electronic Systems", Moscow, Publishing House of Journal "Radiotekhnika", Vol.2, No.2, pp.15-27, 1997.
13. V.F. Kravchenko, V.L. Rvachev, and I.V. Taldykin, On a Method of Electromagnetic Boundary Value Problem Solution for the Complex Shape Inhomogeneous Impedance Region, DAN SSSR, Vol. 302, No.1, pp.72-74, 1988.
14. V.F. Kravchenko, "Excitation and Scattering of Electromagnetic Waves on the Inhomogeneous Impedance Bodies with Rotational Symmetry", DAN SSSR, Vol. 309, No.3, pp.594-598, 1989.
15. V.F. Kravchenko and A.F. Chaplin, "On the Excitation of Superconducting Impedance Plane", DAN SSSR, Vol. 326, No.2, pp.272-275, 1992.
16. V.F. Kravchenko and A.F. Chaplin, "Excitation of Superconducting Circular and Elliptic Cylinder", DAN SSSR, Vol. 326, No.4, pp.633-636, 1992.
17. V.F. Kravchenko and A.F. Chaplin, "Axially Symmetric Excitation of a Superconducting Sphere", DAN, Vol. 327, No.2, pp.208-211, 1992.
18. V.F. Kravchenko, "Scattering of Electromagnetic Waves by a Superconducting Cylinder", DAN, Vol. 328, No.2, pp.178-180, 1993.
19. V.F. Kravchenko , V.L. Rvachev, and A.F. Chaplin, "Electromagnetic Field of Superconducting Antenna Arrays", DAN, Vol.333, No.6, pp.725-726, 1993.
20. V.F. Kravchenko, V.T. Erofeenko, and A.N. Kryuchkov, "Addition Theorems for Basis Electromagnetic Fields", Telecommunications and Radio Engineering, Vol.49, No.10, pp.97-108, 1995.
21. V.F. Kravchenko, V.T. Erofeenko, and V.I. Pustovoit, "Electromagnetic Field Structure of a Magnetic Dipole on a Superconducting Thin Disk", DAN, Vol.52, No.2, pp.278-281, 1995.
22. V.F. Kravchenko and A.B. Kazarov, "About the Excitation and Solid Resonators", The 15-th URSI International Symposium on Electromagnetic Theory, St. Peterburg, Russia, pp.806-808, May 23-26, 1995.
23. V.F. Kravchenko, "Method for Determination of the Speed of Light Based on the Impedance Measurements of Superconductors", Radiotekhnika (Electromagnetic Waves, No.4), No.12, pp.108-117, 1995.
24. V.F. Kravchenko, V.T. Erofeenko, and Lu Bao Lin, "Diffraction of Electromagnetic Waves on Superconducting Thin Shells with Moving Media", DAN, Vol.53, No.1, pp.109-112, 1996.
25. V.F. Kravchenko, A.B. Kazarov, and V.I. Pustovoit, "On a Method of Improvement of the Surface Impedance of Superconductors by Means of Superconducting Cylindrical Resonator", DAN, Vol.345, No.4, pp.472-474, 1995.
26. V.F. Kravchenko, A.B. Kazarov, and V.I. Pustovoit, "Determination of the Main Electrodynamic Characteristics of Superconducting Microstrip Resonators", DAN, Vol. 348, No.2, pp.188-190, 1996.
27. V.F. Kravchenko, V.M. Likhachev, and A.I. Stashkevich, "An Asymptotic Method for Solving the Boundary Value Problem of the Excitation of an Impedance Wedge", DAN, Vol.308, pp.329-334, 1989.

28. V.F. Kravchenko, V.M. Likhachev, and A.I. Stashkevich, "Polarization Structure of the Field of Diffraction of Electromagnetic Waves on Angular Structures With Impedance", DAN, Vol.318, pp.1148-1153, 1991.
29. V.F. Kravchenko, A.B. Kazarov, and V.I. Pustovoit, "Excitation of the Rough Superconducting Wedge by a Filamentary Source", Radiotekhnika, No.1, pp.57-63, 1997.
30. V.F. Kravchenko and R.G. Tyutyukin, "New Method for Determination the Electrodynamical Characteristics of the Superconducting Disk Being Excited by Electrical Dipole", Radiotekhnika, No.2, pp.8-16, 1997.
31. V.F. Kravchenko, "Electromagnetics of Superconducting Structures and Its Application to the Problems of Antenna and Waveguide Technique", Proceedings of the Second International Conference on Antenna Theory and Techniques, Kiev, pp. 16-17, May 20-22, 1997.
32. V.F. Kravchenko and A.B. Kazarov, "Surface Impedance of Superconductors and Its Application in Physics and Engineering", Foreign Radio Electronics. Advances in Modern Radio Science, No.11, pp. 40-55, 1997.
33. V.F. Kravchenko, "Integral Methods and Some of Its Applications to Boundary Value Problems of Diffraction of Electromagnetic Waves on Superconducting Structures", Proceedings of IMA Conference on Boundary Integral Methods: Theory and Applications, University of Salford, UK, pp.76-77, 1997.
34. V.F. Kravchenko, "Methods for Solving Boundary Value Problems of Electrodynamics of Superconducting Structures", Proceedings of the 3rd Workshop on Electromagnetic and Light Scattering - Theory and Applications, Bremen, Germany, pp.169-174, March 16-17, 1998.

Authors Index

A		B	C	D	E	F
<i>Abdulkadyrov V.A.</i>	C21, C22		<i>Bykov V.N.</i>	F26		
<i>Afonin D.G.</i>	H9		<i>Bykov Yu.V.</i>	INV.J2		
<i>Akinshin N.S.</i>	F2, F15		<i>Bystrov R.P.</i>	F1, F2, F3, F4, F5, F6		
<i>Ala-Lauriaho J.</i>	INV.4					
<i>Alekseev E.A.</i>	I1					
<i>Alexeev G.A.</i>	E12, B17					
<i>Ando M.</i>	D24					
<i>Andreev M.V.</i>	I3					
<i>Andrenko A.S.</i>	D24					
<i>Antifeev V.N.</i>	F1, F2, F5, F6					
<i>Antyufeev V.I.</i>	F26					
<i>Arkusha Yu.V.</i>	A8, A15					
<i>Averkov Yu.O.</i>	C13					
<i>Ayzatskiy N.I.</i>	B1.					
B						
<i>Büchler J.</i>	INV.J1					
<i>Böhm H.</i>	A1					
<i>Bacherikov A.N.</i>	L11					
<i>Bakhvalov B.N.</i>	H17					
<i>Balabanov V.N.</i>	INV.11					
<i>Ballard J.</i>	INV.5					
<i>Bandopadhyaya T.K.</i>	E5					
<i>Barantsev S.A.</i>	H21					
<i>Baumgartner M.O.</i>	A3					
<i>Begma A.A.</i>	L17					
<i>Begma L.A.</i>	L17					
<i>Beletskii N.N.</i>	C13, C14					
<i>Belous O.I.</i>	A13, A17, L8					
<i>Belousov Ye.V.</i>	B5					
<i>Bereshnyj V.L.</i>	J3					
<i>Berezhinsky L.I.</i>	L3, L10					
<i>Berezhnyj L.V.</i>	J2					
<i>Bessonov V.A.</i>	H21					
<i>Betskii O.V.</i>	INV.L1					
<i>Blank A.Ya.</i>	C19					
<i>Bludov J.V.</i>	C16					
<i>Bogdashov A.A.</i>	H4					
<i>Borisenko S.A.</i>	C14					
<i>Borsov A.B.</i>	F1, F2, F5, F6					
<i>Borulko V.F.</i>	H22, H23					
<i>Botsula O.V.</i>	A9					
<i>Bratman V.L.</i>	B2					
<i>Brovenko A.V.</i>	D1, D11					
<i>Bubke K.</i>	D4					
<i>Budnikov A.T.</i>	C11					
<i>Bugaev A.S.</i>	C18					
<i>Bulgakov A.A.</i>	C15					
<i>Bulgakov B.M.</i>	A17, L8					
<i>Burov A.B.</i>	INV.10					
<i>Buts V.A.</i>	B7					
<i>Bychkov V.V.</i>	INV.II					
C						
<i>Chayka V.E.</i>	C7, C8					
<i>Chemerovsky V.I.</i>	F9					
<i>Chepel' L.M.</i>	L8					
<i>Cherny I.V.</i>	H12					
<i>Cherpak N.T.</i>	B24, C2, C11					
<i>Cheslavsky G.V.</i>	F23					
<i>Chigryai E.E.</i>	C9					
<i>Chizhov V.V.</i>	H15					
<i>Chornaya L.F.</i>	E1					
<i>Chovnjuk Yu.V.</i>	L7					
<i>Churyumov G.I.</i>	B18, B19					
<i>Claassen M.</i>	A1					
D						
<i>Dachov N.F.</i>	B12					
<i>Dakhov V.M.</i>	H12					
<i>Dan'ko A.Ya.</i>	C11					
<i>Das N.K.</i>	H3					
<i>Demchenko M.Yu.</i>	B6, H29					
<i>Denisov G.G.</i>	H4					
<i>Derkach V.N.</i>	D11, L4, L11					
<i>Detlefsen J.</i>	INV.J1					
<i>Dikmen F.</i>	D16					
<i>Dolia A.N.</i>	F9					
<i>Dovbeshko G.I.</i>	L3, L10					
<i>Dovbyna A.N.</i>	B19					
<i>Drobakhin O.O.</i>	K9					
<i>Dryagin Yu.A.</i>	INV.10					
<i>Dubko S.D.</i>	E2					
<i>Dyubko S.F.</i>	I1					
<i>Dubovitskaya O.V.</i>	L2					
<i>Duxbury, G.</i>	INV.5					
<i>Dyadchenko A.V.</i>	A10					
E						
<i>Efimov V.B.</i>	INV.11					
<i>Erckmann V.</i>	B1					
<i>Eremeev A.G.</i>	INV.J2					
<i>Eremeev D.B.</i>	B19					
<i>Eremenko Z.E.</i>	A12, H27					
<i>Ermak G.P.</i>	B6					
<i>Evtukh A.A.</i>	C7					
F						
<i>Falko V.L.</i>	C4					
<i>Falkovich S.E.</i>	F19					
<i>Fedoseev L.I.</i>	F12					

<i>Fernandes H.C.C.</i>	D6, D7, D8, D9	J
<i>Filipov Yu.F.</i>	A12, H27	
<i>Fisun A.I.</i>	A13, A17, L5, L8	
<i>Fomin I.P.</i>	J2, J3	
<i>Freitas E.L.</i>	D8	
<i>Frolova T.I.</i>	B18	
<i>Fumeaux C.</i>	A2	
<i>Furashov N.I.</i>	E9	
<hr/>		
G		
<i>Gaikovich K.P.</i>	F11	
<i>Ganapolskii E.M.</i>	INV.11, B13, H26	
<i>Garamina L.V.</i>	C19	
<i>Garin B.M.</i>	C9	
<i>Gayvoronskaja S.A.</i>	F25	
<i>Goldenberg A.</i>	INV.9	
<i>Golik A.V.</i>	INV.11	
<i>Golubyatnikov G.Yu.</i>	INV.11	
<i>Gomozov A.V.</i>	H17, H18	
<i>Goncharuk N.M.</i>	C7, C8	
<i>Gorbach N.V.</i>	E4, E11	
<i>Gorbunenko O.A.</i>	F19, F20	
<i>Gorobets N.N.</i>	H10, H11, H12	
<i>Gorobets Yu.N.</i>	H10	
<i>Grechko L.G.</i>	C19	
<i>Greed R.B.</i>	INV.C1	
<i>Grichaniuk A.M.</i>	F26	
<i>Gridasova L.N.</i>	L13	
<i>Gridina N.Ya.</i>	L10	
<i>Grimalsky V.V.</i>	H5	
<i>Grishin A.M.</i>	I4	
<i>Grom Yu.D.</i>	B2	
<i>Gudim I.</i>	H28	
<i>Gusev V.A.</i>	J1	
<i>Gutnic V.G.</i>	E11	
<hr/>		
H		
<i>Herrmann W.</i>	A2	
<i>Herscovici N.I.</i>	H3	
<i>Hirvonen T.</i>	INV.4	
<i>Holopstev V.V.</i>	INV.J2	
<i>Holotyak, T.</i>	F30	
<i>Homenko S.I.</i>	F28	
<i>Hong J.-S.</i>	INV.C1	
<i>Hornbostel A.</i>	INV.E1	
<hr/>		
I		
<i>Ignatov M.Yu.</i>	L4	
<i>Ilchenko M.E.</i>	D3	
<i>Ilyushin V.V.</i>	I1	
<i>Iounevitch E.O.</i>	A5	
<i>Ivanchenko I.</i>	H29	
<i>Ivanilov V.E.</i>	H23	
<i>Ivanyuta A.N.</i>	H16	
<i>Izhyk E.V.</i>	C2, C11	
<hr/>		
<i>Jacob A.F.</i>		J
<i>Jedamzik D.</i>		D4
<i>Judaschke R.</i>		INV.C1
		INV.2
<hr/>		
K		
<i>Kalynov Yu.K.</i>	B2	
<i>Kamenev Yu.E.</i>	B11, B12	
<i>Karacuha E.</i>	D16	
<i>Karyakin E.N.</i>	INV.I1	
<i>Kashpur V.A.</i>	L2, L9	
<i>Kasperek W.</i>	B1	
<i>Kasyanov A.O.</i>	D25	
<i>Khankina S.I.</i>	C4	
<i>Kharkovsky S.N.</i>	H27, H34	
<i>Khlopov G.I.</i>	H33	
<i>Kholod P.V.</i>	F24	
<i>Khomenko E.V.</i>	L1	
<i>Khoroshun V.V.</i>	H13, H14	
<i>Khorunzhii M.O.</i>	B21	
<i>Kirichenko A.Ya.</i>	C2, C11, K10,	
<i>Kirichenko V.A.</i>	F14, F28	
<i>Kirilenko A.A.</i>	INV.H1, A13, D2, D3,	
	D12,	
<i>Kiseliov V.K.</i>	B12, H25, J5	
<i>Kiselova N.E.</i>	L15, L16, L17	
<i>Kishenko Ya.I.</i>	H5	
<i>Kitaj Sh.D.</i>	F10	
<i>Kitaytsev A.A.</i>	A14	
<i>Kiyko V.I.</i>	H10	
<i>Kleiman A.S.</i>	INV.K1	
<i>Klugman J.</i>	H3	
<i>Kneubühl F.K.</i>	A2, A3	
<i>Knyaz'kov B.N.</i>	H24	
<i>Koberidze A.V.</i>	K8	
<i>Kogut A.E.</i>	H34	
<i>Koledintseva M.Yu.</i>	A14	
<i>Kolesnikov V.G.</i>	L6, L12, L13, L15,	
	L16, L17	
<i>Komyak V.A.</i>	F17, F18, H33	
<i>Konov V.I.</i>	C9	
<i>Kopilovich L.E.</i>	G3	
<i>Kopnin A.N.</i>	C9, I2	
<i>Kordoš P.</i>	INV.6	
<i>Korneenkov V.K.</i>	H35	
<i>Korneyenkov V.</i>	H29	
<i>Kornienko Yu.V.</i>	G2, G5, G6	
<i>Korolyuk A.P.</i>	INV.11	
<i>Korshunov I.P.</i>	D19	
<i>Korshunova E.N.</i>	D19	
<i>Korzh V.G.</i>	B5	
<i>Koshevaya S.V.</i>	H5	
<i>Koshparenok V.N.</i>	B21	
<i>Kostenko A.A.</i>	H33	
<i>Kostenko L.V.</i>	E2, H17, H18	
<i>Kovalchuk I.K.</i>	B7	
<i>Kovaljova O.</i>	L14	

Krakovskiy V.A.	C3		M
Krasilnikov A.A.	F12		
Krasnitskaya A.A.	L2	Makarenko B.I.	E2, F26, F27, H19, K1, L1
Kravchenko N.I.	D32	Makarov N.M.	C17, E6, E7
Kravchenko V.F.	D26, D28, D29, D30, D31, D32, D33, D34, D35, F20	Makeev Yu.G.	H36, H37
Krizhanovsky V.V.	H30, H31, H32	Maleev V.Ya.	L2
Kropotkina E.P.	INV.F1, J1	Malihin A.V.	L4
Krupnov A.F.	INV.I1	Malyshev V.Y.	H16
Kudryashov V.E.	L1	Malyshkin A.K.	H9
Kukin L.M.	INV.10	Malyshkin P.A.	D18
Kulagin O.P.	B8, B9, B22	Manuilov V.N.	B2
Kulemin G.P.	INV.8, F7, F8, F14, F16,	Markov V.N.	INV.I1
Kuleshov E.M.	B12	Marquardt J.	H1
Kuleshov Y.M.	H24	Martinenko D.V.	L1
Kulik D.Yu.	INV.H1	Martynuk S.P.	H33
Kulikov Y.Y.	F12	Masalov S.O.	D20
Kuraev A.A.	D29, D30	Maslov V.A.	H6
Kurekin A.A.	F7; F9	Mazur A.B.	C9
Kurekin A.C.	INV.11	McPhail M.	INV.5
Kushta T.M.	J5	McPheat R.	INV.5
Kutuzova B.G.	INV.E1, E8	Medvedev V.V.	A11
Kutuzov V.V.	H34	Medvedev Yu.V.	I4
Kuz'michev I.K.	B15, B16, H8	Melkov G.A.	H16
Kuzmichov V.M.	K2, K3, K4, K5	Meriakri V.V.	INV.I2, I2
Kuzmichova E.V.	K4	Mikhailova D.V.	F21

L

Lancaster M.J.	INV.C1		
Lapy V.K.	J6, J7	Mogila A.A.	F29
Laqua T.H.	B1	Moroz A.V.	E6
Lavrinovich A.A.	B24	Moroz I.P.	H5
Lebedeva N.N.	INV.L1	Mos'pan L.P.	INV.H1, D12
Lehto A.	INV.4	Motornenko A.P.	H37
Leonov I.I.	INV.I1		
Lepeeva E.A.	L14		
Levin G.Ya.	B22	Nagnibeda V.G.	G1
Lima G.A.de B.	D7	Nagornyi D.A.	B5
Lima R.L.M.	D8	Naumenko V.D.	INV.BI
Lioubtchenko V.E.	A5, F22	Naumov A.P.	F10
Lipphardt B.	A2	Nazarchuk Z.T.	K6
Litovchenko V.G.	C7	Nesterenko A.V.	B23
Litvin Yu.M.	C7	Nesterov P.K.	J5
Litvinenko L.N.	E2	Newham D.	INV.5
Litvinov P.V.	D22	Nicolaenko Yu.M.	I4
Ljashchuk O.B.	K6, K7	Nicolenko U.J.	L13
Logvinenko S.V.	J1	Nikiforov P.L.	J1
Logvinov Yu.F.	E3	Nikitin A.A.	A6
Lubyako L.V.	INV.10, B1	Nikitina N.S.	L16
Lukin A.N.	INV.F1, J1	Nikolaev V.A.	F2
Lukin K.A.	INV.F2, F29	Nosdrachev D.A.	F2, F5, F6
Lukin V.V.	F7, F8, F9		
Lukovnikov D.A.	H4		
Lutsenko V.I.	F28, H35	Oberschmidt G.	D4
Luy J.-F.	INV.J1	Obukhoveths V.A.	D25
		Ocheretenko V.L.	J2, J3
		Ofitserov M.M.	B2

O

Oberschmidt G.	D4
Obukhoveths V.A.	D25
Ocheretenko V.L.	J2, J3
Ofitserov M.M.	B2

<i>Onishchuk V.A.</i>	F20	<i>Saltykov D.Yu.</i>	K9
<i>Onufrienko V.M.</i>	D14	<i>Samsonov S.V.</i>	B2
<i>Orlenko A.A.</i>	F24	<i>Saxena P.</i>	E5
<i>Osharin A.M.</i>	E10	<i>Schüemann K.</i>	INV.1, INV.2, INV.BI
<i>Osharina N.N.</i>	F10	<i>Schitov A.M.</i>	INV.I1
<hr/>			
	P	<i>Schroth A.</i>	INV.E1
<i>Panin I.A.</i>	F2.	<i>Semenov M.A.</i>	L9
<i>Panin S.B.</i>	D13	<i>Semenov V.E.</i>	INV.J2
<i>Parkhomenko M.P.</i>	C9	<i>Semenuta V.Ye.</i>	INV.BI
<i>Parshin V.V.</i>	INV.I1	<i>Serebryannikov A.E.</i>	B10
<i>Parshin Y.V.</i>	C9	<i>Sergeev A.G.</i>	INV.11
<i>Passoje J.</i>	H1	<i>Sergeev V.I.</i>	F25
<i>Pavlichenko O.S.</i>		<i>Shablosky Ya.O.</i>	C20
<i>Pavlov G.L.</i>	F5	<i>Shachbazov V.G.</i>	L8
<i>Pedchenko I.E.</i>	H14	<i>Shahabadi M.</i>	INV.1
<i>Pedenko Yu.A.</i>	E3	<i>Shakirin A.I.</i>	D30
<i>Pedyash V.G.</i>	C11	<i>Shapovalov A.S.</i>	A6
<i>Penkin Yu.M.</i>	D21	<i>Sharapov L.I.</i>	E4, E11
<i>Pereira W.P.</i>	D7	<i>Shatrov A.D.</i>	D18, D19
<i>Perov A.O.</i>	D17	<i>Shchegoleva T.Ju.</i>	L6, L12, L13, L14, L15, L16, L17
<i>Petrusenko I.V.</i>	D10	<i>Shilo S.A.</i>	F17, F18
<i>Pinos I.B.</i>	J2	<i>Shokin M.G.</i>	F27
<i>Pogorelov S.V.</i>	K5	<i>Shramkova O.V.</i>	C15
<i>Pogrebnyak V.A.</i>	C6, C18	<i>Shtanjuk A.M.</i>	INV.10, J1
<i>Pojedinchuk A.E.</i>	D1, D11, D13	<i>Shulga V.M.</i>	INV.G1
<i>Pokhil'ko S.N.</i>	K3	<i>Shvetsov A.A.</i>	F13
<i>Polupanov V.N.</i>	H24	<i>Siart U.</i>	INV.J1
<i>Popenko N.</i>	H28	<i>Sidorov D.</i>	L14
<i>Popov V.V.</i>	C10, H15	<i>Silin A.O.</i>	H20
<i>Prilepsky E.D.</i>	F27	<i>Sinitsyn A.K.</i>	D30
<i>Prokhorov E.D.</i>	A8, A9, A10, A11	<i>Sinyavskij G.P.</i>	D23
<i>Prudyus I.</i>	F30	<i>Sirenko S.P.</i>	L8
<i>Pushkaryov K.A.</i>	B4, B5	<i>Sivov A.N.</i>	D19
<i>Puzanov O.O.</i>	D20	<i>Sizova N.D.</i>	D32
<hr/>			
	R	<i>Skalyga N.K.</i>	INV.10, B1
<i>Räisänen A.</i>	INV.4	<i>Skibenko A.I.</i>	J2, J3
<i>Radionov V.P.</i>	B12	<i>Skripnik Yu.A.</i>	J4
<i>Ralchenko V.G.</i>	C9	<i>Skrynnik B.K.</i>	B15
<i>Razskazovsky V.B.</i>	E3	<i>Slesarenko S.S.</i>	A16
<i>Revin I.D.</i>	B6	<i>Smirnova T.A.</i>	B24
<i>Rothuizen H.</i>	A2	<i>Smirnova V.</i>	L14
<i>Rozanov B.A.</i>	INV.G2, F23, G1	<i>Smith K.</i>	INV.5
<i>Rozanov S.B.</i>	INV.F1, INV.G2, J1	<i>Sokolnikov A.V.</i>	F19, F20
<i>Ruban A.I.</i>	B3; B4	<i>Sokolov A.V.</i>	F1, F2, F3, F4, F5, F6
<i>Rud' L.A.</i>	INV.H1, D2, D3	<i>Solodovnik V.A.</i>	H34
<i>Rudenko V.N.</i>	H18	<i>Solokha E.I.</i>	E2, H18
<i>Rvachev V.A.</i>	D28	<i>Solomonov S.V.</i>	INV.F1, J1
<i>Rvachev V.L.</i>	D28, D31, D34	<i>Songfa Li</i>	A4
<i>Ryazantseva N.V.</i>	E4	<i>Soroka A.S.</i>	H19, H20
<i>Rybakov K.I.</i>	INV.J2	<i>Sova A.V.</i>	B10
<i>Ryskin V.G.</i>	F12	<i>Stephanishin Ya.I.</i>	F17
<hr/>			
	S	<i>Storozhenko I.P.</i>	A7, A8
<i>Saarinen K.P.</i>	F7	<i>Strizhachenko A.V.</i>	H15
<i>Sagaidakova N.N.</i>	L9	<i>Stulova L.V.</i>	F21, G4
		<i>Suchkov V.B.</i>	F6
		<i>Sugak V.G.</i>	F14
		<i>Sukhinin B.V.</i>	F15
		<i>Sulima T.N.</i>	L5
		<i>Suvorov E.V.</i>	INV.10, B1

<i>Suvorova O.A.</i>	K10	W
<i>Sverdlov B.A.</i>	E9	
<i>Svich V.A.</i>	H6	
<i>Syvozalizov N.A.</i>	H14	
<hr/>		
	T	
<i>Tarakanov V.V.</i>	INV.11	
<i>Tarasov Yu.V.</i>	E7	
<i>Tcymbal V.N.</i>	INV.11	
<i>Tcymbalov G.M.</i>	C10	
<i>Teperik T.V.</i>	C10	
<i>Teryokhin S.N.</i>	B22	
<i>Timchenko A.I.</i>	D20	
<i>Tishkovets V.P.</i>	D22	
<i>Titov S.V.</i>	E1	
<i>Tkachenko V.I.</i>	INV.H1, A13, D2, D3, H6, H20,	
<i>Tkachev G.B.</i>	C17	
<i>Topkov A.N.</i>	H6	
<i>Torchinov V.V.</i>	D31, D34	
<i>Tretyakov M.Yu.</i>	INV.I1	
<i>Troitskij A.V.</i>	F10	
<i>Troitsky R.V.</i>	F11	
<i>Tsakanyan I.S.</i>	H19, H20	
<i>Tsvyk A.I.</i>	B3, B4, B23	
<i>Tuchkin Y.A.</i>	D16	
<hr/>		
	U	
<i>Uliyanova I.I.</i>	H21	
<i>Unger H.-G.</i>	INV.1	
<i>Uvarov V.N.</i>	A18	
<i>Uzlenkov A.A.</i>	F28	
<i>Uzlenkov V.I.</i>	H35	
<hr/>		
	V	
<i>Vashenko E.V.</i>	F1, F3, F4	
<i>Vavriiv D.M.</i>	INV.BI	
<i>Vdovenko K.V.</i>	D23	
<i>Vekslerchik V.E.</i>	C17	
<i>Velasco Hererra V.M.</i>	F19, F20	
<i>Velichko A.V.</i>	C2	
<i>Veliev E.I.</i>	D14	
<i>Velikiy A.Yu.</i>	K9	
<i>Velychko L.G.</i>	D5	
<i>Vendik O.G.</i>	INV.7	
<i>Vertij A.A.</i>	D11	
<i>Viltchinsky A.S.</i>	F27	
<i>Voitsevya V.S.</i>	J3	
<i>Volkov V.A.</i>	INV.BI	
<i>Volokhov S.A.</i>	INV.I1	
<i>Voloshynovskiy S.</i>	F30	
<i>Volosyuk V.K.</i>	F19, F20,	
<i>Vorobiov S.N.</i>	H8'	
<i>Vorobjov G.S.</i>	B3, B4, B5	
<i>Vyazmitinova S.S.</i>	H11	
<hr/>		
	Y	
<i>Yakovenko I.V.</i>	C12	
<i>Yakovenko V.M.</i>	INV.3, C4, C12, C13	
<i>Yanenko A.F.</i>	J4	
<i>Yanovsky M.S.</i>	H24	
<i>Yaremenko Yu.G.</i>	INV.L1	
<i>Yasumoto K.</i>	H2	
<i>Yatsik V.V.</i>	D15	
<i>Yegorov Y.V.</i>	H16	
<i>Yeremka V.D.</i>	B8, B20, B21, B22	
<i>Yevdokimov A.P.</i>	H30, H31, H32	
<i>Yurchenko L.V.</i>	C5, H7	
<i>Yurchenko V.B.</i>	C5, H7	
<i>Yushchenko A.G.</i>	D3	
<hr/>		
	Z	
<i>Zagorin G.K.</i>	INV.E1, E1	
<i>Zaitsev N.M.</i>	F22	
<i>Zakalyukin A.B.</i>	D29	
<i>Zakutin V.V.</i>	B19	
<i>Zamyatin A.A.</i>	D26, D33	
<i>Zargano G.F.</i>	D23	
<i>Zelensky A.A.</i>	F7, F8, F9	
<i>Zharkova N.A.</i>	G1	
<i>Zhel'tov V.N.</i>	B23	
<i>Zinchenko I.I.</i>	INV.G1	
<i>Zolotuhina L.I.</i>	L4	
<i>Zubez M.V.</i>	L12	
<i>Zubkov A.N.</i>	F15	
<i>Zvyagintsev A.A.</i>	H15	